

National  
Oceanography  
Centre



# SEASTARex

Technical Assistance to Earth Explorer 11 SEASTAR Phase-0 campaign

Final Report

March 2024



METASENSING  
*Radar Solutions*

**Radar**metrics  
Seeing through.



Helmholtz-Zentrum  
**hereon**

**icm** Institut  
de Ciències  
del Mar



## CONTRACT DETAILS

<b>Contract Number</b>	ESA EXPRO 400017623/22/NL/IA
<b>Issuer</b>	ESA-ESTEC
<b>Contract Officer</b>	Irene Aupetit
<b>Technical Officer</b>	Tania Casal

	<b>Name</b>	<b>Affiliation</b>
<b>Author</b>	David L. McCann	NOC
<b>Contributions by</b>	Adrien C.H. Martin	NOC / NOVELTIS
	Karlus Macedo	MetaSensing BV
	Ruben Carrasco Alvarez	HZH
	Jochen Horstmann	HZH
	Louis Marié	Ifremer
	José Márquez-Martinez	Radarmetrics SL
	Marcos Portabella	ICM-CSIC
	Wenming Lin	ICM-CSIC
	Guiseppe Grieco	ICM-CSIC
	Rui Duarte	FEM
	Jean Francois Filipot	FEM
	Adriano Meta	MetaSensing BV
	Christine Gommenginger	NOC
	Petronilo Martin-Iglesias	ESA
	Tania Casal, ESA	ESA
<b>Checked by</b>	Adrien C.H. Marin	NOC / NOVELTIS
<b>Released by</b>	David L. McCann	NOC

## DOCUMENT CHANGE LOG

<b>Issue</b>	<b>Change</b>	<b>Date</b>	<b>Approved</b>
1.0	First Issue	09/02/2024	David McCann
2.0	Submitted version	18/03/2024	David McCann



## TABLE OF CONTENTS

<b>SUMMARY .....</b>	<b>4</b>
<b>1. INTRODUCTION .....</b>	<b>5</b>
<b>2. THE OSCAR INSTRUMENT .....</b>	<b>6</b>
<b>3. CAMPAIGN PLANNING .....</b>	<b>8</b>
3.1 Campaign logistics .....	9
<b>4. CAMPAIGN DATA .....</b>	<b>11</b>
4.1 Airborne data.....	11
4.2 Ground truth data .....	12
<b>5. OSCAR DATA PROCESSING .....</b>	<b>19</b>
5.1 OSCAR data calibration .....	19
5.1.1 Radiometric calibration .....	19
5.1.2 Interferometric calibration.....	21
5.2 OSCAR ocean calibration.....	22
5.3 OSCAR Level-2 processing.....	25
5.3.1 SeaSTAR simultaneous wind and current retrieval .....	25
5.3.2 PenWP wind retrieval.....	28
<b>6. LEVEL 2 RETRIEVAL OF TSCV AND OSVW .....</b>	<b>29</b>
6.1 SEASTAR Simultaneous retrieval of TSCV and OSVW .....	29
6.2 PenWP retrieval of OSVW.....	36
6.3. Circular flights .....	40
<b>7. MEDITERRANEAN CAMPAIGN .....</b>	<b>41</b>
<b>8. CONCLUSIONS AND OUTLOOK.....</b>	<b>43</b>
<b>REFERENCES .....</b>	<b>45</b>
<b>ANNEX A) ANALYSIS OF THE OSCAR POD AND ANTENNA CHARACTERIZATION .....</b>	<b>A</b>
<b>ANNEX B) DATA ACQUISITION REPORT: AIRBORNE DATA .....</b>	<b>B</b>

**ANNEX C) DATA ACQUISITION REPORT: GROUND TRUTH  
DATA ..... C**

**ANNEX D) EVALUATION OF THE SURFACE CURRENT FROM  
OBSERVATION BY STEREO-VIDEO FROM THE LIGHTHOUSE  
OF LA JUMENT ..... D**

**ANNEX E) DATA PROCESSING REPORT: IROISE SEA  
CAMPAIGN ..... E**

**ANNEX F) DATA PROCESSING REPORT: MEDITERRANEAN  
CAMPAIGN ..... F**

**ANNEX G) ANALYSIS OF EXTERNAL CALIBRATION RESULTS  
INCLUDING BASELINE ERRORS ..... G**

**ANNEX H) ALGORITHM THEORETICAL BASELINE DOCUMENT:  
OSCAR LEVEL 2 INVERSION ..... H**

**ANNEX I) MEASUREMENT ERRORS, CALIBRATION, AND SEA-  
SURFACE WIND INVERSION WITH PENWP ..... I**

**ANNEX J) DATA ACQUISITION REPORT FOR THE  
MEDITERRANEAN CAMPAIGN ..... J**

**ANNEX K) PAPER SUBMITTED TO OCEAN SCIENCE ..... K**

## SUMMARY

SEASTARex is an airborne and ground truth scientific campaign to support the SeaSTAR phase 0 candidature for ESA's Earth Explorer 11. Deploying the Ocean Surface Current Airborne Radar (OSCAR) airborne SAR instrument, this scientific campaign represents the first of a SAR instrument of its configuration and the first simultaneous retrieval of total surface current vectors (TSCV) and ocean surface vector winds (OSVW) from interferometric SAR data.

A first campaign was conducted in the Iroise Sea with a wide range of ground truth measurements deployed (HF radar, mooring, X-band marine radar, stereo camera), tasked SAR images, in addition to high-resolution and mature numerical models to simulate ocean waves and current. This campaign consists of three sites: a site over the Ouessant island characterized by strong tidal current gradients, a homogeneous site South of the island where the mooring was deployed and a third area offshore in the Bay of Biscay parallel to an ASCAT pass. The campaign acquired data over four days (17, 22, 25, 26 May 2022). Comparison between OSCAR derived Total Surface Current Vectors and ground truth measurements give correlation and RMSE of 0.08m/s and 8.5° in velocity and direction respectively. These first results have been added to the EE11 SeaSTAR Report for Assessment (ESA, 2023) and a paper was submitted (McCann *et al.*, 2023).

Based on this success and on the unique opportunity to fly simultaneously with NASA/CNES SWOT (Surface Water and Ocean Topography) satellite mission during its daily CalVal repeat phase and a wide range of in situ measurements (e.g. BioSWOT-Med) all relevant to OSCAR and SeaSTAR, a second OSCAR airborne campaign was then planned. This campaign was executed in May 2023 and consisted of three acquisition days (5, 7, 8 May 2023) with a rose pattern centered over the left SWOT sub-swath at (41.09°N, 4.29°W) generating a disk of about 40km diameter. Acquired data during this Med Sea campaign are not analyzed in the frame of this project, but the analysis was supported through a CNES contract and preliminary results are integrated in the EE11 SeaSTAR Assessment Report (ESA, 2023)

# 1. INTRODUCTION

SeaSTAR is a satellite mission concept previously submitted to ESA's Earth Explorer 11 (EE11) programme, dedicated to observing fast-evolving small-scale ocean surface dynamics in all coastal seas, shelf seas and marginal ice zones (ESA, 2023). Its science goals are:

- 1) *To understand the role of fast-evolving small-scale ocean dynamics in mediating exchanges between land, the cryosphere, the atmosphere, the marine biosphere and the deep ocean;*
- 2) *To determine the ocean circulation and dominant transport pathways in the global coastal, shelf and marginal ice zones;*
- 3) *To improve understanding of coastal, shelf and marginal ice zones contributions to the global climate system.*

SeaSTAR proposes to observe these fast-evolving small-scale ocean dynamics with daily revisits and 1 km resolution to study exchanges of heat, carbon and nutrients at boundaries between land, the cryosphere, the atmosphere and the deep ocean. SeaSTAR would measure two-dimensional fields of Total Surface Current Vectors (TSCV), Ocean Surface Vector Winds (OSVW) and Directional Ocean Wave Spectra (DOWS). With its highly innovative technology on a single independent satellite, SeaSTAR is the first mission to offer the ability to characterise fast-evolving processes on daily to multi-annual scales over all coastal and shelf seas and Marginal Ice Zones.

SeaSTAR is based on the concept of along-track interferometric (ATI) synthetic aperture radar (SAR), which measures the Doppler properties of the scattered signal from the sea surface using complex SAR imagery obtained in pairs with a short time lag between. The measured Doppler phase images (interferograms) are related to the ocean total surface motion, which contains contributions from the surface current velocity, wave orbital motion and the microwave scatterer's phase velocity. The present developments in ATI-SAR build on the work done in the Wavemill proof of concept for SeaSTAR (Martin *et al.*, 2016; Martin and Gommenginger, 2017, Martin *et al.*, 2018).

Built and operated by Metasensing BV in Italy and the Netherlands, the Ocean Surface Current Airborne Radar (OSCAR) demonstrator is a unique, 3-look, Ku-band (13.5 GHz) airborne ATI-SAR system capable of making fine-scale measurements of ocean surface motion over a wide swath in a single pass. OSCAR was developed within the framework of an ESA funded project to demonstrate the capability of the SeaSTAR mission concept and ATI-SAR to simultaneously observe total surface current vectors (TSCV) and ocean surface vector winds (OSVW) in two dimensions, at high accuracy, from an airborne platform (Trampuz *et al.*, 2018).

The SEASTARex project is an ESA-funded demonstration and validation campaign to further the scientific readiness level of the SeaSTAR mission concept and act as the first scientific campaign of the OSCAR instrument and 3-look ATI-SAR capability. Involving airborne SAR acquisitions, in situ observations, ground-based remote sensing, numerical modelling and earth observation, SEASTARex drew together expertise from nine international scientific institutions and specialists in the field of oceanography, airborne and ground-based remote sensing, engineering and earth observation sciences.

This report details the work carried out in the SEASTARex project, the main results of the campaign and its contribution to the SeaSTAR EE11 candidature and 3-look ATI-SAR oceanographic remote sensing. This report also collates together the reports submitted to ESA (Annexes A to K) as part of the contract.

## 2. THE OSCAR INSTRUMENT

The Ocean Surface Currents Airborne Radar demonstrator (OSCAR) is a gimbal-based interferometric Ku-band SAR system developed and built by MetaSensing BV within the framework of a European Space Agency funded project and designed to demonstrate squinted ATI with three independent azimuths – two squinted at 45° to the aircraft centerline and one at 90° broadside (Meta *et al.*, 2015; Trampuz *et al.*, 2018; Gebert *et al.*, 2018; Martin *et al.*, 2019). This three-look configuration is unique amongst SAR instruments and was designed specifically for the simultaneous retrieval of TSCV and OSVW. The OSCAR instrument and gimbal are mounted within a radome and flown on a Piper PA-31 airframe. Figure 1 shows the airframe and radome as well the internal mounting of the instrument and the position of the instrument equipment within the cabin of the aircraft. Table 1 shows the general settings and configurations for the instrument during the campaign.

The radome pod and its effect on the instrument data were assessed as part of the HERZ campaign. A full analysis of the radome can be seen in ANNEX A) Analysis of the OSCAR POD and Antenna Characterization.

Table 1: Aircraft and radar settings common to all the acquisitions (land and sea)

Parameter	Value
Aircraft	LN-PNB Piper PA-31-310 Navajo
Height	3000m amsl (FL095 acceptable)
Ground speed (goal, wind dependent)	150 kt (75 m/s, 270 km/h)
Central Frequency	Ku-band
Polarization	V in all beams (squinted and 0-Doppler)
System preset	3-view V
RF peak TX power	50 dBm
IF attenuation	5 dB
PRF	8 kHz
Duty cycle	25%
ATI baseline	17 cm

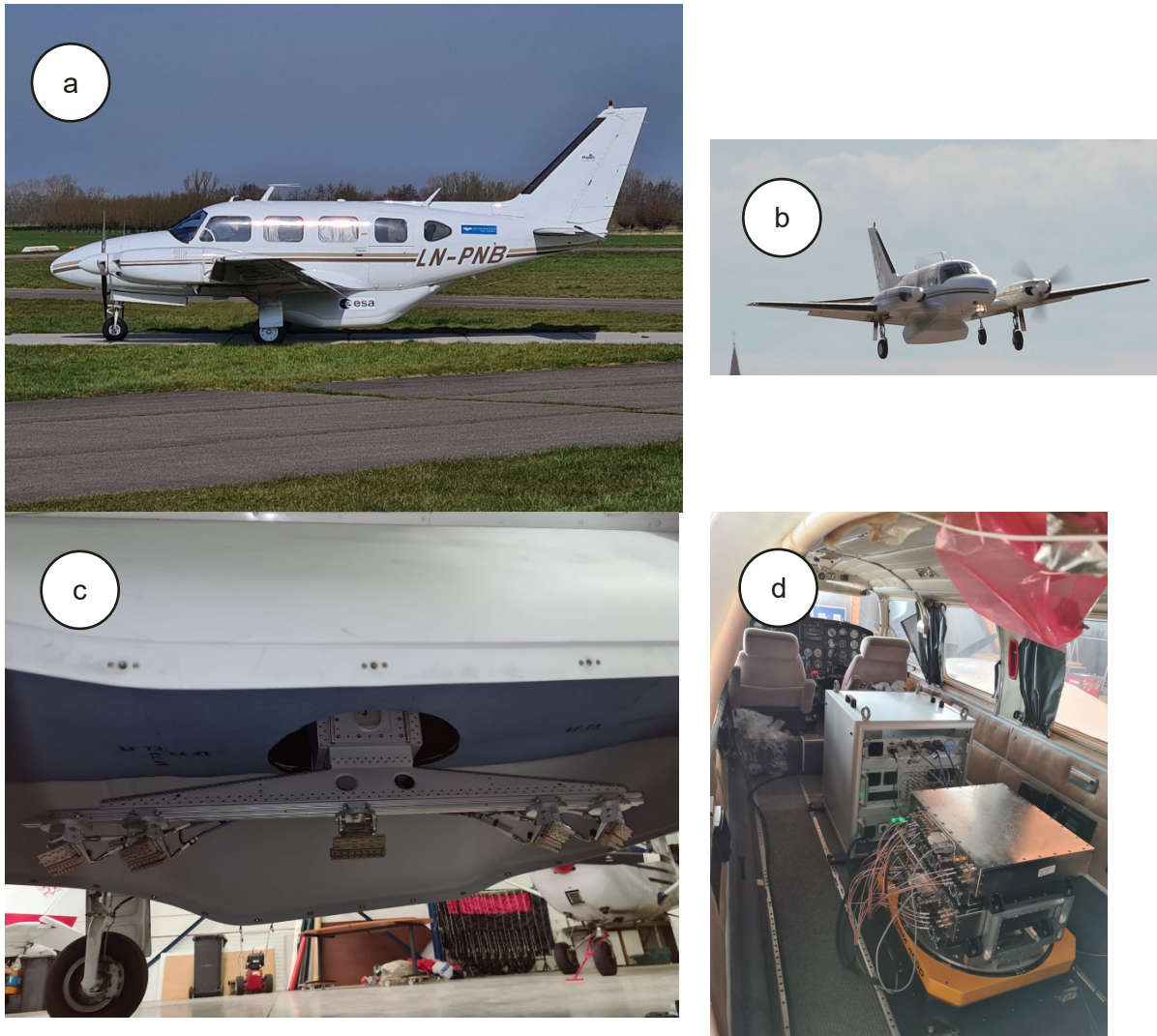


Figure 1. The Piper PA-31 aircraft with OSCAR radome attached (a, b), the OSCAR instrument mounted within the radome (c) and the instrument gimbal, transceivers and recording equipment installed within the cabin of the aircraft (d)

### 3. CAMPAIGN PLANNING

The SEASTARex activity represented the first opportunity to perform a scientific flight campaign with validation against independent ground-truth. The main overall objective of SEASTARex is to acquire experimental airborne data to demonstrate the capability of the OSCAR three-look configuration to measure 2D fields of TSCV and OSVW from Doppler and NRCS data, ideally without the use of auxiliary environmental information. The airborne data and validation results serve to consolidate the calibration and retrieval framework and to contribute to increasing the scientific readiness level of the EE11 SEASTAR candidate (ESA, 2023).

The specific objectives of this campaign are to acquire:

- *Simultaneous acquisitions of OSCAR airborne data and ground truth data during a dedicated campaign over an instrumented and well-characterised ocean site;*
- *Gimbal stabilised and calibrated OSCAR data in NRCS and Doppler (phase and frequency)*

The campaign is separated into four parts:

- *Calibration flight over land (corner reflectors)*
- *Iroise Sea Trefle site with a star flight pattern over homogeneous area: this serves primarily to assess the retrieved TSCV and OSVW over a site well instrumented with ground-truth validation data (HF radar + Trefle mooring) characterised by uniform bathymetry and environmental conditions (current, waves, wind). The Trefle site corresponds to the red circle in Figure 2*
- *Iroise Sea La Jument site with flights over fast-varying currents near La Jument lighthouse: this serves primarily to assess the ability of the OSCAR instrument to image and retrieve credible gradients of TSCV in a very coastal and highly dynamic environment. The site offers ground-truth validation data (X-band marine radar, Stereo-Video and coarse resolution HF radar). The La Jument site corresponds to the red triangle in Figure 2.*
- *Offshore flight: this serves primarily to further calibrate NRCS against spaceborne scatterometer data and assess retrieved OSVW against scatterometers.*



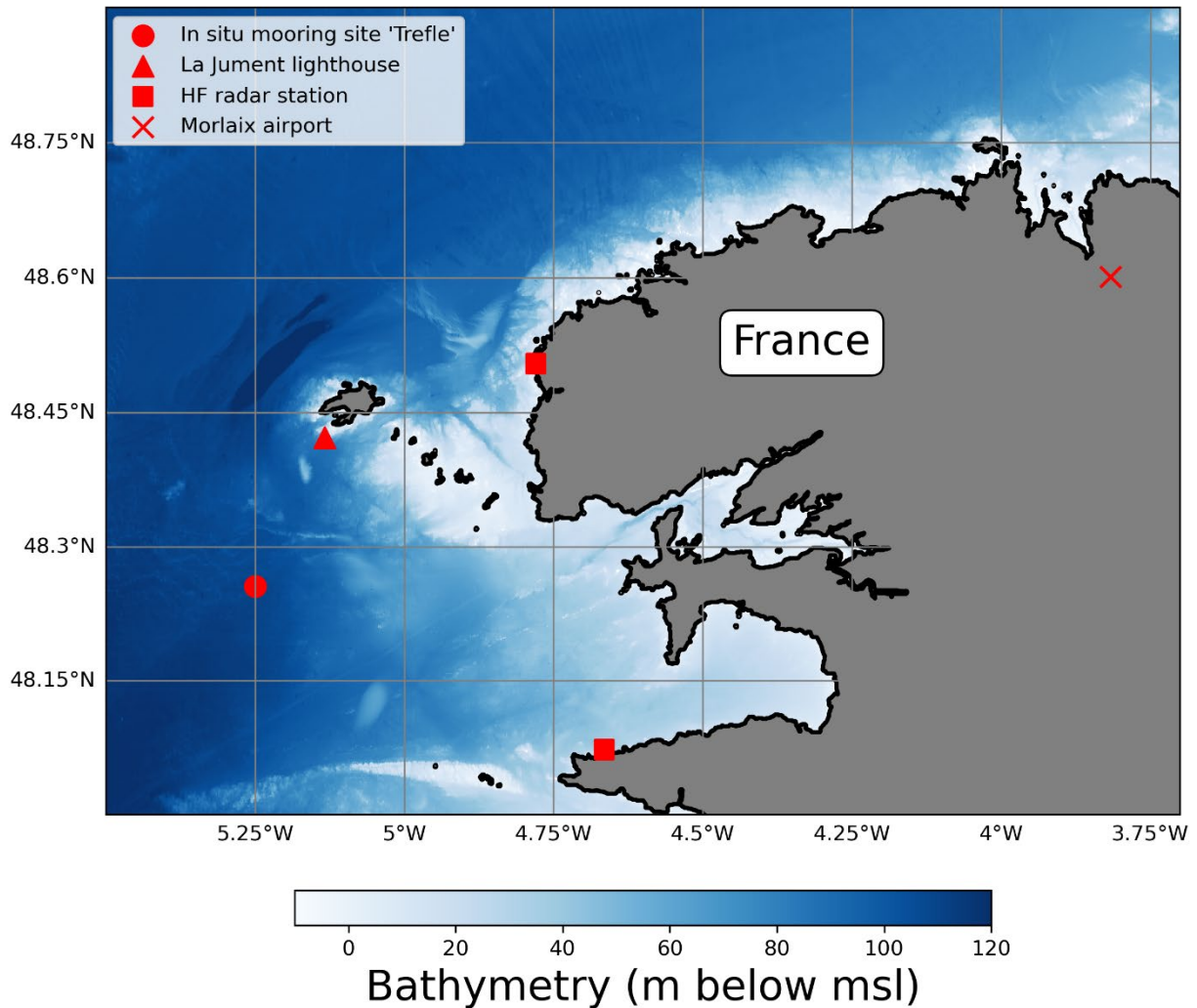


Figure 2. Map of the study area showing the position of the Trefle mooring (red circle), La Jument lighthouse (red triangle), HF radar stations (red squares) and the base of airborne operations at Morlaix airport (red cross). Bathymetry from EMODnet.

### 3.1 CAMPAIGN LOGISTICS

The flight campaign is tailored to meet the project objectives. The objectives of the SEASTARex project are to fly a three-look along-track interferometric SAR instrument (two squinted beams and one broadside beam) to demonstrate the principles and performance of the SeaStar concept using airborne data, and to consolidate the calibration and retrieval framework, to contribute to increasing the scientific readiness level of the EE11 SeaStar candidate.

The key objective of the SEASTARex flight campaign is to acquire airborne data with the OSCAR system which could be later processed to determine TSCV and OSVW performance against independent ground-truth. The processed data are compared to ground monitored data, particularly over the ground truth site, to verify the SeaStar concept.



To achieve these objectives the SEASTARex flight campaign flew over three main sites defined above (Trefle, Jument and Offshore). The aircraft was based at Morlaix airport, some 60kms east of Brest. The geographical coordinates of the three sites are given in Table 2 (Illustrated in Figure 2).

Table 2: Geographical coordinates of the SEASTARex campaign sites.

Site	Latitude	Longitude
Morlaix airport	48°36' N	3°49' W
Trefle mooring	48°15'	5°15' W
La Jument lighthouse	48.422830°	-5.133794°
Offshore area	44°– 48° N	7°18'– 4°55' W

OSCAR data are acquired over the study area following different track plans for the Iroise sea and offshore flights (Figure 3). Originally two repeat flights were planned for the Iroise Sea and one flight offshore. The Iroise Sea flights (Figure 3, a) consist of over-island acquisitions covering the dynamic tidal race of Ouessant around La Jument lighthouse and tracks in a so called 'star pattern' over the homogenous area and Trefle mooring (Figure 4). Additional, experimental circular acquisitions are performed around the Trefle site.

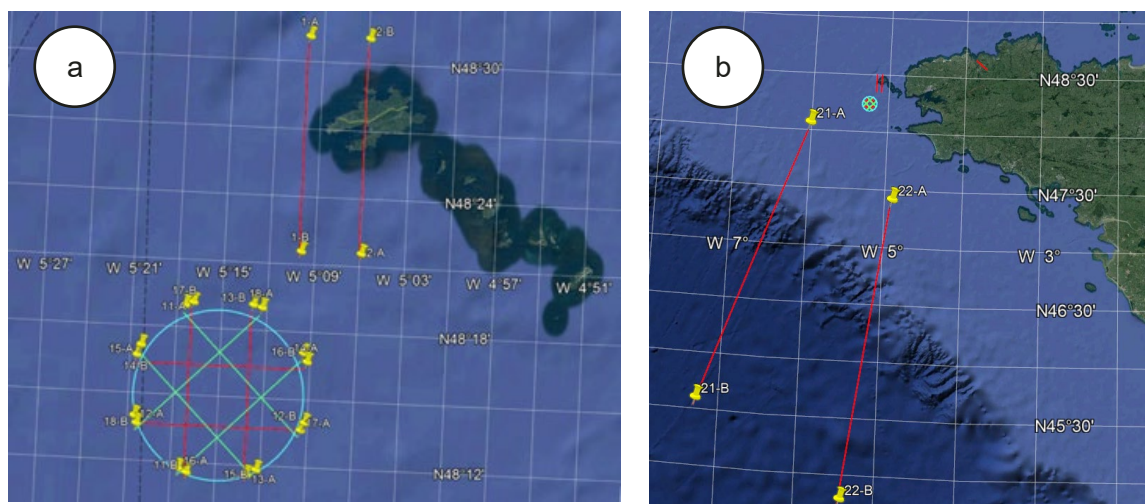


Figure 3. Planned flight tracks for the La Jument (over-island) and Trefle (a) and off-shore flights (b).

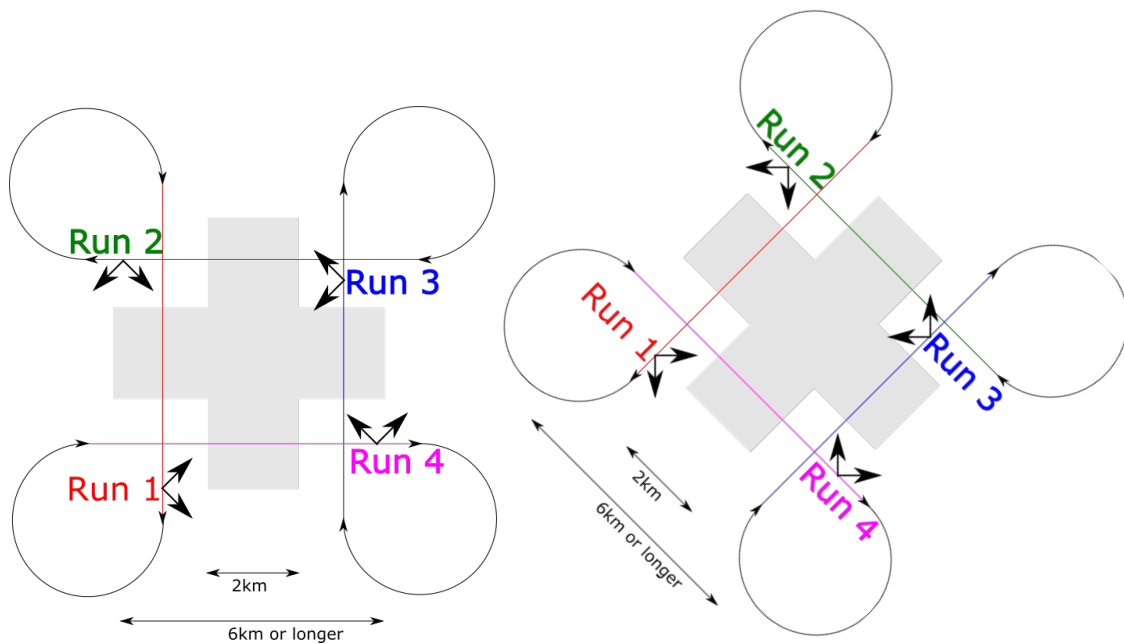


Figure 4. Design of flight tracks in the 'star pattern'. Successive acquisitions are made forming a cross over a common centre (left), with the tracks then rotated 45° to complete the pattern (right). The result is a data set with an equally distributed range of look azimuths centred over the Trefle in situ mooring.

## 4. CAMPAIGN DATA

### 4.1 AIRBORNE DATA

Four flights of the OSCAR system were conducted over the study area between the 17<sup>th</sup> and 26<sup>th</sup> May 2022 (Figure 5). On the 17<sup>th</sup> May (Figure 5, a) the first Iroise Sea flights was aborted during the 'star pattern' due to weather conditions preventing the aircraft to fly over this area. For meteorological and logistics reasons the next Iroise Sea flight occurred on the 22<sup>nd</sup> and 26<sup>th</sup> (Figure 5 b, d). Additional circular acquisitions around the Trefle site were made on the 22<sup>nd</sup> and 26<sup>th</sup> May (Figure 5 b, d). The circular data were not SAR focused, being processed only in a range compressed mode for assessing the variation of NRCS as function of the azimuth to the North in order to assess the wind direction. Back from the 25<sup>th</sup>, due to the weather, the aircraft was unable to land in Morlaix where the aircraft could sleep in a hangar, and sleep outside during the night in Brest airport. On the 26<sup>th</sup>, there was some water in the radome affecting NRCS which was undetected before the flight. The open ocean flight on the 25<sup>th</sup> (Figure 5 c) was completed as 5 separate, contiguous tracks due to a limit on data capture length. Data for the Aft beam were unusable due to acquisition issues.

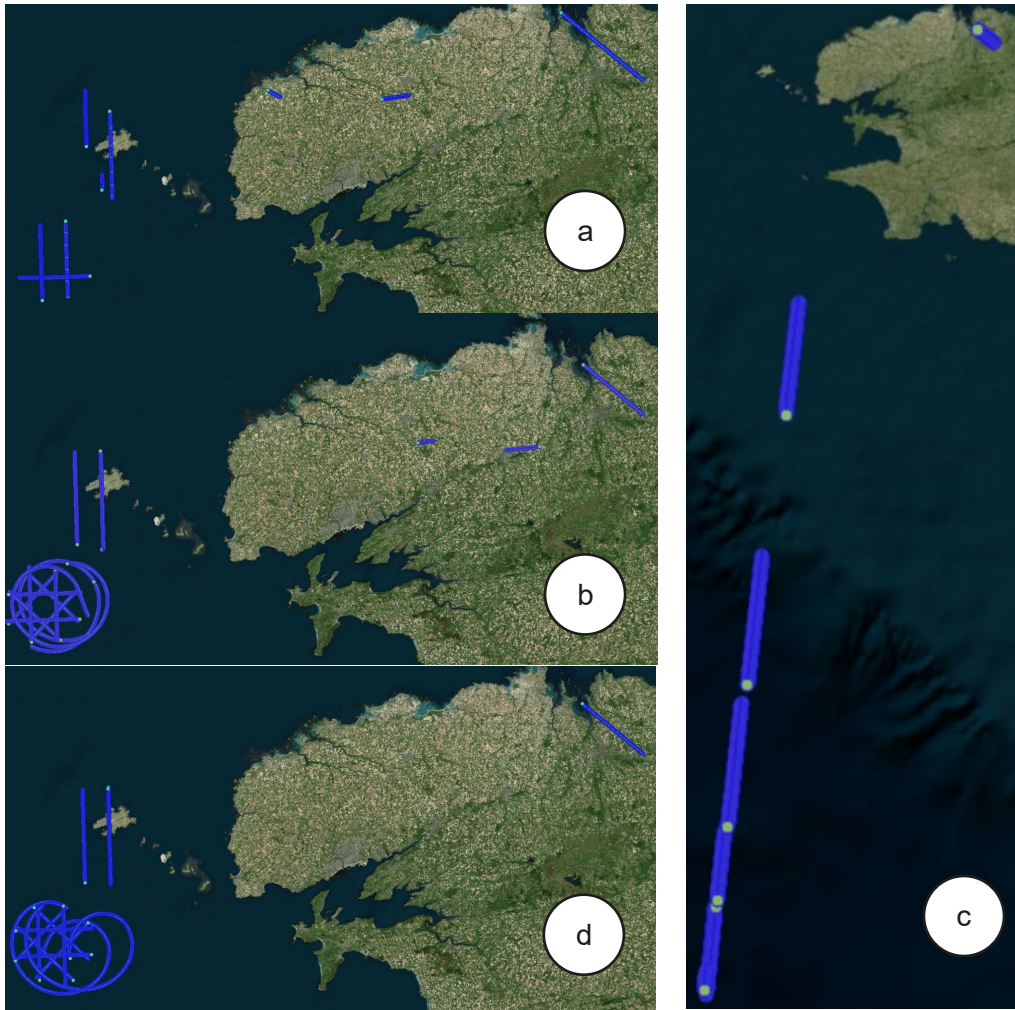


Figure 5. OSCAR flight tracks during the campaign on the 17<sup>th</sup> (a), 22<sup>nd</sup> (b), 25<sup>th</sup> (c) and 26<sup>th</sup> (d) May 2022. Three repeats of the Iroise Sea tracks were performed due to an aborted Trefle site star pattern run on the 17<sup>th</sup>. One open ocean flight was performed on the 25<sup>th</sup> (c)

OSCAR data were recorded and processed by MetaSensing BV. A description of the data and its processing chain can be seen in Section 5. For a full account of the OSCAR airborne SAR data acquired during the campaign, see ANNEX B) Data acquisition report: Airborne data

## 4.2 GROUND TRUTH DATA

An extensive range of ground truth observations were planned and performed as part of the campaign, from in-situ measurements, remote-sensing data, numerical models and earth observation. A full account of the ground truth campaign can be seen in Annex C) Data acquisition report: ground truth data.

As part of the in situ campaign a deployment of the Flux Air-Mer par Eddy correlation (FLAME) buoy was planned for the in situ measurement of OSVW at the Trefle site. Unfortunately, during the deployment operation the buoy capsized. This caused a water ingress which was not noticed at the time and caused a datalogger failure shortly after. During the recovery operation, a shock on the ship

hull caused the destruction of the IRGASon sensor head. This unfortunately leads to a lack of in situ wind data for the campaign, leaving only forecast model data (AROME) for validation.

An experimental deployment of a stereo-video system using zoom lenses were achieved from La Jument Lighthouse for the retrieval of surface current and wave information. The system was calibrated using state-of-the-art methods, and a 30-minute long acquisition collocated with the airborne OSCAR measurements was investigated. Unfortunately, a sensibility analysis showed that the state-of-the-art methods used for the calibration of the stereo-video system are not accurate enough to provide trustworthy sea surface elevation maps. As a result, a reliable estimation of the sea surface current from the stereo video derived 3D wave spectra was not possible. A full account of this work can be seen in ANNEX D) Evaluation of the surface current from observation by Stereo-Video from the lighthouse of La Jument.

Summaries of the ground truth and airborne data captured during the four days of the campaign can be seen in Table 3 to Table 6. Numerous intersecting issues resulted in some ground truth data only being available for certain flight days and issues with the OSCAR system and flight restrictions resulting in some areas receiving better coverage than others.

*A summary of the numerical model data acquired as part of the campaign can be seen in*

Table 7.

Various satellite data were acquired during the primary campaign in the Iroise Sea and the secondary campaign in the Mediterranean Sea. Tables ??? to ??? show dates and times for the SAR and optical satellite data acquired during the Iroise Sea campaign. A full list of SAR and optical satellite data acquired during the Mediterranean campaign can be found in the final report for the CNES funded 'OSCAR-SWOT' project, which can be found at <https://www.noveltis.fr/oscar-swot-final-report/>. For access to these data, please contact David McCann (david.mccann at noc.ac.uk) or Adrien Martin (admartin at noc.ac.uk; adrien.martin at noveltis.fr)

Table 3. Summary of ground truth data acquisition for the 17<sup>th</sup> May 2022.

Instrument	Summary
OSCAR	La Jument tracks <b>OK</b> Trefle tracks <b>incomplete due to poor weather</b>
“TREFLE” buoy	Directional sea state data <b>OK</b> Current data <b>OK</b>
“Pierres Noires” buoy	Directional sea state data <b>OK</b>
“Brittany” buoy	Directional sea state data <b>OK</b>
HF radar sites	Brezellec site (south) <b>OK</b> Garchine site (north) <b>data gaps, low coverage</b>
“La Jument” stéréo-vidéo	Video measurements from 8:30 to 14:00 <b>OK</b> Some gaps due to bad visibility.
“La Jument” X-band radar	Current data <b>OK</b>

Table 4. Summary of ground truth data acquisition for the 22<sup>nd</sup> May 2022.

Instrument	Summary
OSCAR	La Jument tracks <b>OK</b> Trefle tracks <b>OK</b>
“TREFLE” buoy	Directional sea state data <b>OK</b> Current data <b>OK</b>
“Pierres Noires” buoy	Directional sea state data <b>OK</b>
“Brittany” buoy	Directional sea state data <b>OK</b>
HF radar sites	Brezellec site (south) <b>OK</b> Garchine site (north) <b>OK</b>
“La Jument” stéréo-vidéo	Power outage in the lighthouse <b>no data</b>
“La Jument” X-band radar	Power outage in the lighthouse <b>no data</b>

Table 5. Summary of ground truth acquisition for the 25<sup>th</sup> May 2022.

Instrument	Summary
OSCAR	Open ocean tracks <b>complete but one channel faulty</b>
“TREFLE” buoy	Directional sea state data <b>OK</b> <b>No current data</b>
“Pierres Noires” buoy	Directional sea state data <b>OK</b>
“Brittany” buoy	Directional sea state data <b>OK</b>
HF radar sites	Brezellec site (south) <b>OK</b> Garchine site (north) <b>no data</b>
“La Jument” stéréo-vidéo	Power outage in the lighthouse <b>no data</b>
“La Jument” X-band radar	Power outage in the lighthouse <b>no data</b>

Table 6. Summary of ground truth acquisition for the 26<sup>th</sup> May 2022.

Instrument	Summary
OSCAR	La Jument and Trefle tracks <b>complete but water in radome</b>
“TREFLE” buoy	Directional sea state data <b>OK</b> <b>No current data</b>
“Pierres Noires” buoy	Directional sea state data <b>OK</b>
“Brittany” buoy	Directional sea state data <b>OK</b>
HF radar sites	Brezellec site (south) <b>OK</b> Garchine site (north) <b>OK</b>
“La Jument” stéréo-vidéo	Power outage in the lighthouse <b>no data</b>
“La Jument” X-band radar	Power outage in the lighthouse <b>no data</b>



Table 7. Summary of numerical model data collated as part of the campaign

Data	Summary
MARS 2D	Depth-averaged current vectors, 15 minute intervals 17 <sup>th</sup> May, 06:00–09:45 UTC 22 <sup>nd</sup> May, 05:00–07:45 UTC 26 <sup>th</sup> May, 16:00–18:45 UTC Grid resolution 250m
MARS 3D	3D current vectors, hourly 17 <sup>th</sup> May, 06:00–09:00 UTC 22 <sup>nd</sup> May, 05:00–07:00 UTC 25 <sup>th</sup> May, 08:00–12:00 UTC 26 <sup>th</sup> May, 16:00–18:00 UTC Grid resolution 2500m, 40 sigma layers
Wave Watch 3	Wave spectral forecast, hourly 17 <sup>th</sup> May, 07:00–09:00 UTC 22 <sup>nd</sup> May, 05:00–07:00 UTC 25 <sup>th</sup> May, 08:00–12:00 UTC 26 <sup>th</sup> May, 16:00–1800 UTC
AROME	Wind forecast (u10), hourly 17 <sup>th</sup> May, 07:00–09:00 UTC 22 <sup>nd</sup> May, 05:00–07:00 UTC 25 <sup>th</sup> May, 08:00–12:00 UTC 26 <sup>th</sup> May, 16:00–18:00 UTC Grid resolution 1/4°

Table 8. Satellite SAR acquisitions acquired during the Iroise Sea campaign

Date 2022	Data
16/05	NovaSAR (23:37 UTC)
17/05	NovaSAR (10:30UTC, 23:43UTC) Capella (14:47UTC)
18/05	Radarsat-2 (06:21UTC) ICEYE (15:16UTC)
19/05	TerraSAR-X (06:35UTC) Sentinel 1 (06:24UTC)
20/05	ICEYE (14:49UTC) Sentinel 1 (18:13UTC);
21/05	Radarsat-2 (06:33UTC)
22/05	ICEYE (14:48UTC) TerraSAR-X (18:00UTC);
23/05	ICEYE (10:29UTC)
24/05	TerraSAR-X (06:45UTC)
25/05	ICEYE (10:06UTC)
27/05	TerraSAR-X (18:10UTC) Sentinel 1 (18:05UTC)
28/05	NovaSAR (10:48UTC)
29/05	Capella (21:04UTC)
31/05	Capella (01:43UTC)
01/06	Capella (21:36UTC)
17/06	Capella (10:03UTC)
21/06	Capella (10:12UTC)
08/07	Capella (10:16UTC)



Table 9. Optical satellite data acquired during the Iroise Sea campaign

Date 2022	Data	Cloud conditions
17/05	Sentinel 2B (11:21UTC) Sentinel 3A (21:56UTC) Sentinel 3B (21:17UTC) MODIS/Aqua (03:04UTC), VIIRS/SNPP (03:06UTC) VIIRS/N20 (02:17UTC)	Cloudy
18/05	MODIS/Aqua (02:09UTC) VIIRS/SNPP (02:47UTC) VIIRS/N20 (01:58UTC)	Cloudy
19/05	Sentinel 2A (11:21UTC) VIIRS/N20 (13:06UTC)	Mixed
20/05	Sentinel 3A (10:55 UTC) Sentinel 3B (10:16 UTC) MODIS/Aqua (13:05 UTC) VIIRS/SNPP (11:56, 13:36 UTC) VIIRS/N20 (12:47, 14:28 UTC)	Clear sky
21/05	Sentinel 3A (10:29UTC) MODIS/Aqua (02:39, 13:48UTC) VIIRS/SNPP (01:51, 11:37, 13:17UTC) VIIRS/N20 (02:42, 12:28, 14:09UTC)	Clear sky
24/05	Sentinel 3A (10:52UTC) Sentinel 2B (11:21UTC) MODIS/Aqua (12:40UTC) VIIRS/SNPP (12:21, 14:01UTC)	Mixed
26/05	MODIS/Aqua (14:06UTC) VIIRS/SNPP (13:23UTC)	Front, Mixed
27/05	Sentinel 3B (21:58UTC)	Cloudy

## 5. OSCAR DATA PROCESSING

OSCAR SAR data is processed through discrete steps, or data levels, corresponding to the flow chart in Figure 6. L0 to L1p processing are performed by MetaSensing and Radarmetrics. L1p pre-processing MATLAB scripts (for incidence angle and beam squint) are provided by MetaSensing. L1p to L2 processing was performed using the SeaSTAR software package in python (Martin et al, 2023).

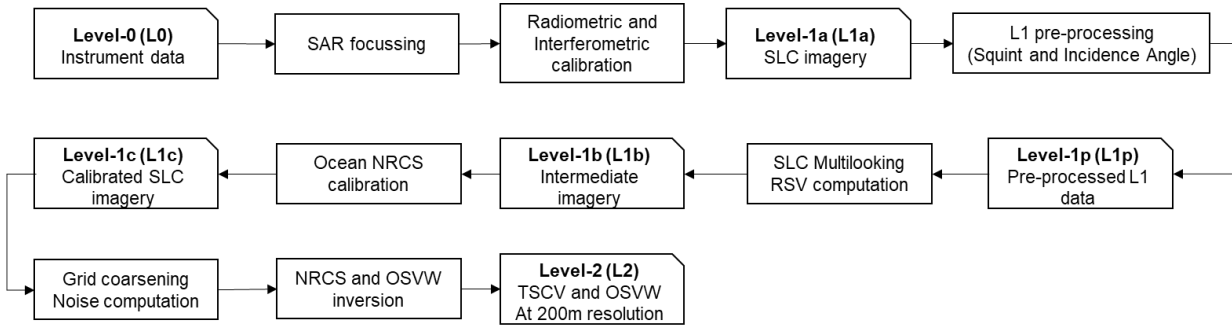


Figure 6. General data processing flow for OSCAR campaign data

The L0 to L1p data processing chain was performed for the Iroise Sea campaign as per the specification detailed in ANNEX E) Data Processing Report: Iroise Sea Campaign. For the Mediterranean Sea campaign, the data processing chain benefitted from lessons learned in the processing of the Iroise Sea dataset, while adjusting for different challenges that were faced. The Mediterranean Campaign data processing report can be seen in ANNEX F) Data Processing Report: Mediterranean Campaign

### 5.1 OSCAR DATA CALIBRATION

Calibration activities are an integral part of the OSCAR flights, with dedicated over-land acquisitions and data captured with corner reflectors at Morlaix airport. Primary radiometric and interferometric calibration was performed by MetaSensing BV and Radarmetrics SL, with further data-based ‘ocean calibration’ performed by NOC and ICM-CSIC. A full account of the primary calibration exercise performed by MetaSensing and Radarmetrics can be seen in Annex G) Analysis of External Calibration Results Including Baseline Errors

#### 5.1.1 Radiometric calibration

Primary radiometric calibration is performed using OSCAR data obtained with corner reflectors of a known radar cross section placed around Morlaix airport and modelling of the instrument’s antenna pattern with additional internal calibration performed by the OSCAR system. Figure 7 shows an example of the corner reflectors used in the primary radiometric calibration, placed within the apron of Morlaix airport. Figure 8 shows an example of high-resolution SAR imagery clearly containing two

corner reflectors on the 25<sup>th</sup> May and the impulse response functions associated with these two targets.



Figure 7. Example of a tri-corner radar reflector ('corner reflector') placed in Morlaix airport for radiometric calibration of OSCAR SAR imagery.

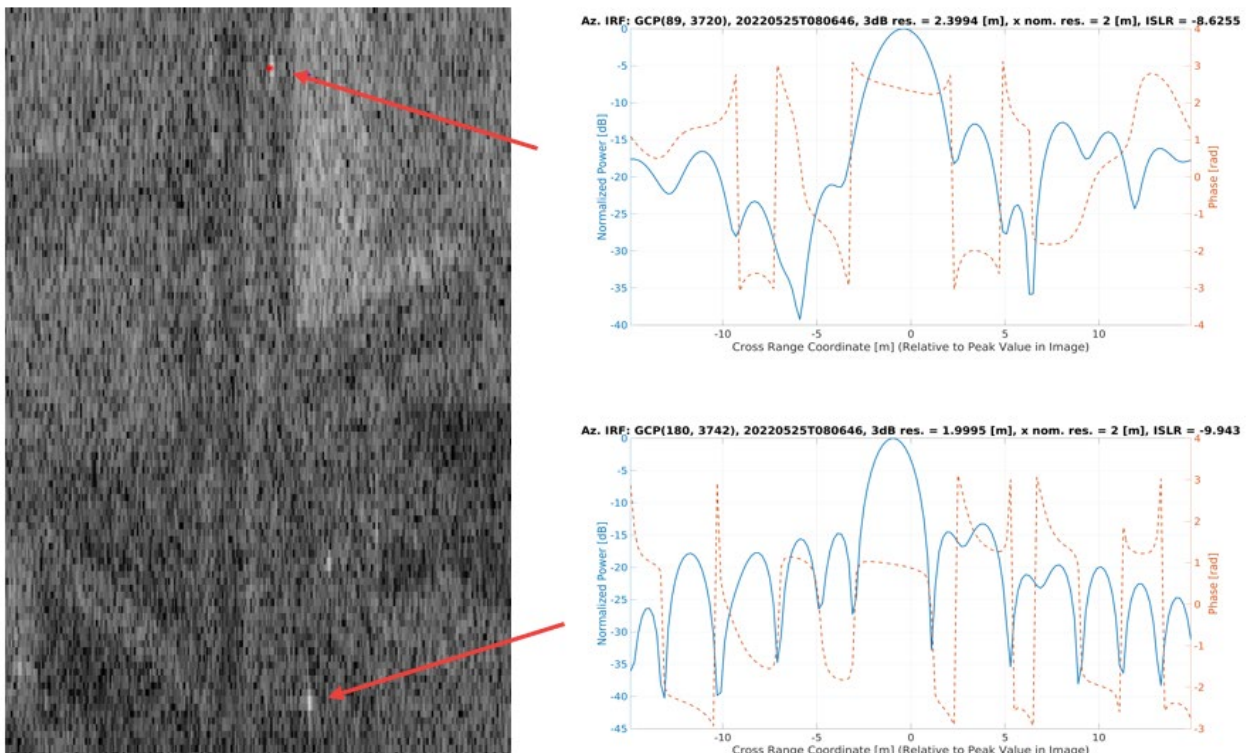


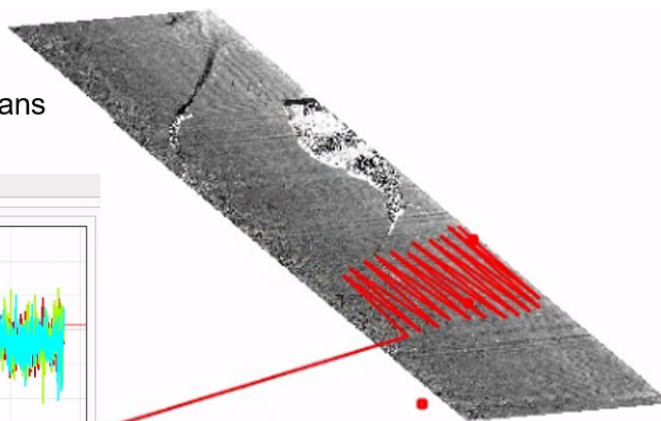
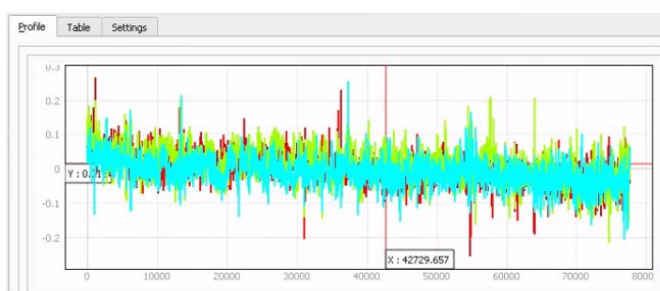
Figure 8. Example impulse response function (IRF) curves from the 25<sup>th</sup> May (right panels) generated from 2m azimuth resolution SAR images (left panel) containing corner reflectors placed at Morlaix airport (highlighted by red arrows).

A full account of the calibration procedure can be seen in Annex G) Analysis of External Calibration Results Including Baseline Errors

### 5.1.2 Interferometric calibration

Primary interferometric calibration is performed using an analysis of over-land data to ascertain ATI baseline errors. A trend in interferometric phase was identified as an unknown across-track ATI baseline error due to uncertainty in the system’s nominal lever arm measurement. The horizontal and vertical lever arm calibrations were found to be 0.1mm x -0.9 mm for the aft channel and 0.4mm x -0.4mm for the fore channel, respectively (Figure 9).

20220517T101737 (channel 33)  
Before lever-arm calibration  
Scaled from -0.2 (back) to 0.2 (white) radians



20220517T101737 (channel 33)  
After lever-arm calibration  
Scaled from -0.2 (back) to 0.2 (white) radians

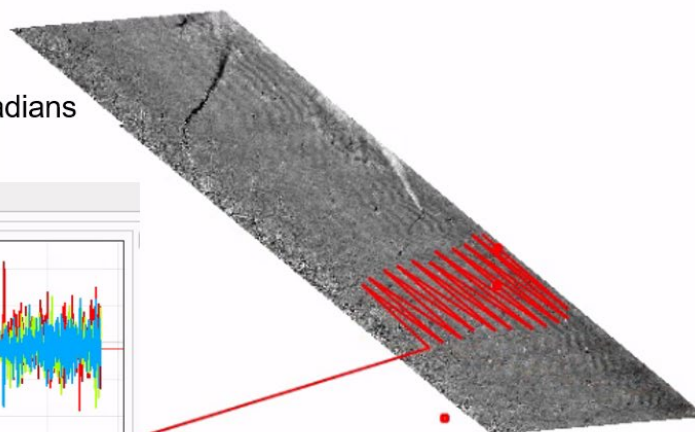
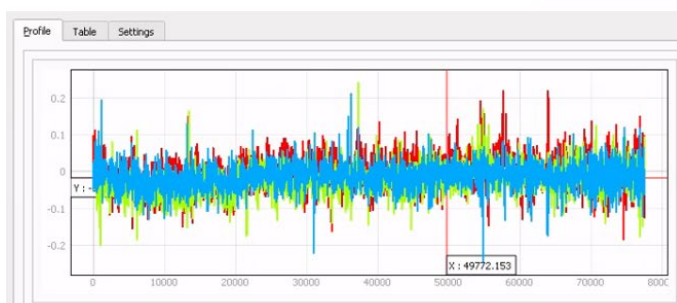


Figure 9. Example of the lever arm calibration to minimize interferometric baseline errors over land (where the phase is assumed to be ~0)

A full account can be seen in Annex G) Analysis of External Calibration Results Including Baseline Errors.



## 5.2 OSCAR OCEAN CALIBRATION

A secondary, data-based validation is performed using the ‘star pattern’ OSCAR data acquired on the 22<sup>nd</sup> May over the Trefle open ocean site. This method relies on the assumption of geophysical spatial and temporal homogeneity over the site (confirmed using ADCP buoy data) and a comparison of OSCAR-derived normalized radar cross section (NRCS) with the NSCAT-4DS model (Wang *et al.*, 2017). To perform the ocean calibration, L1b data from the ‘star pattern’ tracks over the Trefle site on the 22<sup>nd</sup> May are collapsed into Incidence angle – Azimuth space, and second harmonic sinusoidal functions are fitted through the data points. With each track in the star pattern rotated by 45° and the antenna squint being the same, this method allows direct comparison between different beams for a given look direction relative to the wind. Figure 10 shows the output of this analysis, with L1b curves of  $\sigma^0$  plot against the prediction from NSCAT-4DS for all three OSCAR beams.

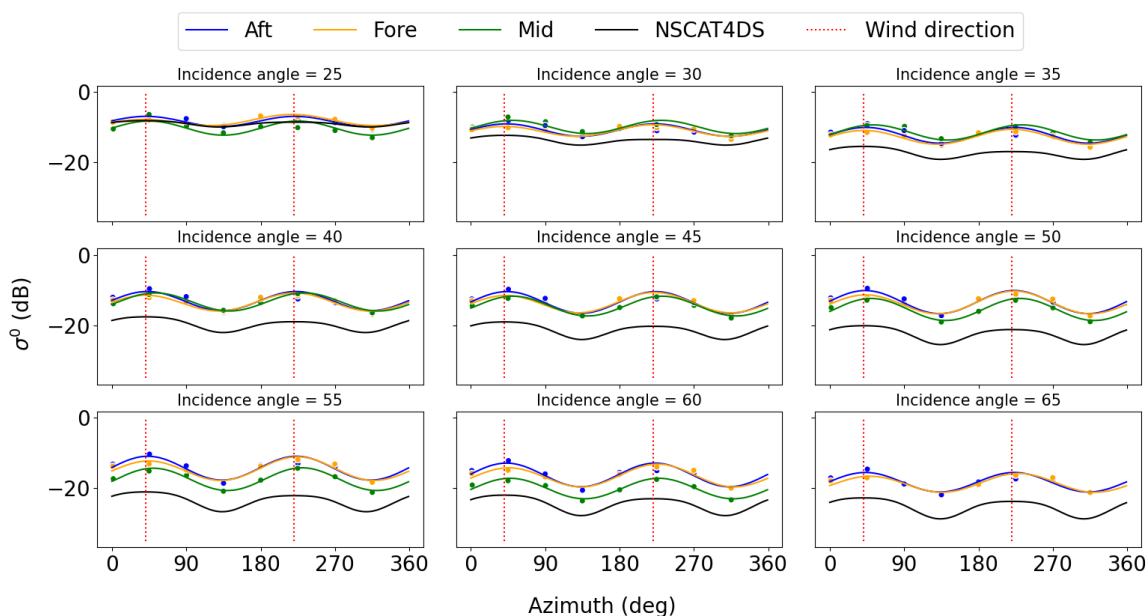


Figure 10. L1a Data (dots) and fitted curves (solid line)  $\sigma^0$  from the aft (blue), fore (orange) and mid (green) beams for the star pattern over the Trefle site on the 22<sup>nd</sup> May, as function of incidence angle (sub-panels with incidence angle in the title) and azimuth. The expected  $\sigma^0$  from NSCAT-4DS using AROME wind input (5.75 m/s, 42°, black line) and the upwind/downwind direction (dashed red).

There is a clear offset between the expected  $\sigma^0$  and OSCAR data, broadly increasing with incidence angle. Figure 11 shows the azimuthal-averaged bias between each OSCAR beam and NSCAT-4DS with respect to incidence angle. The L1b data are calibrated using this ocean calibration method to generate L1c.

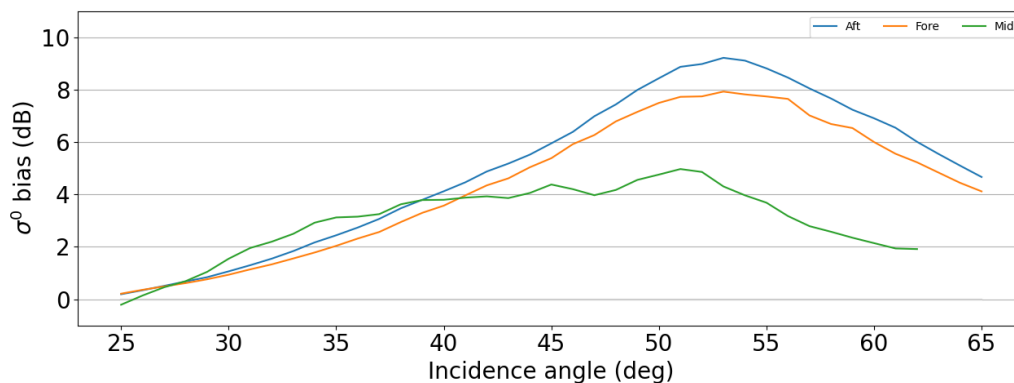


Figure 11. Azimuth-averaged difference between OSCAR and NSCAT-4DS using AROME wind data as input, resulting in ocean calibration curves for the aft (blue), fore (orange) and mid (green) beams.

An alternative set of ocean calibrations for  $\sigma^0$  is performed using a numerical approach and an alternative approach involving PenWP wind retrieval and give similar results. The alternative approach accounts for wind variability between track legs and utilizes the PenWP wind retrieval algorithm (Figure 13). The method uses wind input as an initial condition, in this case using wind data from ECMWF. Figure 12 shows the result of this process, with NRCS calibration curves that are similar to those in Figure 11, albeit with greater magnitude, most likely due to the difference in wind data used to compute the curves in the simplified method (AROME rather than PenWP).

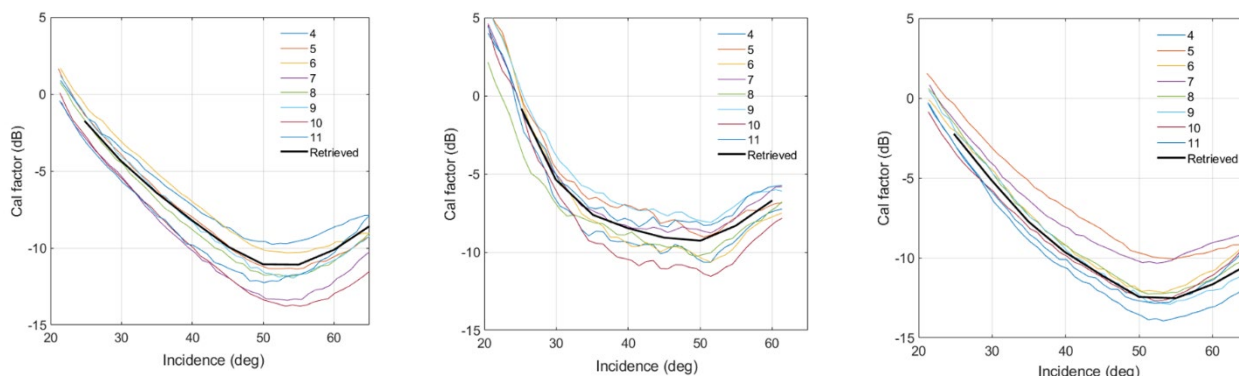


Figure 12. Ocean calibration curves from an alternate ocean calibration method that accounts for leg-to-leg wind variations over the Trefle site on 22<sup>nd</sup> May for the fore beam (left panel), mid beam (middle panel) and aft beam (right panel) using wind input from ECMWF. Coloured lines denote calibration curves for individual star pattern track legs and the solid black line denotes the retrieved calibration curve from the alternative ocean calibration scheme.

A full description and the results of these calibrations can be seen in Annex I) Measurement errors, calibration, and sea-surface wind inversion with PenWP

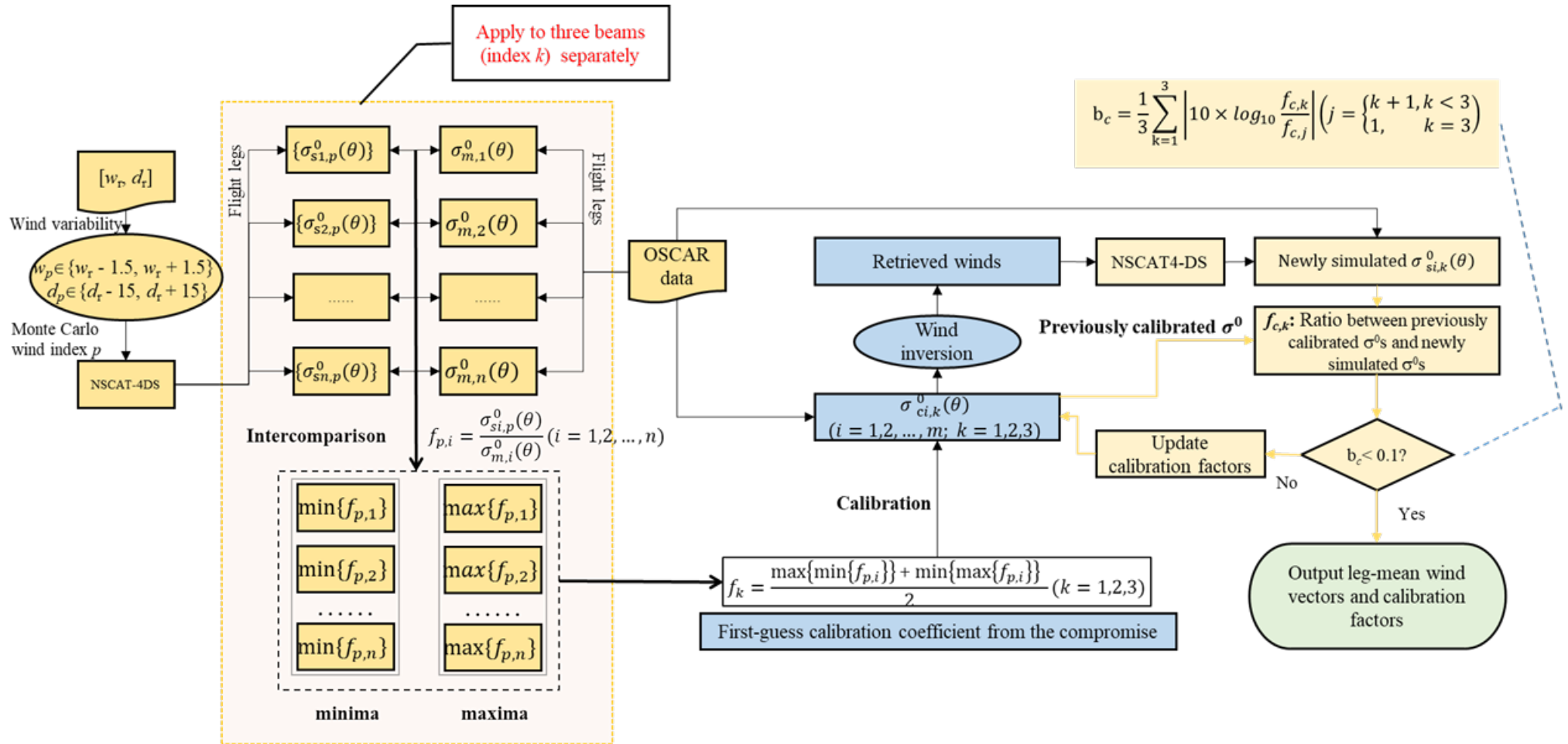


Figure 13. Alternative process for the ocean calibration, accounting for wind variability between track legs and using the PenWP wind inversion methodology.

## 5.3 OSCAR LEVEL-2 PROCESSING

### 5.3.1 SeaSTAR simultaneous wind and current retrieval

The simultaneous retrieval of TSCV and OSVW from OSCAR data was performed using the SeaSTAR project software package in python (Martin et al, 2023), which is an implementation of the algorithms detailed in Annex H) Algorithm Theoretical Baseline Document: OSCAR Level 2 Inversion

The processing was performed on NOC servers with 80 cores running at 2.6GHz. With the L1c input data coarsened to pixels at 200m ground resolution (via a rolling mean), each track took approximately 12-20 minutes to process, depending on track length.

Four main inputs are sent to the retrieval algorithm:

- *Radial Surface Velocity from the Fore and Aft beams*
- *Normalised Radar Cross Section ( $\sigma^0$ ) from all three beams*
- *Geophysical Model Functions (GMFs) for NRCS and RSV*
- *Estimations of noise, in the form of uncertainty in observed  $\sigma^0$  and RSV.*

The simultaneous inversion seeks to find four unknowns, namely two components of the TSCV and two components of the OSVW. If more than four observations with Gaussian noise are available, these four unknowns can be estimated using a quadratic estimator as the objective function to determine TSCV and OSVW.

Based on Bayes' probability theorem, and following Stoffelen & Portabella (2006) and Martin et al. (2018), the Maximum Likelihood Estimator is represented by the cost function, J, defined as:

$$\begin{aligned}
 J(\hat{x}) &= J(u_{10}, c) \\
 &= \frac{1}{N_S + N_D} \sum_{i=1}^{N_S} \left( \frac{KuMod(u_{10}, \chi_i, p_i) - \sigma_{obs,i}^0}{\Delta\sigma_i^0} \right)^2 \\
 &\quad + \frac{1}{N_S + N_D} \sum_{i=1}^{N_D} \left( \frac{KuDop(u_{10}, \chi_i, p_i) + c_{||i} - RSV_{obs,i}}{\Delta RSV_i} \right)^2
 \end{aligned}$$

**Equation 1**

where  $\hat{x}$  is the estimate of the state vector,  $\sigma_{obs,i}^0$  is the observed Normalised Radar Cross Section (NRCS) in azimuth beam direction  $i$ ,  $RSV_{obs,i}$  is the observed Radial Surface Velocity (RSV),  $KuMod$  is the predicted NRCS,  $\sigma_{GMF,i}^0$  in azimuth beam  $i$  obtained with the chosen Geophysical Model Function for Ku-band NRCS,  $KuDop$  is the predicted RSV,  $RSV_{GMF,i}$  in azimuth beam  $i$  obtained with the chosen Geophysical Model Function for Ku-band Wind-wave Artefact Surface Velocity,  $u_{10}$  is the Ocean Surface Vector Wind (OSVW) at 10 metres height,  $c$  is the Total Surface Current Vector (TSCV),  $\Delta\sigma_i^0$  is the uncertainty (standard deviation) on the observed NRCS,  $\sigma_{obs,i}^0$  in azimuth beam direction  $i$ ,  $\Delta RSV_i$  is the uncertainty (standard deviation) on the observed RSV,  $RSV_{obs,i}$  in azimuth



beam direction  $i$ ,  $c_{||i}$  is the component of the TSCV in azimuth beam  $i$ ,  $p_i$  is the polarization,  $\chi_i$  is the azimuth look direction,  $\theta$  is the incidence angle,  $N_S$  is the total number of observations for NRCS and  $N_D$  is the total number of observations for RSV.

$\Delta\sigma_i^0$  and  $\Delta RSV_i$  determine the uncertainty (random noise) on the measurements of  $\sigma_{obs,i}^0$  and  $RSV_{obs,i}$  and contain contribution of both the noise performance of the instrument, the 'geophysical noise', i.e. residual contributions to the noise from geophysical phenomenon and GMF error.

### Uncertainty on NRCS

The NRCS uncertainty  $\Delta\sigma_i^0$  is defined as  $\Delta\sigma^0 = k_p\sigma^0$  where  $k_p$  is the radiometric resolution.  $k_p$  can be estimated as a pure instrument noise, a combination of instrument noise and geophysical noise at a given spatial resolution and a combination of the previous elements with an error to the GMF. Given the fine spatial resolution, the geophysical noise can be negligible and is dominated either by instrument noise  $k_{p,inst}$  or error in the GMF.  $k_{p,inst}$  can be estimated via a robust estimator of distribution (normalized interquartile range,  $IQR/1.349$ ) of  $\sigma_{obs}^0$  from open-ocean data over a geophysically homogenous area for the given resolution of the desired L2 product. Error on the GMF  $k_{p,GMF}$  is estimated via comparison of  $\sigma_{obs}^0$  with the predicted NRCS using NSCAT-4DS using the same open-ocean data, with a standard root mean square error, so that:

$$k_{p,GMF} = \sqrt{\sum (\sigma_{obs}^0 - KuMod)^2}$$

**Equation 2**

$$k_{p,inst} = \frac{IQR(\sigma_{obs}^0)}{1.349} / \langle \sigma_{obs}^0 \rangle$$

**Equation 3**

As computed, the GMF error contain the instrumental and geophysical noise but averaged on a wider spatial resolution (for OSCAR typically 1-10 km). These noise estimates typically vary with incidence angle. The maximum of these two noise contributions are compared (i.e., rather than simply added together), so that a reasonable estimate can be made. In the case of the SEASTARex 2022 Iroise Sea campaign,  $k_p$  was estimated to be equal to 20% and dominated by the instrumental noise. Figure 14 (left panel) shows azimuth-averaged  $K_p$  estimates for the three beams using data over the Trefle site on the 22<sup>nd</sup> May.

### Uncertainty on RSV.

The RSV uncertainty  $\Delta RSV_{obs}$  is estimated using a similar approach to the NRCS uncertainty:

$$\Delta RSV_{inst} = \frac{IQR(RSV_{obs})}{1.349}$$

**Equation 4**

Using open-ocean OSCAR data from the SEASTARex campaign and in situ data from an Acoustic Doppler Current Profiler (ADCP) mooring to estimate the surface current, observed WASV can be estimated ( $RSV_{obs}(\theta, \chi) - c_{||\theta, \chi}$ ) and compared to the predicted WASV from a GMF:

$$\Delta RSV_{inst} = \frac{IQR(RSV_{obs})}{1.349}$$

**Equation 5**

$$WASV_{obs} = RSV_{obs}(\theta, \chi) - c_{||\theta, \chi}$$

**Equation 6**

The RSV GMF error is then estimated as:

$$\Delta RSV_{obs} = \frac{IQR(WASV_{obs} - KuDop)}{1.349}$$

**Equation 7**

The maximum of the two noise contributions is taken. In the case of the SEASTARex campaign,  $\Delta RSV_{obs}$  was estimated to be equal to 0.2 m s<sup>-1</sup>. Figure 14 (right panel) shows azimuth-averaged estimates of  $\Delta RSV$  using data over the Trefle site on the 22<sup>nd</sup> May.

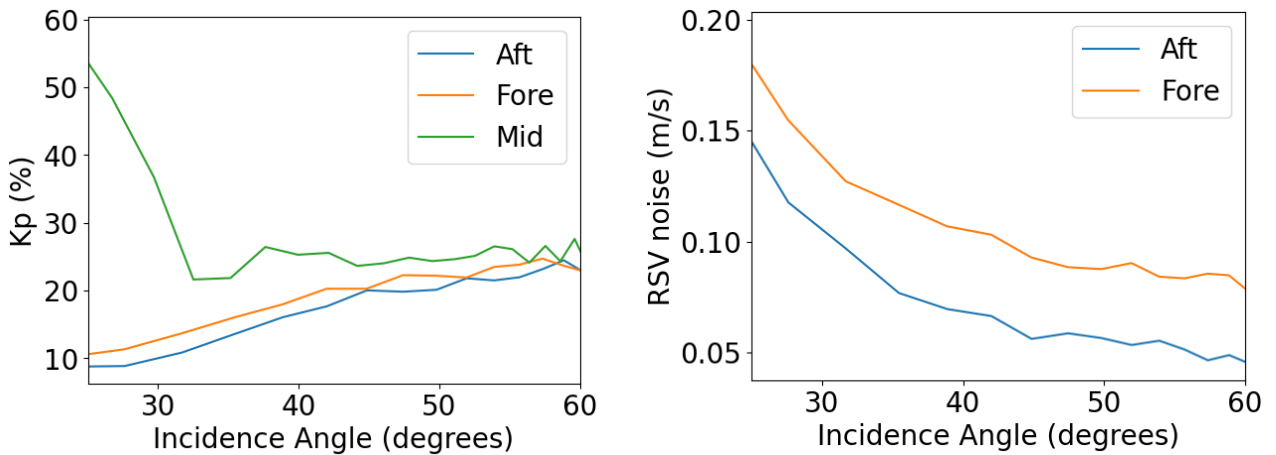


Figure 14. Estimations of the radiometric resolution  $Kp$  and RSV noise, calculated from a normalized IQR applied to OSCAR data recorded over the Trefle site on the 22<sup>nd</sup> May, coarsened to 200m pixel resolution.

The Geophysical Model Function (GMF), which models the contribution of wind and waves to the observed total ocean surface motion, is a critical part of the retrieval of TSCV from doppler data. For the results presented in this work, the GMF of Mouche (2012) was applied, which only considers the contribution of wind to the total surface motion.

The least-squares minimization process outputs up to four ambiguities for TSCV and OSVW, which must then be selected for based on an ambiguity removal criterion. For the results presented in this report, a simple ambiguity removal procedure was adopted to select the ambiguities closest in OSVW

space to a single wind vector obtained by co-locating the track time and track centre to AROME wind forecast data.

Further information regarding the SeaSTAR simultaneous retrieval can be seen in Annex H) Algorithm Theoretical Baseline Document: OSCAR Level 2 Inversion

### 5.3.2 PenWP wind retrieval

As part of the project an additional OSVW retrieval technique was applied to OSCAR data, using an adapted version of the Numerical Weather Prediction Satellite Application Facility (NWP SAF) Pencil-beam scatterometer Wind Processor (PenWP). Similar to the satellite scatterometers, the OSCAR wind retrievals are performed using the maximum likelihood estimator, which cost function is written as:

$$\text{MLE} = \frac{1}{3} \sum_{i=1}^3 (\sigma_{m,i}^0 - \sigma_{s,i}^0)^2$$

**Equation 8**

where  $\sigma_{m,i}^0$  is the calibrated radar backscatter coefficient of the  $i^{\text{th}}$  beam, and  $\sigma_{s,i}^0$  is the simulated radar backscatter through the geophysical model function, i.e., NSCAT-4DS. Note that the general MLE formulation includes a normalization term (i.e., in the denominator) by measurement noise ( $K_p$ ). This term has been neglected, which is equivalent to assume that the measurement noise is similar for all beams. This is done for two reasons: a) we do not have enough data to accurately estimate the  $K_p$  for each beam; b) in ASCAT-type of geometry, it has been shown that including the  $K_p$  term in Equation 8 leads to retrieved wind direction biases (Stoffelen and Portabella, 2006). Further optimization of the inversion process can of course be done in the future by, e.g., z-space transformation (Stoffelen and Portabella, 2006), but this is beyond the scope of this study.

In general, the full-resolution (8m x 8m) backscatter measurements are averaged to a single backscatter value on a WVC of a predefined size, e.g., 200m x 200m. Then, the generic wind inversion module of PenWP is used to retrieve sea surface winds from a set of WVC-mean  $\sigma^0$ s (i.e., three NRCS values, one for each beam). This inversion scheme allows up to 4 ambiguous wind solutions for each WVC, although because of its ASCAT-like viewing geometry it usually leads to 2 wind solution ambiguities 180° apart (Lin *et al.*, 2013). Then the ambiguity which is closest to the background wind field (i.e., ECMWF or ASCAT) is selected as the final wind solution. Note that the wind inversion can be done at other WVC sizes. Also, PenWP also allows the inversion of multiple  $\sigma^0$ s (e.g., at full 8m x 8m resolution) per beam and WVC. However, as shown in (Portabella, 2002), the reduction of noise by  $\sigma^0$  averaging prior to the non-linear inversion leads to higher quality wind retrievals. As such, we perform  $\sigma^0$  averaging prior to inversion.

A full account of this method and the results can be seen in Annex I) Measurement errors, calibration, and sea-surface wind inversion with PenWP.

## 6. LEVEL 2 RETRIEVAL OF TSCV AND OSVW

### 6.1 SEASTAR SIMULTANEOUS RETRIEVAL OF TSCV AND OSVW

Figure 15 shows example results over La Jument on the 17<sup>th</sup> May during an ebb tide, with simultaneously retrieved TSCV in the top two panels (a, b) and OSVW on the bottom (c, d). In this case, and in all remaining simultaneous retrieval results presented in this report the GMF used was that of Mouche et al (2012), i.e. only accounting for doppler variation due to the wind, and a simple ambiguity removal procedure that used a single AROME  $u_{10}$  vector collocated in space and time (nearest neighbor) with the centre of the OSCAR track. Figure 16 shows similar results from the 22<sup>nd</sup> May but during flood tide around the island.

Available ground truth data for comparison are shown for these flight days in Figure 17 (17<sup>th</sup> May) and Figure 18 (22<sup>nd</sup> May). Note the difference in available ground truth data between the flights, with X-band derived surface currents only available on the 17<sup>th</sup> (Figure 17, b) and HF radar derived surface current vectors available for the 22<sup>nd</sup> (Figure 18, b).

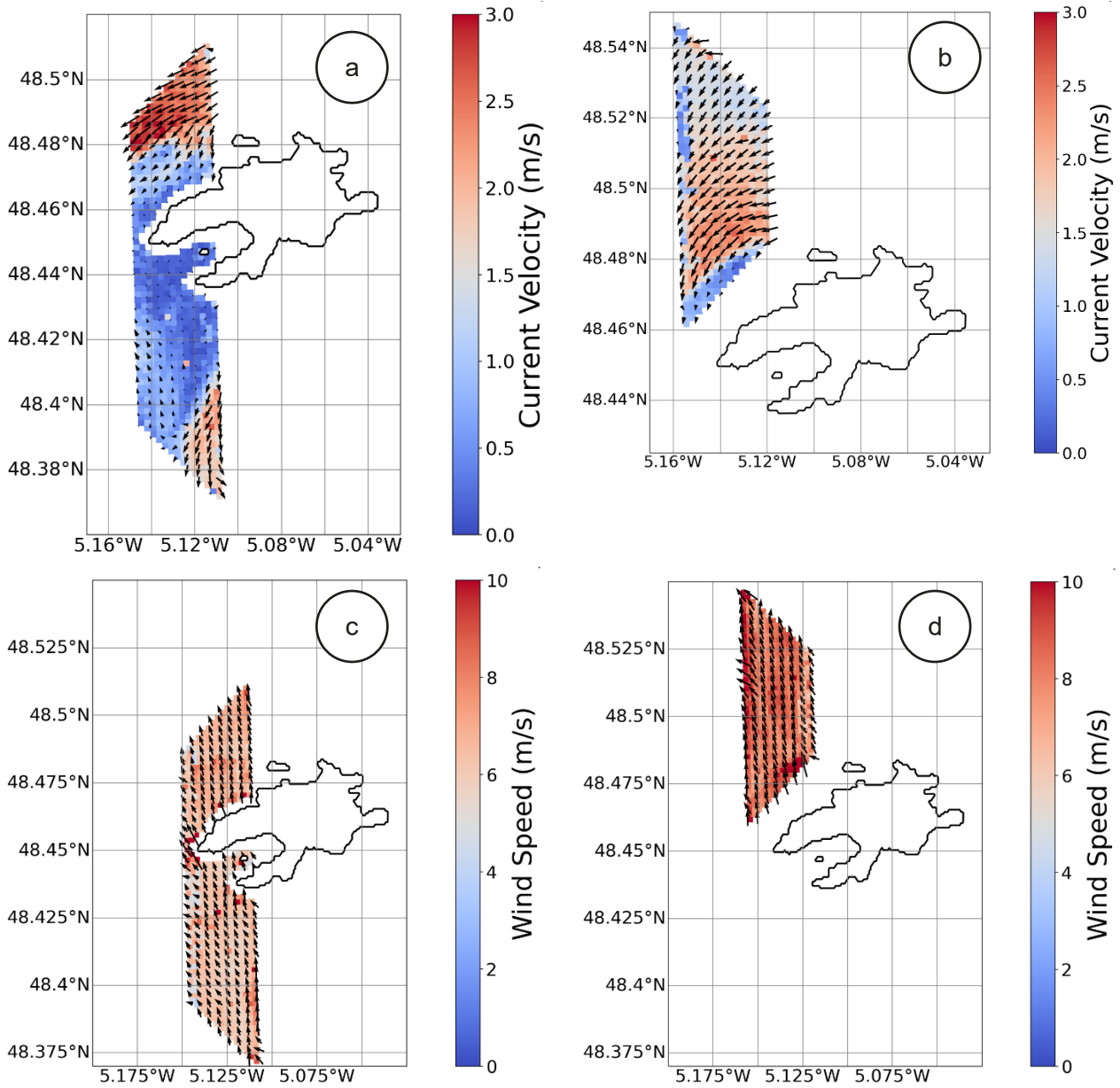


Figure 15. L2 simultaneous retrieval results for the 17<sup>th</sup> May flights: TSCV (a) and OSVW (c) at 09:32 UTC, TSCV (b) and OSVW (d) at 09:38 UTC.

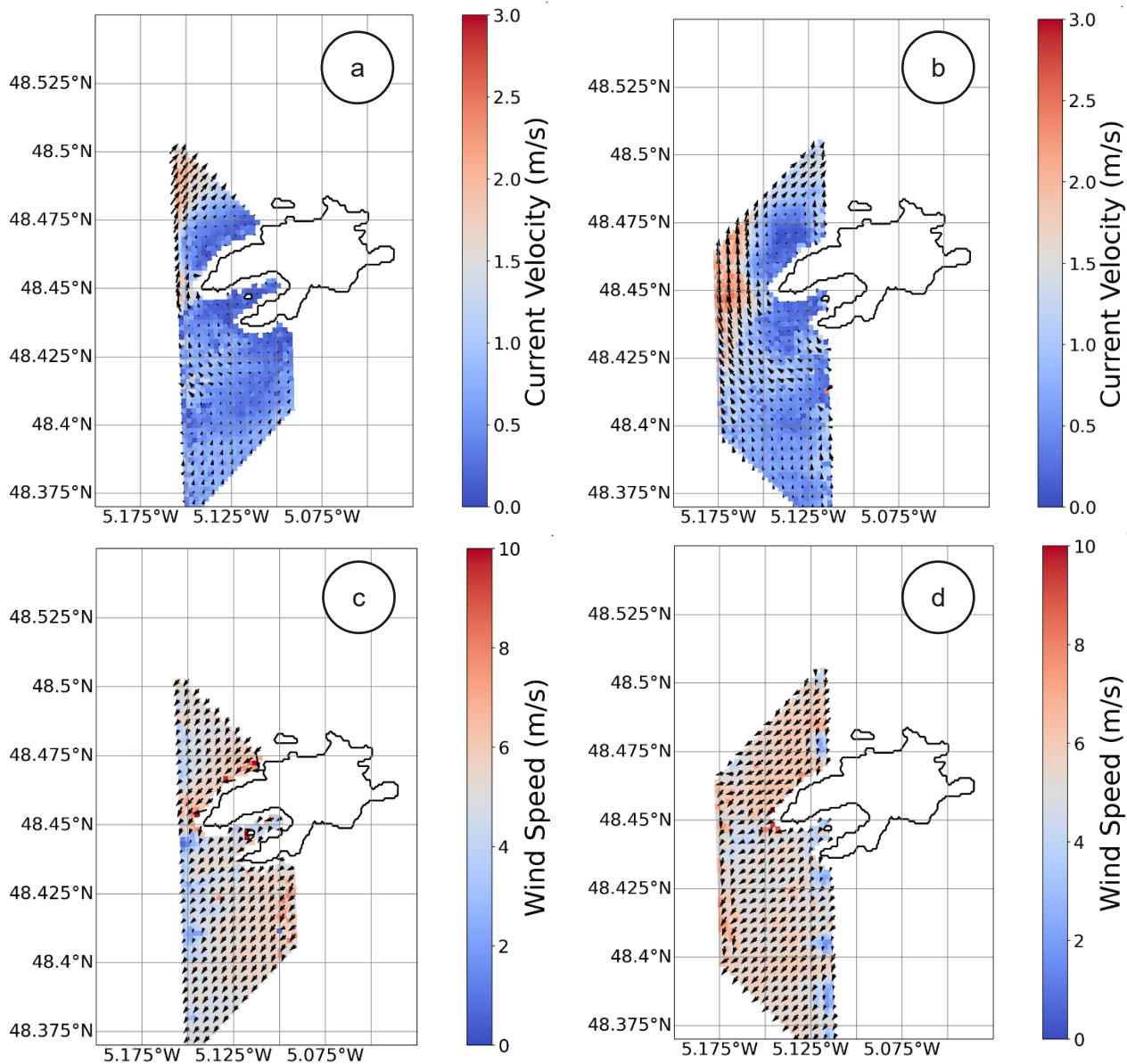


Figure 16. L2 simultaneous retrieval results for the 22<sup>nd</sup> May flights: TSCV (a) and OSVW (c) at 05:39 UTC, TSCV (b) and OSVW (d) at 05:48 UTC.

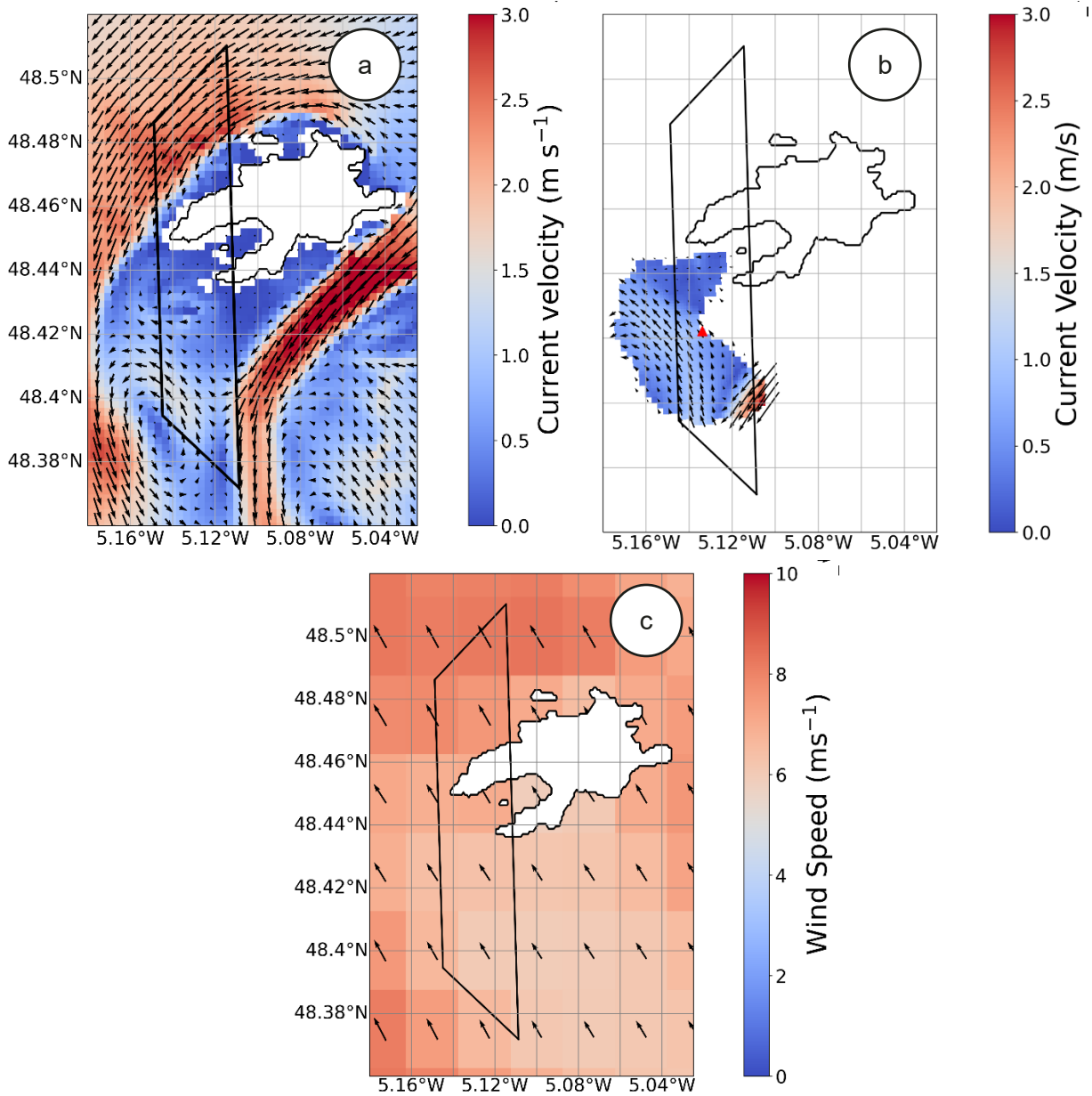


Figure 17. Ground truth data coincident with OSCAR flights on the 17<sup>th</sup> May: MARS2D simulated depth-averaged current vectors at 09:30 UTC (a), X-band radar derived surface currents at 09:35 UTC (b) and AROME predicted  $u_{10}$  wind speed vectors at 09:00 UTC (c). Black polygons denote the outline of an OSCAR track.

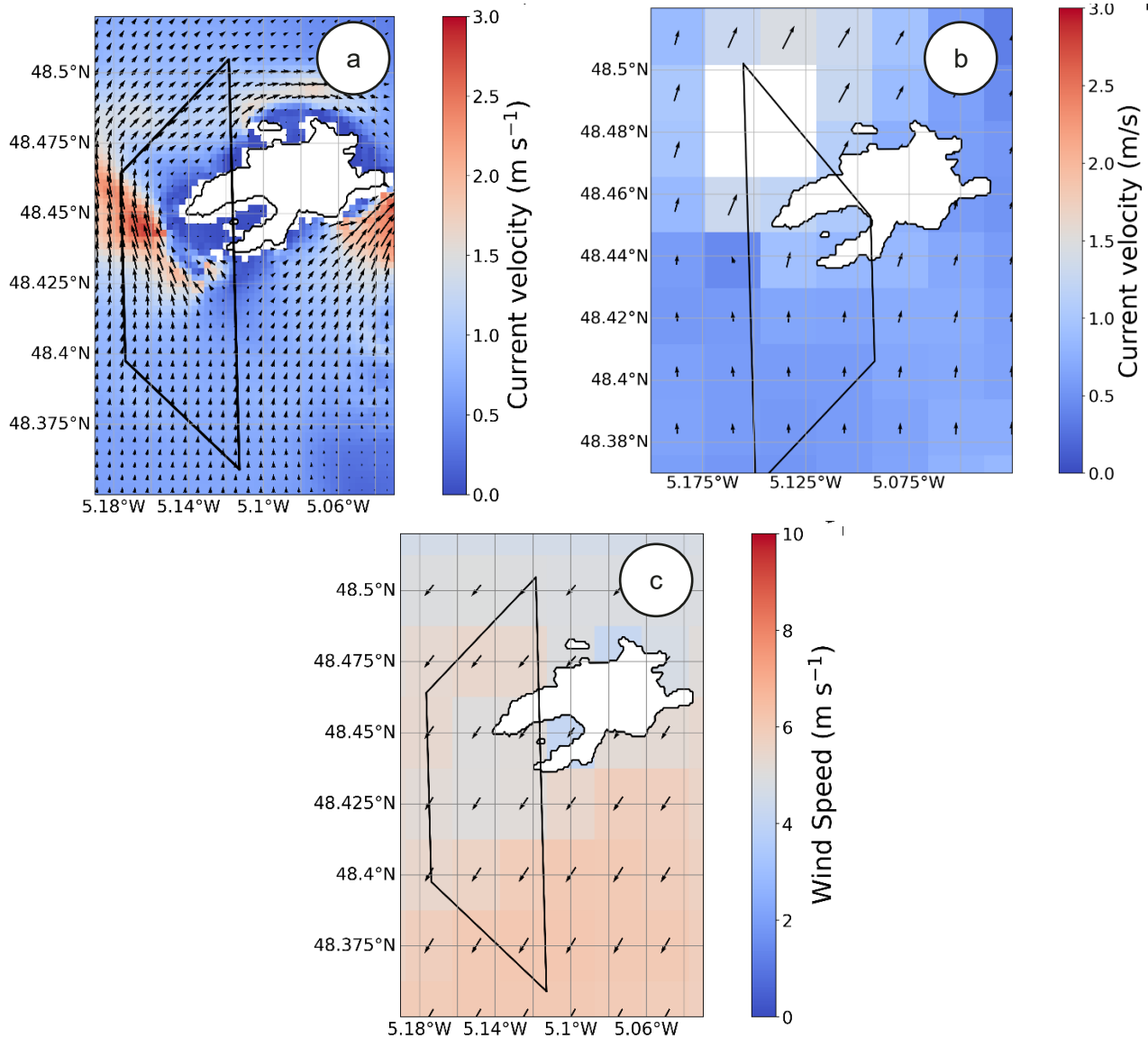


Figure 18. Ground truth data coincident with OSCAR flights on the 22<sup>nd</sup> May: MARS2D simulated depth-averaged current vectors at 05:45 UTC (a), HF radar derived surface current vectors at 05:41 UTC (b) and AROME predicted  $u_{10}$  wind speed vectors at 06:00 UTC (c). Black polygons denote the outline of an OSCAR track.



Figure 19 shows simultaneously retrieved TSCV (a) and OSVW (b) across the ‘star pattern’ flow over the Trefle site on the 22<sup>nd</sup> may. In both cases, data from all 8 ‘star pattern’ tracks were interpolated onto a common grid at 200m pixel resolution and the median value across all crossing tracks displayed. In this way, data at the centre of the ‘star’ contains a median across 8 retrieved values, whilst pixels at the edges may only contain data from a single track. Comparison ground truth data from MARS 2D (c) and AROME (d) are shown, as well as HF derived surface currents (e) and surface current vector components (1.5m depth bin) from the ADCP aboard the Trefle buoy located at the centre of the star pattern (f). The assumption of spatial homogeneity across the star pattern is verified by panels c, d and e, whilst the assumption of temporal homogeneity is verified by panel f (timings of the start and end of the star pattern runs are shown as dashed black lines).

Table 10 shows the results of the validation between OSCAR, ADCP data and AROME modelled winds at the Trefle site on the 22<sup>nd</sup> May, which were used for the SeaSTAR EE11 Report for Assessment (ESA, 2023).

Table 10. Validation parameters for TSCV and OSVW between OSCAR and ground truth, using data from the Trefle ADCP buoy at the centre of the star pattern and data from AROME, interpolated to OSCAR.

	ADCP		AROME	
	TSCV velocity (m/s)	TSCV direction (degrees North)	OSVW speed (m/s)	OSVW direction (degrees North)
<b>OSCAR</b>	0.64	14.4	5.54	49.1
<b>Ground truth</b>	0.62	8.4	5.86	45.8
<b>RMSE</b>	<b>0.08</b>	<b>8.5</b>	<b>0.44</b>	<b>5.4</b>

Further analysis and results can be seen in the submitted paper (McCann et al, 2024), a preprint of which can be found in ANNEX K) Paper submitted to Ocean Science.

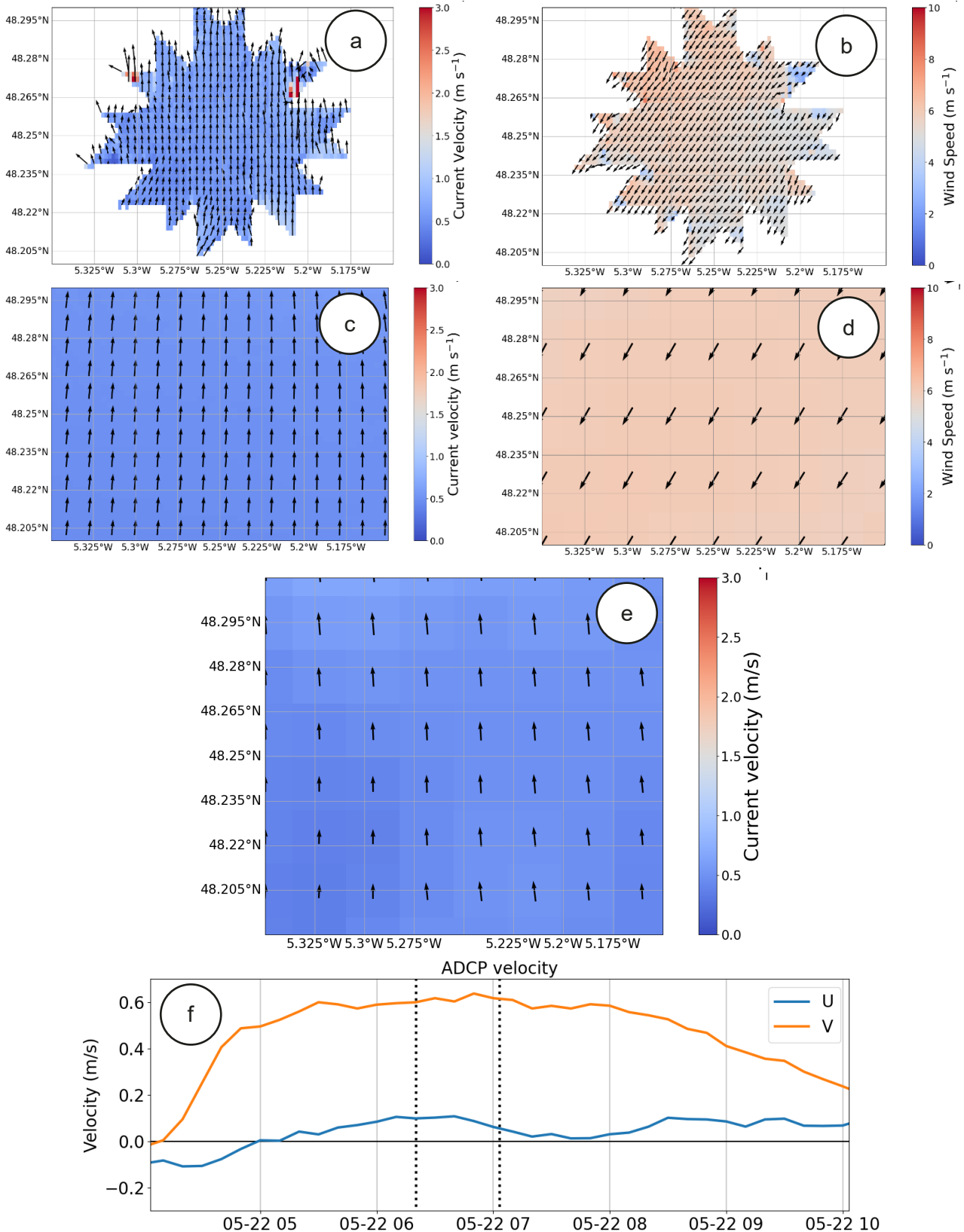


Figure 19. Retrieved results and ground truth data from the Trefle site on the 22<sup>nd</sup> May: Simultaneously retrieved TSCV (a) and OSVW (b) from all ‘star pattern’ tracks, MARS 2D simulated depth-averaged current vectors at 06:30 UTC (c), AROME simulated  $u_{10}$  vectors at 06:00 UTC (d), HF radar derived surface currents at 06:30 UTC (e) and ADCP current vector components (meridional U and zonal V) at 1.5m depth from the Trefle buoy over the flight day with the start and end of the star pattern tracks shown by dashed black lines (f).

## 6.2 PENWP RETRIEVAL OF OSVW

Figure 23 and Figure 25 show examples of PenWP OSVW retrievals at 200m pixel resolution from OSCAR data recorded over the La Jument site on the 22<sup>nd</sup> May. There is good visual agreement in terms of wind velocity gradient with the simultaneous retrieval OSVW result (Figure 19, b) with a general trend of higher wind velocity towards the North-West and lower towards the East and South-East. There are considerable drops in retrieved wind speed at near range observed across all tracks, due to an issue with the OSCAR instrument on the 22<sup>nd</sup> May in the form of intermittent Tx/Rx power.

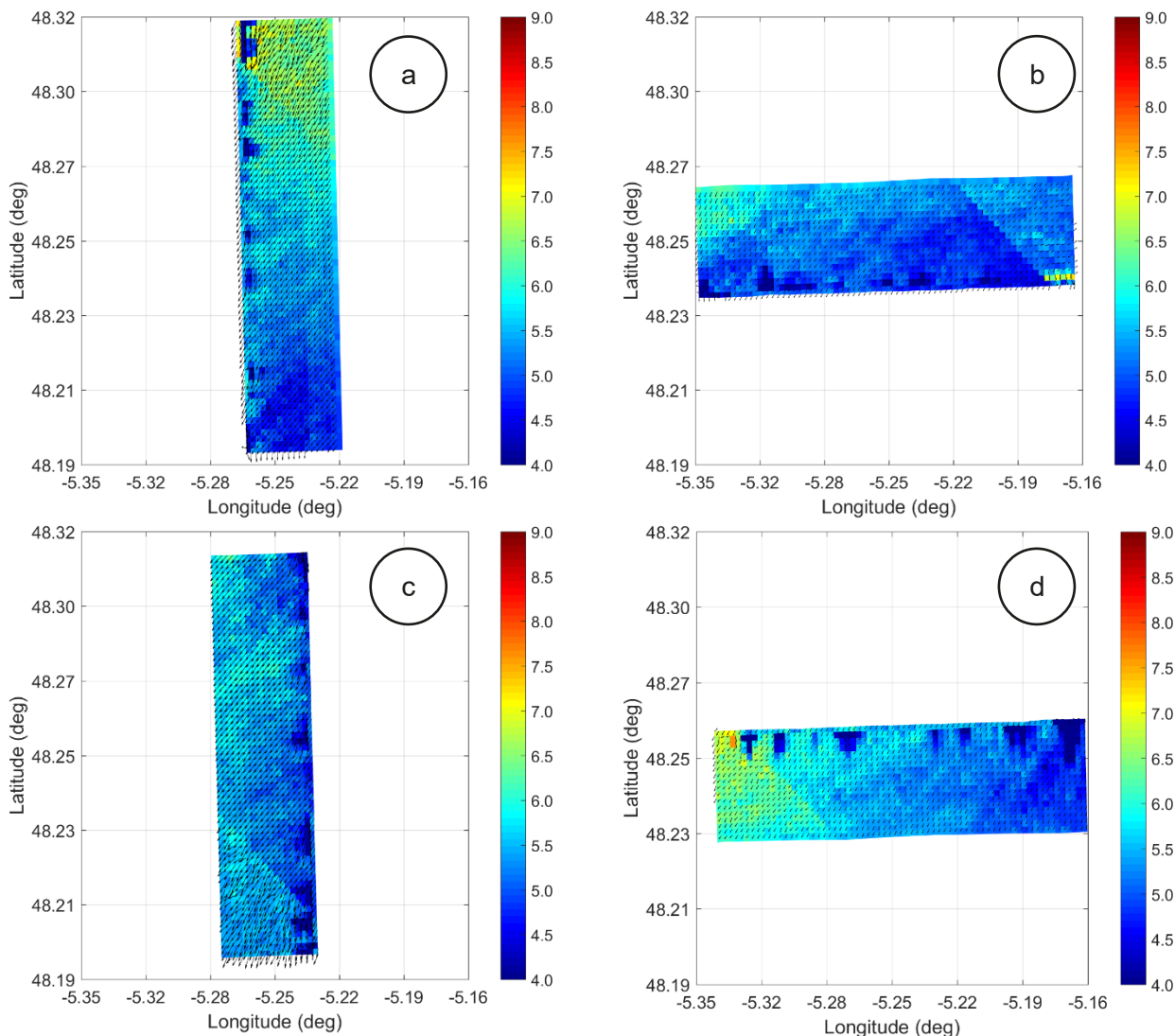


Figure 20. OSCAR PenWP-retrieved winds at 200-m resolution for the star-pattern flight legs 4–7 (a–d, respectively) on the 22<sup>nd</sup> May. For the sake of illustration, the arrows are thinned by a factor of two.

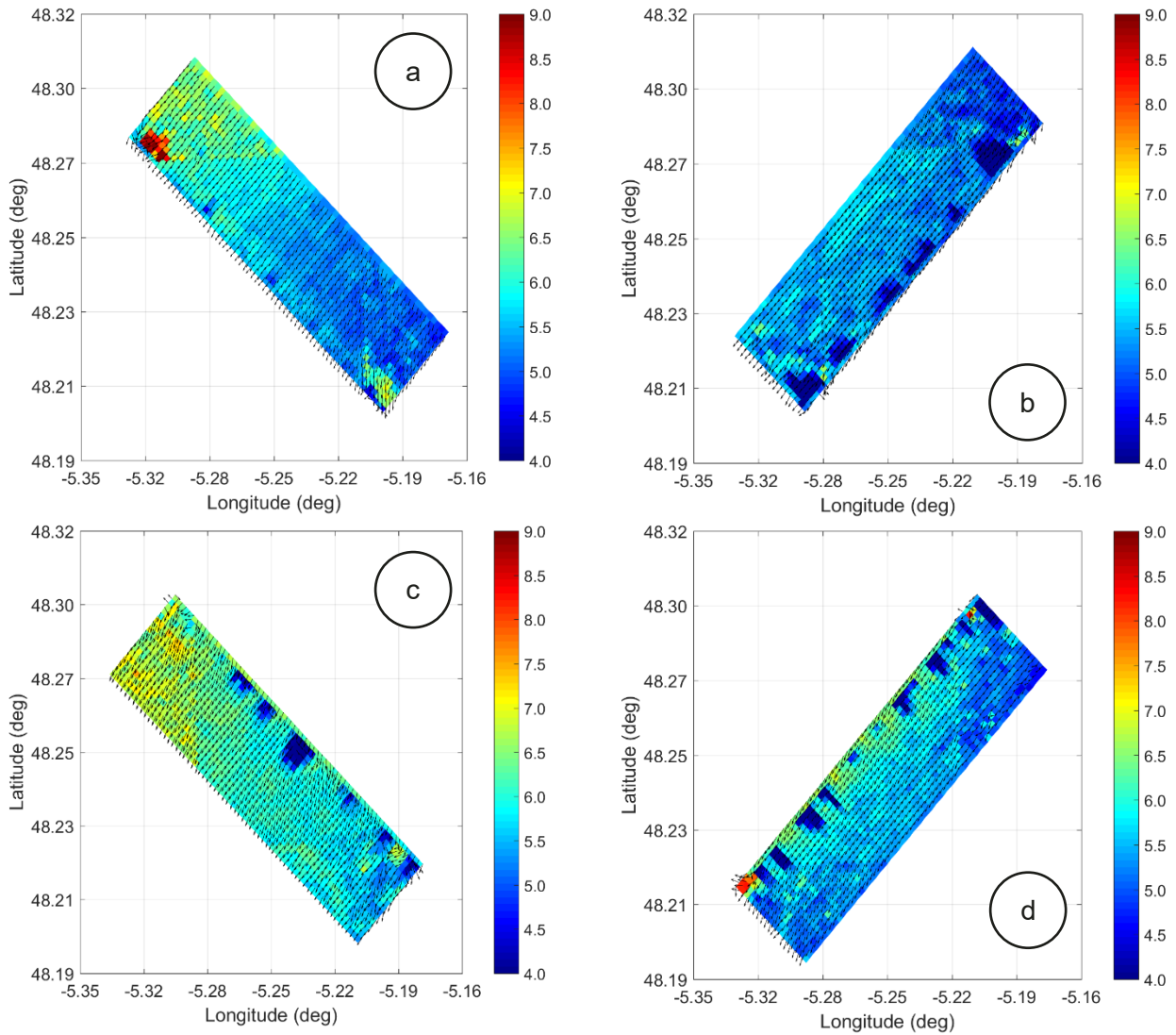


Figure 21. OSCAR PenWP-retrieved winds at 200-m resolution for the star-pattern flight legs 8–11 (a-d, respectively) on the 22<sup>nd</sup> May. For the sake of illustration, the arrows are thinned by a factor of two.

Figure 22 shows PenWP retrieved wind speeds for a single flight leg on the 25<sup>th</sup> May at 104m and 200m resolution. Comparison and validation against ECMWF and ASCAT wind products can be seen in Figure 23.

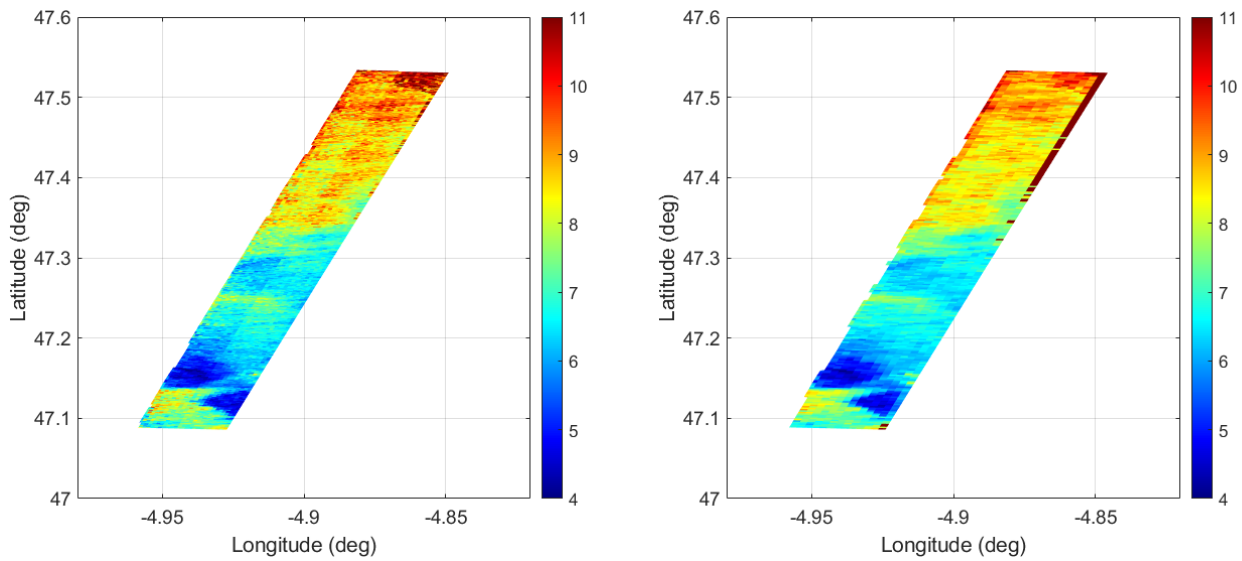


Figure 22. PenWP retrieved wind speed (m/s) at 104-m (left panel) and 200-m (right panel) resolution for offshore flight leg number 2 on the 25<sup>th</sup> May (see Figure 2b for reference on leg numbering). The wind arrows are omitted to better emphasize the wind speed patterns.

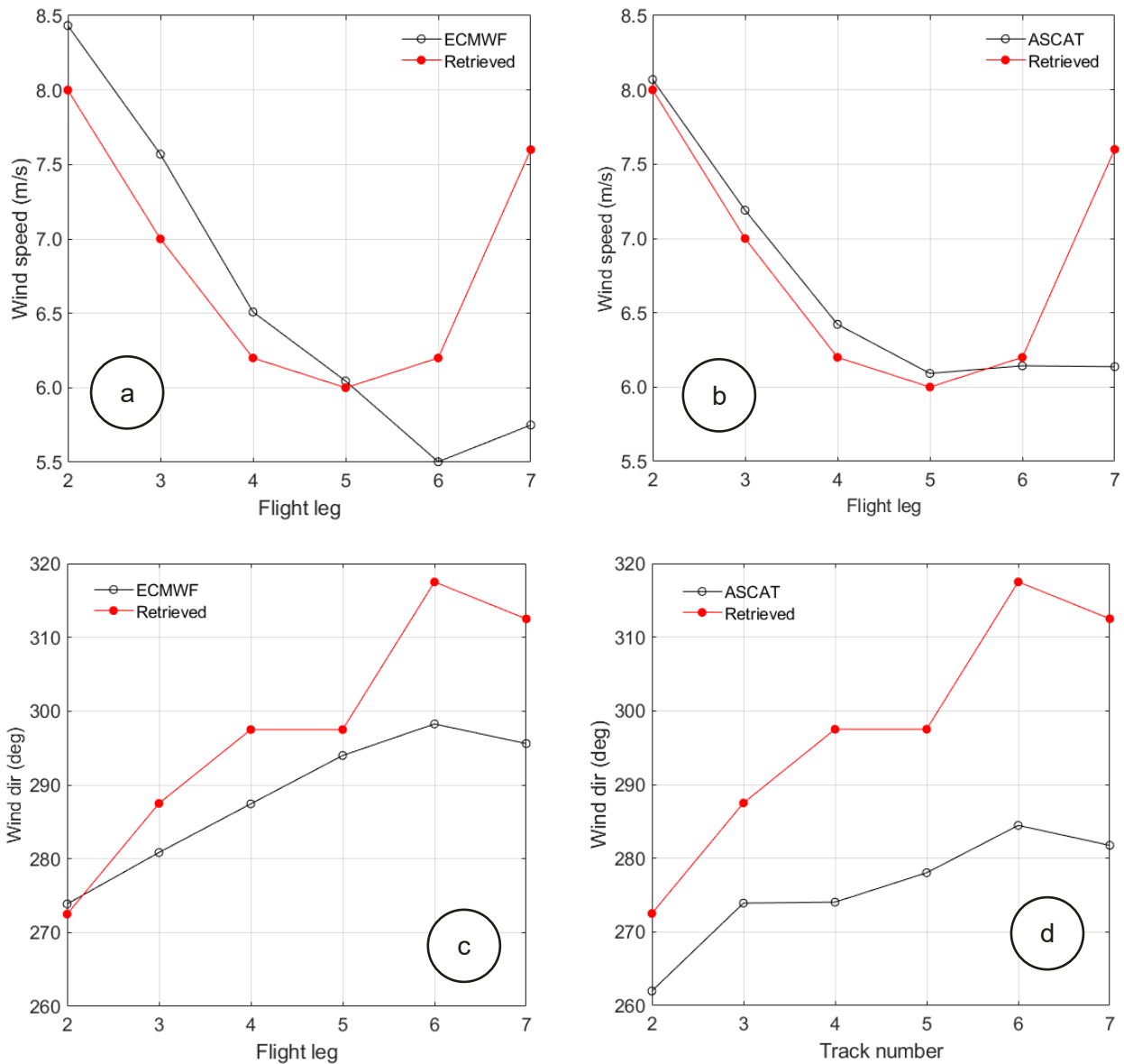


Figure 23. PenWP retrieved wind speed (a, b) and direction (c, d) from the offshore flights on the 25<sup>th</sup> May. Results using the alternative ocean calibration (red) and input data to the calibration (black) are shown (ECMWF winds: a, c; ASCAT winds: b, d)

A full account of the PenWP OSVW retrieval results can be seen in Annex I) Measurement errors, calibration, and sea-surface wind inversion with PenWP



### 6.3. CIRCULAR FLIGHTS

Figure 24 shows results from the circular flight data recorded on the 22<sup>nd</sup> May for the mid beam (broadside). The angles around the plot (radials) correspond to look direction relative to North and the rings (radius) correspond to  $\sigma^0$  in dB. Three traces are plotted, corresponding to increasing incidence angle, and the wind vector from AROME at the Trefle site at time of flight is depicted by the red arrow (as can also be seen in Figure 19, d).

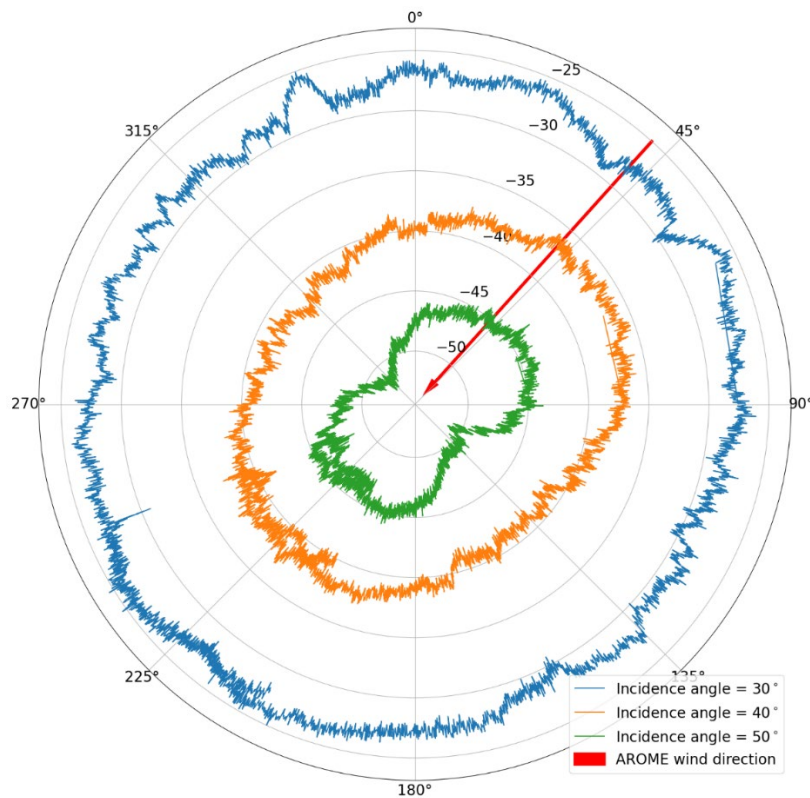
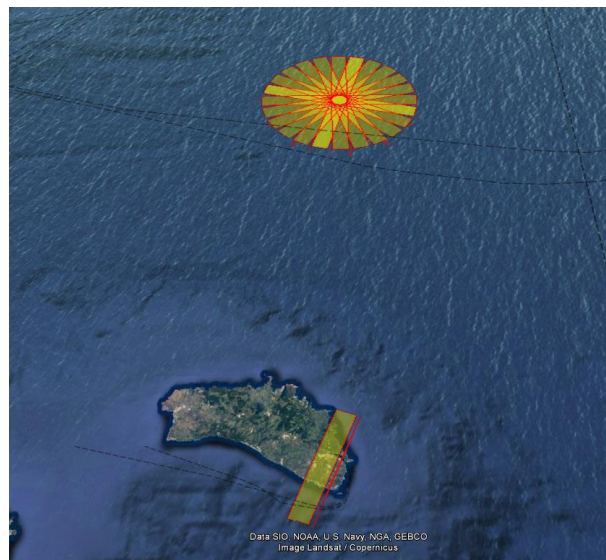


Figure 24. Results from the range compressed circular flight data on the 22<sup>nd</sup> May with radials of radar look direction relative to north and rings of  $\sigma^0$  (dB). The blue, orange and green traces show the  $\sigma^0$  at 30, 40 and 50° incidence angle respectively. The red arrow denotes the wind direction vector at the Trefle site from AROME.

## 7. MEDITERRANEAN CAMPAIGN

As an extension to the SEASTARex contract, a second OSCAR airborne campaign was planned and executed to coincide with the 'CalVal' fast-repeat phase of the NASA/CNES Surface Water and Ocean Topography (SWOT) mission over the southern Mediterranean sea in 2023. As part of the CalVal international activities, the BIOSWOT-Med cruise was planning in situ observations of geophysical and environmental properties under the SWOT overpass and airborne acquisitions were planned to coincide with both.

The campaign ran from the 5<sup>th</sup> to 9<sup>th</sup> May 2023 from the home airport of San Luiz Aerodrome, Menorca. Unfortunately, flight restrictions meant that overflying the BIOSWOT-Med cruise was not possible, however three flights were successfully completed, timed to be coincident with the overpass of SWOT and obtaining airborne imagery over a 50km diameter 'rose pattern' disk (Figure 25).



*Figure 25. Planned OSCAR acquisition swaths for the three flights of the SEASTARex-Med campaign. The island of Menorca in the southern Mediterranean sea is seen in the lower half of the image, with the 50km diameter 'rose pattern' disk in the top half.*

The contract extension did not cover the analysis of these data, with this being planned for future projects. However preliminary analysis of the data shows some very promising results, with geophysical anomalies clearly present in the NRCS data (Figure 26). Preliminary analysis of these data was performed as part of the CNES funded 'OSCAR-SWOT' project, the final report of which can be found at <https://www.noveltis.fr/oscar-swot-final-report/>. For a full account of the OSCAR airborne data collected as part of this work, see ANNEX J) Data acquisition report for the Mediterranean campaign.

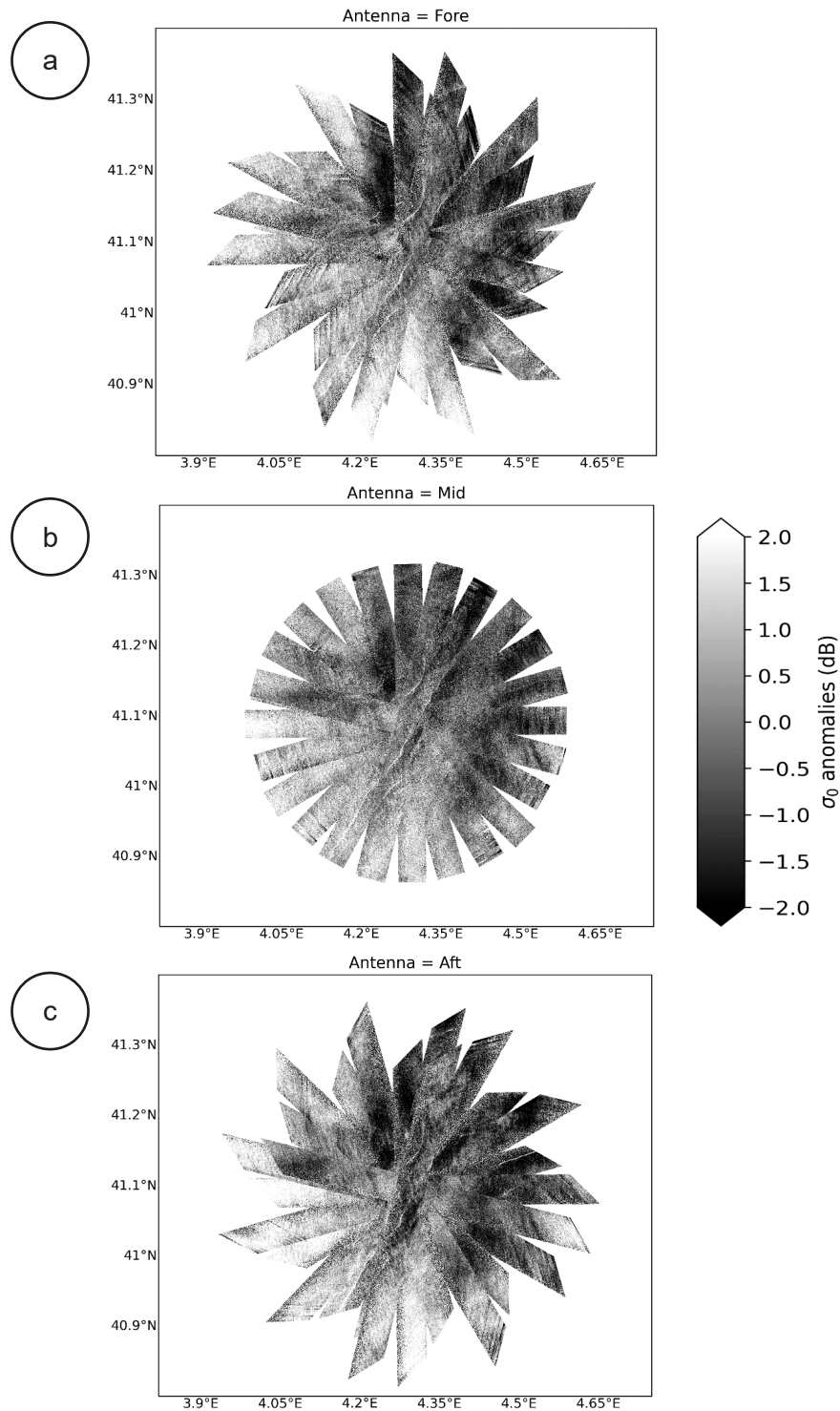


Figure 26. OSCAR NRCS anomalies (median intensity across-track removed) for a sample of the Mediterranean campaign data on the 5<sup>th</sup> May 2023. Fore (a), mid (b) and aft (c) channels shown. The diameter of the disk is 50km.

## 8. CONCLUSIONS AND OUTLOOK

In conclusion, the SEASTARex project has successfully demonstrated the capabilities and potential of the OSCAR airborne instrument in measuring ocean surface currents and winds. This project conducted two extensive campaigns in distinct marine environments, the Iroise Sea and the Mediterranean Sea.

During the Iroise Sea campaign in May 2022, OSCAR measurements were compared against Acoustic Doppler Current Profiler (ADCP), HF radar, and X-band marine radar data. The validation process revealed a high level of agreement between OSCAR and these ground truth measurements, with a root mean square difference (RMSD) better than 10 cm/s for the current in the homogeneous area. For the wind retrieval, very similar results are obtained whereas we retrieved simultaneously wind and current or if we only retrieve the wind using NRCS in the OSCAR 3-look direction. Performance against ECMWF is better than 1m/s. This level of accuracy underscores the effectiveness of the OSCAR instrument in capturing ocean surface dynamics and its potential as a valuable tool for future research and monitoring efforts.

Building on the Iroise Sea OSCAR success, a new campaign was organized in May 2023 to coincide with the BioSWOT campaign, during which OSCAR flew together with SWOT over an area known for its meso- and submesoscale dynamics. The BioSWOT-Med cruise focused on the Western Mediterranean Sea, aiming to investigate the role of fine-scale circulation as a driver of plankton diversity, coinciding with the SWOT satellite's daily "fast-sampling" orbit over the same region. Satellite SAR images from various sources, including RCM, TerraSAR-X, Sentinel-1, RadarSat-2, and PAZ SAR, were collected for comparative analysis with OSCAR and SWOT data. OSCAR data consisted of three days of acquisition acquiring the exact same rose pattern consisting of a disk of about 50km diameter. Preliminary analysis of these data has not been possible in the frame of this project but has been supported by CNES in the OSCAR-SWOT project led by NOVELTIS.

The high-quality OSCAR data have gained recognition within the scientific community, as evidenced by the submission of a peer-reviewed paper (McCann et al. 2024) and oral presentations at various conferences, including Ocean from Space, EGU and the Ocean Science Meeting. Moreover, the OSCAR data have been processed and analyzed in time to be included in the ESA Earth Explorer 11 SeaSTAR Report for Assessment and were presented at the ESA EE11 User Consultation Meeting, further highlighting the significance of the project's achievements.

Future work in the SEASTARex project should focus on deepening the data analysis for the three datasets acquired over the North Sea in the Netherlands, the Iroise Sea, and the Mediterranean Sea. Specific areas of interest include studying the impact of Wave Doppler (aka WASV for Wind-wave Artefact Surface Velocity) on the ATI Doppler shift. This is highly relevant for Harmony, Sentinel-1, and Sentinel-1 NG missions as the Wave Doppler is currently the strongest source of uncertainty. Additionally, research on retrieving Directional Wave spectrum using squinted ATI is of strong interest, as it has the potential to resolve shorter wave wavelengths than standard broadside SAR data and

has not yet been explored in the scientific literature. Proving this increased capability with the airborne data, hence increasing SRL, will enable us to add this as primary observation requirement.

Furthermore, the project could benefit from a campaign in the Marginal Ice Zone, possibly by collaborating with the ICENAV expedition in Winter or Summer 2025 in the Canadian Atlantic waters. This would provide valuable insights into the performance of the OSCAR, hence any squinted ATI SAR mission, like Harmony or SeaSTAR in ice-covered regions.

Beyond the SEASTARex project, a wide range of SAR acquisitions have been tasked in the Iroise Sea and the Mediterranean Sea, thanks to the ESA Third Party Mission Program. The dataset includes a variety of frequencies (Ka-, Ku-, X-, C-, S-band) and has only been partially analyzed for the days of OSCAR flight. Exploring this rich dataset further could lead to additional insights and advancements in the understanding of ocean surface dynamics and its signature in different frequency.

In summary, the SEASTARex project has not only validated the performance of the OSCAR airborne instrument but also paved the way for future advancements in the field of Doppler Oceanography. The project's findings and achievements, along with the proposed future work, will have lasting impacts on our understanding of ocean surface dynamics and their role in various Earth systems.



## REFERENCES

- ESA (2023). Report for Assessment: Earth Explorer 11 Candidate Mission Seastar, European Space Agency, Noordwijk, The Netherlands, ESA-EOPSM-SEAS-RP-4374, 116pp.
- Gebert, N., A. Martin, V. Navarro, and M. Portabella (2018). "Ocean surface current airborne radar (OSCAR) demonstrator." Doppler Oceanography from Space (DOFS), From science to technology and applications, 10-12 October 2018, Brest, France.
- Lin, W., Portabella, M., Stoffelen, A., and Verhoef, A., "On the characteristics of ASCAT wind direction ambiguities," *Atmos. Meas. Tech.*, 6, pp. 1053-1060, doi: 10.5194/amt-6-1053-2013.
- Martin, A.C.H., Gommenginger, C., Marquez, J., Doody, S., Navarro, V., and Buck, C.: Wind-Wave induced velocity in ATI SAR Ocean Surface Currents: First experimental evidence from an airborne campaign, *J. Geophys. Res.-Oceans*, 121(3), 1640–1653, doi: 10.1002/2015JC011459, 2016
- Martin, A.C.H. and Gommenginger, C.: Towards wide-swath high-resolution mapping of total ocean surface current vectors from space: Airborne proof-of-concept and validation, *Remote Sens. Environ.*, 197, 58–71, doi: 10.1016/j.rse.2017.05.020, 2017
- Martin, A.C.H., Gommenginger, C. and Quilfen, Y.: Simultaneous ocean surface current and wind vectors retrieval with squinted SAR interferometry: Geophysical inversion and performance assessment, *Remote Sens. Environ.*, 216, 798–808, doi: 10.1016/j.rse.2018.06.013, 2018
- Martin, A., N. Gebert, C. Trampuz, M. Portabella, V. Navarro, and C. Gommenginger (2019). "Ocean Surface Current Airborne Radar (OSCAR) Demonstrator." Living Planet Symposium 2019, 13-17 May 2019, Milan.
- Martin, A. C. H., McCann, D. L., Gommenginger, C., Macedo, K. A. C., & Le Merle, E. (2023). SeaSTAR project (v2023.10.3), Zenodo, doi: 10.5281/zenodo.10026593
- McCann, D. L., A. C. H. Martin, K. Macedo, R. Carrasco Alvarez, J. Horstmann, L. Marié, J. Márquez-Martínez, M. Portabella, A. Meta, C. Gommenginger, P. Martin-Iglesias and T. Casal (2023). "A new airborne system for simultaneous high-resolution ocean vector current and wind mapping: first demonstration of the SeaSTAR mission concept in the macrotidal Iroise Sea", *EGU sphere preprint*, doi: 10.5194/egusphere-2023-2995.
- Meta, A., S. Placidi, C. Trampuz, V. Navarro, A. Repucci, C. P. Gommenginger, and A. C. H. Martin. (2015). "Ocean Surface Current Airborne Radar Demonstrator (OSCAR)." *Proposal submitted in response to ESA AO/1-8309/15/NL/BJ (Re-Issue of AO/1-7994/14/NL/BJ)*.
- Mouche, A.C.H., Collard, F., Chapron, B., Dagestad, K-F., Guitton, G., Johannessen, J., Kerabol, V. and Hansen, M.W.: On the use of Doppler shift for sea surface wind retrieval from SAR, *IEEE T. Geosci. Remote*, 50(7), 2901–2909, doi: 10.1109/TGRS.2011.2174998, 2012
- Portabella, M., "Wind field retrieval from satellite radar systems," PhD Thesis, University of Barcelona (UB), Barcelona, Spain, <https://digital.csic.es/handle/10261/154354>, 2002.
- Stoffelen, A. and M. Portabella (2006) "On Bayesian scatterometer wind inversion," *IEEE Trans. Geosci. Rem. Sens.*, 44 (6), pp. 1523-1533, doi: 10.1109/TGRS.2005.862502.
- Trampuz, C., N. Gebert, S. Placidi, L. C. Izzy Hendricks, F. Speziali, V. Navarro, A. C. H. Martin, C. P. Gommenginger, M. Suess, and A. Meta (2018). "OSCAR - The airborne interferometric and scatterometric radar instrument for accurate sea current and wind retrieval." *EUSAR 2018, the 12th European Conference on Synthetic Aperture Radar.*, Aachen, 4-7 June 2018.
- Wang, Z., A. Stoffelen, F. Fois, A. Verhoef, C. Zhao, M. Lin and G. Chen (2017). "SST Dependence of Ku- and C-Band Backscatter Measurements", *IEEE Journal of Selected Topics in Applied Earth O*, 10, 5, 2135-2146, doi:10.1109/JSTARS.2016.2600749.



# **ANNEX A) ANALYSIS OF THE OSCAR POD AND ANTENNA CHARACTERIZATION**



# SeaSTARex

## D2: Analysis of the OSCAR POD and Antenna Characterization

**Reference Code** : : MS-SeaSTARex-OSCARPOD  
**Issue** : : 2.0  
**Date** : : 28 Sept 2023

MetaSensing BV  
Schipholweg 55  
2316 ZL Leiden , The Netherlands  
Tel: +31 71 751 5960  
Email: info@metasensing.com

<b>Document change log</b>			
<b>Issue</b>	<b>Change</b>	<b>Date</b>	<b>Author</b>
1.0	First issue	30/08/2023	KM
2.0	Plots added and Review, First Release	28/09/2023	KM

Project: SeaSTARex

Title: D2: Analysis of the OSCARPOD and Antenna Characterization

Ref: MS-SeaSTARex-OSCARPOD

---



# Table of contents

1	Introduction .....	5
2	Methodology.....	6
3	Analysis .....	8
4	Conclusions .....	25
5	References .....	26

# 1 Introduction

This document describes the analysis of the OSCAR antenna patterns when enclosed by the radome to quantify the effects of the radome in the OSCAR data [1]. The OSCAR radome is designed as a pod installed under the aircraft platform used for the OSCAR mission as shown in Figure 1.

The analysis of the OSCAR pod is based on the data obtained during the Hertz campaign. This campaign consists of OSCAR antenna measurements with and without radome in an anechoic chamber in the premises of the European Space Agency (ESA/ESTEC) in Noordwijk, The Netherlands. [2].



Figure 1: Radome hosting the OSCAR system

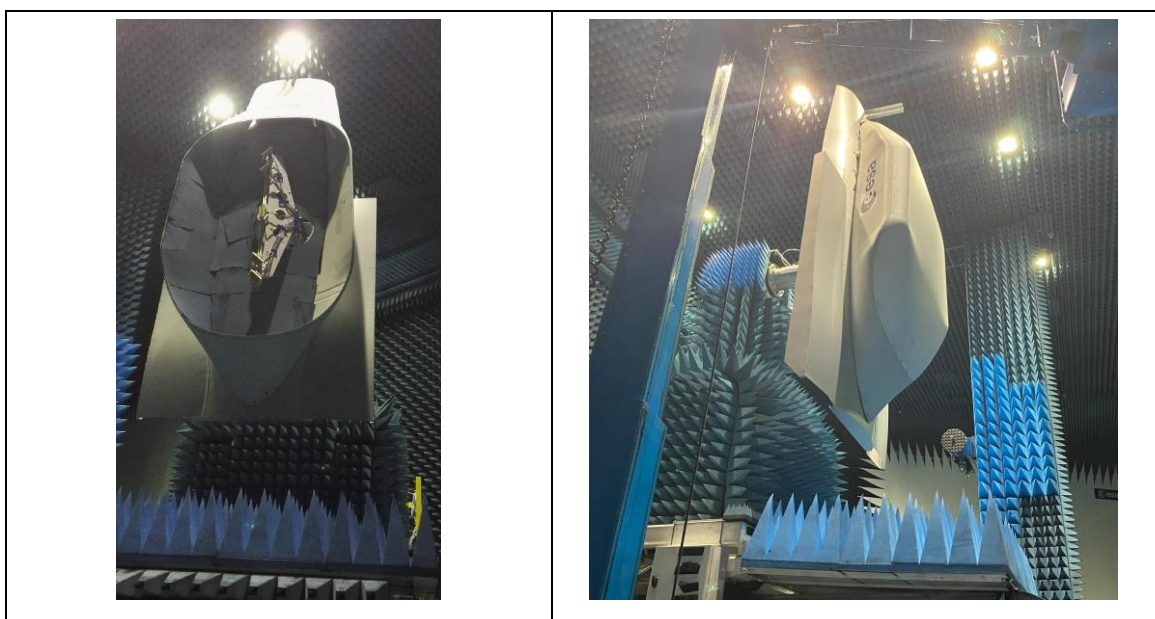


Figure 2: OSCAR radome characterization at ESA-Estec, Noordwijk, The Netherlands



## 2 Methodology

The OSCAR system consists of 5 dual-pol (H and V) antennas. The first 2 antennas form an interferometric pair and are pointing with squint angle of 45 degrees and are called FORE-M (master) and FORE-S (slave). Another interferometric pair consists of 2 antennas pointing to -45 degrees and are called AFT-M and AFT-S. And one single antenna point perpendicular to the nominal flight direction, i.e zero Doppler direction, and it is called 0-DOP antenna. Figure 3 shows a picture of the OSCAR antenna configuration and Table 1 summarizes the antennas point angles.

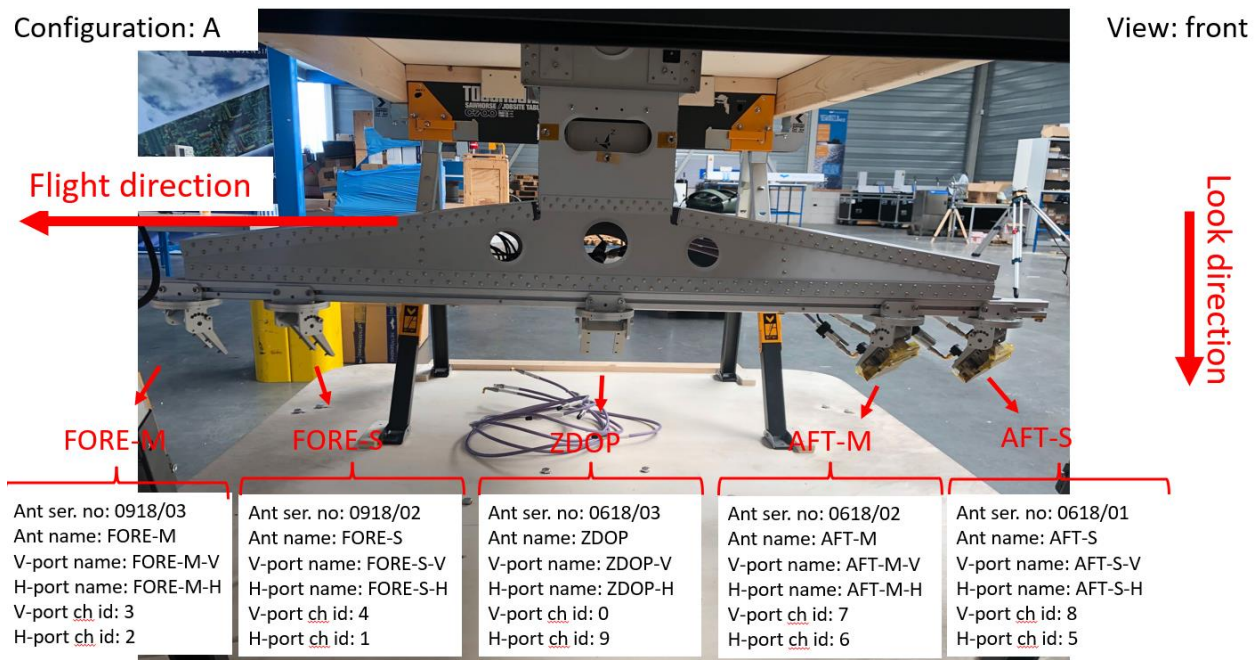


Figure 3: Anttenas of the OSCAR system

Table 1: OSCAR antenna rotation and naming

Antenna name	Angle description	Angle value
<b>AFT-M and AFT-S</b>	Look angle (antenna broadside pointing) from nadir	48°
	Azimuth rotation	-45°
<b>FORE-M and FORE-S</b>	Look angle (antenna broadside pointing) from nadir	48°
	Azimuth rotation	+45°
<b>0-DOP</b>	Look angle (antenna broadside pointing) from nadir	43°
	Azimuth rotation	0°

During the Hertz campaign, the antenna diagrams (VV) were measured in a Spherical Near Field configuration and mounted on the AUT positioner (Figure 2). The antennas were subjected to 5 different yaw, roll, pitch positions to cover the whole movement that the gimbal typically, based on Brest camping data [3], can undergo during the flights, namely:

- Roll 1 deg Pitch 1 deg Yaw 1 deg, (R1P1Y1)
- Roll 0 deg Pitch 0 deg Yaw 10 deg (R0P0Y10)
- Roll 0 deg Pitch 0 deg Yaw -10 deg (R0P0Y-10)
- Roll -10 deg Pitch 0 deg Yaw 0 deg (R-10P0Y0)
- Roll -10 deg Pitch 0 deg Yaw -10 deg (R-10P0Y-10)

The 0-Doppler antennas have been measured only for the nominal configuration: - Roll 1 Pitch 1 Yaw 1 (R1P1Y1).

The data delivered from the Hertz campaign are the gain and phase of the radiation pattern for all five positions described above with and without radome.

Based on the delivered data the differences in terms of gain and interferometric phase between the antenna pattern with radome and without are derived. These differential gains and the interferometric phases corresponds to the effects of the radome in the backscatter images ( $\sigma_0$ ) and interferograms generated by the OSCAR system.

### 3 Analysis

The figures below show the antenna diagram with and without radome for 0-Doppler and FORE Master and Slave antennas diagram (azimuth and elevation) and for all positioner configurations. The AFT Master and Slave antennas behave the same as the FORE antennas and therefore we do not show the plots. We can observe that the gain difference is negligible and below the required radiometric accuracy for OSCAR [1].

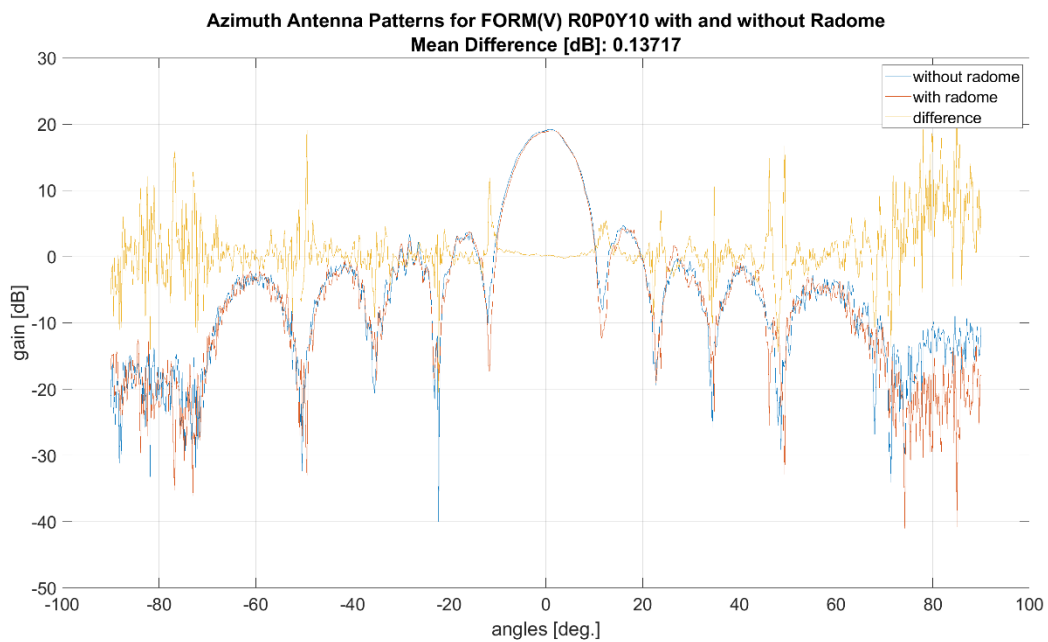


Figure 4: FORE Master Azimuth antenna Diagram for Roll 0 deg Pitch 0 deg Yaw 10 deg.

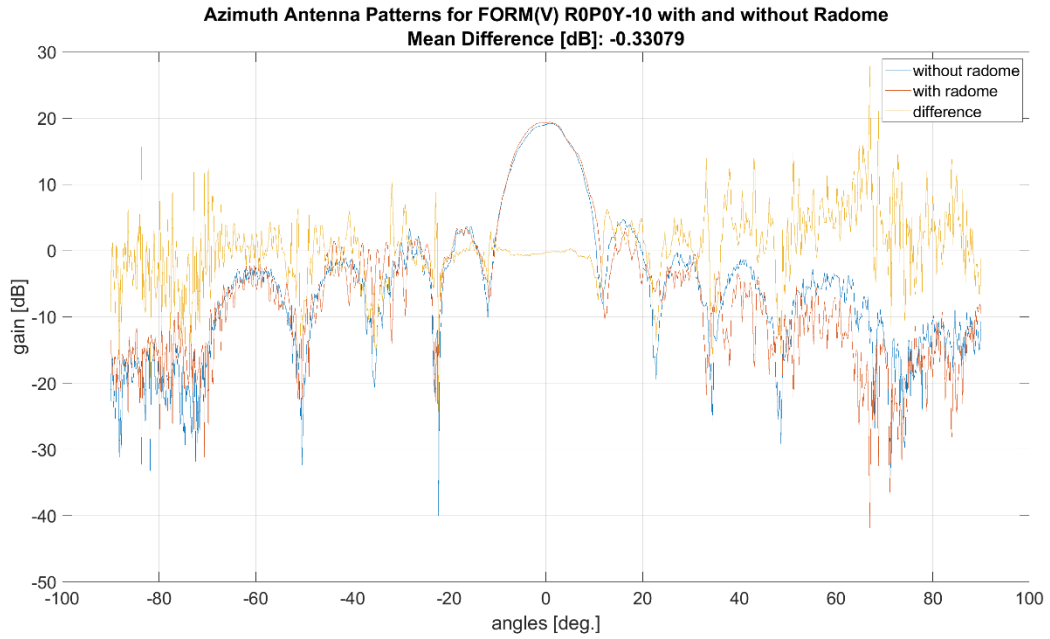


Figure 5: FORE Master Azimuth antenna Diagram for Roll 0 deg Pitch 0 deg Yaw -10 deg.

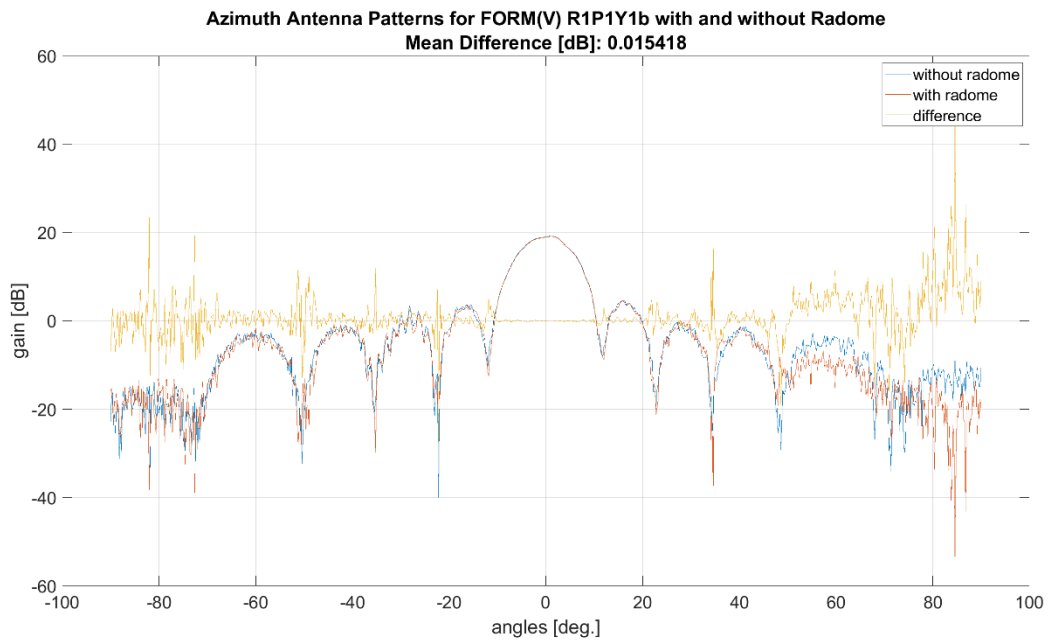


Figure 6: FORE Master Azimuth antenna Diagram for Roll 1 deg Pitch 1 deg Yaw 1 deg.

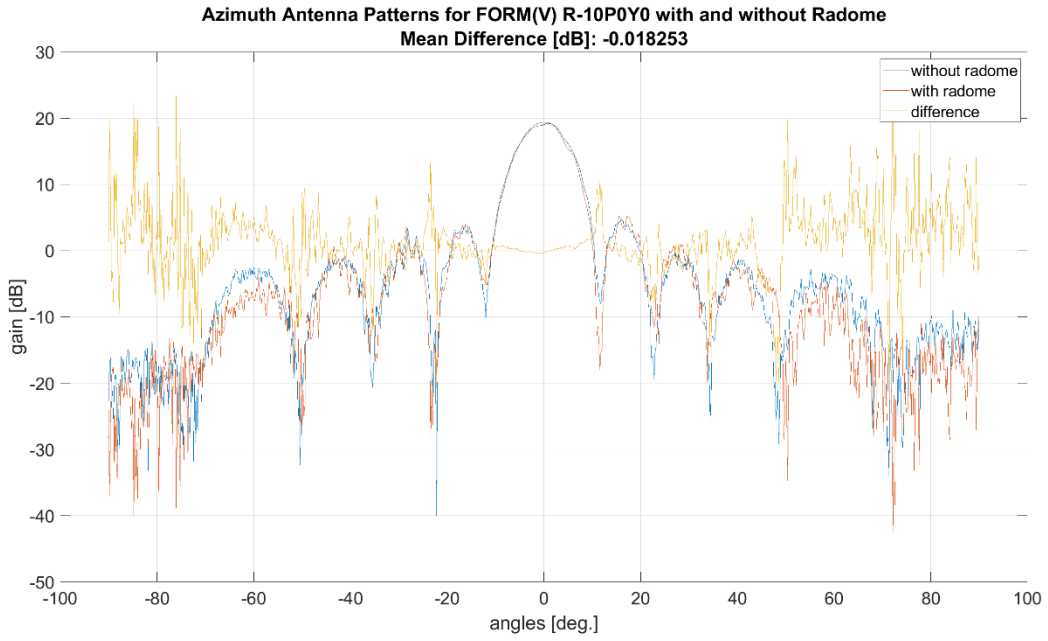


Figure 7: FORE Master Azimuth antenna Diagram for Roll -10 deg Pitch 0 deg Yaw 0 deg.

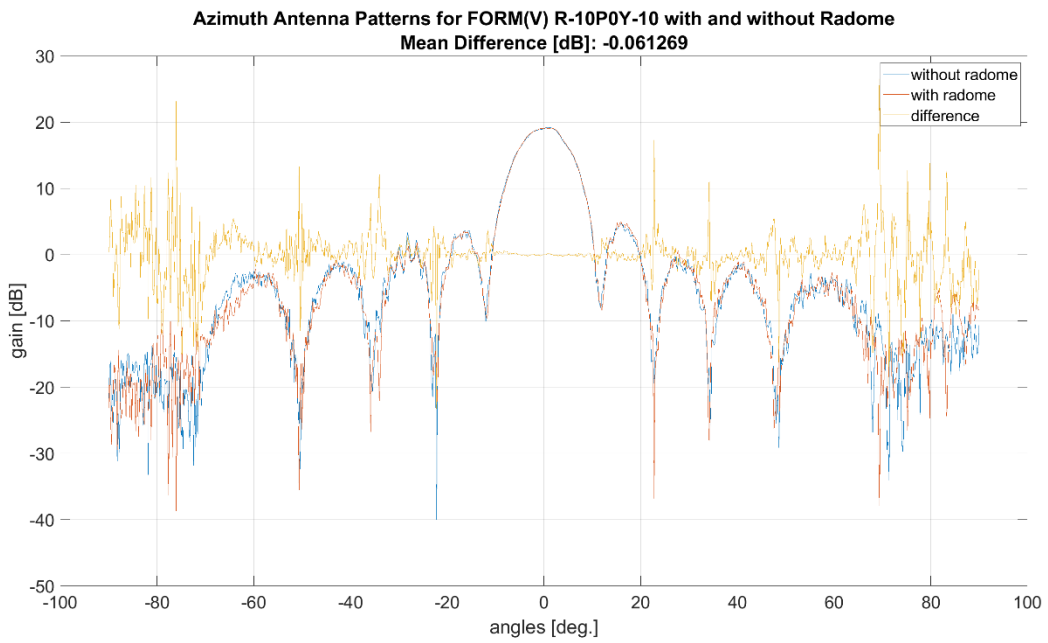


Figure 8: FORE Master Azimuth antenna Diagram for Roll -10 deg Pitch 0 deg Yaw -10 deg.

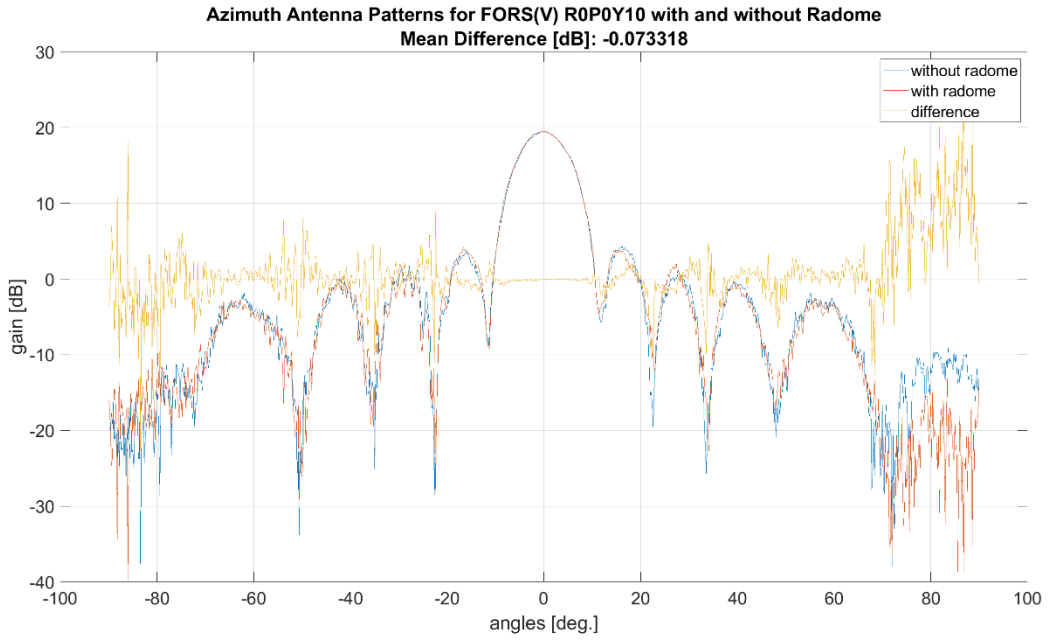


Figure 9: FORE Slave Azimuth antenna Diagram for Roll 0 deg Pitch 0 deg Yaw 10 deg.

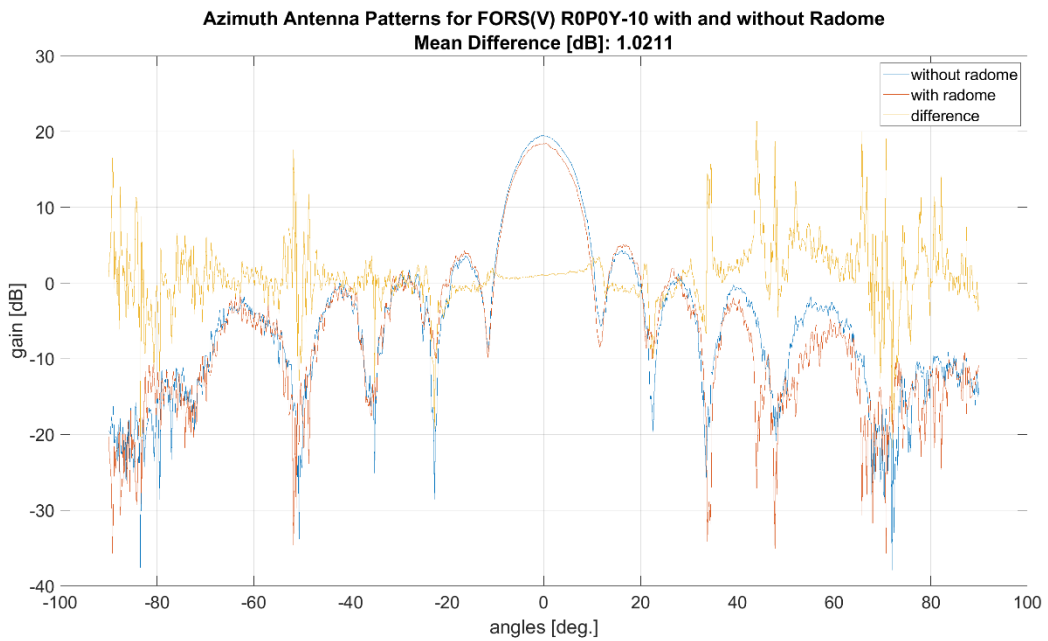


Figure 10: FORE Slave Azimuth antenna Diagram for Roll 0 deg Pitch 0 deg Yaw -10 deg.



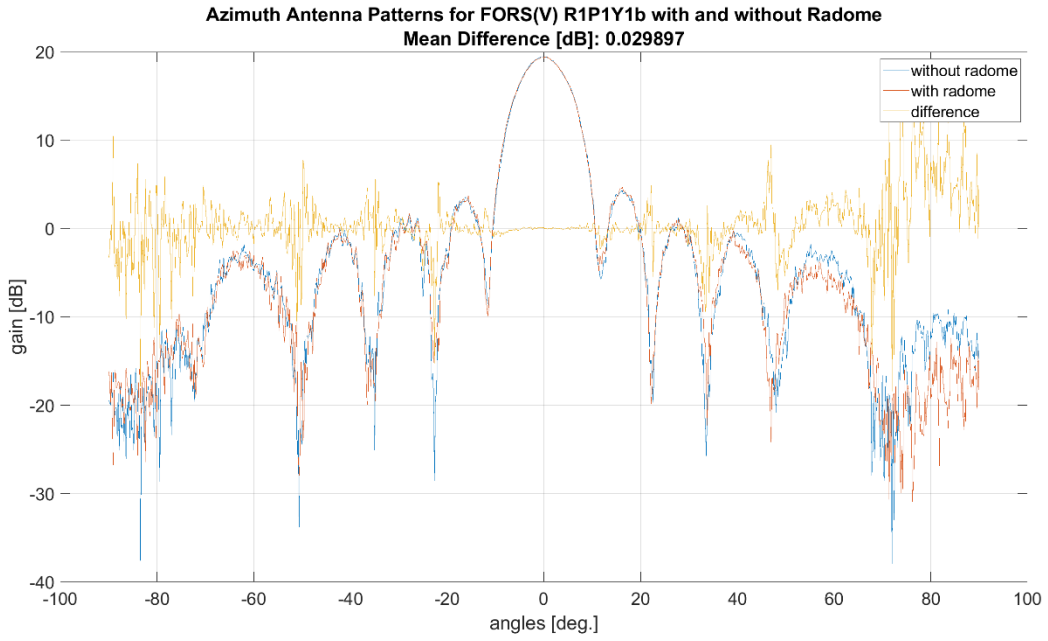


Figure 11: FORE Slave Azimuth antenna Diagram for Roll 1 deg Pitch 1 deg Yaw 1 deg.

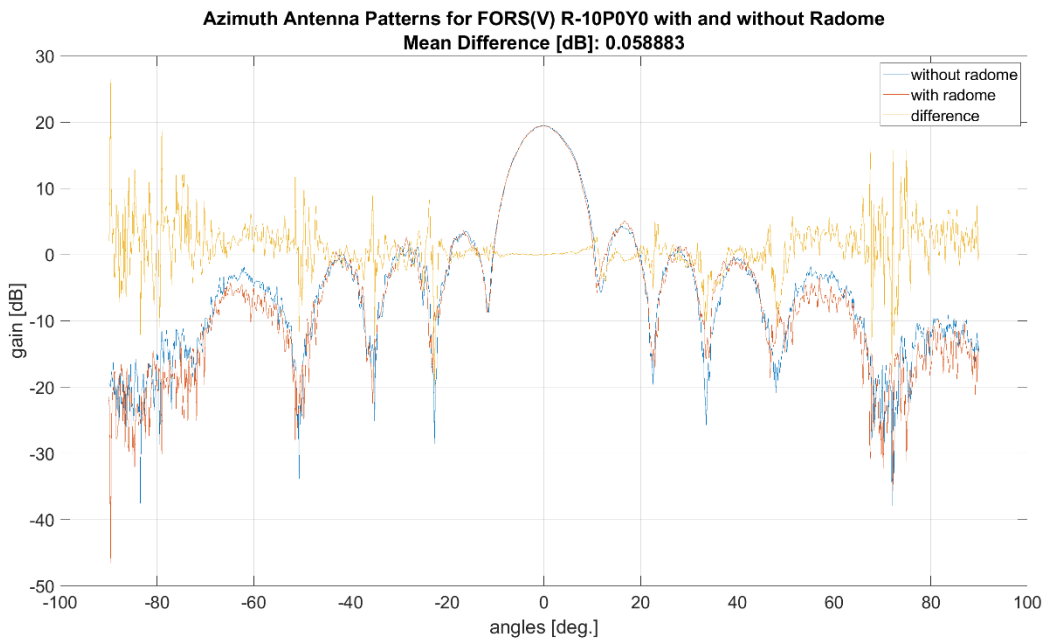


Figure 12: FORE Slave Azimuth antenna Diagram for Roll -10 deg Pitch 0 deg Yaw 0 deg.

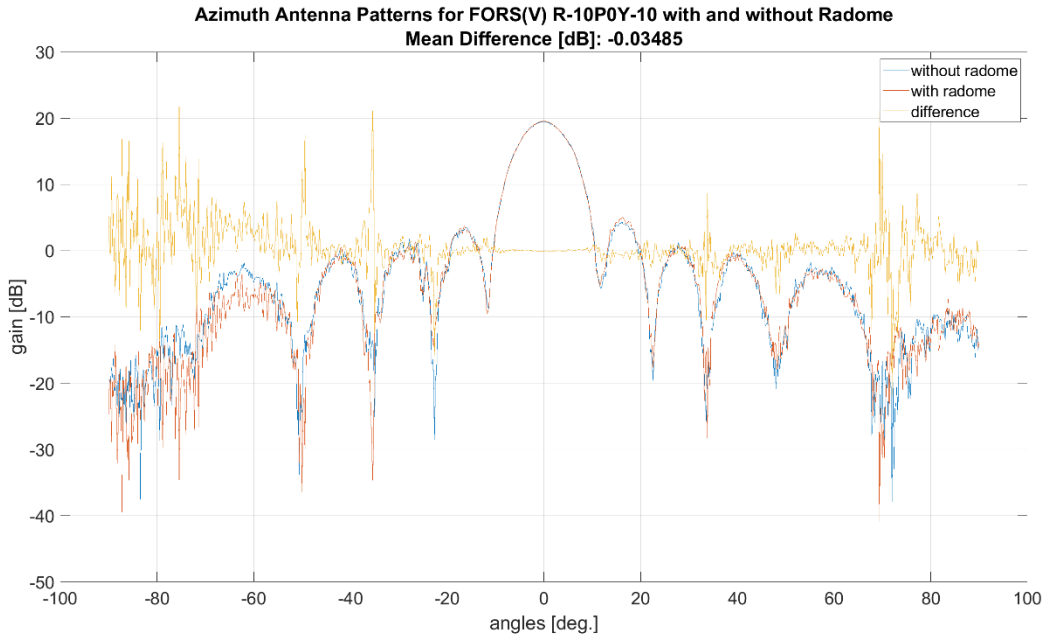


Figure 13: FORE Slave Azimuth antenna Diagram for Roll -10 deg Pitch 0 deg Yaw -10 deg.

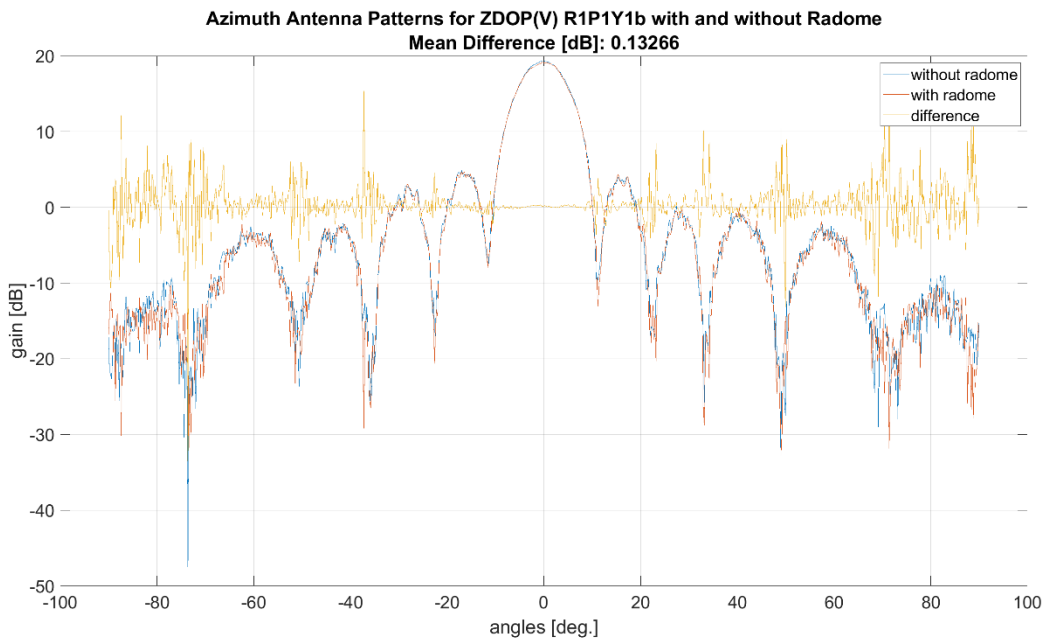


Figure 14: Zero-Doppler Azimuth antenna Diagram for Roll 1 deg Pitch 1 deg Yaw 1 deg.

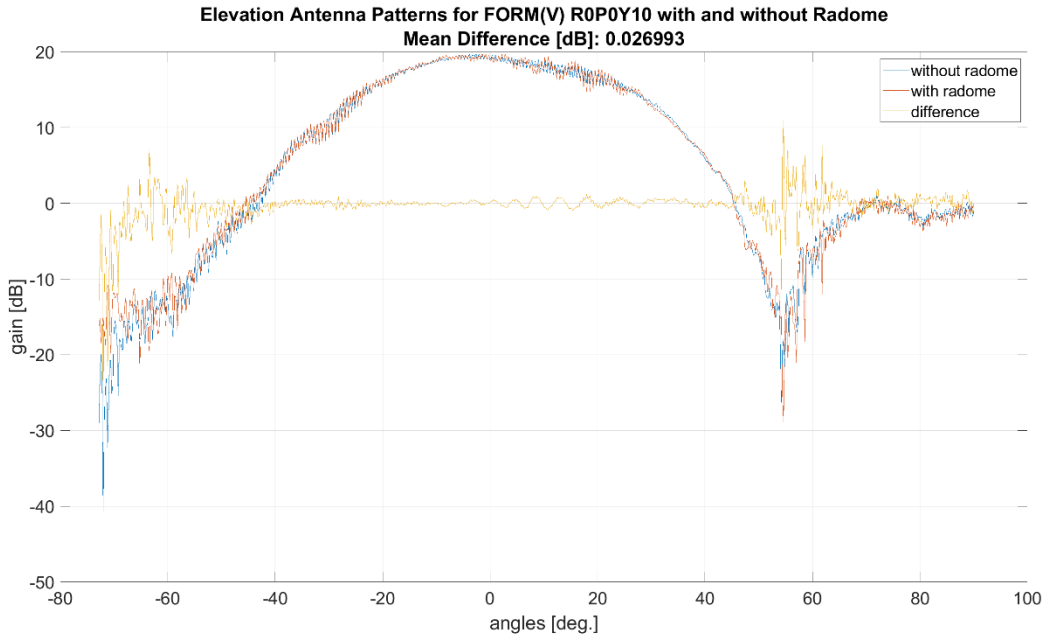


Figure 15: FORE Master Elevation antenna Diagram for Roll 0 deg Pitch 0 deg Yaw 10 deg.

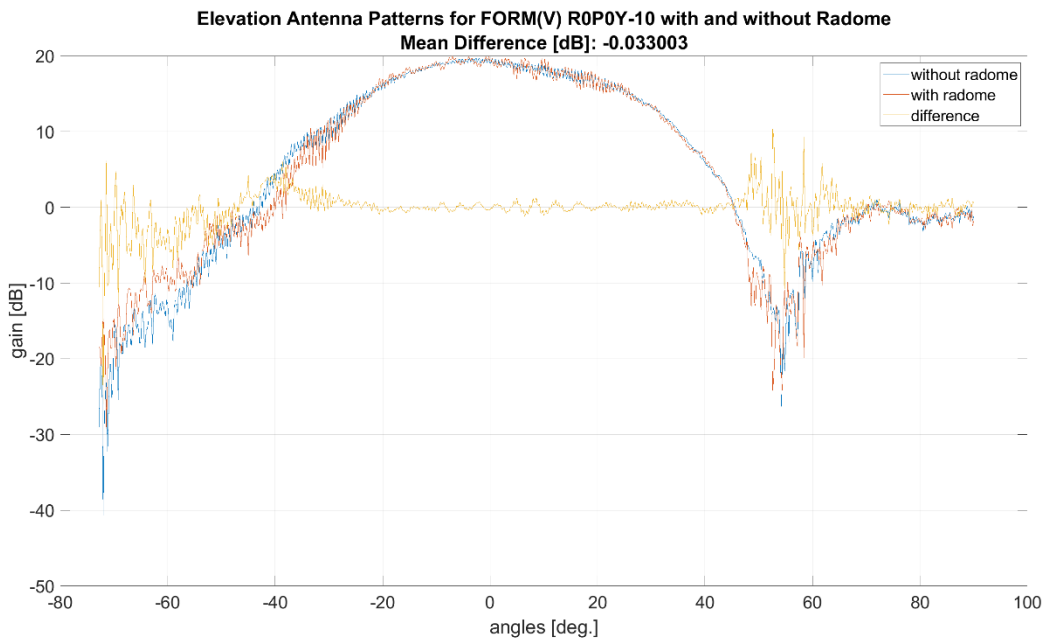


Figure 16: FORE Master Elevation antenna Diagram for Roll 0 deg Pitch 0 deg Yaw -10 deg.

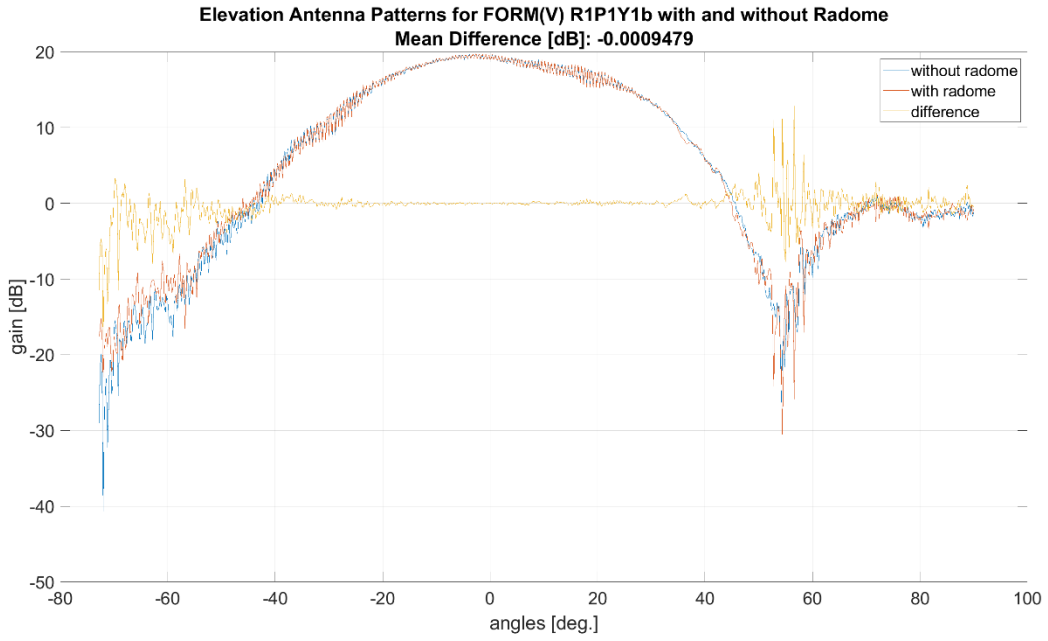


Figure 17: FORE Master Elevation antenna Diagram for Roll 1 deg Pitch 1 deg Yaw 1 deg.

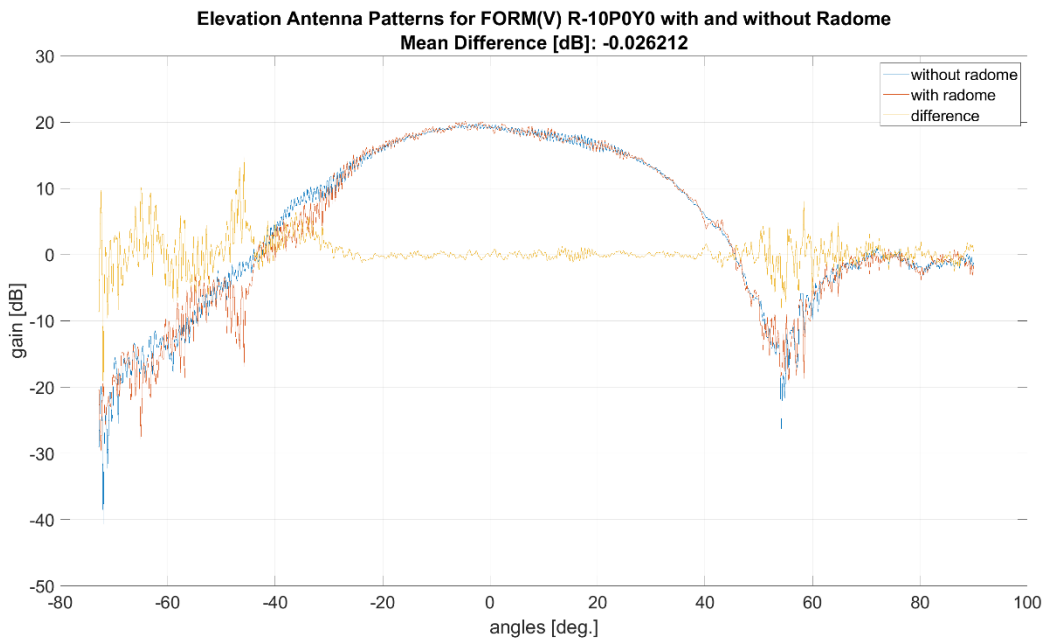


Figure 18: FORE Master Elevation antenna Diagram for Roll -10 deg Pitch 0 deg Yaw 0 deg.

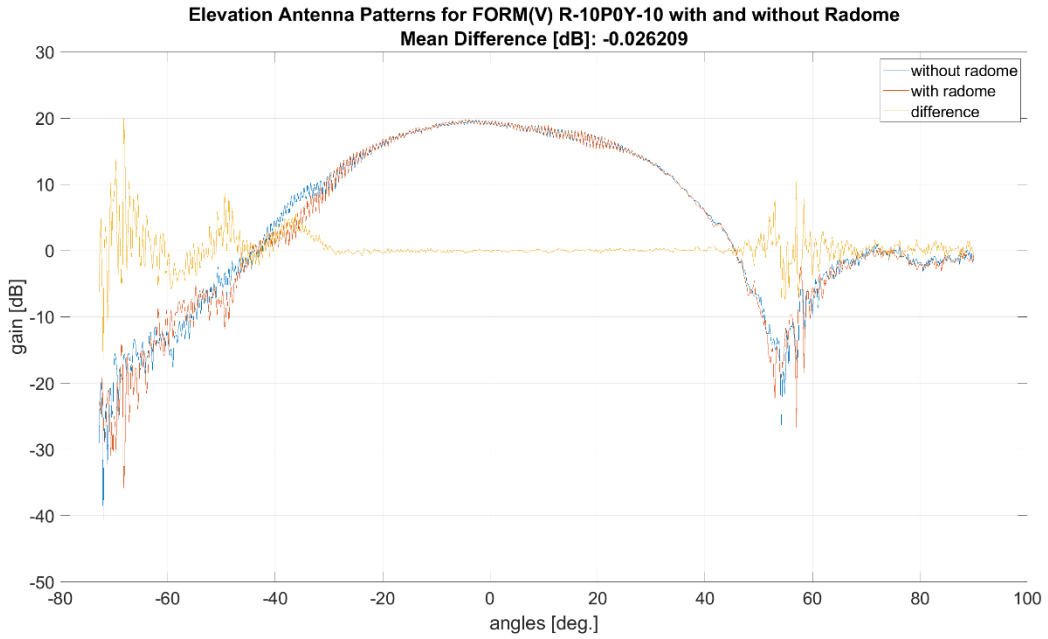


Figure 19: FORE Master Elevation antenna Diagram for Roll -10 deg Pitch 0 deg Yaw -10 deg.

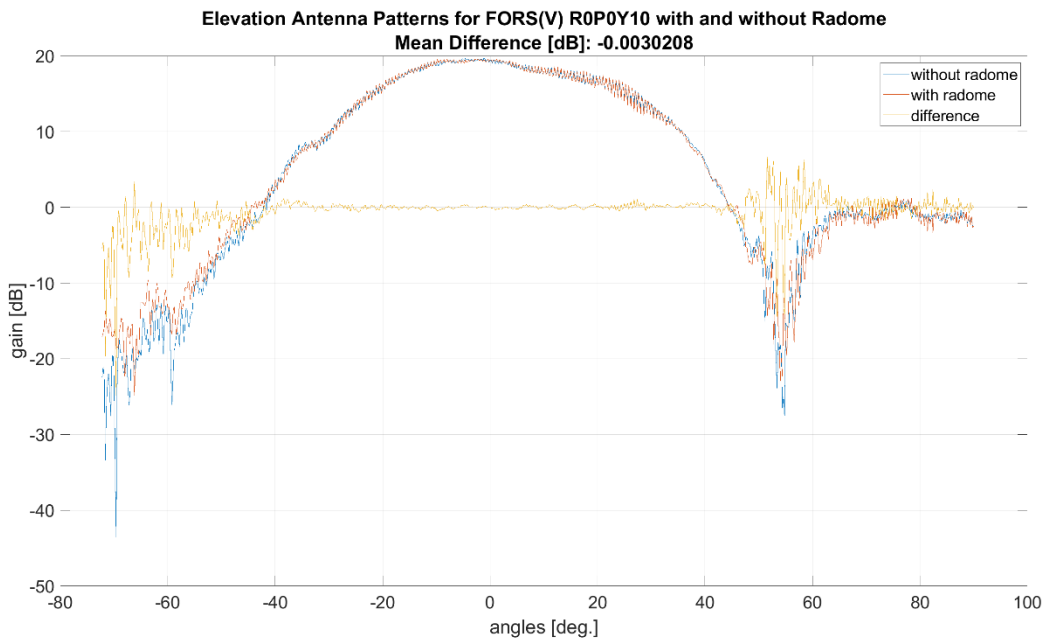


Figure 20: FORE Slave Elevation antenna Diagram for Roll 0 deg Pitch 0 deg Yaw 10 deg.

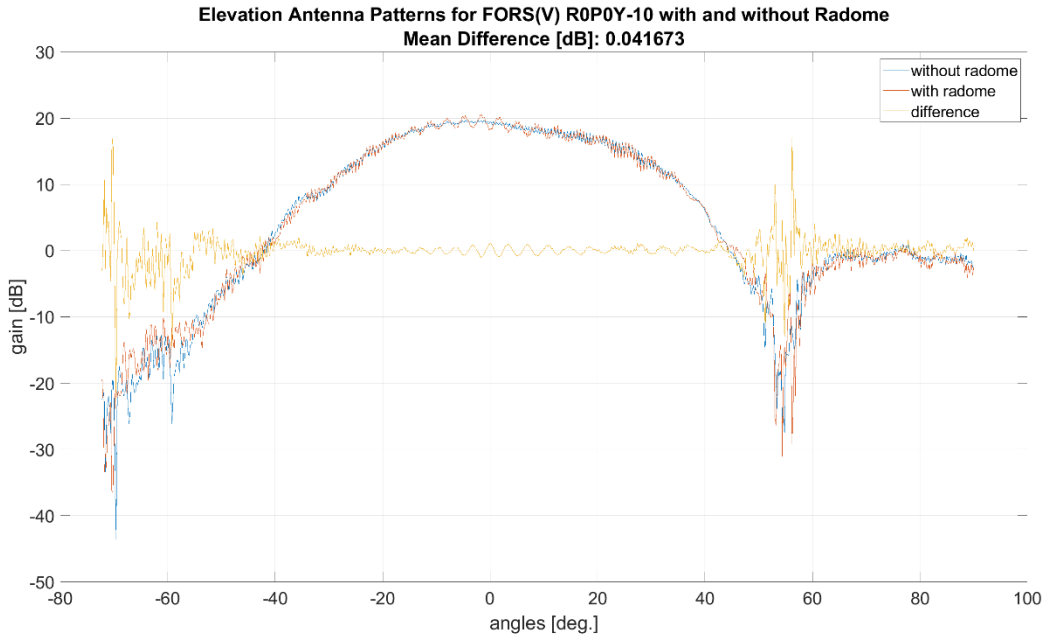


Figure 21: FORE Slave Elevation antenna Diagram for Roll 0 deg Pitch 0 deg Yaw -10 deg.

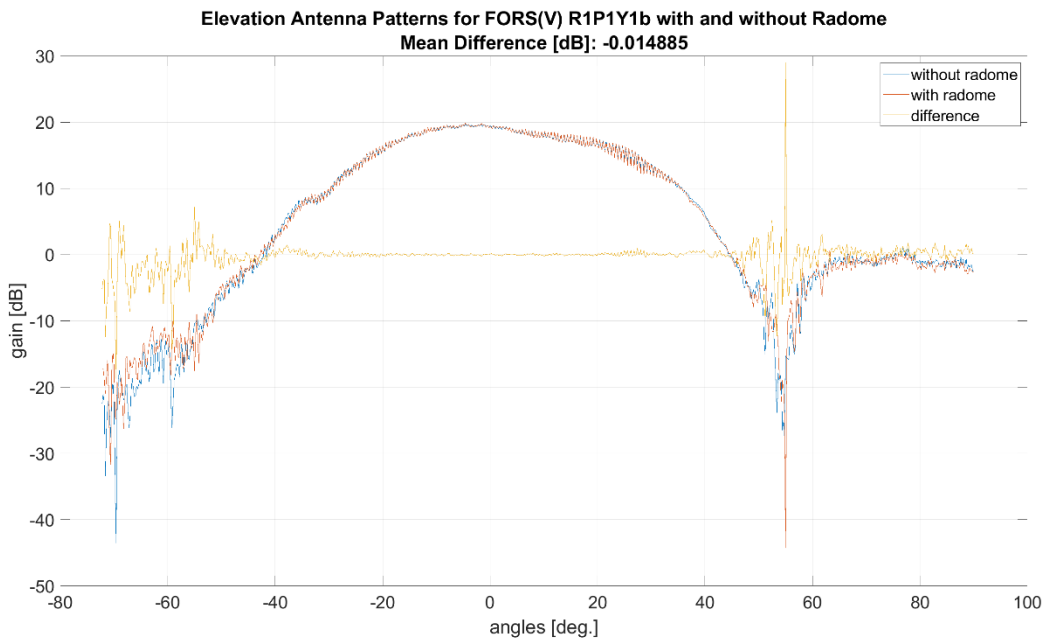


Figure 22: FORE Slaver Elevation antenna Diagram for Roll 1 deg Pitch 1 deg Yaw 1 deg.

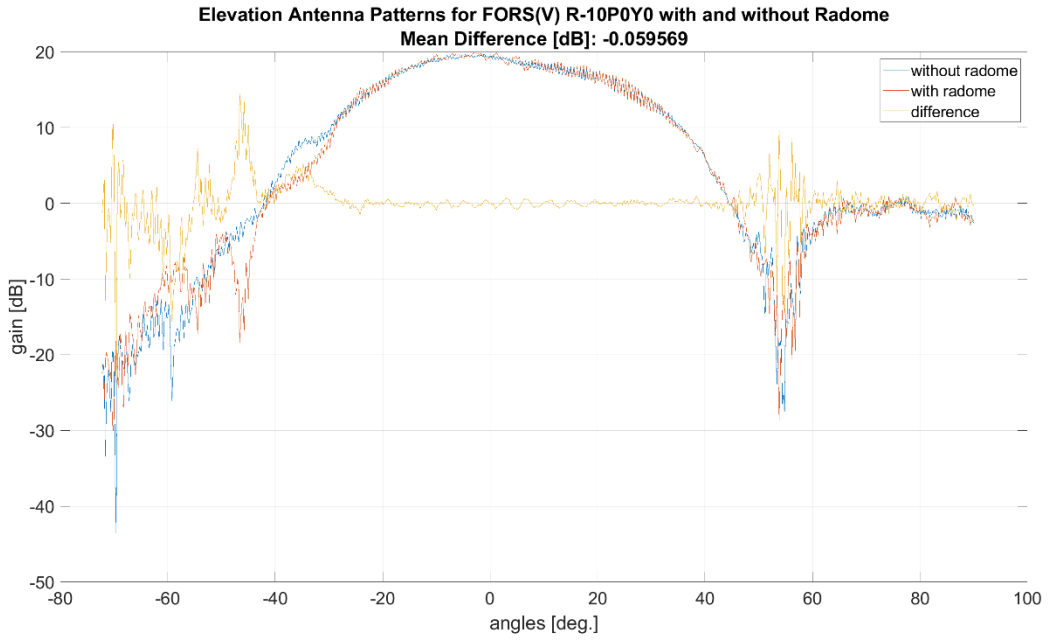


Figure 23: FORE Slave Elevation antenna Diagram for Roll -10 deg Pitch 0 deg Yaw 0 deg.

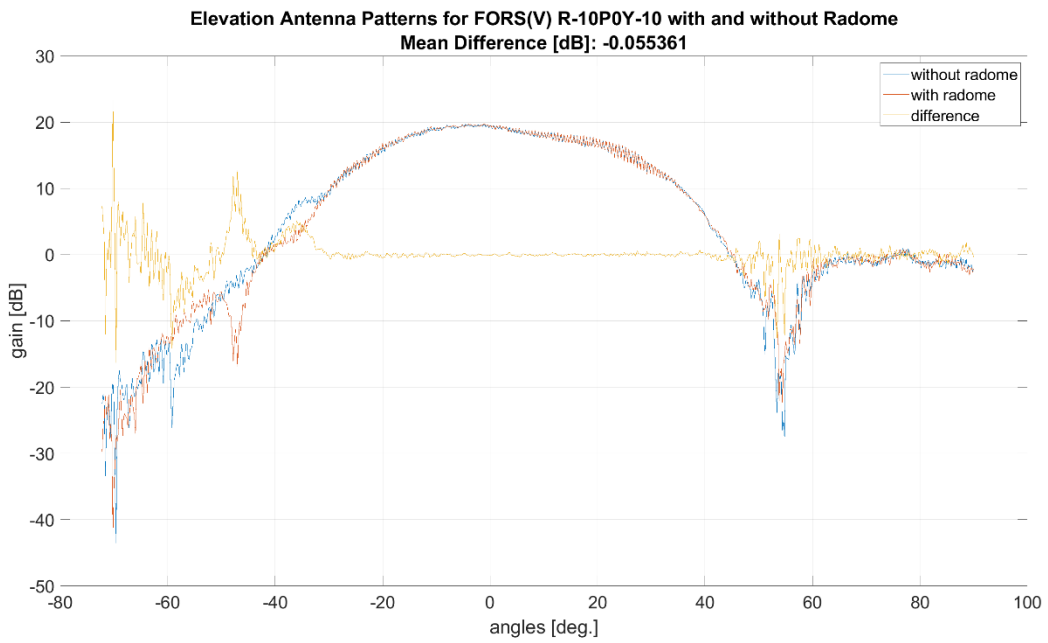


Figure 24: FORE Slave Elevation antenna Diagram for Roll -10 deg Pitch 0 deg Yaw 10 deg.



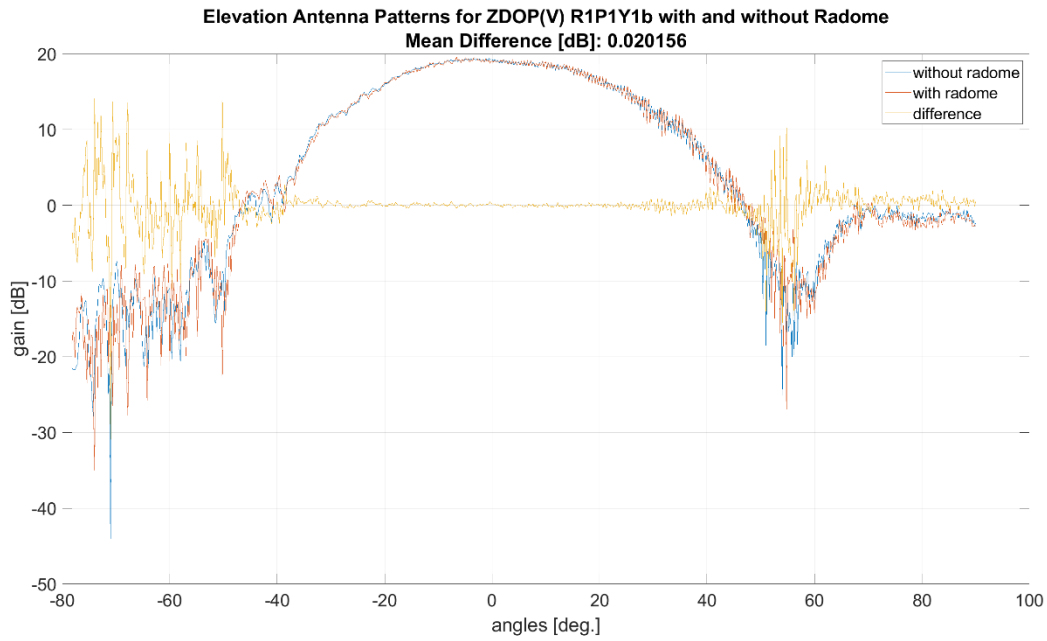


Figure 25: Zero-Doppler Elevation antenna Diagram for Roll 1 deg Pitch 1 deg Yaw 1 deg.

The next figures below show the interferometric phase, induced by the radome, obtained using the master and slave antenna diagrams in elevation and azimuth, zoomed-in within the antenna main lobe. The plots show that the induced phase in the main lobe is within  $1^{\circ}$  variation, which is below the required accuracy of 2.5 deg ATI to have 5m/s vel. err., for the OSCAR system

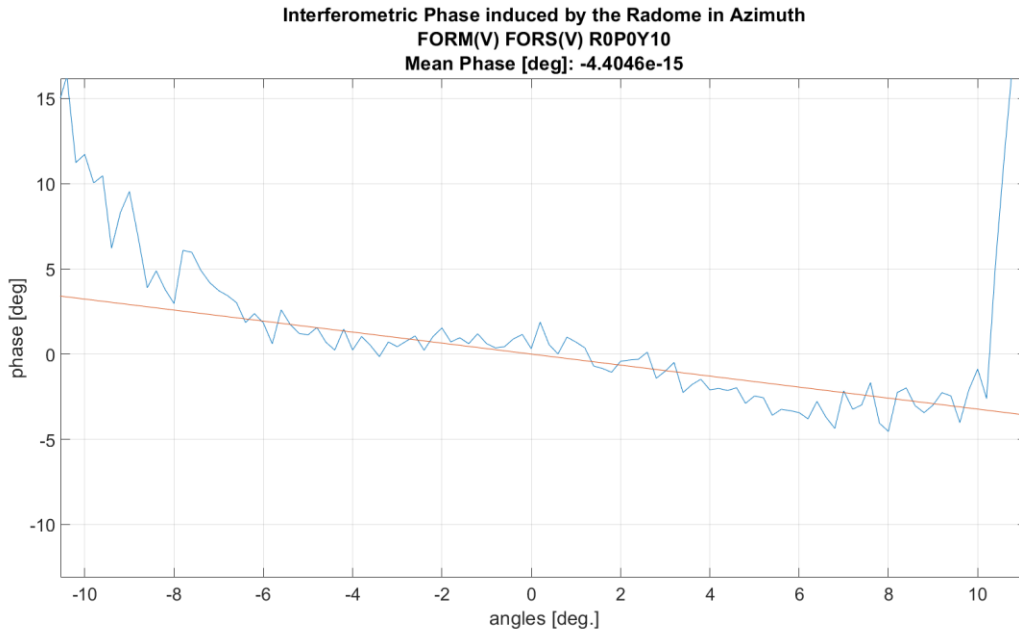


Figure 26: FORE induced interferometric phase in azimuth for Roll 0 deg Pitch 0 deg Yaw 10 deg.

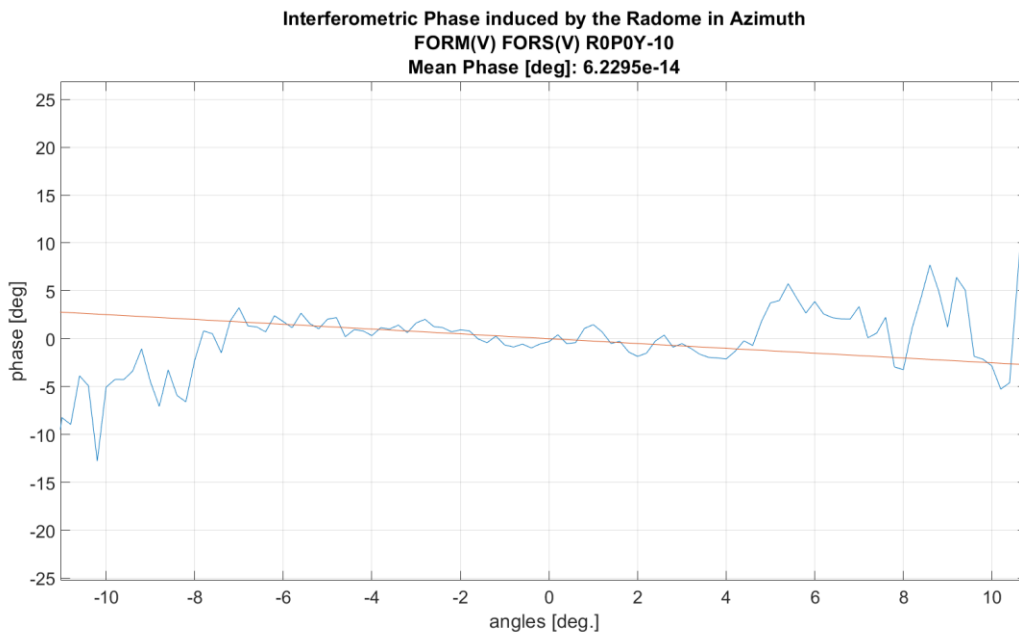


Figure 27: FORE induced interferometric phase in azimuth for Roll 0 deg Pitch 0 deg Yaw -10 deg.

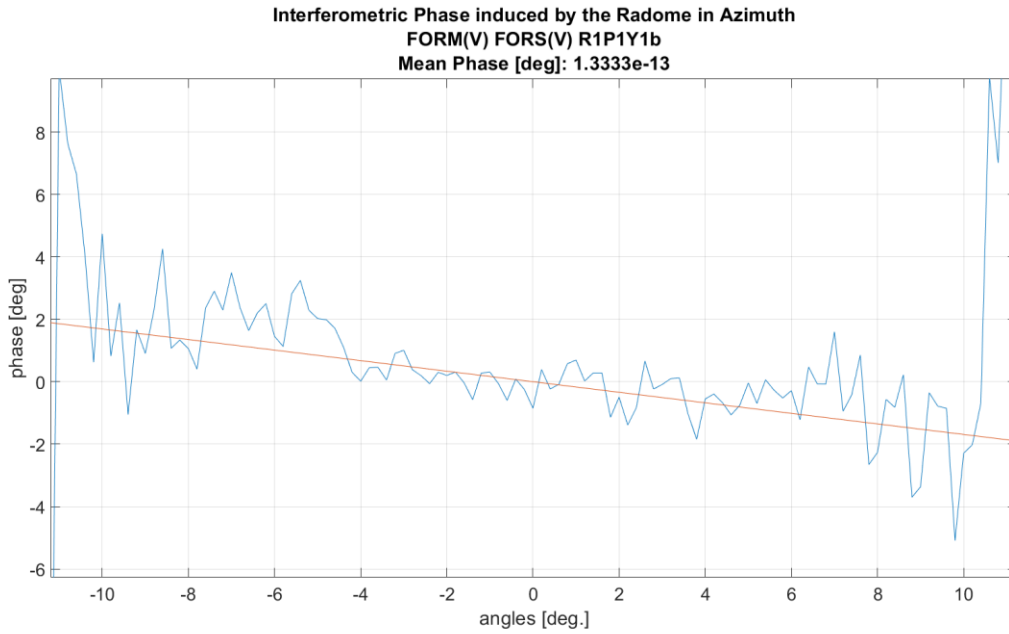


Figure 28: FORE induced interferometric phase in azimuth for Roll 1 deg Pitch 1 deg Yaw 1 deg.

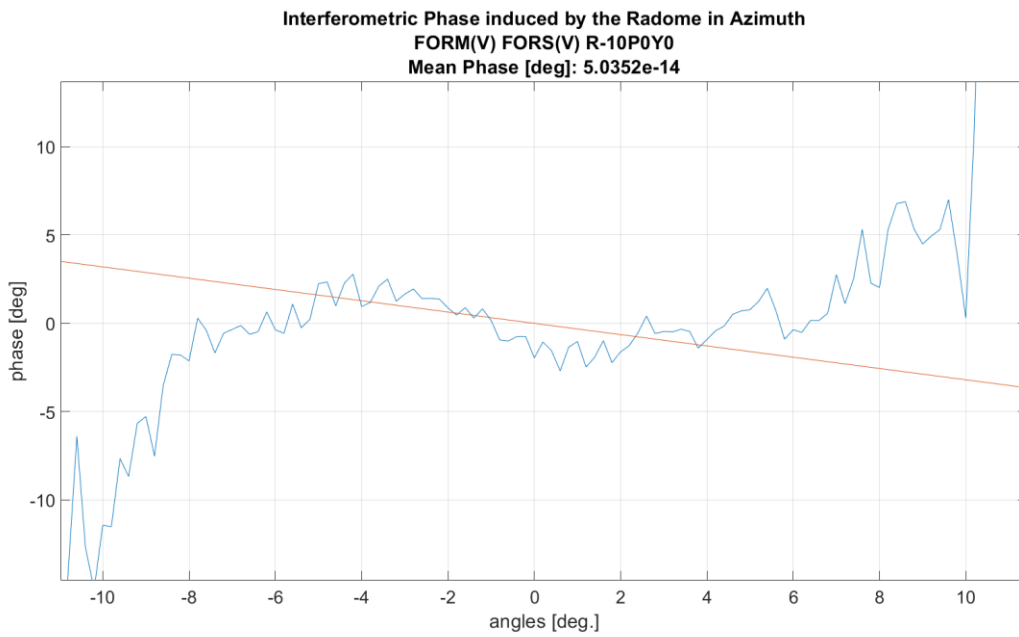


Figure 29: FORE induced interferometric phase in azimuth for Roll -10 deg Pitch 0 deg Yaw 0 deg.

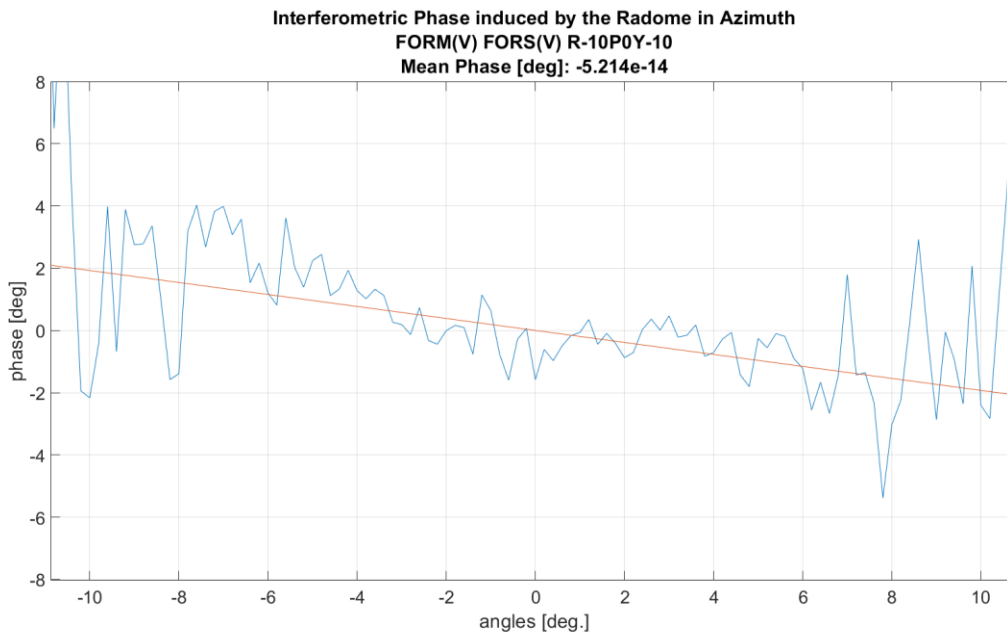


Figure 30: FORE induced interferometric phase in azimuth for Roll -10 deg Pitch 0 deg Yaw -10 deg.

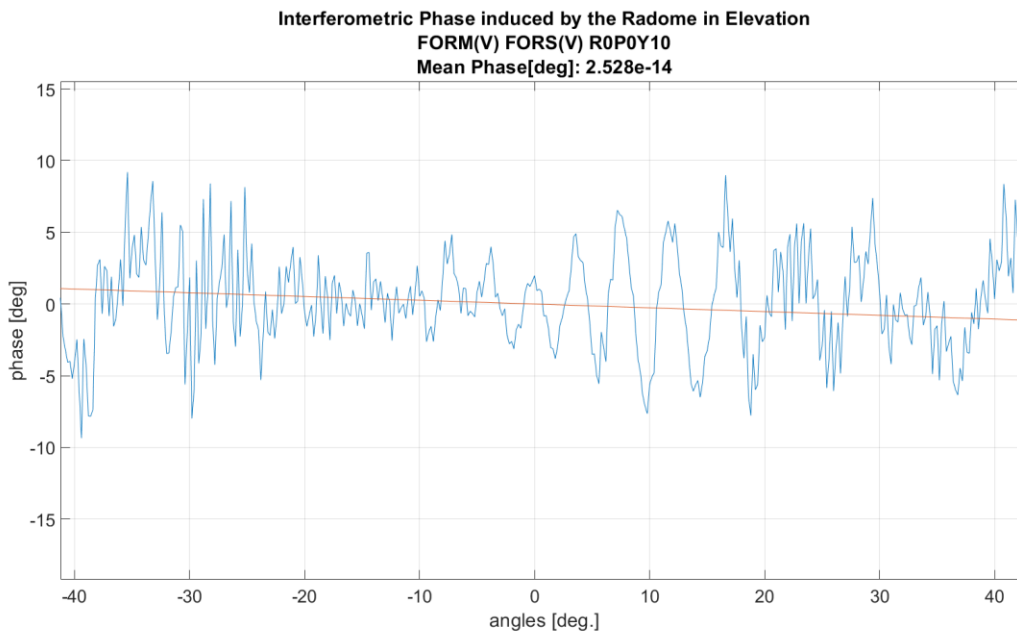


Figure 31: FORE induced interferometric phase in elevation for Roll 0 deg Pitch 0 deg Yaw 10 deg.

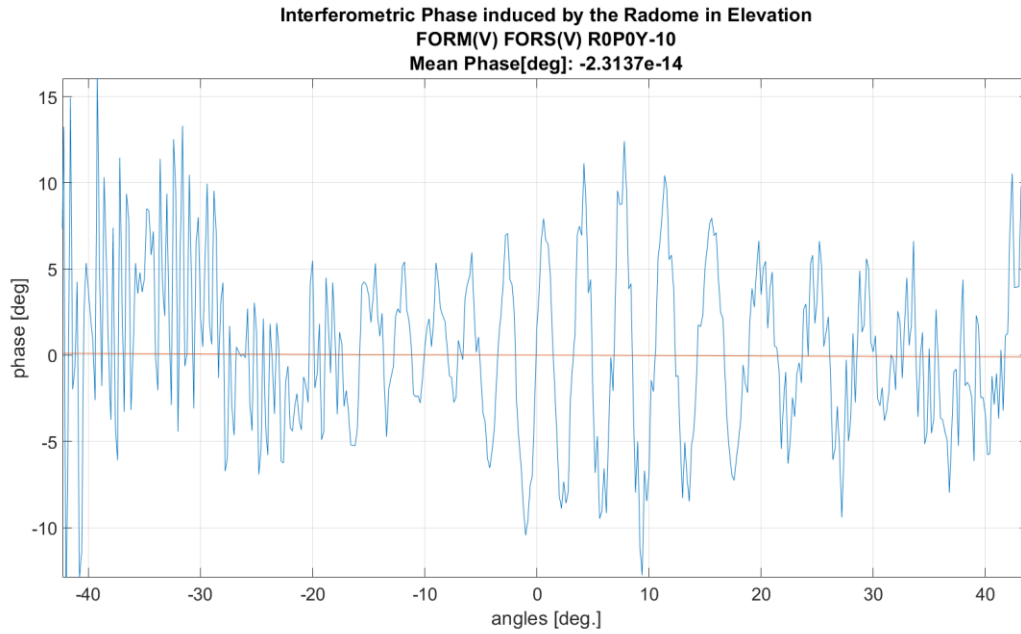


Figure 32: FORE induced interferometric phase in elevation for Roll 0 deg Pitch 0 deg Yaw -10 deg.

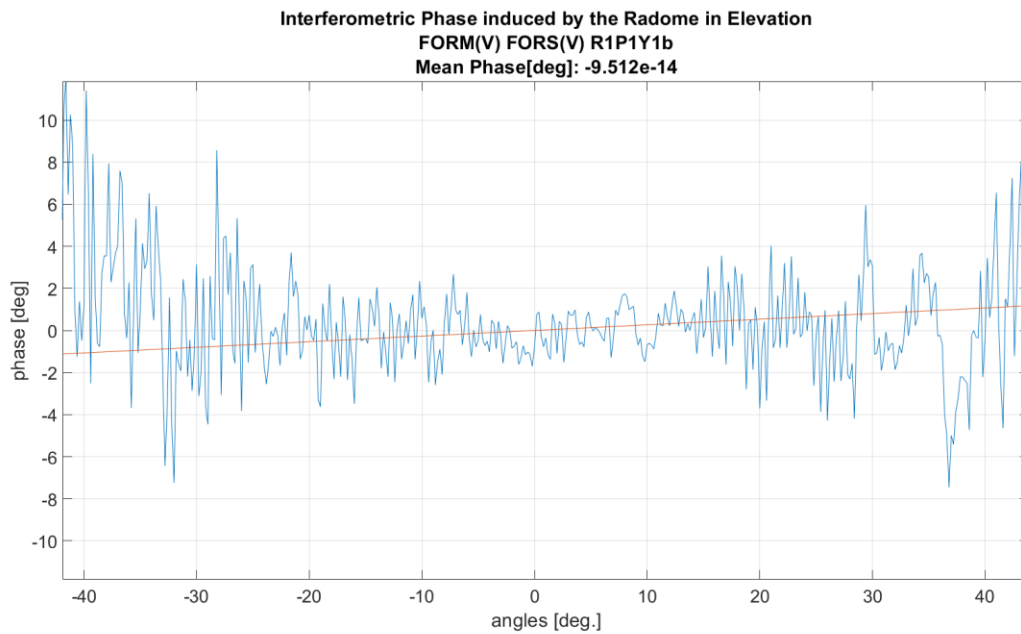


Figure 33: FORE induced interferometric phase in elevation for Roll 1 deg Pitch 1 deg Yaw 1 deg.

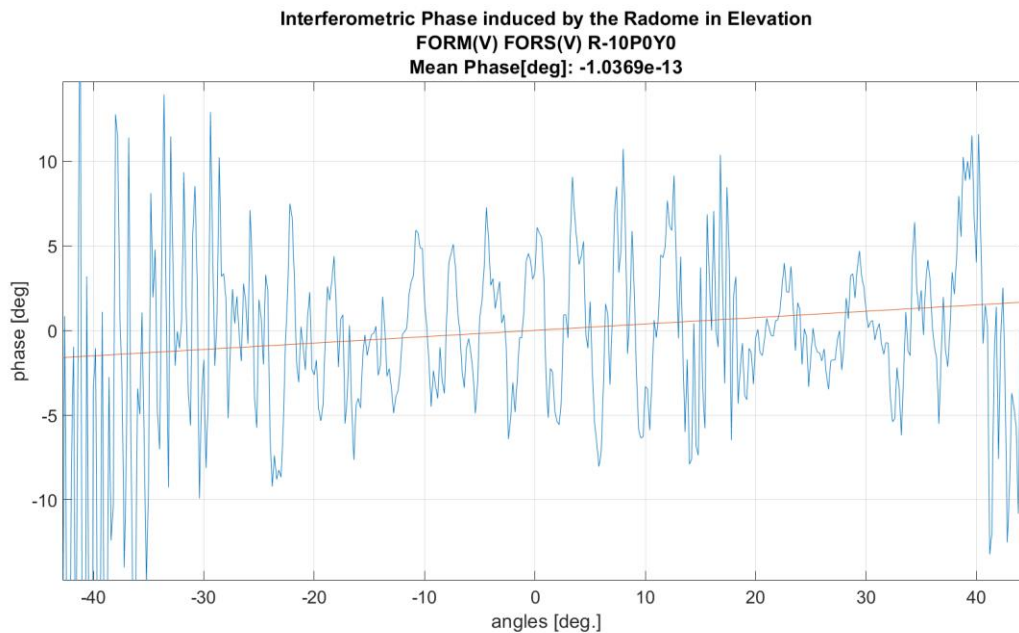


Figure 34: FORE induced interferometric phase in elevation for Roll -10 deg Pitch 0 deg Yaw 0 deg.

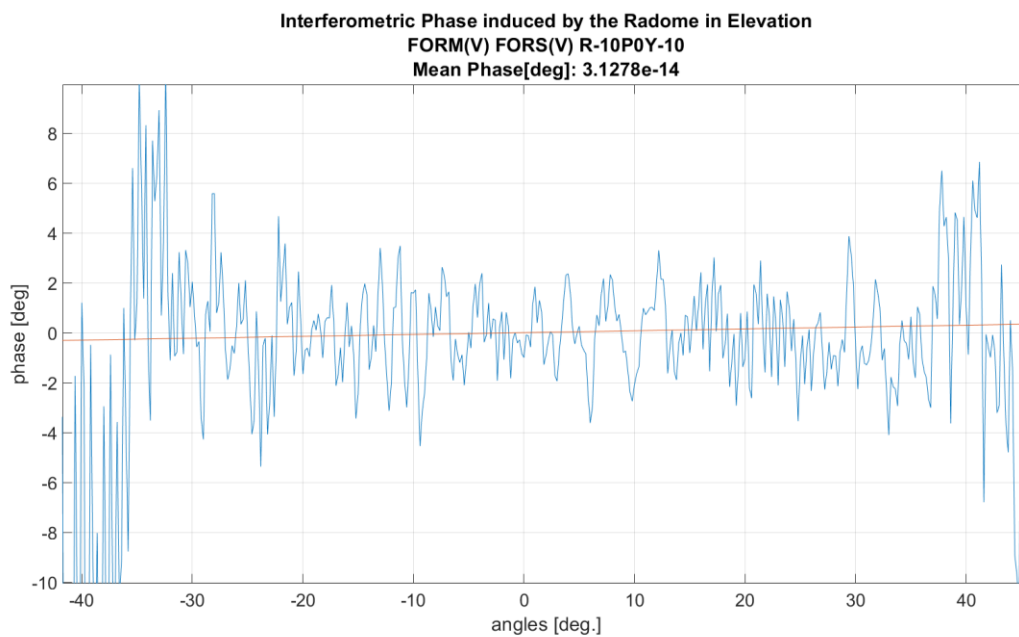


Figure 35: FORE induced interferometric phase in elevation for Roll -10 deg Pitch 0 deg Yaw -10 deg.

## 4 Conclusions

This document shows that the effect of the radome on the OSCAR data is negligible. It is less than 0.1 dB radiometric and less than 1 deg. interferometric phase. While the achievable radiometric accuracy is in the order of 0.5 dB and the ATI phase standard deviation is 2.5 deg, which implies in 5cm/s vel. err as required.

The above has been demonstrated through antenna, with and without radome, measurements under controlled environment, i.e an anechoic chamber in the premises of the European Space Agency (ESA/ESTEC).

The results presented here are in-line with OSCAR SAR data obtained during the SeaSTARex campaign flights. The radiometric and interferometric data derived from those operational flights are within the OSCAR project requirements and campaign desired accuracy and no further undesired effect related to the radome can be observed, demonstrating that the radome distortions if exist are below the required/desired accuracy for the OSCAR system [4].



---

## 5 References

[1] Ocean Surface Current Airborne Radar Demonstrator (OSCAR) – Statement of Work, Appendix 1 to AO/1- 8309/15/NL/BJ.

[2] I. Barbary, “OSCAR 2022 – Test Results (Hertz).” ESA-TECEFA-TR-2022-002759.” 20 Sept. 2022.

[3] MetaSensing SeaSTARex: Data Acquisition Report. MS-SeaSTARex-DAR\_v7.

[4] MetaSensing SeaSTARex: Analysis of External Calibration Results Including Baselines Errors. MS-SEASTAREx-ExtCal\_V1.0.

# **ANNEX B) DATA ACQUISITION REPORT: AIRBORNE DATA**

# SeaSTARex

## D9.1: Data Acquisition Report

**Reference Code** : : MS-SeaSTARex-DAR  
**Issue** : : 8.0  
**Date** : : 29 Feb 2024

MetaSensing BV  
Schipholweg 55  
2316 ZL Leiden , The Netherlands  
Tel: +31 71 751 5960  
Email: [info@metasensing.com](mailto:info@metasensing.com)

Document change log			
Issue	Change	Date	Author
1.0	First issue, system description, internal	07/06/2022	HK
2.0	Data description, table with list of Acquisition/deliverables inserted, Figure 2 updated, Corner reflector description, release	25/08/2022	KM
3.0	Including 17 may flights, picture of water in the radome and inclusion some observations/notes about the campaign	29/08/2022	KM
4.0	Update title, added text and chapters according to feedbacks	15/11/2022	KM
5.0	Added data analysis and Review of Final version	17/11/2022	KM
6.0	Final version after applying internal review	21/11/2022	KM
7.0	Added the list of names of the proceed SAR data	31/01/2023	KM
8.0	Writing in the acq. log the pow instability issues.	29/02/2024	KM



# Table of contents

1	Introduction .....	5
2	System setup .....	7
2.1	System installation.....	7
2.2	IMU installation.....	8
2.3	Antenna installation and lever arms.....	9
2.4	Lever arm of the GSM4000 center of rotation.....	11
2.5	Channels mapping .....	13
3	Corner reflectors .....	14
4	Radar Acquisitions .....	16
5	Results .....	22
5.1	Navigation Data .....	22
5.2	Radar Data .....	24
6	Conclusions .....	34
7	References .....	35

# 1 Introduction

This document is the Data Acquisition Report - DAR for the SeaSTARex airborne SAR data campaign. This DAR provides the details for the airborne SAR data collection with the OSCAR (Ocean Surface Current Airborne Radar) instrument over the Ocean next to Brest (France) and the data analysis. The data collection campaign was executed within the ESA-SeaSTARex project framework. Figure 1 shows the airborne platform used for this campaign. The OSCAR instrument is installed inside the aircraft belly pod, and it is fully operational [1, 2].

The OSCAR instrument is a gimbal-based interferometric Ku-band SAR system developed and built by MetaSensing within the framework of a European Space Agency funded project (Ocean Surface Currents Airborne Radar demonstrator). The OSCAR system is tailored to the observations of the ocean surface motion and retrieval of wind. The OSCAR demonstrator instrument is developed with the observation parameters which directly relate to a potential satellite mission (SeaSTAR) for mesoscale measurements of ocean surface currents in the open-ocean and coastal regions.

The airport base for the campaign was Morlaix - Brittany airport, where the aircraft equipped with the OSCAR system was parked in the hangar. However, on May 25<sup>th</sup> due to bad weather conditions the aircraft could not return to Morlaix airport and had to land and stay in Brest airport. Brest airport did not have a hangar available, hence the aircraft was parked outdoor for the whole night under rainy conditions.

Because of the rainy event during the night, with the aircraft parked outdoor, some water entered the radome/pod and it degraded the SNR in the Zero-Doppler beam on May 26<sup>th</sup>. However, the final SNR is still reasonably high, as shown in Figure 18.





*Figure 1: MetaSensing aircraft with the belly pod hosting the OSCAR system*

## 2 System setup

### 2.1 System installation

Figure 2 shows the OSCAR instrument installation from inside of the aircraft (a) and how the antennas are set-up inside the POD (b). Note that only V-pol channels were enabled during the SeaSTARex Brest campaign.



(a): the OSCAR instrument installed in the cabin

Configuration: A View: front

FORE-M	FORE-S	ZDOP	AFT-M	AFT-S
Ant ser. no: 0918/03 Ant name: FORE-M V-port name: FORE-M-V H-port name: FORE-M-H V-port ch id: 3 H-port ch id: 2	Ant ser. no: 0918/02 Ant name: FORE-S V-port name: FORE-S-V H-port name: FORE-S-H V-port ch id: 4 H-port ch id: 1	Ant ser. no: 0618/03 Ant name: ZDOP V-port name: ZDOP-V H-port name: ZDOP-H V-port ch id: 0 H-port ch id: 9	Ant ser. no: 0618/02 Ant name: AFT-M V-port name: AFT-M-V H-port name: AFT-M-H V-port ch id: 7 H-port ch id: 6	Ant ser. no: 0618/01 Ant name: AFT-S V-port name: AFT-S-V H-port name: AFT-S-H V-port ch id: 8 H-port ch id: 5

(b)

Figure 2: a) HW installation on-board the aircraft and (b) Antenna installation in the POD.

## 2.2 IMU installation

The x-axis of the IMU points towards the right wing of the plane, the y-axis points toward the nose of the plane (along-track forward-looking), and the z-axis points upward to the roof of the aircraft, forming the right-handed coordinate system reference (Figure 3).

The IMU orientation matches the one required by the OSCAR processor.

The definition of the vehicle frame is as follows:

- z-axis – points up through the roof of the vehicle perpendicular to the ground
- y-axis – points out the front of the vehicle in the direction of travel
- x-axis – completes the right-handed system (out the right-hand side of the vehicle when facing forward)

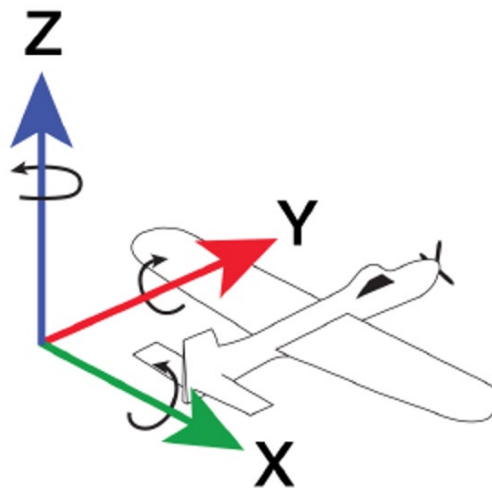


Figure 3: Reference system for the lever arms required by the OSCAR processor.

## 2.3 Antenna installation and lever arms

The tables below report the look angles of the antennas installed during the acquisition campaign and the lever arms of the RF and GPS antennas from the mechanical reference to the IMU phase center in meters.

*Table 1: Look angle of the antennas*

Antenna name	Angle description	Angle value
<b>AFT-M-V and AFT-S-V</b>	Look angle (antenna broadside pointing) from nadir	48°
	Azimuth rotation	-45°
<b>FORE-M-V and FORE-S-V</b>	Look angle (antenna broadside pointing) from nadir	48°
	Azimuth rotation	+45°
<b>0-DOP-V</b>	Look angle (antenna broadside pointing) from nadir	43°
	Azimuth rotation	0°

*Table 2: RF and GPS antennas lever arms from mechanical reference to IMU phase center [m].*

Distances [m] measured during the campaign on 17/02/2022						
Lever arms between IMU and antennas [m]	AFT		FORE		0 - DOP	GPS
Antenna	M	S	M	S		
<b>ΔX</b>	-0.1499	-0.1499	-0.1499	-0.1499	-0.157	-0.090
<b>ΔY</b>	-0.4385	-0.6085	+0.7334	+0.5634	0.0625	0.542
<b>ΔZ</b>	-0.3642	-0.3642	-0.3642	-0.3642	-0.3682	+1.524

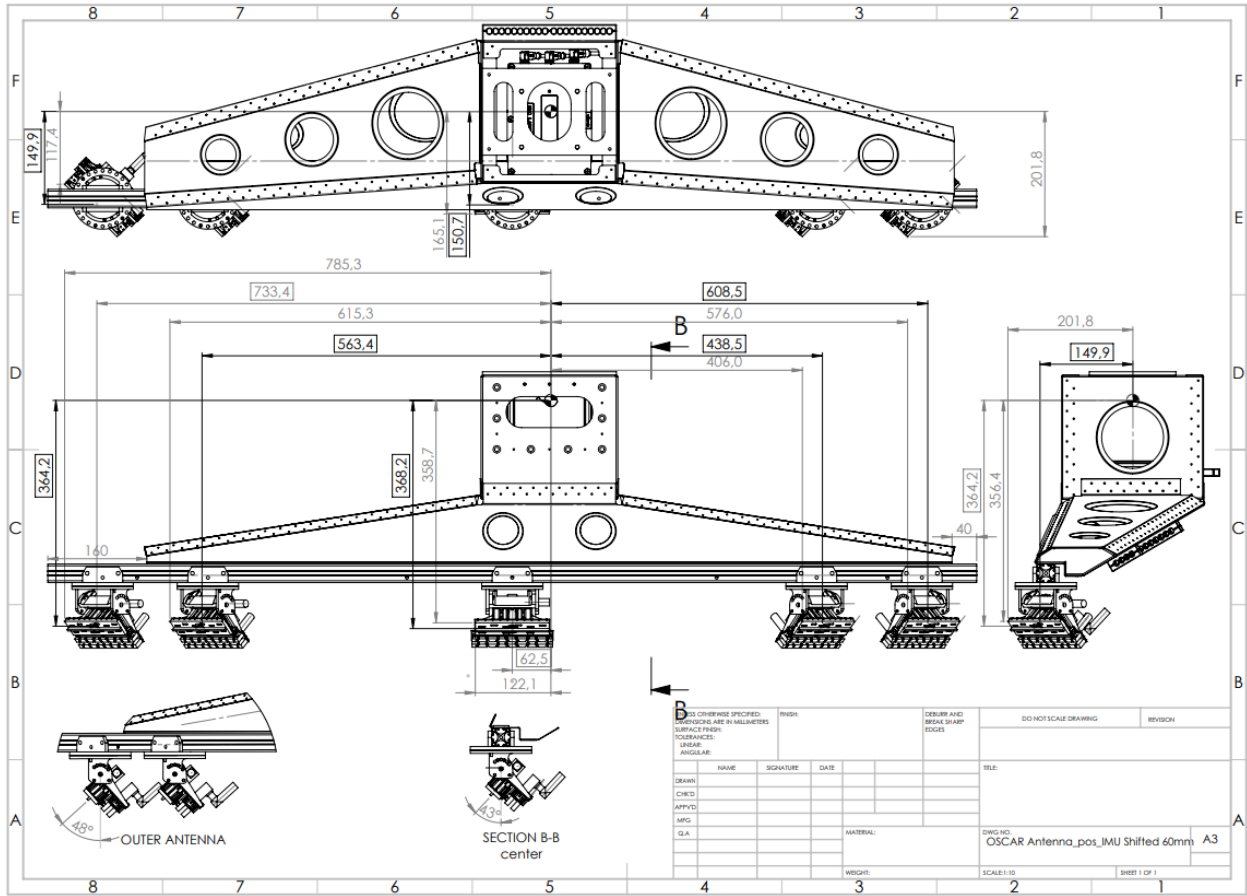


Figure 4: Measurements (units mm) of the X,Y,Z offsets, used to compute the RF antenna lever arms from the IMU reference. The mechanical reference point taken on the antennas is indicated with a red circle.

## 2.4 Lever arm of the GSM4000 center of rotation

In this section, the position of the center of rotation of the GSM4000 mount is given (see Figure 5 and Figure 6).

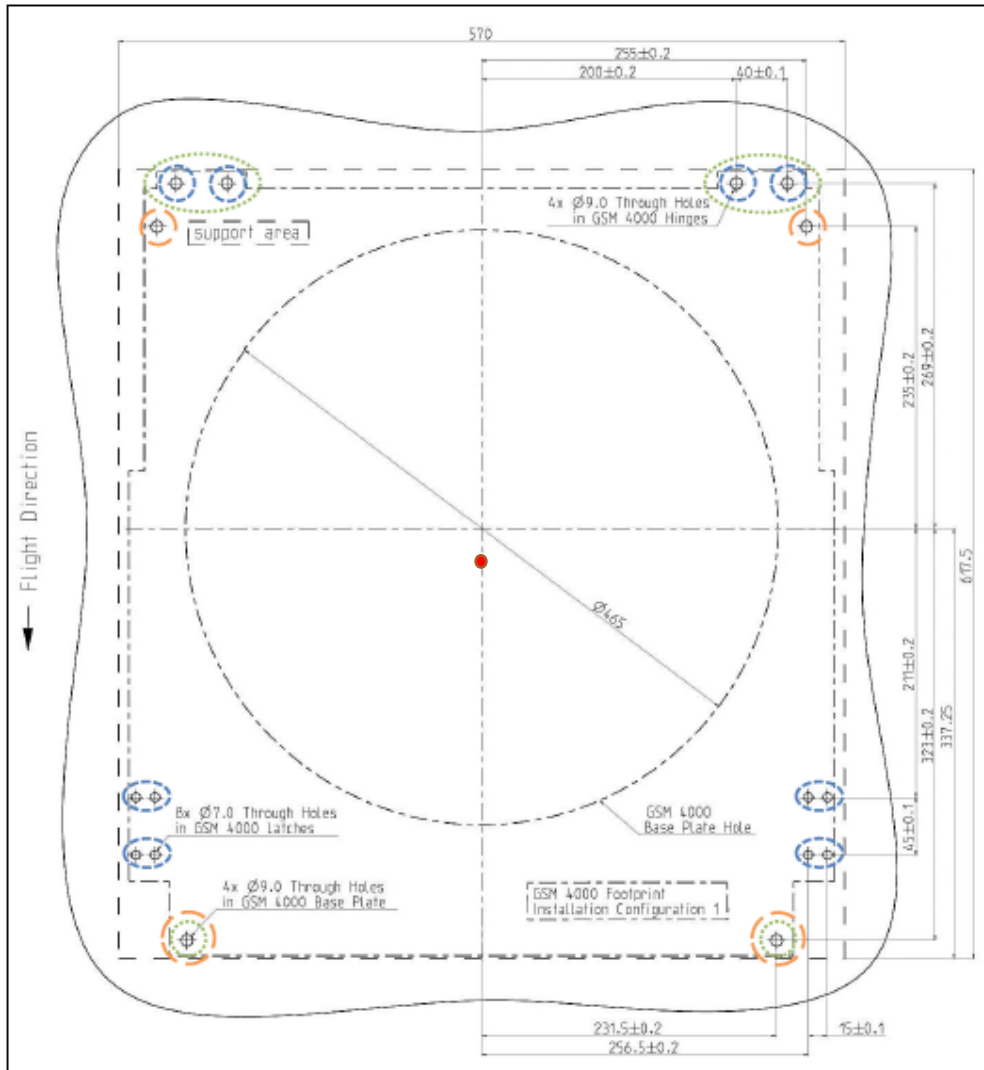


Figure 5: Top view of the mount. The center of rotation is located on the (vertical) axis passing through the center of the ring (red dot above).

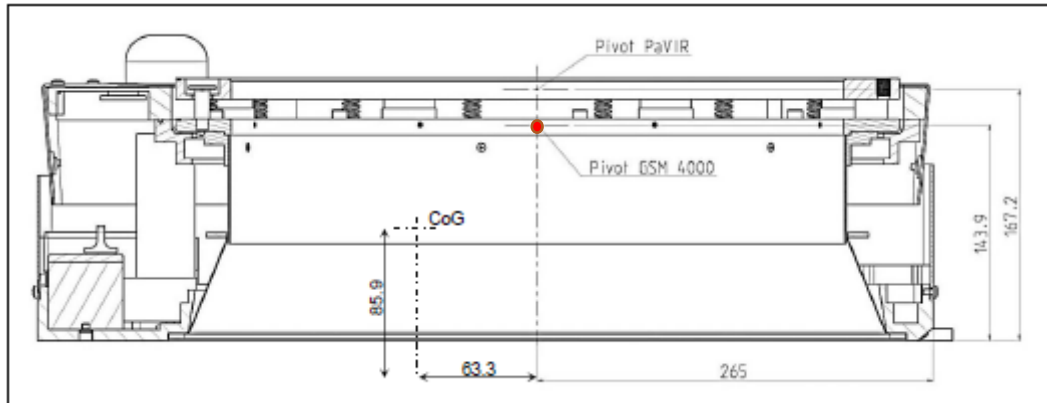


Figure 6: Side view of the mount. The center of rotation is located at the position (red dot) indicated with “Pivot GSM 4000”, i.e., 143.9mm (we can assume 144mm) above the floor.

The geometrical center of the IMU enclosure is located on the vertical axis passing through the center of the ring of the GSM4000 mount. Therefore, the offsets of the GSM4000 center of rotation with respect to the IMU origin and reference system is given in Table 3.

Table 3: Lever arm of the GSM4000 center of rotation from the IMU reference system [m].

Lever arms between IMU and GSM 4000 pivot [m]	
$\Delta X$	-0.0005
$\Delta Y$	+0.0025
$\Delta Z$	-0.2624



## 2.5 Channels mapping

The below table reports the channel numbers and configuration occurred during the SeaSTARex campaign, according to the OSCAR installation.

*Table 4: Brest Campaign channel mapping.*

Channel number	Configuration	Description
00	0DOP-V	Zero-Doppler Vertical Polarization
33	FORE-M-V	Fore view – Master – Vertical Polarization
34	FORE-S-V	Fore view – Slave – Vertical Polarization
77	AFT-M-V	Aft view – Master – Vertical Polarization
78	AFT-S-V	Aft view – Slave – Vertical Polarization

### 3 Corner reflectors

In Figure 7 the corner reflectors location is shown on the Google map. **Error! Reference source not found.** The following table reports the corner reflectors location, radar cross section (RCS) and the description of installation in the field.

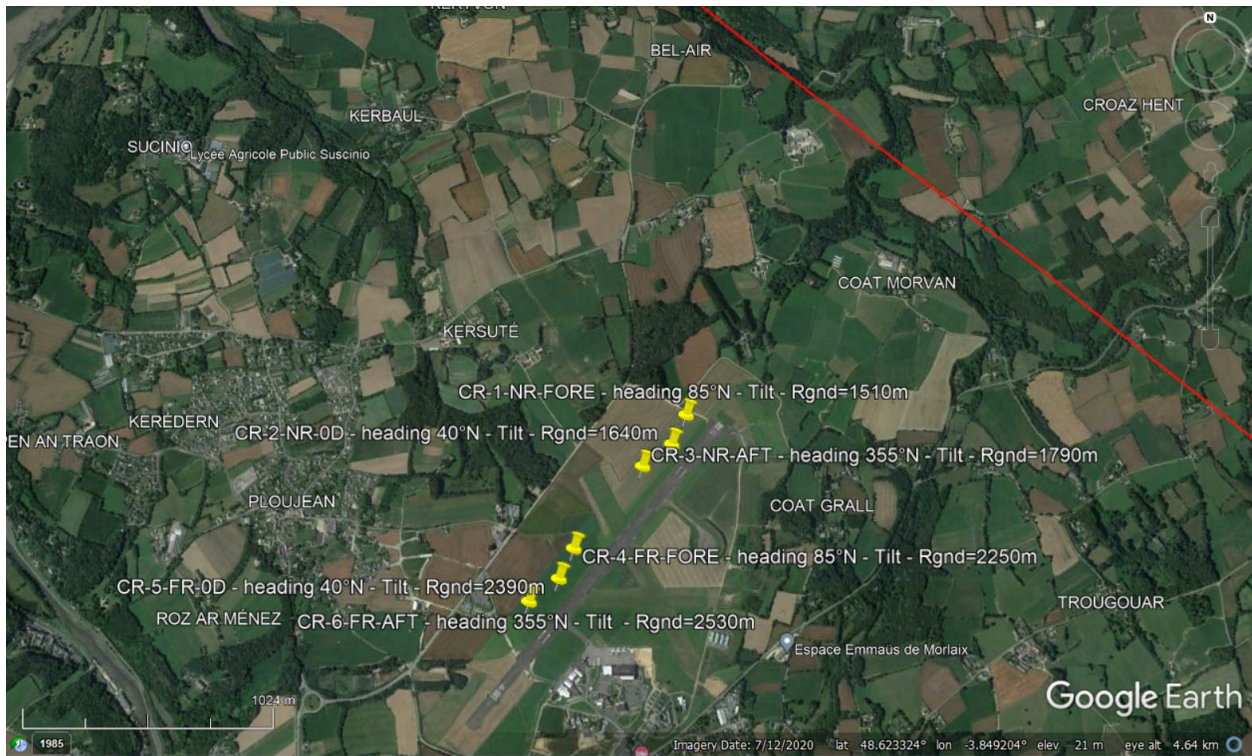


Figure 7: Position of the corner reflectors with naming.

The corner reflectors have been checked for absence of dew before each take off, except on May 26<sup>th</sup>.

*Table 5: Corner reflectors field installation*

#	CR-1	CR-2	CR-3	CR-4	CR-5	CR-6
Type	Triang 40cm	Triang 40cm	Triang 40cm	Squar 30cm	Squar 30cm	Squar 30cm
Peak RCS [dBm2]	23.38	23.38	23.38	27.92	27.92	27.92
Azimuth pointing mag=geo	85°N	40°N	355°N	85°N	40°N	355°N
Local incidence angle	35.5°	28.7°	40.2°	46.7°	38.5°	50.0°
Baseplate tilt from horizon (front up +)	4.5°	11.3°	-0.2°	-6.7°	1.5°	-10.0°
GPS coordinates (TO BE UPDATED WITH MEASURE D)	48°36'31.00" N 3°48'40.00"W	48°36'27.00" N 3°48'43.00"W	48°36'24.00" N 3°48'49.00"W	48°36'13.00" N 3°49'3.00"W	48°36'9.00" N 3°49'6.00"W	48°36'6.00"N 3°49'12.00" W
Height (amsl)	80m	80m	80m	80m	80m	80m
Ground range from nominal track	1.51km	1.64km	1.79km	2.25km	2.39km	2.53km

## 4 Radar Acquisitions

This chapter reports all the tracks acquired during the Brest campaign. Each track corresponds to a raw data file identified by the name which originates from the time of acquisition. Please note that the raw data files (listed below) and the corresponding final delivered processed data (listed below and described in the next section) have different filenames because of a time difference of **24 seconds**. This is because the ingested data in the OSCAR processor is renamed according to the GPS time, while the raw data filename is based on the instrument internal clock.

In general, the tracks were flown with a flight height of about 3000 m, with exception of tracks over the sea on 17<sup>th</sup> May.

*Table 6: List of the deliverable tracks flown on 17/05 (There were a 45 min delay of the campaign because the radar computer was not initializing properly the GNSS receiver)*

Track	Raw data name	Processed data name	Issue
<b>Track land 1</b>	20220517T082221	20220517T082245	–
<b>Track land 2</b>	20220517T082908	20220517T082932	-
<b>Track 11</b>	20220517T085949	20220517T090013	-
<b>Track 12</b>	20220517T090745	20220517T090809	-
<b>Track 13</b>	20220517T091455	20220517T091519	-
<b>Track 2</b>	20220517T093215	20220517T093239	-
<b>Track 1</b>	20220517T093754	20220517T093818	-
<b>Track 1b</b>	20220517T094315	20220517T094339	-
<b>Calib over land</b>	20220517T101713	20220517T101737	-

Figure 8 shows a spatial overview of all tracks flown on 17<sup>th</sup> May listed above.



Figure 8: Tracks flown on May 17, 2022.

Table 7: List of the deliverable tracks flown on 22/05 (No issue encountered during flight)

Track	Raw data name	Processe data name	Issue
Track 1	20220522T053918	20220522T053942	00 Pow Instab.
Track 2	20220522T054741	20220522T054805	00 Pow Instab.
Track 1	20220522T055434	20220522T055458	00 Pow Instab.
Track 10 (Circular)	20220522T060319	20220522T060343	00 Pow Instab.
Track 11	20220522T061954	20220522T062018	00 Pow Instab.
Track 12	20220522T062556	20220522T062620	00 Pow Instab.
Track 13	20220522T063215	20220522T063239	00 Pow Instab.
Track 14	20220522T063842	20220522T063906	00 Pow Instab.
Track 15	20220522T064435	20220522T064459	00 Pow Instab.
Track 16	20220522T065044	20220522T065108	00 Pow Instab.
Track 17	20220522T065645	20220522T065709	00 Pow Instab.
Track 18	20220522T070253	20220522T070317	00 Pow Instab.
Track 10 (Circular)	20220522T070714	20220522T070738	00 Pow Instab.
Track 2	20220522T072309	20220522T072332	00 Pow Instab.
Calib over land	20220522T074803	20220522T074827	00 Pow Instab.

The 00 Pow Instable means the TX/RX power only in channel 00 is not stable. Power varies beyond the expected backscatterer power. This is observed at raw data level and is causing radiometric issues at L1 data. Other channels work fine.



Figure 9 shows a spatial overview of all tracks flown of 22<sup>nd</sup> May.

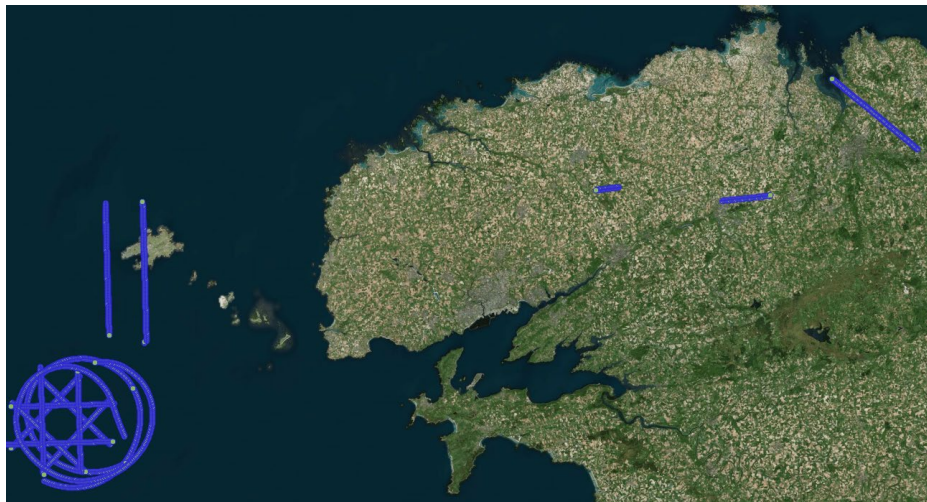


Figure 9: Tracks flown on May 22, 2022.

During the flight on 25<sup>th</sup> May, the aft beam at the end of track 20220525T085428 stopped recording data due to a power security protection mode. All the other tracks that follow have been acquired with 0-Doppler and fore-beam only.

Table 8: List of the deliverable tracks flown on 25<sup>th</sup> May

Track	Raw data name	Processed data name	Issue
<b>Calib over land</b>	20220525T080622	20220525T080646	-
<b>Track 22a</b>	20220525T085428	20220525T085452	Aft ch. fail end
<b>Track 22a</b>	20220525T091717	20220525T091741	Aft channe; off
<b>Track 22a</b>	20220525T092910	20220525T092934	Aft channel off
<b>Track 22a</b>	20220525T093926	20220525T093950	Aft channel off
<b>Track 22a</b>	20220525T095047	20220525T095111	Aft channel off
<b>Track 22b</b>	20220525T095723	20220525T095747	Aft channel off



*Figure 10: Tracks flown on 25<sup>th</sup> May, 2022*

*Table 9: List of the deliverable tracks flown on 26/05*

Track	Raw data name	Processed data name	Issue
<b>Track 2</b>	20220526T162854	20220526T162918	Low SNR in 00
<b>Track 1</b>	20220526T163556	20220526T163620	Low SNR in 00
<b>Track 10 (Circular)</b>	20220526T164943	20220526T165007	Low SNR in 00
<b>Track 13</b>	20220526T170606	20220526T170630	Low SNR in 00
<b>Track 14</b>	20220526T171306	20220526T171330	Low SNR in 00
<b>Track 11</b>	20220526T172128	20220526T172152	Low SNR in 00
<b>Track 12</b>	20220526T172755	20220526T172819	Low SNR in 00
<b>Track 17</b>	20220526T173712	20220526T173737	Low SNR in 00
<b>Track 18</b>	20220526T174423	20220526T174448	Low SNR in 00
<b>Track 15</b>	20220526T175106	20220526T175131	Low SNR in 00
<b>Track 16</b>	20220526T175802	20220526T175826	Low SNR in 00
<b>Track 10 (Circular)</b>	20220526T180236	20220526T180301	Low SNR in 00
<b>Track 2</b>	20220526T182114	20220526T182139	Low SNR in 00
<b>Track 1</b>	20220526T182749	20220526T182813	Low SNR in 00
<b>Calib over land</b>	20220526T185508	20220526T185533	Low SNR in 00

The 0-Doppler beam has lower SNR than previous acquisitions. This issue has been traced back to accumulated water in the bottom of the radome as described in the introduction of this document.





Figure 11: Tracks flown on 26<sup>th</sup> May

Figure 11 shows the accumulated water in the bottom of the radome (during 25<sup>th</sup> May and 26<sup>th</sup> May), which decreased the SNR of the Zero-Doppler beam on the 26<sup>th</sup> of May, which is the one pointing directly to the bottom of the radome and in direction of the water.

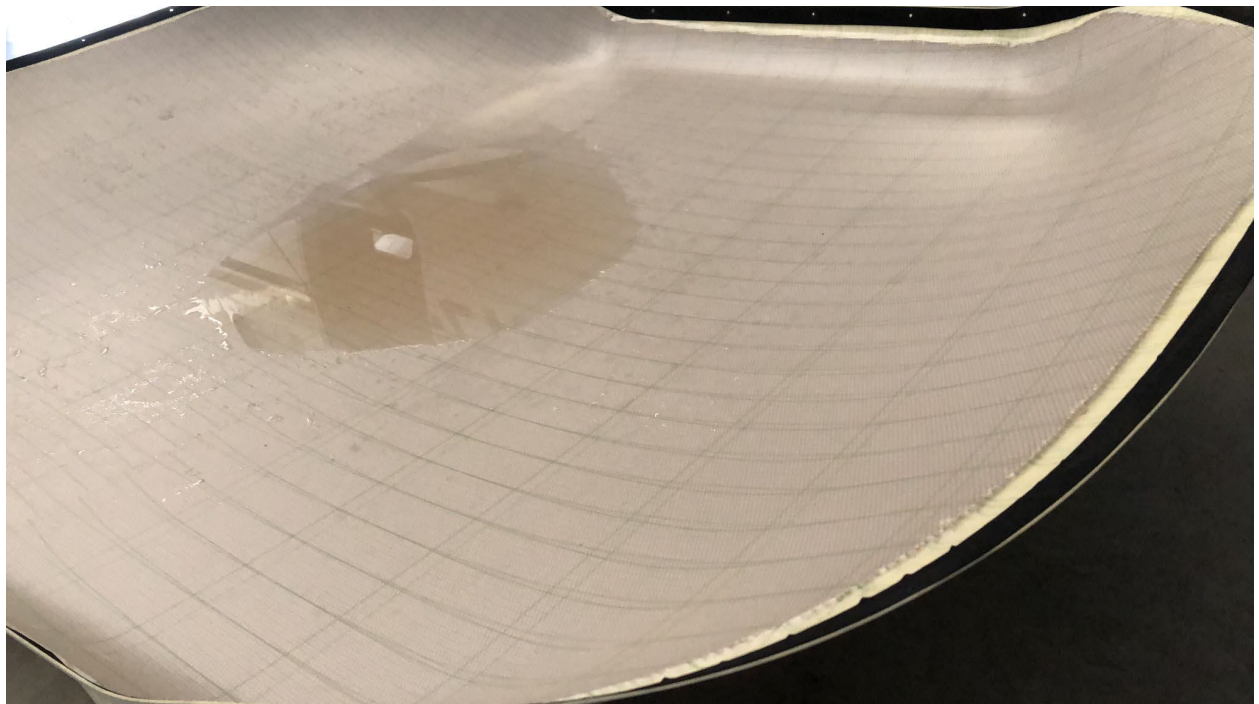


Figure 12: Accumulated water in the bottom of the radome.

## 5 Results

### 5.1 Navigation Data

The navigation data logged during the flights have been post-processed to improve the accuracy of the navigation solution. As a result, 3D positioning and attitude are estimated with an average accuracy of about 1 cm and 0.004°, respectively.

*Table 10: Statistics of the estimated position [m] (left) and attitude [arcmin] (right) accuracy of the navigation data for the OSCAR sensor during the SeaSTARex campaign.*

Day	Position	Attitude
17	Time range: Start: 201477.0 2210 07:57:57.0 05/17/2022 End: 210884.0 2210 10:34:44.0 05/17/2022 Number of samples: 9,408  Stat East North Height 2D 3D Std: 0.00061 0.00083 0.00161 0.00096 0.00179 Rms: 0.00489 0.00627 0.00969 0.00796 0.01254 Avg: 0.00486 0.00622 0.00955 0.00790 0.01241 Max: 0.00922 0.01113 0.01762 0.01336 0.02211 Min: 0.00398 0.00508 0.00769 0.00647 0.01037	Time range: Start: 201477.0 2210 07:57:57.0 05/17/2022 End: 210884.0 2210 10:34:44.0 05/17/2022 Number of samples: 9,408  Stat Roll Pitch Heading/ 2D 3D Std: 0.0383 0.0386 0.1017 0.0544 0.1106 Rms: 0.1111 0.1121 0.2288 0.1578 0.2779 Avg: 0.1042 0.1053 0.2049 0.1482 0.2550 Max: 0.2786 0.2790 0.6151 0.3943 0.7307 Min: 0.0525 0.0542 0.0915 0.0761 0.1292
22	Time range: Start: 18371.0 2211 05:06:11.0 05/22/2022 End: 28991.0 2211 08:03:11.0 05/22/2022 Number of samples: 10,621  Stat East North Height 2D 3D Std: 0.00066 0.00081 0.0011 0.0009 0.0013 Rms: 0.00453 0.00565 0.0102 0.0072 0.0126 Avg: 0.00449 0.00559 0.0102 0.0072 0.0125 Max: 0.01810 0.02413 0.0318 0.0302 0.0437 Min: 0.00394 0.00490 0.0084 0.0063 0.0112	Time range: Start: 18371.0 2211 05:06:11.0 05/22/2022 End: 28991.0 2211 08:03:11.0 05/22/2022 Number of samples: 10,621  Stat Roll Pitch Heading/ 2D 3D Std: 0.0312 0.0322 0.0766 0.0449 0.0836 Rms: 0.1064 0.1066 0.2095 0.1506 0.2580 Avg: 0.1017 0.1016 0.1949 0.1438 0.2441 Max: 0.1847 0.1847 0.4880 0.2612 0.5535 Min: 0.0595 0.0559 0.1056 0.0817 0.1406
25	Time range: Start: 287478.0 2211 07:51:18.0 05/25/2022 End: 302581.0 2211 12:03:01.0 05/25/2022 Number of samples: 15,104  Stat East North Height 2D 3D Std: 0.00086 0.00110 0.0020 0.0012 0.0023 Rms: 0.00729 0.00849 0.0136 0.0112 0.0176 Avg: 0.00724 0.00842 0.0134 0.0111 0.0175 Max: 0.00942 0.01154 0.0187 0.0148 0.0239 Min: 0.00492 0.00537 0.0086 0.0073 0.0115	Time range: Start: 287478.0 2211 07:51:18.0 05/25/2022 End: 302581.0 2211 12:03:01.0 05/25/2022 Number of samples: 15,104  Stat Roll Pitch Heading/ 2D 3D Std: 0.0436 0.0442 0.0515 0.0621 0.0736 Rms: 0.1568 0.1575 0.2392 0.2223 0.3266 Avg: 0.1507 0.1512 0.2336 0.2135 0.3181 Max: 0.2264 0.2347 0.4644 0.3260 0.5093 Min: 0.0557 0.0565 0.0869 0.0793 0.1328
26	Time range: Start: 402822.0 2211 15:53:42.0 05/26/2022 End: 415986.0 2211 19:33:06.0 05/26/2022 Number of samples: 13,165  Stat East North Height 2D 3D Std: 0.00077 0.00083 0.0012 0.0011 0.0014 Rms: 0.00651 0.00683 0.0123 0.0094 0.0155 Avg: 0.00646 0.00678 0.0122 0.0094 0.0154 Max: 0.00952 0.00996 0.0191 0.0135 0.0234 Min: 0.00504 0.00530 0.0106 0.0074 0.0133	Time range: Start: 402822.0 2211 15:53:42.0 05/26/2022 End: 415986.0 2211 19:33:06.0 05/26/2022 Number of samples: 13,165  Stat Roll Pitch Heading/ 2D 3D Std: 0.0299 0.0306 0.0881 0.0427 0.0906 Rms: 0.1089 0.1094 0.2247 0.1544 0.2726 Avg: 0.1047 0.1051 0.2067 0.1483 0.2571 Max: 0.1684 0.1695 0.5499 0.2389 0.5845 Min: 0.0573 0.0584 0.1031 0.0818 0.1399

Figure 13 shows the plot of the antenna and attitude dynamic (after considering the lever arms) describing the antenna behavior along the flight. It is important to note that it has been verified that the antenna movement is within expectations, including for the circular flights. Especially, it can be verified that the gimbal worked fine keeping the roll, pitch, and heading (relative to nominal track) basically constant around zero degrees, besides the yaw (due to changes in the velocity). It has been checked that all flights behave similarly.

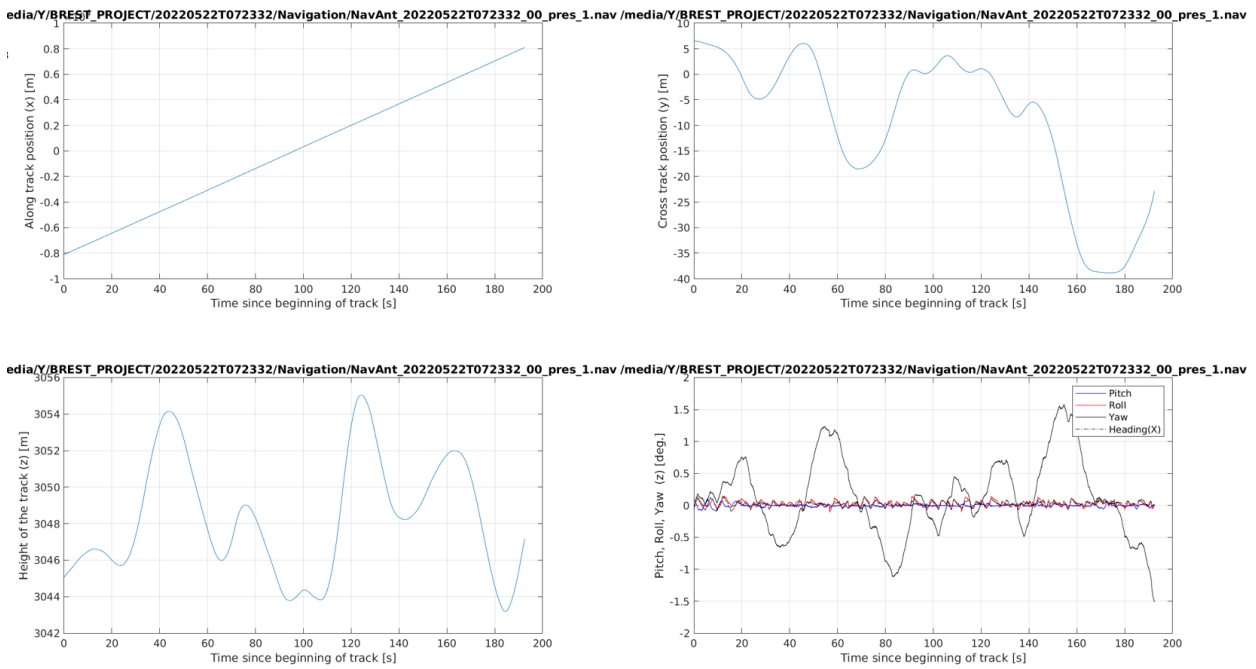


Figure 13: Plots of the antenna position and attitude dynamic

## 5.2 Radar Data

From the in-flight checks during the campaign, the data looked healthy. The live preview was giving enough information to confirm that the system was performing nominally. In the plots below, example of a normal, i.e. good SNR, no RFI issues (as expected) Range-Doppler map as seen during the flights, coherence maps and interferograms between channels of the same view of two interesting acquisitions are shown.

As already commented there were HW issue of the aft beam on May 25<sup>th</sup>.

As already commented the accumulated water affected the SNR on May 26<sup>th</sup>, although reasonably returns, with sufficient SNR, are visible in the Range Doppler maps, the SNR was lower than the acquisitions during previous days.



Data take: 20220525T085428

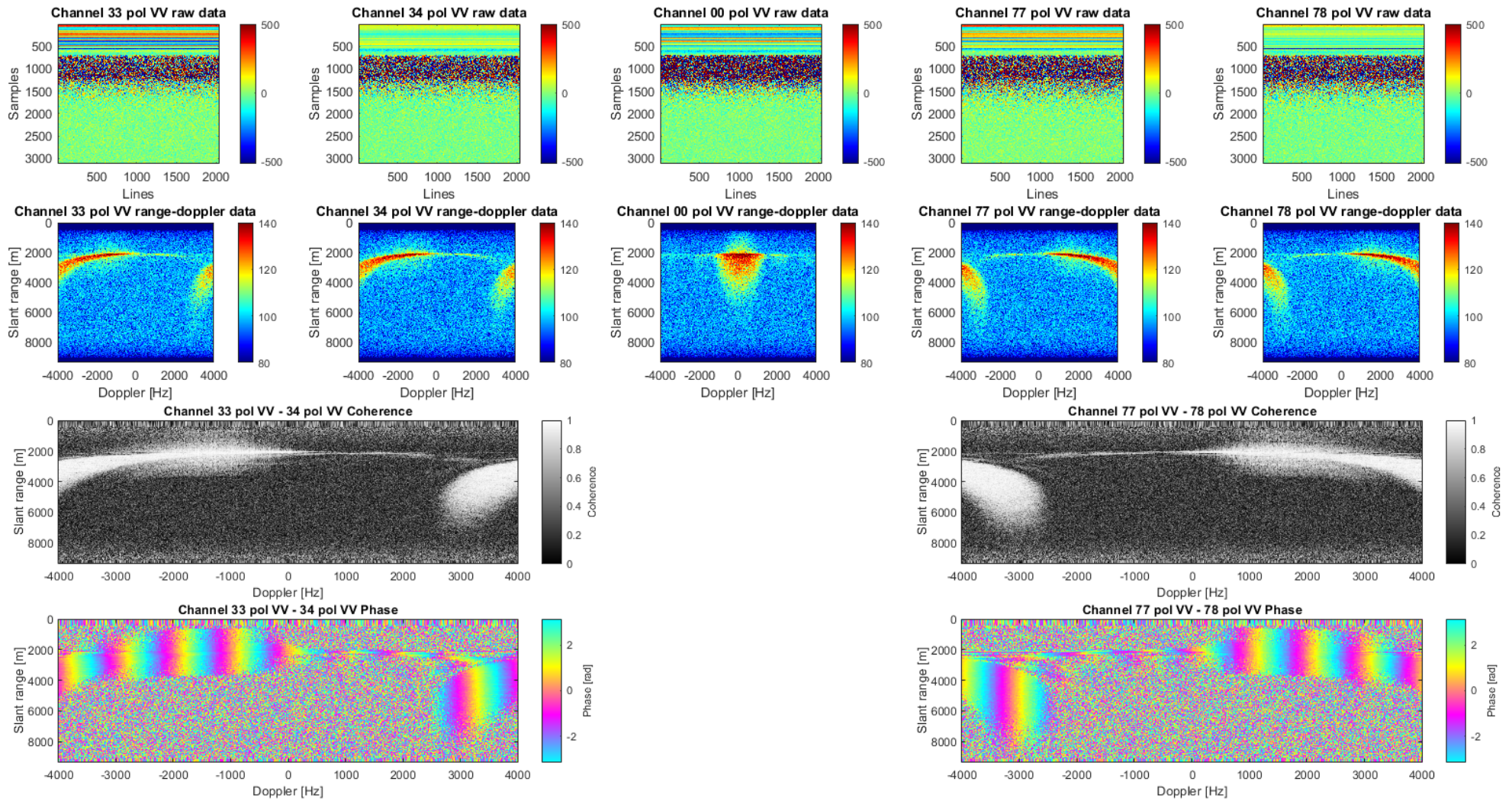


Figure 14: RD maps, coherency map and interferograms of the 0-Doppler (00), fore (33-34) and aft (77-78) beams.

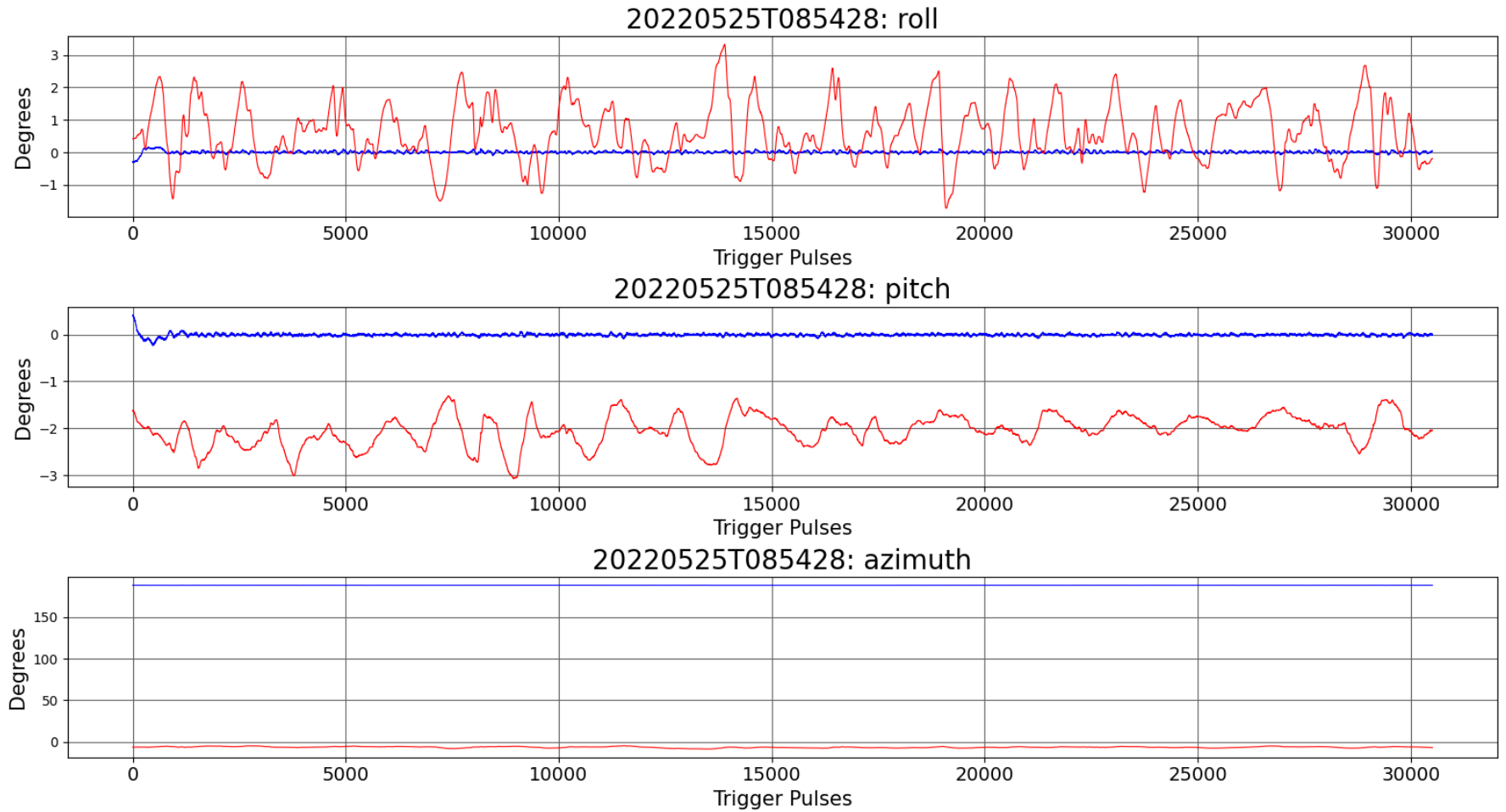
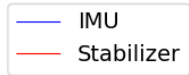


Figure 15: IMU and gimbal attitude along the track (zoom on azimuth)



The figure below shows a healthy AFT beam of the second track of the 25<sup>th</sup>

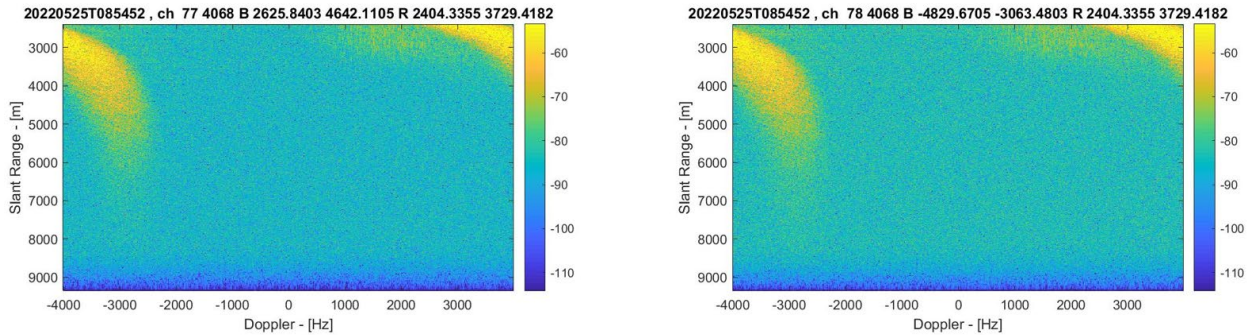


Figure 16: RD-map of the AFT beam on the 2<sup>nd</sup> track of the 25<sup>th</sup>

The figure below shows the AFT beam RD map of the 3<sup>rd</sup> track of the May 25<sup>th</sup>, confirming that the AFT beam is lost beginning with the 3<sup>rd</sup> track and subsequent on the May 25<sup>th</sup> acquisitions. The other beams have RD maps as expected.

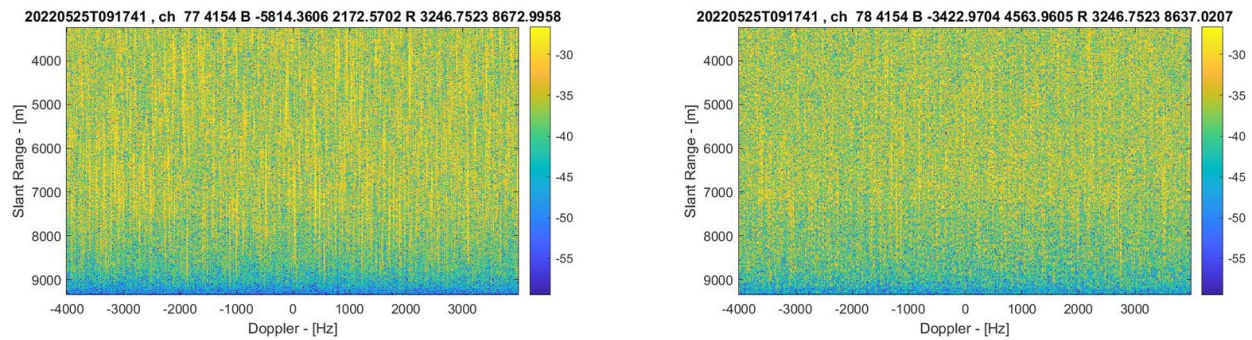


Figure 17: Loss of the AFT beam on the 4<sup>th</sup> track of the 25<sup>th</sup> May.

The figure below shows the RD map of the Zero-Doppler beam of track number 2 on the 26<sup>th</sup> May next to the same track on May 22<sup>th</sup>. It is clear the loss of SNR on the 26<sup>th</sup> May data.

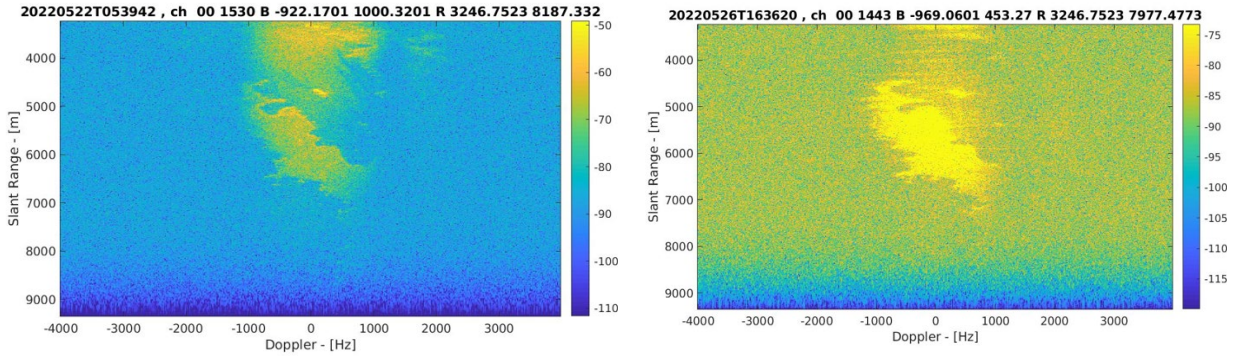


Figure 18: SNR issues of the Zero-Doppler beam of the 26<sup>th</sup> May. Comparison of the RD map of track number 2 form the 22/05 (left) and 26/06 (right).

The figure below illustrates the 00 power instability issue that occurred only on 22 May only on channel 00 for the calibration track and for a track over ocean. The top image shows the profile coming from scanning the raw data (L-0 data) and below the corresponding L1 data. Note that the problem affects stronger the NRCS in near range.

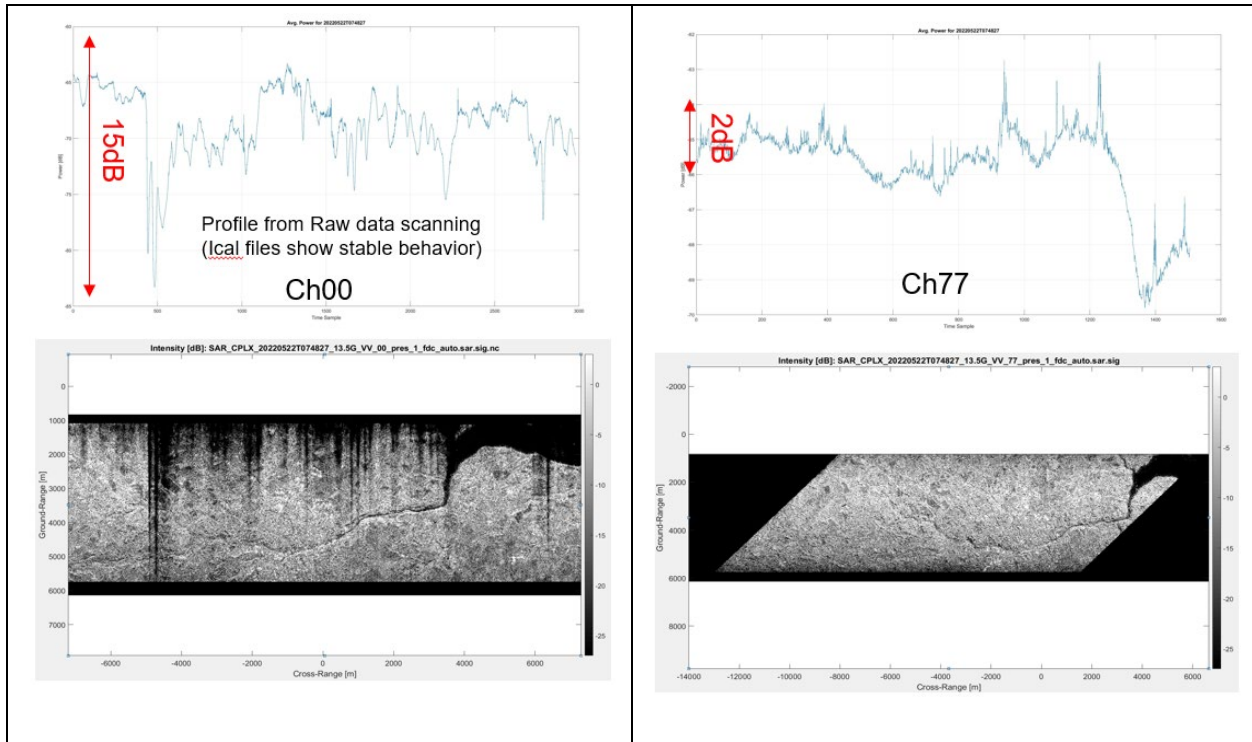


Figure 19: Channel 00 pow. Instability issue on the 22<sup>th</sup> May over land. Top show the profile coming from scanning the raw data (L-0 data) and below the corresponding L1 data.



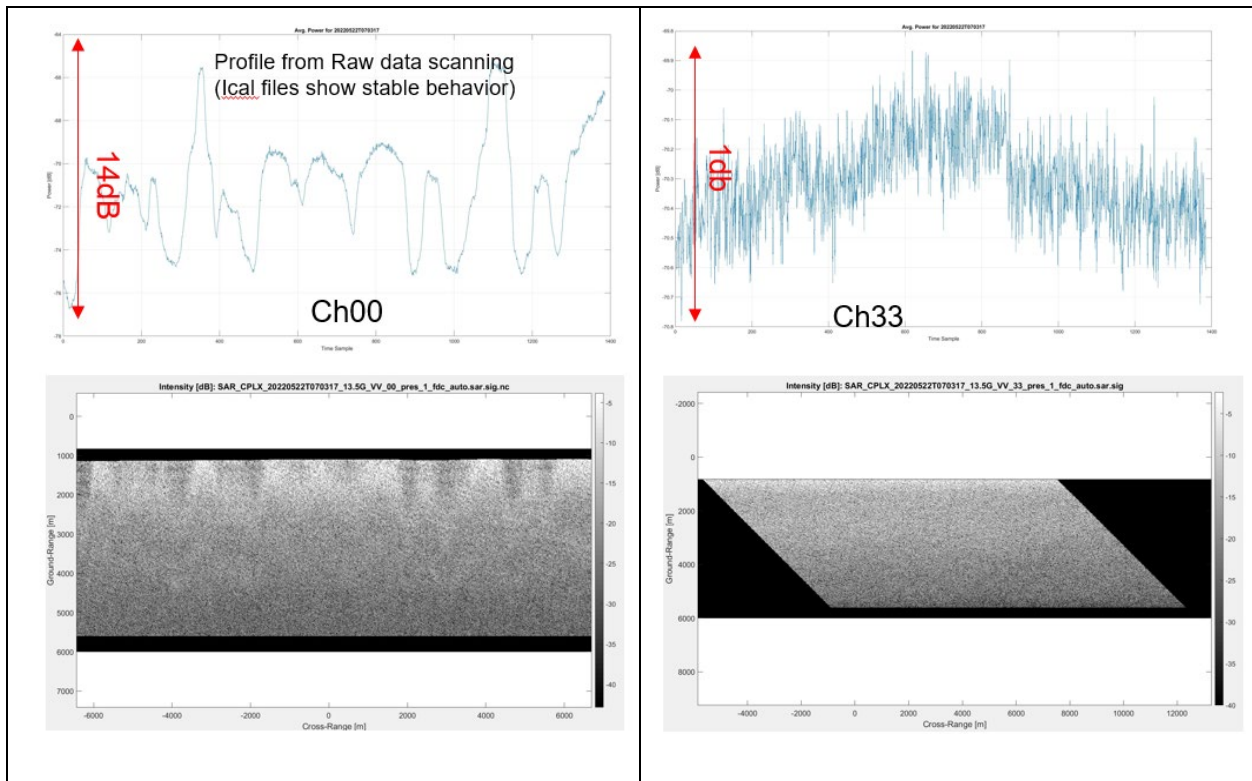


Figure 20: Channel 00 pow. Instability issue on the 22<sup>th</sup> Ma over ocean. Top show the profile coming from scanning the raw data (L-0 data) and below the corresponding L1 data.

The data of all beams have been processed within the maximum possible available swath. The data are processed using the OSCAR processor, developed by MetaSensing, and making use of the GBP (Global Back Projection) algorithm. The data are processed up to L1a level, i.e. radiometrically (sigma-0) and geometrically calibrated SLC.

The processed data are delivered together with the metadata encapsulated in the NetCDF file format [3]. The processed data have 11.5 m x 8 m slant range x azimuth resolution (after Hanning windowing), respectively. The look angle can be adjusted to be between 28 to 68 degrees.

The figures below show the SLC SAR images for all the 3 beams for one of the calibration tracks. Note that the images were processed with the early L1-processor version from released before January 2023. Therefore the images are clipped in both range and azimuth and the here presented SLC image the look angles vary from 50 to 68 degrees.

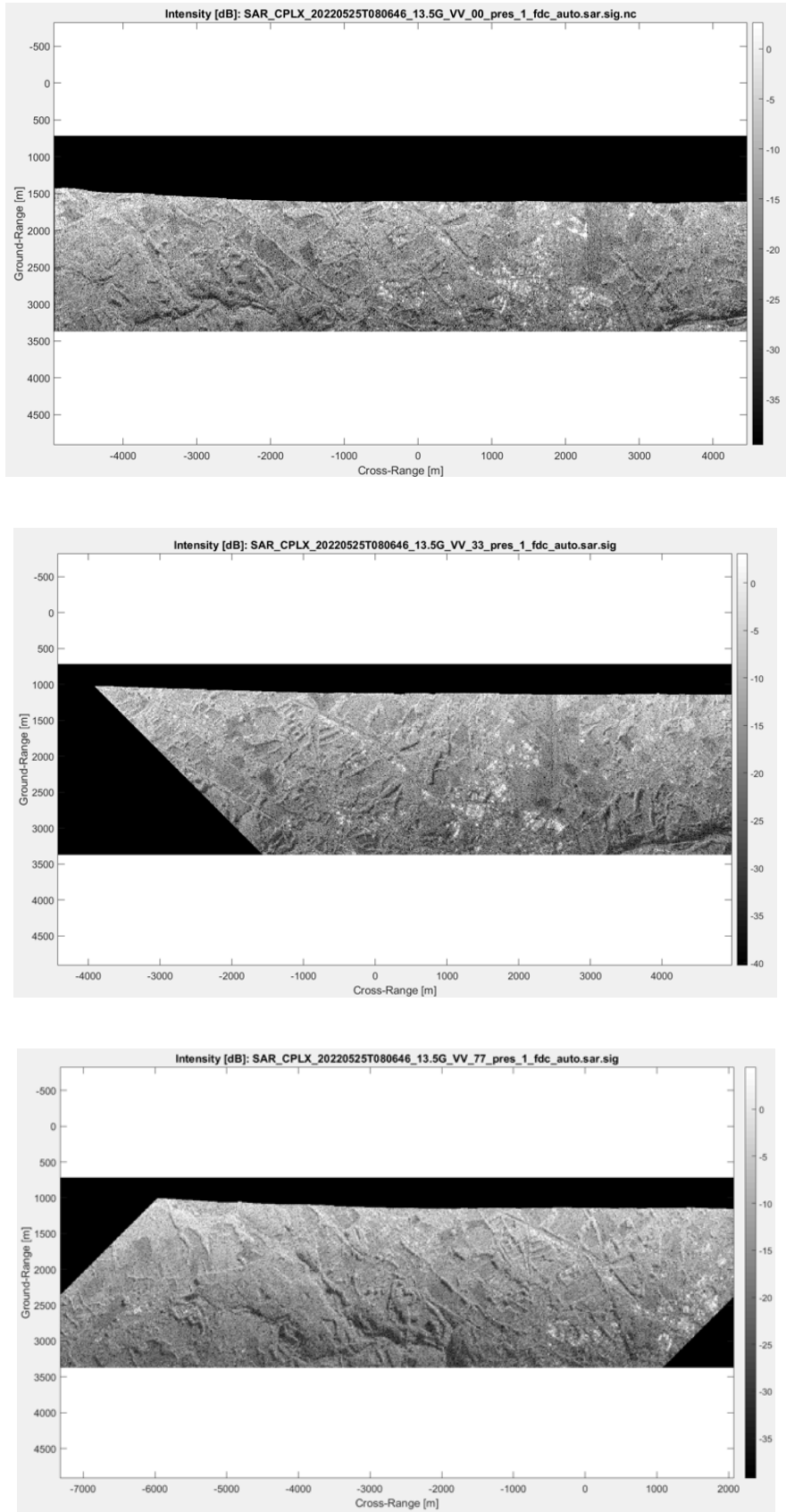


Figure 21: SAR Intensity images of the calibration of the May 25th acquisitions Top is Zero-Doppler beam, Middle is FORE beam and Bottom is AFT beam

The figures below show the interferometric phase and coherence for the AFT and FORE beams. It is visible that the phase is calibrated and there is no presence of phase undulations due to motion errors.

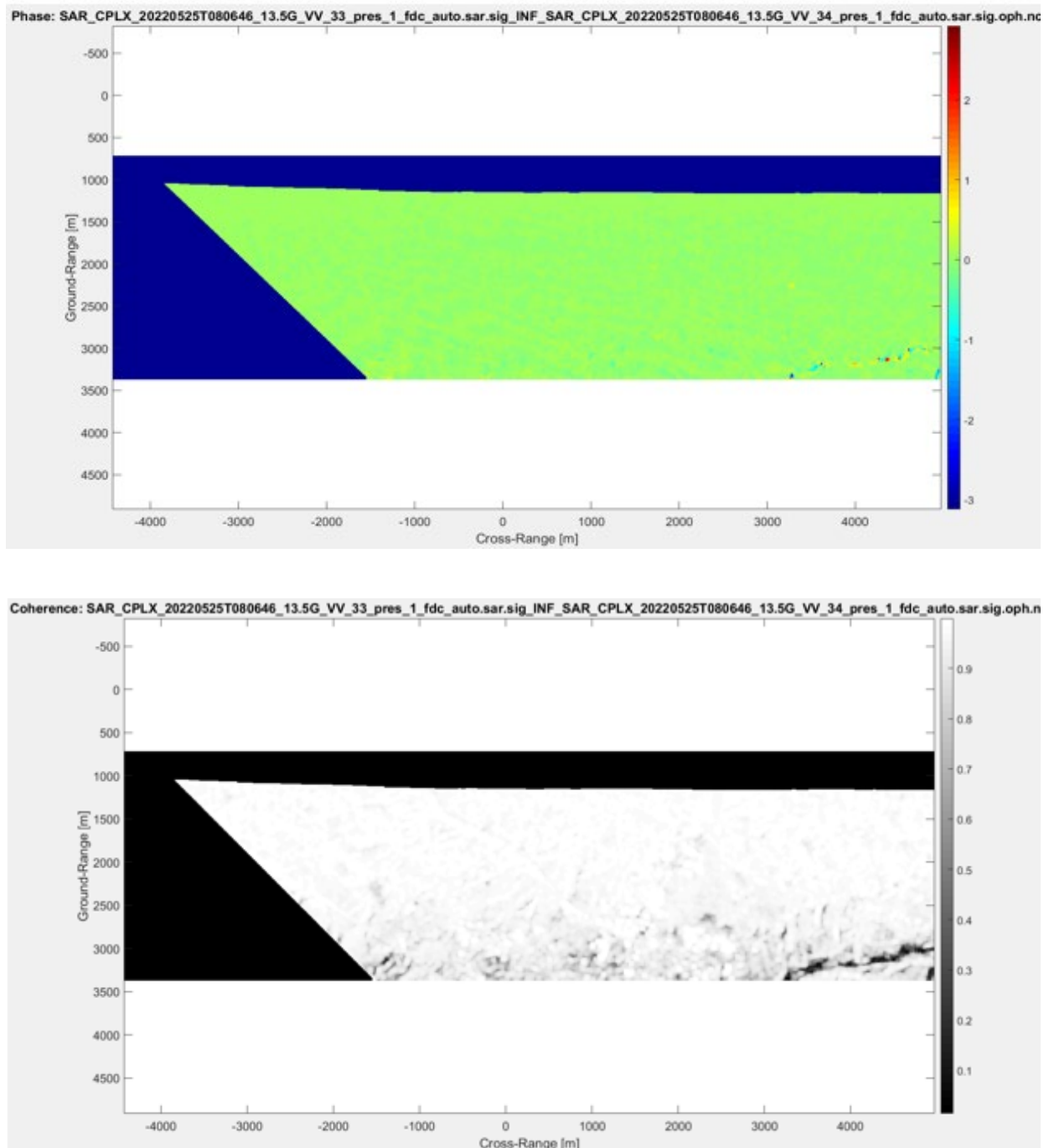


Figure 22: Interferometric phase (top) and coherence (bottom) of the FORE beam.

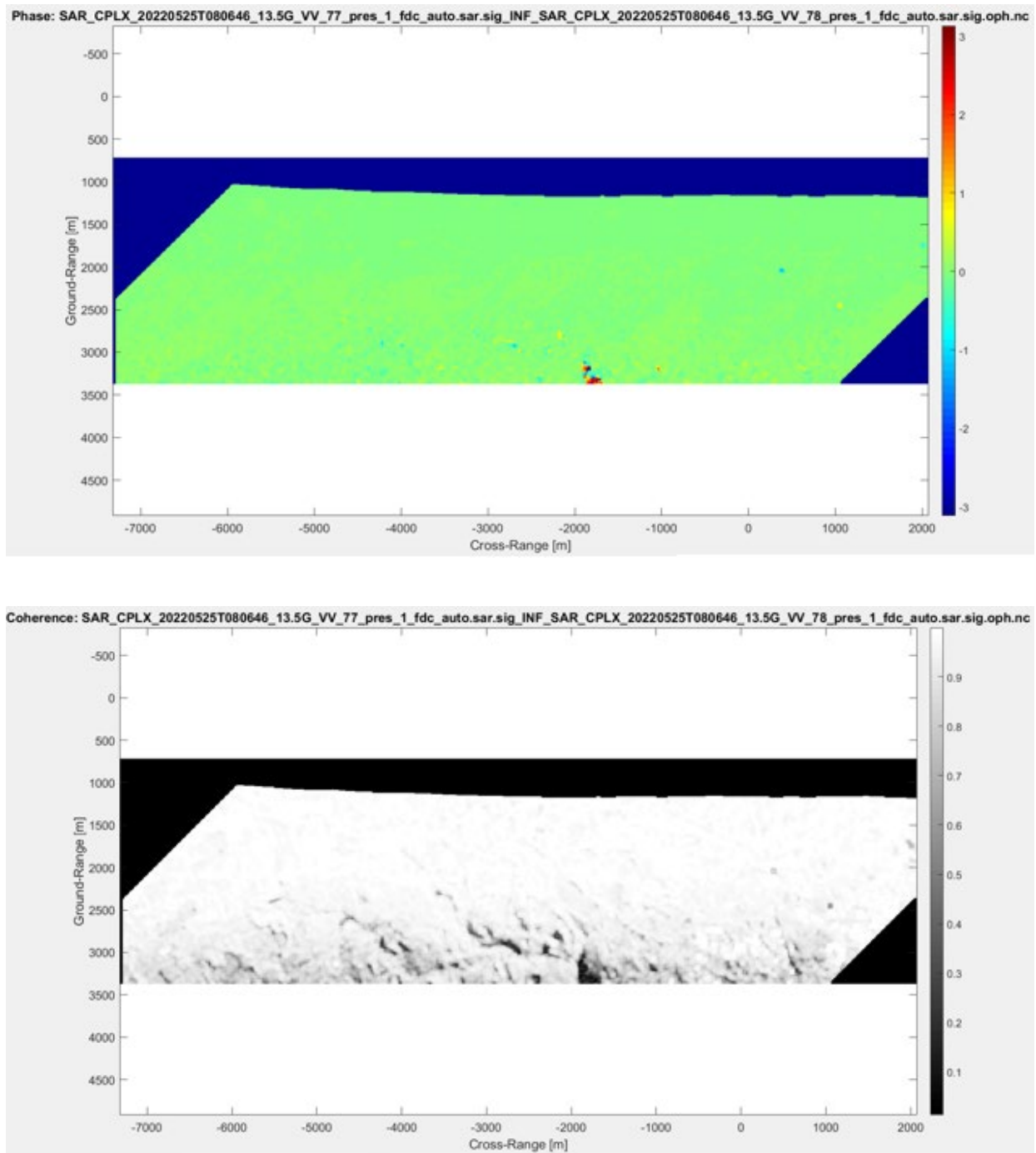


Figure 23: Interferometric phase (top) and coherence (bottom) of the AFT beam.

Furthermore, we show the same for a track over Water/Land. The SAR image is geolocated over a GIS platform. It is visible that the phase is sensible to the movements of the ocean, while over land is practically zero (using the same calibration factor applied to track over Land).

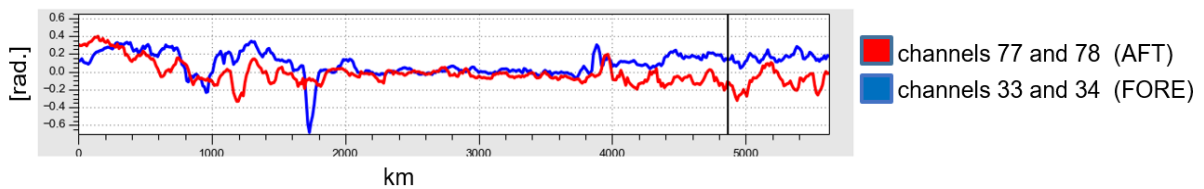
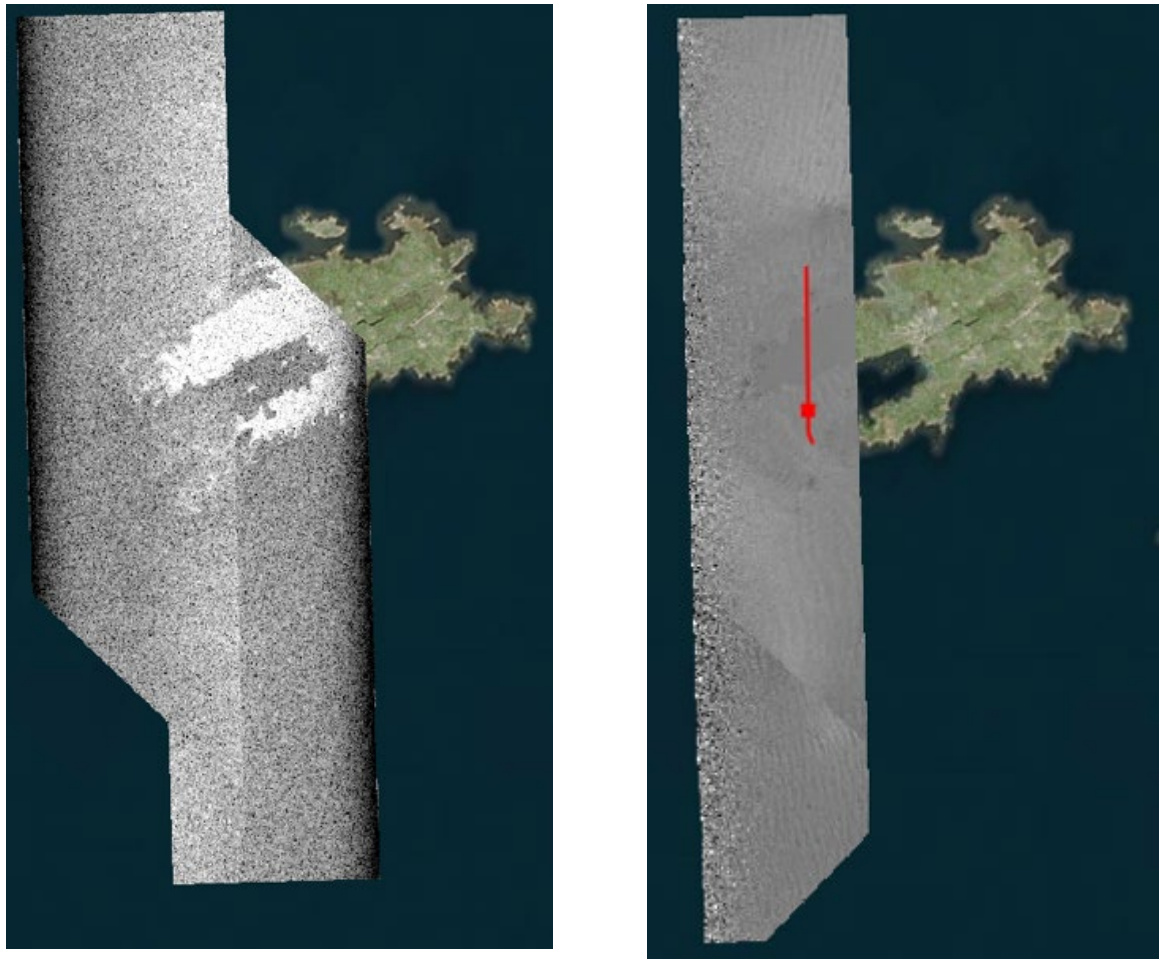


Figure 24: Georeferenced SAR images (top left) and interferometric phase (top right) with red line corresponding to the phase profiling plot in the bottom.

## 6 Conclusions

This Data Acquisition Report - DAR provides the information about the data collection needed for the data processing and analysis. Moreover, the DAR proves that the SAR data of the SeaSTARex campaign in BREST were correctly acquired with the OSCAR instrument, besides some detected, reported and analyzed issues.

The only significant issue was the loss of the AFT beam from the 4<sup>th</sup> track of the 25<sup>th</sup> May acquisition. A power instability issue has been detected only on channel 00 of day 22, affecting mostly the near range portion of the data. A minor issue is the SNR degradation on channel 00 of May 26<sup>th</sup>. In summary 75% of total data acquired is in accordance with the specifications/requirements/expectations. All data have been processed with the OSCAR processor and analyzed up to geometrically, radiometrically, and interferometrically calibrated SLC level to demonstrate that the acquired metadata and data are healthy.

Finally the OSCAR processor, used to process the data and generate the images above, is able to correctly process and deliver data within the SeaSTARex project requirements.



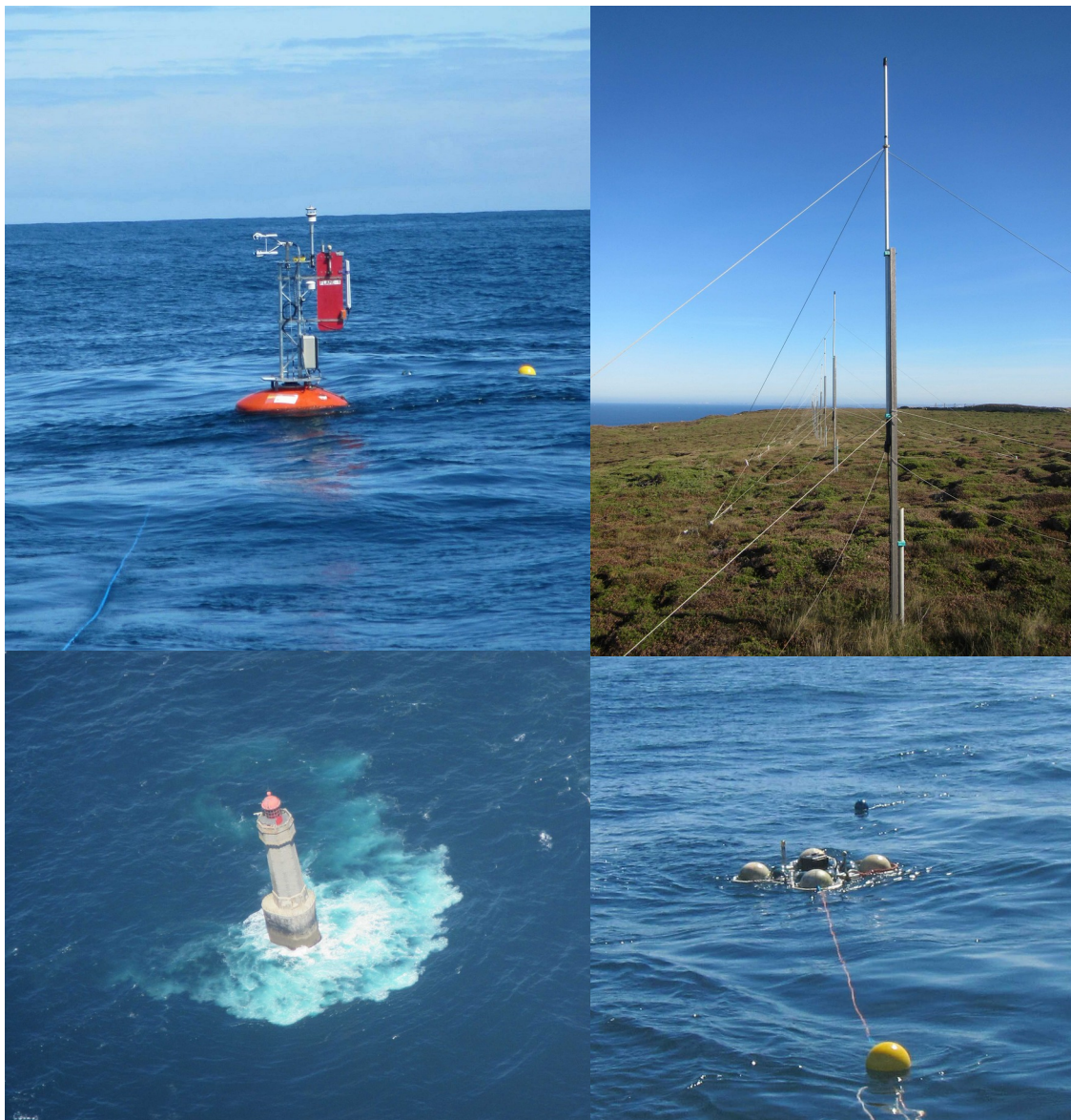
## 7 References

- [1] C. Gommenginger, et al, “SEASTAR: A Mission to Study Ocean Submesoscale Dynamics and Small-Scale Atmosphere-Ocean Processes in Coastal, Shelf and Polar Seas”, Proposal selected for Phase 0 of Earth Explorer 11 candidate mission, ESA-ESTEC.
- [2] Ocean Surface Current Airborne Radar Demonstrator (OSCAR) – Statement of Work, Appendix 1 to AO/1- 8309/15/NL/BJ.
- [3] MetaSensing NetCDF. File Format Description. MS-SAR-NetCDF-FFD\_v3.

# **ANNEX C) DATA ACQUISITION REPORT: GROUND TRUTH DATA**



# SEASTARex



## D9.2: Data Acquisition Report (DAR)

Ground Truth measurements

ESA Contract No. 4000116410/16/NL/BJ



L. Marié, O. Peden, IFREMER, France

R. Duarte, J.-F. Filipot, FEM, France

R. Carrasco, J. Horstmann, HZH, Germany

A. Martin, David McCann, NOC, UK

v1.0, Nov 8<sup>th</sup>, 2022


### Document change record

Author	Modification	Issue	Rev	Date
L. Marié	Initial release	DRAFT	0	06/2022
A. Martin			0.1	09/2022
L. Marié	Inclusion of information regarding X-band and Stereo-Video data.		0.2	11/2022
L. Marié	Version with modifications suggested during PM2.	1	0	11/2022

### Applicable Documents

Reference	Title
[AD-1]	D8 SeaSTARex Campaign Implementation Plan (CIP), ESA-ESTEC Contract number 400017623/22/NL/IA, ESA

### Signatures

Institution	Signature
ESA	
IFREMER	Louis Marié 

## Contents

1	Introduction.....	4
1.1	Context.....	4
1.2	Campaign location and timing.....	5
1.3	Campaign environment.....	6
1.4	Synoptic environmental conditions.....	7
1.5	Campaign Components.....	10
2	In-situ data.....	11
2.1	“FLAME” buoy data.....	11
2.2	“TREFLE” buoy data.....	12
2.3	“Pierres Noires” buoy data.....	13
2.4	NDBC 62163 “Brittany” buoy data.....	13
3	Ground-based remote sensing data.....	13
3.1	HF radar data.....	13
3.2	“La Jument” Stereo-Video data.....	13
3.3	“La Jument” X-band radar data.....	14
4	Satellite remote sensing data.....	15
4.1	SAR satellite data.....	15
4.2	Optical satellite data.....	16
4.3	Other satellite data.....	17
5	Summary of operations.....	18
5.1	2022/05/17.....	18
5.2	2022/05/22.....	18
5.3	2022/05/25.....	19
5.4	2022/05/26.....	19
6	Summary.....	20
	Acknowledgements.....	20

# 1 Introduction

## 1.1 Context

The SEASTARex activity represents the first opportunity to perform a scientific flight campaign with validation against independent ground-truth. The main overall objective of SEASTARex is to acquire experimental airborne data to demonstrate the capability of the OSCAR three-look configuration to measure 2D fields of TSCV and OSVW from Doppler and NRCS data, ideally without the use of auxiliary environmental information. The airborne data and validation results would serve to consolidate the calibration and retrieval framework and to contribute to increasing the scientific readiness level of the EE11 SEASTAR candidate (Gommenginger et al., 2019).

The specific objectives of this campaign are to perform:

- Simultaneous acquisitions of OSCAR airborne data and ground truth data during a dedicated campaign over an instrumented and well-characterized ocean site;
- Acquisition of gimbal stabilized and calibrated OSCAR data in NRCS and Doppler (phase and frequency).



Figure 1: Sentinel-2 MSI true colour image from 14/02/2017 over the Iroise Sea. The Trefle mooring site is indicated by red square 'T' and the La Jument site by red square 'J'. Tidal coefficients are indicated on the right-hand side of the calendar, with the red and blue side bars indicating the weeks identified for the airborne campaign.

The campaign can be separated in four parts:

- **Calibration flight over land (corner reflectors)**
- **Iroise Sea "Trefle" site with a star flight pattern over homogeneous area:** this serves primarily to assess the retrieved TSCV and OSVW over a site well instrumented with ground-truth validation data (HF radar + Trefle mooring) characterized by uniform bathymetry and environmental conditions (current, waves, wind). The "Trefle" site corresponds to the red box 'T' in Figure 1.

- **Iroise Sea “La Jument” site with flights over fast-varying currents near “La Jument” lighthouse:** this serves primarily to assess the ability of the OSCAR instrument to image and retrieve credible gradients of TSCV in a very coastal and highly dynamic environment. The site offers ground-truth validation data (X-band marine radar, Stereo-Video and coarse resolution HF radar). The “La Jument” site corresponds to the red box ‘J’ in Figure 1.
- **Offshore flight:** this serves primarily to further calibrate NRCS against spaceborne scatterometer data and assess retrieved OSVW against scatterometers.

## 1.2 Campaign location and timing

The campaign was performed in the vicinity of Brest from 2022/05/16 to 2022/05/27.

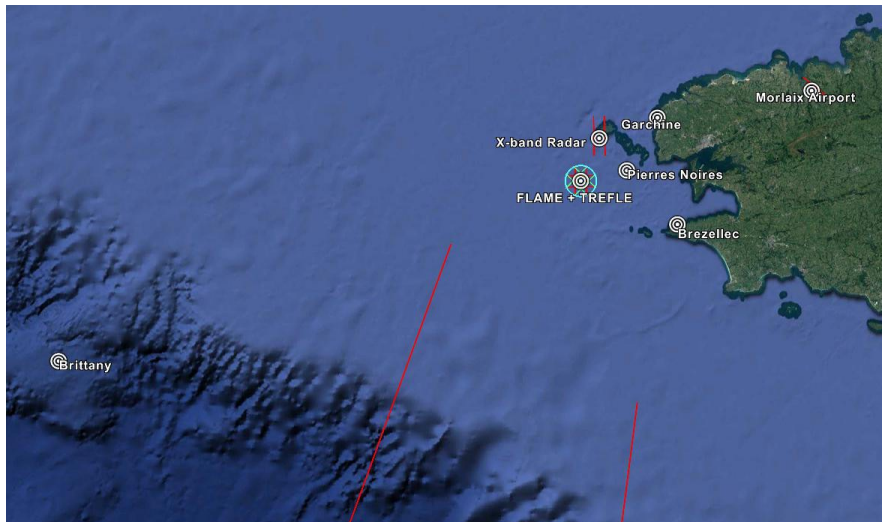


Figure 2: Map of the campaign area, showing the main “ground truth” assets.

Ocean observations were performed in three different zones with contrasting phenomenology:

- in the vicinity of the island of Ushant, an area known for its strong and spatially and temporally highly variable currents and sea states.
- to the south of Ushant, in an area where in contrast the currents and sea states are known to be spatially quite homogeneous.
- to the south of Brittany, along the Metop-B and Metop-C ground tracks (see Figure 2).



### 1.3 Campaign environment

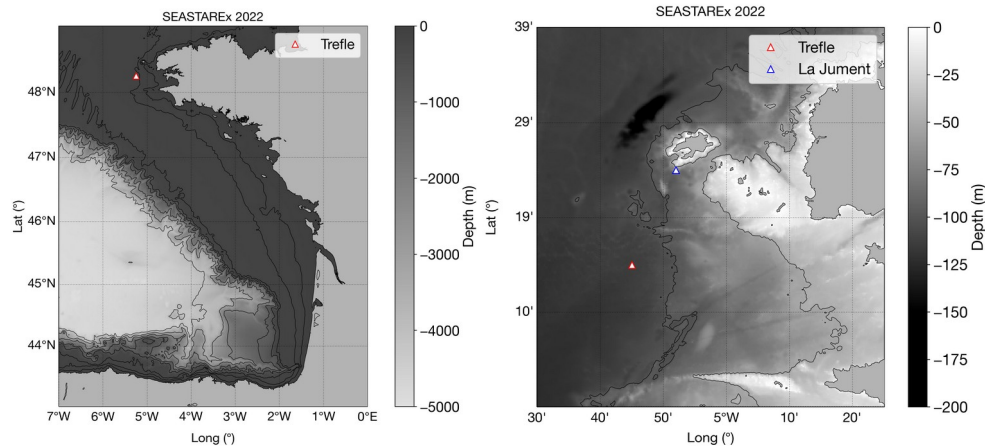


*Figure 3: (Left) Bathymetric chart of the Bay of Biscay. (Right) Bathymetric chart of the Iroise Sea. The thin lines mark (starting from the coast) the 50 m, 100 m, 150 m, 500 m, 1000 m, 2000 m, 3000 m and 4000 m isobath. On the right, only the 50 m, 100 m and 150 m isobath can be seen.*

Figure 3 shows bathymetric charts of the study area. The left panel shows a general view of the Bay of Biscay, showing in particular the location of the shelf break, which the 2022/05/25 flight overpassed, while the right panel shows a close-up of the Iroise Sea region, over which the 2022/05/17, 2022/05/22 and 2022/05/26 flights took place. As can clearly be seen in the right panel, this area has a quite rough topography, with numerous islands, channels and headlands. The “Trefle” mooring was deployed offshore of these complicating influences, in an area with a flat bathymetry and comparatively simpler dynamics. The “La Jument” lighthouse, on the opposite, was in the area of the island of Ushant, which is well known for very strong tidal currents, and rough seas.

## 1.4 Synoptic environmental conditions

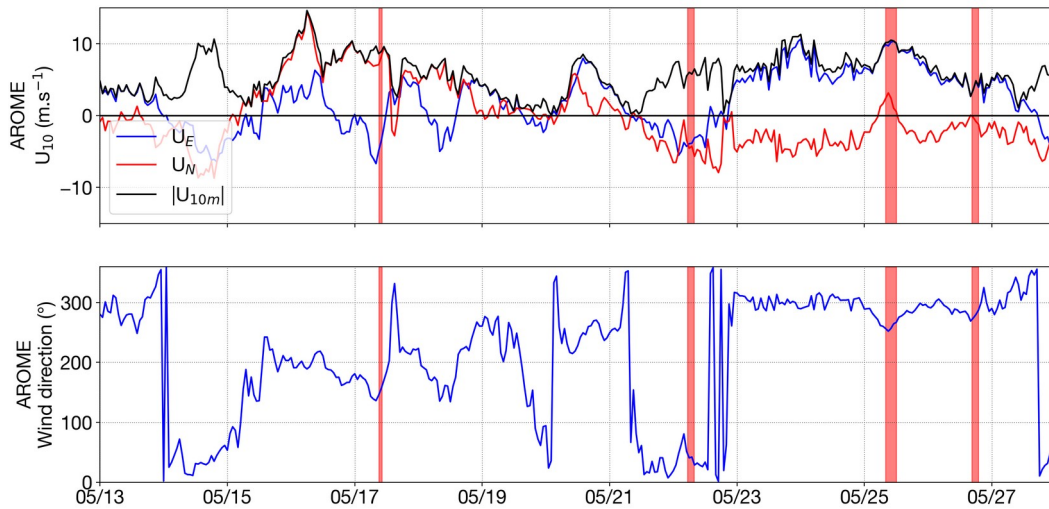


Figure 4: Time series of Meteo-France analyzed 2-m wind at the Trefle mooring location over the duration of the campaign. The red rectangles highlight the different flights.

Figure 4 shows a time series of Meteo-France analyzed wind at the Trefle mooring location, over the duration of the campaign. As can be seen in this figure, during the 2022/05/17 flight the wind was blowing at approximately 10 m/s from the South, during the 2022/05/22 flight the wind was blowing at approximately 6 m/s from the North-East, during the 2022/05/25 flight the wind was blowing at approximately 10 m/s from the West, and during the 2022/05/26 flight the wind was blowing at approximately 2 m/s from the West.

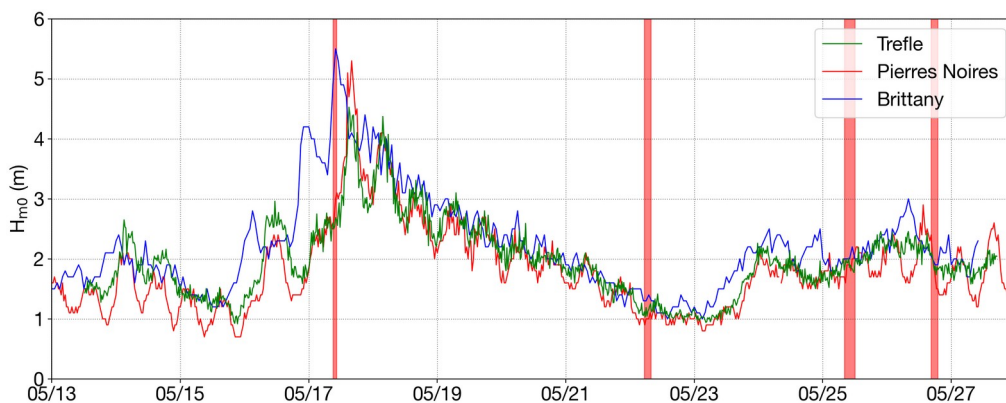


Figure 5: Time series of significant wave height recorded in the Iroise Sea by the Trefle and “Pierres Noires” buoy, and at the shelf break by the “Brittany” NDBC buoy (see Figure 2 for location of those last two buoys).

Figure 5 shows a time series of significant wave height recorded over the study area by the three buoys that were operating at the time of the campaign. As can be seen in this figure, the 2022/05/17 flight occurred shortly before a strong (5 m  $H_s$ ) sea state episode swept the study area (the waves had already arrived at Brittany, but not yet at the Trefle location). On the opposite, the 2022/05/22 flight occurred on a very mild day, with  $H_s$  of the order of 1 m. For the 2022/05/25 and 2022/05/26 flights, the waves were only marginally higher, of the order of 2 m. This figure also shows a clear and strong modulation of the sea state by tidal currents.

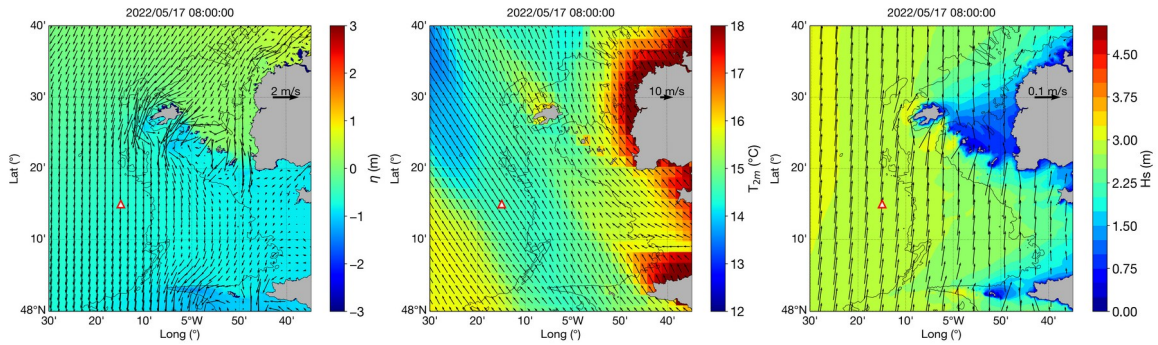


Figure 6: MARS2D simulated current (left) AROME wind and surface temperature (center) and WW3 simulated significant wave height and direction (right) over the Iroise Sea on 2022/05/17. On all plots, the thin lines mark the 50 m, 100 m and 150 m isobaths.

The panels in Figure 6 show the conditions prevailing during the 2022/05/17 flight in terms of current (left) wind (center) and waves (right). During this flight, the current (of mostly tidal origin) was flowing from the North-West to the South-East, and opposing the wind. The large swell event was arriving from the West.

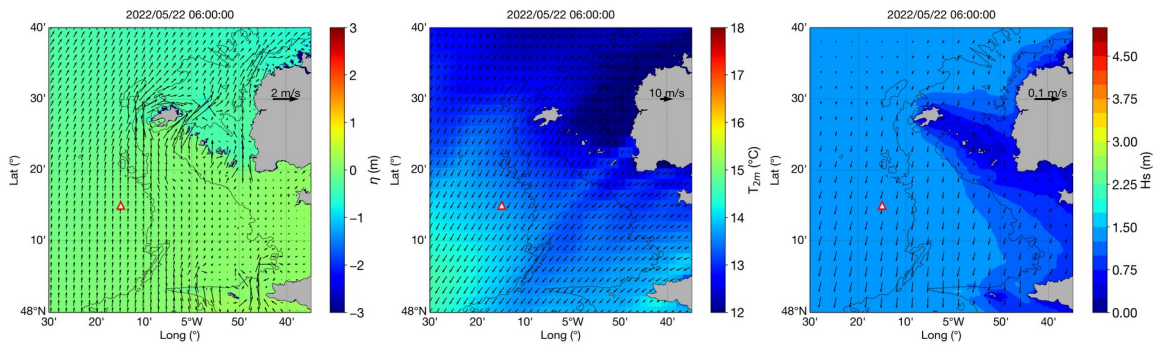


Figure 7: MARS2D simulated current (left) AROME wind and surface temperature (center) and WW3 simulated significant wave height and direction (right) over the Iroise Sea on 2022/05/22. On all plots, the thin lines mark the 50 m, 100 m and 150 m isobaths.

The panels in Figure 7 show the conditions prevailing during the 2022/05/22 flight in terms of current (left) wind (center) and waves (right). During this flight, the current (of mostly tidal origin) was flowing from the South into the English Channel, and opposing the North-Easterly wind. The sea state was very mild.

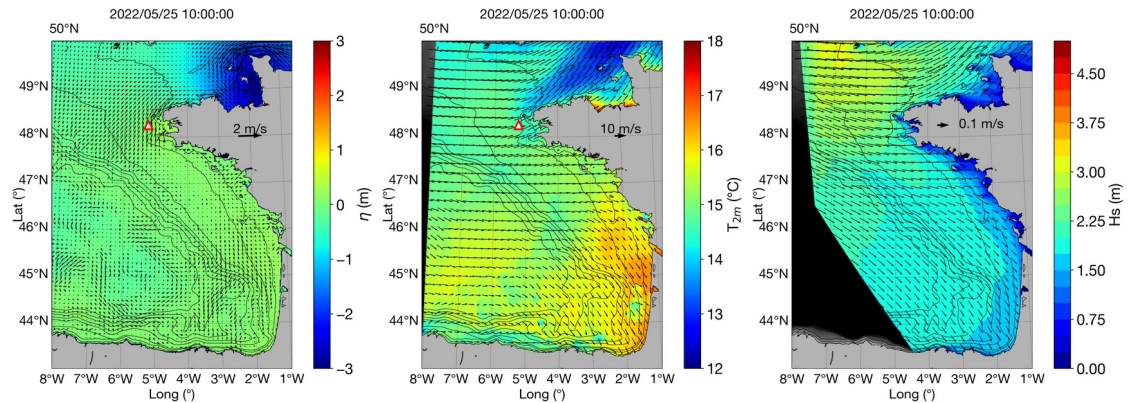
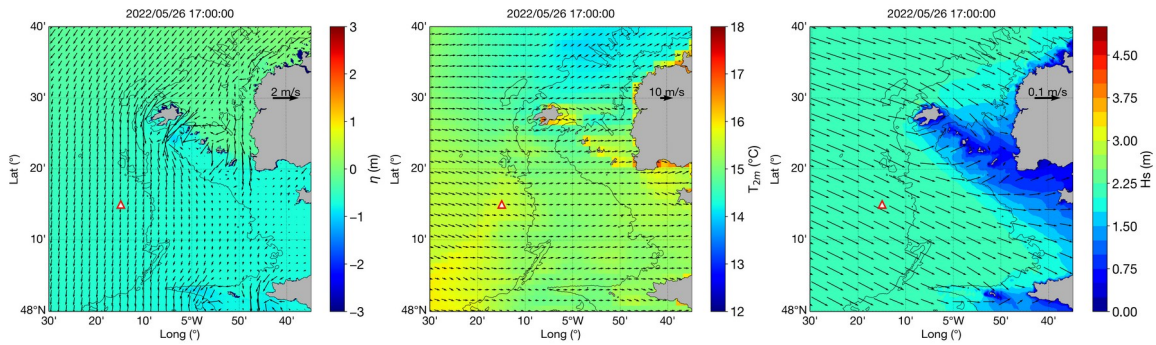


Figure 8: MARS3D simulated current (left) AROME wind and surface temperature (center) and WW3 simulated significant wave height (right) over the Bay of Biscay on 2022/05/25. On all plots, the thin lines mark the 50 m, 100 m and 150 m isobaths.



*Biscay on 2022/05/25. On all plots, the thin lines mark the 50 m, 100 m, 150 m, 500 m, 1000 m, 2000 m, 3000 m, 4000 m isobaths.*

The panels in Figure 8 show the conditions prevailing during the 2022/05/25 flight in terms of current (left) wind (center) and waves (right). Recalling that this flight mostly sampled the open-ocean regime at the level of the shelf break, we can see that currents in this area were much weaker, that the wind was blowing from the West at roughly 10 m/s, and that the sea state was quite mild.



*Figure 9: MARS2D simulated current (left) AROME wind and surface temperature (center) and WW3 simulated significant wave height and direction (right) over the Iroise Sea on 2022/05/26. On all plots, the thin lines mark the 50 m, 100 m and 150 m isobaths.*

The panels in Figure 9 show the conditions prevailing during the 2022/05/26 flight in terms of current (left) wind (center) and waves (right). The current was quite weak and flowing out of the English Channel. The wind was also weak and blowing from the West. Finally, the significant wave height was of the order of 2 m. Altogether, one can consider that this flight sampled a set of relatively mild conditions for such a midlatitude open-ocean location.

## 1.5 Campaign Components

The airborne component involved the OSCAR Ku-band SEASTAR demonstrator, deployed onboard the PA-31 Piper Navajo aircraft (NL-PNB) operated by MetaSensing from the Morlaix airport (LFRU). The plane arrived in Morlaix on 2022-05-16, made a back-and-forth trip to the Netherlands from 2022-05-18 to 2022-05-21 for 50-hours flight time maintenance, and finally left from Morlaix on 2022-05-27.

An overall four flights were performed:

- on 2022/05/17, from 08:10 UTC to 10:25 UTC, targetting the “Ushant” and “Homogeneous” zones.
- on 2022/05/22, from 05:10 UTC to 08:00 UTC, targetting the “Ushant” and “Homogeneous” zones.
- on 2022/05/25, from 08:00 UTC to 12:00 UTC, flying offshore along the Metop-B and Metop-C ASCAT swaths.
- on 2022/05/26, from 16:00 UTC to 19:30 UTC targetting the “Ushant” and “Homogeneous” zones.

The “ground truth” component involved:

- a dual mooring, deployed on 2022/05/13 and recovered on 2022/05/31. This mooring was composed of a “FLAME” buoy, equipped with a high-frequency sonic anemometer, which was damaged at deployment and did not provide data (see section 2.1 ), and a “TREFLE” data equipped with a 300 KHz RDI Workhorse ADCP and a Xsens MTI-G IMU, which provided measurements of sea state and ocean currents (see section 2.2 ).
- a HF radar system composed of two sites located at “Pointe de Brezellec” and “Pointe de Garchine”, which provided sea surface current observations during the 2022/05/22 and 2022/05/26 flights (see section 3.1 ).
- an X-band radar system located on the “La Jument” lighthouse, to the southwest of the island of Ushant (see section 3.2 ).

Other assets, which were not specifically deployed for the campaign, but whose datasets are freely available and can be used in conjunction with the airborne data, are:

- a Datawell DWR MKIII buoy operated by the french government agency CEREMA near the “Pierres Noires” lighthouse.
- NDBC buoy # 62163 (“Brittany”), located at the shelf break to the west of the area, jointly operated by Météo France and the UK Met Office.

## 2 In-situ data

### 2.1 “FLAME” buoy data



*Figure 10: Photograph of the FLAME buoy shortly after its deployment. The Campbell Scientific Irgason sonic anemometer/gas analyzer and the Gill Metpak Pro compact meteorological station are visible at the top of the mast. The hull (in orange) contains the batteries. The vane (in red) ensures that the anemometers face the wind at all times.*

The FLAME (“Flux Air-Mer par Eddy correlation”, see figure 10) buoy is an autonomous platform that has been designed and built at LOPS to perform direct eddy-correlation measurements of momentum, sensible and latent heat fluxes at the air-sea interface.

Its main instrument is a Campbell Irgason integrated sonic anemometer / IR gas analyzer, which measures at 60 Hz the turbulent wind velocity, sonic temperature and humidity fluctuations.

This instrument is complemented by an SBG Ellipse-N IMU, which measures the sensor position, orientation and motion, and a Gill Metpak pro compact meteorological sensor package, which performs 1 Hz measurements of air temperature, air humidity and air pressure.

The datastreams from the three sensors are timestamped and recorded by a datalogger built around a Raspberry Pi/3B microcomputer. This microcomputer can be remotely controlled by a field Wifi bridge.

Every 15 minutes, the GPS location of the buoy is transmitted by the Iridium satellite communication system.

The batteries and ballasting weight are contained in the hull of the buoy, and a vane forces the anemometers to face the wind at all times.

The buoy was deployed at 9:15 TU on 2022/05/13, at N48°15.28', W5°14.99', and recovered at the same location at 10:40 TU on 2022/05/31.

During the deployment operation, the buoy capsized. This caused a water ingress, which was not noticed at the time, and caused a datalogger failure shortly after. During the recovery operation, a shock on the ship hull caused the destruction of the IRGASon sensor head.

**In conclusion, the SEASTARex FLAME buoy deployment did not yield any usable wind data.**

## 2.2 “TREFLE” buoy data

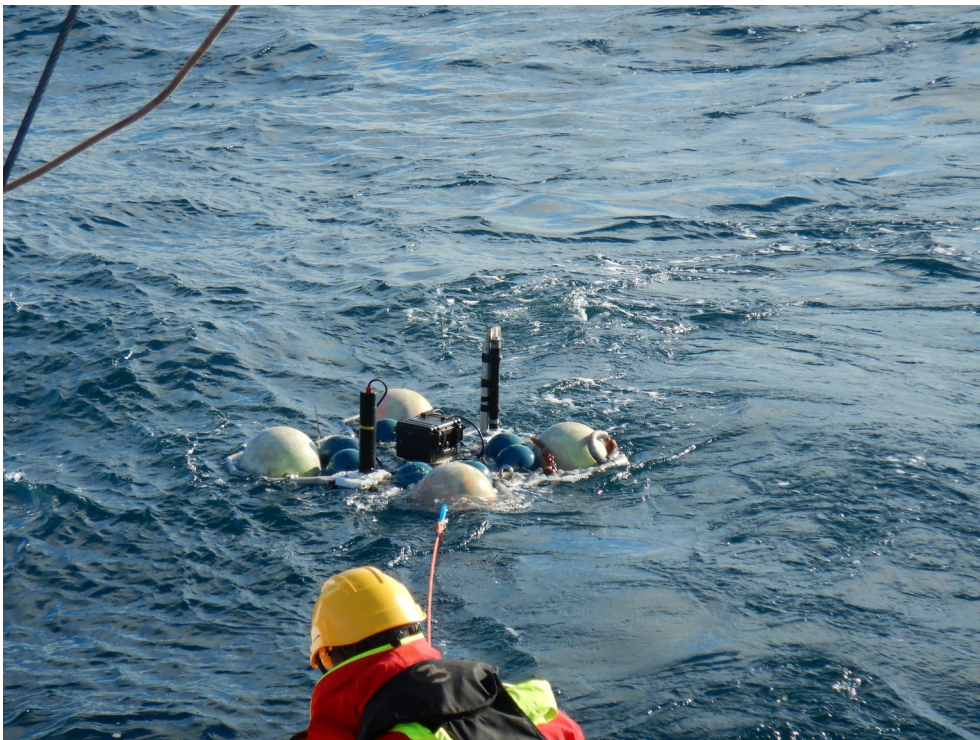


*Figure 11: Photograph of the Trêfle buoy shortly after its deployment. The black box contains the datalogger and its batteries. It is mounted on the end cap of the Workhorse RDI 300 kHz ADCP. A flashing beacon can be seen on the right.*

The “Trêfle” buoy is a platform designed and built at LOPS to perform autonomous current measurements from the sea surface. For the SEASTARex campaign, it was equipped with an RDI Workhorse 300 kHz Acoustic Doppler Current Profiler.

These instruments are complemented with a X-Sens MTI-G IMU, used to compensate the velocity measurements for platform motion, and to provide sea state measurements. These datastreams are timestamped and recorded using a datalogger built from a Persistor™ microcomputer.

The Trêfle buoy was deployed at 9:15 TU on 2022/05/13, at N48°15.28', W5°14.99', and recovered at the same location at 10:40 TU on 2022/05/31.

**It worked mostly satisfactorily, and provided usable sea state data until 17:20 TU on 2022/05/27, when the IMU and datalogger battery pack was exhausted, and usable**



**ADCP data until 01:50 on 2022/05/24, when the ADCP battery pack was exhausted. No ADCP data are thus available for the 2022/05/25 and 2022/05/26 flights.**

### 2.3 “Pierres Noires” buoy data

This buoy is a Datawell DWR MKIII directional wave buoy, operated by CEREMA on behalf of the french government. It is located at N 48°17.42', W 4°58.1', to the north of the “Homogeneous” area. **It provided usable directional wave measurements over the entire duration of the campaign.**

### 2.4 NDBC 62163 “Brittany” buoy data

This buoy is a meteorological buoy jointly operated by the UK Met Office and Meteo France. It is located at the shelf break, at N 47°33', W 8°28.2', quite far to the west of the campaign area. **It provided usable directional wave measurements over the entire duration of the campaign but, due to an anemometer failure, did not provide wind measurements.**

## 3 Ground-based remote sensing data

### 3.1 HF radar data

The “Ushant” and “Homogeneous” areas are within coverage of a two-sites HF-radar system, originally installed by Shom, the french hydrographic service, in 2005, and operated during the campaign by IFREMER.

Two sites equipped with 12.380 MHz “WERA” instruments manufactured by Helzel Messtechnik GmbH are located in “Pointe de Garchine” and “Pointe de Brezellec”, respectively to the north and to the south of the study area.

Each site provides maps of the radial component of current on a cartesian grid at 2 km posting every 10 minutes.

The Brezellec site performed nominally during the campaign, and the data record is available over the full duration of the campaign.

Significant difficulties were however experienced on the Garchine site, **restricting the data availability to the 2022/05/22 and the 2022/05/26 flights.**

### 3.2 “La Jument” Stereo-Video data

The “La Jument” Lighthouse is equipped with a stereo video system that has been in service since the year 2017, and is operated remotely by FEM.

Presently it is composed of two FLIR 5.0 MP cameras installed at the top of the lighthouse separated by 5 meters and equipped with zooms lenses (4x) facing to the SW.

The system permits the reconstruction of the sea surface height over an area that ranges from about 200m to 600m from the lighthouse and 100m width.

The images are acquired time synchronized at 5 Hz and then processed with the WASS system to compute the surface elevation using stereo triangulation.

This allows one to have a good resolution of the evolving wave field and compute its temporal and spatial statistics. The ocean currents are also inferred from the 3D wave spectra.

During the campaign the **2022/05/17 data were acquired nominally**. Some gaps occur due to rain and bad visibility.

On the other days, due to a failure of the set-up power supply at the lighthouse, **no data acquisition has been possible**.

### 3.3 “La Jument” X-band radar data

The “La Jument” Lighthouse is equipped with a recording 12-kW X-band (9.3 GHz) marine radar, with vertical transmit and receive polarizations (VV-pol). The instrument is mounted at a height of about 43 m.a.s.l. and runs in a rotational mode covering a range of roughly 3260 m at 0.5 Hz around the lighthouse.

During this experiment, the X-band marine radar was used to observe ocean waves in space and time.

This allows the measurement of the two-dimensional wave spectra from which parameters such as the peak wave direction and peak wave period can be determined. In addition, the radar data give surface wave properties such as wavelength and phase velocity, which in turn enable one to retrieve the surface current vector. The surface currents measurements result from the difference between the observed phase velocity and that given by the linear dispersion relation of surface gravity waves. A surface current vector is produced every 200 m.

During the campaign the **2022/05/17 data were acquired nominally**.

On the other days, due to a failure of the set-up power supply at the lighthouse, **no data acquisition has been possible**.

## 4 Satellite remote sensing data

### 4.1 SAR satellite data

Date	Day	Data type and time range
16/05	Monday	NovaSAR (23:37 UTC)
17/05	Tuesday	NovaSAR (10:30UTC, 23:43UTC), Capella (14:47UTC)
18/05	Wednesday	Radarsat-2 (06:21UTC), ICEYE (15:16UTC)
19/05	Thursday	TerraSAR-X (06:35UTC); S1 (06:24UTC)
20/05	Friday	ICEYE (14:49UTC); S1 (18:13UTC);
21/05	Saturday	Radarsat-2 (06:33UTC)
22/05	Sunday	ICEYE (14:48UTC); TerraSAR-X (18:00UTC);
23/05	Monday	ICEYE (10:29UTC)
24/05	Tuesday	TerraSAR-X (06:45UTC)
25/05	Wednesday	ICEYE (10:06UTC)
26/05	Thursday	
27/05	Friday	TerraSAR-X (18:10UTC), S1 (18:05UTC)
28/05	Saturday	NovaSAR (10:48UTC)

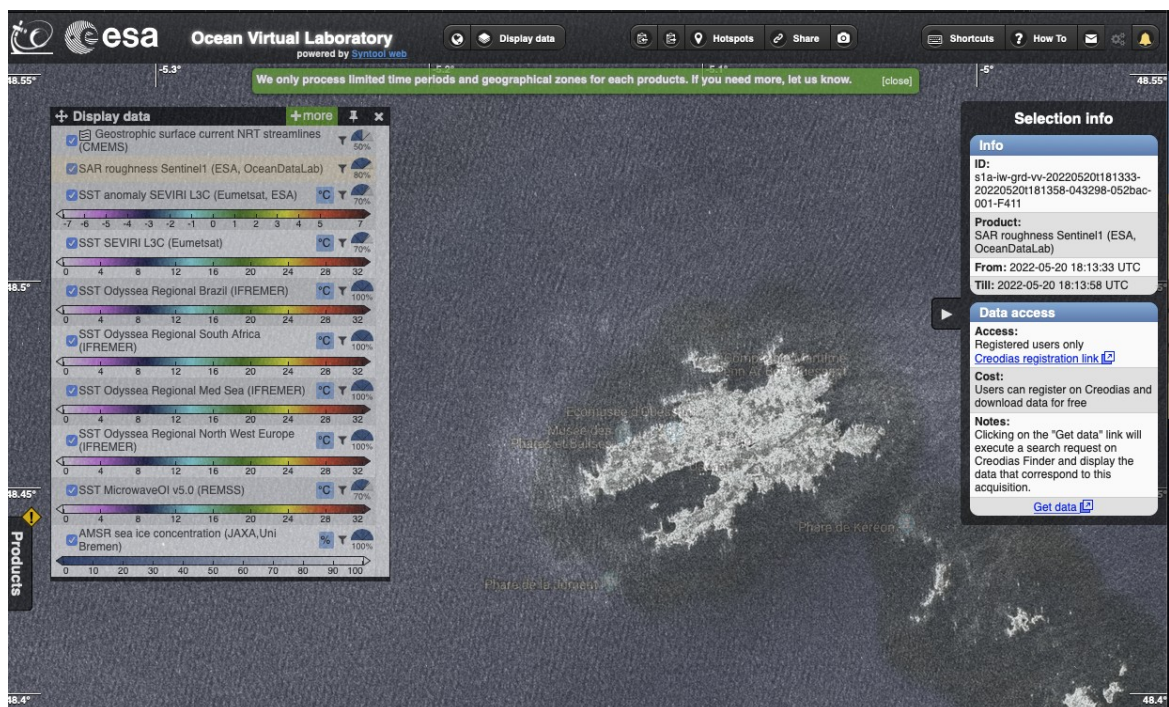


Figure 12: Sentinel-1 data for the 20/05/2022. Zoom over Ouessant.

Six additional Capella acquisitions were also performed on:

2022/05/29 21:04UTC, 2022/05/31 01:43UTC, 2022/06/01 21:36UTC,  
2022/06/17 10:03UTC, 2022/06/21 10:12UTC, 2022/07/08 10:16UTC.



## 4.2 Optical satellite data

Date	Day	Data type and time range	Cloud conditions
16/05	Monday	No usable SST scene.	Mixed
17/05	Tuesday	S2B (1121), S3A (2156), S3B (2117) MODIS/Aqua (0304), VIIRS/SNPP (0306), VIIRS/N20 (0217)	Cloudy
18/05	Wednesday	MODIS/Aqua (0209), VIIRS/SNPP (0247), VIIRS/N20 (0158)	Cloudy
19/05	Thursday	S2A (1121), VIIRS/N20 (1306)	Mixed
20/05	Friday	S3A (1055), S3B (1016), MODIS/Aqua (1305), VIIRS/SNPP (1156,1336), VIIRS/N20 (1247,1428)	Clear sky
21/05	Saturday	S3A (1029), MODIS/Aqua (0239,1348), VIIRS/SNPP (0151,1137,1317), VIIRS/N20 (0242,1228,1409)	Clear sky
22/05	Sunday	No usable SST scene.	Cloudy
23/05	Monday	No usable SST scene.	Cloudy
24/05	Tuesday	S3A (1052), S2B (1121), MODIS/Aqua (1240), VIIRS/SNPP (1221,1401)	Mixed
25/05	Wednesday	No usable SST scene.	Cloudy
26/05	Thursday	MODIS/Aqua (1406), VIIRS/SNPP (1323)	Front, Mixed
27/05	Friday	S3B (2158)	Cloudy
28/05	Saturday	No usable SST scene.	Clear sky

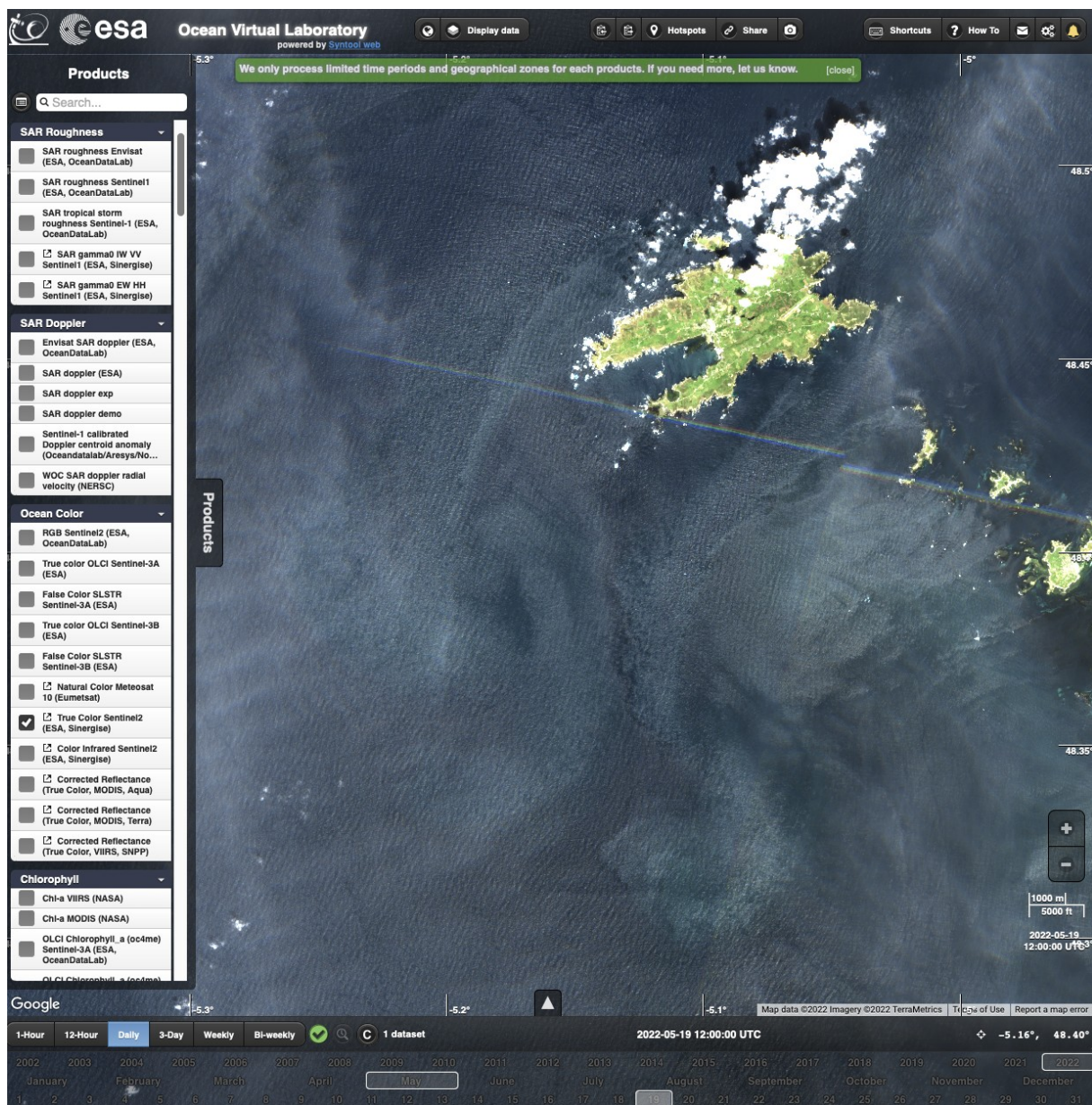


Figure 13: True color Sentinel-2 data on the 19/05 at 11:21 UTC. Zoom over Ushant.

### 4.3 Other satellite data

CFOSAT: 17/05, 24/05, 30/05

Altimeters: 16/05 (S3B 2139), 18/05 (HY-2B); 19/05 (S6A 0946); 20/05 (S3B 2136); 21/05 (J3); 26/05 (S3B 1058);

ASCAT: 2022/05/25 (Metop-B 0916, 2105), (Metop-C 1009, 2018).

## 5 Summary of operations

The daily schedule of the campaign was the following:

### 5.1 2022/05/17

Instrument	Summary
OSCAR airborne radar	Flight over the “Ushant” and “Homogeneous” zones, from 08:10 UTC to 10:25 UTC
“TREFLE” buoy	Directional sea state data <b>OK</b> Current data <b>OK</b>
“Pierres Noires” buoy	Directional sea state data <b>OK</b>
“Brittany” buoy	Directional sea state data <b>OK</b>
HF radar sites	Brezellec site (south) <b>OK</b> Garchine site (north) <b>data gaps, low coverage</b>
“La Jument” stéréo-vidéo	Video measurements from 8:30 to 14:00 <b>OK</b> Some gaps due to bad visibility.
“La Jument” X-band radar	Current data <b>OK</b>

### 5.2 2022/05/22

Instrument	Summary
OSCAR airborne radar	Flight over the “Ushant” and “Homogeneous” zones, from 05:10 UTC to 08:00 UTC
“TREFLE” buoy	Directional sea state data <b>OK</b> Current data <b>OK</b>
“Pierres Noires” buoy	Directional sea state data <b>OK</b>
“Brittany” buoy	Directional sea state data <b>OK</b>
HF radar sites	Brezellec site (south) <b>OK</b> Garchine site (north) <b>OK</b>
“La Jument” stéréo-vidéo	Power outage in the lighthouse <b>no data</b>
“La Jument” X-band radar	Power outage in the lighthouse <b>no data</b>

### 5.3 2022/05/25

Instrument	Summary
OSCAR airborne radar	Flight over the Metop B/C ASCAT swath, from 08:00 UTC to 12:00 UTC
“TREFLE” buoy	Directional sea state data <b>OK</b> <b>No current data</b>
“Pierres Noires” buoy	Directional sea state data <b>OK</b>
“Brittany” buoy	Directional sea state data <b>OK</b>
HF radar sites	Brezellec site (south) <b>OK</b> Garchine site (north) <b>no data</b>
“La Jument” stéréo-vidéo	Power outage in the lighthouse <b>no data</b>
“La Jument” X-band radar	Power outage in the lighthouse <b>no data</b>

### 5.4 2022/05/26

Instrument	Summary
OSCAR airborne radar	Flight over the “Ushant” and “Homogeneous” zones, from 16:00 UTC to 19:30 UTC
“TREFLE” buoy	Directional sea state data <b>OK</b> <b>No current data</b>
“Pierres Noires” buoy	Directional sea state data <b>OK</b>
“Brittany” buoy	Directional sea state data <b>OK</b>
HF radar sites	Brezellec site (south) <b>OK</b> Garchine site (north) <b>OK</b>
“La Jument” stéréo-vidéo	Power outage in the lighthouse <b>no data</b>
“La Jument” X-band radar	Power outage in the lighthouse <b>no data</b>

## 6 Summary

This reports provides an overview of the data collected as part of the SEASTARex field campaign, funded by ESA as part of the design and feasibility studies of the “SEASTAR” EE11 candidate mission.

The field campaign took place in the Iroise Sea, in the vicinity of Brest, France, from 17/05/2022 to 26/05/2022.

It involved an airborne data acquisition component, which collected radar radiometry and Doppler observations using the OSCAR airborne Ku-band radar, deployed from a PA-31 Piper Navajo aircraft operated by MetaSensing, as well as in-situ (sea state and surface current measurements using moored buoys) and ground-based remote sensing components (HF radar surface current and X-band radar surface current and sea state measurements).

The SEASTARex data collection effort went well, favored by unexpectedly mild conditions for the area and period of year. With the exception of the FLAME eddy correlation buoy, and one of the HF radar sites which experienced some data availability issues, the instruments performed nominally during at least part of the experiment, yielding a very large, high quality data set.

## Acknowledgements

This study was supported by the SeaSTARex contract from the European Space Agency (400017623/22/NL/IA). This study was possible thanks to the previous work done over the ESA OSCAR contract and the long and constant determination of ESA staff amongst them Tania Casal, Petrolino Martin-Iglesias and Nico Gebert, MetaSensing staffs who developed the instrument and in particular, Christian Trampuz and Hugo Kerhuel.

The in situ measurements owe much to the dedication of the “TSM” ship crew.

We thanks the pilot for his skilled maneuvers to follow our strange patterns over the sea.

**ANNEX D) EVALUATION OF THE  
SURFACE CURRENT FROM  
OBSERVATION BY STEREO-VIDEO FROM  
THE LIGHTHOUSE OF LA JUMENT**



# Evaluation of the surface current from observation by Stereo-Video from the lighthouse of La Jument

Rapport vf

23/06/2023

## SUIVI DU DOCUMENT

<b>Auteurs</b>	LECKLER, Fabien DUARTE, Rui GUINOT, Florent FILIPOT, Jean-François	France Energies Marines
<b>Titre du document</b>	Evaluation of the surface current from observation by Stereo-Video from the lighthouse of La Jument.	
<b>Statut du document</b>	Final Version	
<b>Date de sauvegarde</b>	23/06/2023	
<b>Date de diffusion</b>	23/06/2023	
<b>Version du document</b>	Final	
<b>Nom du fichier</b>	220620_Rapport_NOC_2022_024_SEASTAREX_vf.pdf	
<b>Nombre de pages</b>	22	
<b>Niveau de diffusion</b>	NOC / FEM	

## APPROBATION

Version	Date	Approuvé par	Titre
V1	12/06/2023	Filipot, Jean-François (FEM)	Scientific Director (FEM)

Signature :

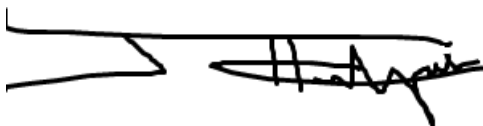


# Table des matières

- Liste des figures ..... 4
- Liste des tableaux ..... 4
- Objective..... 5
- Estimation of the surface current speed ..... 5
- Deployment ..... 5
- Camera calibration..... 7
  - 1 Intrinsic calibration ..... 7
  - 2 Extrinsic calibration..... 9
- Sea surface elevation maps ..... 10
- Carried out acquisition..... 12
- Statistical validation of the elevation maps..... 13
- Conclusions ..... 21
- References ..... 22

## Liste des figures

Figure 1: Location of the La Jument lighthouse from which the stereo video system was deployed. ....	6
Figure 2: Stereo video system deployed on top of La Jument lighthouse, next to the X-band radar. ....	6
Figure 3: Projection of the chessboards used for the calibration of the left camera. ....	7
Figure 4: Distortion model obtained after calibration for the left camera. The arrows represent the distortion, in pixels. ....	8
Figure 5: Projection of the chessboards used for the calibration of the right camera. ....	8
Figure 6: Distortion model obtained after calibration for the right camera. The arrows represent the distortion, in pixels. ....	9
Figure 7: Relative positions of the two cameras, plotted in the frame of reference of the right camera. ....	10
Figure 8: Illustration of the processing chain for sea surface reconstruction. Top figures: similar points detected in stereo images; bottom left: stereo-triangulation of points in the right camera frame; bottom right: rotation and translation of the point cloud to a geo-reference. Figure taken from Leckler (2013). ....	11
Figure 9: Illustration of the principle of stereo-triangulation. Image taken from Benetazzo (2006). ....	12
Figure 10: Retrieved sea surface elevations reprojected on the left image and the corresponding gridded surface obtained for the first image pair. ....	12
Figure 11: Sequence of retrieved elevation maps. Only one image out of five is shown. ....	13
Figure 12: Data availability at each grid point. ....	14
Figure 13: Significant wave height map obtained from the variance of the elevation at each grid point. Values are masked if data availability is less than 99%. ....	14
Figure 14: Selected areas for statistical analysis, plotted over the first retrieved elevation map. ....	15
Figure 15: Left: PDF of the elevations obtained in each area. The black dashed line correspond the expected Gaussian distribution for linear waves. Right: Frequency spectra computed at each grid points contained in each area (thin lines) and mean frequency spectrum over the whole area (main line). The areas are shown on Figure 13. ....	16
Figure 16: Comparison of elevation PDFs (left) and frequency wave spectra (right) obtained for each area. ....	17
Figure 17: 3D wave spectrum obtained for the area 1 (the closest one from the lighthouse). Left panel represents the frequency-wavenumber spectrum (i.e. 3D wave spectrum integrated over directions), and right panels are slices of the 3D spectrum at given frequencies $fc$ . The linear dispersion relation without current is represented by black lines. ....	17
Figure 18 : 3D wave spectrum obtained for the area 2. Left panel represents the frequency-wavenumber spectrum (i.e. 3D wave spectrum integrated over directions), and right panels are slices of the 3D spectrum at given frequencies $fc$ . The linear dispersion relation without current is represented by black lines. ....	18
Figure 19 : 3D wave spectrum obtained for the area 3. Left panel represents the frequency-wavenumber spectrum (i.e. 3D wave spectrum integrated over directions), and right panels are slices of the 3D spectrum at given frequencies $fc$ . The linear dispersion relation without current is represented by black lines. ....	18
Figure 20 : 3D wave spectrum obtained for the area 4 (the furthest one from the lighthouse). Left panel represents the frequency-wavenumber spectrum (i.e. 3D wave spectrum integrated over directions), and right panels are slices of the 3D spectrum at given frequencies $fc$ . The linear dispersion relation without current is represented by black lines. ....	19
Figure 21 : 3D wave spectrum obtained for the area 1 (the closest one from the lighthouse) after an arbitrary scaling of the surface with a factor 3. Left panel represents the frequency-wavenumber spectrum (i.e. 3D wave spectrum integrated over directions), and right panels are slices of the 3D spectrum at given frequencies $fc$ . The linear dispersion relation without current is represented by black lines. ....	19
Figure 22: Sensibility analysis of camera intrinsic parameter. Variation of the focal length with $f = (1 + \delta)f_{init}$ ....	20
Figure 23: Sensibility analysis of extrinsic parameter. Variation of the yaw angle with $\theta = \theta_{init} + \Delta\theta$ . ....	21

## Liste des tableaux

Aucune entrée de table d'illustration n'a été trouvée.

## Objective

---

An innovative satellite mission concept, named SEASTAR, was proposed by the National Oceanography Centre (NOC) in 2020 in response to the ESA Earth Explorer 11 call. The SEASTAR instrument aims to provide accurate 2-D fields of Total Surface Current Vectors (TSCV) and Ocean Surface Vector Winds (OSVW) at 1-km resolution.

In the context of the development of SEASTAR, a dedicated scientific campaign was done over the Iroise Sea in May 2022, combining airborne, ground truth measurements and output from existing numerical oceanographic models for waves and currents in the area. The present study aims to provide an innovative estimation of the sea surface current from a stereo-video system.

The objective of the study is thus to reconstruct the sea surface elevation maps in order to extract a measure of the 3D wave spectrum,  $E(f, k, \theta)$ , with  $f$  the wave frequency,  $k$ , the wavenumber,  $\theta$ , the wave direction. Then, the surface current is estimated using the difference between the observed and theoretical wave dispersion relations.

## Estimation of the surface current speed

---

Considering the wave as linear, the wave angular frequency,  $\sigma = 2\pi f$ , is linked to the wave number,  $k$ , by the dispersion relation :

$$\sigma^2 = gk \tanh(kd)$$

with  $d$  the water depth and  $g$  the gravitational constant.

In the presence of an uniform current  $U$ , and neglecting the bottom friction, the absolute angular wave frequency,  $\omega$ , as measured in the reference frame attached to the bottom, equals

$$\omega = \sigma + \mathbf{k} \cdot \mathbf{U}$$

The uniform current,  $U$ , only introduces a simple Doppler frequency shift. The current can thus be estimated using the deviation of the observed dispersion relation from the theoretical dispersion relation without current (see *Leckler et al. (2015)* for example). Such an estimation is very sensitive to the quality of the reconstructed sea surfaces and thus requires a very accurate sea surface reconstruction that has not been reached.

The rest of the document will be dedicated to the description of a field experiment designed to estimate  $U$  from stereo-video reconstruction of surface wave and to the data quality analysis, with regards to the above objective.

## Deployment

---

A stereo-video system has been deployed from the La Jument lighthouse, southwest of the Ushant Island (see Figure 1). The tower offers a privileged location for such a deployment, providing a fixed platform in mid-to-deep water. The deployed system consists of two high resolution cameras (FLIR Blackfly S USB3, BFS-U3-50S5M-C: 5.0 MP, 35 FPS, Sony IMX264, Mono) equipped with optics (Kowa LMVZ166HC 1" 16-64mm F1.8 Manual Iris Vari-Focal C-Mount Lens) connected to an acquisition station. The distance between the two cameras is 5m. Figure 2 shows the deployed system.

Note that in contrast with the stereo-video systems usually used in published studies, the use of zoom lenses, required to estimate the current far away from the lighthouse, raises difficulties that are discussed latter.

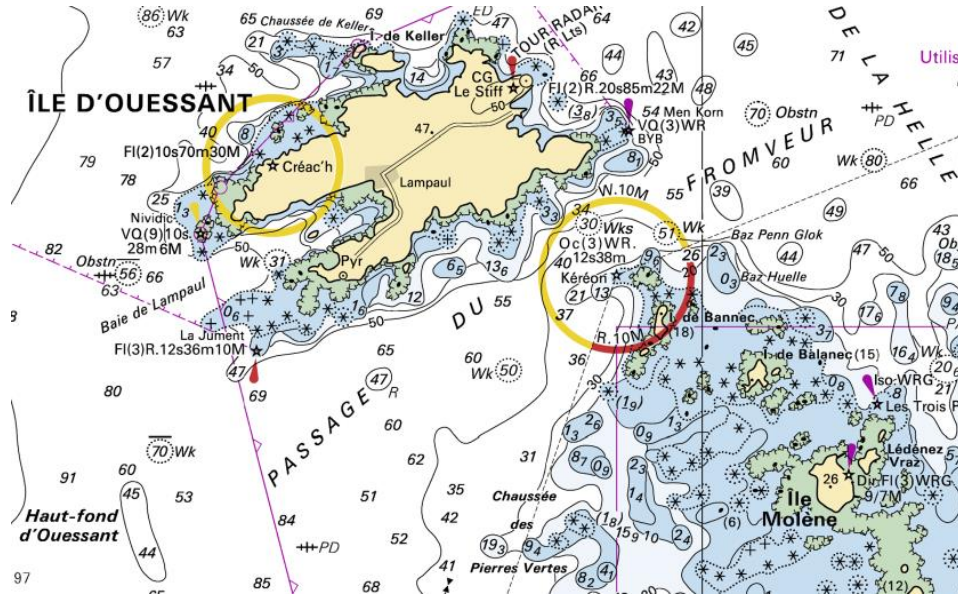


Figure 1: Location of the La Jument lighthouse from which the stereo video system was deployed.



Figure 2: Stereo video system deployed on top of La Jument lighthouse, next to the X-band radar.



# Camera calibration

## 1 Intrinsic calibration

In order to process the images from the stereo-video system, a calibration of the cameras is necessary. This one aims at obtaining with a great precision the intrinsic parameters of each camera (focal length, central point, distortion coefficients, ...). The calibration has been done here with the Matlab® toolbox written by Jean-Yves Bouguet<sup>1</sup>. The details of the calibration procedure are available in *Leckler (2013)*<sup>2</sup>. For each camera, numerous images of a chessboard of known dimensions were acquired and 257 and 259 chessboard images were selected for the left (Figure 3) and right (Figure 5) cameras, respectively. The calibration results are of very good quality with root mean square reprojection errors less than 0.5 pixel for both cameras. The obtained distortion models are plotted in Figure 4 and Figure 6, respectively.

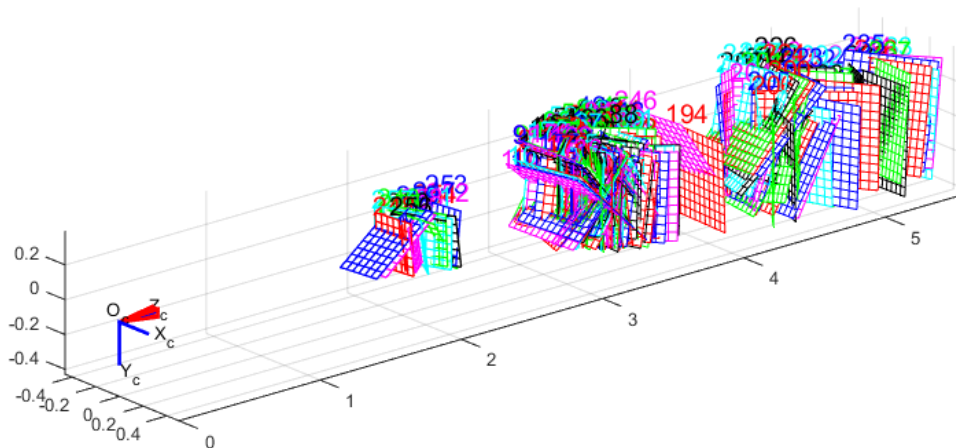


Figure 3: Projection of the chessboards used for the calibration of the left camera.

<sup>1</sup> [http://www.vision.caltech.edu/bouguetj/calib\\_doc/](http://www.vision.caltech.edu/bouguetj/calib_doc/)

<sup>2</sup> <https://tel.archives-ouvertes.fr/tel-01622848/document>

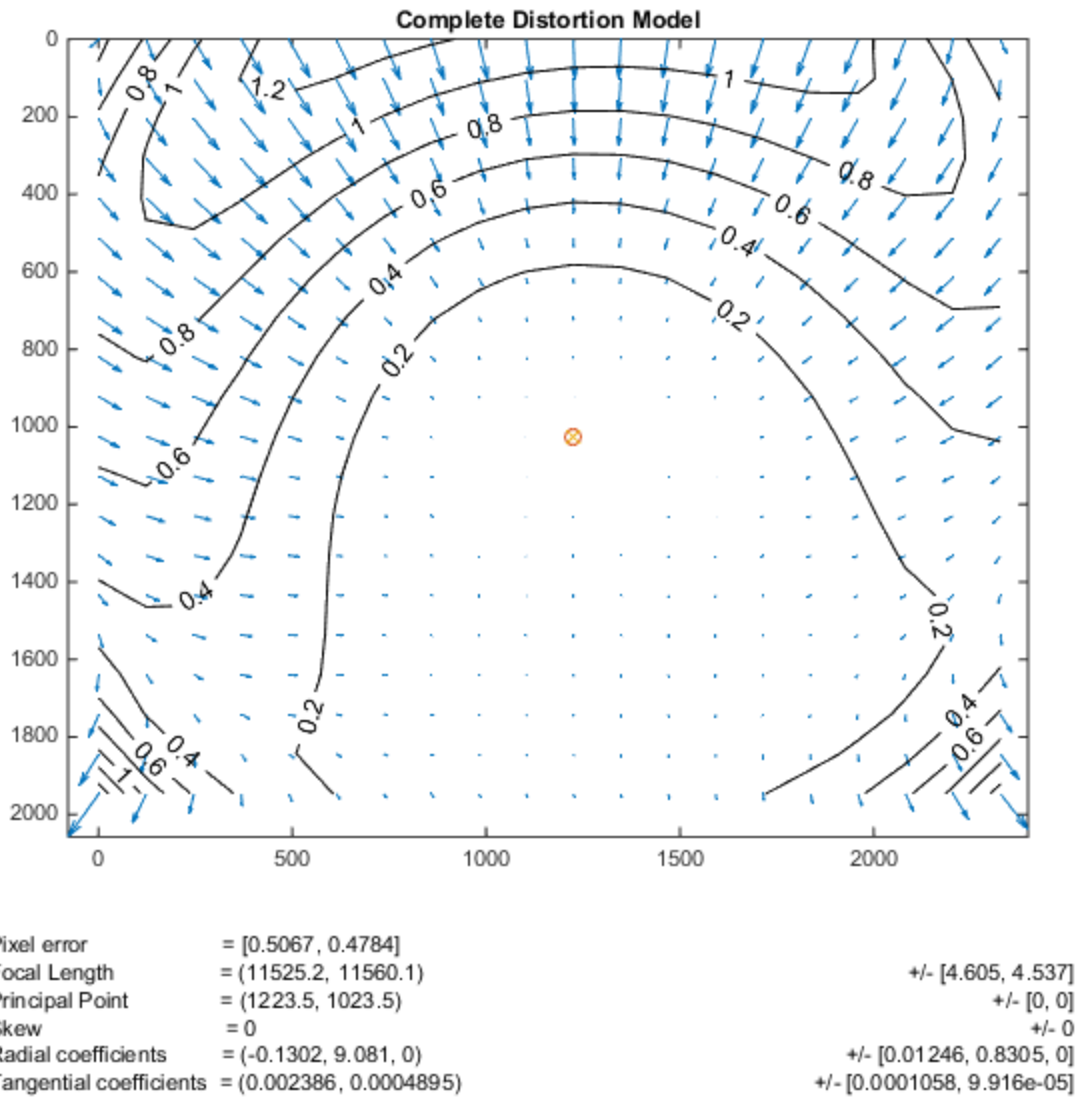


Figure 4: Distortion model obtained after calibration for the left camera. The arrows represent the distortion, in pixels.

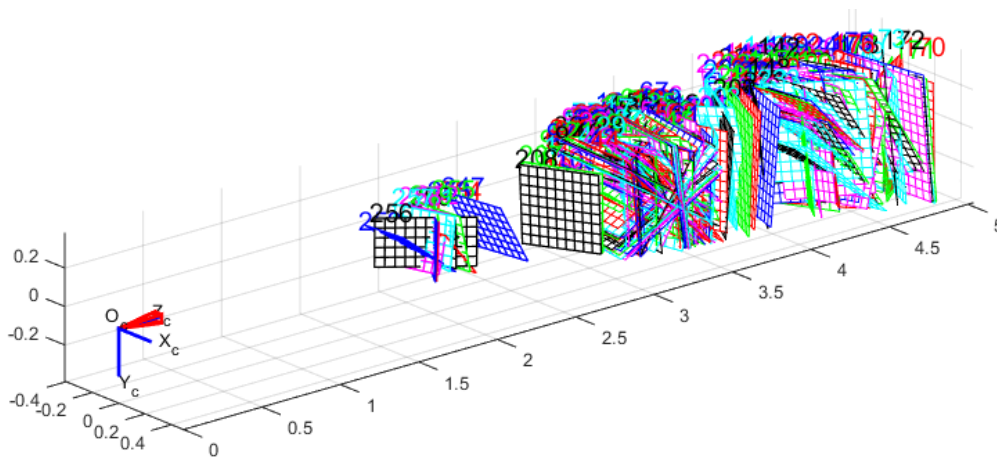


Figure 5: Projection of the chessboards used for the calibration of the right camera.

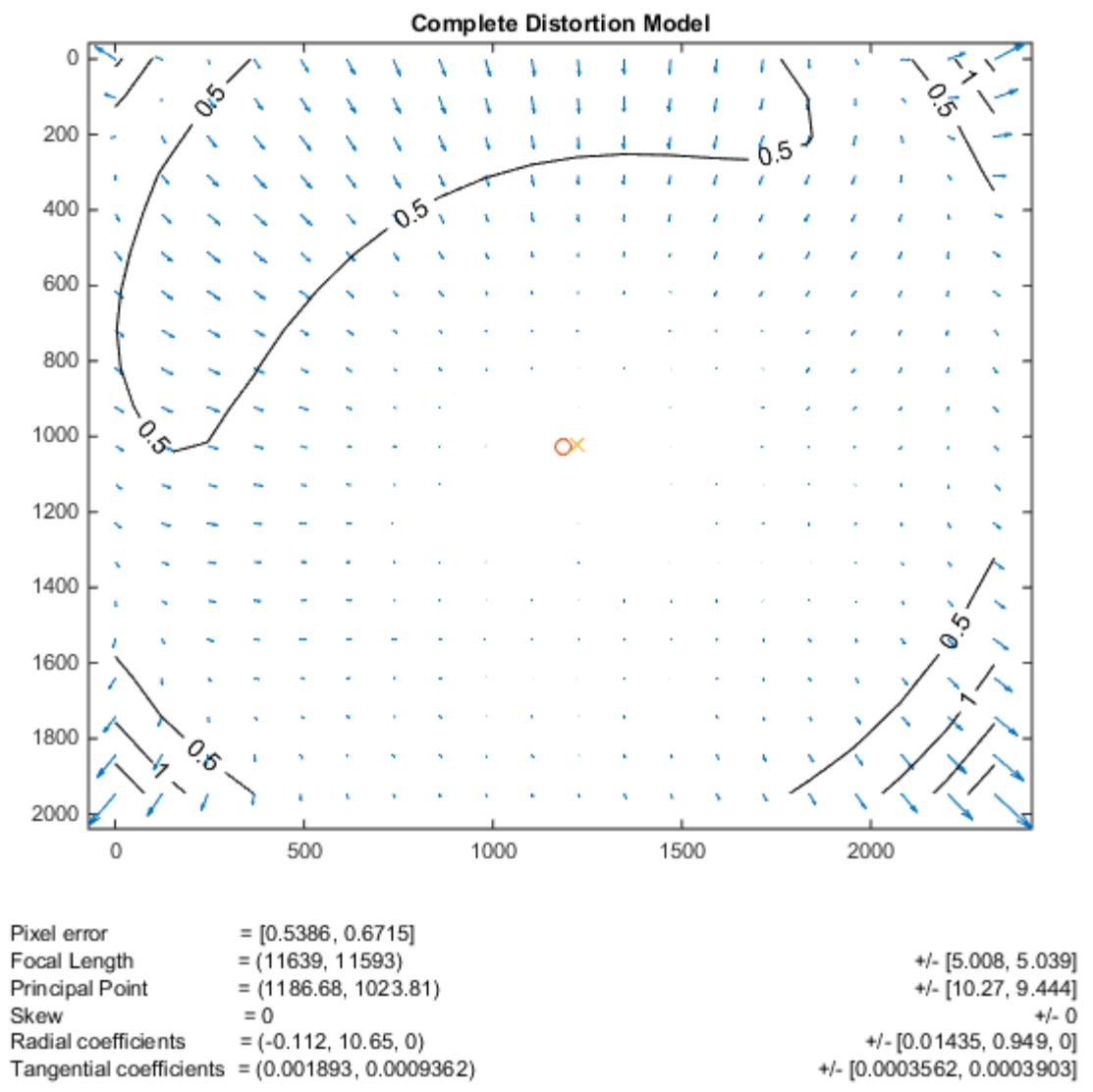


Figure 6: Distortion model obtained after calibration for the right camera. The arrows represent the distortion, in pixels.

## 2 Extrinsic calibration

In order to triangulate the points, it is necessary to know the relative position of the cameras (i.e., the rotation matrices and translation vectors to move from the frame of one of the cameras to the frame of the other) with high accuracy. For this step we use here the auto-calibration functionality of the WASS stereo reconstruction system (see Bergamasco et al., 2017 for details of the method). This method directly uses the sea surface images to determine the rotation matrix between the reference frames of each of the cameras as well as a translation unit vector between it. Since the sea surface images do not have a target of known dimension, the absolute distance between the cameras cannot be determined. The obtained unit vector is then multiplied by the absolute distance measured manually during the installation of the system to obtain the translation vector between the two cameras. The results of the auto-calibration show very small angles between the reference frames of the two cameras (i.e. the viewing angles of the two cameras are quasi-linear) with absolute angles of 0.05, -1.47 and 0.61 degrees along the X, Y and Z axes respectively. The distance between the cameras is 5.0 m. The relative position of the cameras is shown in Figure 7.

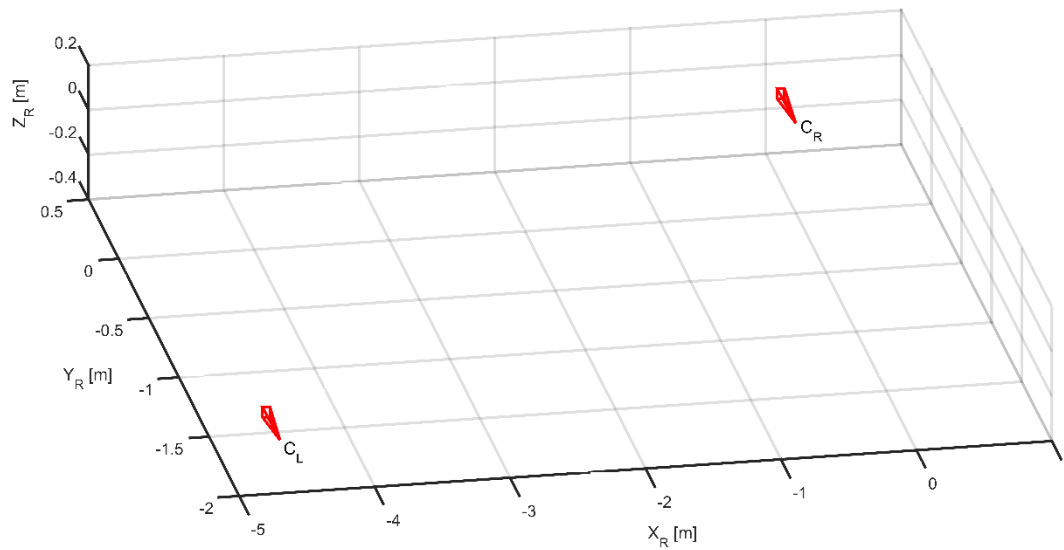


Figure 7: Relative positions of the two cameras, plotted in the frame of reference of the right camera.

## Sea surface elevation maps

The reconstruction of sea surfaces from the synchronous image pairs from the cameras is performed using the WASS stereo reconstruction processing proposed by *Bergamasco et al. (2017)*.

The processing chain consists of four main steps (see Figure 8) :

1. The detection of similar points on the two images. This step consists in finding for each pixel on one of the images, the corresponding point on the other image ;
2. The triangulation of the points. With the knowledge of the intrinsic parameters of the cameras and the relative position of the cameras (see previous paragraph), the points are triangulated in the three-dimensional reference frame of one of the cameras ( $X_c, Y_c, Z_c$ ). The principle of stereo-triangulation is represented in Figure 9.
3. The definition of the mean plane and the rotation-translation of the points. For each pair of stereo images, a point cloud is obtained and a plane passing through these points is calculated using the least squares method. The average of all the planes thus obtained is then considered as the plane corresponding to the sea surface at rest, in the camera frame. The rotation matrix and the translation vector allowing to transform this plane into a horizontal plane, with the vertical Z axis directed upwards, are calculated. Applied to the point cloud, this transformation allows us to obtain a point cloud on the sea surface, in a geo-reference system ( $X_w, Y_w, Z_w$ ), with the two horizontal axes  $X_w$  et  $Y_w$  corresponding respectively to the  $j$  (horizontal) and  $i$  (vertical) axes of the images.
4. Surface gridding. This last step aims at making the data more easily exploitable. The gridded surfaces are delivered with a horizontal resolution of 50cm. The surface elevation values on the grid are calculated as follows :
  - a. For each grid cell in which at least one point ( $x_{w,i}, y_{w,i}, z_{w,i}$ ) is found, the median value of all the points in the cell is kept.
  - b. An optimal interpolation is then applied on the grid to fill the data gap.

N.B. : Note that the optimal interpolation does not fill all the grid points without data. The degraded quality of some parts of the image, or the lack of sufficient texture in the image can make the detection of similar points (Step 1) difficult.

Some parts of the surface may also not be visible on the images (shadow effect due to steep/high crests) that may end up gaps in the reconstructed surfaces.

For a detailed description of the method used for sea surface reconstruction, the reader may refer to *Benetazzo (2006), Leckler (2013) and Bergamasco et al. (2017)*.

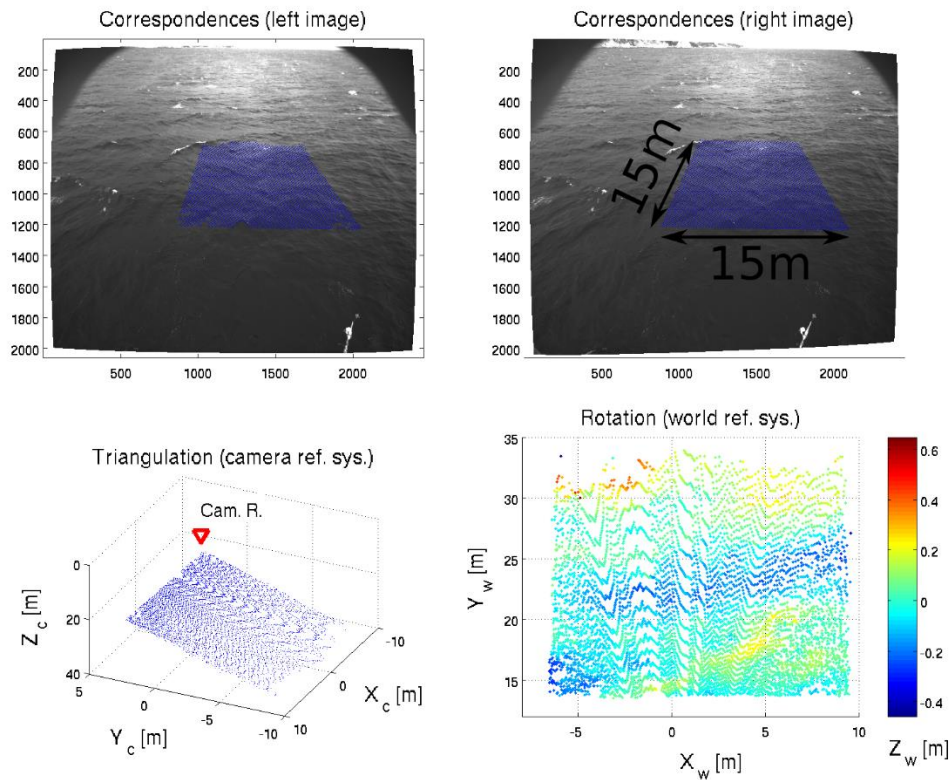


**Figure 8: Illustration of the processing chain for sea surface reconstruction. Top figures: similar points detected in stereo images; bottom left: stereo-triangulation of points in the right camera frame; bottom right: rotation and translation of the point cloud to a geo-reference. Figure taken from Leckler (2013).**

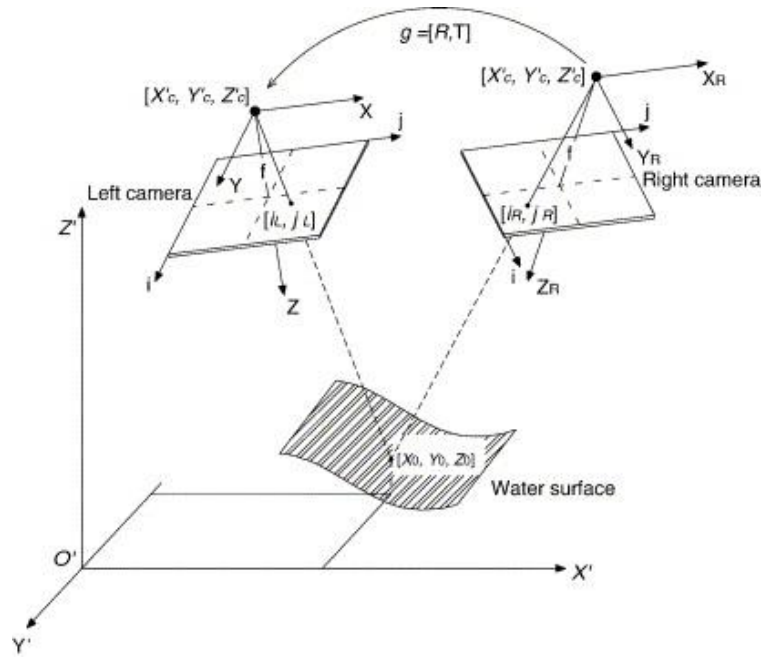


Figure 9: Illustration of the principle of stereo-triangulation. Image taken from Benetazzo (2006).

## Carried out acquisition

The unique acquisition was carried out on 2022/05/17 from 11:35 to 12:35 (30 minutes) with a 5Hz framerate. As a result, 9000 synchronous stereo image pairs were acquired and processed to retrieved surface elevation maps, following the processing described above. Retrieved sea surface elevations reprojected on the left image and the corresponding gridded elevation map obtained for the first image pair are shown on the Figure 10. The sequence of retrieved elevation maps is shown as illustration on Figure 11. All reconstructed surface elevation maps are delivered in NetCDF format.

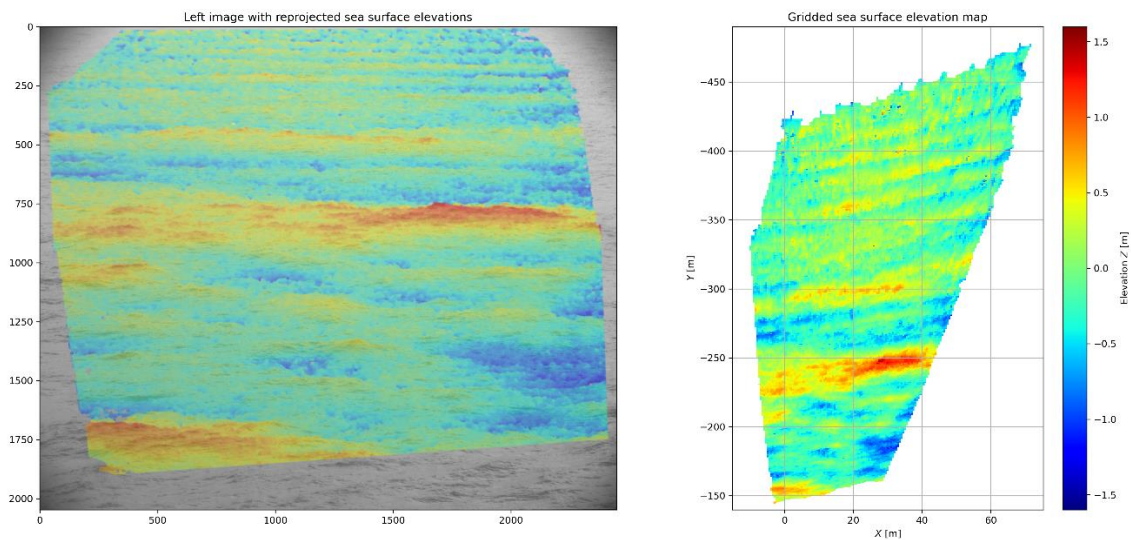


Figure 10: Retrieved sea surface elevations reprojected on the left image and the corresponding gridded surface obtained for the first image pair.



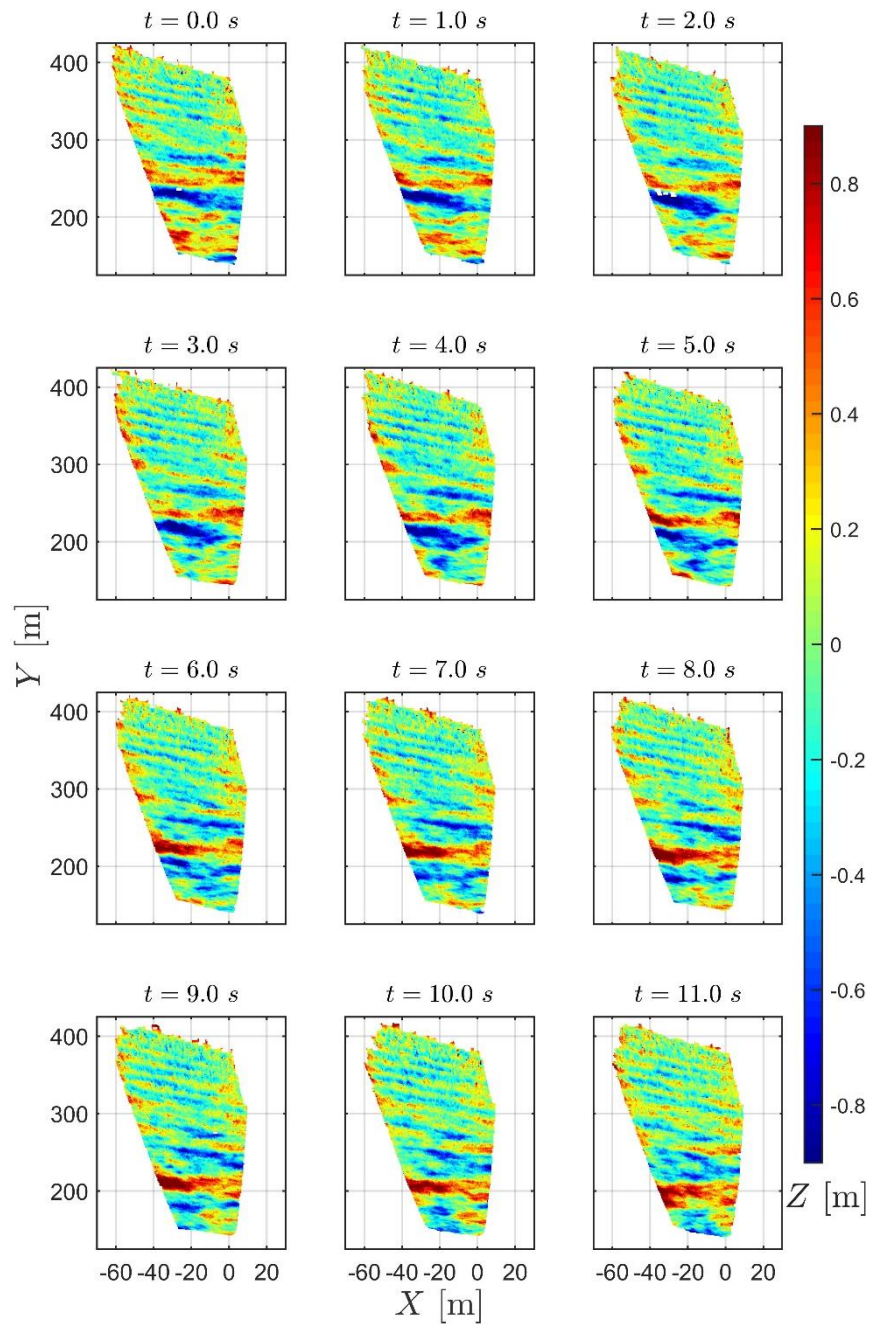


Figure 11: Sequence of retrieved elevation maps. Only one image out of five is shown.

## Statistical validation of the elevation maps

No *in-situ* measurements of the surface elevation are available in the field of view of the stereo-video system. Thus, no direct validation of the retrieved sea surface elevations can be achieved. A statistical validation is proposed here.

Note that the reconstructed surface area evolves with time due to the evolution of the sea surface elevations. For the following analysis, grid cells whose availability is less than 99% are not used. Figure 12 shows the map of data availability and the dotted line corresponds to the 99% data availability contour. Only grid points with data availability greater than 99% are kept for further analysis.

The significant wave height map, computed from the variance of the elevations at each grid cell, is shown on Figure 13. Note that the right camera is at  $(X_{camR}, Y_{camR}) = (0,0)$  in the map reference system. The large gradient observed on retrieved significant wave heights is not expected in this area.

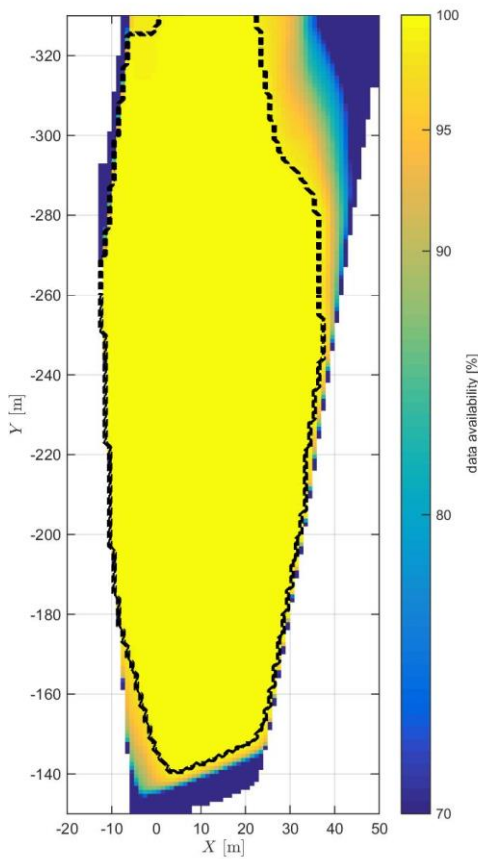


Figure 12: Data availability at each grid point.

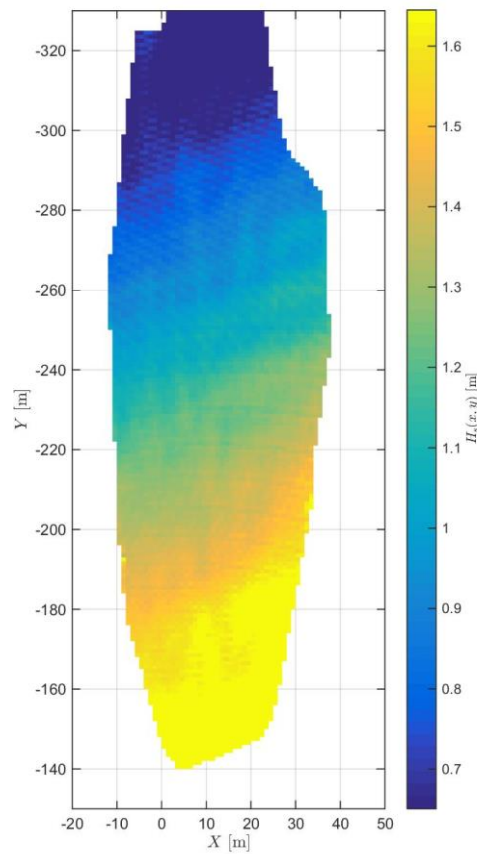


Figure 13: Significant wave height map obtained from the variance of the elevation at each grid point. Values are masked if data availability is less than 99%.

To analyze the consistency on the reconstructed area, four areas have been selected (see Figure 14). The Probability Density Function (PDF) of the elevations are plotted on the left panels of the Figure 15 and frequency wave spectra are plotted on the right panels, for each area. The PDFs of the elevation (resp. frequency wave spectra) computed in each area are compared on left (resp. right) panel of the Figure 16.

The PDFs of the sea surface elevations retrieved with the stereo system well fit the theoretical Gaussian distribution for linear waves. For extreme values, the observed PDFs deviates from the theoretical curve. This may be due to the presence of some spurious values in the reconstructed surfaces.

Frequency wave spectra computed over each grid points in each area show a good consistency with each other, with a very few spreading around the wave energy peak. Consistency between spectra then slightly decreases with shorter waves, but the energy decay follows quite well the  $f^{-4}$  theoretical decay, up to about  $f = 0.4 \text{ Hz}$  where wave signal is fully covered by noise.

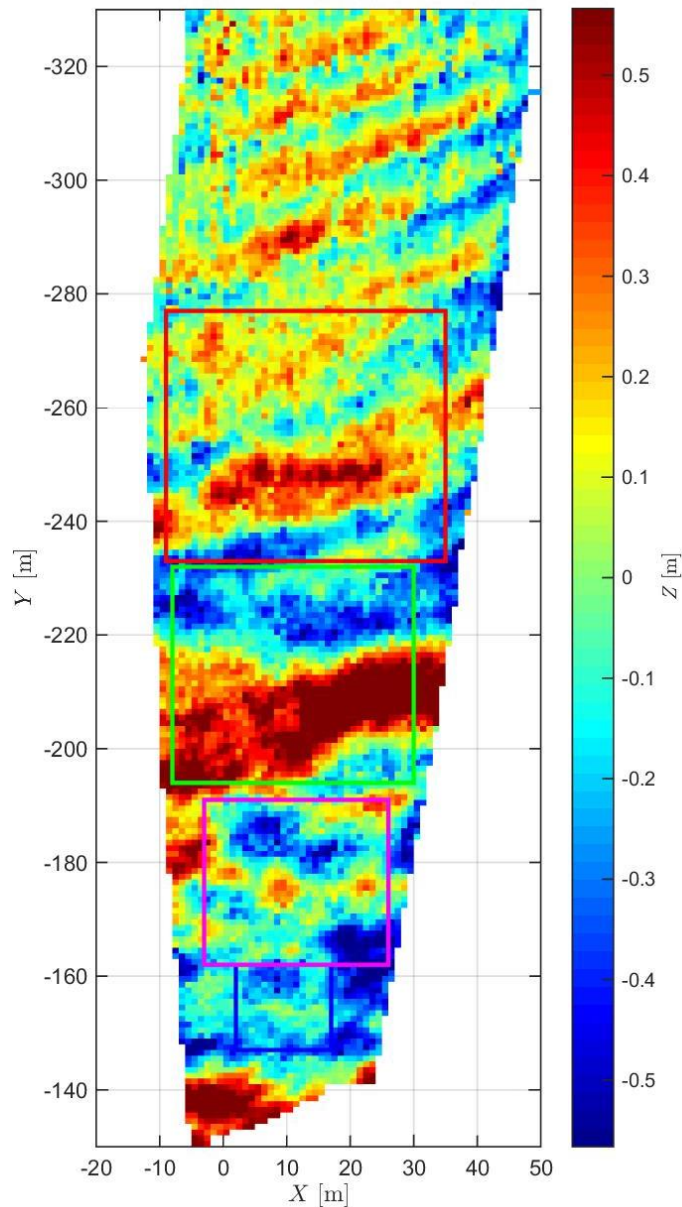
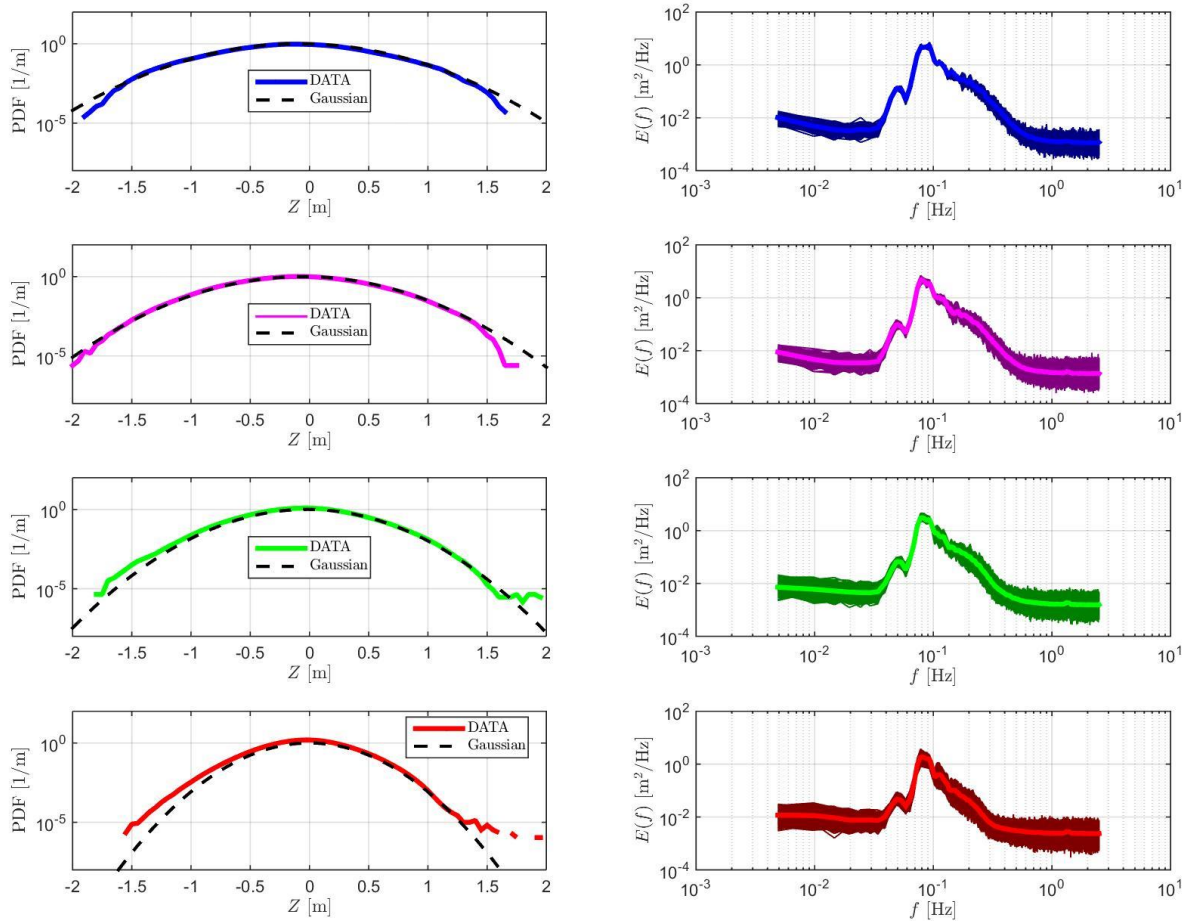


Figure 14: Selected areas for statistical analysis, plotted over the first retrieved elevation map.

The comparisons between the different area investigated (see Figure 16) shows a relative good consistency of the reconstructed surfaces in the two areas closest to the cameras in comparison with the third and fourth farthest areas. Despite wave statistics in the different areas could be affected with different environmental conditions (bathymetry, current, ...), the large differences observed between the four areas are most likely due to poor reconstruction of the sea surfaces.



**Figure 15: Left: PDF of the elevations obtained in each area. The black dashed line correspond the expected Gaussian distribution for linear waves. Right: Frequency spectra computed at each grid points contained in each area (thin lines) and mean frequency spectrum over the whole area (main line). The areas are shown on Figure 14**

The 3D wave spectra,  $E(f, k, \theta)$ , with  $f$  the wave frequency,  $k$ , the wavenumber,  $\theta$ , the wave direction were computed in each areas (see Figure 14). The Figure 17, Figure 18, Figure 19 and Figure 20 show the obtained 3D wave spectra for the areas, respectively from the closest one to the furthest one from the lighthouse. The frequency-wavenumber spectra (left panels of the figures) shows a well know distribution of the wave energy, with the main patch corresponding to the free linear waves and the secondary one corresponding to the first harmonic bounded waves. Nevertheless, the wave energy distribution is very far from the theoretical linear wave dispersion relation (black lines on the figures). Such an offset cannot be due to current and confirms the poor reconstruction of the sea surfaces.

The Figure 21 shows the 3D wave spectrum obtained in the first area after an arbitrary scaling of the reconstructed sea surfaces with a factor 3 in each direction (i.e.  $X' = 3X$ ,  $Y' = 3Y$ ,  $Z' = 3Z$ ). The energy corresponding to the free linear waves linear dispersion is now closer to the linear dispersion.



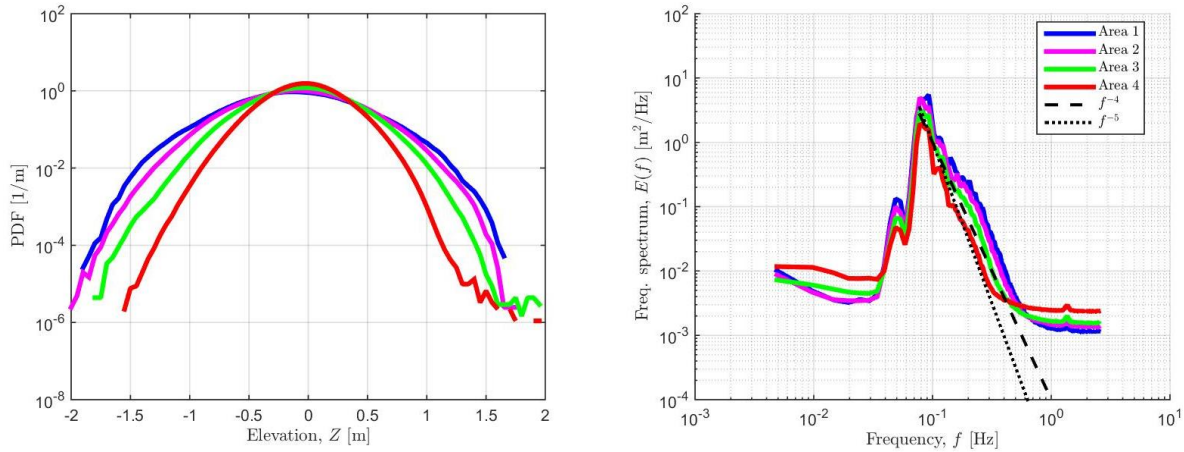


Figure 16: Comparison of elevation PDFs (left) and frequency wave spectra (right) obtained for each area.

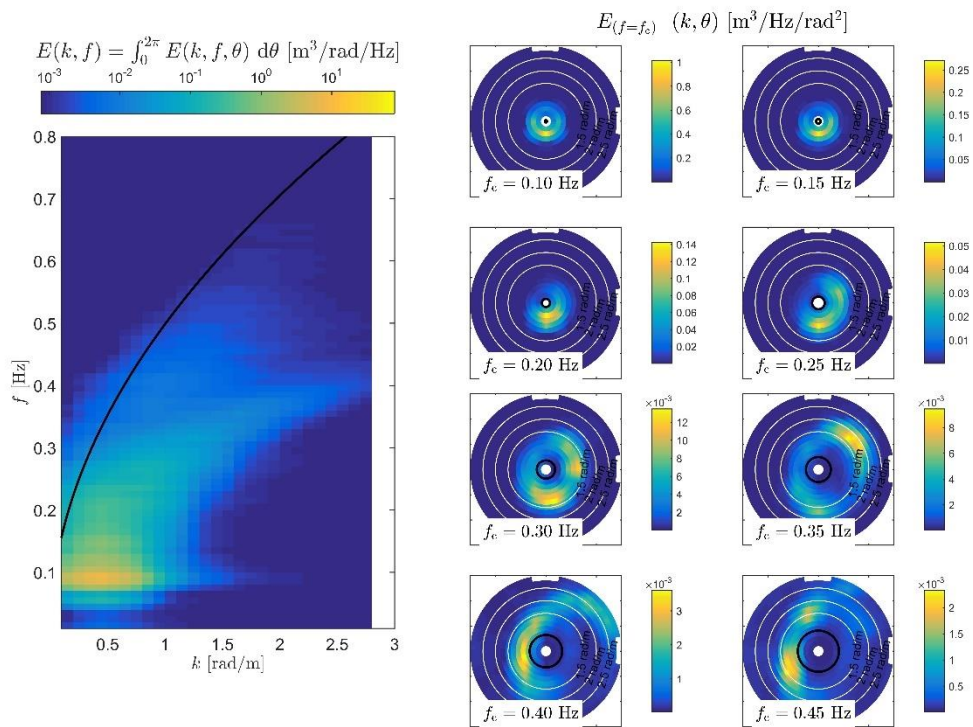


Figure 17: 3D wave spectrum obtained for the area 1 (the closest one from the lighthouse). Left panel represents the frequency-wavenumber spectrum (i.e. 3D wave spectrum integrated over directions), and right panels are slices of the 3D spectrum at given frequencies  $f_c$ . The linear dispersion relation without current is represented by black lines.

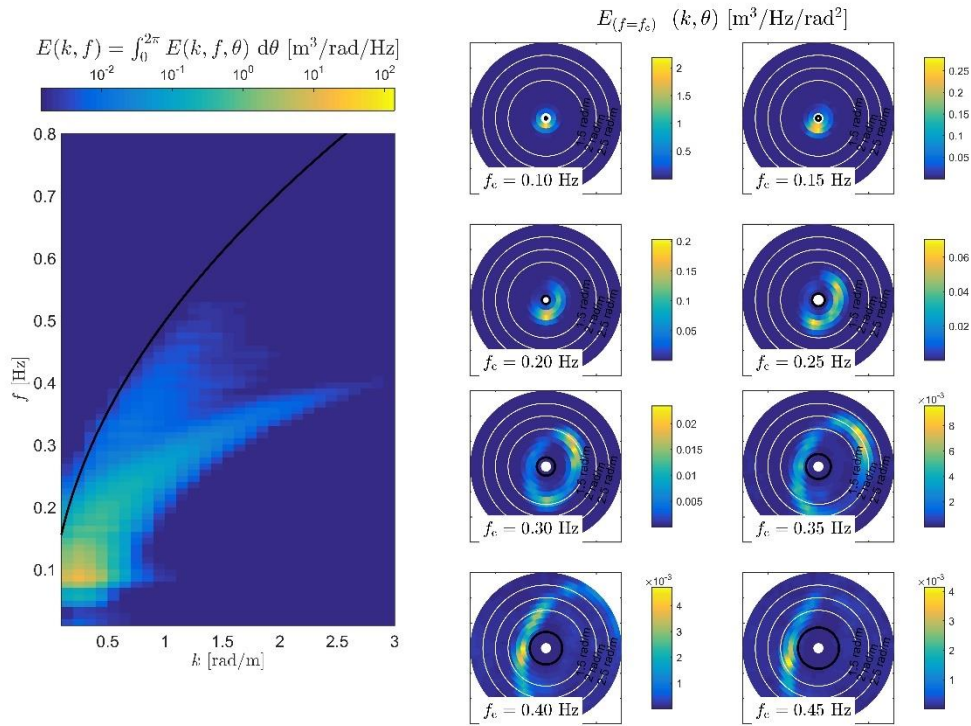


Figure 18 : 3D wave spectrum obtained for the area 2. Left panel represents the frequency-wavenumber spectrum (i.e. 3D wave spectrum integrated over directions), and right panels are slices of the 3D spectrum at given frequencies  $f_c$ . The linear dispersion relation without current is represented by black lines.

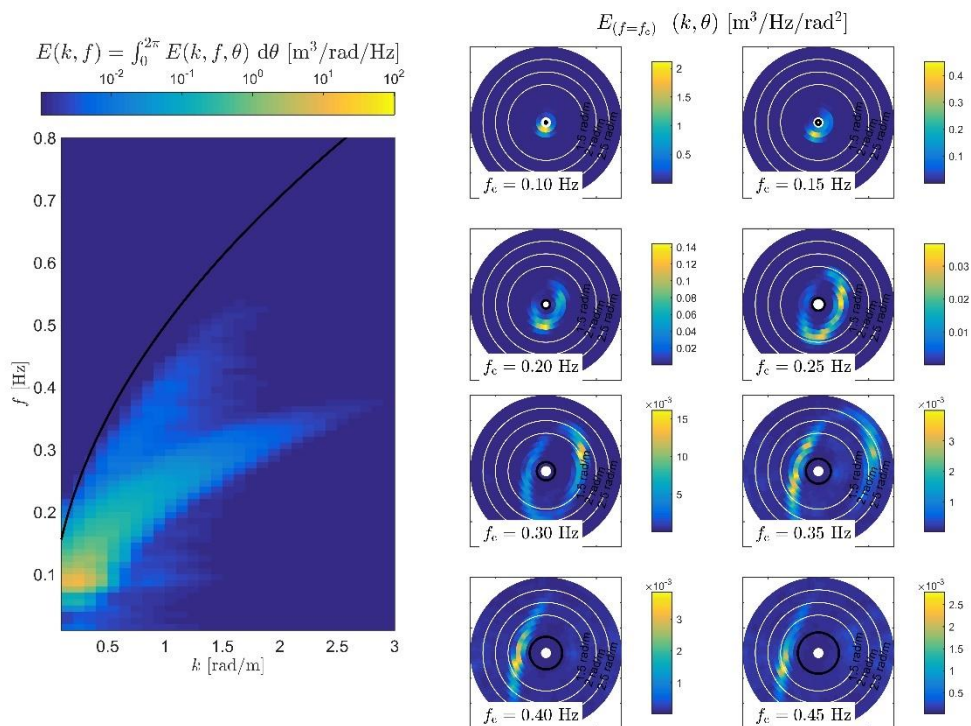


Figure 19 : 3D wave spectrum obtained for the area 3. Left panel represents the frequency-wavenumber spectrum (i.e. 3D wave spectrum integrated over directions), and right panels are slices of the 3D spectrum at given frequencies  $f_c$ . The linear dispersion relation without current is represented by black lines.



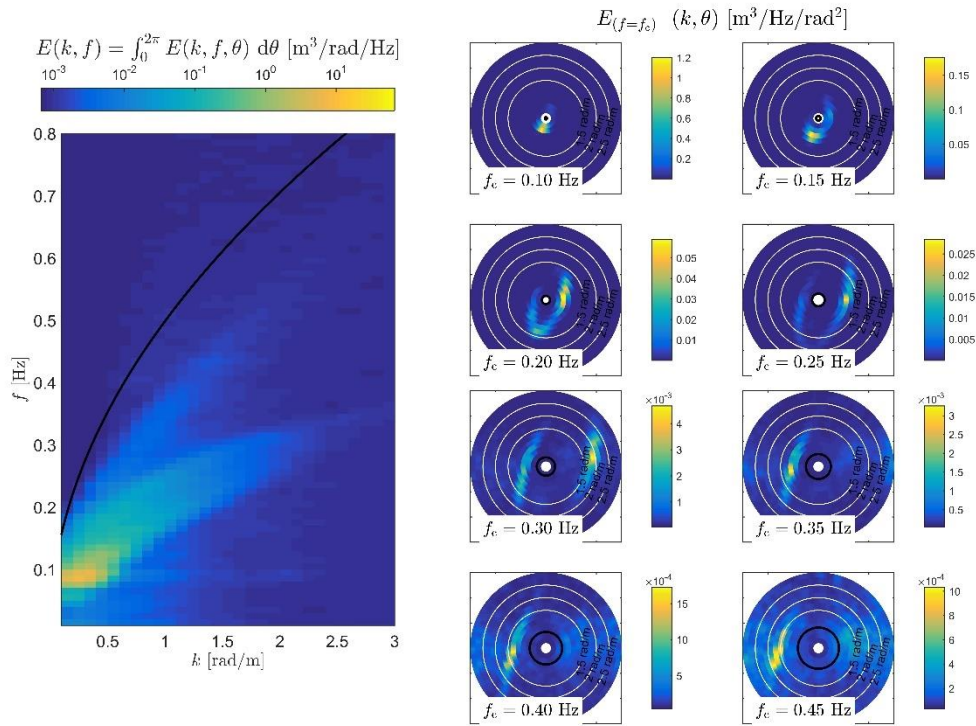


Figure 20 : 3D wave spectrum obtained for the area 4 (the furthest one from the lighthouse). Left panel represents the frequency-wavenumber spectrum (i.e. 3D wave spectrum integrated over directions), and right panels are slices of the 3D spectrum at given frequencies  $f_c$ . The linear dispersion relation without current is represented by black lines.

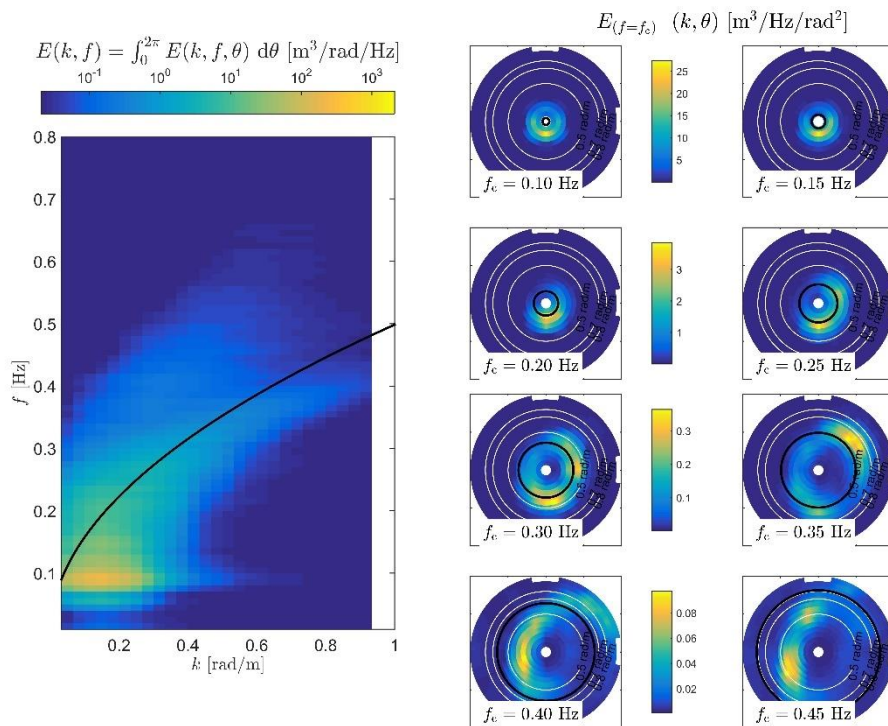


Figure 21 : 3D wave spectrum obtained for the area 1 (the closest one from the lighthouse) after an arbitrary scaling of the surface with a factor 3. Left panel represents the frequency-wavenumber spectrum (i.e. 3D wave spectrum integrated over directions), and right panels are slices of the 3D spectrum at given frequencies  $f_c$ . The linear dispersion relation without current is represented by black lines.

To investigate the reasons of such failing in the reconstruction processing, a sensibility analysis was done on the main camera parameters. Note that the sensibility analysis was done using the Matlab<sup>®</sup> processing chain developed by *Leckler (2013)* which allows more flexibility than the WASS processing chain of *Bergamasco et al. (2017)*. In this processing, the word reference system is defined slightly differently, but scales are respected. Note also, that due to much larger computational time, only a restricted part of the image has been processed. Two parameters were found to be very sensible and strongly impact reconstructed sea surfaces. The Figure 22 shows the reconstructed surfaces obtained with a variation  $\delta = \pm 0.1\%$  of the focal length for both cameras obtained by the intrinsic calibration. The Figure 23 shows the reconstructed surfaces obtained with a variation  $\Delta\theta = \pm 0.2$  degrees of the yaw angle of extrinsic parameters obtained by the extrinsic autocalibration provided with WASS processing chain of *Bergamasco et al. (2017)*. For each obtained surface, a significant wave height is estimated with  $h_{m0} = 4 \sqrt{\text{var}(Z)}$ . The variation amplitude of these parameters was chosen to fit the parameter estimation uncertainties.

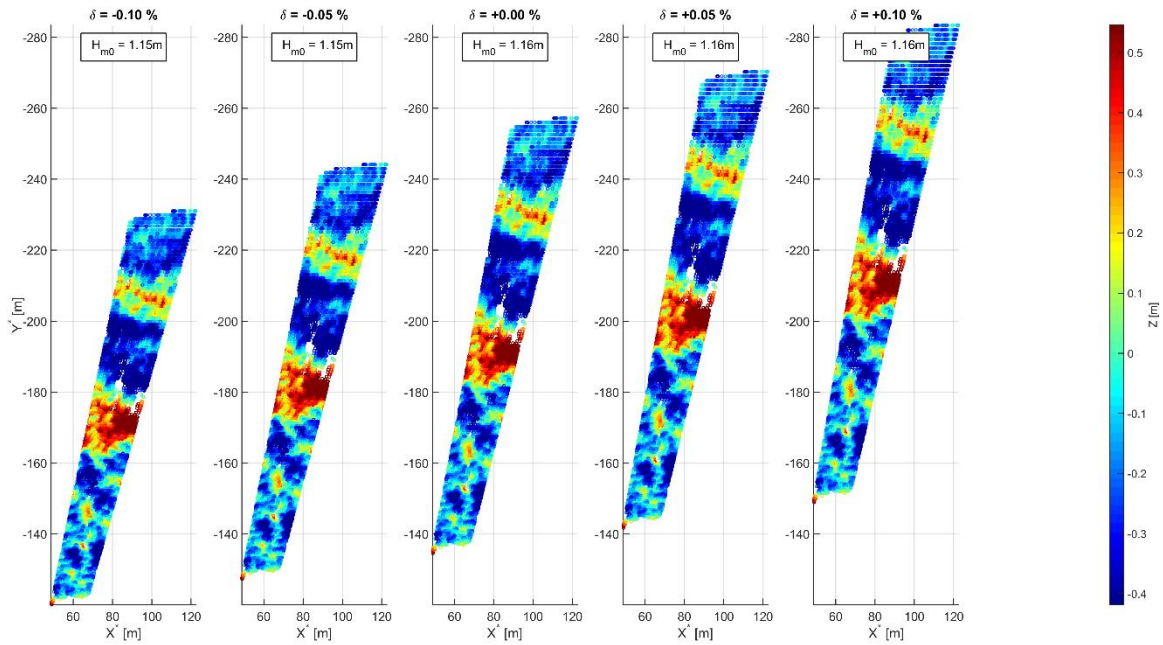


Figure 22: Sensibility analysis of camera intrinsic parameter. Variation of the focal length with  $f = (1 + \delta)f_{init}$

The sensibility analysis shows that the obtained reconstructed surfaces are strongly affected with variations of the key parameters (focal length and yaw angle between cameras) in their range of uncertainties. Due to the poor quality of the reconstructed sea surfaces, and its large impact on the observed wave dispersion, the estimation of the surface current is here not possible.

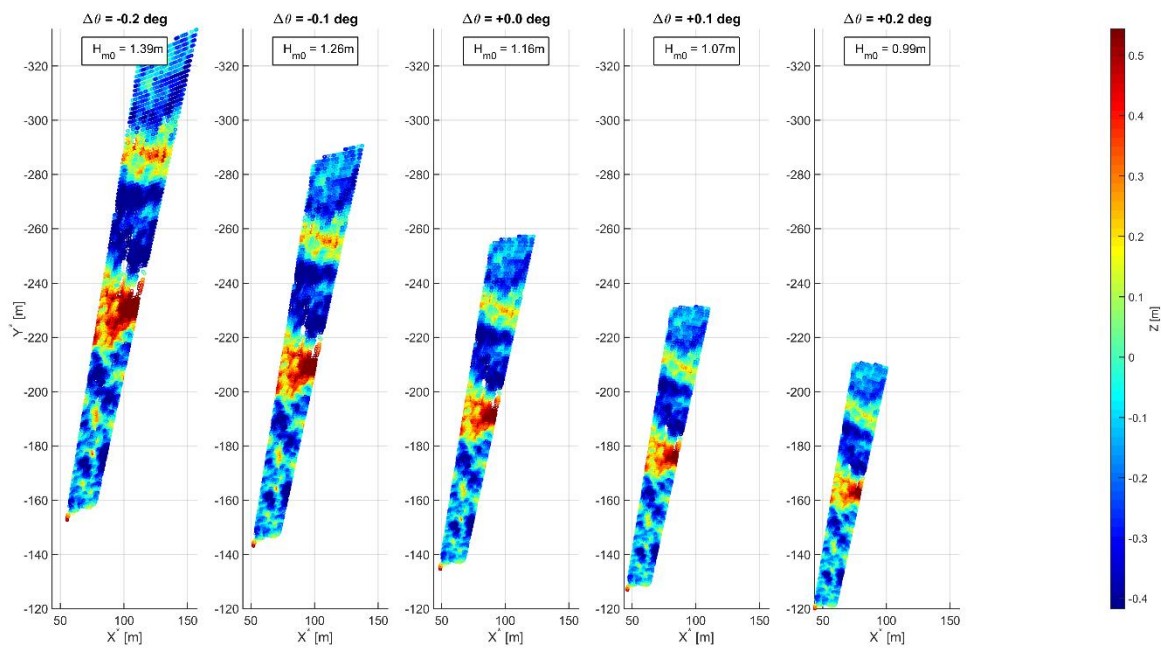


Figure 23: Sensibility analysis of extrinsic parameter. Variation of the yaw angle with  $\theta = \theta_{init} + \Delta\theta$

## Conclusions

An experimental deployment of a stereo-video system using zoom lenses were achieved from the La Jument Lighthouse. The system was calibrated using the state-of-the-art methods, and the 30-minutes long acquisition collocated with the airborne SEASTAR measurements was investigated. Nevertheless, the sensibility analysis showed that the state-of-the-art methods used for the calibration of the stereo-video system are not enough accurate to provide trusting sea surface elevation maps. Moreover, the lack of independent measurements of the sea surface elevation in the field of view of the cameras does not allow for a proper validation of the retrieved sea surface qualifications. As a result, a reliable estimation of the sea surface current from the 3D wave spectra was not possible.

Future deployments of the stereo-system with zoom lenses required more accurate calibration tools. Moreover they must be coupled with independent sea surface elevation measurements (e.g. wave lidar, ADCP with acoustic surface tracking, or pressure sensor) in the field of view of the camera to allows for a proper validation of the obtained elevations.

## References

---

- Benetazzo, A. (2006). Measurements of short water waves using stereo matched image sequences. *Coastal engineering*, 53(12), 1013-1032.
- Bergamasco, F., Torsello, A., Sclavo, M., Barbariol, F., & Benetazzo, A. (2017). WASS: An open-source pipeline for 3D stereo reconstruction of ocean waves. *Computers & Geosciences*, 107, 28-36.
- Leckler, F. (2013). *Observation and modelisation of wave breaking* (Doctoral dissertation, Université de Bretagne occidentale-Brest).
- Leckler, F., Ardhuin, F., Peureux, C., Benetazzo, A., Bergamasco, F., & Dulov, V. (2015). Analysis and interpretation of frequency–wavenumber spectra of young wind waves. *Journal of Physical Oceanography*, 45(10), 2484-2496.

# **ANNEX E) DATA PROCESSING REPORT: IROISE SEA CAMPAIGN**

# SeaSTARex

## Processing Specification

**Reference Code** : : MS-SeaSTARex-ProcSpec  
**Issue** : : 5.0  
**Date** : : 09-10-2023

MetaSensing BV  
Schipholweg 55  
2316 ZL Leiden , The Netherlands  
Tel: +31 71 751 5960  
Email: info@metasensing.com

Copyright © 2023 MetaSensing BV



The information disclosed in this document, including all designs and related materials, is the valuable property of MetaSensing and/or its licensors. MetaSensing and/or its licensors, as appropriate, reserve all patent, copyright, and other proprietary rights to this document, including all design, manufacturing, reproduction, use, and sales rights thereto, except to the extent said rights are expressly granted to others.

The product(s) discussed in this document are warranted in accordance with the terms of the Warranty Statement accompanying each product.

To allow for design and specification improvements, the information in this document is subject to change at any time, without notice. Reproduction of this document or portions thereof without prior written approval MetaSensing is prohibited.

## Document Status Log

Issue	Change description	Date	Written
1.0	First Release	15-Mar-2023	KM
2.0	Review	29-Mar-2023	TB
3.0	Final Review and Release	29/09/2023	KM
4.0	Review of Calibration Equations and Release	04/10/2023	KM
5.0	Cal. Equation correction and Release	09/10/2023	KM

---

1	Preface.....	4
1	Introduction.....	5
2	SAR by Means of the Backprojection Algorithm.....	6
3	OSCAR Processing Chain .....	8
3.1	Pre-processor.....	8
3.2	Navigation Synchronization.....	10
3.3	GBP Focusing .....	11
3.4	Packager.....	14
3.5	Calibration.....	15
4	OSCAR Processor Log .....	17

## 1 Preface

This document describes how the SeaStarEx data are processed. The SeaStarEx data were acquired by the OSCAR instrument and therefore processed by its processor, the OSCAR processor. This document explains in terms of SAR concept and SAR algorithms how the OSCAR processor implementation developed by MetaSensing and used for the SeaStarEx campaign works. In the end of the document, a table with time history description of the bug fixing and improvements of the OSCAR processor since its first release is given. For software implementation and operation details please refer to the OSCAR processor manual and architecture documentation [1].

# 1 Introduction

MetaSensing is an Italian-Dutch company offering radar sensors and services. MetaSensing's radar products cover a wide range of applications such as: mapping, detection, deformation, oceanography, weather, glaciology, forestry, topography, surveillance, and harbor management. During the past few years, the MetaSensing SAR systems have been deployed for several projects in the framework of radar backscatter imaging ( $\sigma^0$ ), interferometry (ATI, XTI), bistatic, (nadir) altimeter and tomography.

The OSCAR Processor is the advanced Airborne Synthetic Aperture Radar processor developed by MetaSensing to focus SAR data. It is a proprietary software tool to generate SAR images from the data acquired by the airborne OSCAR instrument developed by MetaSensing. It allows to do all processing in steps up to interferogram generation. The processor performs navigation synchronization, range compression, focusing to generate Single Look Complex (SLC) SAR data, antenna pattern removal, calibration, coherence and phase estimations. For usage and installation requirements, please refer to OSCAR Processor manual and file format definition documents [1, 2].

The OSCAR Processor is based on the Global Back Projection algorithm for the generation of the SAR Single Look Complex (SLC) images. It is meant and developed to be used with SAR raw data coming from an antenna working with a 3d axis stabilizer, e.g. the OSCAR instrument. The OSCAR Processor uses GPU/CUDA and it requires NVIDIA card installed on the processing computer. The use of parallel processing in GPU drastically reduces the computational time required by the Global Back Projection. Next, the steps within the OSCAR processor in which SeaStarEx data, acquired by OSCAR instrument, have gone through are described and explained at algorithm level.

## 2 SAR by Means of the Backprojection Algorithm

The OSCAR Processor algorithm is based on a time-domain global backprojection (GBP) method [3, 4]. Opposite to the frequency-domain approach, separate motion compensation and range migration correction (RCMC) steps are not required because the GBP algorithm handles non-ideal motion/sampling implicitly and can precisely perform beam-steering. Therefore, the GBP algorithm can be used for any imaging geometry. This gives flexibility to use the same algorithm core to process data acquired at diverse configurations (side-looking, nadir-looking, bistatic), trajectories or modes.

The GBP algorithm works interpolating each received echo at the desired positions to be focused. Because the radar echo has been sampled according to the Nyquist criterion, it can be interpolated with arbitrary accuracy at any illuminated image position. By coherently adding the contributions of each echo to each desired position, the focusing is performed. The contribution of each echo is computed according to the acquisition geometry obtained from the navigation data of each pulse.

The OSCAR processing architecture is shown below. This software has 3 modules: the Pre-processor, the Focuser, and the Packager as show in the Figure below.

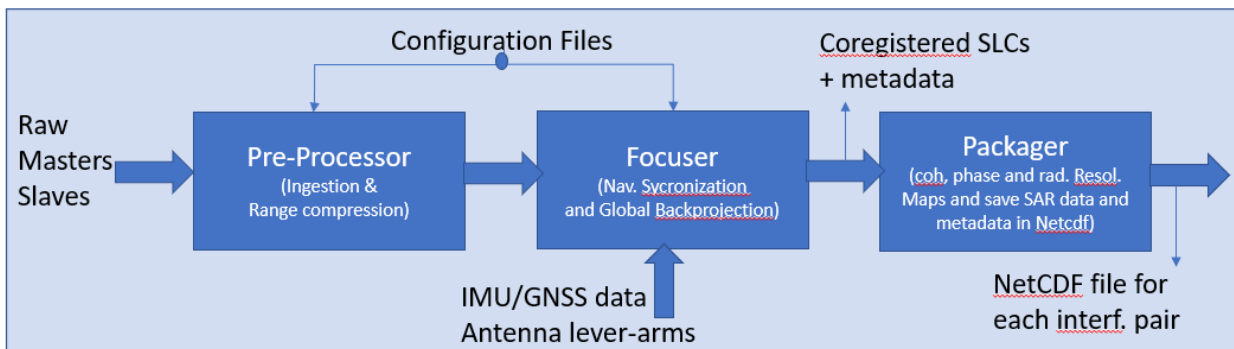


Figure 1 – OSCAR processing architecture

The first module, called Pre-processor, reads the radar raw data header to extract radar parameters, timing information and radar echoes. Upon echoes extraction, these are classified as imaging or calibration and are subsequently range compressed. This procedure is repeated on a file-by-file basis until covering all raw data files present in a directory. When the complete flight line has been processed, the metadata associated with both imaging and calibration data is produced as well as a data take summary.

The Focuser module, the second in the SAR data processing pipeline, plays a critical role in performing navigation synchronization and SAR focusing. To achieve precise position and attitude solutions, third-party software such as Novatel's Inertial Explorer is used, with resulting text files fed into the processor. These solutions are then combined with radar timing information and interpolated to form the radar state vector product, which is used for further processing of the SAR data.

Lower precision solutions are available in real time, but this is not included in the block diagram since it is not the nominal operation workflow. Similarly, data recorded from the gimbal is read and interpolated using the imaging pulses information. Afterwards, the focusing implements the back-projection algorithm adding coherently each pulses according to its navigation data. Because each coherently added echo is positioned in a georeferenced grid (UTM), the output of the second module is already ground georeferenced SLC data. If the same grid is used to focus all the channels, the output SLC data are already co-registered with one another.

The third and last module, called Packager, computes the intensity SAR image, the radiometric resolution image and the interferograms for all possible combinations, i.e., the coherence and phase images. The module also packages the SAR data and metadata of each interferometric pair channel into a NetCDF file format.

To ensure accurate calibration of the SeaStarEx data, several key parameters including range delay, lever-arms, antenna pattern, and sigma-0 offset must be set in the OSCAR processor configuration files [1]. Computation of these parameters is facilitated by the MetaSAR-PRO Add-On software tool [5]. In the following section, we explain the concept and algorithm employed in the calibration setup for the SeaStarEx campaign. Providing additional context about the purpose and significance of calibration in the SAR data processing pipeline could help readers better understand the importance of these parameters and their impact on the quality of the resulting data.



## 3 OSCAR Processing Chain

### 3.1 Pre-processor

The Pre-Processor is responsible for ingesting the raw data, internal calibration data and navigation data. It outputs the data re-arranged by channels in a format accepted by the Focuser step. Using the information included in the header, i.e. instrument configuration and user settings such as used Pulse Repetition Frequency (PRF), Sampling Frequency ( $F_s$ ), etc, the time-tagged observation data is arranged in a raw-data matrix, one for each receiving channel: rows represent slow time domain, which parametrizes the along track position of the platform (sampled at PRF), while columns represent the fast time domain, which parametrizes the received echoes (sampled at  $F_s$ ).

During ingestion the pre-processor also performs range compression using the radar raw data. Raw data of each channel (deramped frequency-modulated continuous waveforms) are the input for the range compression step. The range compression for OSCAR is implemented as a the well-known technique of Pulse Compression with a transmitted pulse replica. The pulse compression is implemented with Fast Fourier Transform (FFT) in range. Before this step, up-sampling is performed on deramped data to minimize the impact of quantization on system resolution. Furthermore, a hamming window is applied to trade-off side-lobes level and resolution.

In the end of the pre-processor the range compressed data arranged by channels are saved in a sub-folder called “rc” as shown below (more details of the file format description please refer to MS-OSCAR-PRO-FFD document).

OSCAR\_FUNCAMP\_FINAL > 20220411T100134 > rc

Name	Date modified	Type	Size
20220411T100134_00_rc	11/22/2022 1:47 PM	File	5,336,925 KB
20220411T100134_00_rc.json	11/22/2022 1:48 PM	JSON File	29 KB
20220411T100134_00_rc.json.old	11/22/2022 1:47 PM	OLD File	159 KB
20220411T100134_33_rc	11/22/2022 1:47 PM	File	5,336,925 KB
20220411T100134_33_rc.json	11/22/2022 1:48 PM	JSON File	29 KB
20220411T100134_33_rc.json.old	11/22/2022 1:48 PM	OLD File	159 KB
20220411T100134_34_rc	11/22/2022 1:47 PM	File	5,336,925 KB
20220411T100134_34_rc.json	11/22/2022 1:48 PM	JSON File	29 KB
20220411T100134_34_rc.json.old	11/22/2022 1:48 PM	OLD File	159 KB
20220411T100134_77_rc	11/22/2022 1:47 PM	File	5,336,925 KB
20220411T100134_77_rc.json	11/22/2022 1:48 PM	JSON File	29 KB
20220411T100134_77_rc.json.old	11/22/2022 1:48 PM	OLD File	159 KB
20220411T100134_78_rc	11/22/2022 1:47 PM	File	5,336,925 KB
20220411T100134_78_rc.json	11/22/2022 1:48 PM	JSON File	29 KB
20220411T100134_78_rc.json.old	11/22/2022 1:48 PM	OLD File	159 KB
RangeAxis_20220411T100134.axi	11/23/2022 10:36 AM	AXI File	4 KB

Figure 2: Pre-processor Output.

Figure 3 shows a Range-Doppler map of the OSCAR range compressed data for each of its 5 channels, which has been acquired in April 12, 2022 (20220412T102907) during the function campaign.

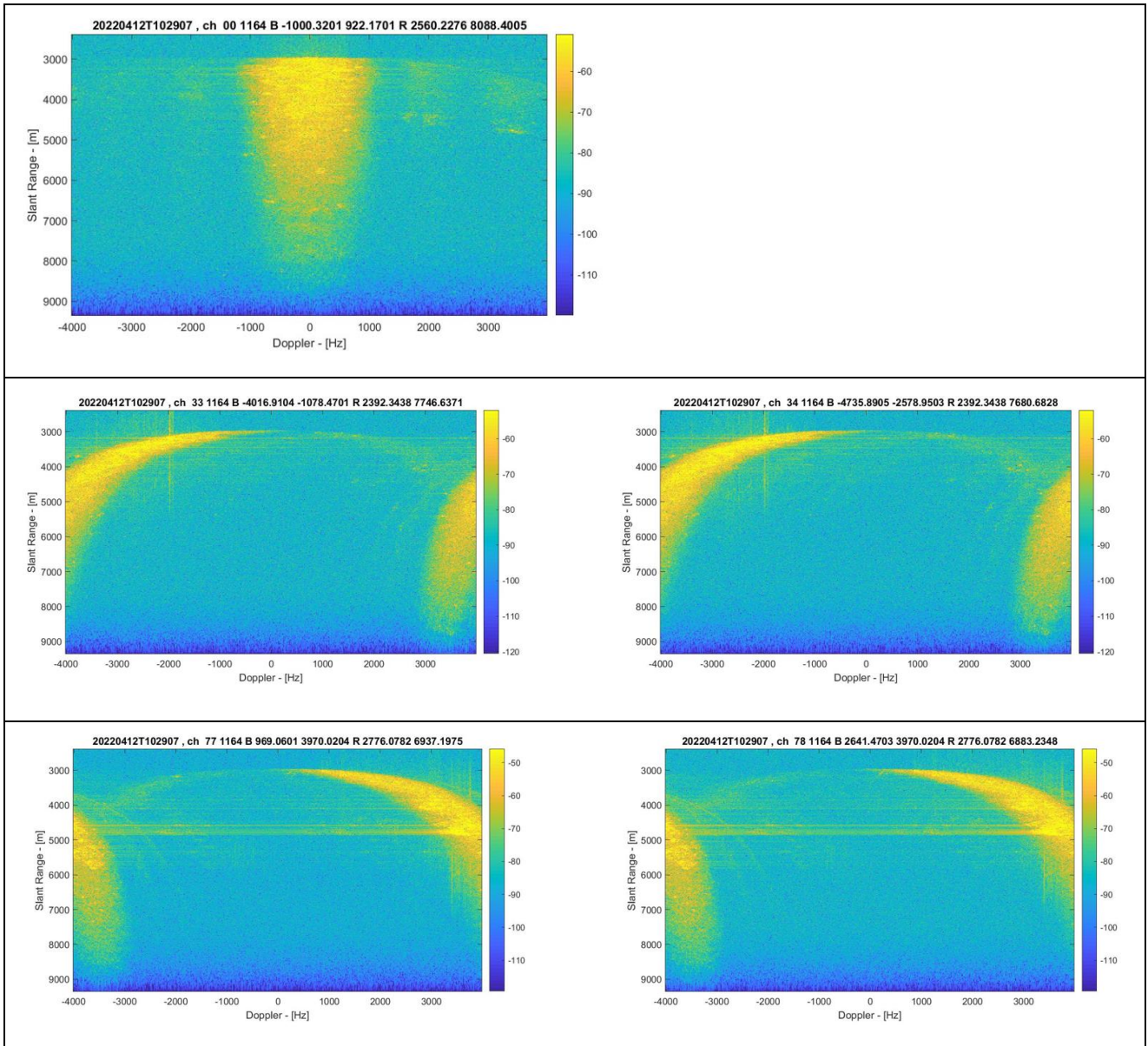


Figure 3: Example of Range-Doppler map for a OSCAR range-compressed data. The colormap is expressed in dB.

### 3.2 Navigation Synchronization

The starting point for the Focuser is the navigation synchronization. The navigation synchronization consists basically in interpolating the navigation data into the slow-time frame of the range-compressed data defined by the PRF and the start time of the first pulse. Below an illustration of the input for the Navigation Synchronization step, e.g. a part of a typical .txt file with the navigation data coming from an independent navigation unit (time tag, position and attitude of the antenna). This file is ingested by the processor and with the help of the lever-arms of each antenna, the position of antenna is known for each the transmitted pulses.

```

Project:      20220411_085657
Program:     Inertial Explorer Version 8.90.2428
Profile:     SAR
Source:      GNSS/INS Epochs(Smoothed TC Combined)
SolFile:     C:\PostprocessingNav\Oscar_202204\logs\20220411_085657\20220411_085657.cts
ProcessInfo: 20220411_085657 by Unknown on 4/14/2022 at 11:42:28

Datum:       WGS84
Master 1:    Name COUD, Status ENABLED
              Antenna height 0.072 m, to ARP [AERAT1675_120(SPKE)]
              Lat, Lon, El Hgt 51 01 22.60211, 2 22 26.80399, 56.794 m [WGS84, N/A]
Remote:      Antenna height 0.000 m, to LIPC [Generic(NONE)]
IMU to GNSS Antenna Lever Arms:
              x=-0.090, y=0.542, z=1.524 m (x-right, y-fwd, z-up)
Body to IMU Rotations:
              xRot=0.000, yRot=0.000, zRot=0.000 degrees

Map projection Info:
  UTM Zone:   31

  GPSTime      Week      Easting  Northing  H-Ell  Latitude  Longitude  Roll      Pitch      Heading
  (sec)        (weeks)  (m)      (m)      (m)    (deg)     (deg)     (deg)     (deg)     (deg)
118736.000  2205.00000  707801.621  5792258.84  48.961  52.2414483458  6.0437056863 -0.5125508548  0.2155352634 -137.77095665
118736.005  2205.00000  707801.621  5792258.84  48.961  52.2414483457  6.0437056859 -0.5088998642  0.2174821497 -137.77089138
118736.010  2205.00000  707801.621  5792258.84  48.961  52.2414483456  6.0437056858 -0.5098621184  0.2212812727 -137.77070743
118736.015  2205.00000  707801.621  5792258.84  48.961  52.2414483455  6.0437056860 -0.5153966335  0.2262979782 -137.77045532
118736.020  2205.00000  707801.621  5792258.84  48.961  52.2414483454  6.0437056860 -0.5169701532  0.2302100149 -137.77015589

```

Figure 4: Navigation data before synchronization (time tag, position and attitude of the antenna).

### 3.3 GBP Focusing

Following navigation synchronization, the focuser step begins by implementing the backprojection algorithm for SAR processing. This algorithm involves beam steering in Doppler for the range compressed data, with individual steering performed for each sample on an arbitrary surface grid. As the OSCAR instrument features a 3D stabilizer, beam steering is accomplished using a fixed ground squint for all samples. Specifically, in the azimuth compression stage, the squint definition value is typically set to the ground squint formed by the OSCAR antenna in a straight flight, with backward pointing antennas (AFT channels) set to -45 degrees, forward pointing antennas (FORE channels) set to -135 degrees, and Zero-Doppler Channels set to -90 degrees. The resolution is defined by the desired integration time around this squint. This fixed squint setup was used for processing the SeaStarEx data. For more details on the pointing geometry and naming conventions used in the OSCAR instrument, please refer to the OSCAR Data Acquisition Report [6].

The coordinate system  $T_{xyz}$  used for the backprojection processing is a Cartesian system aligned with the flight line direction and with origin in the center of the track (not the output grid).

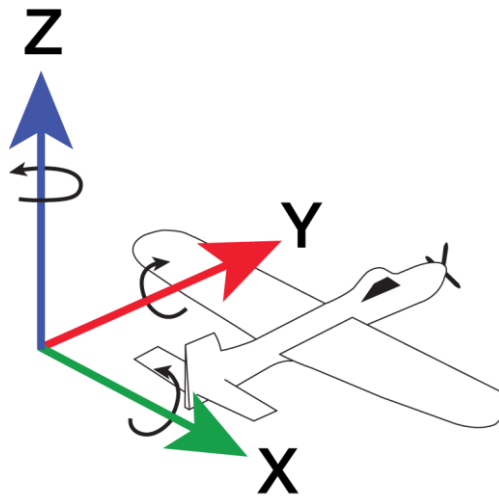


Figure 5 – Coordinate system used by the OSCAR Processor

To generate such a coordinate system, the processor uses a two-step approach. First, it uses the local level frame ENU with its origin being the point mentioned above (commonly referred to as peg point). The conversion starts from geographic latitude and longitude (LLH) data measured by the navigation system (not ECEF data) and then converted to ENU coordinates.

Once the data is in the local level frame, then a rotation process converts ENU coordinates in what is internally called rENU (rotated ENU) frame as follows:

$$p_{ENU} = [E, N, U]^T$$

$$M_{rENU} = R_z(-p_{peg}(3))$$

$$p_{peg}(3) = [heading]$$

$$p_{rENU} = M_{rENU}p_{ENU}$$

Where  $R_z$  is the rotation matrix about z-axis as described in <sup>1</sup> for 3 dimensions. Note that a point in  $rENU$  coordinates can be converted back to  $ENU$  by transposing  $M_{rENU}$ .

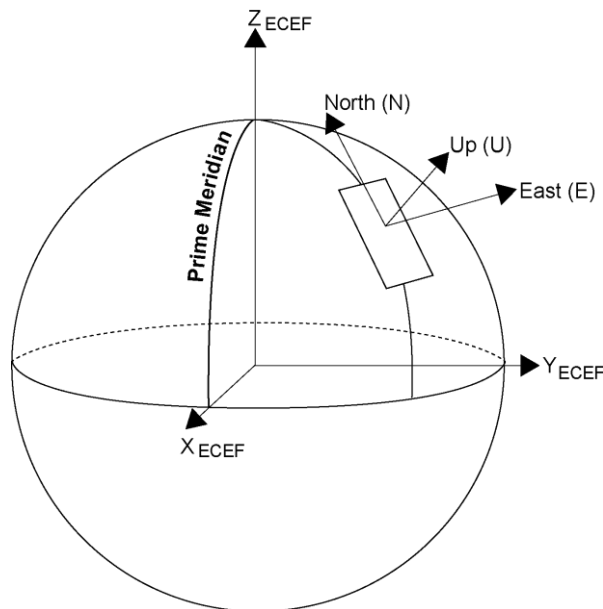


Figure 6 - ENU frame description

The body frame definition describes the order and direction of the Euler angles rotations. Additionally, it is the frame used to describe lever arms or necessary rotations to indicate the antenna broadside direction.

**Rotation order is always dictated by yaw-pitch-roll**, therefore the axis sequence in this case is z-x'-y'' (and not z-y'-x'').

---

1

[https://en.wikipedia.org/wiki/Rotation\\_matrix](https://en.wikipedia.org/wiki/Rotation_matrix)

The geometry of the output grid can be set to follow any direction: for example, the SeaStarEx processed data processing are directly projected in UTM (Universal Transverse Mercator) coordinates.

The navigation information is used to determine the vectors joining the position of the beam center and the position of the point-target in the grid. With the knowledge of the ranges and angles relative to each point-target the pulses are coherently summed to form the focused beam. This is repeated for each point-target of the grid.

From the range-compressed, the backprojection algorithm proceeds as follows:

1) First, construct the spatial domain target function array (output array)  $f[i, j]$ , where  $i$  and  $j$  represents the row and column indices of the reconstruction grid slant-range index, and fill it with zeros.

2) Read the coordinates  $T_{xyz}$  for each output pixel.

3) For a given pixel point  $[i, j]$  on the output grid, with NCS coordinates  $T_{xyz}$ , and a given antenna position on the synthetic aperture  $P(u)$ , obtain the precise slant-range values to the target:

$$r(u, i, j) = \sqrt{(T_x |x - P_x(u)|)^2 + (T_y |y - P_y(u)|)^2 + (T_z |z - P_z(u)|)^2}$$

Range Cell Migration and Motion Compensation are integrated in backprojection by considering the actual antenna positions, as obtained by the geometry module, in the determination of the slant range to the target.

4) Find  $\omega_{close} = k_{close} \Delta\omega$  as the nearest upsampled range-domain frequency point to:

$$\omega_{ij}(u) = \frac{2\alpha(r^{tx} + r^{rx})}{c}$$

The  $\alpha$  refers to the chirp rate. Note that interpolation of range-compressed data at  $\omega_{ij}$  may be required if oversampling is not enough, or not performed at all (not recommended).

5) Then coherent summation is performed by using the following formula:

$$f[i, j] = f[i, j] + S_D [u, \omega_{close}] e^{j\frac{4\pi}{\lambda}[r(u, i, j) - r_{ref}(i, j)]}$$

The  $S_D$  refers to the range compressed data.



### 3.4 Packager

The Packager is responsible to save in the NetCDF format the SAR data and its corresponding metadata. The metadata related to the antenna position and the position of each pixel in the image are converted from  $T_{xyz}$  to the standard geographical system. The parameters of the radar acquisition and of the processing are also saved. For each saved variable a name and description is given within the NetCDF [2]. Besides creating the NetCDF, the packager also computes and make the visualizations of the image intensity (in dB), radiometric resolution, coherence and phase. Below the equations used for power, phase, and coherence computations.

$$power = \frac{1}{L} \sum_{l=1}^L \left( \frac{|S|^2}{2} \right)$$

$$X = \frac{1}{L} \sum_{l=1}^L \left( \frac{S_{master} \cdot conj(S_{slave})}{\sqrt{|S_{master}|^2 \cdot |S_{slave}|^2}} \right)$$

$$phase = arg(X)$$

$$coherence = |(X)|$$

Where  $S_{master}$  and  $S_{slave}$  refer to the back-projected data from master and slave antennas, and L refers to the desired number of looks.

### 3.5 Calibration

The Geometric calibration was done according to the given geographical coordinates of the corner reflectors in the field. The slant range of the corners were computed according to the flight geometry as well as the slant range of the corresponding corner reflector response in the image.

The resulting slant range delay obtained is given to the backprojection algorithm so that the focused pixels are already geolocated and orthorectified in correct geographical positions in focuser output.

The phase calibration is based on the given antenna lever-arms given in the Data Acquisition Report [6]. Since the navigation system and lever-arms are very accurate, there is no need of any further residual motion compensation. Small phase trend in range were visible in the SeaStarEx due to a small unknown global XTI baseline offset. This global baseline offset has been retrieved from the interferograms from the calibration (overland data) using the algorithm described in [7]. A XTI baseline offset in the sub-millimeter scale in both horizontal and vertical components have been measured. These values were added into the lever-arms values, ingested into the processor and the data re-processed, and the all-phases of all 4 calibration tracks over land show no trends.

The radiometric calibration is implemented to provide SAR imagery in which the pixel values can be directly related to the radar backscatter of the scene. Based on the well-known radar equation, the SAR image can be radiometrically calibrated by dividing the value of each image pixel by a calibration factor  $K$ , to give the normalized RCS [8, 9]:

$$\sigma_{i,j}^0 = \frac{|A_{i,j}|^2 F}{K} \frac{R_{i,j}^3}{G_{TX}(\theta_{i,j})G_{RX}(\theta_{i,j})} \sin\theta_{i,j}^{inc} - NESZ$$

where:

$A$  is the amplitude of the complex focused SAR image.

$G_{TX}$  is antenna gain for the transmitting antenna.

$G_{RX}$  is antenna gain for the receiving antenna.

$R_{i,j}$  is the slant range to ref. track.

$\theta_{i,j}^{inc}$  are local incidence angles.

$\theta_{i,j}$  are the antenna pointing angles.

$K$  is absolute calibration constant.

$NESZ$  is the noise equivalent sigma nought

We use the DEM, navigation data and correct antenna pointing to compute the incidence angles. With the antenna pattern we derive the antenna gain for each antenna pointing.

At least one corner reflector should be deployed over a specific area to estimate the absolute calibration constant  $K$ .

- 1- Compute the calibration factor:

$$F = \frac{R_{i,j}^3}{G_{TX}(\theta_{i,j})G_{RX}(\theta_{i,j})} \sin\theta_{i,j}^{inc}$$

- 2- With a target with a certain amplitude value  $A_{target}$  and known  $RCS$  we compute the calibration constant  $K$

$$K = \frac{|A_{target}|^2 F}{RCS} \delta_{az} \delta_{sr}$$

where  $\delta_{az} \delta_{sr}$  are the azimuth and slant range resolution, respectively.

- 3- Compute sigma nought

$$\sigma_{i,j}^0 = \frac{|A_{i,j}|^2 F}{K} - NESZ$$

An explanation of the steps to do the calibration and verification with SeaSTAREx data are described in [10].



## 4 OSCAR Processor Log

Release	Status description	Fixes/Improvements	date
1.0	Initial Release *	-----	23/June/ 2022
1.1	Phase undulation in the order of 1 to 2 radians along azimuth that resembles motion errors	Solved a bug in the Navigation Synchronization step. Interpolation was not being done corrected. Sample spacing being computed wrong. Interpolation has been corrected and spacing computed according to the PRF.	13/Sept/2022
1.2	Near range data being clipped after pre-processing	Bug solved in the pre-processor step. Length to be discarded due to transmitted pulse length was wrong computed. Length to be discarded is now correctly computed.	26/Jan /2023
1.3	Data being clipped in beginning and end of the cross-range dimension	Solved the issue with the grid definition not taking into consideration the whole swath of the AFT and FOR beams. The Grid definition during focusing was changed to accommodate the whole swath of all 3 channels.	26/Jan/2023
1.4	The last change created an issue that eventually the grids for each channel has different dimension (also they are the same) . This is not desired. It is more practical to deliver the gris with exactly the same dimensions	A step was added to equalize the grids between channels saved in the netcdf, if desired..	21/Mar//2023

\*The first stable version of the OSCAR processor was used with the SeaStarEx data and its result presented during a SeaStarEx progress meeting on 23 June 2022.

## References

- [1] *MetaSensing OSCAR Processor: Manual, Interface and Architecture. MS-OSCAR-PRO-MAN-ICD-ARCHIT\_v3.pdf*
- [2] *MetaSensing NetCDF. File Format Description. MS-OSCAR-PRO-FFD\_v7.pdf*
- [3] L.M. H.Ulander, H. Hellsten, and G.Stenström, "Synthetic-aperture radar processing using fast factorized back-projection," *IEEE Trans. Aerosp. Electron. Syst.*, vol. 39, pp. 760–776, Jul. 2003.
- [4] L.M. H. Ulander, H. Hellsten and G. Stenstrom, "Synthetic-aperture radar processing using fast factorized back-projection," in *IEEE Transactions on Aerospace and Electronic Systems*, vol. 39, no. 3, pp. 760-776, July 2003.
- [5] *MetaSAR-PRO\_ADDON\_User\_Manual\_v1\_20220113*
- [6] *MetaSensing Data Acquisition Report. MS-SEASTAREx-DAR\_V7.0*
- [7] K. A. C. de Macedo et al., "Long-Term Airborne DInSAR Measurements at X- and P-Bands: A Case Study on the Application of Surveying Geohazard Threats to Pipelines," in *IEEE Journal of Selected Topics in Applied Earth Observations and Remote Sensing*, vol. 5, no. 3, pp. 990-1005, June 2012, doi: 10.1109/JSTARS.2012.2187275.
- [8] A. Freeman, J. Curlander, *Radiometric Correction and Calibration of SAR Images* [Radiometric Correction and Calibration of SAR Images \(asprs.org\)](http://asprs.org).
- [9] Airbus. *Calculation of beta naught and sigma naught for TerraSAR-X data.* [1 \(intelligence-airbusds.com\)](http://intelligence-airbusds.com)
- [10] *MetaSensing Analysis of External Calibration Results Including Baselines Errors. MS-SEASTAREx-DAR\_V7.0*

# **ANNEX F) DATA PROCESSING REPORT: MEDITERRANEAN CAMPAIGN**



# SeaSTARex-Med

## D3: Mediterranean Data Processing Report

**Reference Code** : : MS-SeaSTARex-Med-DPR  
**Issue** : : 1.0  
**Date** : : 08 Mar 2024

MetaSensing BV  
Schipholweg 55  
2316 ZL Leiden , The Netherlands  
Tel: +31 71 751 5960  
Email: info@metasensing.com

<b>Document change log</b>			
<b>Issue</b>	<b>Change</b>	<b>Date</b>	<b>Author</b>
1.0	First version and release	08/03/2024	KM

# Table of contents

1	Introduction .....	4
2	Processing Chain .....	5
3	Data Analysis.....	9
3.1	Navigation Data.....	9
3.2	Impulse Responses.....	12
3.3	Sigma-0.....	17
3.4	Geolocation.....	20
3.5	Interferograms.....	22
4	Conclusions .....	25
5	References .....	26

# 1 Introduction

This document describes the analysis of the L1 data acquired with the OSCAR system during the SeaSTARex-Med airborne SAR data campaign carried out 05, 07 and 08, May 2023 over the Mediterranean Sea next to Menorca Island, Spain [1, 2, 3] and processed with the OSCAR processor. This document analysis the final L1 calibrated data delivered in December 2023 of all 3 antenna squinted angles (-45, 0, 45 deg.) for all acquisition days processed up to coregistered SLC (Single-Look Complex) level [3, 4]. Figure 1 shows the airborne platform used for this campaign. The OSCAR instrument is installed inside the aircraft belly pod, and it is fully operational.

The OSCAR instrument is a gimbal-based interferometric Ku-band SAR system developed and built by MetaSensing within the framework of a European Space Agency funded project (Ocean Surface Currents Airborne Radar demonstrator). The OSCAR system is tailored to the observations of the ocean surface motion and retrieval of wind. The OSCAR demonstrator instrument is developed with the observation parameters which directly relate to a potential satellite mission (SeaSTAR) for mesoscale measurements of ocean surface currents in the open-ocean and coastal regions [1, 2, 3].



*Figure 1: MetaSensing aircraft with the belly pod hosting the OSCAR system*

## 2 Processing Chain

The L1 data of SeaSTARex has been processed with the OSCAR processor. The OSCAR Processor algorithm is based on a time-domain global backprojection (GBP) method [4]. The OSCAR processor can be divided into 3 main modules as shown in the Figure below.

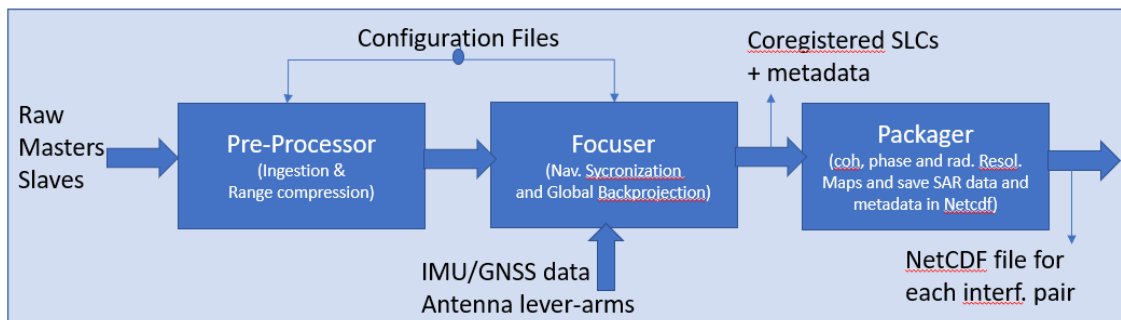


Figure 2 – OSCAR processing architecture.

Detailed description of each OSCAR processor module can be found in [4]. Description on how the OSCAR processor is used in the context of the SeaStarEx processing and calibration is found in [5, 6].

In the data production perspective, the processing for the SeaSTARex is carried out using the OSCAR processor in conjunction with the post-processing tool MetaSAR-Pro AddOn [7].

Below the block diagram showing how the tasks are split. Mainly, the MetaSAR-Pro AddOn is responsible to compute the calibration parameters used by the focuser and implements the OSCAR Packager module according to the SeaSTARex requirements [8].

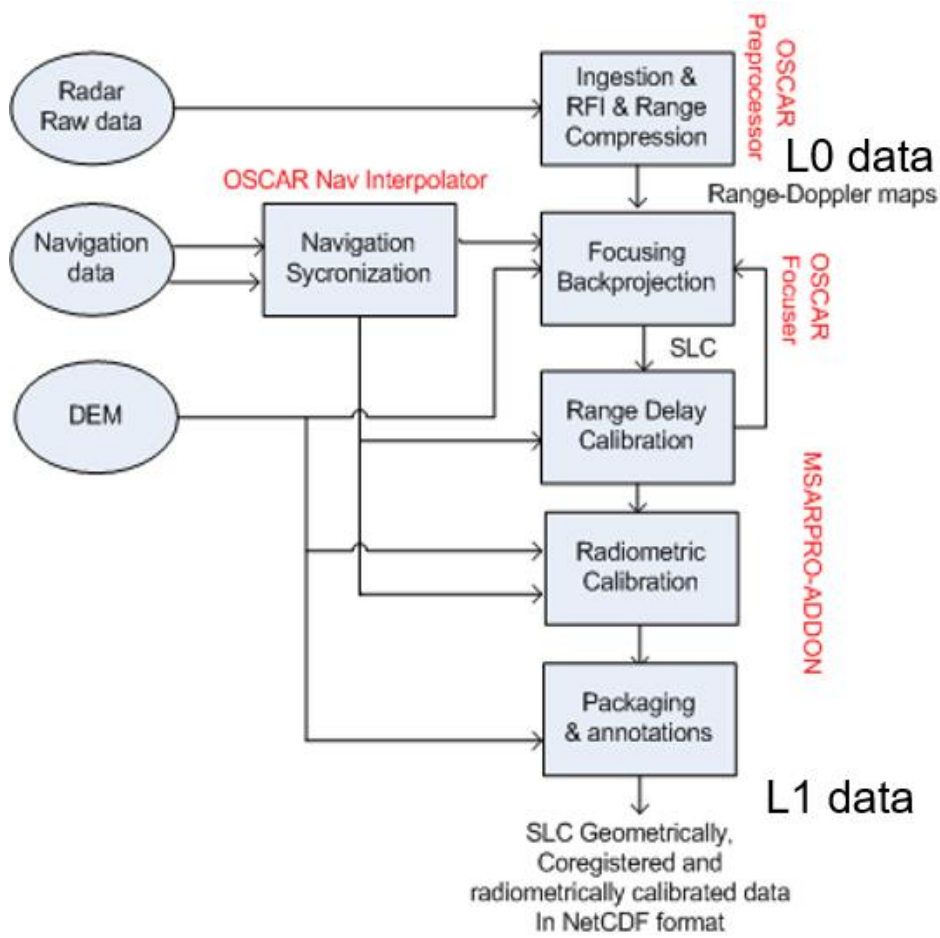


Figure 3 – SeaStarEx processing chain.

After the processing the first tracks of the Mediterranean campaign we found an issue in the phase related to systematic error coming out from the fact the True North has a divergence angle, or grid convergence angle, related to Grid North as shown below. This angle difference causes a systematic phase error that is correct at calibration level by taking into consideration the divergence angle during the computation of the sensor-to-target ranges.

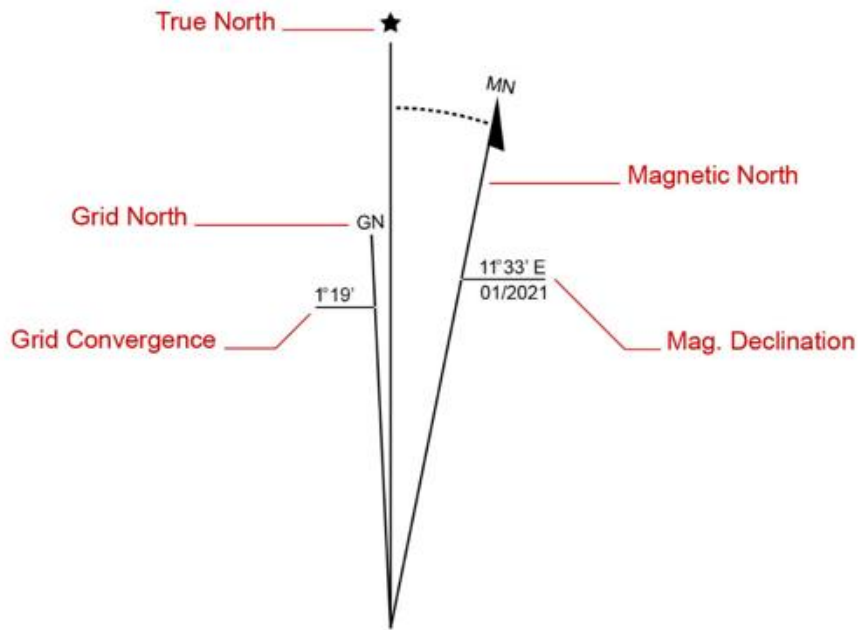


Figure 4 – Grid convergence illustration.

Below the update processor log.

Table 1: Update Processor Log

Release	Status description	Fixes/Improvements	date
1.0	Initial Release *	-----	23/June/ 2022
1.1	Phase undulation in the order of 1 to 2 radians along azimuth that resembles motion errors	Solved a bug in the Navigation Synchronization step. Interpolation was not being done corrected. Sample spacing being computed wrong. Interpolation has been corrected and spacing computed according to the PRF.	13/Sept/2022
1.2	Near range data being clipped after pre-processing	Bug solved in the pre-processor step. Length to be discarded due to transmitted pulse length was wrong computed. Length to be discarded is now correctly computed.	26/Jan /2023



1.3	Data being clipped in beginning and end of the cross-range dimension	Solved the issue with the grid definition not taking into consideration the whole swath of the AFT and FOR beams. The Grid definition during focusing was changed to accommodate the whole swath of all 3 channels.	26/Jan/2023
1.4	The last change created an issue that eventually the grids for each channel have different dimensions (also they are the same) . This is not desired. It is more practical to deliver the grids with the same dimensions	A step was added to equalize the grids between channels saved in the netcdf, if desired.	21/Mar//2023
1.5	Systematic undulations observed in Med Campaign.	Issue linked to the grid convergence angle not being considered during process/calibration. Issue fixed at calibration level (MSAR-Pro ADD-ON).	23/Dec/2023

### 3 Data Analysis

#### 3.1 Navigation Data

We show below the analysis for the navigation data for each campaign day. From top to bottom it shows the quality of navigation data (being green the highest quality index), it shows how accurate the attitude (in arcmin) and positioning (in meters) of the antenna are. The number of satellites available during all the flights was between 11 and 15 for all days.

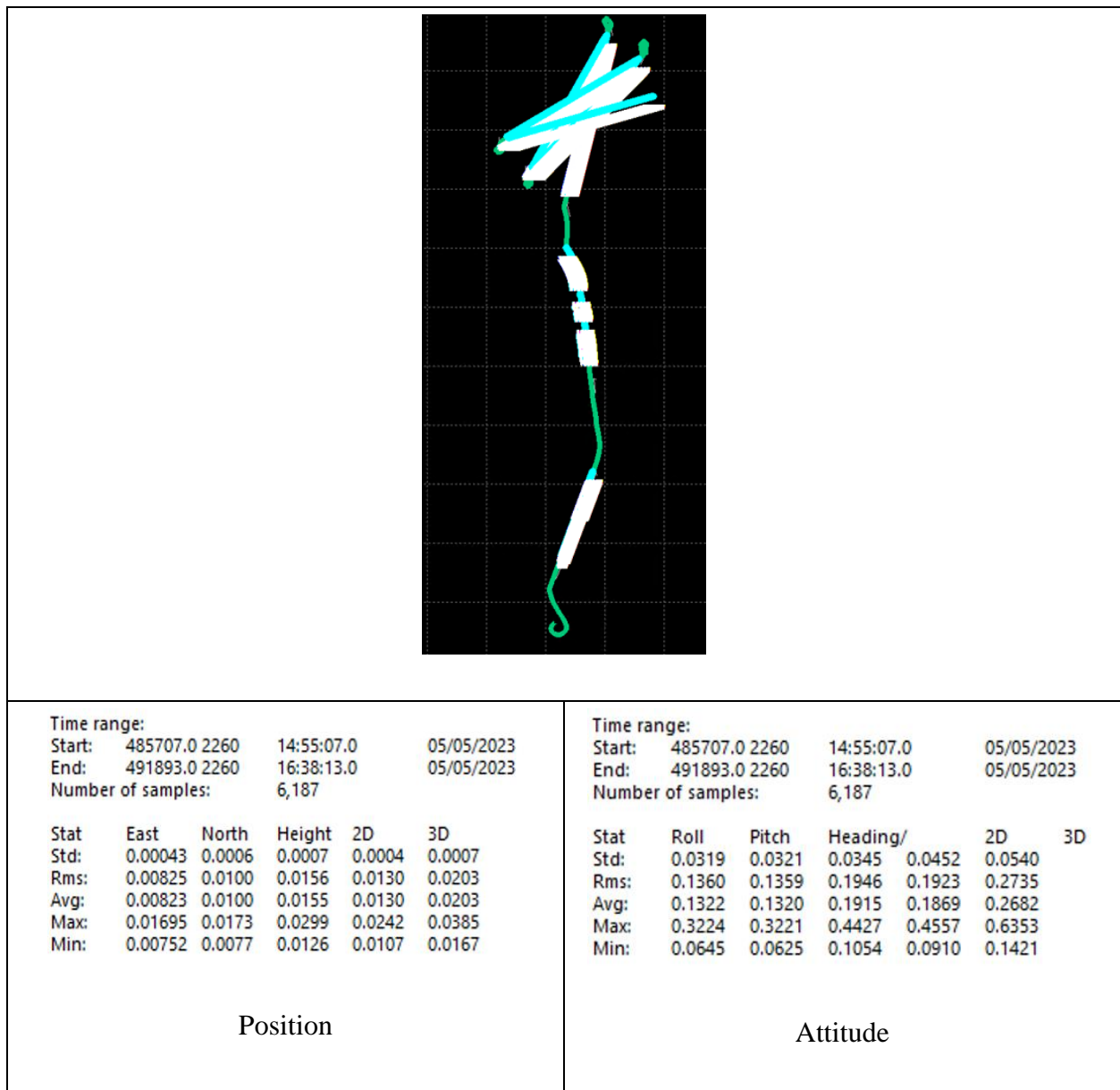


Figure 5: Navigation accuracy of the flights in 05 May 2023

Note that because of interruption of the navigation HW starting in track 6 to 14. Those were post-processed independently without any further effect or loss of accuracy on the L1 data.

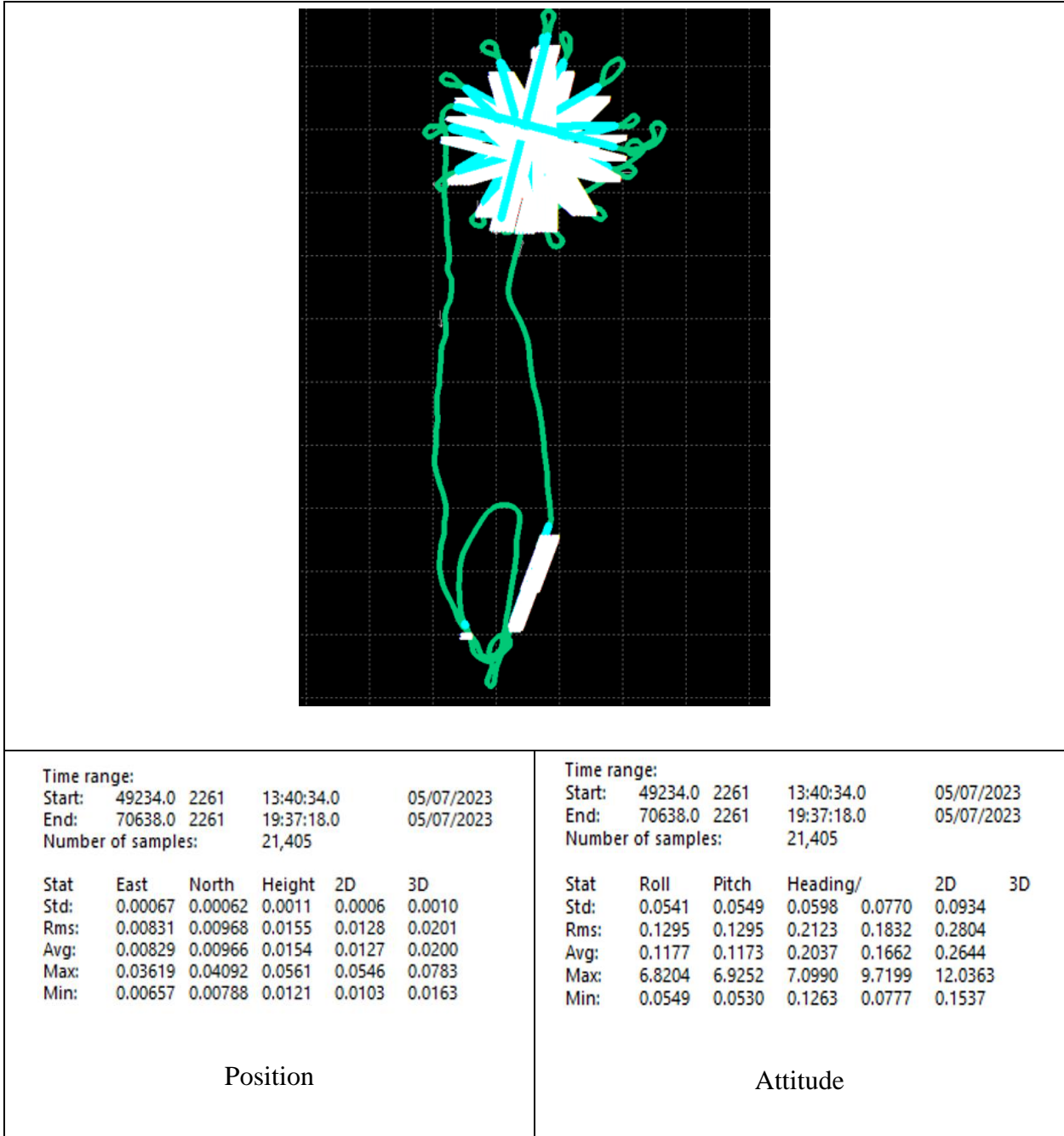


Figure 6: Navigation accuracy of the flights in 07 May 2023

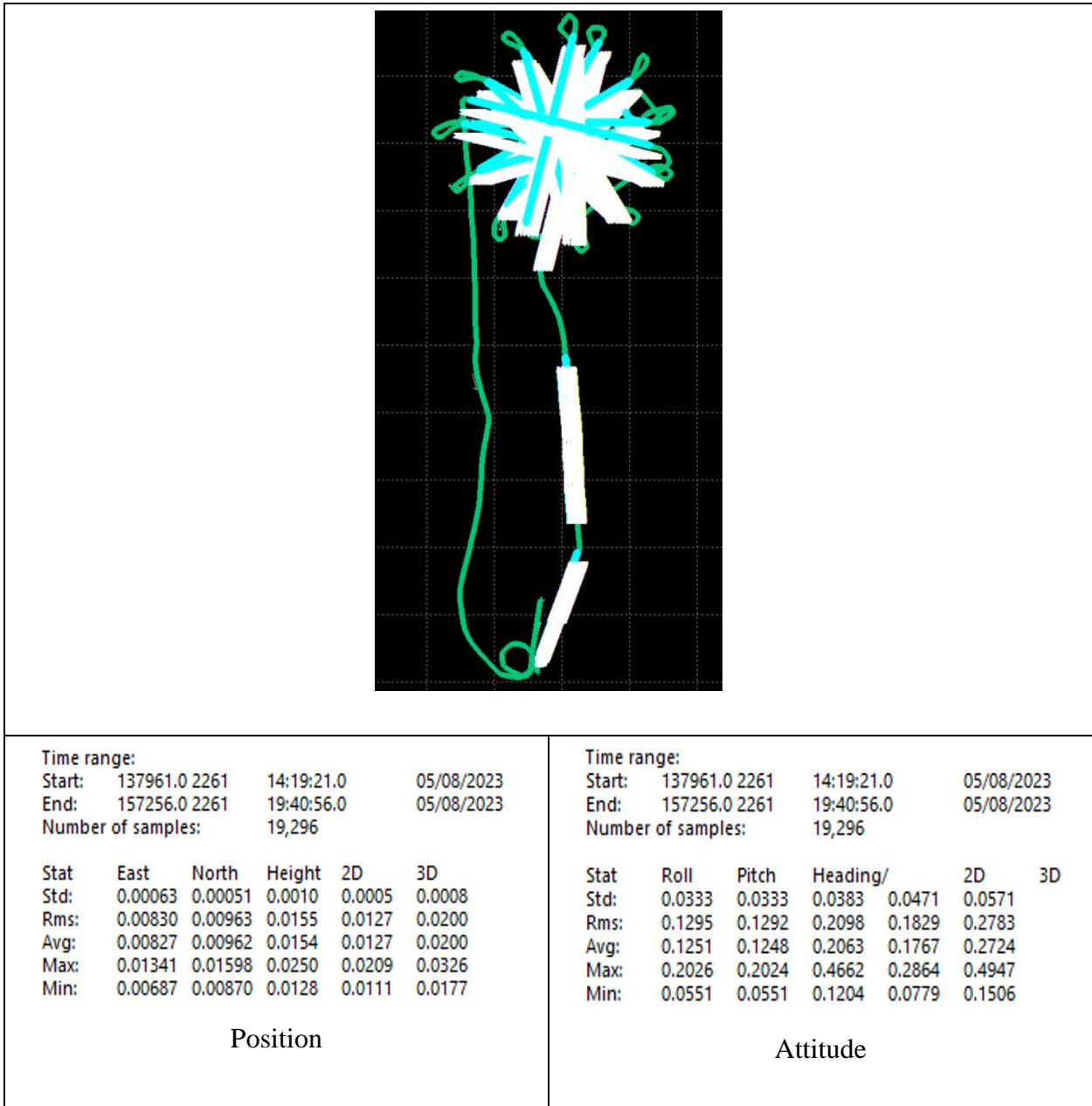


Figure 7: Navigation accuracy of the flights in 08 May 2023

In summary, the position accuracy is 1.5cm on average and 0.004 degrees in attitude all over the flights in all directions (3D).

## 3.2 Impulse Responses

Next, we show the Impulse Response Function (IRF) of the corner reflectors placed within the radar swath. For each corner the resolution, phase stability and side-lobe-ratio are measured to verify that the system and processor work as expected and generate images close to theoretical radiometric response (accuracy and resolution). Although the corner analysis is valid locally, a visual inspection to verify the homogeneity of the whole images in terms of resolution and texture confirms that the response seen in the corners applies equally spatially throughout the focused images. This is done for all calibration tracks, for all squints and for all days, further confirming the temporal stability of the system. This visual inspection is done and presented in the next section.

A good IRF indicates that the calibration of the SAR Images is sufficient in terms of antenna position, coming from the navigation system (shown before) and internal calibration (calibration pulses) and an external DEM (digital elevation model).

Below the table that describes the corner naming, size, orientation, and location taken from the DAR [3]. Figure 8 shows the GoogleEarth overview of the corner's location on the field, showing a total of 3 corners, each point according to the squint orientation of the OSCAR antenna (-45, 0, 45 deg). Note there are 2 labels CRF\_G and CRF\_A in the picture referring to 2 measurements of the same corner. The average position of the CRF is written on the table for calibration/verifications purposes.

Figure 9 summarizes the corner reflector responses showing the zoomed-in image and the profiles of the IRF for each day at different squints.

Note that this time all corners are visible at resolution of 8m, differently from Brest Campaign. Probably in Brest the grass was high (plus wind), while in Menorca we have bare soil around the corners. We used the standard peak estimation method [11, 12]. To derive the  $\sigma_0$  images.





Figure 8: Position of the corner reflectors with naming.

Table 2: Corner reflectors field installation

CR#	Type	Length [m]	RCS* [dB]	Lat (N) [deg]	Lon [deg]	I	Azimuth tilt** [deg]	Elevation tilt *** [deg]	Notes
CRF	Square	0.30	27.92	39.86606,	4.25413		155	7	
CRZ	Square	0.30	27.92	39.892656	4.274708		110	12	
CRB	Square	0.30	27.92	39.86509	4.25384		65	7	

\* if not filled a theoretical number derived from length is used)

\*\* True North

\*\*\* Relative to the ground

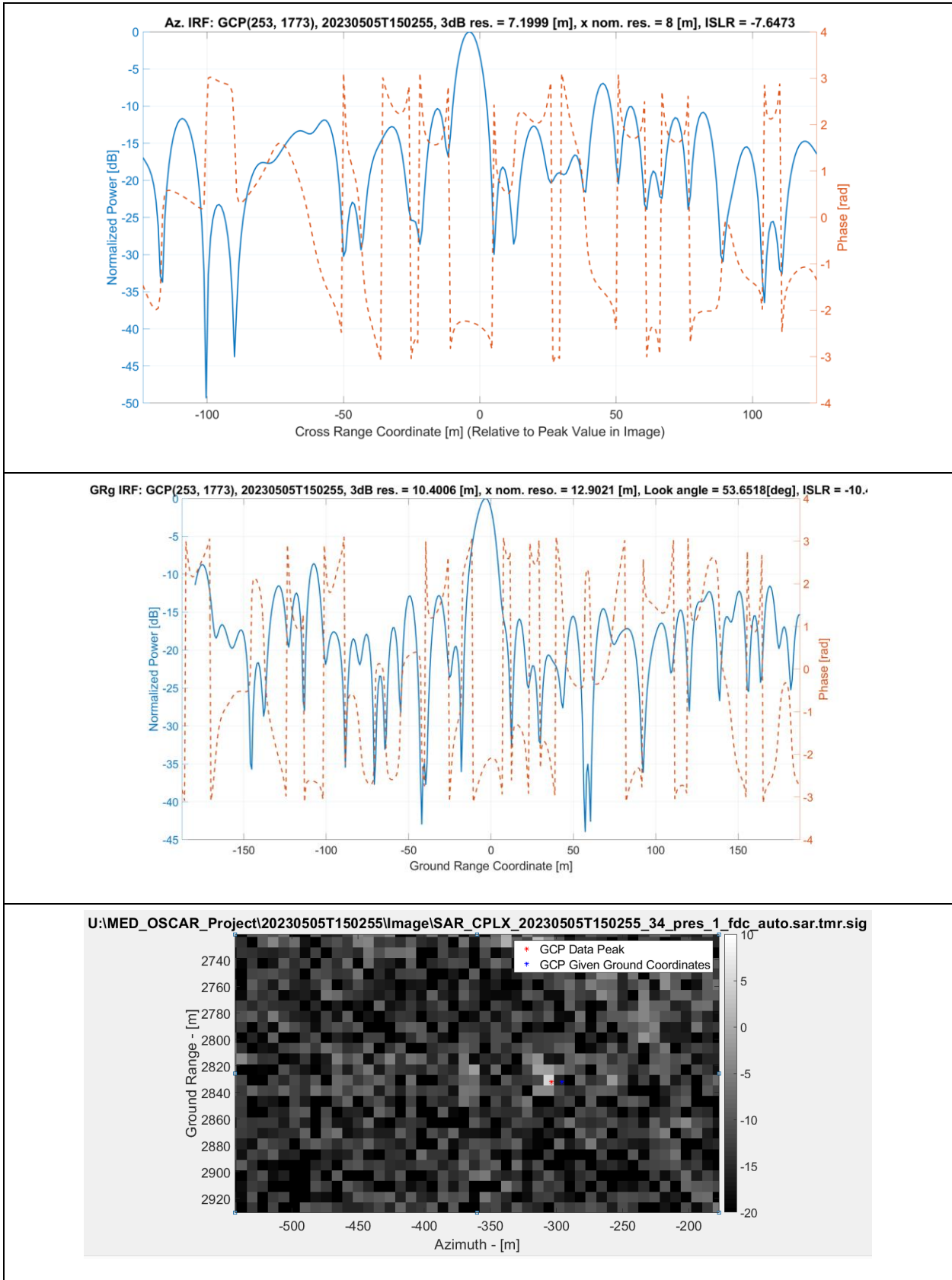


Figure 9 Corner Reflector response of day 05 May 2023.



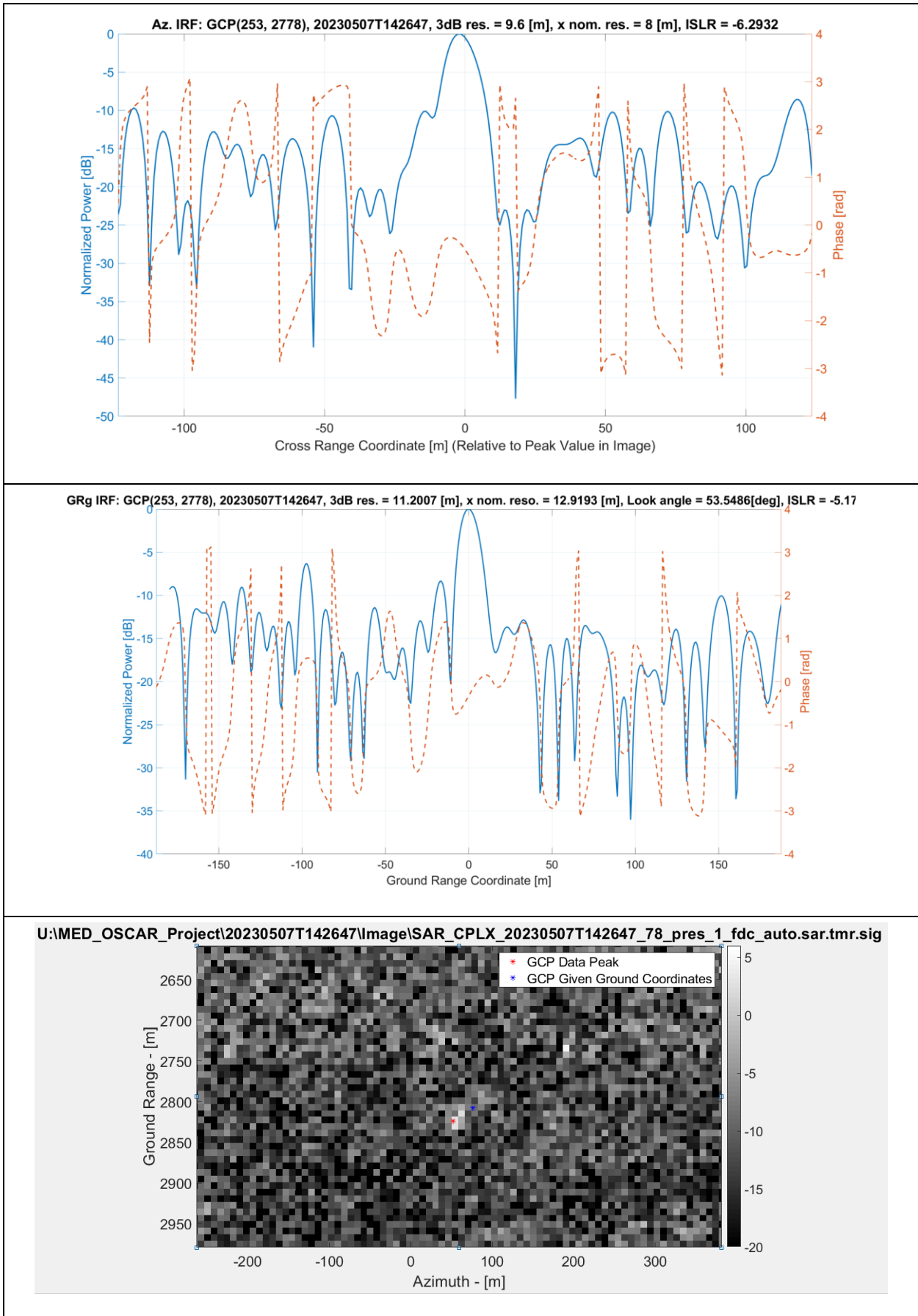


Figure 10 Corner Reflector response of day 07 May 2023.

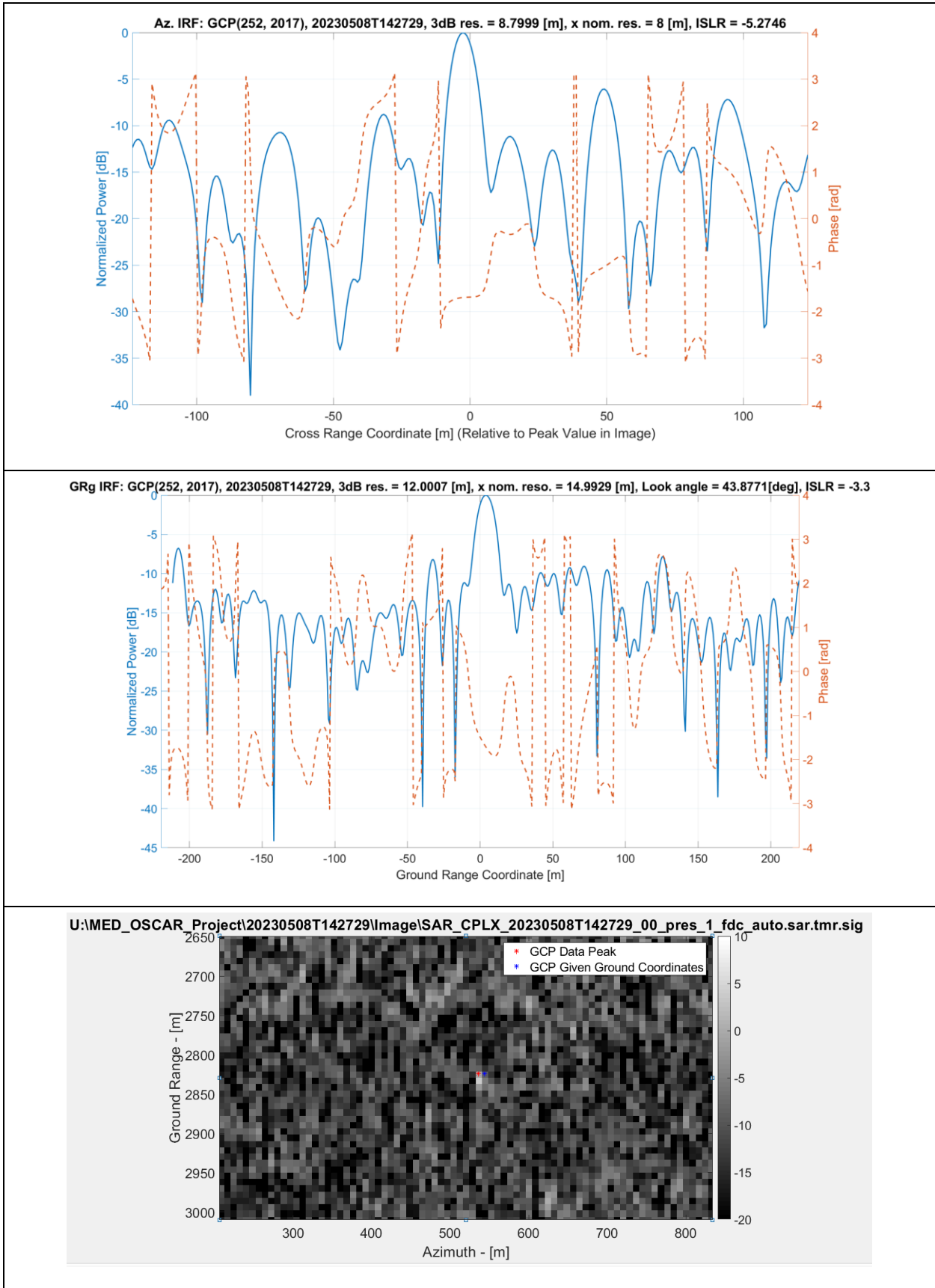


Figure 11 Corner Reflector response of day 08 May 2023.

### 3.3 Sigma-0

We calibrate the images to sigma-0 values using an antenna pattern diagram, external DEM and the knowledge of a radiometric offset derived from the RCS (radar cross section) of the corners. Only one single radiometric offset per channel is applied to all the images showing a very stable behavior of the system. Through the corners of different calibration tracks and pointing we estimate the difference between the theoretical NRCS of the corners and observed NRCS values of the delivered 8m (az.) reso. images. The table below compiles all corners observations used to verify that the radiometric sigma-0 mean and standard deviation is  $0.62 \pm 1.17$  dB. Note that we attribute larger variation among the corner in Mediterranean compared to Brest campaign, especially in day 05 because of the gimbal offset observed in gimbal data in the calibration track as reported in acquisition log documented in the DAR. In general, we identified more variations of the Gimbal in Med campaign as reported in acquisition log in the DAR [3].

*Table 3: Corners used for Calibration and Verification*

Track	CRA: Observed minus Theoretical Sigma-0	CRZ: Observed minus Theoretical Sigma-0	CRF: Observed minus Theoretical Sigma-0
20230505T150255	1.0	3	-0.9
20230507T142647	-0.2	-0.5	0.5
20230508T142729	1.5	0.5	-0.2
Mean and standard deviation:  0.62 ± 1.17 dB.			

Inspecting visually all calibration images over the processed ground swath of 5 km we see image textures over land with no dependency of topography, range or antenna motion, indicating a sufficient radiometric calibration in space and time.

Figure 12 shows a simultaneous visualization of all 3 squinted images acquired on 17 May. As expected because of the differences between the squints (-45, 0, 45) there is clear dependency of the  $\sigma_0$  with the antenna pointing. Nevertheless, in areas where a more isotropic backscatter is expected the values are within a radiometric variation of ca. 1dB.

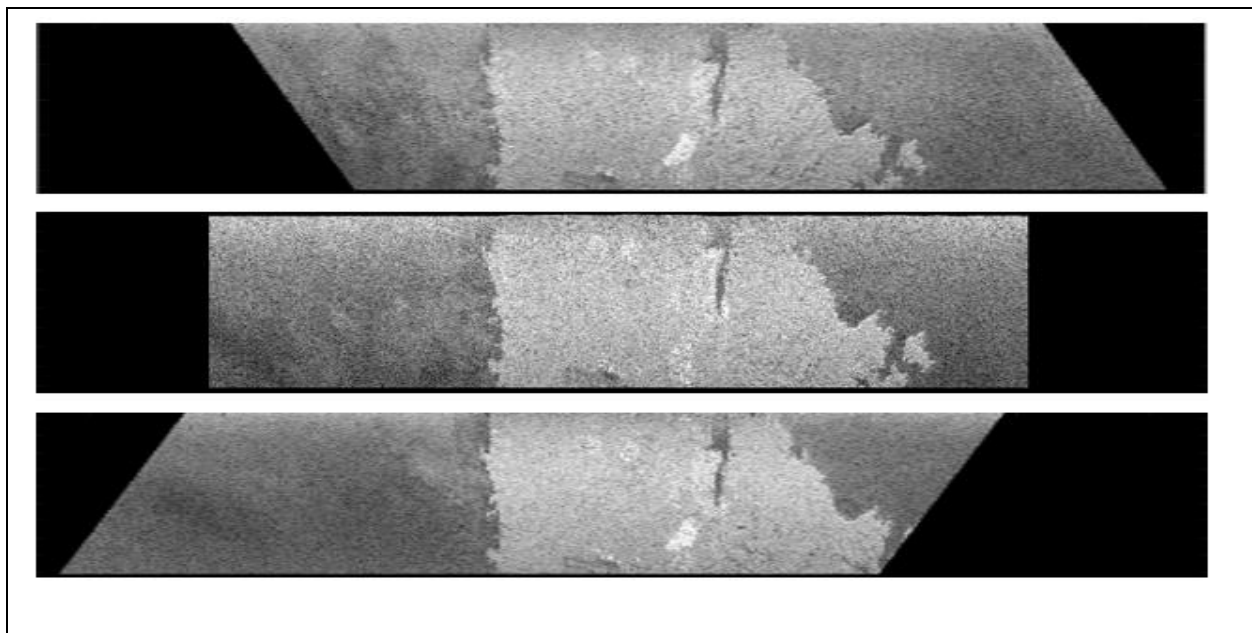


Figure 12: Simultaneous visualization of the current  $\sigma_0$  images (5km swath) from all 3 antennas (-45, 0, 45 degs) acquired in 08 May, 2023. The color scale goes from -30 to 5 dB. The images show no dependency of topography, range or antenna motion.

Unfortunately, if we do a profile of the along range over land in the Mediterranean Sea data of day 8, for example, we do see a variation that resembles an antenna pattern. Nevertheless, while investigating this issue, we re-calibrated the same Med data over land after updating our SW/methodology and we show in figure below that we get a  $\sigma_0$  profile as expected over land and without antenna patterns trend.

Note that the terrain in Menorca is hilly than is also good to show the profile obtained with the latest process data (Netherlands campaign) which also used the latest SW/methodology for calibration. Below we show that for the Netherlands data we get also as well the expected decreasing response from near to far range with a plateau like response in mid-range (flattened  $\sigma_0$ ), as expected over flat land, without any antenna pattern dependence. Therefore, eventually we need to re-calibrate the antenna pattern of the whole Mediterranean data.

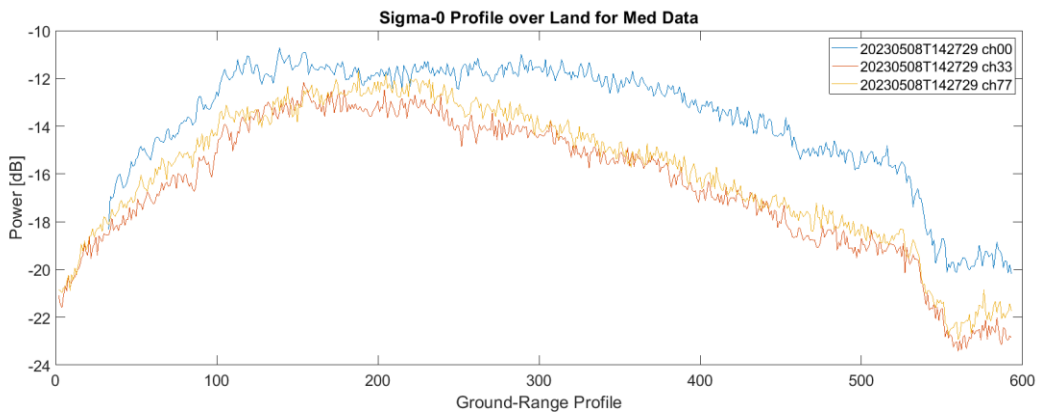


Figure 13: Antenna pattern trend observed in Sigma-0 over land profile of the current Med data.

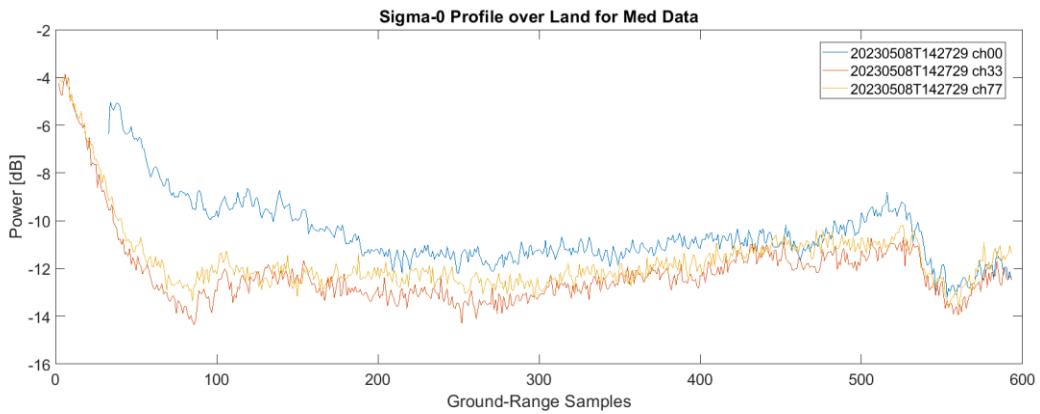


Figure 14: As expected Sigma-0 over land profile of the Med data after re-calibrating, i.e using latest SW/methodology version.

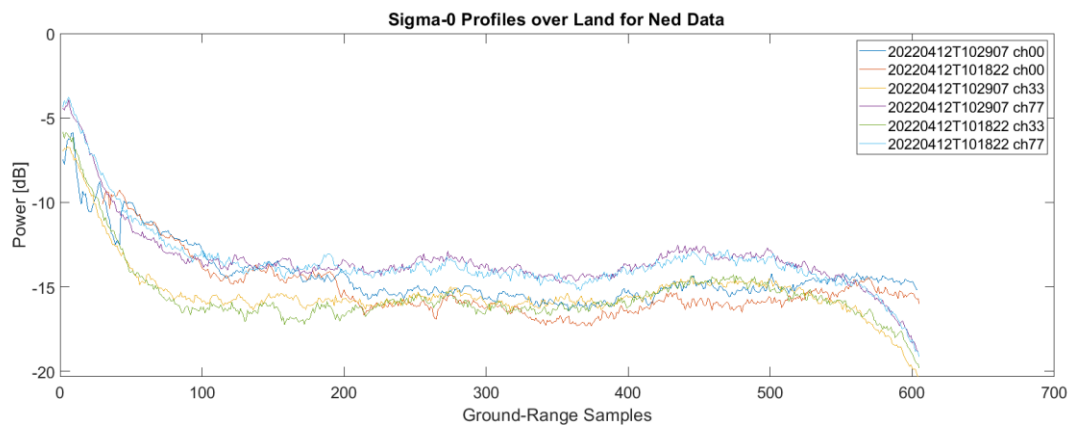


Figure 15: As expected Sigma-0 profile over land of the Ned data (mostly flat), processed with the latest SW/methodology version.

### 3.4 Geolocation

The correct geolocation of the images depends basically on the estimation of the range delay of the system. The along track timing of the data is guaranteed through the knowledge of the antenna position which is given by the navigation system and its accuracy is in the order of 2 centimeters as shown before. Furthermore, we used 30m resolution SRTM.

The estimation of the range delay is based on corner reflector response and the geographical position of the corners measured in the field. Note that field measurements are made by a handheld GPS and have accuracy with 5 to 10m. Only one range delay offset has been applied for the whole data set (all days, all squints).

Our absolute geolocation accuracy as here described is basically over flat areas. From the corner reflectors from different days and different squints, we obtain absolute geolocation accuracy of 5.33 m, i.e., within the resolution cell of the final images.

Relatively speaking, all the images are perfectly geolocated with one another due to the fact we use the same grid to back project that data of different channels.

It is important to note that for the absolute geographical position we also identify features in the images that could support that we correctly estimate the range delay and correctly geolocate the data, such as streets, runway, coast lines, river lines. Below is an example of a georeferenced SAR image overlaid with optical imagery highlighting the well alignment with river and coast line.





Figure 16: Georeferenced SAR image (ch00) of 05 May 2023 overlaid with standard optical image for access the geolocation accuracy.



### 3.5 Interferograms

The interferometric calibration of Med data consists in correcting the systematic offset and trend of the phase measurements to enable the retrieval of velocity measurements. This is done using the methodology/processing explained in [5, 6], i.e. the calibration track is used to properly set the lever-arms, using Zero-meter Baseline Estimation (ZIBE) approach [see 6], in such way the velocity outcome is null m/s over land. This is the case since the nominal cross-track baseline is practically null meter in the OSCAR instrument and the DEM (SRTM 30m) has been taken into consideration during phase flattening operation. Also, The OSCAR consists of single-pass along track interferometer, where the baselines are well known up to the millimeter scale due to the accurately measured lever-arms, gimbal stabilization, and accurate navigation data (as shown in section 3.1), thus no non-linear motion errors are expected.

Below the nominal lever-arms of the OSCAR instrument flown in Med followed by the coordinate system used.

Table 4: Nominal antenna lever arms used in Med (mechanical reference to IMU phase center [m]).

Lever arms between IMU and antennas	AFT		FORE		0 - DOP
Antenna	M	S	M	S	
$\Delta X$ [m]	-0.1496	-0.1496	-0.1501	-0.1501	-0.1507
$\Delta Y$ [m]	-0.4387	-0.6087	+0.7331	+0.5631	0.0621
$\Delta Z$ [m]	-0.3642	-0.3642	-0.3642	-0.3642	-0.3653

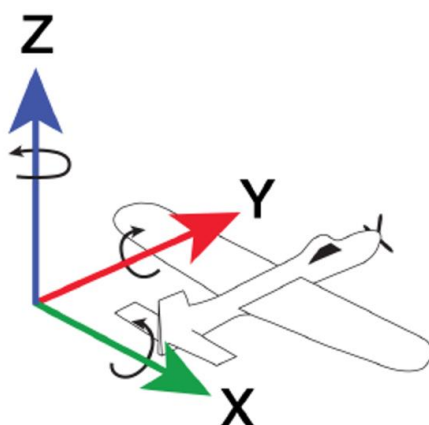


Figure 17: Reference system for the lever arms required by the OSCAR processor.

The interferograms generated with nominal lever-arms show a trend along range over land which is related to an unknown cross-track baseline component. This is an unknown cross-track baseline component that comes from a small uncertainty in the nominal lever-arms measurements. We use the phase trend to invert it into horizontal and vertical baseline components, which is then added to the nominal lever-arm values. Below are the lever-arms used to obtain the current calibrated Med interferograms. It's a difference of 0.1mm x -0.9 mm (hor x vert) for AFT channels (77x78) and of 0mm x -0.8mm for FOR channels (33x 34).

*Table 5: Calibrated antenna lever arms used in Med (mechanical reference to IMU phase center [m]).*

Lever arms between IMU and antennas	AFT		FORE		0 - DOP
	M	S	M	S	
<b>Antenna</b>					
<b><math>\Delta X</math> [m]</b>	-0.1496	-0.1497	-0.1501	-0.1505	-0.1507
<b><math>\Delta Y</math> [m]</b>	-0.4387	-0.6087	+0.7331	+0.5631	0.0621
<b><math>\Delta Z</math> [m]</b>	-0.3642	-0.3651	-0.3642	-0.3650	-0.3653

The next figure shows the interferograms (ch33) obtained after lever-arms calibration over the calibration of track of each day, namely day 05, 07, and 08 May 2023.

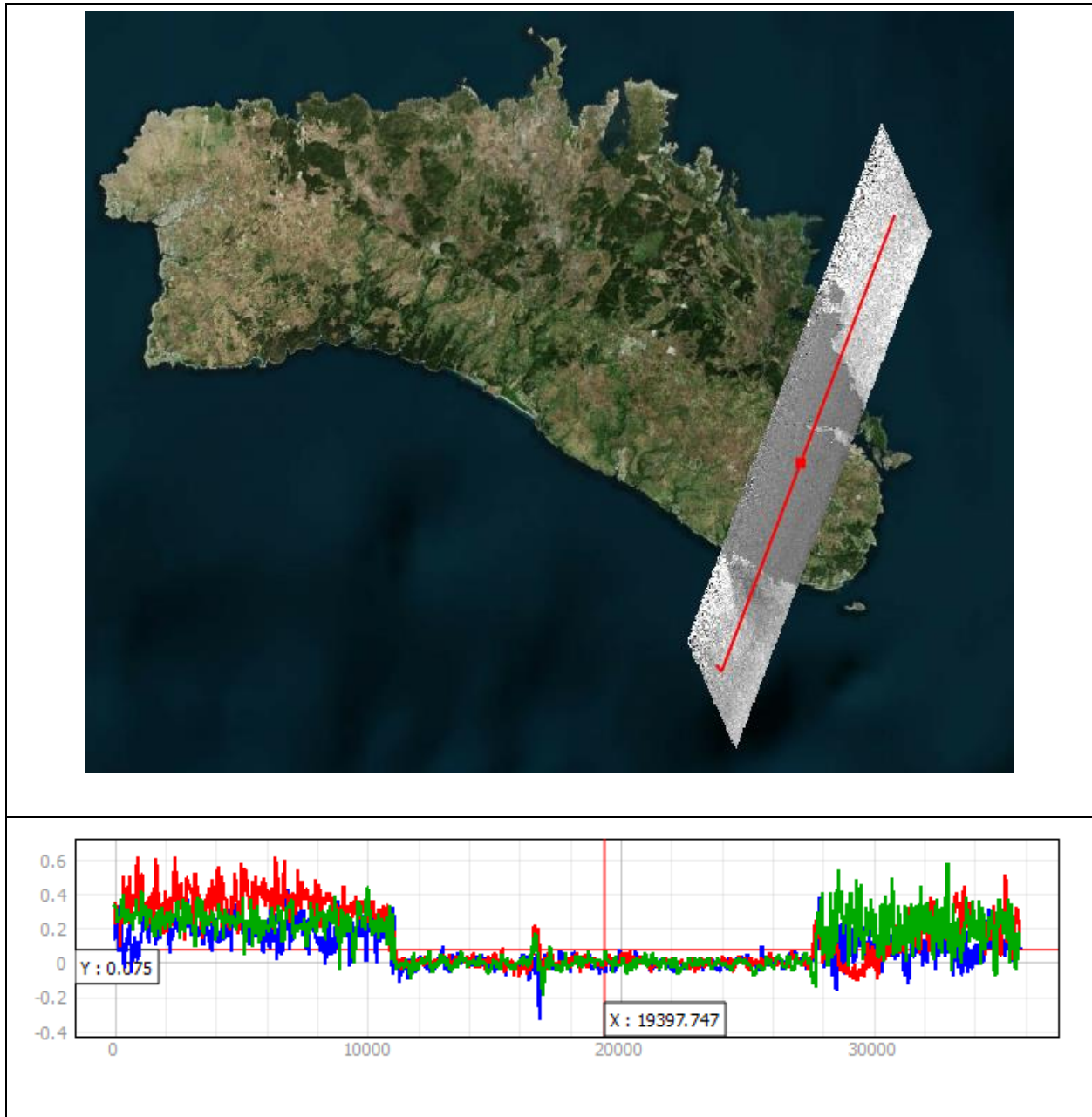


Figure 18: Calibration track with profile (top) where calibrated phase of ch33 is checked for each day.  
Green is day 05, blue is day 07 and red is day 08 May 2023.

## 4 Conclusions

This document provides information about how the Med data are processed and calibrated. In the document, the data are analyzed to demonstrate the level of quality and accuracy in terms of geometric, radiometric, and interferometric aspects. The verification is done based on corner reflectors and on the intensity and interferometric images over land.

For the radiometric calibration, it shows that all corner reflectors are visible at 8m azimuth resolution and the IRF are within the theoretical/expected/required values. Furthermore, visual inspection of all images for all days shows that the radiometric behavior of the images is within the expectations besides the antenna pattern related feature. We demonstrated that we can remove this feature by redoing the antenna pattern calibration with the latest SW/methodology.

For the geometric calibration, the visible corners are used as well optical imagery to verify that the geolocation of the data is within the resolution cell of 8 m.

For the interferometric calibration, interferogram over land shows that the phase behaves stable along the flight. Fine adjustment in the lever arms and phase offset further sets the phase over land with basically average equal zero radians and standard deviation of 2.4 degrees after posting of 60m x 60m over ground (40 looks).

.

## 5 References

- [1] C. Gommenginger, et al, “SEASTAR: A Mission to Study Ocean Submesoscale Dynamics and Small-Scale Atmosphere-Ocean Processes in Coastal, Shelf and Polar Seas”, Proposal selected for Phase 0 of Earth Explorer 11 candidate mission, ESA-ESTEC.
- [2] Ocean Surface Current Airborne Radar Demonstrator (OSCAR) – Statement of Work, Appendix 1 to AO/1- 8309/15/NL/BJ.
- [3] MetaSensing Data Acquisition Report- Mediterranean Sea MS-SEASTARExMED-DAR\_V6.0.
- [4] MetaSensing OSCAR Processor: Manual, Interface and Architecture. MS-OSCAR-PRO-MAN-ICD-ARCHIT\_v3.pdf
- [5] MetaSensing Processor Specification: SeaSTARex MS-SEASTAREx-PROCESSING\_SPECIFICATION\_v5
- [6] MetaSensing External Calibration: SeaSTARex. MS-SEASTAREx-ExtCal\_V5.0
- [7] MetaSAR-PRO\_ADDON\_User\_Manual\_v1\_20220113
- [8] MetaSensing NetCDF. File Format Description. MS-SAR-NetCDF-FFD\_v3.

# **ANNEX G) ANALYSIS OF EXTERNAL CALIBRATION RESULTS INCLUDING BASELINE ERRORS**

# SeaSTARex

## D3: Analysis of External Calibration Results Including Baselines Errors

**Reference Code** : : MS-SeaSTARex-ExtCal  
**Issue** : : 5.0  
**Date** : : 09 Oct 2023

MetaSensing BV  
Schipholweg 55  
2316 ZL Leiden , The Netherlands  
Tel: +31 71 751 5960  
Email: info@metasensing.com



Document change log			
Issue	Change	Date	Author
1.0	First version	21/08/2023	KM
2.0	Table with corners used for cal. Verification and disc on SCR	29/09/2023	KM
3.0	Review and Release	29/09/2023	KM
4.0	Review of Equations and Release	04/10/2023	KM
5.0	Equation correction and Release	09/10/2023	KM

# Table of contents

1	Introduction .....	4
2	Methodology.....	5
3	Results .....	7
3.1	Navigation Data.....	7
3.2	Corner Reflectors.....	11
3.3	Sigma0.....	24
3.4	Geolocation.....	26
3.5	Interferograms .....	27
4	Conclusions .....	31
5	References .....	32

# 1 Introduction

This document describes the analysis of the external calibration conducted for the SeaSTARex airborne SAR data campaign carried out 17, 22, 25, and 26 May 2022 over the sea/ocean area next to Brest, France [1, 2, 3]. This document provides the calibration results that demonstrate that the airborne SAR data collected with the OSCAR (Ocean Surface Current Airborne Radar) instrument over the Ocean next to Brest (France), in all 3 antenna squinted angles (-45, 0, 45 deg.), and processed with the OSCAR processor up to coregistered SLC (Single-Look Complex) level [3, 4] are calibrated within the desired accuracy in terms of geolocation, radiometry, and interferometric phase. Figure 1 shows the airborne platform used for this campaign. The OSCAR instrument is installed inside the aircraft belly pod, and it is fully operational.

The OSCAR instrument is a gimbal-based interferometric Ku-band SAR system developed and built by MetaSensing within the framework of a European Space Agency funded project (Ocean Surface Currents Airborne Radar demonstrator). The OSCAR system is tailored to the observations of the ocean surface motion and retrieval of wind. The OSCAR demonstrator instrument is developed with the observation parameters which directly relate to a potential satellite mission (SeaSTAR) for mesoscale measurements of ocean surface currents in the open-ocean and coastal regions [1, 2, 3].



*Figure 1: MetaSensing aircraft with the belly pod hosting the OSCAR system*

## 2 Methodology

The external calibration performed for the OSCAR data collected for the SeaSTARex Campaign can be divided into three types: Geometric, Radiometrically and Interferometric calibrations. Geometric calibration is related to the correct geolocation of the data, which comes projected into a known geographical grid after SAR back-projection focusing [5]. Radiometric calibration consists in determining the calibration factors which convert the digital values of the data into radar backscatter ( $\sigma_0$ ) values. Interferometric calibration consists in determining the baseline offset values. i.e., fine adjust the measured lever-arms values, to remove residual phase errors.

The Geometric calibration was done according to the given geographical coordinates of the corner reflectors measured in the field. The slant range of the corners were computed according to the given flight geometry (given by the navigation system) and compared to the slant range of the corresponding corner reflector response in the focused SAR image. The resulting slant range delay obtained is given to the SAR processor so that after focusing all pixels are placed in the correct geographical positions.

The Interferometric calibration is based on a fine adjustment of an XYZ offset in the nominal (measured) antenna lever-arms given in the Data Acquisition Report [3]. Since the navigation system and lever-arms are very accurate, plus the fact that the gimbal maintains the antenna stable, there is no need of any further variable (advanced) residual motion compensation/calibration built in the processor chain. Only a small phase trend along range can be visible in the SeaStarEx due to a small unknown global XTI baseline offset. This global baseline offset has been retrieved from the OSCAR ATI interferograms over land (where phase should be zero, with help of an external 30m SRTM data) using the algorithm described in [6]. A XTI baseline offset in the order of 0.2mm in both horizontal and vertical components have been measured for the SeaSTARex data. These values were added into the lever-arms values, ingested into the processor and the data re-processed. After re-processing all-phases of all 4 calibration tracks over land show no trends.

The radiometric calibration is implemented to provide SAR imagery in which the pixel values can be directly related to the radar backscatter of the scene. Based on the well-known radar equation, the SAR image can be radiometrically calibrated by dividing the value of each image pixel by a calibration factor  $K$ , to give the normalized RCS [7, 8]:

$$\sigma_{i,j}^0 = \frac{|A_{i,j}|^2}{K} \frac{R_{i,j}^3}{G_{TX}(\theta_{i,j})G_{RX}(\theta_{i,j})} \sin\theta_{i,j}^{inc} - NESZ$$

where:

$A$  is the amplitude of the complex focused SAR image.

$G_{TX}$  is antenna gain for the transmitting antenna.

$G_{RX}$  is antenna gain for the receiving antenna.

$R_{i,j}$  is the slant range to ref. track.

$\theta_{i,j}^{inc}$  are local incidence angles.

$\theta_{i,j}$  are the antenna pointing angles.

$K$  is absolute calibration constant.

$NESZ$  is the noise equivalent sigma nought.

We use the DEM, navigation data and correct antenna pointing to compute the incidence angles. With the antenna pattern we derive the antenna gain for each antenna pointing.

At least one corner reflector should be deployed over a specific area to estimate the absolute calibration constant  $K$ .

1- Compute the calibration factor:

$$F = \frac{R_{i,j}^3}{G_{TX}(\theta_{i,j})G_{RX}(\theta_{i,j})} \sin\theta_{i,j}^{inc}$$

2- With a target with a certain amplitude value  $A_{target}$  and known  $RCS$  we compute the calibration constant  $K$

$$K = \frac{|A_{target}|^2 F}{RCS} \delta_{az} \delta_{sr}$$

where  $\delta_{az} \delta_{sr}$  are the azimuth and slant range resolution, respectively.

3- Compute sigma nought

$$\sigma_{i,j}^0 = \frac{|A_{i,j}|^2 F}{K} - NESZ$$

### 3 Results

#### 3.1 Navigation Data

We show below the analysis for the navigation data for each campaign day. From top to bottom it shows the quality of navigation data (being green the highest quality index), it shows how accurate the attitude (in arcmin) and positioning (in meters) of the antenna are. The number of satellites available during all the flights were between 11 and 15 for all days..

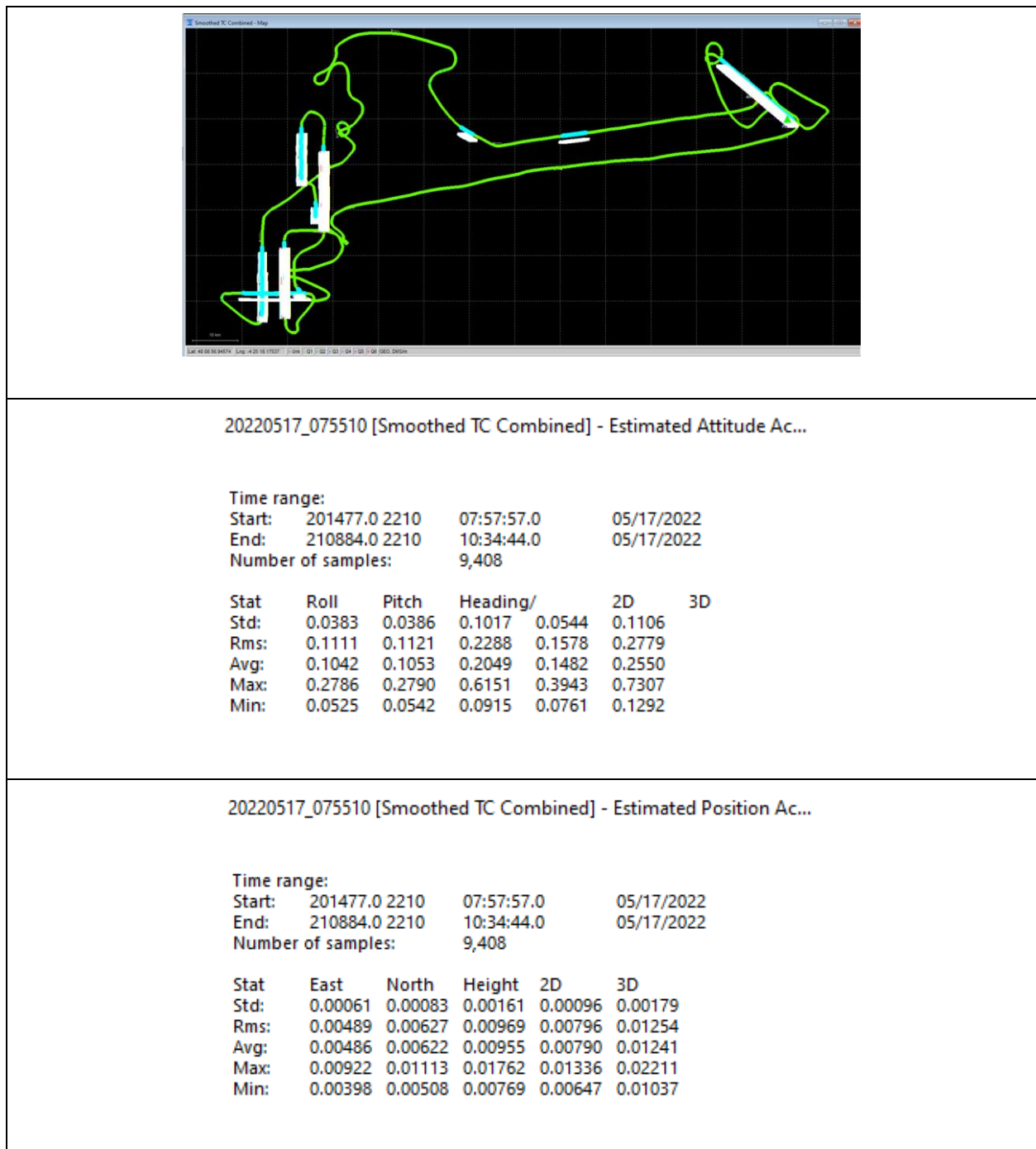
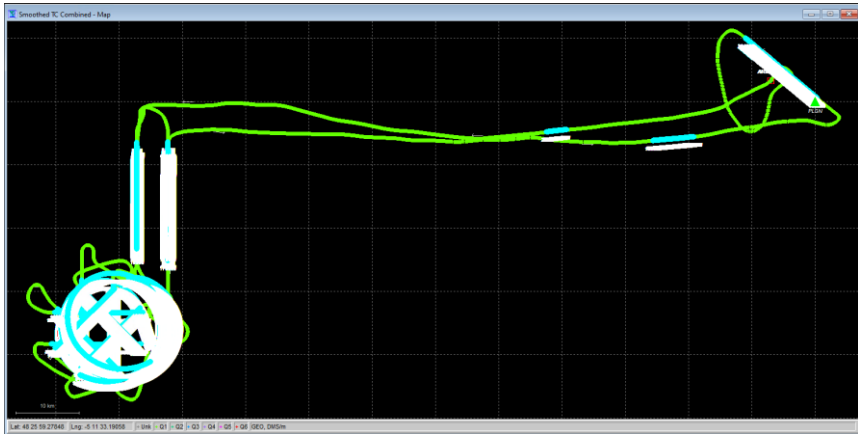


Figure 2: Navigation accuracy of the flights in 17 may 2022



breast\_may22\_050541 [Smoothed TC Combined] - Estimated Attitude ...

Time range:

Start:	18371.0	2211	05:06:11.0	05/22/2022
End:	28991.0	2211	08:03:11.0	05/22/2022
Number of samples:	10,621			

Stat	Roll	Pitch	Heading/	2D	3D
Std:	0.0312	0.0322	0.0766	0.0449	0.0836
Rms:	0.1064	0.1066	0.2095	0.1506	0.2580
Avg:	0.1017	0.1016	0.1949	0.1438	0.2441
Max:	0.1847	0.1847	0.4880	0.2612	0.5535
Min:	0.0595	0.0559	0.1056	0.0817	0.1406

breast\_may22\_050541 [Smoothed TC Combined] - Estimated Position ...

Time range:

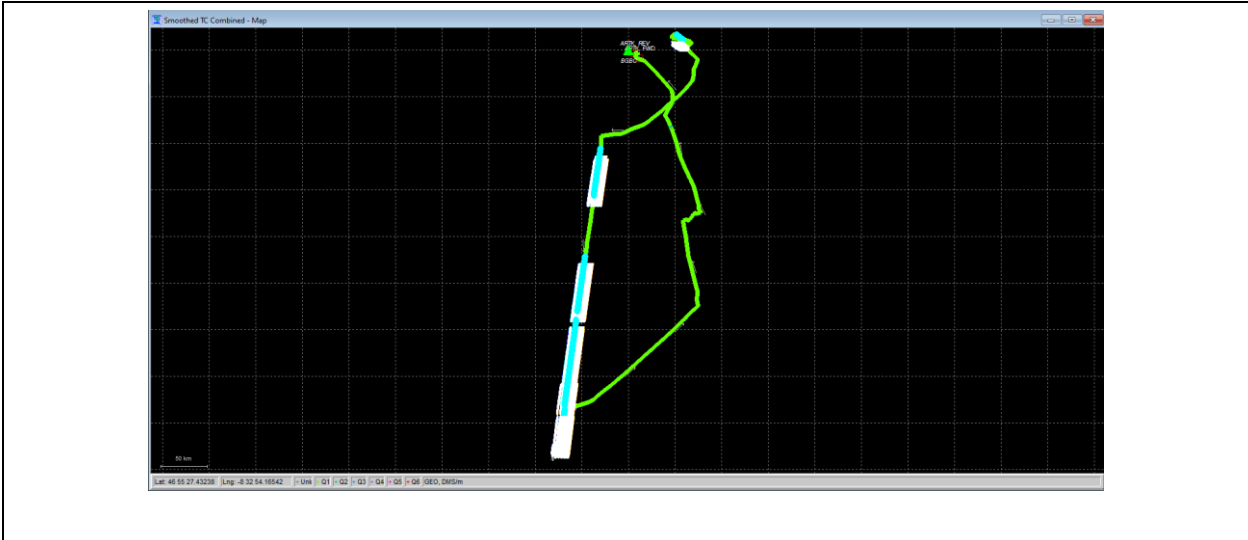
Start:	18371.0	2211	05:06:11.0	05/22/2022
End:	28991.0	2211	08:03:11.0	05/22/2022
Number of samples:	10,621			

Stat	East	North	Height	2D	3D
Std:	0.00066	0.00081	0.0011	0.0009	0.0013
Rms:	0.00453	0.00565	0.0102	0.0072	0.0126
Avg:	0.00449	0.00559	0.0102	0.0072	0.0125
Max:	0.01810	0.02413	0.0318	0.0302	0.0437
Min:	0.00394	0.00490	0.0084	0.0063	0.0112

Figure 3: Navigation accuracy of the flights in 22 may 2022





brestr\_mnay\_25\_second\_20220525\_075048 [Smoothed TC Combined] ...

Time range:

Start: 287478.0 2211 07:51:18.0 05/25/2022  
 End: 302581.0 2211 12:03:01.0 05/25/2022  
 Number of samples: 15,104

Stat	Roll	Pitch	Heading/		2D	3D
Std:	0.0436	0.0442	0.0515	0.0621	0.0736	
Rms:	0.1568	0.1575	0.2392	0.2223	0.3266	
Avg:	0.1507	0.1512	0.2336	0.2135	0.3181	
Max:	0.2264	0.2347	0.4644	0.3260	0.5093	
Min:	0.0557	0.0565	0.0869	0.0793	0.1328	

brestr\_mnay\_25\_second\_20220525\_075048 [Smoothed TC Combined] ...

Time range:

Start: 287478.0 2211 07:51:18.0 05/25/2022  
 End: 302581.0 2211 12:03:01.0 05/25/2022  
 Number of samples: 15,104

Stat	East	North	Height	2D	3D
Std:	0.00086	0.00110	0.0020	0.0012	0.0023
Rms:	0.00729	0.00849	0.0136	0.0112	0.0176
Avg:	0.00724	0.00842	0.0134	0.0111	0.0175
Max:	0.00942	0.01154	0.0187	0.0148	0.0239
Min:	0.00492	0.00537	0.0086	0.0073	0.0115

Figure 4: Navigation accuracy of the flights in 25 may 2022

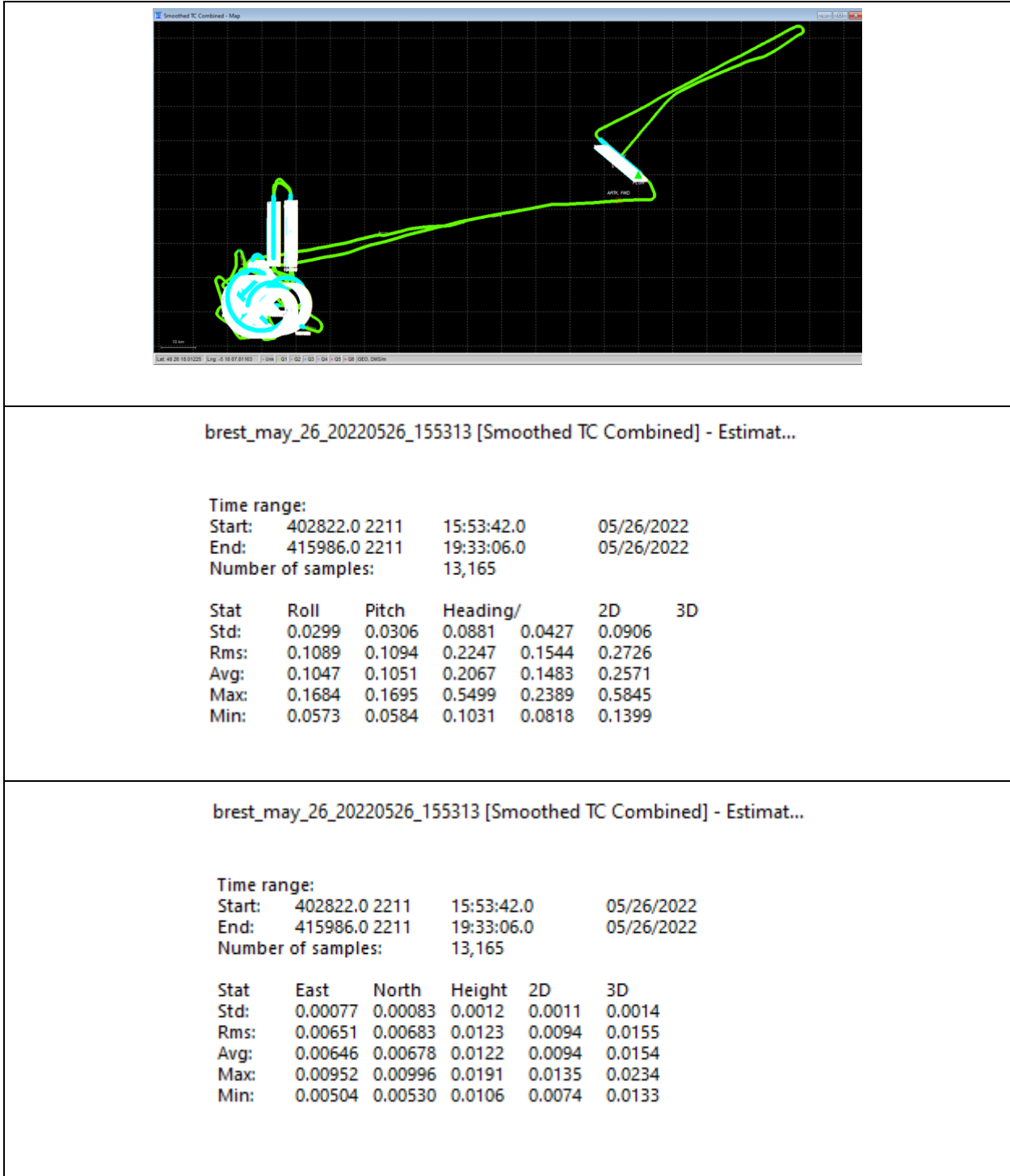


Figure 5: Navigation accuracy of the flights in 26 may 2022

In summary, the position accuracy is 1.5cm on average and 0.004 degrees in attitude all over the flights in all directions (3D).

## 3.2 Corner Reflectors

Next, we show the Impulse Response Function (IRF) of all corner reflectors placed within the radar swath. For each corner the resolution, phase stability and side-lobe-ratio are measured to verify that the system and processor work as expected and generate images close to theoretical radiometric response (accuracy and resolution). Although the corner analysis is valid locally, a visual inspection to verify the homogeneity of the images in terms of resolution and texture confirms that the response seen in the corners applies equally spatially throughout the focused images. This is done for all calibration tracks, for all squints and for all days, further confirming the temporal stability of the system. This visual inspection is done and presented in the next section after sigma0 calibration.

A good IRF indicates that the calibration of the SAR Images is sufficient in terms of antenna position, coming from the navigation system (shown before) and internal calibration (calibration pulses) and an external DEM (digital elevation model).

Below the table that describes the corner naming, size, orientation, and location [3]. Figure 6 shows the GoogleEarth overview of the corner's location on the field, showing a total of 6 corners, where every 2 corners point according to the squint orientation of the OSCAR antenna (-45, 0, 45 deg).

Figure 7 shows the IRFs SAR image zoom-in of every corner and corresponding IRF azimuth profile. Please note that for the IRF visualization of all the calibration images were focused with 2m azimuth resolution (but range resolution still coarse and limited to 11.5 m resolution in slant range due to transmitted bandwidth) to properly see all the responses of all 2 corners in all 3 squinted directions in all 4 calibration tracks, totaling 24 IRF responses. The final delivered Brest data are 11.5m slant range x 8m azimuth resolution [3] and therefore some corners might not be clearly visible depending on clutter surrounding them.

Nevertheless, three corners (CR-6 -45deg on day 17<sup>th</sup>, CR-5 Zero Doppler on day 25<sup>th</sup>, and CR-4 45 deg. squint on day 25<sup>th</sup>) are visible in the 11.5m (slant) x 8m (azimuth) resolution images. Figure 9, Figure 10 and Figure 11 show the azimuth and range IRF profile of these corners.

Please note that only well focused IRF are used in the calibration process. We attribute the variation of IRF quality due to the clutter in its surroundings. The fact that we do not see most of the corners at 8 m reso in azimuth and we do see basically all of them at 2m resolution indicates that clutter power plays a significant role, rather than data processing focusing quality.

Indeed it is proven that the interferometric phase can be more sensible than the IRF amplitude response data when unfocused data is present. Indeed, all well focused corners present a very stable phase behavior and that translates into a very stable ATI interferometric phase. The very stable flat ATI response over land [3] indicates that the images are well focused along the whole swath [9, 10].

Figure 8 shows the surroundings of the corners. It is made of high grass. The heights of the grass were modified around the corners and that varies depending on the location. Wind also might play a role in the final clutter affecting the IRF differently.

In summary, we use the standard peak estimation method [11, 12]. To derive the  $\sigma_0$  images. Only well focused corners, with a good SCR (signal clutter ratio) are used to derive the radiometric calibration parameters.

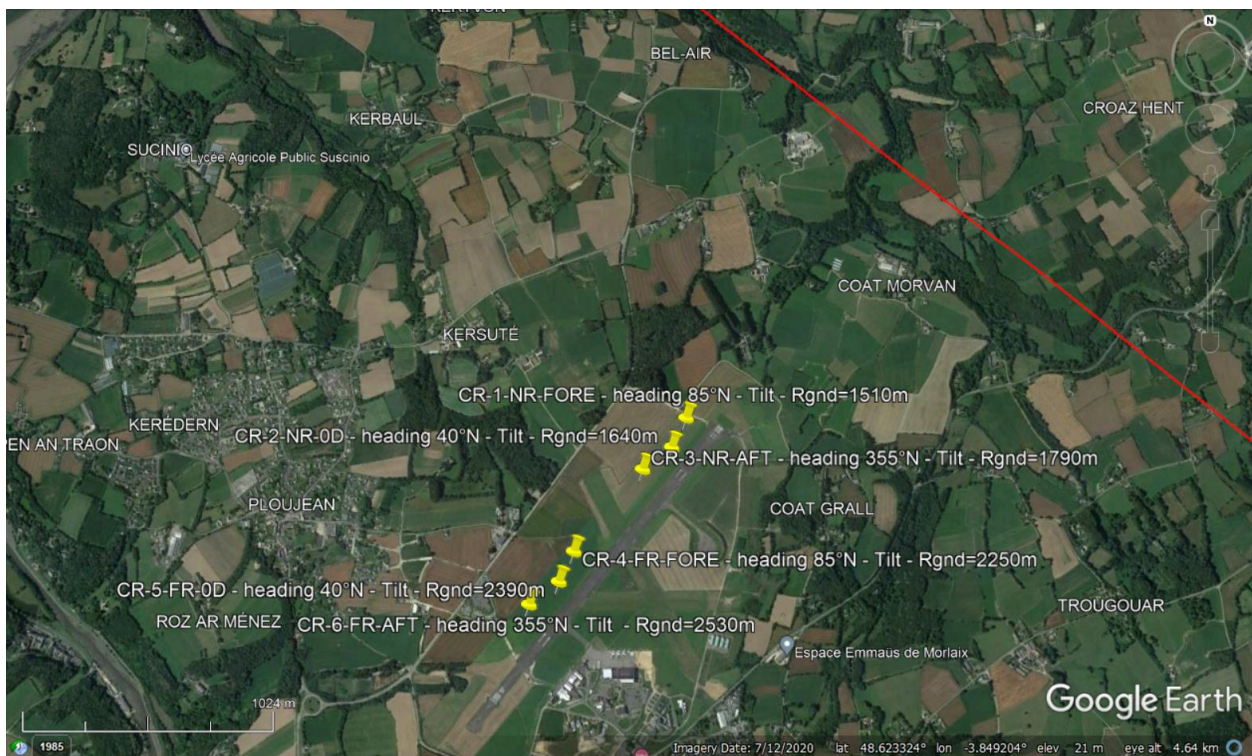
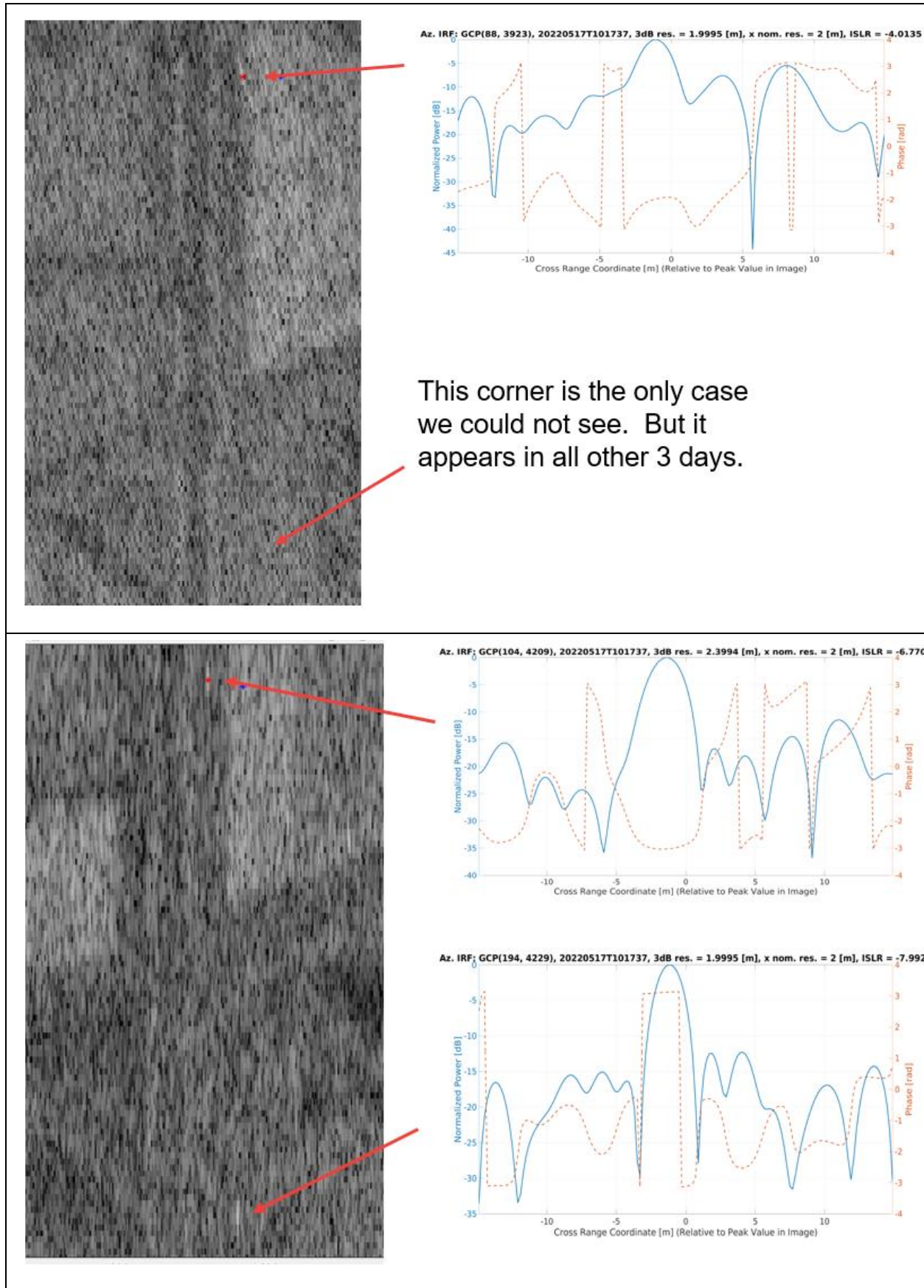


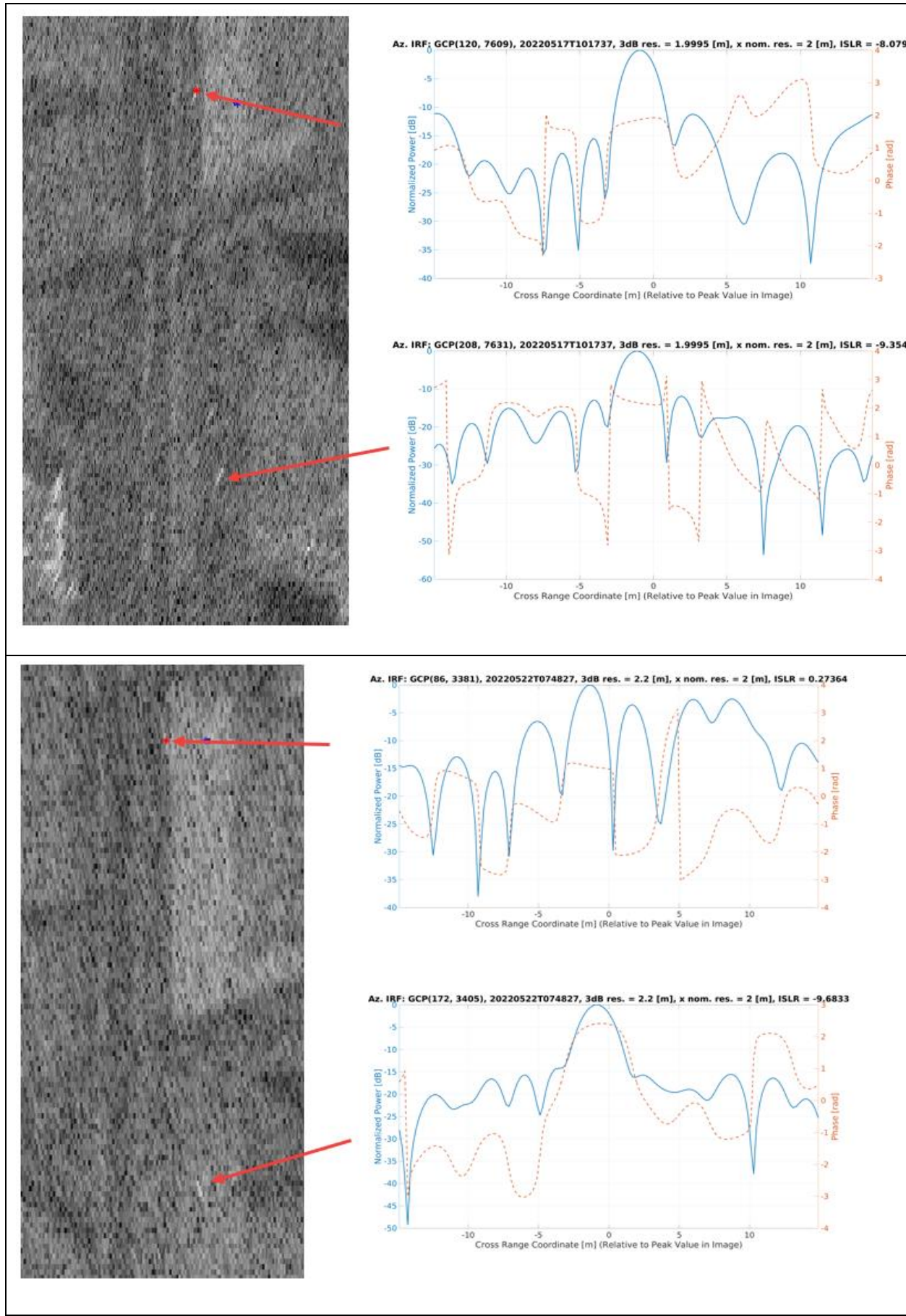
Figure 6: Position of the corner reflectors with naming.

Table 1: Corner reflectors field installation

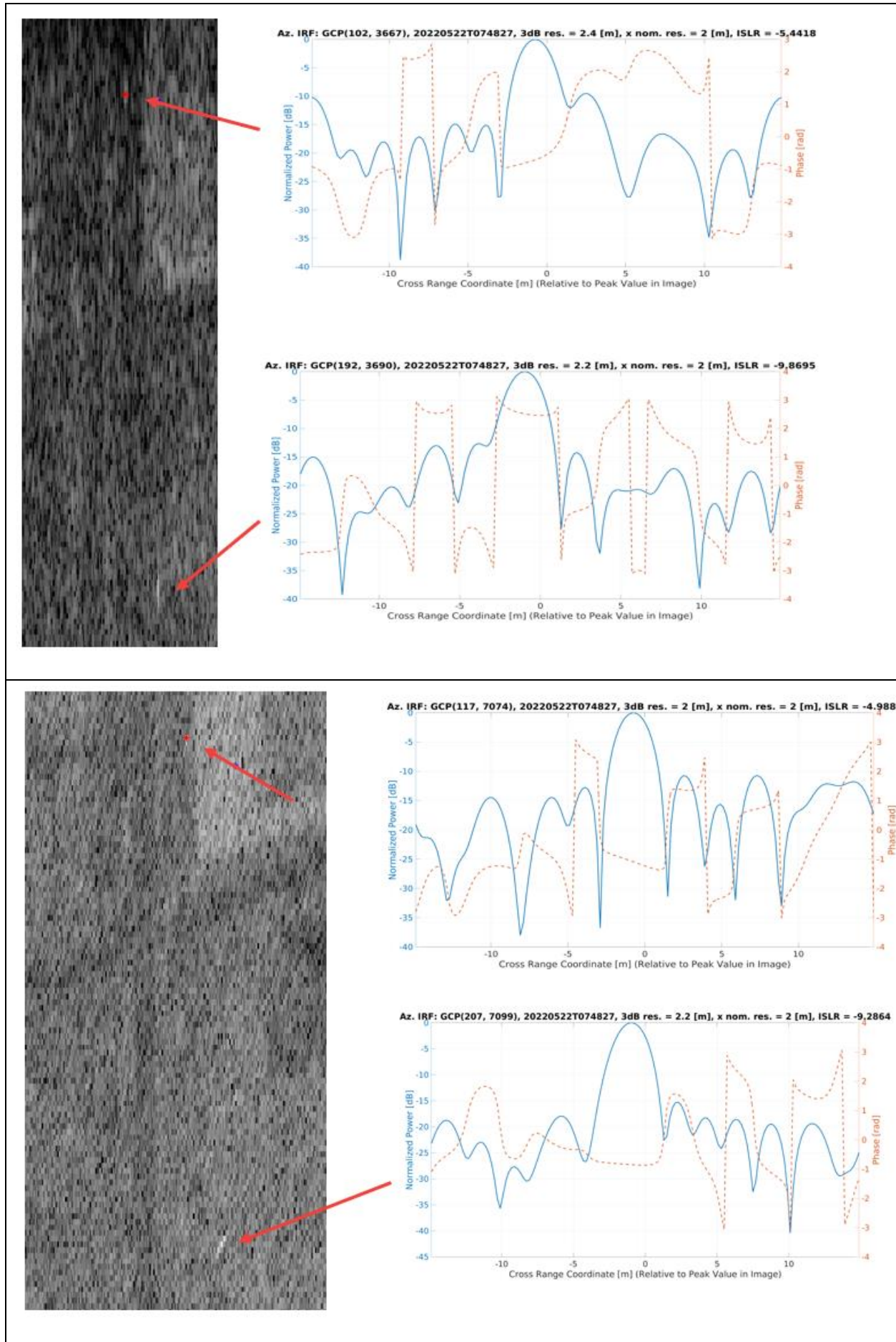
#	CR-1	CR-2	CR-3	CR-4	CR-5	CR-6
Type	Triang 40cm	Triang 40cm	Triang 40cm	Squar 30cm	Squar 30cm	Squar 30cm
Peak RCS [dBm2]	23.38	23.38	23.38	27.92	27.92	27.92
Azimuth pointing mag=geo	85°N	40°N	355°N	85°N	40°N	355°N
Local incidence angle	35.5°	28.7°	40.2°	46.7°	38.5°	50.0°
Baseplate tilt from horizon (front up +)	4.5°	11.3°	-0.2°	-6.7°	1.5°	-10.0°
GPS coordinates	48°36'31.00" N 3°48'40.00" W	48°36'27.00" N 3°48'43.00"W	48°36'24.00" N 3°48'49.00"W	48°36'13.00" N 3°49'3.00"W	48°36'9.00" N 3°49'6.00"W	48°36'6.00"N  3°49'12.00" W
Height (amsl)	80m	80m	80m	80m	80m	80m
Ground range from nominal track	1.51km	1.64km	1.79km	2.25km	2.39km	2.53km

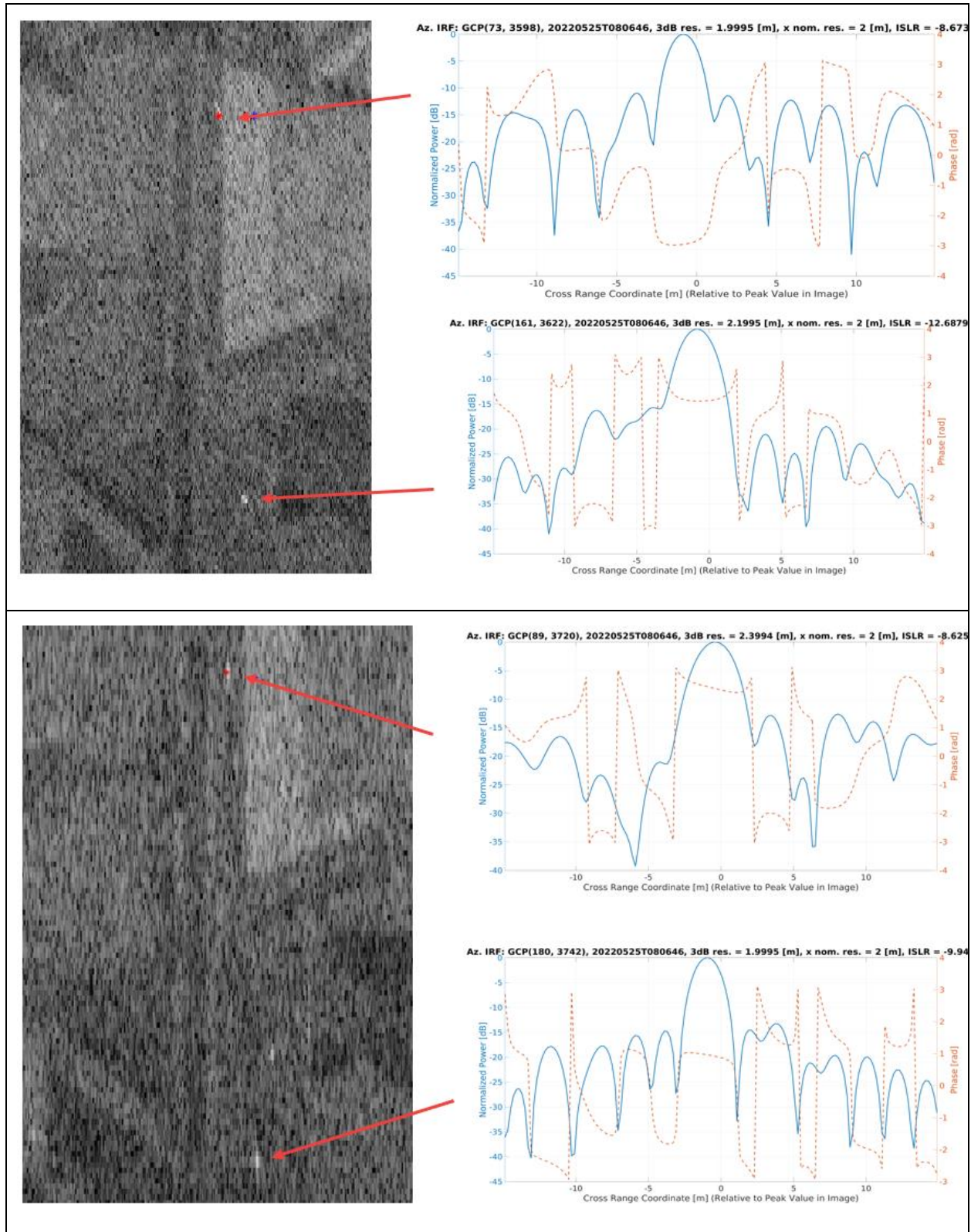




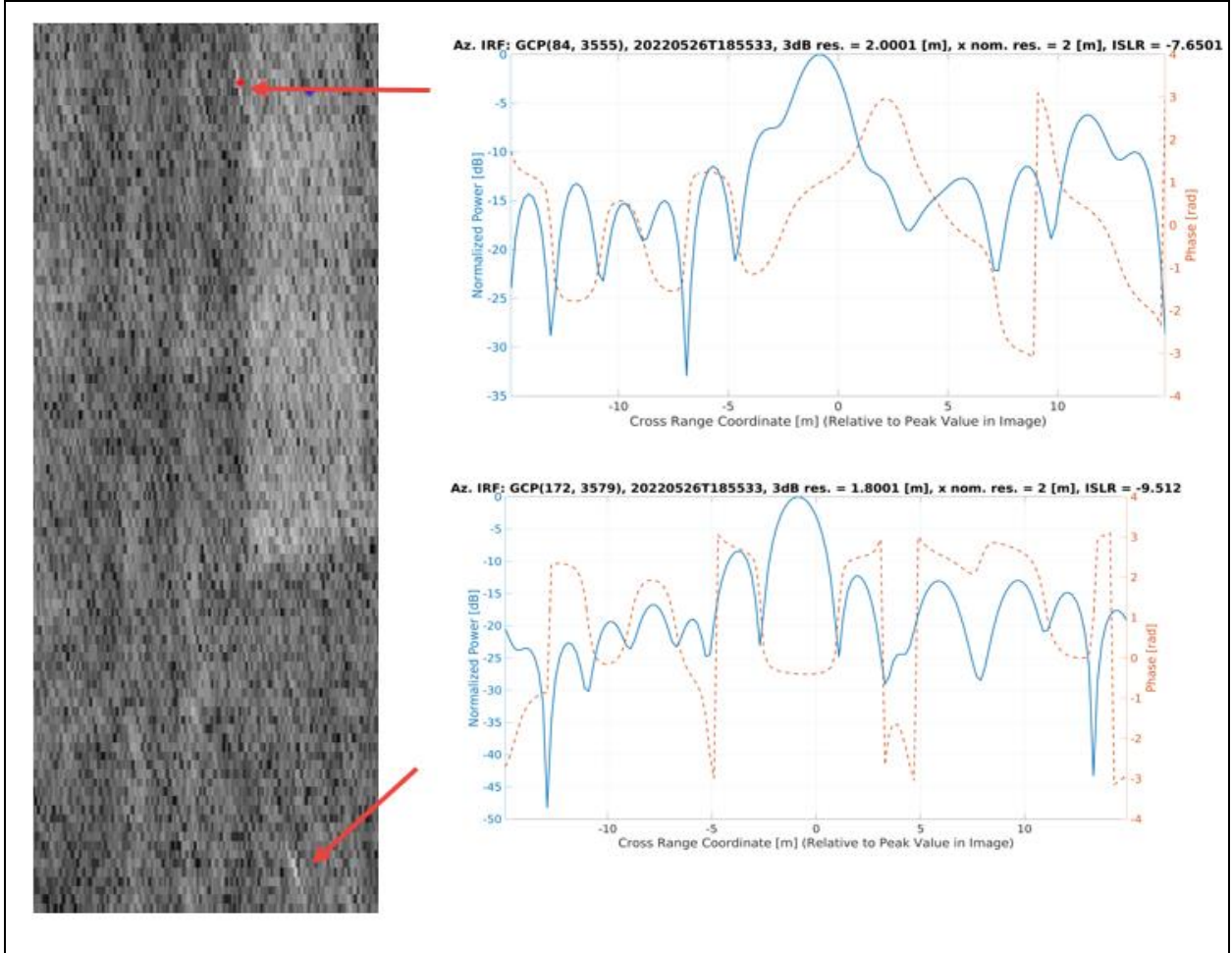
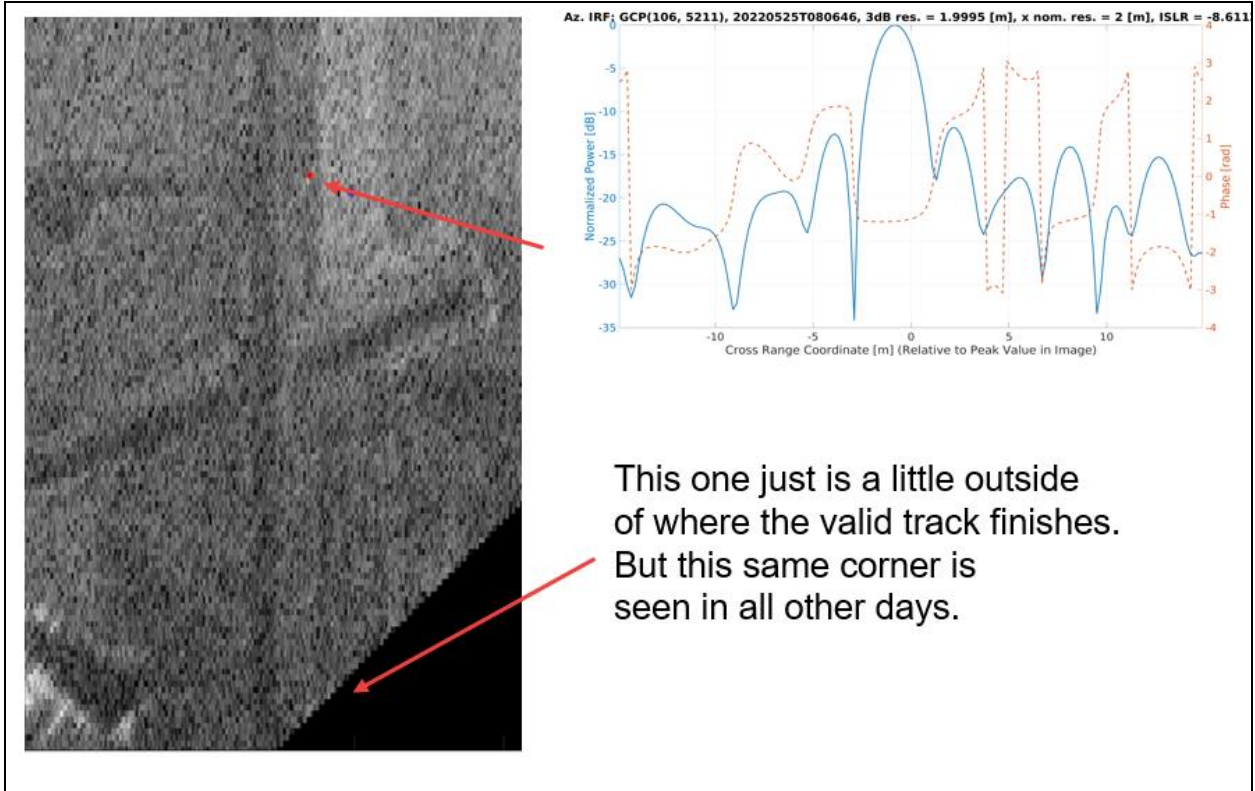












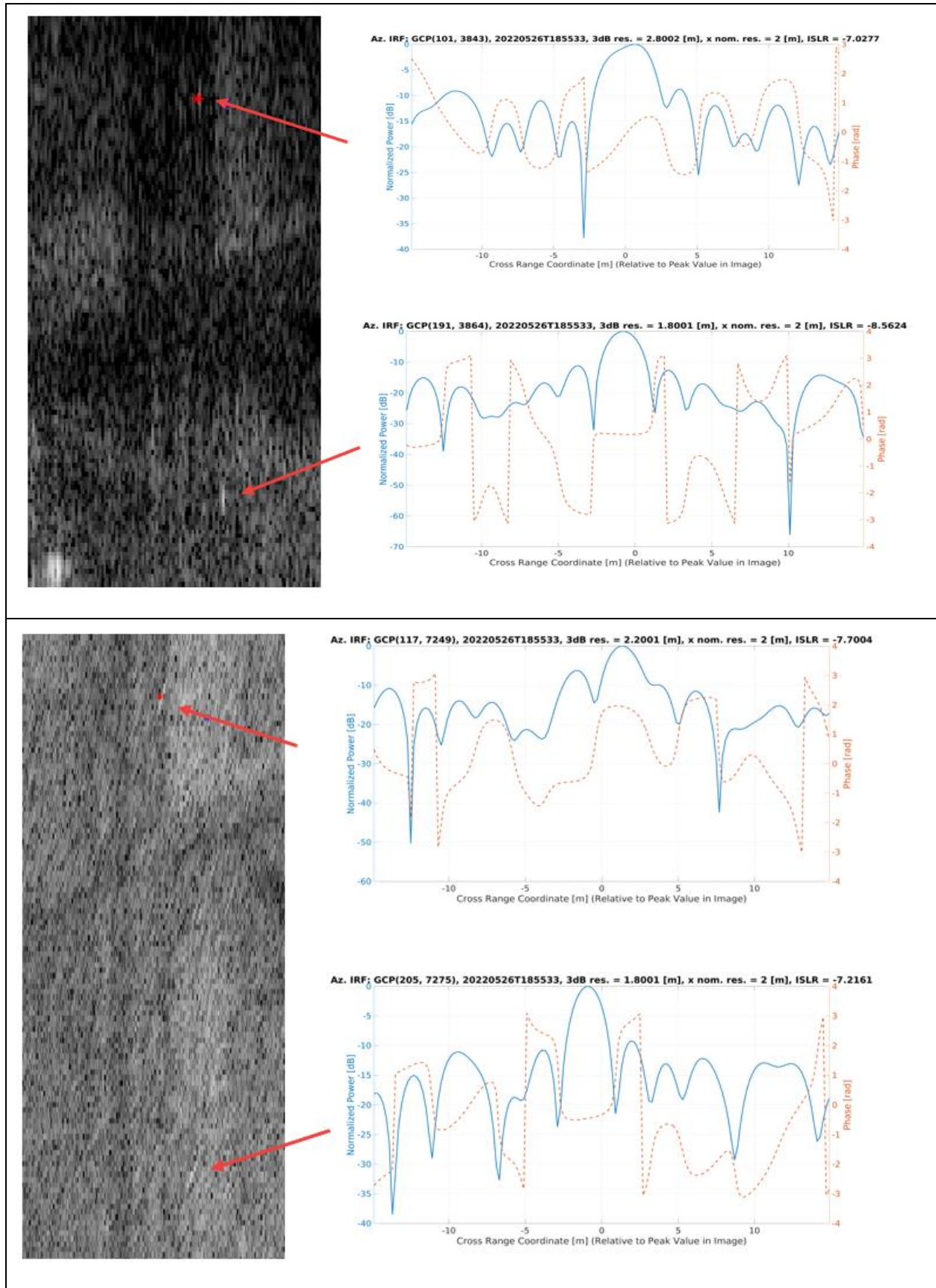


Figure 7: All 24 corner reflector IRFs from the calibration tracks (2m az. resolution images). From top to bottom: CR-1 and CR-4 , CR-2 and CR-5, CR-3 and CR-6 of acquisition 17 May; CR-1 and CR-4 , CR-2 and CR-5, CR-3 and CR-6 of acquisition 22 May; CR-1 and CR-4 , CR2 and CR-5, CR-3 and CR-6 of acquisition 25 May; CR-1 and CR-4 , CR-2 and CR-5, CR-3 and CR-6 of acquisition 26 May 2023 .





Figure 8: Example of surrounding of the corner reflectors..

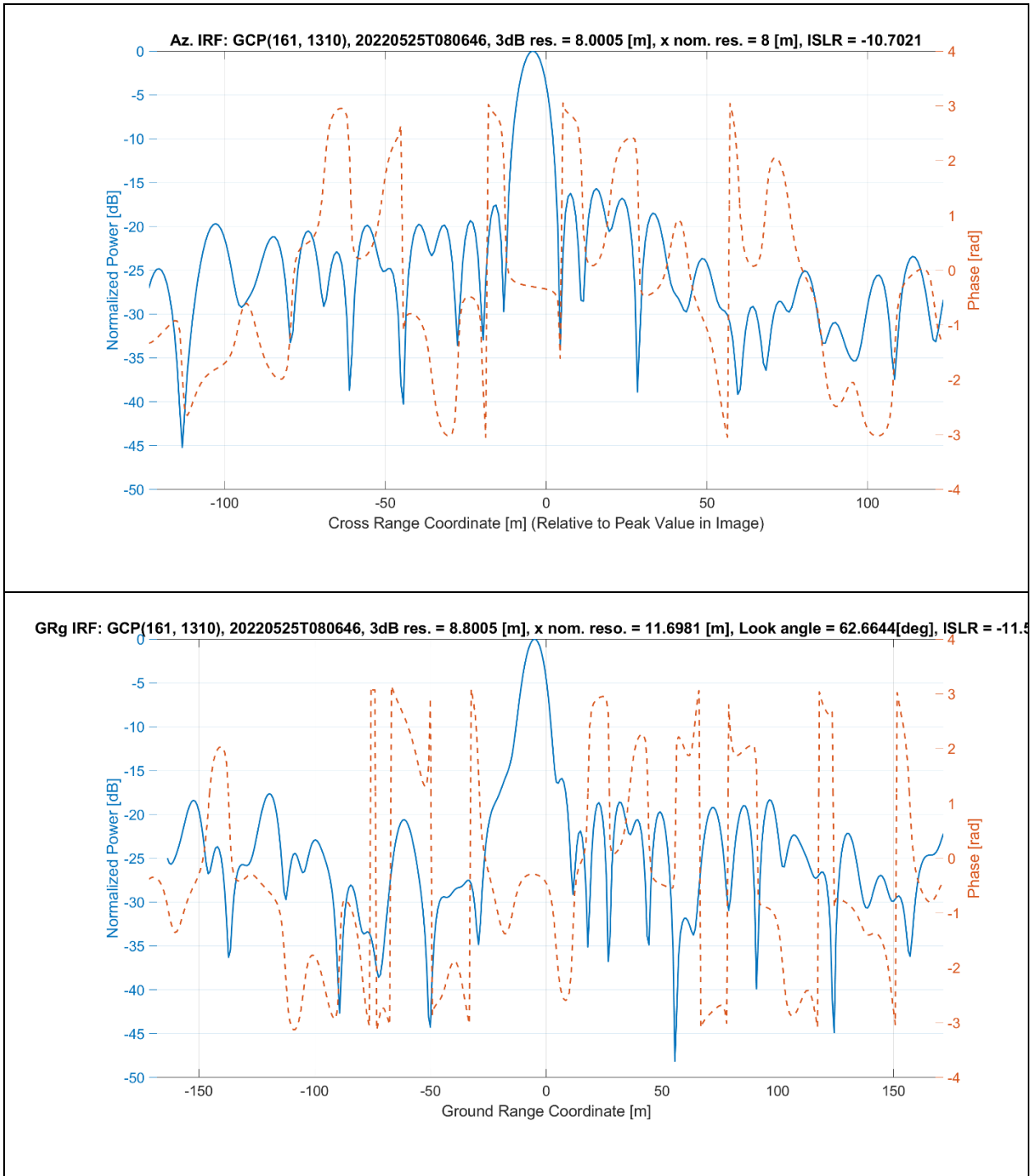


Figure 9: CR-4 IRF of a 11.5mx8m resolution SAR image of channel 33 (squint 45 deg) acquired in 25 may 2032

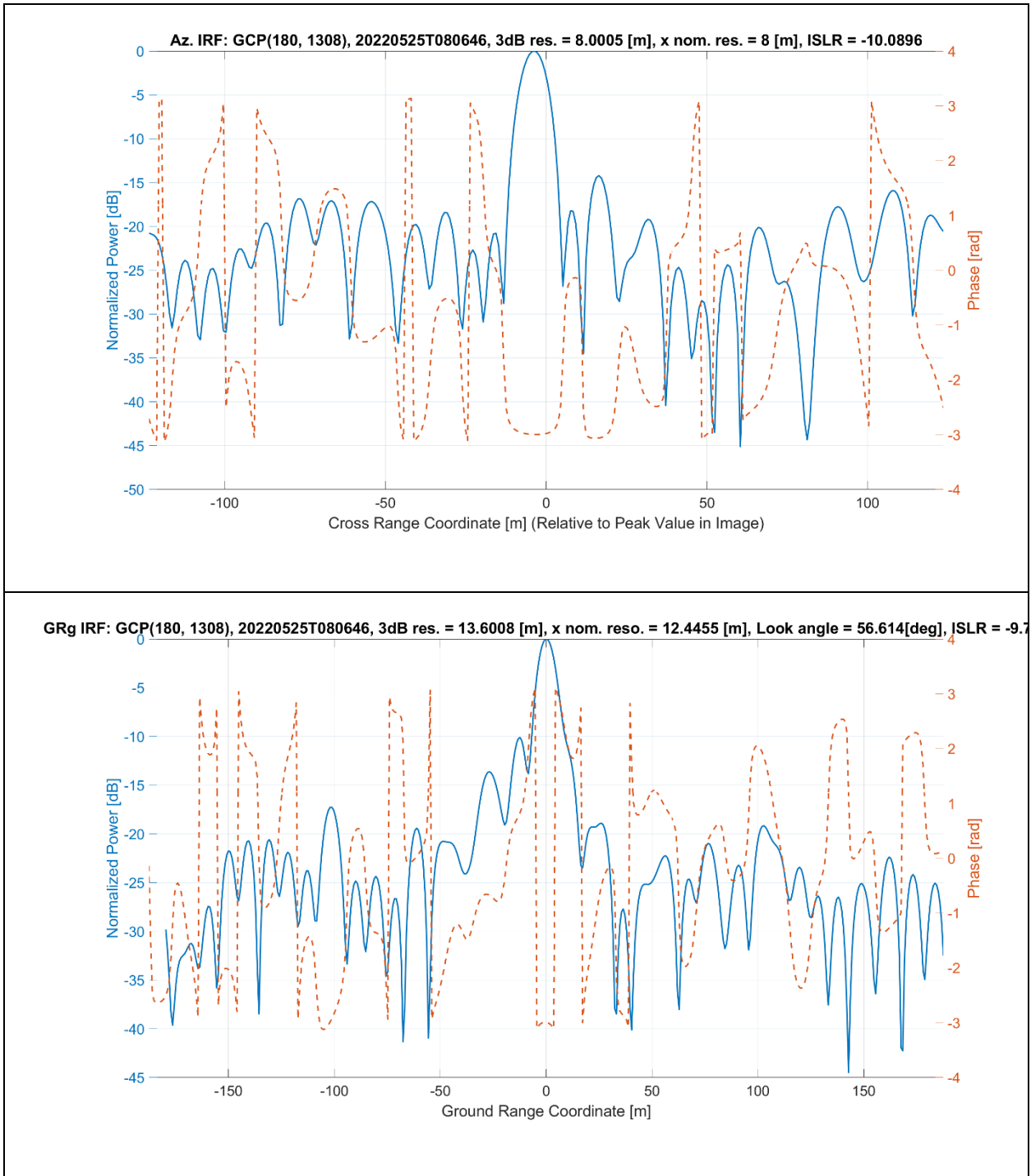


Figure 10: CR-5 IRF of a 11.5mx8mm resolution SAR image of channel 00 (squint 0 deg) acquired in 25 may 2032



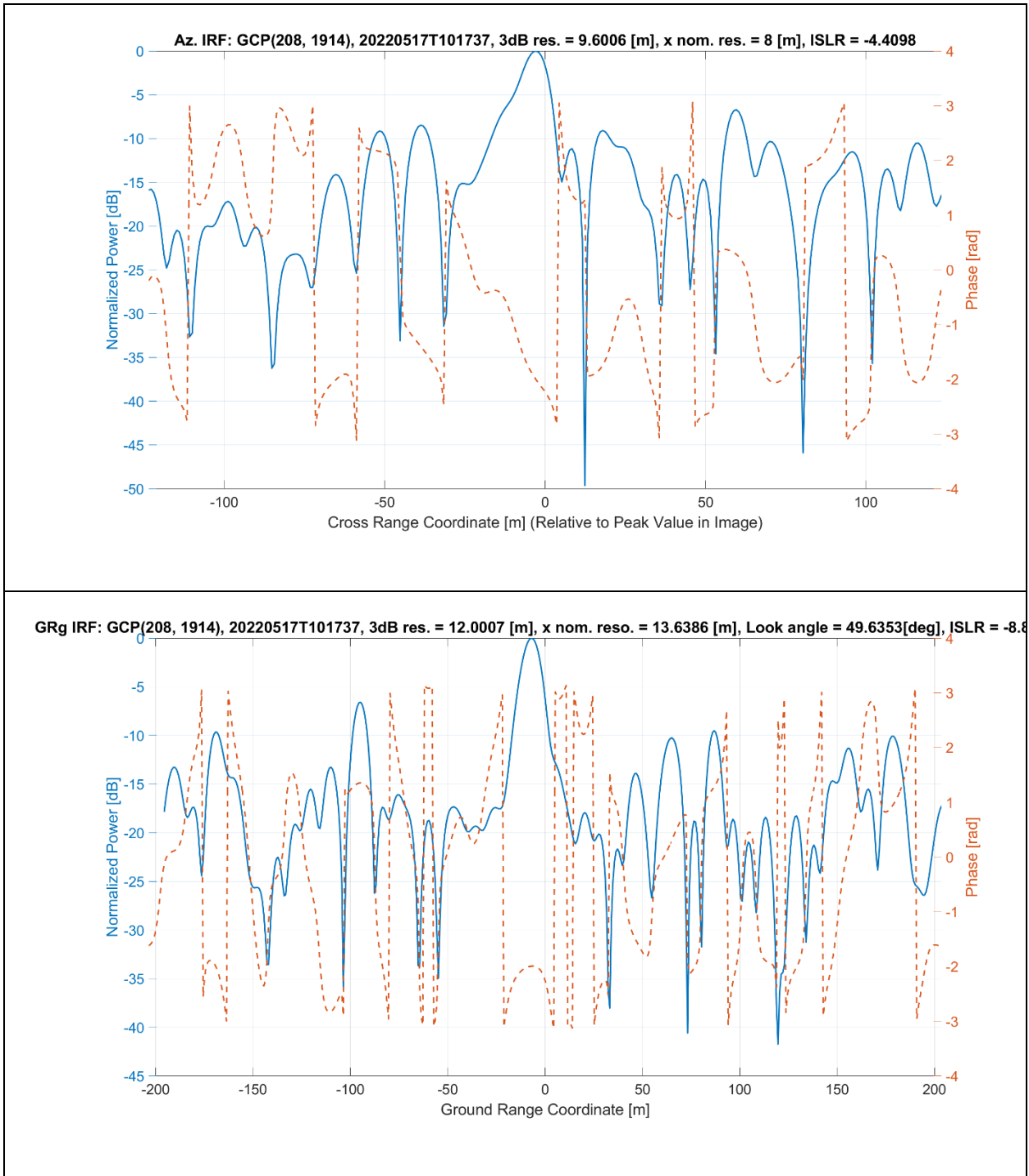


Figure 11: CR-6 IRF of a 11.5mx8mm resolution SAR image of channel 77 (squint -45 deg) acquired in 17 may 2032

### 3.3 Sigma0

Now we show that the sigma0 images are derived correctly from the clear visible IRF corners (as discussed in section 3.2). We derive the sigma0 values through the use of an antenna pattern diagram, external DEM and the knowledge of a radiometric offset derived from the RCS (radar cross section) of the corners. Only one single radiometric offset is applied to all the images showing a very stable behavior of the system. Through the corners of different calibration tracks and pointing we estimate that the difference between RCS of the corners and sigma0 values for the delivered 8m (az.) reso. images. The table below summarizes the 3 corners used to verify that the radiometric sigma0 mean and standard deviation is  $0.57 \pm 0.2$  dB.

*Table 2: Corners used for Calibration and Verification*

Track	Corner	Sigma 0 error (Observed – Theoretical)
20220517T101737	CR-6	0.3623
20220525T080646	CR-5	0.6382
20220525T080646	CR-4	0.7126
Mean and standard deviation		$0.57 \pm 0.2$ dB.

Inspecting visually all calibration images over the processed ground swath of 5km we see image textures over land with no dependency of topography, range or antenna motion, indicating a sufficient radiometric calibration in space and time. Figure 12 shows a simultaneous visualization of all 3 squinted images acquired on 17 may. There we see no dependency of the sigma 0 in range (besides the expected incidence angle dependency) or along azimuth. As expected because of the differences between the squints (-45, 0, 45) there are clear dependency of the sigma 0 with the antenna pointing . Nevertheless in areas where a more isotropic backscatter is expected the values are within a radiometric variation less than 1dB.

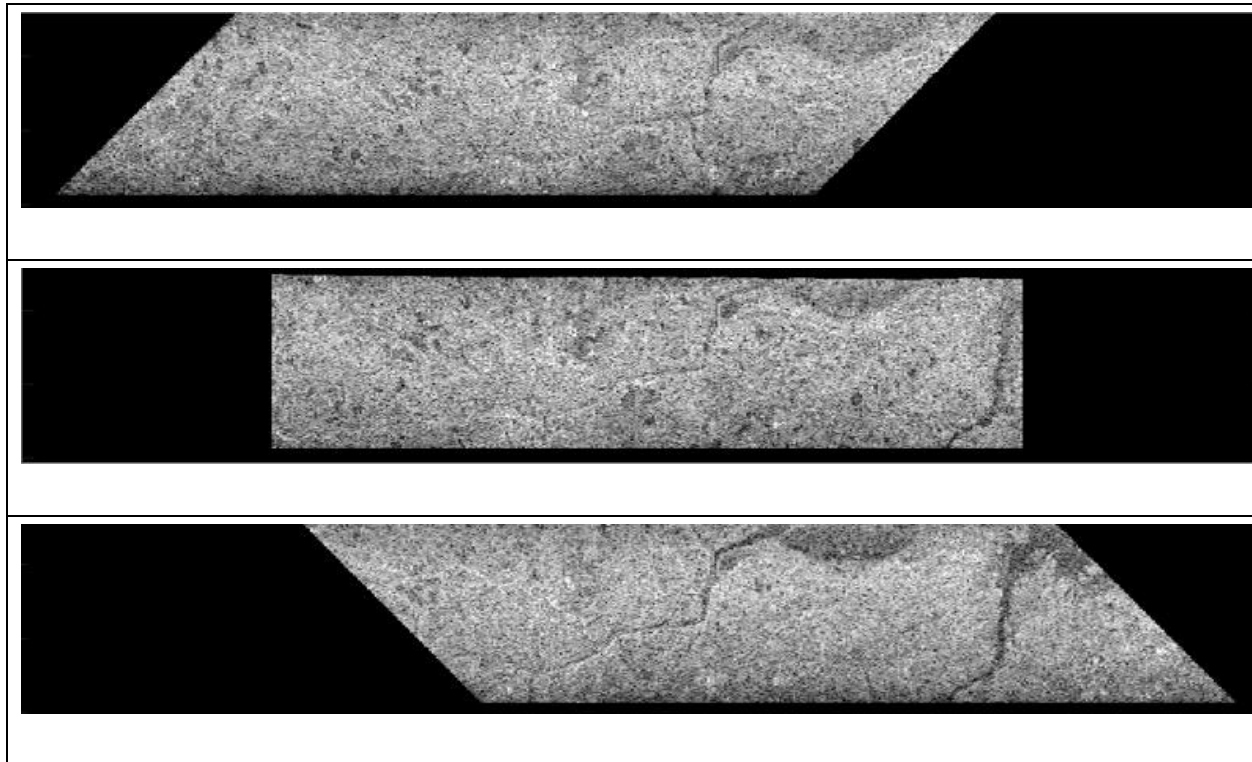


*Figure 12: Simultaneous visualization of sigma0 images (5km swath) from all 3 antennas (-45, 0, 45 degs) acquired in 17 May , 2022. The color scale goes from -30 to 5 dB. The images show no dependency of topography, range or antenna motion, indicating sufficient radiometric calibration.*

### 3.4 Geolocation

The correct geolocation of the images depends basically on the estimation of the range delay of the system. The along track timing of the data is guaranteed through the knowledge of the antenna position which is given by the navigation system and its accuracy is in the order of 2 centimeters as shown before. Furthermore, we used 30m resolution SRTM.

The estimation of the range delay is based on corner reflector response and the geographical position of the corners measured in the field. Note that field measurements are made by a handheld GPS and have accuracy with 5 to 10m. Only one range delay offset has been applied for the whole data set (all days, all squints).

Our absolute geolocation accuracy as here described is basically over flat areas. From the corner reflectors from different days and different squirts, we obtain absolute geolocation accuracy of 7.16m, i.e., within the resolution cell of the final images.

Relatively speaking, all the images are perfectly geolocated with one another due to the fact we use the same grid to back project that data of different channels.

It is important to note that for the absolute geographical position we also identify features in the images that could support that we correctly estimate the range delay and correctly geolocate the data, such as streets, runway, coast lines, river lines. Below is an example of a georeferenced SAR image overlaid with an optical image highlighting the well alignment with river.



Figure 13: Georeferenced SAR image of 17 May 2022 overlaid with standard optical image for access the geolocation accuracy.

### 3.5 Interferograms

The interferometric calibration of Brest data consists in correcting the systematic offset and trend of the phase measurements to enable the retrieval of velocity measurements. This is done using the calibration track to properly set the phase value in such way the velocity outcome is null m/s over land. This is the case since the nominal cross-track baseline is practically null meter in the OSCAR instrument and the DEM (SRTM 30m) has been taken into consideration during phase flattening operation. Also, The OSCAR consists of single-pass along track interferometer, where the baselines are well known up to the millimeter scale due to the accurately measured lever-arms, gimbal stabilization, and accurate navigation data (as shown in section 3.1), so no motion errors are expected. Therefore, the expected SAR phase is basically flat over land.

Below the nominal lever-arms of the OSCAR instrument flown in Brest followed by the coordinate system used.

Table 3: Nominal antenna lever arms used in Brest (mechanical reference to IMU phase center [m]).

Lever arms between IMU and antennas	AFT		FORE		0 - DOP
	M	S	M	S	
<b>Antenna</b>					
<b><math>\Delta X</math> [m]</b>	-0.1496	-0.1496	-0.1501	-0.1501	-0.1507
<b><math>\Delta Y</math> [m]</b>	-0.4387	-0.6087	+0.7331	+0.5631	0.0621
<b><math>\Delta Z</math> [m]</b>	-0.3642	-0.3642	-0.3642	-0.3642	-0.3653

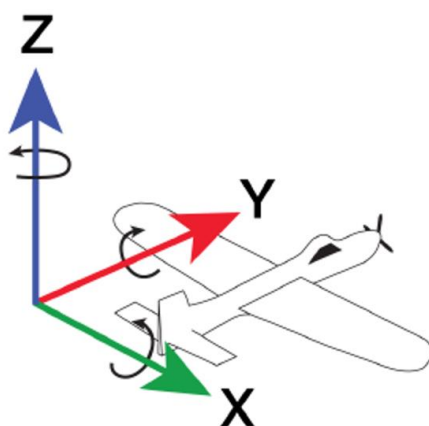


Figure 14: Reference system for the lever arms required by the OSCAR processor.

The interferograms generated with nominal lever-arms show a trend along range which is related to an unknown cross-track baseline component. This is an unknown cross-track baseline component can because of small uncertainty in the nominal lever-arms measurements. We use the phase trend to invert it into horizontal and vertical baseline components, which is then added to the nominal lever-arm values. Below are the final lever-arms used in the to obtain the final calibrated Brest interferograms. It's a difference of 0.1mm x -0.9 mm (hor x vert) for AFT channels (77x78) and of 0.4mm x -0.4mm for FOR channels (33x 34).

*Table 4: Calibrated antenna lever arms used in Brest (mechanical reference to IMU phase center [m]).*

Lever arms between IMU and antennas	AFT		FORE		0 - DOP
Antenna	M	S	M	S	
<b>ΔX [m]</b>	-0.1496	-0.1497	-0.1501	-0.1505	-0.1507
<b>ΔY [m]</b>	-0.4387	-0.6087	+0.7331	+0.5631	0.0621
<b>ΔZ [m]</b>	-0.3642	-0.3651	-0.3642	-0.3638	-0.3653

Figure 15 and Figure 16 shows the interferograms obtained with the nominal lever-arms and calibrated lever-arms, respectively, over the whole 5km swath of 3 different calibration tracks, namely day 17, 22, and 26 May 2022. The colors represent the profile from the interferometric data of each calibration track.



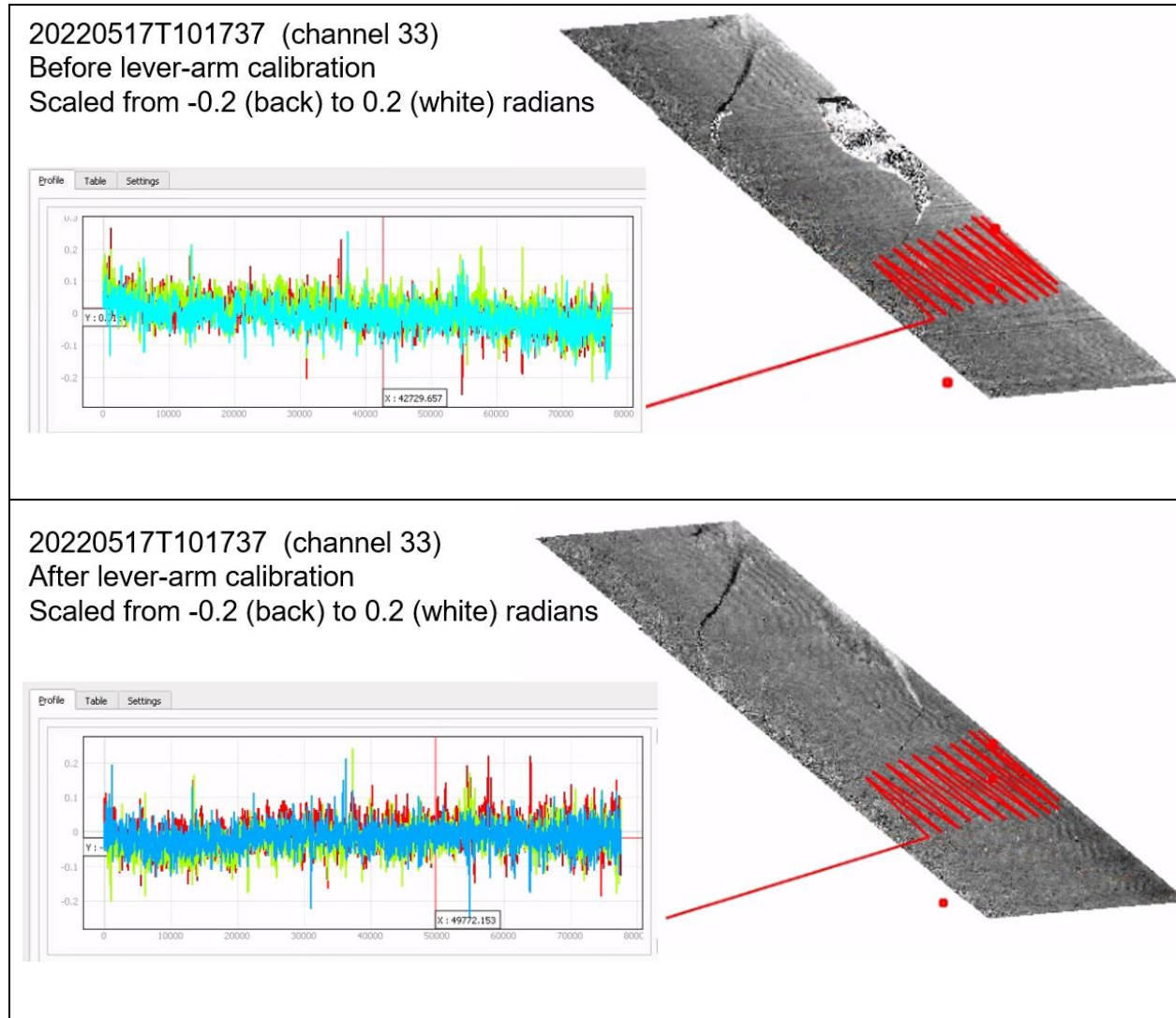


Figure 15: Uncalibrated (top) and calibrated (bottom) Brest (FORE) interferogram .

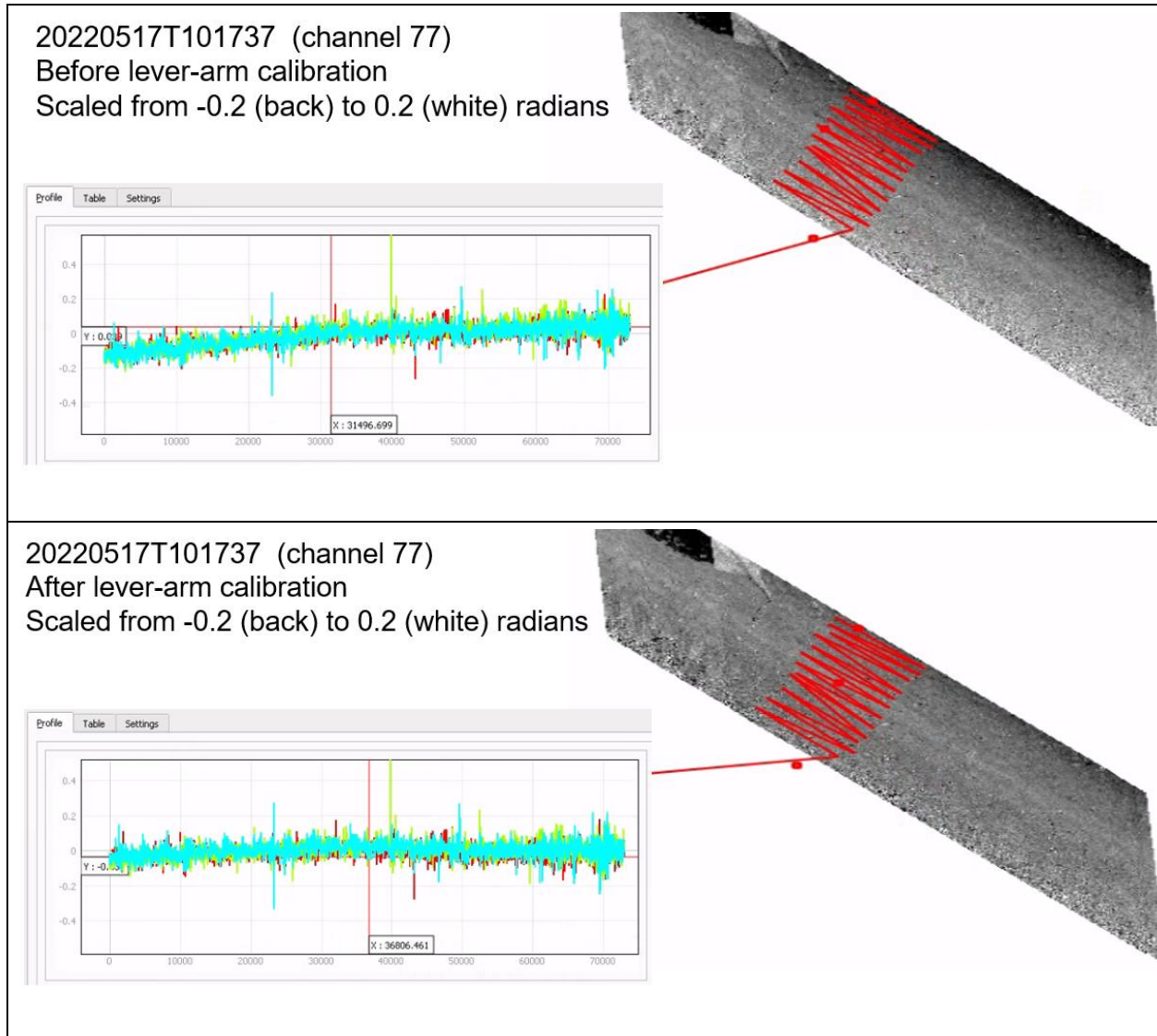


Figure 16: Uncalibrated (top) and calibrated (bottom) Brest (AFT) interferogram

## 4 Conclusions

This document provides information about how the data calibration is performed and verified. All the 3 aspects of the calibration related to the level 1 products are covered, namely, geometric, radiometric, and interferometric calibrations. The verification is done based on corner reflectors and on the intensity and interferometric images over land.

For the radiometric calibration, it shows that not all corner reflectors respond in the same way. Especially at 8m az. resolution some corners are not visible. Nevertheless, based on 3 corner that has a good SCR (signal clutter ratio) in the 8m az., reso, the statistic of radiometric accuracy is carried out, indicating an accuracy of  $< 0.5$  dB. Furthermore visual inspection of all images for all days shows that the radiometric behavior of the images are within the expectations and do not show any feature related to topography or motion.

For the geometric calibration, the visible corners are used as well optical imagery to verify that the geolocation of the data is within the resolution cell of 8 m.

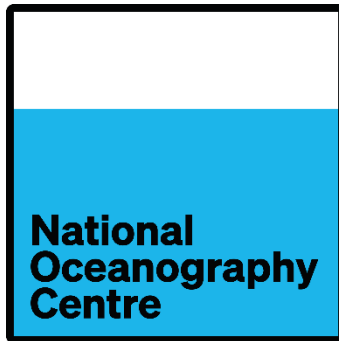
For the interferometric calibration, interferogram over land shows that the phase behaves stable along the flight. Fine adjustment in the lever arms and phase offset further sets the phase over land with basically average equal zero radians and standard deviation of 2.4 degrees after posting of 60m x 60m over ground (40 looks).

.

## 5 References

- [1] C. Gommenginger, et al, “SEASTAR: A Mission to Study Ocean Submesoscale Dynamics and Small-Scale Atmosphere-Ocean Processes in Coastal, Shelf and Polar Seas”, Proposal selected for Phase 0 of Earth Explorer 11 candidate mission, ESA-ESTEC.
- [2] Ocean Surface Current Airborne Radar Demonstrator (OSCAR) – Statement of Work, Appendix 1 to AO/1- 8309/15/NL/BJ.
- [3] MetaSensing Data Acquisition Report. MS-SeaSTARex-DAR\_v7.
- [4] MetaSensing NetCDF. File Format Description. MS-SAR-NetCDF-FFD\_v3.
- [5] L.M. H.Ulander, H. Hellsten, and G.Stenström, “Synthetic-aperture radar processing using fast factorized back-projection,” IEEE Trans. Aerosp. Electron. Syst., vol. 39, pp. 760–776, Jul. 2003.
- [6] K. A. C. de Macedo et al., "Long-Term Airborne DInSAR Measurements at X- and P-Bands: A Case Study on the Application of Surveying Geohazard Threats to Pipelines," in IEEE Journal of Selected Topics in Applied Earth Observations and Remote Sensing, vol. 5, no. 3, pp. 990-1005, June 2012, doi: 10.1109/JSTARS.2012.2187275.
- [7] A. Freeman, J. Curlander, Radiometric Correction and Calibration of SAR Images [Radiometric Correction and Calibration of SAR Images \(asprs.org\)](http://asprs.org).
- [8] Airbus. Calculation of beta naught and sigma naught for TerraSAR-X data. [1 \(intelligence-airbusds.com\)](http://intelligence-airbusds.com)
- [9] K. A. C. de Macedo, R. Scheiber and A. Moreira, "An autofocus approach for residual motion errors with application to airborne repeat-pass SAR interferometry," 2007 IEEE International Geoscience and Remote Sensing Symposium, Barcelona, Spain, 2007
- [10] K. A. C. de Macedo, C. Wimmer and J. R. Moreira, "Highly accurate and precise airborne single-pass interferometry for DEM generation over challenging terrain," 2014 IEEE Geoscience and Remote Sensing Symposium, Quebec City, QC, Canada, 2014.
- [11] A. L. Gray, P. W. Vachon, C. E. Livingstone and T. I. Lukowski, "Synthetic aperture radar calibration using reference reflectors," in IEEE Transactions on Geoscience and Remote Sensing, vol. 28, no. 3, pp. 374-383, May 1990, doi: 10.1109/36.54363.
- [12] I. M. H. Ulander, "Accuracy of using point targets for SAR calibration," in IEEE Transactions on Aerospace and Electronic Systems, vol. 27, no. 1, pp. 139-148, Jan. 1991, doi: 10.1109/7.68156.

**ANNEX H) ALGORITHM THEORETICAL  
BASELINE DOCUMENT: OSCAR LEVEL 2  
INVERSION**



ESA EXPRO 400017623/22/NL/IA

---

**EE11 SEASTAR SEASTARex  
D-4 Algorithm Theoretical Baseline Document  
OSCAR Level 2 Inversion**

---

V1.0

19 October 2023

The copyright of this document is jointly owned by the authors: The National Oceanography Centre and NOVELTIS.

It is supplied in confidence and shall not be used for any purpose other than that for which it is supplied and shall not in whole or in part be reproduced, copied, or communicated to any person without written permission from the owners.

**This Document is Commercial in Confidence**



Authors	Affiliation		
D. McCann A.C.H. Martin C. Gommenginger	NOC NOC, NOVELTIS NOC		
Approved	Affiliation	Signatures	Date
A.C.H. Martin	NOC, NOVELTIS		
ESA Acceptance			

Issue	Date	Comments
V1.0	19 October 2023	First version for review by ESA

## Contents

1. Introduction .....	1
2. OSCAR: instrument and inversion principle.....	2
2.1 The OSCAR instrument .....	2
2.2. Overview of the OSCAR L2 inversion and key characteristics .....	2
3. OSCAR processing chain.....	3
3.1 OSCAR data products .....	3
3.1.1 Level-0 (L0).....	3
3.1.2 Level-1 (L1).....	3
3.1.3 Level-2 (L2).....	4
3.2. L1 Processing.....	4
3.3. Calibration .....	5
3.3.1. Calibration of NRCS.....	5
3.3.2. Calibration of RSV / phase .....	5
4. L2 inversion.....	6
4.1. Simultaneous inversion.....	6
4.1.1. Noise characterisation.....	7
4.1.2. Cost Minimisation and Output .....	8
4.1.3 Ambiguity Removal .....	9
4.2. Sequential inversion .....	10
4.3. Geophysical Model Functions.....	11
4.3.1. GMF for Sigma0 ( $\sigma_0$ ) .....	11
4.3.2. GMF for Radial Surface Velocity (RSV).....	11
References .....	14

## List of Acronyms

ATBD	Algorithm Theoretical Baseline Document
EE11	Earth Explorer 11
ERVW	Earth Relative Vector Winds
MATER	Mission Assumptions and Technical Requirements
NRCS	Normalised Radar Cross Section
OSWV	Ocean Surface Vector Winds
RSV	Radial Surface Velocity (projected on the ocean surface)
TSCV	Total Surface Current Vectors
WASV	Wind-wave Artefact Surface Velocity

## 1. Introduction

This document is Deliverable D-4 of the Technical Assistance to Earth Explorer 11 SEASTAR Phase 0 campaign study (SEASTARex; ESA EXPRO 400017623/22/NL/IA) referring to the activities by NOC in WP4200 'OSCAR L2 processor Development'. This Technical Note presents the Algorithm Theoretical Baseline Document (ATBD) for the retrieval of Level 2 Primary products of the EE11 SeaSTAR mission concept from data recorded by the Ocean Surface Current Airborne Radar (OSCAR) demonstrator. The SeaSTAR Level 2 Primary products are Total Surface Current Vectors (TSCV) and the Ocean Surface Vector Winds (OSVW).

The content is arranged as follows:

- Section 2 provides a short overview of the OSCAR instrument and the inversion principle.
- Section 3 gives the details of the OSCAR data processing chain with the description of the data products, Level-1 processing chain and calibration.
- Section 4 gives details of the Level-2 (L2) inversion.

## 2. OSCAR: instrument and inversion principle

### 2.1 The OSCAR instrument

SeaSTAR is one of four satellite mission candidates currently under investigation in Phase 0 of the ESA Earth Explorer 11 programme. SeaSTAR proposes to measure small-scale ocean dynamics below 10 km at interfaces of the Earth System between the atmosphere, the ocean surface, the ocean interior, land and the cryosphere.

The Ocean Surface Current Airborne Radar (OSCAR) is a demonstration instrument for the SeaSTAR mission concept, built and operated by Metasensing BV. OSCAR is a unique 3-look, single-pass, Ku-band (13.5 GHz) ATI-SAR instrument and scatterometer, with two complimentary interferometric antenna pairs ('fore' and 'aft'), squinted at  $\pm 45^\circ$  from the aircraft centre-line, and a single 'zero-Doppler' antenna pointing broadside ('mid'). All channels pointed to the port (left) side of the aircraft and transmitted and received in vertical polarisation ('VV'). The instrument is mounted on a 3-axis gimbal (Fig. 1a) with a mounted Inertial Measurement Unit (IMU) paired with high-precision Global Navigation Satellite System (GNSS) receiver to accurately stabilize the instrument pointing relative to the aircraft and resolve the pointing geometry of the beams to a high precision. The SAR system and gimbal are mounted in a purpose-built radome for Ku-band and Ka-band frequencies and installed on a PA-31 Piper Navajo airframe.

### 2.2. Overview of the OSCAR L2 inversion and key characteristics

The SeaSTAR L2 retrieval algorithm retrieves TSCV and OSVW either simultaneously; in one step, without the need for ancillary information (following the work of Martin et al, 2018) or sequentially; in two steps, using ancillary wind data to estimate the WASV directly and therefore compute TSCV (following the work of Martin and Gommenginger, 2017).

The simultaneous inversion is based on a Bayesian approach inspired by L2 algorithms used in scatterometry to retrieve OSVW (Stoffelen, 1998; OSI SAF, 2022). A cost function is defined and subsequently minimised using least-square fitting to determine the wind and current vectors that are most consistent with the radar observables (NRCS and Radial Surface Velocity in different azimuth directions). As for scatterometry, the minimisation returns up to four solutions (Portabella, 2002) leading to an ambiguity problem. An ambiguity selection procedure is then applied to identify the most likely solution.

The action of the atmosphere on the moving ocean is known as the relative wind (OSVW), which accounts for the relative orientation of the wind vector and the current vector. Winds and currents are closely coupled at the ocean surface and it is a common observation that ocean surface roughness flattens (resp. raises) when currents flow with (resp. against) the wind.

The ocean roughness response to the relative wind will affect Bragg-type microwave scattering at moderate incidence angles. This phenomenon manifests frequently in SAR images as enhanced or reduced backscatter e.g., in regions of strong alternating tidal currents. Simultaneous retrieval of TSCV and OSVW makes it possible to account for this effect by correctly representing the response of the microwave signals to the ocean roughness generated by the relative wind. An Earth Relative Vector Wind (ERVW) can then be retrieved using the vectorial addition of OSVW and TSCV.

## 3. OSCAR processing chain

### 3.1 OSCAR data products

OSCAR data products are categorised into the following data processing Levels:

#### 3.1.1 Level-0 (L0)

Raw SAR data from OSCAR instrument channels. These are data processed by Metasensing BV.

#### 3.1.2 Level-1 (L1)

##### Level-1p (L1p)

Level-1 product as delivered by MetaSensing before pre-processing to add geometric auxiliary data (Incidence angle and beam squint).

##### Level-1a (L1a)

Single Look Complex (SLC) images providing amplitude and phase (fore-master VV; fore-slave VV; aft-master VV; aft-slave VV; broadside VV). L1a data is obtained after pre-processing to compute and add incidence angle and beam squint data fields to the L1a data files.

At a flight altitude of 3km and a 5km wide swath, OSCAR incidence angles are within the range of 20 to 72° for the fore and aft squinted channels and 15 to 62° for the broadside mid channel.

Antenna beam squint varies with incidence angle. Typical ranges for OSCAR data are 42–47° for the squinted fore channel, -47 to -44° for the aft squinted channel and -2 to 1.5° for the broadside mid channel, with all angles defined from 90° to the aircraft centreline.

##### Level-1b (L1b)

Intermediate data products after multilooking and radial surface velocity computation including Normalised Radar Cross Section, Interferograms ( $\phi$ , fore VV; aft VV), and Radial Surface Velocity (fore VV, aft, VV.); The default multilooking is a rolling window of 3 pixels.

$$NRCS_{lin} = |\overline{SLC_{Master} \cdot SLC_{Slave}^*}|$$

**Equation 1**

$$\phi = \text{angle}(\overline{SLC_{Master} \cdot SLC_{Slave}^*})$$

**Equation 2**

$$RSV = \frac{\phi}{\Delta t \cdot k_{EM} \cdot \sin \theta}$$

**Equation 3**

With the horizontal line indicating the rolling average, \* the complex conjugate,  $\Delta t$  the time lag between the Master and the Slave ( $\Delta t = \frac{B_{ATI}^{eff}}{V_{platform}}$  with a platform velocity V and an effective



Along-Track Interferometry Baseline  $B_{ATI}^{eff}$ ,  $k_{EM}$  the electromagnetic wavenumber and  $\theta$  the incidence angle.

### Level-1c (L1c)

Radiometrically and interferometrically calibrated L1b products after land-based and open ocean calibration curves have been applied.

$$NRCS_{dB}^{L1c} = NRCS_{dB}^{L1b} - NRCS_{calibration\ factor}$$

**Equation 4**

$$\phi^{L1c} = \phi^{L1b} - \phi_{calibration\ factor}$$

**Equation 5**

### 3.1.3 Level-2 (L2)

TSCV and OSVW are obtained on a coarsened L1c grid. The current recommended grid for OSCAR data is 200 x 200 m, coarsened using the mean values of NRCS and RSV across this area but is conditional of the presence of longer swell.

The Level-2 (L2) geophysical inversion algorithm presented in this document relates to the retrieval of L2 products from Level-1c (L1c) products as input.

The input observables to the L2 inversion come from L1c products (with calibration applied). Should L1c not be available, L1b observables can also be used as input.

For OSCAR, each L2 inversion takes 5 separate L1c input observables:

- Normalised Radar Cross Section fore  $\sigma_{obs,1}^0$
- Normalised Radar Cross Section aft  $\sigma_{obs,3}^0$
- Normalised Radar Cross Section broadside  $\sigma_{obs,2}^0$
- Radial Surface Velocity fore  $RSV_{obs,1}$
- Radial Surface Velocity aft  $RSV_{obs,3}$

Note that there is no Radial Surface Velocity measurement in the broadside look direction ( $RSV_{obs,2}$ ) as this channel does not function in an interferometric mode.

## 3.2. L1 Processing

The OSCAR L1 processing chain begins with L1a data supplied by Metasensing after pre-processing. The following steps are then followed to prepare the data for L2 retrieval:

- Pre-processing of L1p data files to compute Incidence Angle and Squint data fields and add these to the L1a data
- L1a to L1b processing, involving the computation of:
  - Multilooking (3 pixel rolling mean window as default)
  - Antenna azimuth from squint and aircraft heading
  - Baseline time lag

- Radial Surface Velocity (RSV)
- L1b to L1c processing, involving:
  - Any additional calibration (radiometric and/or interferometric)
  - Coarsening (using the mean value) of the L1c data to the required L2 processing ground resolution, e.g., 200 x 200m<sup>2</sup>

### 3.3. Calibration

#### 3.3.1. Calibration of NRCS

The observed NRCS must be calibrated before input to the L2 simultaneous inversion algorithm. This radiometric calibration is primarily performed using observations of radar reflectors of a known Radar Cross Section (RCS), here termed ‘absolute calibration’. A second method, ‘residual calibration’, is performed using the comparison of  $\sigma_{obs,i}^0$  over a range of look directions to  $\sigma_{GMF,i}^0$  for the given geophysical conditions to estimate the incidence angle dependent NRCS calibration curve for each beam direction.

##### *Residual radiometric calibration*

Additional relative radiometric calibration was performed using OSCAR data acquisitions over a geophysically homogenous open-ocean site over a range of azimuth look directions. Using the assumption of temporal and spatial homogeneity, the variations in  $\sigma_{obs,i}^0$  relative to  $\sigma_{GMF,i}^0$  can be assumed to be due to the residual, incidence angle dependent calibration factors for each beam. These incidence-angle dependent  $\sigma_i^0$  bias curves are applied to the L1b data to form the radiometrically calibrated L1c imagery.

#### 3.3.2. Calibration of RSV / phase

The primary interferometric calibration is performed by Metasensing (i.e., before L1a) using over-land OSCAR data to minimise the observed phase over land. Additional interferometric calibration can be performed at L1c via two methods:

##### *Residual over-land interferometric calibration*

Additional checks to the over-land calibration are performed by assessment of the observed phase (L1b interferograms) over areas that are known to be land. Averaging these data (or taking the median) with respect to incidence angle then provides incidence angle dependent curves of interferometric bias for the fore and aft channels than can be applied at L1c

##### *Residual over-ocean interferometric calibration*

Applying a similar method to the residual radiometric calibration, star pattern data over a geophysically homogenous area can be used to assess the residual incidence angle dependent phase bias. Grouping the observed interferogram data by incidence angle and look azimuth and fitting curves through the data points, a set of line equations are computed dependent on incidence angle and look azimuth. The mean (or ‘DC’) component of these curves, with dependence on incidence angle only, is then used to create incidence angle dependent curves of relative interferometric bias. It only gives information about a relative bias with incidence angle, and needs to be adjusted to an absolute bias using for example land.

## 4. L2 inversion

### 4.1. Simultaneous inversion

The simultaneous inversion seeks to find four unknowns, namely two components of the TSCV and two components of the OSVW. If more than four observations with Gaussian noise are available, these four unknowns can be estimated using a quadratic estimator as the objective function to determine TSCV and OSVW.

Based on Bayes' probability theorem, and following Stoffelen & Portabella (2006) and Martin et al. (2018), the Maximum Likelihood Estimator is represented by the cost function,  $J$ , defined as:

$$\begin{aligned}
 J(\hat{x}) &= J(u_{10}, c) \\
 &= \frac{1}{N_S + N_D} \sum_{i=1}^{N_S} \left( \frac{KuMod(u_{10}, \chi_i, p_i) - \sigma_{obs,i}^0}{\Delta\sigma_i^0} \right)^2 \\
 &\quad + \frac{1}{N_S + N_D} \sum_{i=1}^{N_D} \left( \frac{KuDop(u_{10}, \chi_i, p_i) + c_{||i} - RSV_{obs,i}}{\Delta RSV_i} \right)^2
 \end{aligned}$$

**Equation 6**

with

$\hat{x}$	the estimate of the state vector	
$\sigma_{obs,i}^0$	the observed Normalised Radar Cross Section (NRCS) in azimuth beam direction $i$	Linear units
$RSV_{obs,i}$	the observed Radial Surface Velocity (RSV) in azimuth beam direction $i$	Hz
$i$	the azimuth beam number	1 (fore squint), 3 (aft squint), 2 (broadside)
$KuMod$	the predicted NRCS, $\sigma_{GMF,i}^0$ , in azimuth beam $i$ obtained with the chosen Geophysical Model Function for Ku-band NRCS.	Linear units
$KuDop$	the predicted RSV, $RSV_{GMF,i}$ in azimuth beam $i$ obtained with the chosen Geophysical Model Function for Ku-band Wind-wave Artefact Surface Velocity.	Hz
$u_{10}$	the Ocean Surface Vector Wind (OSVW) at 10 metres height	m/s
$c$	the Total Surface Current Vector (TSCV)	m/s
$\Delta\sigma_i^0$	the uncertainty (standard deviation) on the observed NRCS, $\sigma_{obs,i}^0$ in azimuth beam direction $i$	linear

$\Delta RSV_i$	the uncertainty (standard deviation) on the observed RSV, $RSV_{obs,i}$ in azimuth beam direction $i$	Hz
$c_{  i}$	the component of the TSCV in azimuth beam $i$	m/s
$p_i$	the polarisation	e.g. VV
$\chi_i$	the azimuth look direction	degrees
$\theta$	the incidence angle	rad
$N_S$	the total number of observations for NRCS	
$N_D$	the total number of observations for RSV	

The cost function,  $J$ , is a unit-less function of 4 unknown variables ( $\overline{u}_{10}$ ,  $\vec{c}$ ). Minimising the cost function finds the values of TSCV ( $\vec{c}$ ) and OSVW ( $\overline{u}_{10}$ ) that best reduce the quadratic differences between the measured observables ( $\sigma_{obs,i}^0$ ,  $RSV_{obs,i}$ ) and the predicted quantities ( $\sigma_{GMF,i}^0$ ,  $RSV_{GMF,i}$ ).

The cost function can be customised to apply to instrument configurations with different numbers of azimuth beams and polarisations. Martin et al. (2018) presented this geophysical inversion scheme for a 2-look squinted ATI SAR configuration, with two squinted beams pointing  $\pm 45^\circ$  from broadside. In that instance, the number of azimuth look directions,  $N$ , was equal to 2, but depending on the configuration with single polarisation (VV) or dual-polarisation (VV, HH) for these two beams. For OSCAR, there is  $N_S = 3$  azimuth look directions for NRCS and  $N_D = 2$  azimuth directions for RSV as described in section 2.

#### 4.1.1. Noise characterisation

$\Delta\sigma_i^0$  and  $\Delta RSV_i$  determine the uncertainty (random noise) on the measurements of  $\sigma_{obs,i}^0$  and  $RSV_{obs,i}$  and contain contribution of both the noise performance of the instrument, the ‘geophysical noise’, i.e. residual contributions to the noise from geophysical phenomenon and GMF error.

##### Uncertainty on NRCS

The NRCS uncertainty  $\Delta\sigma_i^0$  is defined as  $\Delta\sigma^0 = k_p\sigma^0$  where  $k_p$  is the radiometric resolution.  $k_p$  can be estimated as a pure instrument noise, a combination of instrument noise and geophysical noise at a given spatial resolution and a combination of the previous elements with an error to the GMF. Given the fine spatial resolution, the geophysical noise can be negligible and is dominated either by instrument noise  $k_{p,inst}$  or error in the GMF.  $k_{p,inst}$  can be estimated via a robust estimator of distribution (normalized interquartile range,  $IQR/1.349$ ) of  $\sigma_{obs}^0$  from open-ocean data over a geophysically homogenous area for the given resolution of the desired L2 product. Error on the GMF  $k_{p,GMF}$  is estimated via comparison of  $\sigma_{obs}^0$  with the predicted NRCS using NSCAT-4DS using the same open-ocean data, with a standard root mean square error, so that:

$$k_{p,GMF} = \sqrt{\sum (\sigma_{obs}^0 - KuMod)^2}$$

Equation 7

$$k_{p,inst} = \frac{IQR(\sigma_{obs}^0)}{1.349} / \langle \sigma_{obs}^0 \rangle$$

Equation 8

As computed, the GMF error contain the instrumental and geophysical noise but averaged on a wider spatial resolution (for OSCAR typically 1-10 km). These noise estimates typically vary with incidence angle. The maximum of this two noise contributions are compared (i.e., rather than simply added together), so that a reasonable estimate can be made. In the case of the SEASTARex 2022 Iroise Sea campaign,  $k_p$  was estimated to be equal to 20% and dominated by the instrumental noise.

### Uncertainty on RSV.

The RSV uncertainly  $\Delta RSV_{obs}$  is estimated using a similar approach to the NRCS uncertainty:

$$\Delta RSV_{inst} = \frac{IQR(RSV_{obs})}{1.349}$$

Equation 9

Using open-ocean OSCAR data from the SEASTARex campaign and in situ data from an Acoustic Doppler Current Profiler (ADCP) mooring to estimate the surface current, observed WASV can be estimated ( $RSV_{obs}(\theta, \chi) - c_{||\theta, \chi}$ ) and compared to the predicted WASV from a GMF:

$$\Delta RSV_{inst} = \frac{IQR(RSV_{obs})}{1.349}$$

Equation 10

$$WASV_{obs} = RSV_{obs}(\theta, \chi) - c_{||\theta, \chi}$$

Equation 11

The RSV GMF error is then estimated as:

$$\Delta RSV_{obs} = \frac{IQR(WASV_{obs} - KuDop)}{1.349}$$

Equation 12

The maximum of the two noise contributions is taken. In the case of the SEASTARex campaign,  $\Delta RSV_{obs}$  was estimated to be equal to 0.2 m s<sup>-1</sup>.

### 4.1.2. Cost Minimisation and Output

The cost function is a 4-dimensional function in OSVW and TSCV space with variations along dimensions:

- u zonal wind component (OSVW East-West)

- v meridional wind component (OSVW North-South)
- cu zonal current component (TSCV East-West)
- cv meridional current component (TSCV North-South)

The cost function minimisation is performed using non-linear least-square fitting (e.g. Trust Region Reflective algorithm, Nelder–Mead technique, Levenberg–Marquardt). As for scatterometry, the cost function presents up to four local minima. Depending on instrument configuration (number of beams, polarisation capability), instrument performance ( $\Delta\sigma^0$ ,  $\Delta df$ ) and the wind direction relative to the instrument look directions, the local minima can be more or less well defined and separated (Figure 2; Martin et al., 2018). Further ambiguity removal needs to be applied to identify the most likely solution.

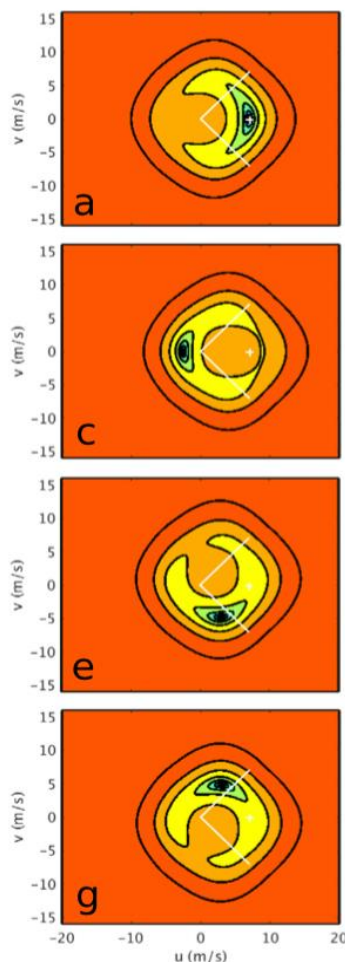


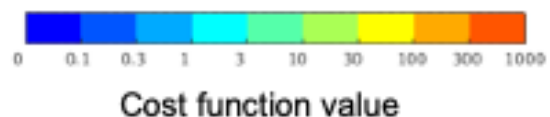
Figure 2: Illustration of the cost function for a single-polarisation instrument (VV) with two squinted beams  $\pm 45^\circ$  in fore and aft (white lines).

The 4D cost function is mapped in 2D OSVW space against zonal ( $u$ ) and meridional ( $v$ ) wind components for given values of TSCV. The four panels show slices for TSCV values of  $(cu, cv) = (0.6, 0.0), (3.2, 0.0), (1.7, 1.2)$  and  $(1.7, -1.2)$  m/s.

The true OSVW is 8 m/s, eastward (shown by the small white cross). The true TSCV is  $(0.6;0)$ .

Lower values of the cost function indicate the higher likelihood of the solution for the wind and current vector. The top panel correctly identifies a cost function minimum for the true values of OSVW and TSCV.

Ambiguity removal needs to be applied to identify the most likely solution.



### 4.1.3 Ambiguity Removal

The minimisation of the cost function returns four ambiguous solutions that need to be separated to identify the final solution.

Three ambiguity removal approaches can be considered to identify the final solution:

1. Deepest cost function minimum: in principle, the local minimum with the lowest cost value should identify the best solution. This method is very attractive as it depends solely on SeaSTAR data. However, the method is not 100% reliable and can give

erroneous results depending on the level of instrument noise ( $\Delta\sigma^0$ ,  $\Delta RSV$ ) and the wind direction relative to the instrument look directions.

2. Using a *priori* knowledge: in some cases, local minima can identify OSVW and TSCV conditions that are physically unlikely in given regions or conditions. In some cases, a *priori* knowledge of the likely magnitude or direction of the TSCV or the OSVW may be sufficient to nudge the inversion towards the right answer.
3. Using ancillary information: likewise, one could consider the use of ancillary information from another satellite or a model to budget the retrieval towards the right answer. This approach is not optimal since there are no reliable sources of information about TSCV and OSVW at the fine resolution considered by SeaSTAR.

For the purposes of the SEASTARex campaign, removal method number 3 was applied, using wind vector ( $\overline{u_{10}}$ ) data from the AROME operational wind model to select the ambiguity closest in  $\overline{u_{10}}$  space.

#### 4.2. Sequential inversion

A simplified computation of TSCV can be performed using direct computation of the GMF to find the predicted quantity  $RSV_{GMF,i}$ . This is implemented as a computation of retrieved TSCV only, using prior knowledge of geophysical parameters required to compute the GMFs (e.g., the wind vector  $u_{10}$ ). In this way, the WASV is computed directly using the chosen Ku band GMF and the TSCV component along the look direction  $i$  is defined as:

$$c_{||i} = RSV_{obs,i} - KuDop(u_{10}, \chi_i, \varphi_i, \theta_i, p_i)$$

**Equation 13**

where  $\varphi_i$  is the wind direction relative to the beam look direction and  $\theta_i$  is the incidence angle. The magnitude ( $|c|$ ) and direction ( $\psi$ ) of the TSCV are computed from the orthogonal combination of the TSCV components of the two squinted antenna look directions:

$$|c| = \sqrt{\frac{(c_{||1}^2 + c_{||3}^2) - 2(c_{||1}^2 * c_{||3}^2) \cos(\psi_{squint})}{\sin(\psi_{squint})^2}}$$

**Equation 14**

where  $\psi_{squint}$  is the range dependent effective angle at the surface between the fore and aft-looking antennas, and:

$$\psi = \begin{cases} \chi_1 - \cos^{-1}\left(\frac{c_{||1}}{|c|}\right) & \text{if } c_{||3} > c_{||1} \cos(\psi_{squint}) \\ \chi_1 \cos^{-1}\left(\frac{c_{||1}}{|c|}\right) & \text{otherwise} \end{cases}$$

**Equation 15**

In the case of OSCAR,  $\psi_{squint} = 90^\circ$  and so  $\cos(\psi_{squint}) = 0$ .



### 4.3. Geophysical Model Functions

#### 4.3.1. GMF for Sigma0 ( $\sigma^0$ )

The radar backscatter of the ocean ( $\sigma^0$ ) depends on the wind speed, wind direction relative to the radar azimuth look direction, incidence angle, radar wavelength (here Ku-band) and polarisation.

Assuming the instrument  $\sigma^0$  has been correctly calibrated, existing Geophysical Model Functions can be used.

For Ku-band NRCS, several GMFs are available in the literature, including NSCAT-2 (Wentz et al. 1999), Ku-2011 (Ricciardulli et al. 2015), NSCAT-4 (KNMI, 2014; Wang et al., 2019) and NSCAT-4DS (KNMI, 2019). Martin et al., (2018) used NSCAT-2 (Wentz et al. 1999) as the GMF for Ku-band NRCS (Figure 1a, c).

NSCAT-4 GMF was derived from the NSCAT-2 GMF and was recently superseded by NSCAT-4DS, which improved consistency for both wind Direction and Speed (hence the DS extension). The NSCAT-4DS GMF is used in most of the near-real time Ku-band scatterometer wind products produced by the OSI SAF (KNMI, 2019).

For SeaSTAR (at end of EE11 phase 0) and OSCAR, the baseline GMF for NRCS is NSCAT-4DS, which has the added advantage of being available as a python script ([https://scatterometer.knmi.nl/nscat\\_gmf/](https://scatterometer.knmi.nl/nscat_gmf/)).

#### 4.3.2. GMF for Radial Surface Velocity (RSV)

##### *Wind-wave Artefact Surface Velocity (WASV)*

The Doppler frequency shift (or RSV) sensed by microwave instruments is related to the velocity of the ocean surface in the radial line of sight of the radar relative to the platform.

Once corrected for platform motion, the Radial Surface Velocity consists of the sum of two parts: an oceanographic velocity that relates to the component of the TSCV in the radar line-of-sight projected in the slant range of the instrument; and a microwave scattering velocity caused by the motion of the surface scatterers responsible for the backscatter. The two parts appear explicitly in the second term in Equation 1.

The microwave scattering velocity is an artefact of the remote sensing process that does not contribute to the displacement of water. It is known as the Wind-wave Artefact Surface Velocity (WASV; Martin et al., 2016) or Wave Doppler. The WASV is a large systematic signal that needs to be removed from RSV measurements in each azimuth direction to retrieve correct TSCVs.

##### *WASV GMFs*

Developing GMFs of microwave Radial Surface Velocity is a relatively recent topic (~ 2012) compared to developing GMFs for NRCS (started in 1982). There are currently three main GMFs in the literature, including Mouche et al. (2012; known as C-Dop), Yurovsky et al. (2019) and Moiseev et al. (2021).

The C-Dop model (Mouche et al., 2012) was derived empirically from Envisat ASAR Doppler Centroid Anomaly data at C-band (5.4 GHz) measured over the global ocean. It is

parameterised as a function of wind speed, wind direction and incidence angle and is available at C-band (Figure 1b,d).

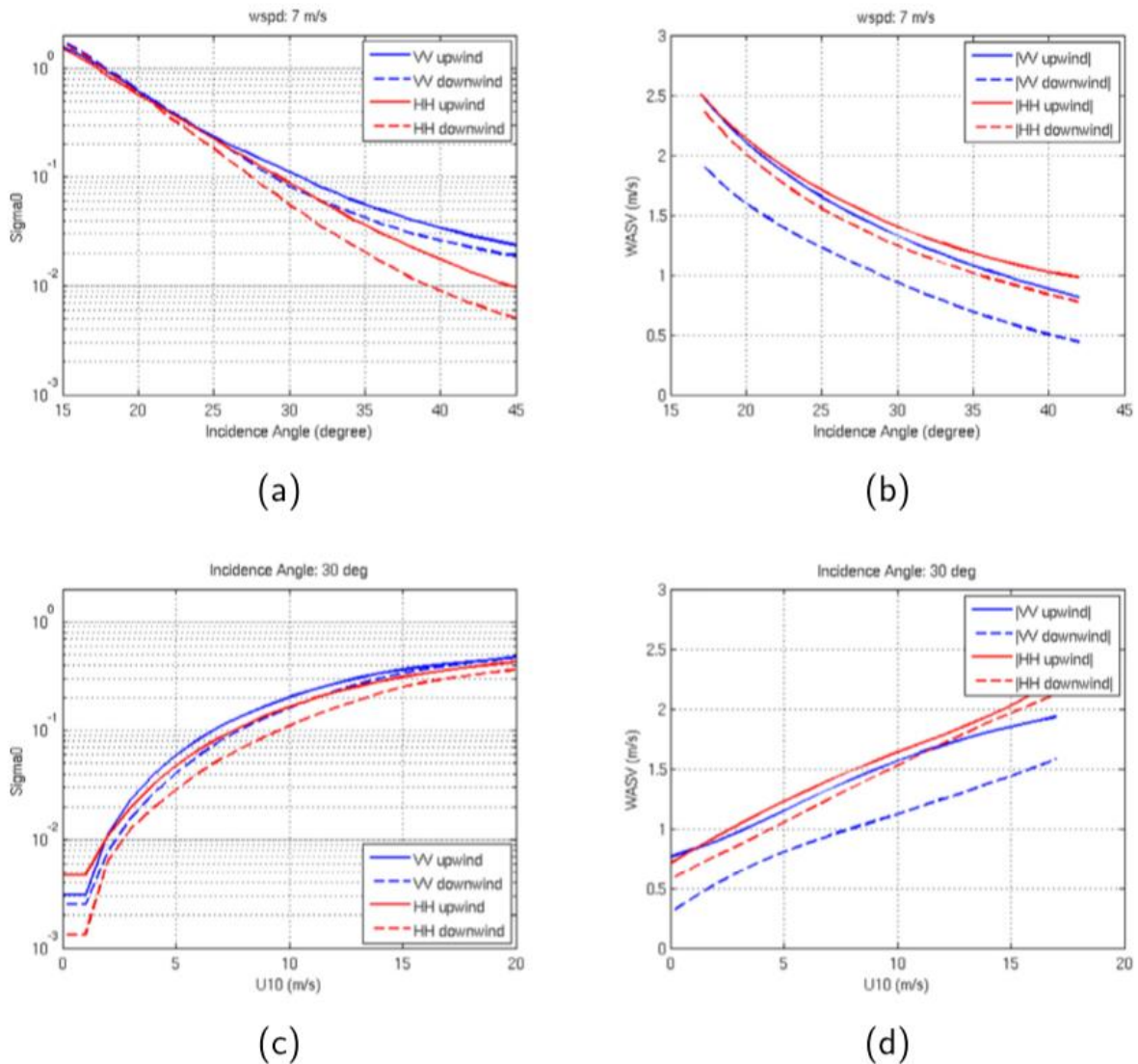


Figure 1: Geophysical Model Functions for (left) Ku-band  $\sigma^0$  from Wentz and Smith (1999) and (right) Wind-wave Artefact Surface Velocity (WASV) at Ku-band scaled from Mouche et al. (2012) C-Dop model. GMFs shown as function of: (top row) incidence angles for a wind speed of 7 m/s; (bottom row) wind speed for an incidence angle of 30°. Blue and red colours show VV and HH polarisation respectively. Plain and dashed lines show upwind and downwind respectively [see Figure 1 in Martin et al., 2018].

Yurovsky et al. (2019) is a semi-empirical model based on Ka-band Doppler scatterometer data (37.5 GHz) obtained from a sea platform in the Black Sea. It offers a parameterisation as a function of wind speed, wind direction and incidence angle, as well as a more advanced formulation that also accounts for sea state parameters like significant wave height and frequency of wind sea and swell. The Yurovsky et al. (2019) GMF is available at Ka-band.

Finally, Moiseev et al. (2021) was built from C-band Sentinel-1 Radial Velocity data. Like Yurovsky et al. (2019), it provides a simple parameterisation with wind vector and incidence

angle, as well as more advanced formulations with sea state dependencies. It was developed for C-band but, unlike Yurovsky et al. (2019), the algorithm is not publicly available.

#### *WASV GMFs at Ku-band*

There are currently no published Doppler GMFs for Ku-band. However, empirical evidence shows that the WASV is not strongly dependent on radar frequency.

Yurovsky et al. (2019) demonstrated the applicability and validity of its Ka-band formulation to numerous observations in the literature obtained at all radar frequencies from Ka-band to C-band. Recent work by Martin et al. (2022) with Sentinel-1 C-band Doppler data confirmed, using validation against HF radar data, that the Yurovsky et al. (2019) GMF is the most appropriate choice to retrieve unbiased ocean surface current from C-band SAR. The baseline GMF is Yurovsky et al. (2019) and Mouche et al. (2012).

## References

- KNMI, 2014. NSCAT-4 geophysical model function. Available from [http://projects.knmi.nl/scatterometer/nscat\\_gmf/](http://projects.knmi.nl/scatterometer/nscat_gmf/).
- KNMI, 2019. NSCAT-4DS geophysical model function. Available from [https://scatterometer.knmi.nl/nscat\\_gmf/](https://scatterometer.knmi.nl/nscat_gmf/).
- Martin, A.C.H., Gommenginger, C., 2017. Towards wide-swath high-resolution mapping of total ocean surface current vectors from space: airborne proof-of-concept and validation. *Remote Sens. Environ.* 197, 58–71. <http://dx.doi.org/10.1016/j.rse.2017.05.020>.
- Martin, A. C. H., C. P. Gommenginger, and Y. Quilfen, 2018. Simultaneous ocean surface current and wind vectors retrieval with squinted SAR interferometry: Geophysical inversion and performance assessment, *Remote Sensing of Environment*, <https://doi.org/10.1016/j.rse.2018.06.013>.
- Mouche, A., Chapron, B., 2015). Global C-Band Envisat, RADARSAT-2 and Sentinel-1 SAR measurements in copolarization and cross-polarization. *J. Geophys. Res. Oceans* 120, 7195–7207. <http://dx.doi.org/10.1002/2015JC011149>.
- OSI SAF, 2022. Algorithm Theoretical Basis Document for the scatterometer wind products, EUMETSAT Ocean and Sea Ice Satellite Application Facility (OSI SAF), Version 2.1, 12/10/2022. [https://scatterometer.knmi.nl/publications/pdf/osisaf\\_ss3\\_atbd.pdf](https://scatterometer.knmi.nl/publications/pdf/osisaf_ss3_atbd.pdf)
- Ricciardulli, L. and Wentz, F.J., 2015. A scatterometer geophysical model function for climate-quality winds: QuikSCAT Ku-2011. *Journal of Atmospheric and Oceanic Technology*, 32(10), pp.1829-1846. <https://doi.org/10.1175/JTECH-D-15-0008.1>
- Stoffelen, A., Portabella, M., 2006). On Bayesian scatterometer wind inversion. *IEEE Trans. Geosci. Remote Sens.* 44, 1523–1533. <http://dx.doi.org/10.1109/TGRS.2005.862502>.
- Wang, Z., Stoffelen, A., Zhang, B., He, Y., Lin, W. and Li, X., 2019. Inconsistencies in scatterometer wind products based on ASCAT and OSCAT-2 collocations. *Remote Sensing of Environment*, 225, 207-216. <https://doi.org/10.1016/j.rse.2019.03.005>.
- Wentz, F.J., Smith, D.K., 1999). A model function for the ocean-normalized radar cross section at 14 GHz derived from NSCAT observations. *J. Geophys. Res. Oceans* 104, 11499–11514. <http://dx.doi.org/10.1029/98JC02148>.
- Yurovsky, Y.Y., Kudryavtsev, V.N., Grodsky, S.A. & Chapron, B., 2019. Sea Surface Ka-Band Doppler Measurements: Analysis and Model Development. *Remote Sens.* 2019, 11, 839. <https://doi.org/10.3390/rs11070839>.

# **ANNEX I) MEASUREMENT ERRORS, CALIBRATION, AND SEA-SURFACE WIND INVERSION WITH PENWP**

## **SEASTARex:**

# **Measurement errors, calibration, and sea-surface wind inversion of the OSCAR normalized radar cross sections**

**AUTHORS: W. Lin, G. Grieco, M. Portabella**

Doc. No.: D7

Issue. No.: 1.0

Version: 1.0.0

Date: 16 February 2024

Document prepared under ESA Contract Number: 4000137991/22/NL/IA

## Table of contents

<b>1</b>	<b>Introduction.....</b>	<b>3</b>
1.1	Study objective .....	3
1.2	Document objective and organisation.....	4
1.3	Applicable and reference documents.....	4
<b>2</b>	<b>Datasets.....</b>	<b>4</b>
2.1	OSCAR data .....	4
2.2	ASCAT data.....	6
2.3	ECMWF data .....	7
2.4	SEASTARex flights.....	7
<b>3</b>	<b>Noise characterization.....</b>	<b>9</b>
3.1	Methodology.....	11
3.2	Results.....	12
<b>4</b>	<b>Ocean calibration.....</b>	<b>16</b>
4.1	Numerical Ocean Calibration.....	16
4.1.1	Methodology .....	16
4.1.2	Results .....	18
4.2	Alternative calibration approach.....	20
4.2.1	Methodology .....	20
4.2.2	Results .....	23
<b>5</b>	<b>Wind retrievals.....</b>	<b>27</b>
5.1	OSCAR wind retrievals at different WVC sizes.....	28
5.2	Intercomparison with ECMWF and ASCAT winds.....	33
<b>6</b>	<b>Summary and conclusions.....</b>	<b>36</b>
<b>7</b>	<b>REFERENCES .....</b>	<b>37</b>



## 1 INTRODUCTION

Within the SEASTARex project, the following tasks have been carried out by ICM:

- To support MetaSensing for the planning of the airborne acquisitions over sea (flight patterns and schedule) for the test flight in The Netherlands and for the open ocean “wind” campaign south of Brittany.
- To support MetaSensing in the development of the OSCAR L-1 processor, which should contain all the required input parameters to the Numerical Weather Prediction Satellite Application Facility (NWP SAF) Pencil-beam scatterometer Wind Processor (PenWP), i.e., Normalized Radar Cross Section (NRCS), viewing geometry, Kp, acquisition time/position, and flight parameters), as well as in the definition of the so-called wind vector cells (WVCs) and the NRCS integration/aggregation strategy.
- To adapt the PenWP scatterometer processor to produce wind retrievals from the OSCAR L-1 input.
- To perform a preliminary ocean (target) calibration of the OSCAR NRCS data, using collocated European Centre for Medium-range Weather Forecasts (ECMWF) wind output and Advanced Scatterometer onboard Metop (ASCAT) wind data as calibration reference.
- To perform an analysis of the L2 ocean surface vector winds derived from NRCS-only inversion for the OSCAR ocean flights.

This report summarizes the ICM R&D activities associated with the above tasks, with a particular focus on measurement Kp characterization, NRCS ocean calibration and wind retrievals based on the data acquired during the SEASTARex campaign near Brittany in May 2022. In particular, the analysis focuses on the May 22<sup>nd</sup> and 25<sup>th</sup> flights, for which the OSCAR calibration over land and the instrument performance over ocean were reported to be nominal [SEASTARex\_DAR, 2023] [MS-SEASTARex ExtCal, 2023].

### 1.1 Study objective

The aim of this study is to analyze the SEASTARex campaign data acquired by the Ocean Surface Current Airborne Radar (OSCAR), with a particular focus on noise characterization, calibration, and sea-surface wind inversion of the normalized radar cross sections.

## 1.2 Document objective and organisation

This document describes the methodologies used for the OSCAR NRCS Kp characterization and calibration as well as the main findings, and a preliminary analysis of the retrieved winds using the PenWP code adapted for OSCAR NRCS data ingestion. In Section 2, the different datasets used in this report, i.e., OSCAR, ASCAT, and ECMWF, are briefly described. In Section 3, the NRCS noise characterization methodologies and results are presented. Section 4 focuses on the NRCS ocean calibration, while Section 5 presents a preliminary analysis of the OSCAR-derived wind fields. Finally, the summary and conclusions can be found in Section 6.

## 1.3 Applicable and reference documents

[MS-SAR-NetCDF-FFD_v3]	MetaSensing NetCDF. File Format Description.
[MS-SAR Calibration, 2023]	Metasensing SAR Radiometric Calibration Procedure. Issue: 3.0. Date: 23 March 2023
[MS-SEASTARex ExtCal, 2023]	Analysis of External Calibration Results Including Baselines Errors. Issue: 5.0. Date: 9 October 2023.
[SEASTARex DAR, 2023]	D9.1: Data Acquisition Report. Issue: 7.0. Date: 31 January 2023.
[SEASTARex CIP, 2022]	Campaign Implementation Plan. Issue 2.0. Date: 27 June 2022.
[SEASTARex PenWP, 2024]	PenWP adaptation and user manual. Issue 1.0. Date: 21 February 2024.

## 2 DATASETS

This Section briefly describes the main datasets (OSCAR, ASCAT, and ECMWF) used in this study together with a short explanation of the SEASTARex flight campaign.

### 2.1 OSCAR data

The OSCAR SAR Single Look Complex (SLC) images are stored in NetCDF files, one for each of the three beams [MS-SAR-NetCDF-FFD\_v3]. The version of the files used in this study was released on March 1<sup>st</sup>, 2023, and data were downloaded from ESA-ESTEC ftp site. The mid

beam data are acquired on channel number 0, while the master and slave fore (aft) beam images are acquired on channels 33 and 34 (77 and 78), respectively. The files used in this study have a pixel spacing of 8 m in both azimuth and range directions. Each NetCDF file contains several fields, the most relevant of which for this study are reported in Table 1. For more details on the NetCDF file content, see [MS-SAR-NetCDF-FFD\_v3]. Also note that OSCAR images are radiometrically calibrated according to the procedure described in [MS-SAR Calibration].

*Table 1. List of relevant fields (left column) included in the NetCDF files and their corresponding description (right column).*

Field name	Description
OrbitLatitude	Latitude of the antenna
OrbitLongitude	Longitude of the antenna
OrbitHeight	Antenna height above WGS84
OrbitHeading	Heading of the airiplane relative to North
CrossRange	Dimension of the image along cross-range direction
GroundRange	Dimension of the image in ground range direction
LatImage	latitude of the pixels in the image
LonImage	longitude of the pixels in the image
SigmaImageSingleLookRealPart	Real part of the calibrated voltage signal of the master image
SigmaImageSingleLookImaginaryPart	Imaginary part of the calibrated voltage signal of the master image
SigmaImageSingleLookRealPartSlave	Real part of the calibrated voltage signal of the slave image
SigmaImageSingleLookImaginaryPartSlave	Imaginary part of the calibrated voltage signal of the slave image

The Normalized Radar Cross Section ( $\sigma_0$ ) in linear units used in the entire document is obtained using the following equation:

$$\sigma_0 = \Re[v]^2 + \Im[v]^2 \quad (1)$$

where,  $v$  stands for the echoed “voltage signal” and R and I for real and imaginary parts, respectively. For the sake of clarity,  $R[v]$  and  $I[v]$  correspond to “SigmaImageSingleLookRealPart” and “SigmaImageSingleLookImaginaryPart” in the case of a master image. Similarly, the NRCS can be computed for the master images. Moreover, an average of the master and slave can be computed following Equation 1.

## 2.2 ASCAT data

The OSI SAF Level 2 12.5-km Advanced Scatterometer onboard Metop-B (ASCAT-B) wind product, reprocessed with the Eumetsat NWP-SAF ASCAT Wind Data Processor (AWDP) version 3.3, for the month of May 2022, is used in this work. In particular, the ASCAT-B overpass of May 25<sup>th</sup>, as shown in Figure 1.

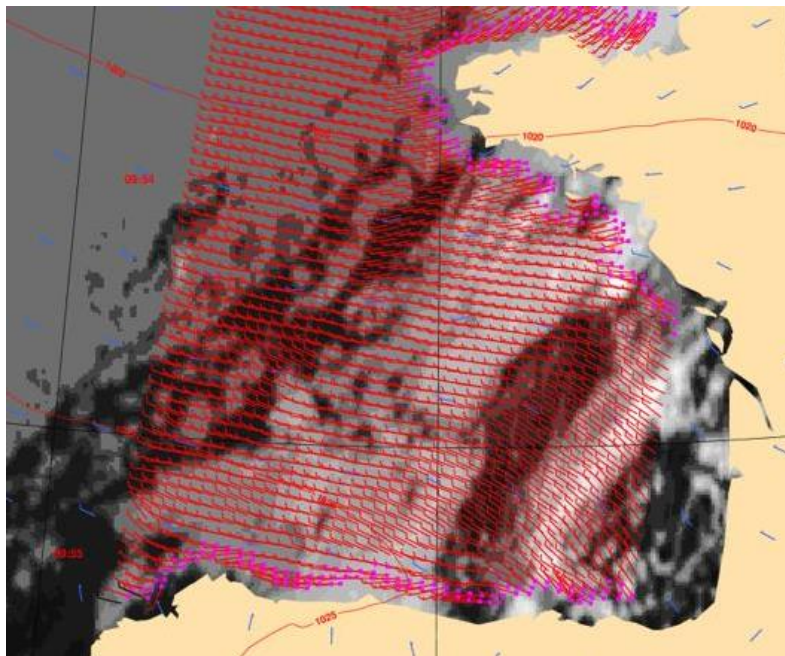


*Figure 1. OSI SAF ASCAT-B coastal wind field (red flags), corresponding to an overpass around 09:54 UTC on May 25<sup>th</sup>, 2022. A full (half) barb represents a wind speed of 5 m/s (2.5 m/s). The magenta markers denote land presence. Blue flags correspond to the HIRLAM model wind field forecast.*

## 2.3 ECMWF data

The ECMWF data consist of analyses and hourly forecasts, initialized twice daily from the analyses at 00 and 12 UTC. The hourly ECMWF 10-m equivalent neutral winds (U10N) have been downloaded through the ECMWF Meteorological Archival and Retrieval System (MARS) (<https://www.ecmwf.int/en/forecasts/datasets/archive-datasets>). Then a spatial and temporal interpolation of ECMWF U10S to the OSCAR acquisition is carried out. That is, three subsequent ECMWF forecast fields around the OSCAR acquisition time are used to perform the interpolation, two forecast fields corresponding to UTC times before the OSCAR observing time and one after. Each of the three selected ECMWF forecasts is spatially interpolated to each OSCAR WVC position. Then, a time interpolation of the three forecasts to the satellite acquisition time is performed to get the final collocated ECMWF U10S [Lin et al., 2016].

## 2.4 SEASTARex flights

Figure 2 shows the two SEASTARex flights, whose data have been used in this work, corresponding to May 22<sup>nd</sup> (a) and May 25<sup>th</sup> (b), 2022. Note that for the May 22<sup>nd</sup> flight, only the star pattern tracks to the South of the island have been used (see a more detailed schematic in Figure 3), while the circular track data are not yet available. Also note that on May 25<sup>th</sup>, there are 6 flight legs, 5 heading South (i.e., legs #2-6) and the last one (leg #7) heading North (which is superimposed to the southernmost leg heading South, i.e., leg #6). Also relevant, on May 25<sup>th</sup>, the aft beam only operated for leg #2 (i.e., the northernmost leg). For the remaining 5 legs, only the fore and mid beams were operating.

Further details on the flight campaign can be found in [SEASTARex CIP, 2022], [SEASTARex\_DAR, 2023].



Figure 2. SEASTARex flight tracks for May 22<sup>nd</sup> (a) and May 25<sup>th</sup> (b), 2022. Note that the leg numbering for the open ocean flight (b) is also provided.

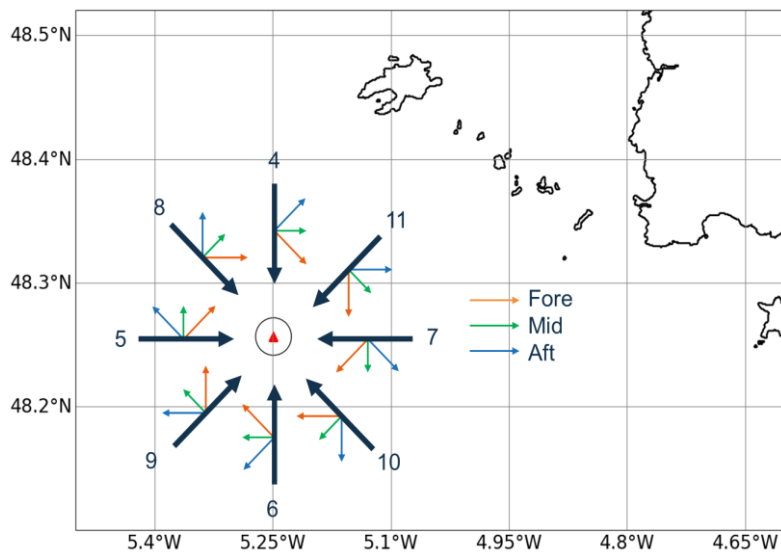


Figure 3. Detailed information on the star pattern of Figure 2a. The aircraft heading (black arrows) and the OSCAR viewing geometry of the fore (orange), mid (green), and aft (blue) beams is shown for each leg. Note that the leg numbering is also provided.

Table 2 lists the initial time and the assigned number for each of the flight tracks (legs) used in this study.

*Table 2. List of the SEASTARex flight legs used in this study. Left column: list of the initial acquisition times, in the format YYYYMMDDThhmmss, where YYYY stands for year, MM for month, DD for day, hh for hour, mm for minutes and ss for seconds. Right column: leg number of the day. For each track, all three files corresponding to the fore, mid and aft beam data have been used. The version of the files used in this study was released on March 1<sup>st</sup>, 2023.*

Initial track time	Leg number for each flight
20220522T062018	4
20220522T062620	5
20220522T063239	6
20220522T063906	7
20220522T064459	8
20220522T065108	9
20220522T065709	10
20220522T070317	11
20220525T085452	2
20220525T091741	3
20220525T092934	4
20220525T093950	5
20220525T095111	6
20220525T095747	7

### 3 NOISE CHARACTERIZATION

The electric field of a single-look radar signal backscattered by the sea surface can be reasonably modeled with the Rayleigh distribution when the illuminated area is large enough.



More in general, in case of a multi-look radar, a chi-square function can properly explain the experimental normalized radar cross section ( $\sigma_0$ ) distribution, given that one knows its expected value ( $\mu$ ) and the specific standard deviation ( $K_p$ ) [Grieco et al., 2022], as reported in the following equation:

$$f_{\sigma_0,k} = \frac{k}{\mu^2} \left( \frac{k\sigma_0}{\mu} \right)^{\frac{k}{2}-1} \exp \frac{-k\sigma_0}{\mu} \quad (2)$$

where  $k$  is the number of degrees of freedom. In fact, the number of degrees of freedom of the chi-square distribution is double the equivalent number of looks, which is inversely proportional to  $K_p^2$ . The  $K_p$  can be empirically estimated by dividing the standard deviation of a set of  $\sigma_0$  measurements with a given acquisition geometry over a homogeneous area by its expected value [Grieco et al., 2022].

In case of single look radars, the chi-square distribution with two degrees of freedom reduces to the negative exponential function, which writes as follows:

$$f_{\sigma_0,NE} = \lambda e^{-\lambda\sigma_0} \quad (3)$$

In Equations 2 and 3,  $f$  stands for probability distribution function and NE for Negative Exponential.

In case of high-resolution radars, such as Synthetic Aperture Radars (SARs), important departures from this model can happen, and a non-Rayleigh speckle model is required. The threshold size of the illuminated area seems to be related to several factors, such as the size of the individual scatterers and the sea state, as suggested by [Jakeman and Pusey, 1976]. In the same paper, the authors argue that the key aspect is related to the number of independent scatterers in the illuminated area: when it is reasonably high, at least higher than 10, the Rayleigh distribution is adequate. The authors of this paper demonstrate that when this criterion is not matched, a statistical model based on K-distributions is more adequate, and can properly explain several experimental findings. Recently, [Migliaccio et al, 2019] proposed a K-distribution configuration for Sentinel-1 SLC images, with an extensive analysis of the moments. The configuration proposed writes as follows:

$$f_{\sigma_0,K} = \frac{2}{\Gamma(\nu)\mu^{\frac{\nu+1}{2}}} \nu^{\frac{\nu+1}{2}} \sigma_0^{\frac{\nu-1}{2}} K_{\nu-1} \left( \frac{2}{\sqrt{\mu}} \right) \sqrt{\nu\sigma_0} \quad (4)$$

In Equation 4, the subscript  $K$  of  $f$  stands for K-distribution,  $\nu$  is the shape parameter and  $K_{\nu-1}$  is the modified Bessel function of the second kind of order  $\nu-1$ .  $\nu$  is set by equating the experimental and the theoretical normalized second order moment of the K-distribution.

In this document, we will investigate the consistency of the distributions of the OSCAR acquisitions with the two models introduced above. Furthermore, we will investigate the presence of any eventual biases between master and slave images and their trend with the incidence angle. Finally, a simple strategy for  $\sigma_0$  speckle noise reduction will be shown.

### 3.1 Methodology

The python package *random* has been used to generate random values fitting the exponential distribution. As said, the parameter  $\lambda$  of the exponential distribution is inversely proportional to  $\mu$ . Since  $\mu$  depends on the incidence angle, it has been estimated for each bin of one degree width, from its minimum to its maximum values. The incidence angle range for OSCAR acquisitions spans roughly between 20° and 70°.

The generation of random values fitting the K-distribution adopted in this study is more complex because the package *random* does not support neither K-distribution nor Bessel functions. To overcome this issue, an alternative original approach based on the cumulative distribution function matching technique has been successfully explored, and is described as follows:

- A sample of  $n$  uniformly distributed random values between 0 and 1 is generated with the uniform random generator *rand* of the python package *random* (note that any alternative packages or libraries are equivalent);
- The cumulative distribution function of the uniform distribution ( $F_U$ ) is linear, therefore the samples generated in the previous step correspond to the values of  $F_U$ ;
- The K-distribution model described in Equation 4 is implemented and evaluated for a wide range of SAR values, spanning from -50 dB to 10 dB, which likely covers the entire range of  $\sigma_0$ s acquired by OSCAR.  $\mu$  is estimated as in the case of the exponential distribution, and  $\nu$  is assessed by equating the experimental and the theoretical normalized second order moment of the K-distribution. Note that both parameters depend on the incidence angle;
- The cumulative distribution function of the K-distribution ( $F_K$ ) is estimated with the following formula:

$$F_K(x_i) = \sum_{k=1}^i \frac{f_K(x_{k+1}) - f_K(x_k)}{2} dx_k \quad (5)$$

Note that Equation 5 is a numerical implementation of the indefinite integral of Equation 4, using a trapezoidal formula;

- For each value  $x_U$  of the uniform random sample, the corresponding K-distributed random value  $x_K$  is obtained by equating  $F_U(x_U)$  and  $F_K(x_K)$ . This approach has been tested for the exponential distribution, obtaining results equivalent to those obtained with the mentioned python package. Note that the finer the definition grid of  $f$  is, the more accurate is the method. Furthermore, this approach can be extended to any kind of distribution.

### 3.2 Results

The results shown in this section refer to the OSCAR images dated 25<sup>th</sup> of May 2022 at 8:54 UTC (i.e., leg #2), fore beam.

The red curve in Figure 4 represents the distribution of the  $\sigma_0$ s acquired by the master channel of the fore beam. The black (green) curve represents the simulated values with the K-distribution (exponential). It is apparent that K-distributed  $\sigma_0$ s fit experimental data better than those generated with the exponential function. In particular, the simulated  $\sigma_0$ s with the exponential function explain significantly less variability than the real data. This is also confirmed by the empirical  $K_p$  estimates, which span from a minimum of 1.11 to a maximum value of 1.43, while theoretical values for the exponential distribution should be close to 1. This example proves that K-distribution implemented following [Migliaccio et al., 2019] is adequate to simulate real SAR  $\sigma_0$ s.

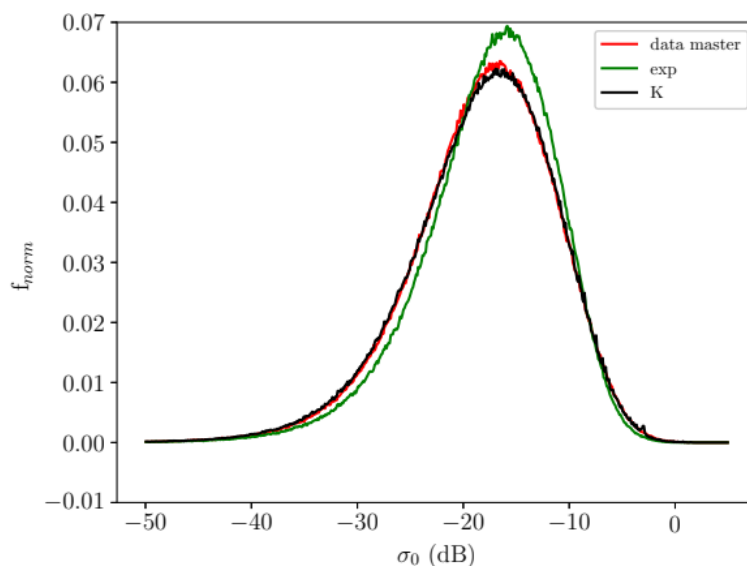


Figure 4. Red curve: distribution of experimental  $\sigma_0$ s acquired on the 25th of May 2022 at 8:54 UTC (i.e., leg #2), with the fore beam, master channel. Black (green) curve: simulation

of  $\sigma_0$ s with  $K$ -distribution (exponential). Note that data refer to the entire range of incidence angles.

Other cases have been examined with similar results, and are therefore not reported for the sake of brevity.

Figure 5 shows the real  $\sigma_0$ s distributions for the master (blue curve) and slave (orange curve) channels of the same image, for the entire range of incidence angles, whose acquisition time is reported in the panel. The operator E stands for “expected value” and the superscript MAS and SLA stand for master and slave, respectively. Finally, the letter F next to the acquisition time stands for fore beam. Differences are averaged over the entire range of values, with an overall master low bias of 0.9 dB. The trend of the aft beam is similar, with an overall master low bias of 0.98 dB. Note that these values are not constant, with variations of about 0.1 dB from leg to leg within the same flight (day). Moreover, these biases also vary from day to day, with a mean (over all legs) variation for each beam lower than 0.1 dB (not shown).

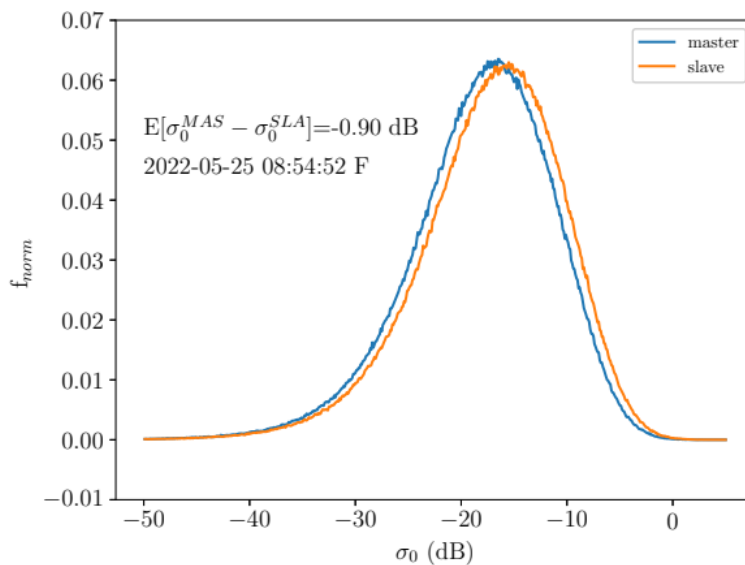


Figure 5. Blue (orange) curve: distribution of  $\sigma_0$ s acquired by the master (slave) channel of the fore beam, dated 25<sup>th</sup> of May 2022 at 8:54 UTC. The operator E stands for “expected value”, MAS for master and SLA for slave. Finally, the letter F next to the acquisition time stands for “fore”.

Figure 6 shows the mean  $\sigma_0$  differences in logarithmic units as a function of incidence angle for the same image. These differences are estimated on incidence angle bins of one degree width. The biases are all negative, but the difference is not constant with incidence angle, spanning roughly from -0.5 dB to -1.1 dB.

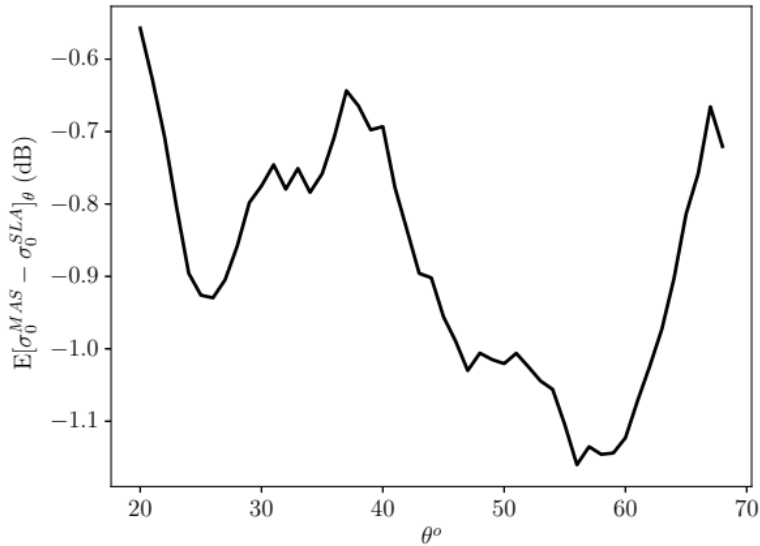


Figure 6. Mean  $\sigma_0$  difference between master and slave channels as a function of incidence angle ( $\theta$ ) for the acquisition dated 25<sup>th</sup> of May 2022 at 8:54 UTC.

Figures 7-9 show the normalized density plots (2D histograms) of the averaged  $\sigma_0$ s as a function of incidence angle, for the fore beam master channel. The averaging is performed on increasing WVC sizes, from 6x6 to 12x12 and 19x19 image pixels, which correspond to about 50x50m<sup>2</sup>, 100x100m<sup>2</sup> and 150x150m<sup>2</sup>, respectively. The incidence and  $\sigma_0$  ranges are 20°-70° and -28dB to 0dB, respectively. The bin size is 3°x0.3dB, and the normalization is done with respect to the bin having the maximum value for each incidence angle interval. This way, the reader can appreciate the conditional distribution of averaged  $\sigma_0$ s for each incidence angle interval. Several WVC sizes are tested in order to assess the capability to reduce the speckle noise prior to wind retrieval. Finally, the averaged  $\sigma_0$ s with respect to incidence angle are shown with the black dashed curve.

A few things are apparent: i) this approach is effective in reducing the speckle noise, as expected. In fact, the y-direction widths of the density plots reduce when the averaging area is increased; ii) the data distribution is not uniform with respect to incidence angle, being more dense at higher values, as expected. This is the reason for the white troughs in the left most part of Figures 8 and 9, being more evident in the latter; iii) the average  $\sigma_0$  is not monotonically decreasing with incidence angle, as it would be expected. Instead, in the range between 40°-50°, the average  $\sigma_0$  is even increasing. This is likely due to poor data calibration, as it will be discussed in Section 4.

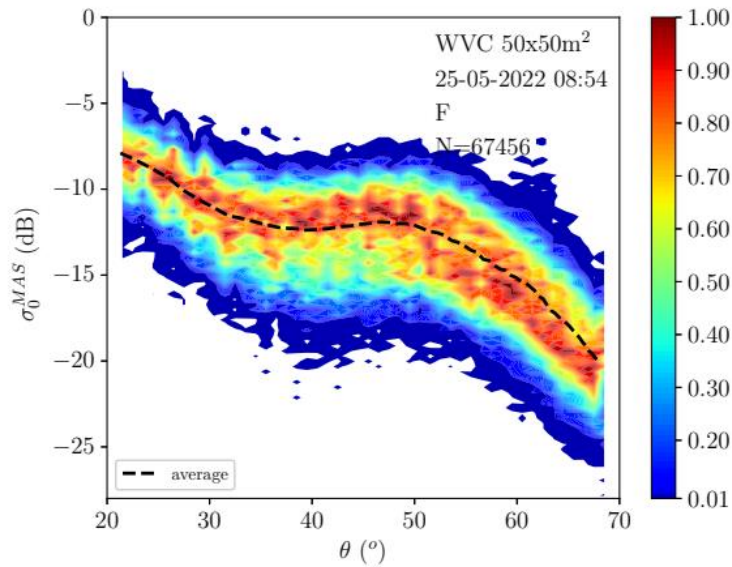


Figure 7. 2D normalized histogram of  $\sigma_0$  in logarithmic units from the master channel of the fore beam, averaged over a WVC size of 6x6 pixels (about 50x50 m<sup>2</sup>), as a function of incidence angle. The bin size is 3°x0.3 dB in the ranges 20°-70° and -28 to 0 dB. Normalization is done with respect to the bin with the maximum value for each incidence angle interval. The average  $\sigma_0$  with incidence angle is represented by the black dashed curve. The image acquisition time is reported on the panel, together with the total number of cells (N) and the WVC size.

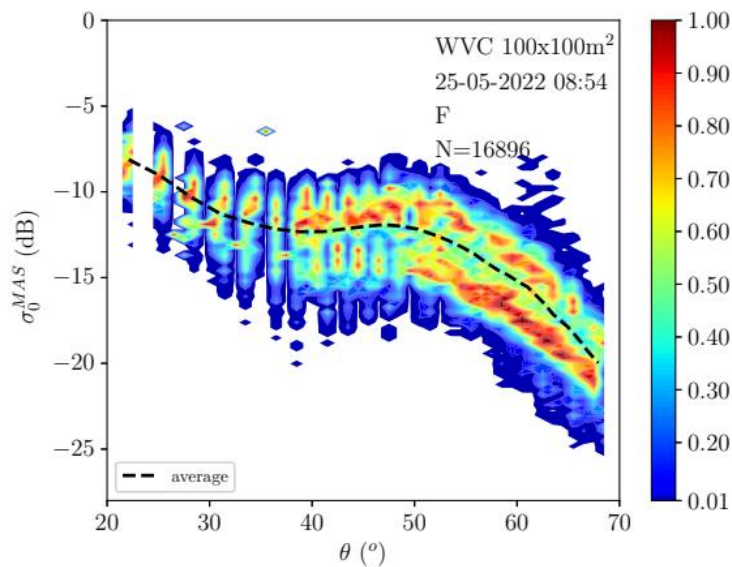


Figure 8. Same as Figure 7, but for a WVC size of 12x12 pixels (about 100x100 m<sup>2</sup>).

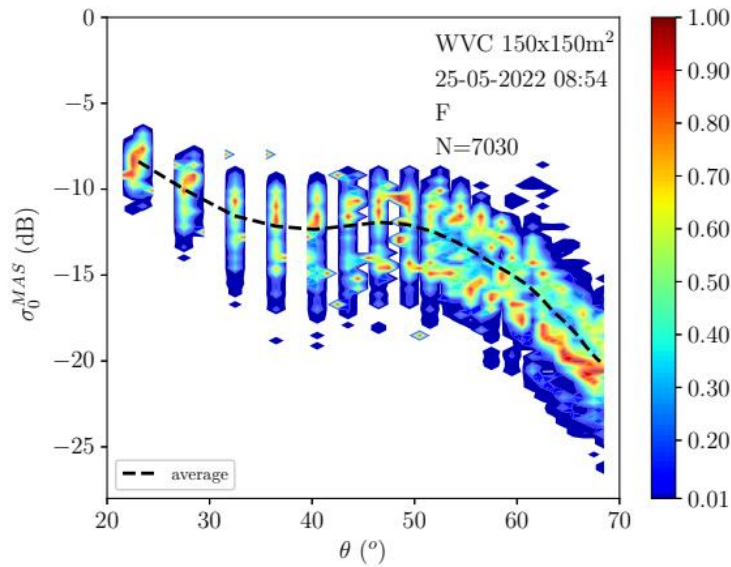


Figure 9. Same as Figure 7, but for a WVC size of 19x19 pixels (about 150x150 m<sup>2</sup>).

## 4 OCEAN CALIBRATION

This Section presents two ocean calibration approaches and their main results when applied to OSCAR NRCS data.

### 4.1 Numerical Ocean Calibration

A well-established method for calibrating scatterometer measurements, the so-called Numerical Ocean Calibration (OC) [Verspeek et al., 2010] [Verspeek et al., 2012], resides in the direct comparison of measured  $\sigma_\theta$  data with simulated values from collocated Numerical Weather Prediction model (NWP) winds using the Geophysical Model Function (GMF), i.e., the empirically-derived function that relates the sea-surface wind vector to  $\sigma_\theta$ , accounting for instrument viewing geometry (azimuth and incidence angles), polarization, and operating frequency. In this Section, the OC methodology is presented and adapted for OSCAR NRCS calibration purposes.

#### 4.1.1 Methodology

The OC method is based on the analysis of a large measurement dataset to estimate the Fourier coefficients that can be directly compared to those in the scatterometer GMF. A prerequisite



for an accurate OC is to get a uniformly sampled wind direction distribution for all wind speeds. To arrange a uniform wind direction distribution, the collocated model (e.g., ECMWF) wind data are separated into wind speed bins and azimuth angle bins. The differences of measured and simulated  $\sigma_0$ s are averaged over all wind azimuth bins weighted according to the wind azimuth occurrence. Next they are averaged over all wind speed bins weighted according to the wind speed occurrence. The OC method needs only a few days of collocated scatterometer and ECMWF winds to produce a reasonable calibration. The collocated ECMWF equivalent neutral 10-meter winds are converted to simulated  $\sigma_0$  values using the scatterometer GMF. Both measured and simulated  $\sigma_0$  pairs are then averaged following the already described procedure.

Finally, the OC provides backscatter residuals, i.e., the difference between the two  $\sigma_0$  values as a function of incidence angle for each antenna. When these residuals are stable over time they may be used as correction factors for errors in the instrument, for monitoring instrument health or for GMF development. Further details on the OC methodology can be found in [Verspeek et al., 2012].

Given that the SEASTARex campaign data is limited in terms of observation area and flight time, the sea surface wind speeds and directions are similar for all the flight legs during a certain day, thus a simplified version of the OC is used for OSCAR NRCS calibration purposes. That is the wind speed and/or azimuth occurrence are not taken into account, the mean difference between the simulated and measured  $\sigma_0$ s is calculated directly, and then is used as calibration coefficients. Figure 10 shows a schematic illustration of the OC work flow. For each OSCAR antenna beam, a calibration factor as a function of incidence angle can be derived using either collocated ASCAT or ECMWF wind data as input. Since OSCAR is a Ku-band system, the latest version of the PenWP Ku-band GMF, i.e., NSCAT-4DS [Wang et al., 2017], is used.

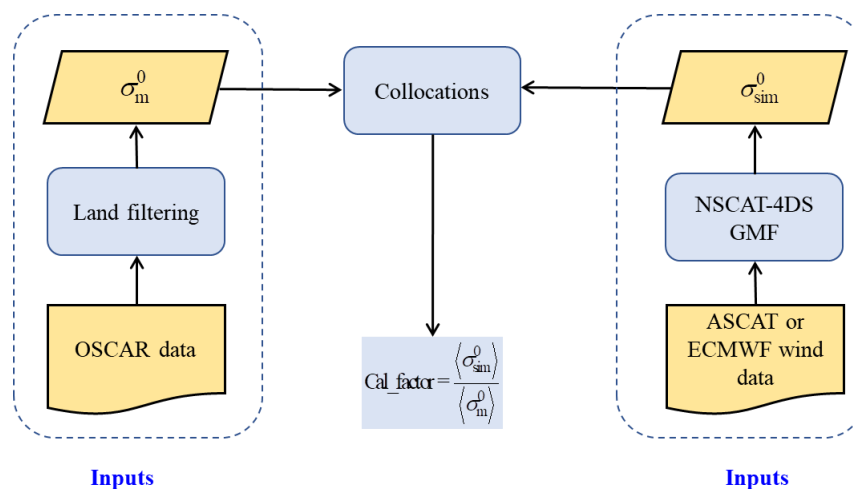


Figure 10. Schematic illustration of the OC process.

### 4.1.2 Results

Figure 11 shows the OC results for OSCAR NRCS data acquired during the star pattern flights on May 22<sup>nd</sup> (see Figure 3). Here, the calibration coefficient (y-axis) is simply derived from a logarithm operation, i.e.,  $Cal\_Coeff (dB) = 10 \times \log_{10}(Cal\_factor)$ . No ASCAT wind data are available in the flight area since the latter is too close to the coast. As such, collocated ECMWF wind data are used as input (see Figure 10). For each incidence angle interval of 1°, the calibration factor is computed by averaging over all OSCAR original resolution (8 x 8 m<sup>2</sup>) WVCs in each leg the measured and simulated NRCS differences (see Figure 10).

Note that the calibration curves have a variation of more than 10 dB over the entire incidence angle range [20°,65°]. Such a remarkable variation cannot be explained by errors in the input ECMWF winds or the NSCAT-4DS GMF, since 10 dB would represent more than a 10 m/s error. As such, the measured backscatter deviations from the expected (simulated) values are attributed to an anomaly in the OSCAR instrument behavior or in the image reconstruction algorithm. This needs further investigation.

This anomalous incidence angle behavior can however be corrected with OC. Note as well the spread of up to 4 dB between the calibration curves from different legs. This spread is far too large to be associated it with leg-to-leg instrument calibration changes, since all the legs correspond to the same flight and the instrument is operating continuously over a couple of hours.

One possible reason for such changes is wind variability. Indeed, the OSCAR NRCS measurements are of very high resolution (around 8m), compared to the resolution of the ECMWF model winds (used as input to OC), which is estimated to be around 100-150 km [Vogelzang et al., 2011]. Moreover, the star pattern flight takes about 2 hours, while coastal winds are indeed highly variable.

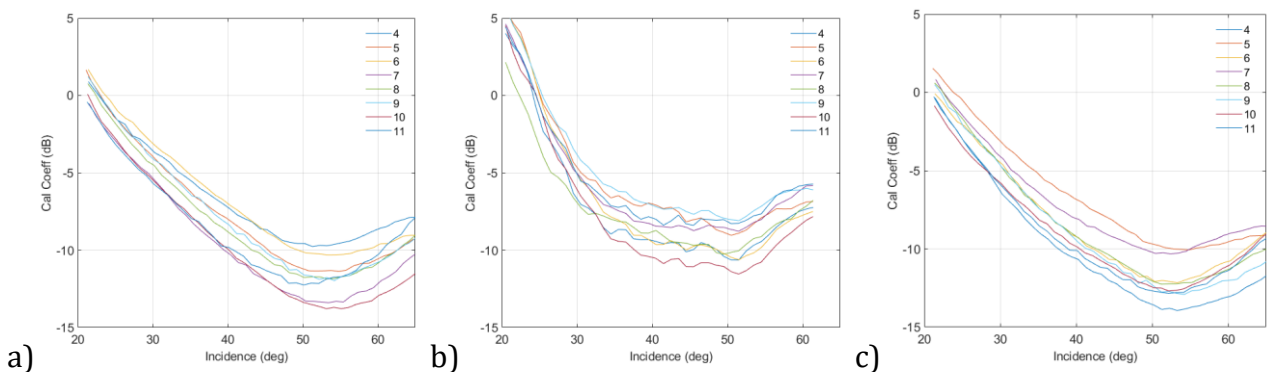


Figure 11. OSCAR calibration factors as a function of incidence angle, for the fore (a), mid (b), and aft (c) beams, and for all the star pattern legs on May 22<sup>nd</sup> (see Figure 3).

Figure 12 shows the same calibration curves but for the open ocean flight on May 25<sup>th</sup> and only the fore and the mid beams, since the aft beam only worked for leg #2. Similar to the star

pattern flight (see Figure 11), the calibration curves have a variation of more than 10dB over the entire incidence angle range [20°,65°]. Note also the spread of a few dB between the calibration curves from different legs. However, in this case, legs #2-5 are relatively close to each other, while legs #6-7 (i.e., the southernmost legs) show a distinct behavior.

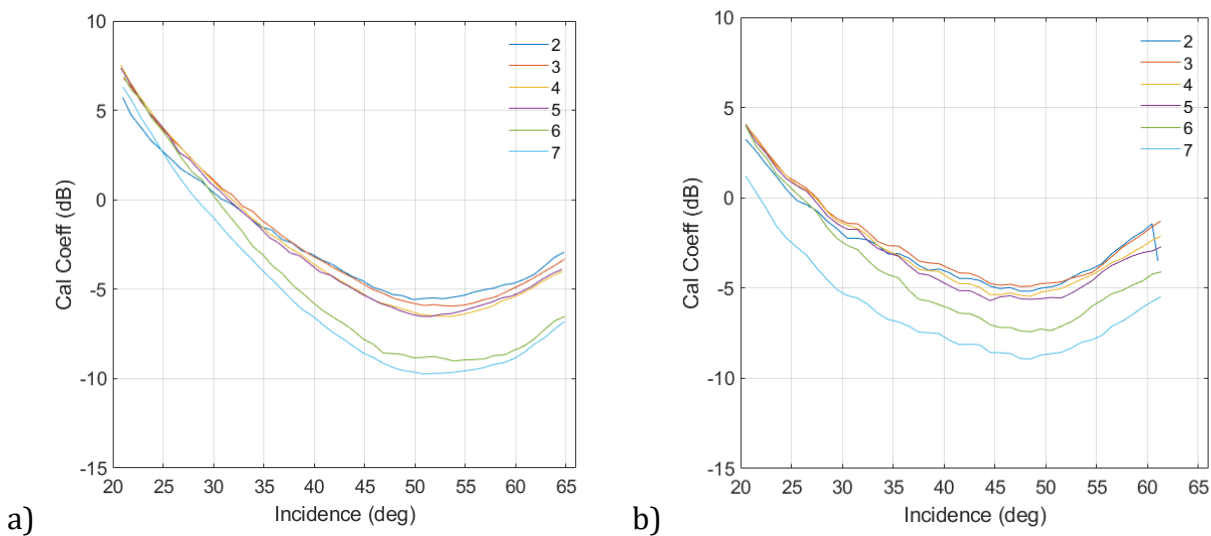


Figure 12. Same as Figure 11, but for all the open ocean legs on May 25<sup>th</sup> (see Figure 2b), and for the fore (a) and mid (b) beams only.

Figure 13 shows the same as Figure 12, but using collocated ASCAT winds (instead of ECMWF winds) as input to OC (see Figure 10). Note that the curves are significantly closer to each other than in Figure 12. Indeed, this seems to be associated to the fact that ASCAT winds resolve much smaller scales (around 20km) than ECMWF winds (around 100-150km), and as such, the former are able to depict more of the small scale variability depicted by OSCAR.

It can therefore be concluded that the (different) curve spread shown in Figures 12 and 13 seems to be mainly related to the unresolved (small) scales by the input ECMWF and ASCAT winds, respectively, rather than to instrument calibration changes along the flight.

Finally, note that the calibration curve for leg #7 (light blue) shows a distinct behavior w.r.t. the other legs. This is the only leg in which the plane is heading North, after a 180° course change, i.e., the last flight leg before the instrument was switched off. This different behavior could be due to a sudden wind change, not capture by ASCAT (note that ASCAT winds are almost “instantaneous” over the entire leg, while OSCAR measurements are taken at different times) or to an instrument behavior change due to the plane manouevre (turn). This needs further investigation.

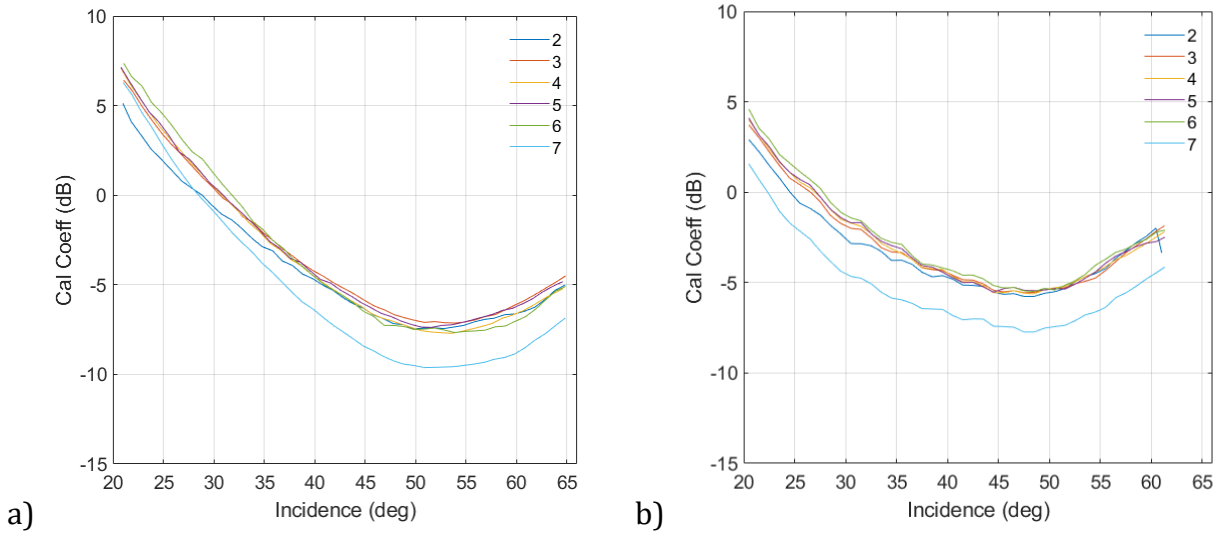


Figure 13. Same as Figure 12, but using collocated ASCAT winds instead of ECMWF winds as OC input.

## 4.2 Alternative calibration approach

In this Section, we develop a new OC methodology to account for leg-to-leg wind variations which are captured by OSCAR but not by the input winds, i.e., ECMWF or ASCAT.

### 4.2.1 Methodology

As discussed in Section 4.1, in order to properly calibrate OSCAR NRCS, the small-scale wind variability, depicted by OSCAR but not by ASCAT and (notably) ECMWF winds, needs to be accounted for. As such, an alternative OC approach is presented here, in which the goal is to find a single calibration curve for all the legs within the same flight (day) by accounting for leg-to-leg true wind variations, which are sensed by OSCAR but not by the input-to-OC wind sources (ASCAT or ECMWF). Specifically, each flight leg is about 15~20 km long (i.e., in the along-track direction), such that for calibration purposes, the sea surface wind is assumed to be constant over the same leg, but may vary from leg to leg. As such, the alternative OC consists of two steps, as illustrated in Figure 14.

First, we simulate the Ku-band radar backscatter measurements for all the OSCAR flight legs in one particular day by taking the sea surface wind variability into account. That is, the Monte Carlo method is used to simulate the leg-mean  $\sigma_{os}$  under a variety of wind conditions, and then the difference between the measured and the simulated  $\sigma_{os}$  as a function of incidence angle is calculated for each antenna beam and for each wind condition. Following the assumption that the calibration coefficients do not vary within the same flight, and that the unknown ‘true’ sea

surface wind is within the simulated wind conditions, we may estimate the ocean calibration coefficient for each antenna beam in the following way:

- For each flight leg, the maximum and the minimum  $\sigma_0$  differences over all the simulated wind conditions are selected firstly for each incidence angle bin;
- At each incidence angle bin, the maximum value of the above minima and the minimum value of the maxima corresponding to those flight legs, are averaged to represent the first-guess ocean calibration coefficient.
- In practice, the mean ECMWF or ASCAT wind vector  $[w_r, d_r]$  over the flight area is used as initial condition, over which the Monte Carlo simulation is run using the following wind speed  $[w_r - 1.5\text{m/s}, w_r + 1.5\text{m/s}]$  and wind direction  $[d_r - 15^\circ \text{ to } d_r + 15^\circ]$  ranges, with bin sizes of 0.1 m/s and  $2^\circ$ , respectively.

Second, we calibrate the measured leg-mean  $\sigma_0$ s using the above first-guess calibration coefficient, and then perform wind inversion for each flight leg using the maximum likelihood estimator [Portabella and Stoffelen 2002], which leads to typically 2-4 ambiguity solutions for each flight leg. The solution closest to the reference wind vector  $[w_r, d_r]$  is then selected as the retrieved wind vector.

Subsequently, the retrieved winds are used to simulate the radar backscatter measurements, and the ratio between the previously calibrated  $\sigma_0$ s and the newly simulated ones, denoted as  $f_{c,k}$ , is estimated for each antenna beam ( $k = 1, 2, 3$ , indicating the fore-, mid-, and aft-beam respectively). Ideally,  $f_{c,k}$  should be very close to 1. However, in case that the first-guess calibration coefficient does not well represent the simulated wind variability conditions,  $f_{c,k}$  may be slightly larger or smaller than 1, indicating that the  $k^{\text{th}}$  beam is not consistent with the GMF under the given (retrieved) wind conditions. Therefore, an iterative approach is carried out until the calibration converges. This is done as follows:

- 1) compute the beam consistency factor, which is defined as the mean value of the differences in dB among the three consistency indicators, as follows

$$b_c = \frac{1}{3} \sum_{k=1}^3 \left| 10 \times \log_{10} \frac{f_{c,k}}{f_{c,j}} \right| \left( j = \begin{cases} k+1, & \forall k < 3 \\ 1, & k = 3 \end{cases} \right); \quad (6)$$

- 2) if  $b_c < 0.1$  dB, it is assumed that the three beams are consistent with each other, thus one may stop the iteration and output the retrieved wind vector and the calibration coefficients;
- 3) if  $b_c \geq 0.1$  dB then the calibration coefficient is updated, i.e.,  $f_{c,k\text{new}} = f_{c,k\text{previous}} \times f_{c,k}$ , and then wind inversion is performed again;
- 4) repeat steps 1-3 until convergence (i.e.,  $b_c < 0.1$  dB) is reached.

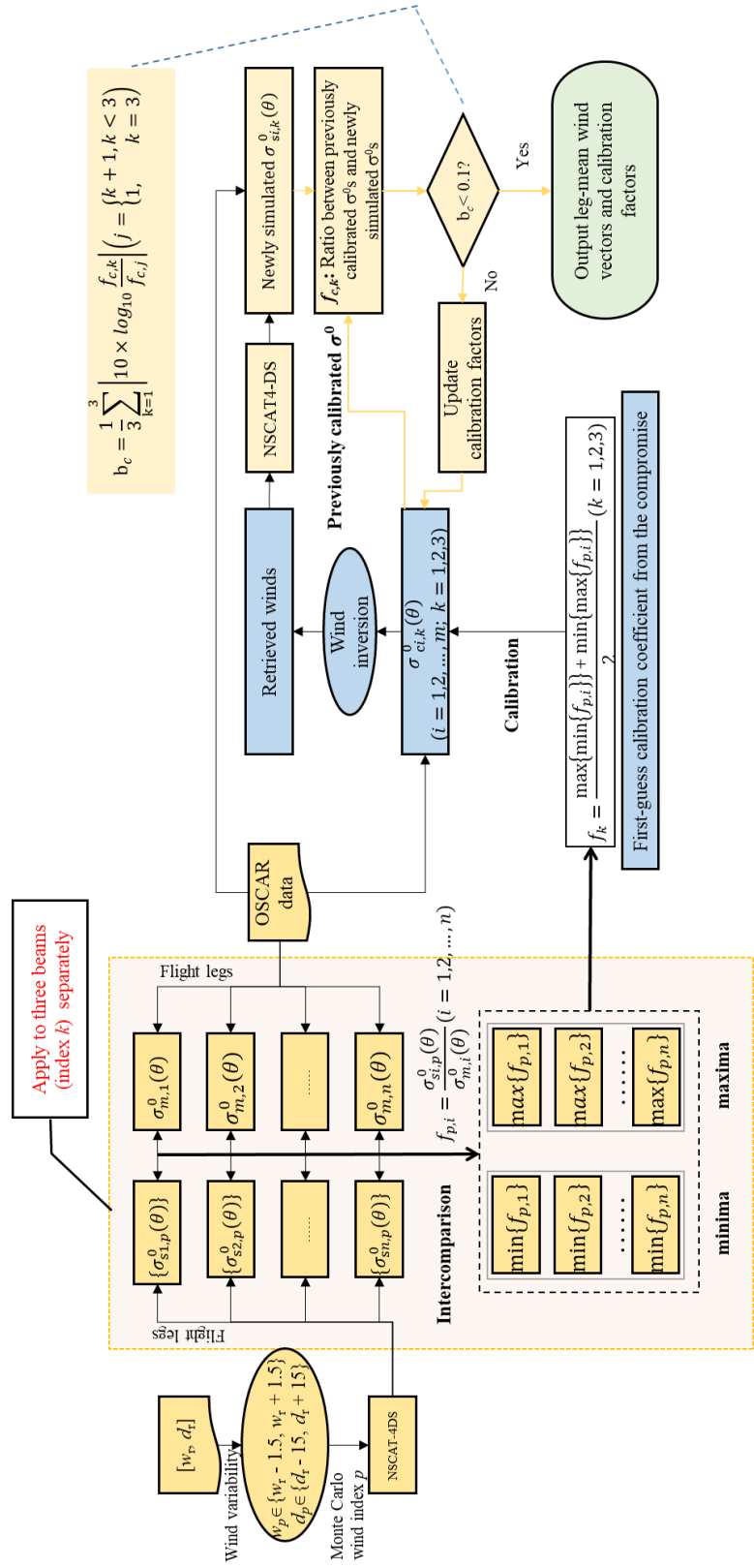


Figure 14. Schematic illustration of the alternative OC scheme.

## 4.2.2 Results

Figure 15-17 show the same as Figures 11-13, respectively, but including the retrieved calibration curve (solid thick curve) using the alternative OC approach from Section 4.2.1. As expected, the new calibration curve is in general a compromise between all the individual (leg-wise) curves retrieved by the nominal OC (see coloured curves).

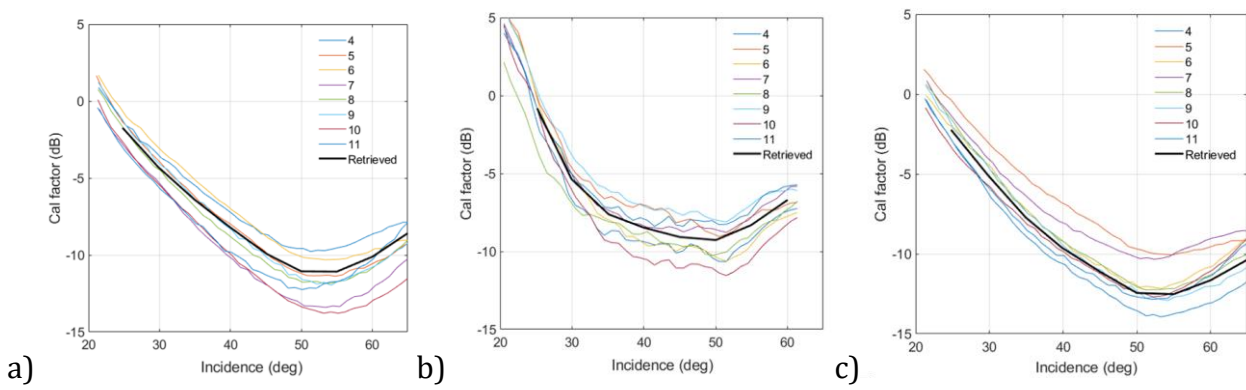


Figure 15. Same as Figure 11, but including the retrieved calibration curve (solid thick curve) using the alternative OC approach from Section 4.2.1.

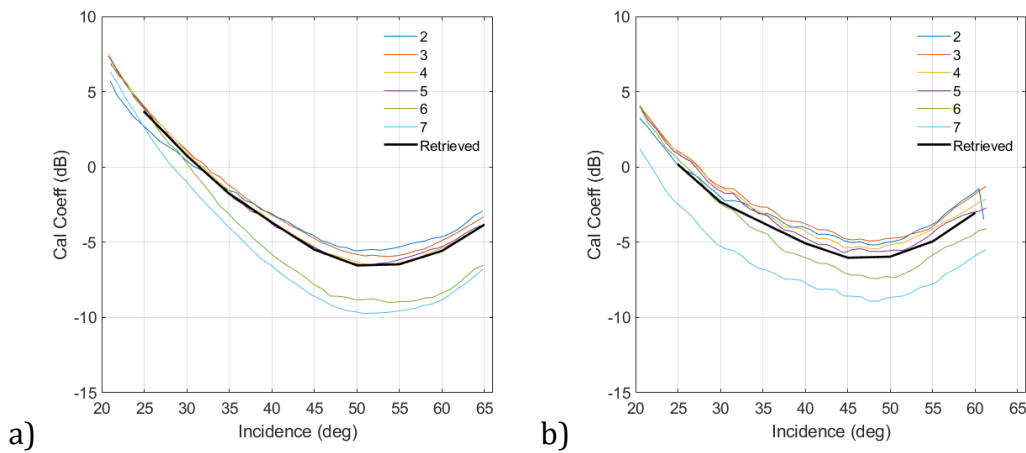


Figure 16. Same as Figure 12, but including the retrieved calibration curve (solid thick curve) using the alternative OC approach from Section 4.2.1.



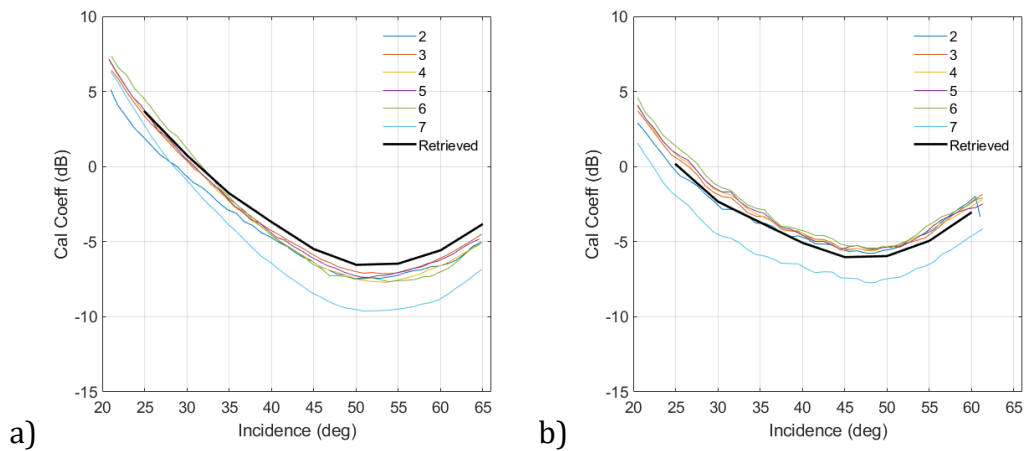


Figure 17. Same as Figure 13, but including the retrieved calibration curve (solid thick curve) using the alternative OC approach from Section 4.2.1.

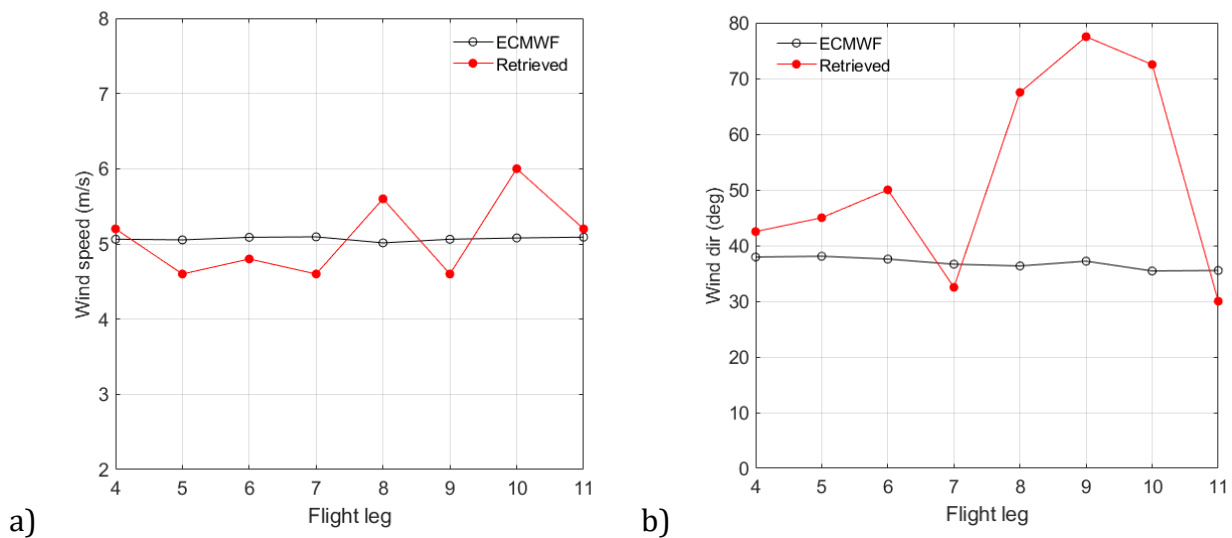


Figure 18. Retrieved wind speed (left) and direction (right) from the alternative OC (red) and input-to-OC wind (black), i.e., ECMWF, for all the the star pattern flight legs on May 22<sup>nd</sup>.

Figure 18 shows the retrieved wind speed (left) and wind direction (right) by the alternative OC approach for each leg (red curves), in comparison with the ECMWF (black curves) input winds for the star pattern flight on May 22<sup>nd</sup>. As shown in Section 4.2.1, the alternative OC approach not only derives a single calibration curve but also the leg-to-leg wind vector variations that lead to a single calibration curve. Note the relatively small retrieved wind speed variation from leg to leg, while the wind direction does significantly change for legs #8-10 (i.e., around a 30°-40° change). However, in general, while both low winds and coastal are

usually highly variable, these results indicate that wind conditions were not much variable for this specific occasion.

Figures 19 and 20 show, respectively, the retrieved wind speed and wind direction by the alternative OC approach for each leg, in comparison with the ECMWF (left) and ASCAT (right) input winds for the open ocean flight on May 25<sup>th</sup>.

As shown in Figure 18, the leg-mean retrieved wind speeds are more consistent with the collocated ASCAT wind speeds (right) than with the ECMWF speeds (left). In line with the calibration curve results (see Figure 17), the main discrepancy between retrieved (red) and input (black) wind speeds is for leg #7, which, as already discussed, has a very distinct behavior from that of the other legs.

In contrast with the retrieved wind speeds (Figure 18), the leg-mean retrieved wind directions shown in Figure 20 are more consistent with the collocated ECMWF wind directions (left) than with the ASCAT directions (right). This inconsistency can also be seen in the backscatter domain in Figure 17a, where the retrieved calibration curve (solid black line) for the fore beam is above all the leg-wise calibration curves (coloured lines) for incidence angles above 35°. This may be due to the initial wind vector values used in the alternative OC approach to generate the wind ensemble, i.e., the leg-to-leg variable wind conditions assumed by the methodology. Indeed, a different initial wind vector may slightly change the retrieved calibration and wind vector results. Also note that the alternative OC approach undergoes a wind retrieval process (see Figure 14) with only two beams, i.e., the fore and aft beams, since on May 25<sup>th</sup> the aft beam only operated for one leg (i.e., #2). [Note that an ad-hoc approach to calibrate the aft beam for leg #2 is followed in Section 5, just for wind retrieval illustration purposes.] As shown in [Portabella, 2002], the scatterometer wind inversion based on only two views (beams) is ill-posed and can lead to larger uncertainties and biases in the retrieved winds.

In any case, the alternative OC approach shows that, by assuming certain leg-to-leg variable wind conditions, a single calibration curve can be derived which represents a good compromise among the different individual (leg-wise) calibration curves obtained by the nominal OC.

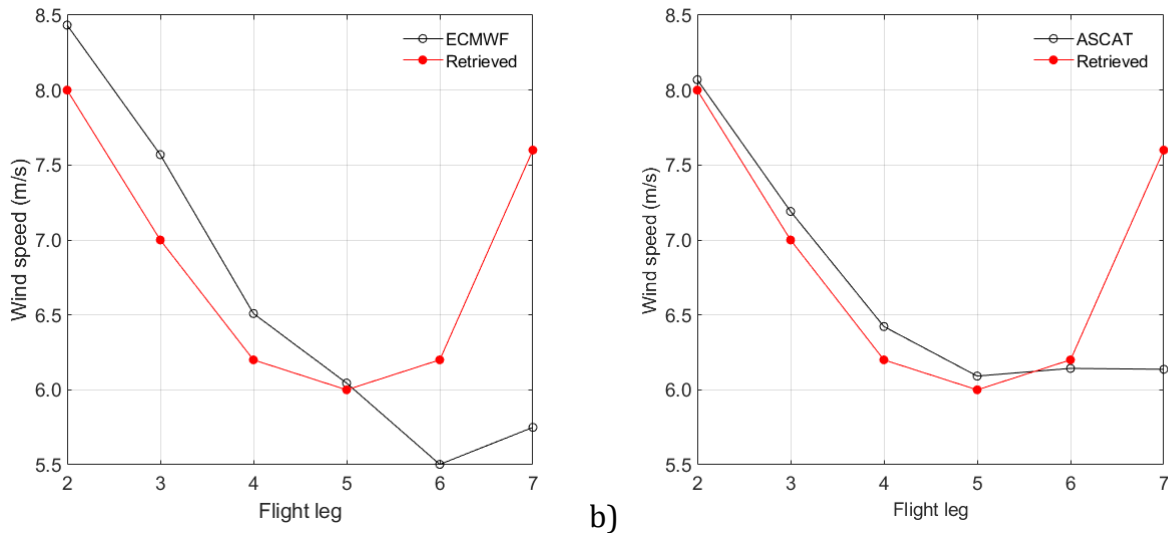


Figure 19. Retrieved wind speed from the alternative OC (red) and input-to-OC wind speed (black), i.e., ECMWF (left) and ASCAT (right), for all the open ocean flight legs on May 25<sup>th</sup>.

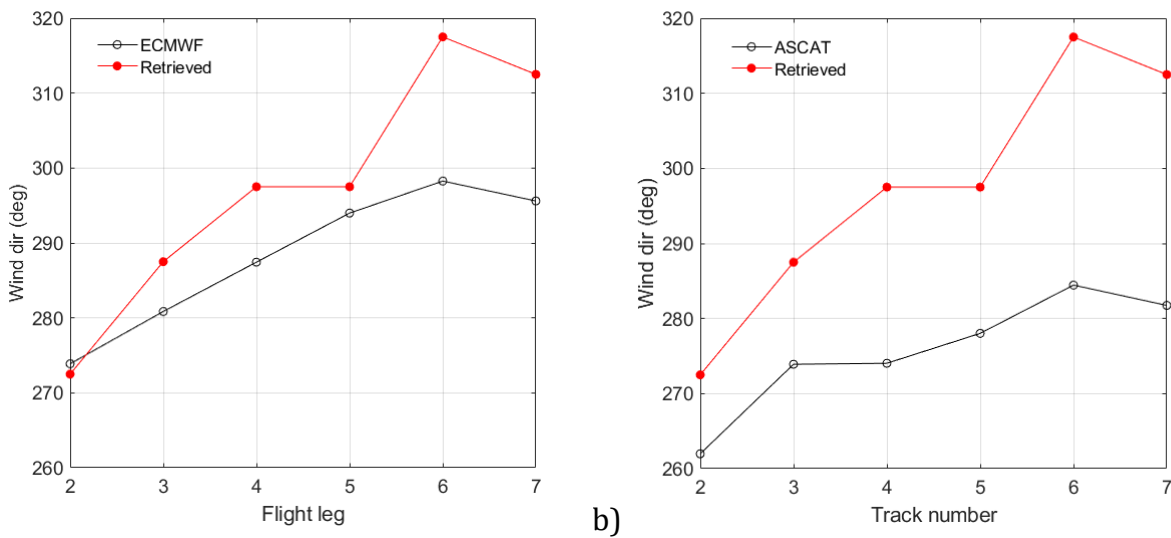


Figure 20. Retrieved wind direction from the alternative OC (red) and input-to-OC wind direction (black), i.e., ECMWF (left) and ASCAT (right), for all the open ocean flight legs on May 25<sup>th</sup>.

Finally, Figure 21 shows the retrieved calibration curves by the alternative OC approach for both, the May 22<sup>nd</sup> and the May 25<sup>th</sup> flights, and for the different beams. It is clear that the retrieved calibration curves of May 22<sup>nd</sup> substantially differ from those of May 25<sup>th</sup>. Such differences of up to 5.5 dB cannot be explained by errors in the initial wind conditions (i.e., by errors in the input ECMWF or ASCAT winds). Moreover, while the fore beam curves for both

days are parallel, those of the mid beam have a different incidence angle dependence, indicating that the instrument behavior changed from one flight to the next. Further investigation is needed at Level 1 in order understand the causes of these instrumental anomalies.

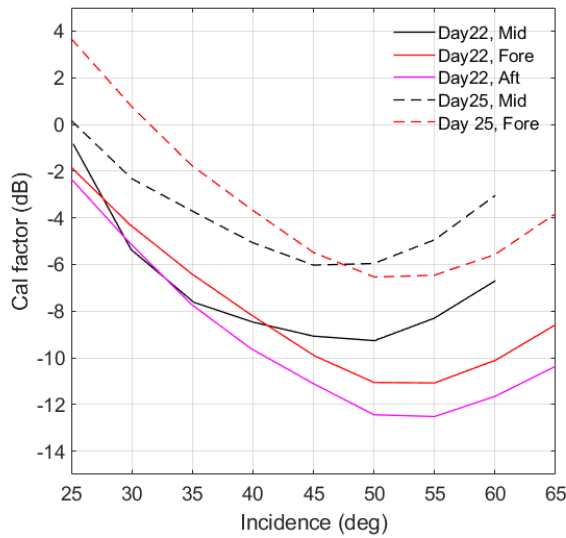


Figure 21. Retrieved calibration curves for the May 22<sup>nd</sup> (solid) and May 25<sup>th</sup> (dashed) flights, for the fore (red), mid (black), and aft (purple) beams. Note that for the May 25<sup>th</sup> flight, no calibration curve is retrieved from the aft beam due to lack of acquisitions (the aft beam only operated for leg #2).

## 5 WIND RETRIEVALS

Similar to the satellite scatterometers, the OSCAR wind retrievals are performed using the maximum likelihood estimator, which cost function is written as:

$$MLE = \frac{1}{3} \sum_{i=1}^3 (\sigma_{m,i}^0 - \sigma_{s,i}^0)^2 \quad (7)$$

where  $\sigma_{m,i}^0$  is the calibrated radar backscatter coefficient of the  $i^{\text{th}}$  beam, and  $\sigma_{s,i}^0$  is the simulated radar backscatter through the geophysical model function, i.e., NSCAT-4DS. Note that the general MLE formulation includes a normalization term (i.e., in the denominator) by measurement noise (Kp). This term has been neglected, which is equivalent to assume that the measurement noise is similar for all beams. This is done for two reasons: a) we do not have enough data to accurately estimate the Kp for each beam; b) in ASCAT-type of geometry, it has been shown that including the Kp term in Equation 7 leads to retrieved wind direction

biases [Stoffelen and Portabella, 2006]. Further optimization of the inversion process can of course be done in the future by, e.g., z-space transformation [Stoffelen and Portabella, 2006], but this is beyond the scope of this study.

In general, the full-resolution (8m x 8m) backscatter measurements are averaged to a single backscatter value on a WVC of a predefined size, e.g., 200m x 200m. Then, the generic wind inversion module of PenWP is used to retrieve sea surface winds from a set of WVC-mean  $\sigma^0$ s (i.e., three NRCS values, one for each beam). This inversion scheme allows up to 4 ambiguous wind solutions for each WVC, although because of its ASCAT-like viewing geometry it usually leads to 2 wind solution ambiguities 180° apart [Lin et al., 2013]. Then the ambiguity which is closest to the background wind field (i.e., ECMWF or ASCAT) is selected as the final wind solution. Note that the wind inversion can be done at other WVC sizes. Also, PenWP also allows the inversion of multiple  $\sigma^0$ s (e.g., at full 8m x 8m resolution) per beam and WVC. However, as shown in [Portabella, 2002], the reduction of noise by  $\sigma^0$  averaging prior to the non-linear inversion leads to higher quality wind retrievals. As such, we perform  $\sigma^0$  averaging prior to inversion.

In this Section, a preliminary, qualitative analysis of the OSCAR-derived wind fields is presented, together with a comparison of such fields against collocated ASCAT and ECMWF wind fields. The aim is to show that the OSCAR NRCS have been successfully integrated into PenWP, while a comprehensive validation of the retrieved winds is beyond the scope of this project due to the limited amount of OSCAR acquisitions and collocated (high-resolution) reference winds. For detailed information about the PenWP adaptation and user manual, see [SEASTARex PenWP, 2024].

## 5.1 OSCAR wind retrievals at different WVC sizes

PenWP has been tested at different WVC grid sizes, in particular at 104-m and 200-m resolution. Figures 22 and 23 (24 and 25) show the OSCAR-derived fields at 104-m (200-m) resolution for the star pattern legs #4-7 and #8-11, respectively, on May 22<sup>nd</sup>. The calibration curves shown in Figure 21 (Section 4.2.2) have been applied to OSCAR NRCS prior to wind retrieval.

As expected, the OSCAR retrieved wind variance is reduced with increasing WVC size, as qualitatively visible by the reduced wind speed granularity and wind arrow spatial variations of Figures 24 and 25 when compared against Figures 22 and 23.

The OSCAR wind fields indeed show small-scale variance, which can be attributed to the presence of noise, signal (true wind), or most likely a mixture of both. Some artifacts are clearly visible, with clear geometric patterns, e.g., the diagonal features in Figures 22 and 24, which can be clearly associated to small jumps in the fore and/or aft  $\sigma^0$  values. Moreover, the relatively high winds at the shortest-range (lowest incidence angles or inner-most WVC)

edges of the swaths in legs #10 (Figures 23c and 25c) and #11 (Figures 23d and 25d) or the low wind “blobs” that appear at short range in all the flight legs do not seem to be of geophysical origin.

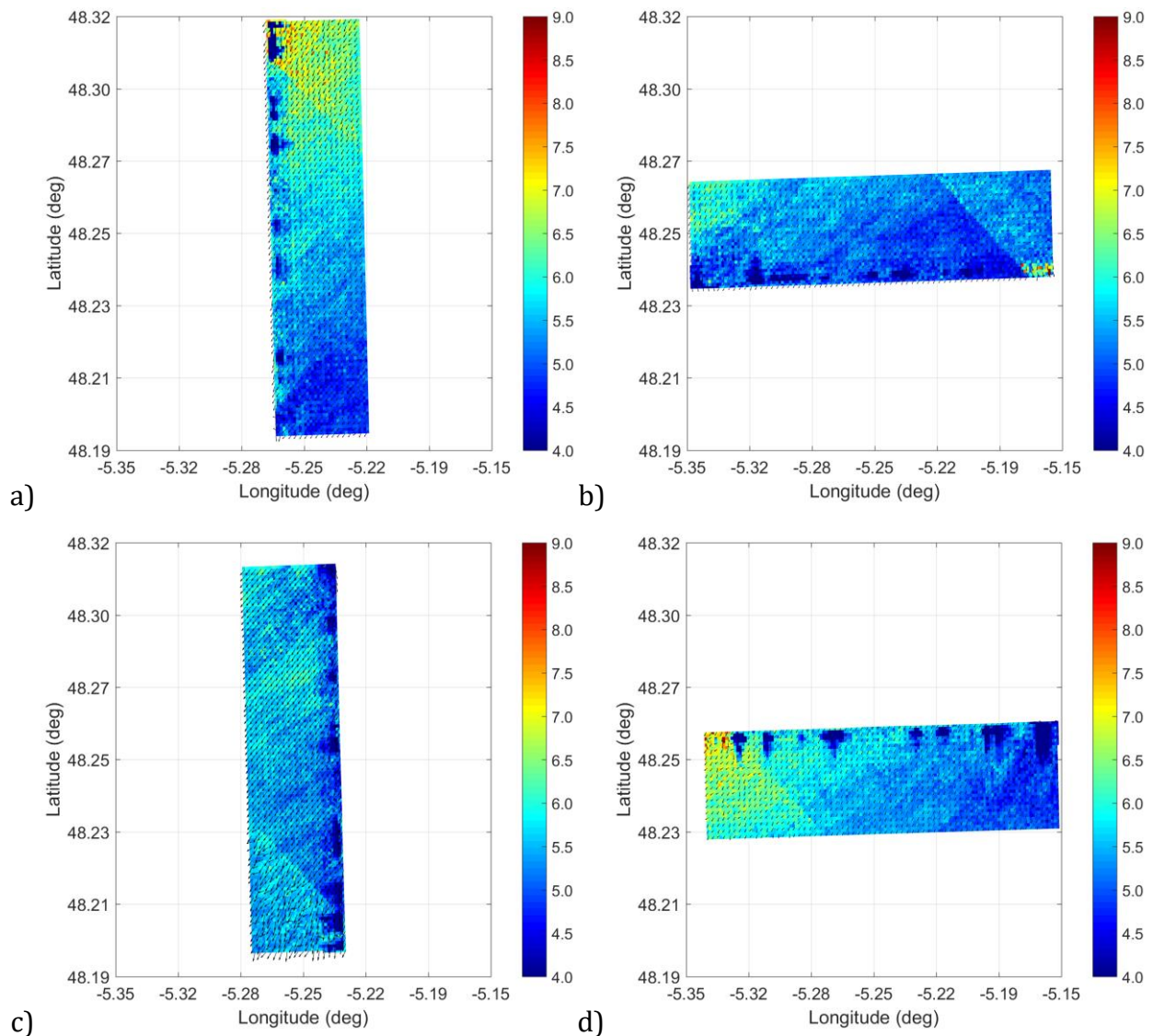


Figure 22. OSCAR-retrieved winds at 104-m resolution for the star-pattern flight legs #4-7 (a-d, respectively) on May 22<sup>nd</sup> (see Figure 3 for reference on leg numbering). For the sake of illustration, the arrows are thinned by a factor of two.



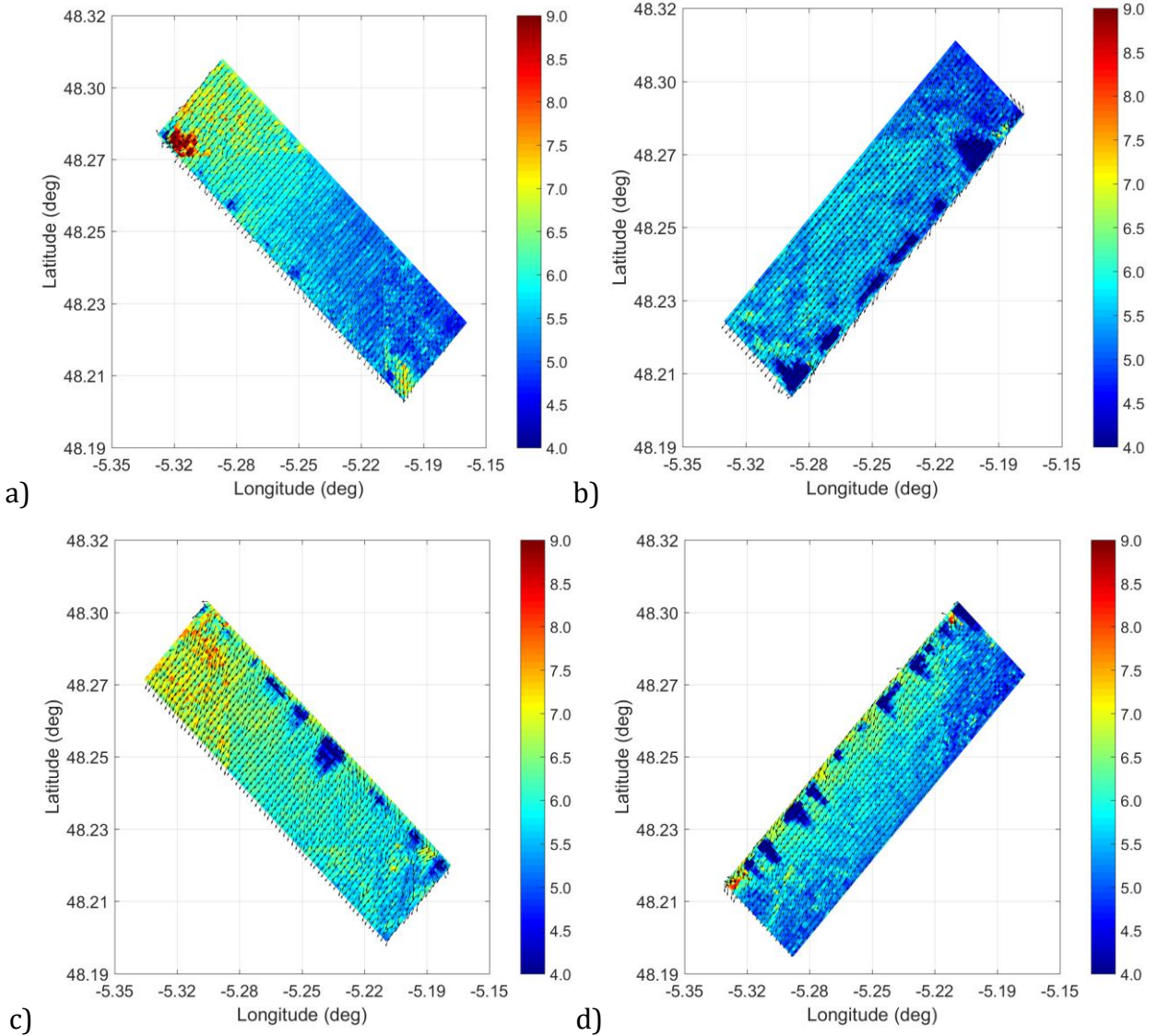


Figure 23. Same as Figure 22 but for legs #8-11 (a-d, respectively).



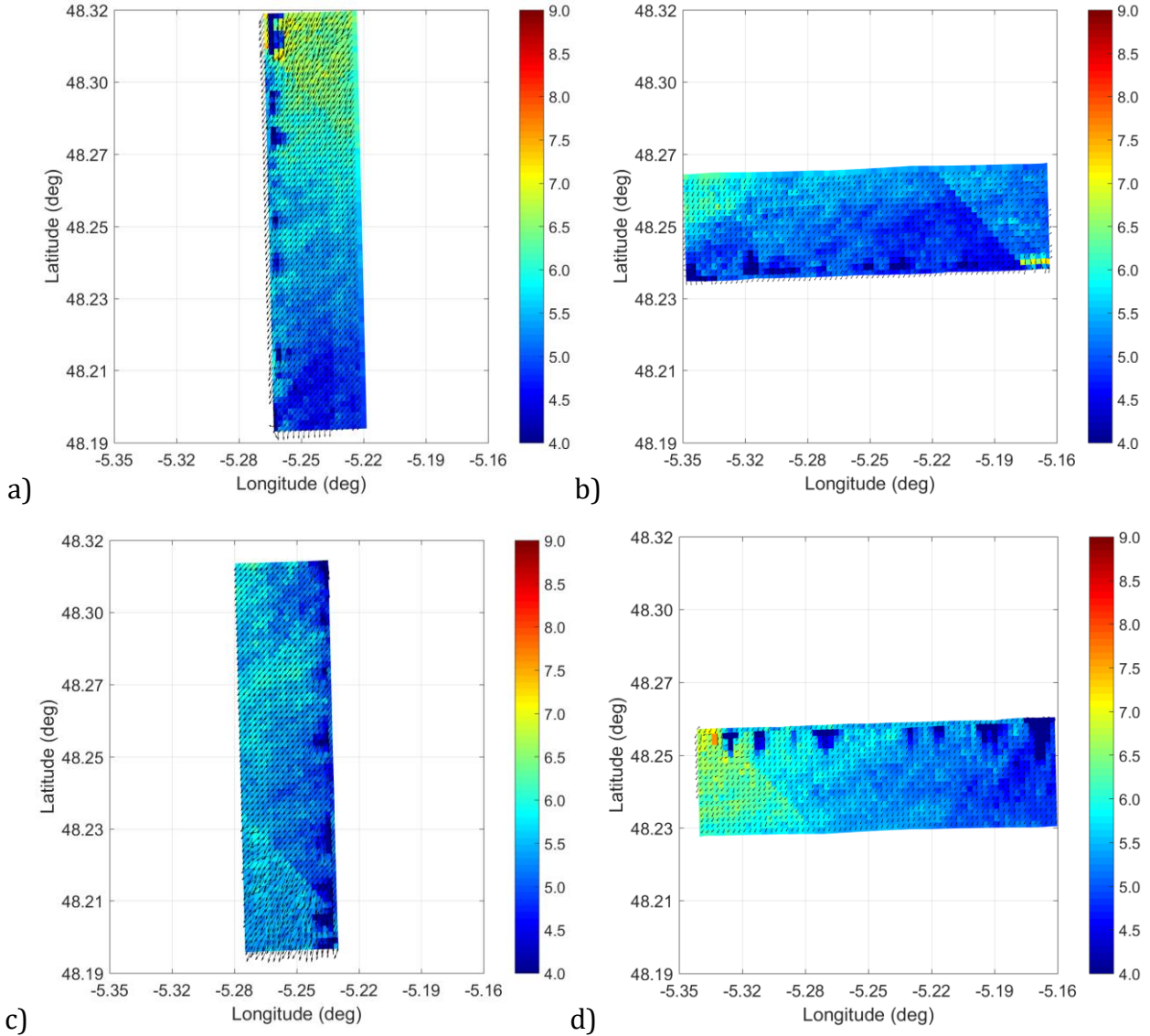


Figure 24. OSCAR-retrieved winds at 200-m resolution for the star-pattern flight legs #4-7 (a-d, respectively) on May 22<sup>nd</sup> (see Figure 3 for reference on leg numbering). For the sake of illustration, the arrows are thinned by a factor of two.

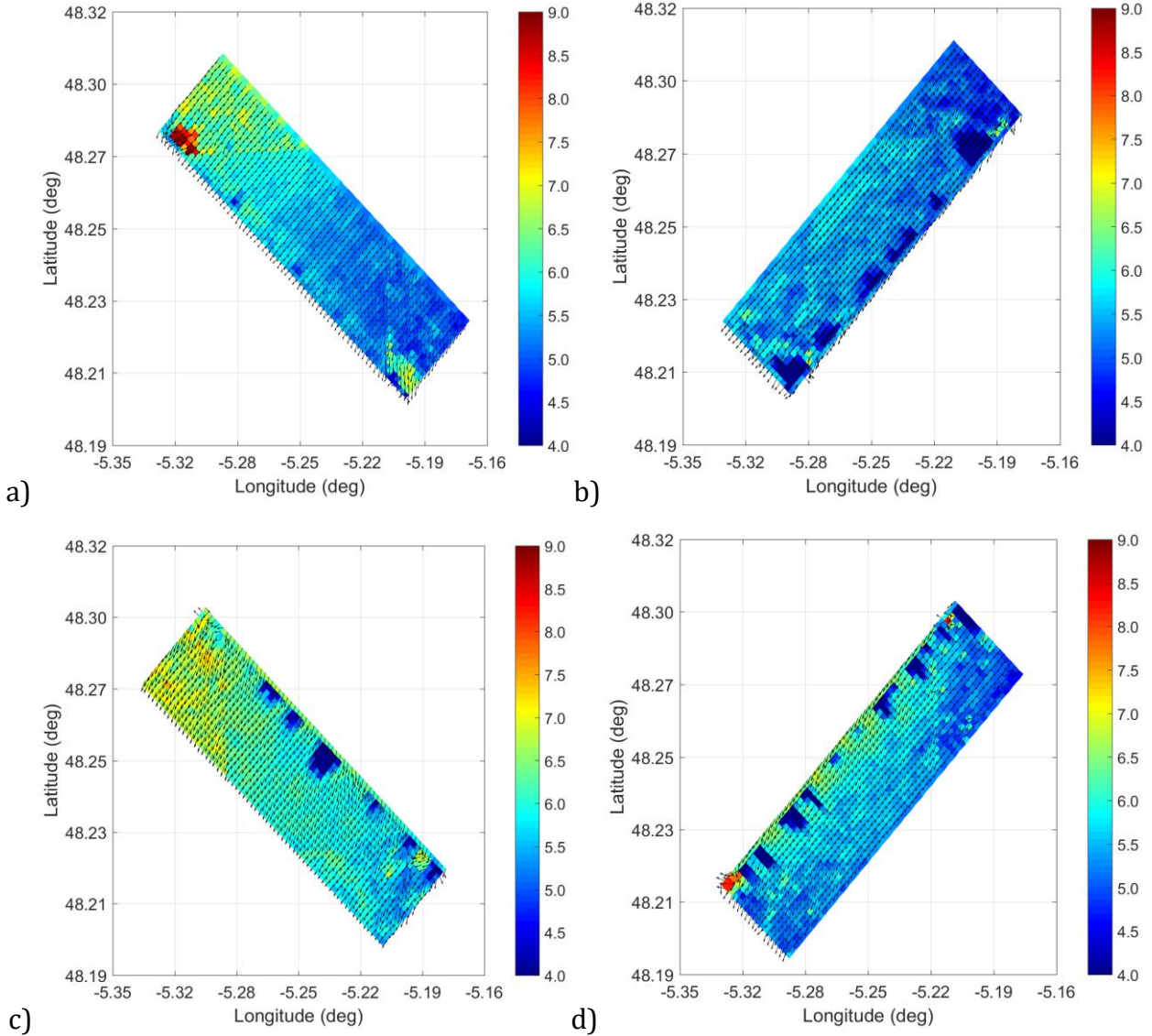


Figure 25. Same as Figure 24 but for legs #8-11 (a-d, respectively).

As already reported in Section 2.4, the OSCAR aft beam only operated for leg #2 on May 25<sup>th</sup>. While PenWP can actually run on 2-beam (e.g., fore and mid) only mode, the quality of the retrievals is far from optimal [Portabella, 2002]. As such, we have attempted to calibrate the aft beam using the retrieved winds from the alternative OC applied to the fore and mid beams (see Section 4.2.2). Indeed, such retrieved wind for leg #2 can be used as input to OC (such that a calibration curve can be derived for the mentioned beam). Then, the fore, mid, and aft beams are calibrated using their corresponding calibration factors prior to wind retrieval.

Figure 26 shows the OSCAR-derived wind speed map for leg #2 on May 25<sup>th</sup>, at 104-m (left) and 200-m (right) resolution. Again, as expected, the 104-m map shows more granularity than the 200-m map. While the patterns are very similar, there is more spatial detail in the 104-m map. Note also the presence of some image and/or retrieval artifacts, e.g., the along-track geometric feature in the middle of the swath in Figure 26a or the high-wind feature at the far-range edge of the swath in Figure 26b.

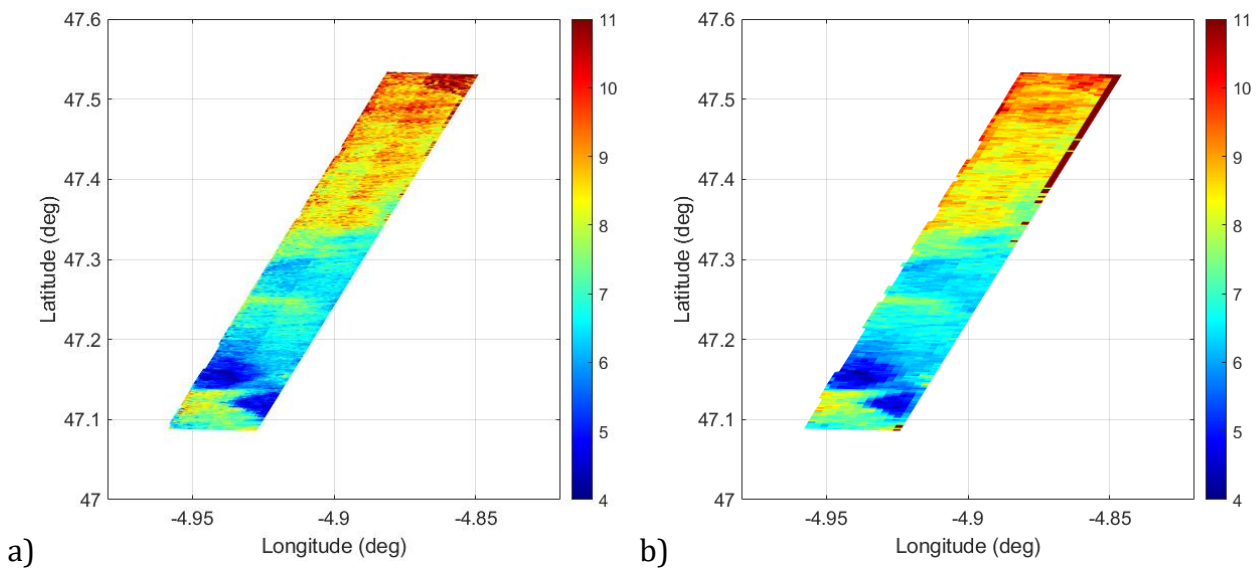


Figure 26. OSCAR-retrieved wind speed at 104-m (left) and 200-m (right) resolution for flight leg #2 on May 25<sup>th</sup> (see Figure 2b for reference on leg numbering). The wind arrows are ignored to better emphasize the wind speed patterns.

## 5.2 Intercomparison with ECMWF and ASCAT winds

Figures 27 and 28 show the intercomparison of the OSCAR-retrieved winds versus ECMWF on May 22<sup>nd</sup> and ASCAT on May 25<sup>th</sup>, at both 104-m and 200-m resolution.

Note the generally narrow vertical distributions of the scatterplots, indicating, on the one hand, the difference in spatial resolution between the relatively high-resolution OSCAR winds and the relatively-low resolution ASCAT and ECMWF winds, and on the other hand, the likely presence of substantial noise in the OSCAR acquisitions. Also note that, in general, the scatter around the diagonal is smaller for the OSCAR 200-m resolution winds than for the 104-m resolution winds, indicating the expected noise reduction by NRCS integration (averaging).

However, for leg #2 on May 25<sup>th</sup> (Figure 28), the standard deviation (STD) values (see legend) indicate otherwise, i.e., the 200-m resolution shows larger values than the 104-m. It seems that the presence of outliers is more dominant in the 200-m resolution winds (Figures 28b & 28d) than in the 104-m resolution winds (Figures 28a & 28c), as also corroborated by visual inspection of the OSCAR-derived wind maps in Figure 26. This needs further investigation.

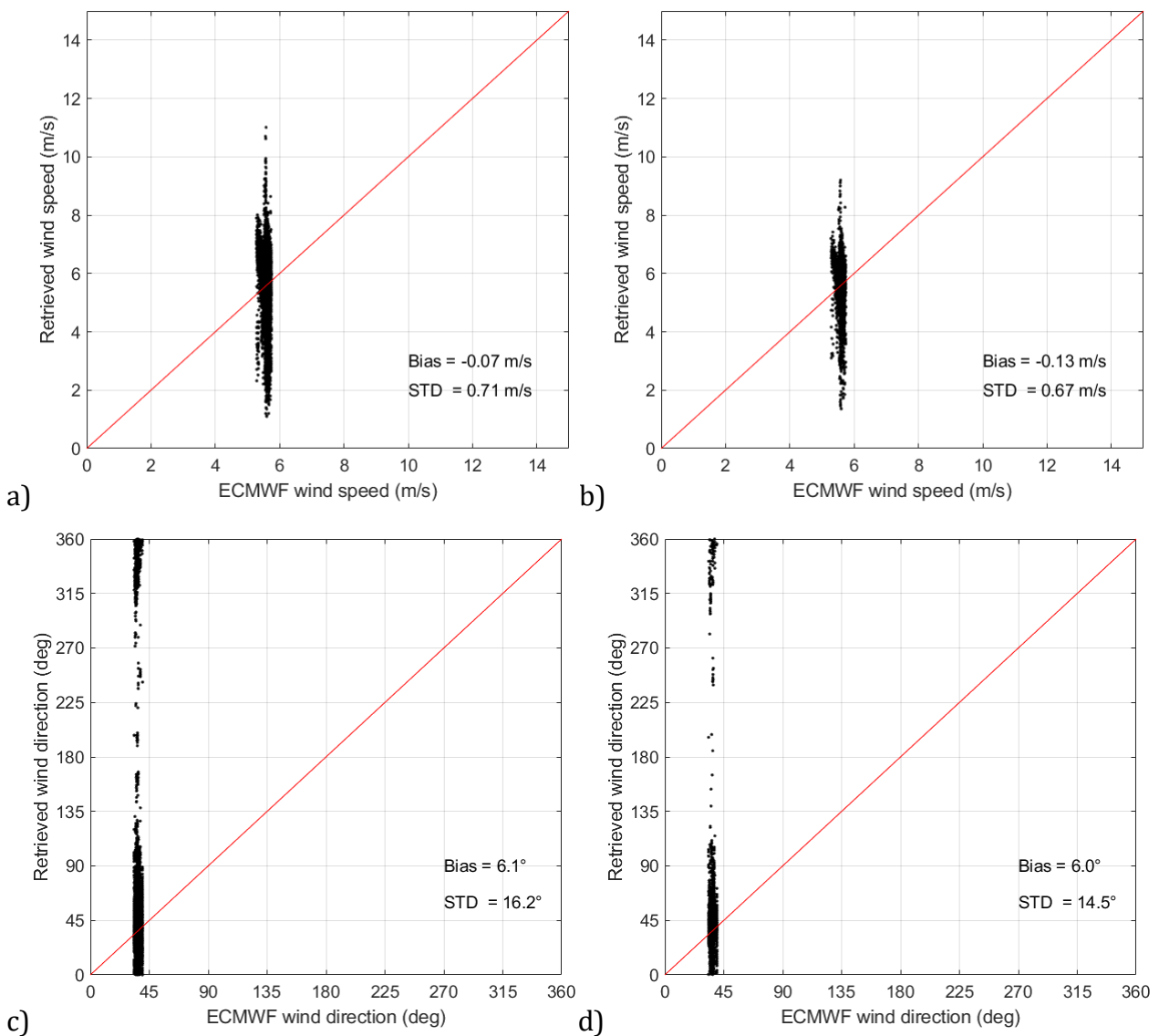


Figure 27. Scatterplots of OSCAR-retrieved versus ECMWF wind speeds (top) and directions (bottom), at 104-m (left) and 200-m (right) resolution for the star pattern flight legs #4-11 on May 22<sup>nd</sup>. The mean (bias) and standard deviation (STD) of the OSCAR vs ECMWF differences are shown in the legend.

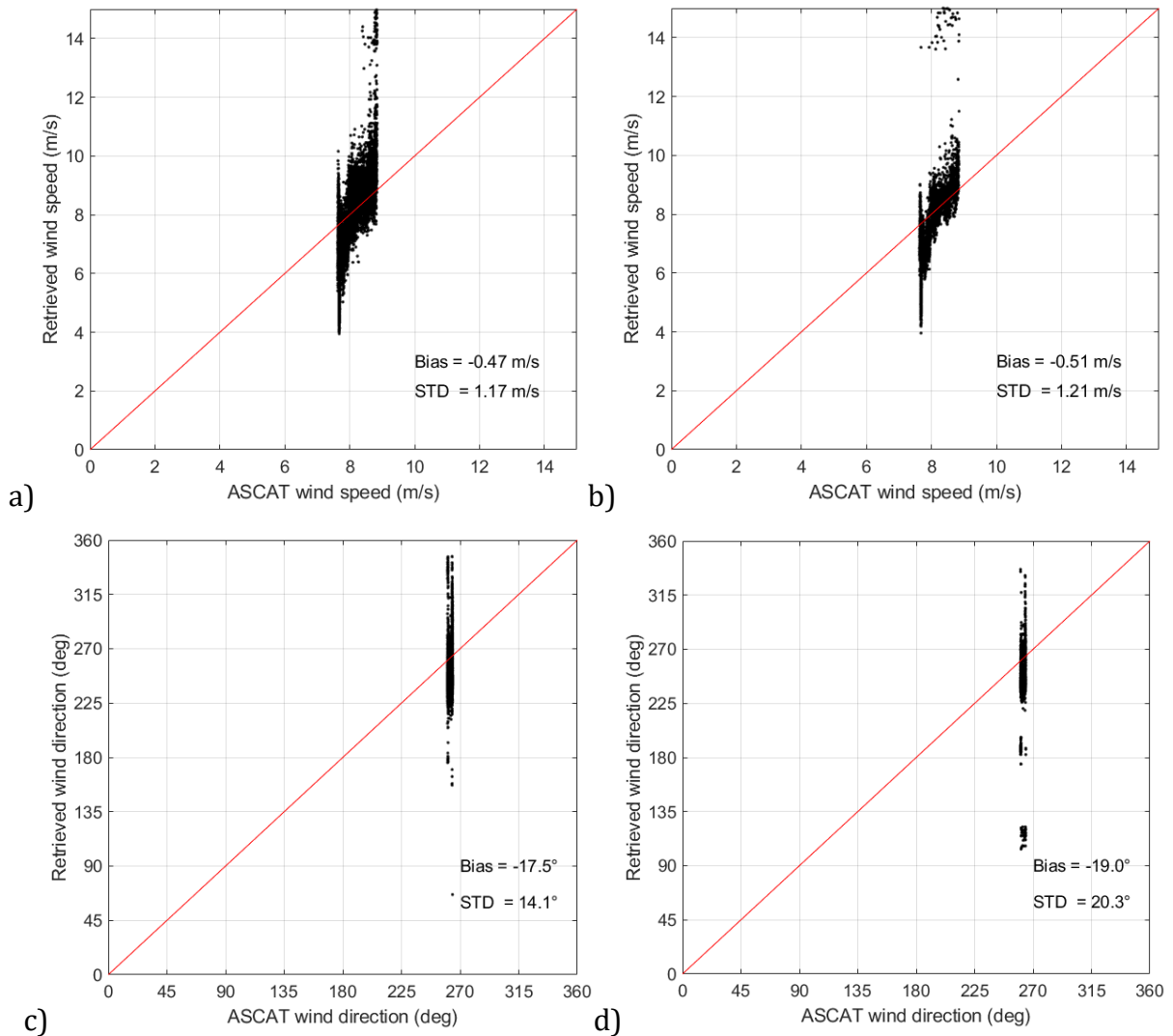


Figure 28. Scatterplots of OSCAR-retrieved versus ASCAT wind speeds (top) and directions (bottom), at 104-m (left) and 200-m (right) resolution for flight leg #2 on May 25<sup>th</sup>. The mean (bias) and standard deviation (STD) of the OSCAR vs ASCAT differences are shown in the legend.

Table 3 summarizes the intercomparison results between the OSCAR-derived and the reference (ECMWF, ASCAT) winds. Note that since the star pattern is too close to the coast, there are no ASCAT (valid) winds available for comparison on May 22<sup>nd</sup>.

Note that, as expected, OSCAR-derived winds better agree with ASCAT winds than with ECMWF winds, since the former resolves smaller scales than the latter. Note also that the statistical scores show substantially larger values for leg #2 on May 25<sup>th</sup> than for the star pattern flight on May 22<sup>nd</sup>. This could be due to several reasons. On the one hand, the mean winds and their variability (see e.g. the larger wind speed range on the x-axis of Figures 28a

& 28b w.r.t. Figures 27a & 27b) are significantly larger on May 25<sup>th</sup>. Also note the substantially larger bias in the wind speed and (notably) the wind direction on May 25<sup>th</sup> than on May 22<sup>nd</sup>. Indeed, the calibration of the aft beam on May 25<sup>th</sup> is less robust since it's only done for one leg. However, looking at the differences in the calibration curves for the fore and aft beams (see Figure 21), it is concluded that the instrument behavior significantly changed on May 25<sup>th</sup> w.r.t. May 22<sup>nd</sup>. Therefore, it is recommended to further investigate instrument anomalies on May 25<sup>th</sup> before any further wind validation is carried out.

*Table 3. Bias, standard deviation (STD), and vector root-mean square (VRMS) of the differences between OSCAR-derived and reference (ECMWF or ASCAT) winds. The OSCAR resolution, reference wind source and flight date are specified in the first column.*

Experiments (Resolution, Reference, Date)	Speed (m/s)		Direction (°)		VRMS (m/s)
	Bias	STD	Bias	STD	
<b>104 vs ECMWF, May 22<sup>nd</sup></b>	-0.07	0.71	6.1	16.2	1.71
<b>200 vs ECMWF, May 22<sup>nd</sup></b>	-0.13	0.67	6.0	14.5	1.55
<b>104 VS ECMWF, May 25<sup>th</sup></b>	-0.66	1.29	-23.0	16.6	4.19
<b>200 VS ECMWF, May 25<sup>th</sup></b>	-0.78	1.18	-24.5	23.6	4.41
<b>104 VS ASCAT, May 25<sup>th</sup></b>	-0.47	1.17	-17.5	14.1	3.28
<b>200 VS ASCAT, May 25<sup>th</sup></b>	-0.51	1.21	-19.0	20.3	3.66

## 6 SUMMARY AND CONCLUSIONS

In this study, a summary of the OSCAR NRCS noise characterization and calibration efforts, as well as of the OSCAR wind retrieval development is presented, based on the data acquired during the SEASTARex campaign near Brittany, in particular those acquisitions from the flights on May 22<sup>nd</sup> and 25<sup>th</sup>, 2022.

Two empirical approaches to characterize measurement noise ( $K_p$ ) are implemented, one based on the exponential behavior of a chi-square distribution of  $\sigma_{os}$ , while the second is based on a K-distribution which accounts for non-Rayleigh contributions due to speckle noise, which is more suitable for SAR systems like OSCAR. Indeed, the K-distribution model better fits the OSCAR  $\sigma_o$  distribution, showing its potential for noise characterization of SAR systems like OSCAR. It is also found that OSCAR slave images are biased low (around 0.9-1 dB) with respect



to the master images, while the averaged  $\sigma_0$ s show an unexpected behavior with respect to incidence angle.

Then, the numerical ocean calibration (OC) method is applied to calibrate OSCAR  $\sigma_0$ s, using the (Ku-band) NSCAT-4DS GMF and collocated auxiliary winds from ECMWF and ASCAT. The calibration coefficients show a strong incidence angle dependence (of more than 10 dB), indicating either an instrument anomaly, a problem with the SAR image reconstruction/focusing, or a poor (land-based) calibration. Also, a large spread (of up to 4 dB) in the leg-based calibration curves is observed. An alternative OC which accounts for wind variations from one leg to the next is proposed in order to retrieve a unique, consistent calibration curve. The alternative OC shows differences of up to 5.5 dB between single calibration curves obtained for two different days (May 22<sup>nd</sup> and 25<sup>th</sup>). Moreover, while the fore beam curves for both days are parallel, those of the mid beam are not, indicating that the incidence angle behavior of the instrument changed from one flight (day) to the next. Further investigation is needed at Level 1 in order understand the causes of these instrumental anomalies.

Finally, the NWP SAF PenWP has been adapted to retrieve sea surface winds from OSCAR acquisitions. The retrieved calibration coefficients from the alternative OC are applied to OSCAR NRCS prior to wind inversion, while an interface between OSCAR L1 data and PenWP is created to allow wind retrievals at different WVC grid sizes. The PenWP inversion can handle multiple  $\sigma_0$ s per beam or just one integrated (averaged)  $\sigma_0$  per beam. Indeed, the variance of the retrieved wind fields is reduced with increasing WVC grid size, indicating a reduction of both noise (Kp) and spatial resolution (i.e., reduced small-scale variance). Similarly, the agreement between OSCAR-derived winds and collocated ECMWF and ASCAT winds increases with increasing WVC grid size, as expected. The exception is leg #2 on May 25<sup>th</sup>, which shows a more dominant role of the outliers in the statistical scores for the relatively larger WVC grid size. At last, the OSCAR-derived fields show a few artifacts linked to viewing geometry and to short-range anomalous behavior of the instrument, which need further attention.

## 7 REFERENCES

- [Fisher, 1972] R. E. Fischer, "Standard Deviation of Scatterometer Measurements from Space," in *IEEE Transactions on Geoscience Electronics*, vol. 10, no. 2, pp. 106-113, doi: 10.1109/TGE.1972.271276, 1972.
- [Grieco et al, 2022] Grieco, G.; Stoffelen, A.; Verhoef, A.; Vogelzang, J.; Portabella, M. Analysis of Data-Derived SeaWinds Normalized Radar Cross-Section Noise. *Remote Sens.*, 14, 5444, <https://doi.org/10.3390/rs14215444>, 2022.



- [Jakeman and Pusey, 1976] E. Jakeman and P. Pusey, "A model for non-Rayleigh sea echo," in *IEEE Transactions on Antennas and Propagation*, vol. 24, no. 6, pp. 806-814, doi: 10.1109/TAP.1976.1141451, 1976.
- [Lin et al., 2013] Lin, W., Portabella, M., Stoffelen, A., and Verhoef, A., "On the characteristics of ASCAT wind direction ambiguities," *Atmos. Meas. Tech.*, **6**, pp. 1053-1060, <https://doi.org/10.5194/amt-6-1053-2013>, 2013.
- [Lin et al., 2016] W. Lin, M. Portabella, A. Stoffelen, J. Vogelzang, A. Verhoef, "On Mesoscale Analysis and ASCAT Ambiguity Removal," *Quarterly Journal of the Royal Meteorological Society*, vol. 142, no. 697, pp. 1745-1756, 2016.
- [Migliaccio et al, 2019] M. Migliaccio, L. Huang and A. Buono, "SAR Speckle Dependence on Ocean Surface Wind Field," in *IEEE Transactions on Geoscience and Remote Sensing*, vol. 57, no. 8, pp. 5447-5455, doi: 10.1109/TGRS.2019.2899491, 2019.
- [Portabella, 2002] Portabella, M., "Wind field retrieval from satellite radar systems," PhD Thesis, University of Barcelona (UB), Barcelona, Spain, <https://digital.csic.es/handle/10261/154354>, 2002.
- [Portabella and Stoffelen 2002] Portabella, M., and Stoffelen, A., "Characterization of residual information for SeaWinds quality control," *IEEE Trans. Geosci. Rem. Sens.*, **40** (12), pp. 2747-2759, <https://doi.org/10.1109/TGRS.2002.807750>, 2002.
- [Stoffelen and Portabella, 2006] Stoffelen, A., and Portabella, M., "On Bayesian scatterometer wind inversion," *IEEE Trans. Geosci. Rem. Sens.*, **44** (6), pp. 1523-1533, <https://doi.org/10.1109/TGRS.2005.862502>, 2006.
- [Verspeek et al., 2010] Verspeek, J., Stoffelen, A., Portabella, M., Bonekamp, H., Anderson, C., and Figa Saldaña, J., "Validation and calibration of ASCAT data using ocean backscatter and CMOD5.n," *IEEE Trans. Geosci. Rem. Sens.*, <https://doi.org/10.1109/TGRS.2009.2027896>, 48 (1), pp. 386-395, 2010.
- [Verspeek et al., 2021] Verspeek, J., Stoffelen, A., Verhoef, A., and Portabella, M., "Improved ASCAT wind retrieval using NWP ocean calibration," *IEEE Trans. Geosci. Rem. Sens.*, **50** (7), pp. 2488-2494, <https://doi.org/10.1109/TGRS.2011.2180730>, 2012.
- [Vogelzang et al., 2011] [Vogelzang et al., 2011] J. Vogelzang, A. Stoffelen, A. Verhoef, and J. Figa-Saldaña, "On the quality of high-resolution scatterometer winds," *J. Geophys. Res., Oceans*, vol. 116, no. C10, pp. 1-14, 2011.
- [Wang et al., 2017] Wang, Z. et al., "SST Dependence of Ku- and C-Band Backscatter Measurements," in *IEEE Journal of Selected Topics in Applied Earth Observations and Remote Sensing*, 10 (5), pp. 2135-2146, doi: 10.1109/JSTARS.2016.2600749, 2017.

# **ANNEX J) DATA ACQUISITION REPORT FOR THE MEDITERRANEAN CAMPAIGN**

# SeaSTARex-MED

## Data Acquisition Report

**Reference Code** : : MS-SeaSTARexMED-DAR  
**Issue** : : 6.0  
**Date** : : 28 Feb 2024

MetaSensing BV  
Schipholweg 55  
2316 ZL Leiden , The Netherlands  
Tel: +31 71 751 5960  
Email: info@metasensing.com

Document change log			
Issue	Change	Date	Author
1.0	First issue, system description, internal	20/06/2023	KM
2.0	Text	20/09/2023	KM
3.0	Acquisition Log	26/10/2023	KM
4.0	Navigation data, Data check, Review and Release	27/02/2024	KM
5.0	Correction in table 9 and Release	27/02/2024	KM
6.0	Correction related to Adrien comments and Release	28/02/2024	KM

# Table of contents

1	Introduction .....	4
2	System setup .....	5
2.1	Lever arms .....	8
2.2	Channel Mapping and Configuration.....	9
2.3	Corners.....	10
3	Acquisition Log .....	11
4	Data Check .....	17
4.1	Navigation Data .....	17
4.2	Raw Data .....	20
4.3	Processed Data.....	23
5	Conclusions .....	27
6	References .....	27

# 1 Introduction

This document is the Data Acquisition Report - DAR for the SeaSTARex-Med airborne SAR data campaign. This DAR provides the details of the airborne SAR data collection with the OSCAR (Ocean Surface Current Airborne Radar) instrument over the Ocean next to Mallorca Island (Spain) and verifies the quality of the acquired data. The data collection campaign was executed within the ESA-SeaSTARex project framework. The image below shows the flown tracks and imaged areas during campaign on 05, 07 and 08 May 2023.

The OSCAR instrument is installed inside the aircraft belly pod, and it is a fully operational instrument. The OSCAR instrument is a gimbal-based interferometric Ku-band SAR system developed and built by MetaSensing within the framework of a European Space Agency funded project (Ocean Surface Currents Airborne Radar demonstrator). The OSCAR system is tailored to the observations of the ocean surface motion and retrieval of wind. The OSCAR demonstrator instrument is developed with the observation parameters which directly relate to a potential satellite mission (SeaSTAR) for mesoscale measurements of ocean surface currents in the open-ocean and coastal regions [1, 2].

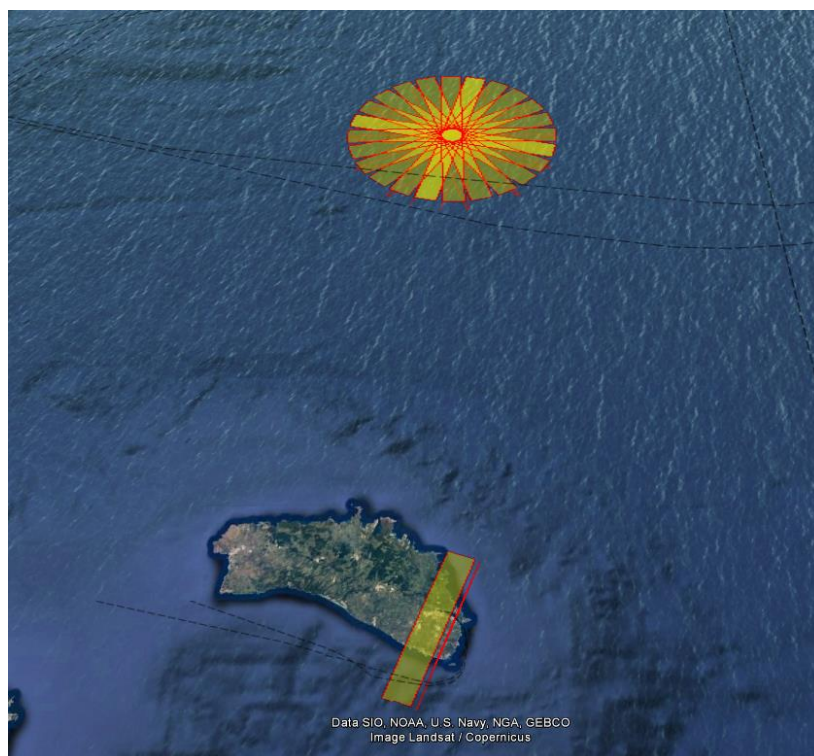


*Figure 1 – flown tracks and imaged areas during SeaSTARex-Med campaign over Mallorca Island (Spain), on 05, 07 and 08 May 2023.*

## 2 System setup

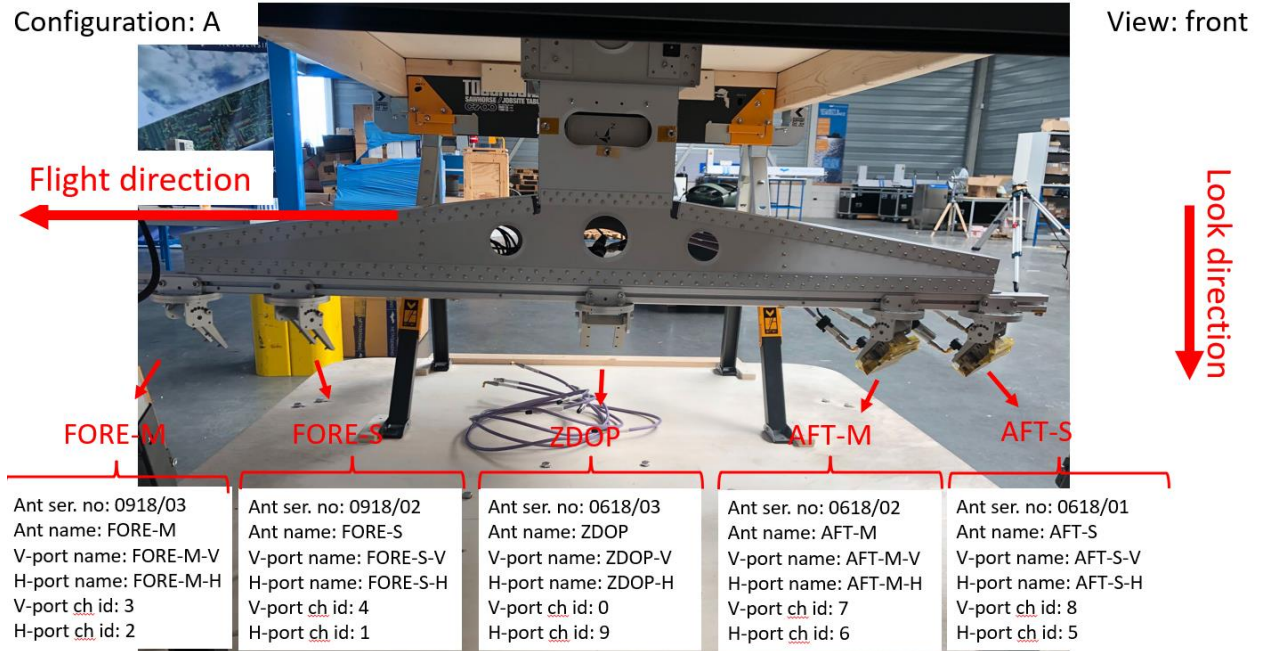
Figure 2 shows the OSCAR instrument installation from inside of the aircraft (a) and how the antennas are set-up inside the POD (b). Note that only V-pol channels were enabled during the SeaSTARex Medt campaign.



(a): the OSCAR instrument installed in the cabin

Configuration: A

View: front



(b)

Figure 2: a) HW installation on-board the aircraft and (b) Antenna installation in the POD.



Next a drawing with the position configurations of the antennas and GSM4000 navigation system inside of the aircraft

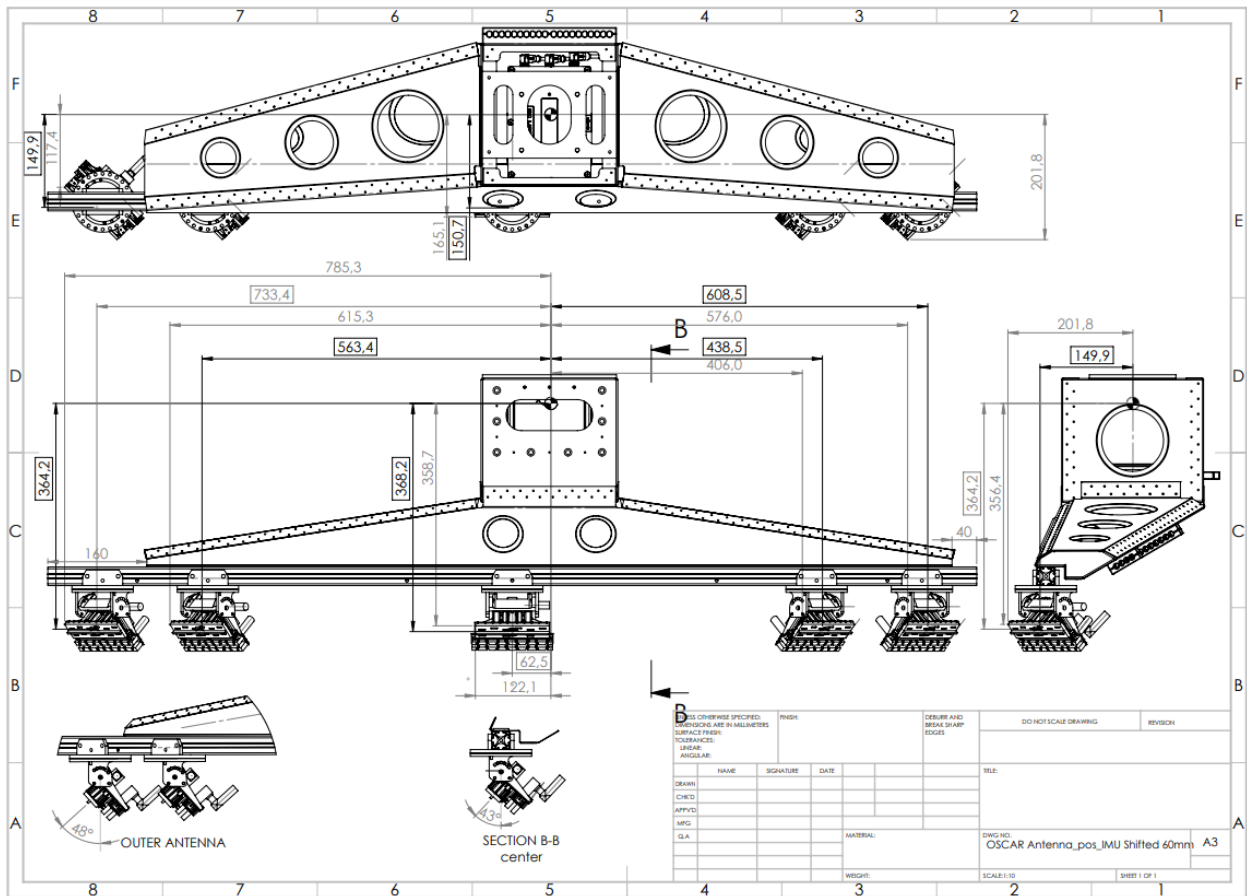


Figure 3: Measurements (units mm) of the X,Y,Z offsets, used to compute the RF antenna lever arms from the IMU reference. The mechanical reference point taken on the antennas is indicated with a red circle.

Next, the position of the center of rotation of the GSM4000 mount is given (see Figure 4 and Figure 5).

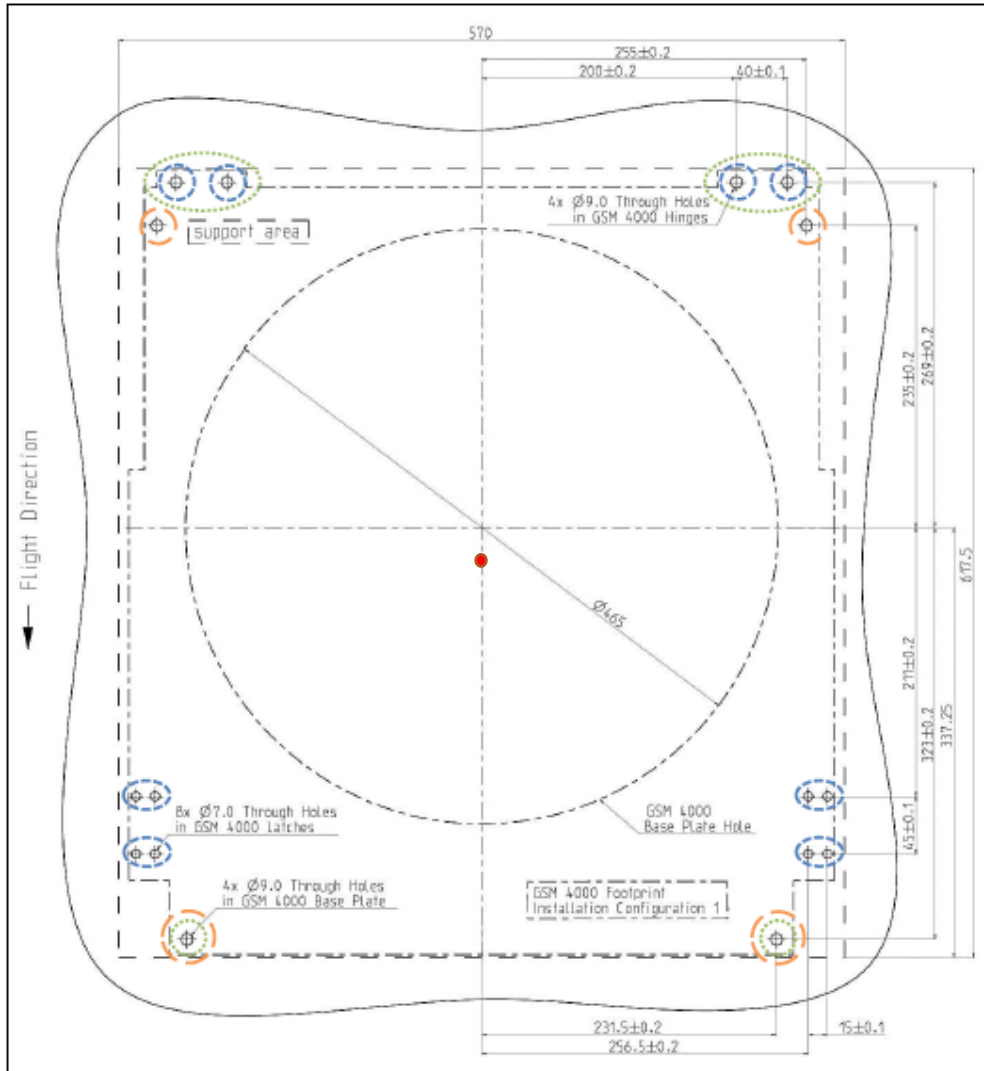


Figure 4: Top view of the mount. The center of rotation is located on the (vertical) axis passing through the center of the ring (red dot above).

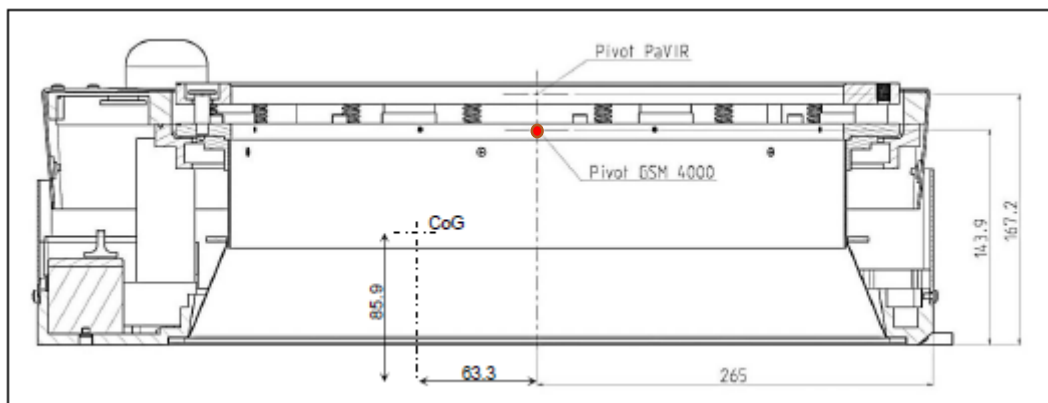


Figure 5: Side view of the mount. The center of rotation is located at the position (red dot) indicated with "Pivot GSM 4000", i.e., 143.9mm (we can assume 144mm) above the floor.

## 2.1 Lever arms

From the system set-up drawings, we derive the lever-arms and rotations below. The distances are relative to a cartesian coordinate system with the IMU center in the origin and the x-axis points of the IMU center towards the right wing of the plane, the y-axis points toward the nose of the plane, and the z-axis points upward to the ceiling of the plane. The lever arms are given in the next table. The RF connector was used as references point for the antennas.

Table 1: Look angle of the antennas.

Antenna name	Angle description	Angle value
<b>AFT-M-V and AFT-S-V</b>	Look angle (antenna broadside pointing) from nadir	48°
	Azimuth rotation	-45°
<b>FORE-M-V and FORE-S-V</b>	Look angle (antenna broadside pointing) from nadir	48°
	Azimuth rotation	+45°
<b>0-DOP-V</b>	Look angle (antenna broadside pointing) from nadir	43°
	Azimuth rotation	0°

Table 2: RF and GPS antennas lever arms from mechanical reference to IMU phase center [m].

Distances [m] measured during the campaign on 17/02/2022 also applies to Med						
Lever arms between IMU and antennas [m]	AFT		FORE		0 - DOP	GPS
Antenna	M	S	M	S		
<b>ΔX</b>	-0.1499	-0.1499	-0.1499	-0.1499	-0.157	-0.090
<b>ΔY</b>	-0.4385	-0.6085	+0.7334	+0.5634	0.0625	0.542
<b>ΔZ</b>	-0.3642	-0.3642	-0.3642	-0.3642	-0.3682	+1.524

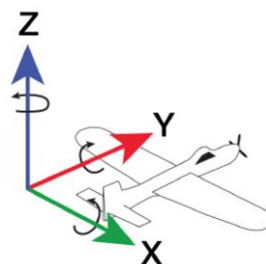


Figure 6: Reference system for the lever arms.

The geometrical center of the IMU enclosure is located on the vertical axis passing through the center of the ring of the GSM4000 mount. Therefore, the offsets of the GSM4000 center of rotation with respect to the IMU origin and reference system is given in Table 3.

*Table 3: Lever arm of the GSM4000 center of rotation from the IMU reference system [m].*

<b>Lever arms between IMU and GSM 4000 pivot [m]</b>	
<b><math>\Delta X</math></b>	-0.0005
<b><math>\Delta Y</math></b>	+0.0025
<b><math>\Delta Z</math></b>	-0.2624

## 2.2 Channel Mapping and Configuration

The below table reports the channel numbers and configuration occurred during the SeaSTARex-Med campaign, according to the OSCAR installation.

*Table 4: Brest Campaign channel mapping.*

Channel number	Configuration	Description
00	0DOP-V	Zero-Doppler Vertical Polarization
33	FORE-M-V	Fore view – Master – Vertical Polarization
34	FORE-S-V	Fore view – Slave – Vertical Polarization
77	AFT-M-V	Aft view – Master – Vertical Polarization
78	AFT-S-V	Aft view – Slave – Vertical Polarization

## 2.3 Corners

Below the corner reflectors location is shown on the Google map. The following table reports the corner reflectors location, radar cross section (RCS) and the description of installation in the field.



Figure 7: Position of the corner reflectors with naming.

Table 5: Position and orientation of the deployed trihedral corner reflectors.

CR#	Type	Length [m]	RCS* [dB]	Lat (N) [deg]	Lon I [deg]	Azimuth tilt** [deg]	Elevation tilt *** [deg]	Notes
CRF	Square	0.30	27.92	39.86606,	4.25413	155	7	
CRZ	Square	0.30	27.92	39.892656	4.274708	110	12	
CRB	Square	0.30	27.92	39.86509	4.25384	65	7	

\* if not filled a theoretical number derived from length is used)

\*\* True North

\*\*\* Relative to the ground

### 3 Acquisition Log

This chapter reports all the tracks acquired during the Mediterranean campaign. Each track corresponds to a raw data file identified by the name which originates from the time of acquisition. Please note that the raw data files (listed below) and the corresponding final delivered processed data (listed below and described in the next section) have different filenames because of a time difference of 3min and 45 sec in 05 may; 24 seconds in 07 may; and 37 seconds in 08 may. This is because the ingested data in the OSCAR processor is renamed according to the GPS time, while the raw data filename is based on the instrument internal clock.

The tracks were flown with a flight height of about 3000 m.

*Table 6: List of the deliverable tracks flown on May 5 2023*

Track (Direction [deg])	Raw data name	Processed data name	Issue
<b>Track Cal (020)</b>	20230505T145920	20230505T150255	Off2
<b>Track 1 (013)</b>	20230505T152643	20230505T153018	-
<b>Track 2 (208)</b>	20230505T154041	20230505T154416	-
<b>Track 3 (043)</b>	20230505T155532	20230505T155907	Var1
<b>Track 4 (238)</b>	20230505T160906	20230505T161242	-
<b>Track 5 (073)</b>	20230505T162428	20230505T162803	-
<b>Track 6 (268)</b>	20230505T163822	20230505T164157	-
<b>Track 7 (103)</b>	20230505T165447	20230505T165823	Var2
<b>Track 8 (298)</b>	20230505T170947	20230505T171323	-
<b>Track 9 (133)</b>	20230505T172546	20230505T172922	Var1
<b>Track 10 (328)</b>	20230505T173947	20230505T174322	-
<b>Track 11 (163)</b>	20230505T175441	20230505T175816	-
<b>Track 12 (358)</b>	20230505T180835	20230505T181210	-
<b>Track 13 (193)</b>	20230505T182336	20230505T182711	-
<b>Track 14 (283)</b>	20230505T184749	20230505T185124	-

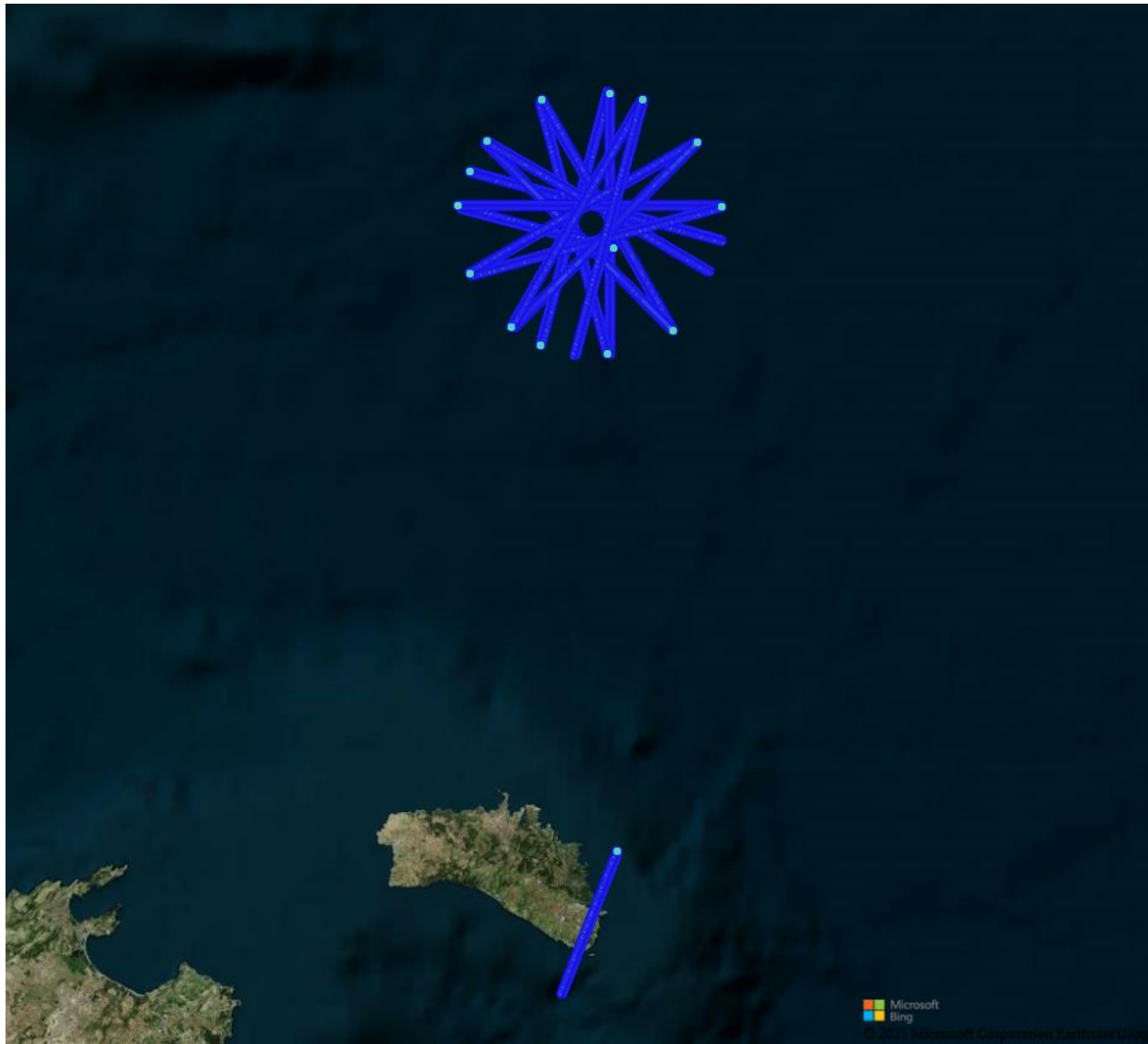


Figure 8: Tracks flown on May 5, 2023.



Table 7: List of the deliverable tracks flown on May 07 2023

Track (Direction [deg])	Raw data name	Processed data name	Issue
<b>Track Cal. (20)</b>	20230507T142623	20230507T142647	-
<b>Track 1 (013)</b>	20230507T145624	20230507T145648	Off1
<b>Track 2 (208)</b>	20230507T151218	20230507T151242	-
<b>Track 3 (043)</b>	20230507T152734	20230507T152758	-
<b>Track 4 (238)</b>	20230507T154403	20230507T154427	-
<b>Track 5 (073)</b>	20230507T155927	20230507T155951	-
<b>Track 6 (268)</b>	20230507T161408	20230507T161432	-
<b>Track 7 (103)</b>	20230507T162924	20230507T162948	-
<b>Track 8 (298)</b>	20230507T164409	20230507T164433	Off1
<b>Track 9 (133)</b>	20230507T165930	20230507T165954	-
<b>Track 10 (328)</b>	20230507T171355	20230507T171419	Off25
<b>Track 11 (163)</b>	20230507T172920	20230507T172944	Off1
<b>Track 12 (358)</b>	20230507T174423	20230507T174447	Off25
<b>Track 13 (193)</b>	20230507T180109	20230507T180133	Var5
<b>Track 14 (283)</b>	20230507T183456	20230507T183521	Var2

- Off consists of an abnormal behavior of the gimbal which results in a heading, roll or pitch offset or trend, although reasonably constant, during the acquisition. Therefore, instead of the planned 0 and 45 deg squints, the antenna is slightly 1 deg off (off1) or 2 degrees off (Off2) and so on. We identified the extreme case off25, gimbal error, resulting in images with ca. 25 degrees squint offset. An example illustrating the problem follows in section 4.0.
- Var consists of an abnormal behavior of the gimbal which results in a heading, roll pitch local variations, usually in small period of time during the acquisition. When the local peaks reach values in the order of 1deg we call Var1, and when reach values in the order of 2 we call Var2 and so on.

Figure 9 shows a spatial overview of all tracks flown on May 07 2023 listed above.



Figure 9: Tracks flown on May 7, 2023.

Table 8: List of the deliverable tracks flown on May 08 2023

Track (Direction [deg])	Raw data name	Processed data name	Issue
<b>Track Cal. (20)</b>	20230508T142652	20230508T142729	-
<b>Track 1 (013)</b>	20230508T145740	20230508T145818	TX/Rx fail *
<b>Track 2 (208)</b>	20230508T151753	20230508T151830	-
<b>Track 3 (043)</b>	20230508T153319	20230508T153356	TX/Rx fail *
<b>Track 4 (238)</b>	20230508T155044	20230508T155121	-
<b>Track 5 (073)</b>	20230508T160509	20230508T160546	-
<b>Track 6 (268)</b>	20230508T163223	20230508T163300	-
<b>Track 7 (103)</b>	20230508T164808	20230508T164845	-
<b>Track 8 (298)</b>	20230508T170312	20230508T170349	-
<b>Track 9 (133)</b>	20230508T172008	20230508T172045	-
<b>Track 10 (328)</b>	20230508T173349	20230508T173426	TX/Rx fail *
<b>Track 11 (163)</b>	20230508T175050	20230508T175127	-
<b>Track 12 (358)</b>	20230508T180400	20230508T180437	TX/Rx fail *
<b>Track 13 (193)</b>	20230508T182140	20230508T182217	-
<b>Track 14 (283)</b>	20230508T184535	20230508T184612	-

- TX/RX problem only Zero-Doppler channel. No receiving signal within the the second half of the tracks. Example illustrating the problem follows in section 4.0.

Figure 10 shows a spatial overview of all tracks flown on May 08 2023 listed above.



Figure 10: Tracks flown on May 8, 2023.

## 4 Data Check

### 4.1 Navigation Data

The navigation data logged during the flights have been post-processed to improve the accuracy of the navigation solution. As a result, 3D positioning and attitude are estimated with an average accuracy of about 1 cm and 0.004°, respectively.

*Table 9: Statistics of the estimated position [m] (left) and attitude [arcmin] (right) accuracy of the navigation data for the OSCAR sensor during the SeaSTARex-Med campaign.*

Day	Position	Attitude
05	Time range: Start: 485707.0 2260 14:55:07.0 05/05/2023 End: 491893.0 2260 16:38:13.0 05/05/2023 Number of samples: 6,187  Stat East North Height 2D 3D Std: 0.00043 0.0006 0.0007 0.0004 0.0007 Rms: 0.00825 0.0100 0.0156 0.0130 0.0203 Avg: 0.00823 0.0100 0.0155 0.0130 0.0203 Max: 0.01695 0.0173 0.0299 0.0242 0.0385 Min: 0.00752 0.0077 0.0126 0.0107 0.0167	Time range: Start: 485707.0 2260 14:55:07.0 05/05/2023 End: 491893.0 2260 16:38:13.0 05/05/2023 Number of samples: 6,187  Stat Roll Pitch Heading/ 2D 3D Std: 0.0319 0.0321 0.0345 0.0452 0.0540 Rms: 0.1360 0.1359 0.1946 0.1923 0.2735 Avg: 0.1322 0.1320 0.1915 0.1869 0.2682 Max: 0.3224 0.3221 0.4427 0.4557 0.6353 Min: 0.0645 0.0625 0.1054 0.0910 0.1421
07	Time range: Start: 49234.0 2261 13:40:34.0 05/07/2023 End: 70638.0 2261 19:37:18.0 05/07/2023 Number of samples: 21,405  Stat East North Height 2D 3D Std: 0.00067 0.00062 0.0011 0.0006 0.0010 Rms: 0.00831 0.00968 0.0155 0.0128 0.0201 Avg: 0.00829 0.00966 0.0154 0.0127 0.0200 Max: 0.03619 0.04092 0.0561 0.0546 0.0783 Min: 0.00657 0.00788 0.0121 0.0103 0.0163	Time range: Start: 49234.0 2261 13:40:34.0 05/07/2023 End: 70638.0 2261 19:37:18.0 05/07/2023 Number of samples: 21,405  Stat Roll Pitch Heading/ 2D 3D Std: 0.0541 0.0549 0.0598 0.0770 0.0934 Rms: 0.1295 0.1295 0.2123 0.1832 0.2804 Avg: 0.1177 0.1173 0.2037 0.1662 0.2644 Max: 6.8204 6.9252 7.0990 9.7199 12.0363 Min: 0.0549 0.0530 0.1263 0.0777 0.1537
08	Time range: Start: 137961.0 2261 14:19:21.0 05/08/2023 End: 157256.0 2261 19:40:56.0 05/08/2023 Number of samples: 19,296  Stat East North Height 2D 3D Std: 0.00063 0.00051 0.0010 0.0005 0.0008 Rms: 0.00830 0.00963 0.0155 0.0127 0.0200 Avg: 0.00827 0.00962 0.0154 0.0127 0.0200 Max: 0.01341 0.01598 0.0250 0.0209 0.0326 Min: 0.00687 0.00870 0.0128 0.0111 0.0177	Time range: Start: 137961.0 2261 14:19:21.0 05/08/2023 End: 157256.0 2261 19:40:56.0 05/08/2023 Number of samples: 19,296  Stat Roll Pitch Heading/ 2D 3D Std: 0.0333 0.0333 0.0383 0.0471 0.0571 Rms: 0.1295 0.1292 0.2098 0.1829 0.2783 Avg: 0.1251 0.1248 0.2063 0.1767 0.2724 Max: 0.2026 0.2024 0.4662 0.2864 0.4947 Min: 0.0551 0.0551 0.1204 0.0779 0.1506

Figure 11 shows the plot of the antenna and attitude dynamic (after considering the lever arms) describing the antenna behavior along the flight. It is important to note that it has been verified that the antenna movement is within expectations, including for the circular flights. Especially, it can be verified that the gimbal worked fine keeping the roll, pitch, and heading (relative to nominal track) basically constant around zero degrees, besides the yaw (due to changes in the velocity). It has been checked that all flights behave similarly.

Some tracks present small drift, offset or variations in the heading(X), roll or pitch. If those are less than 1 degree we did not detect any significant radiometric differences in the final results comparing them with tracks without any small drift or offset. The antenna patterns (delivered within the netcdf files) show that the variations of more than 1 deg in heading or pitch might lead to 1dB to 2dB variation in the sigma-0. In elevation, the antenna patterns show that variation of more than 5 degrees could lead to 1dB variation in the sigma-0. Therefore, we find the acquisition log the tracks in which, there were any offset (off), trend (off) or local variation (var) in the heading or pitch that exceeds 1 degree or in the roll that exceed 5 degrees. Two tracks presented extreme heading offset of -25 (gimbal error). Those cases will be illustrated in the next section.

Note that concerning the phase we observe that such variations greater than 1 degree do not cause any observable phase disturbance since the phase is used to generate single-pass interferograms. After the interferometric beat most of those errors caused by this variation cancel out since they are basically the same in each antenna.

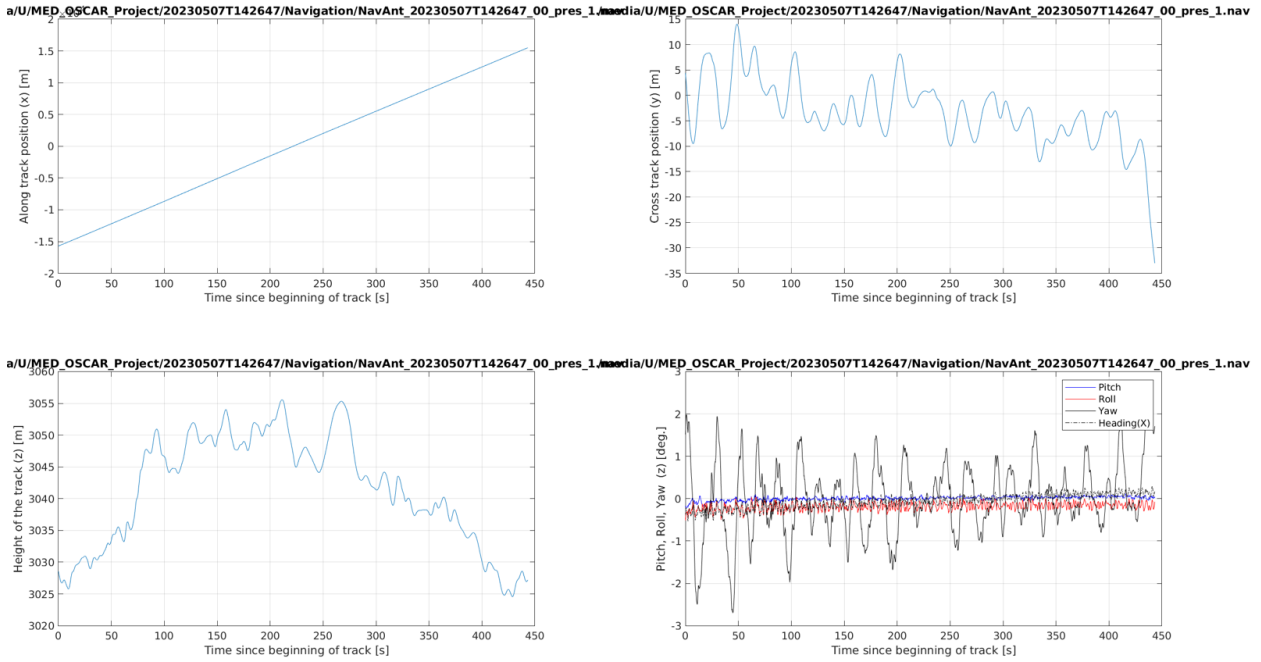


Figure 11: Plots of an antenna position and attitude dynamic from Med data

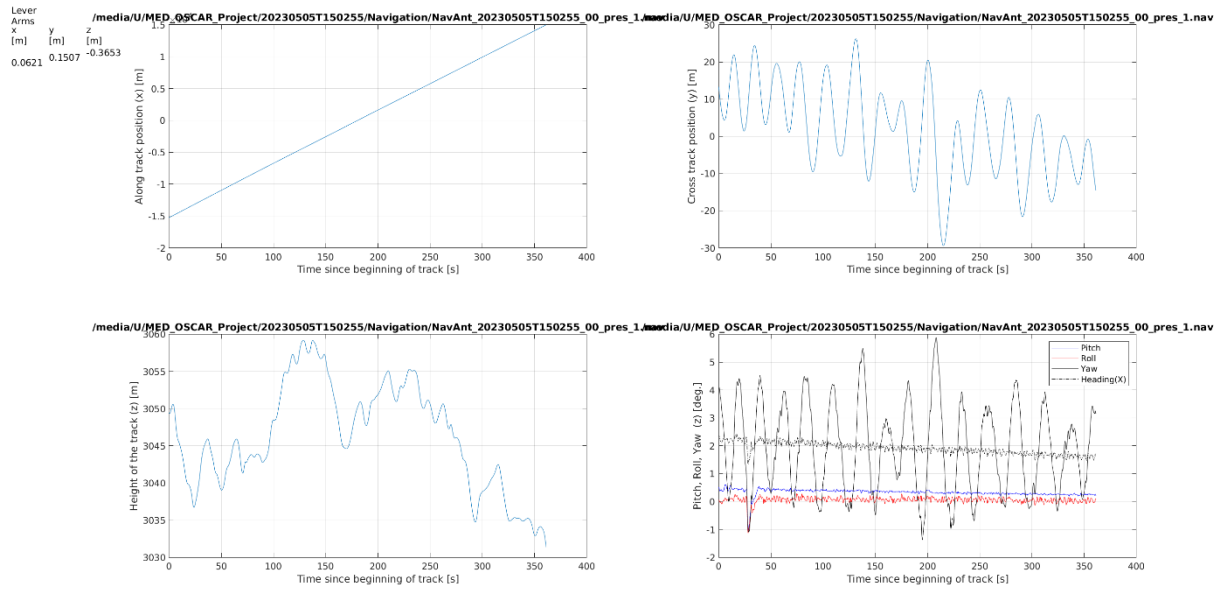


Figure 12: Plots of an antenna position and attitude dynamic from Med data with offset or/and trend issue (off2).



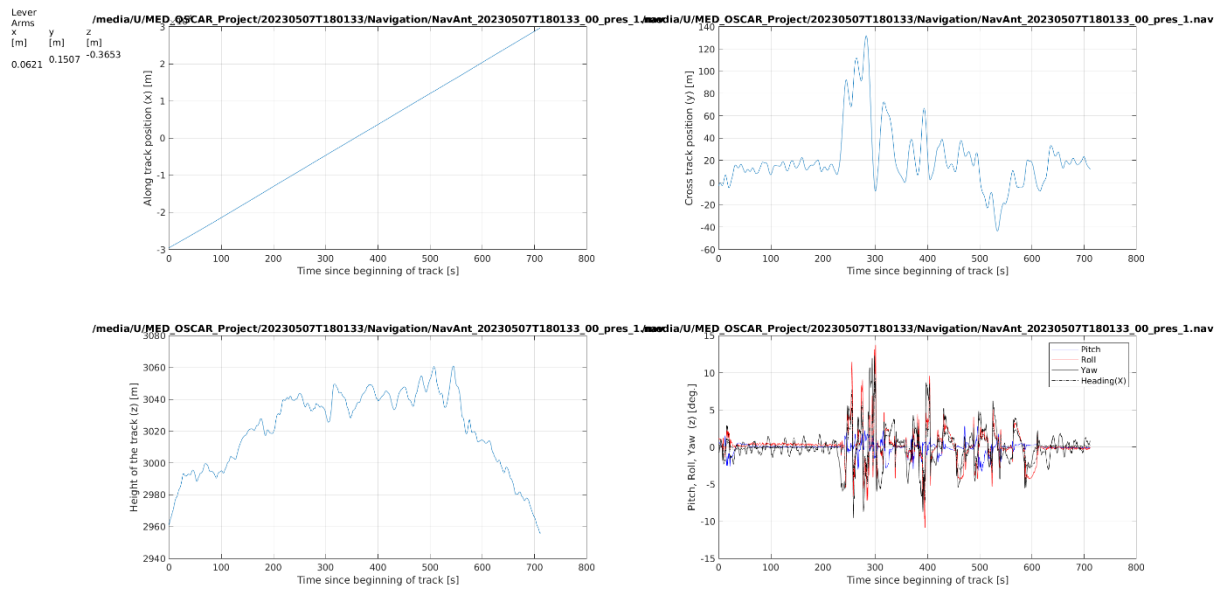
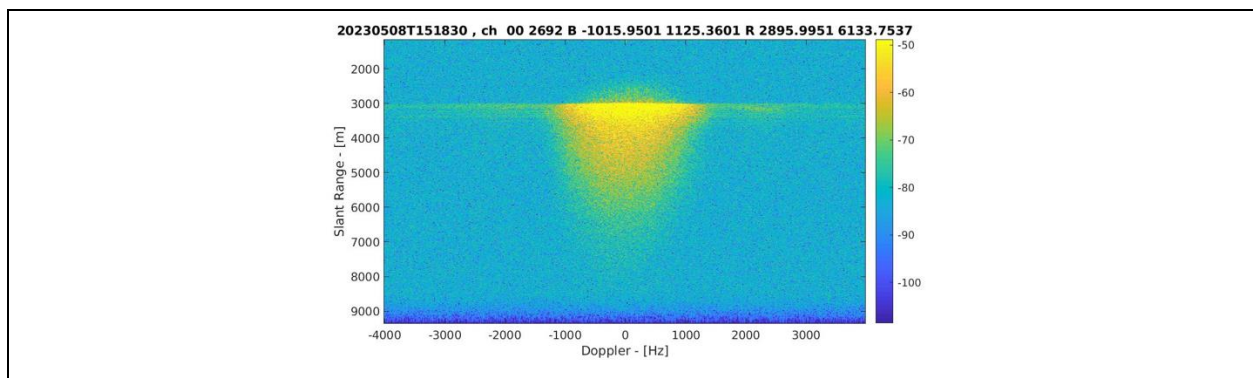


Figure 13: Plots of an antenna position and attitude dynamic from Med data with variation issue (var5)

## 4.2 Raw Data

The plots below confirm that the system was performing nominally, and that data acquired are healthy in most of the data (see acquisition log) . In the plots below, example of a normal, i.e. good SNR, no RFI issues (as expected) We also show the coherence maps and interferograms between channels of the same view.



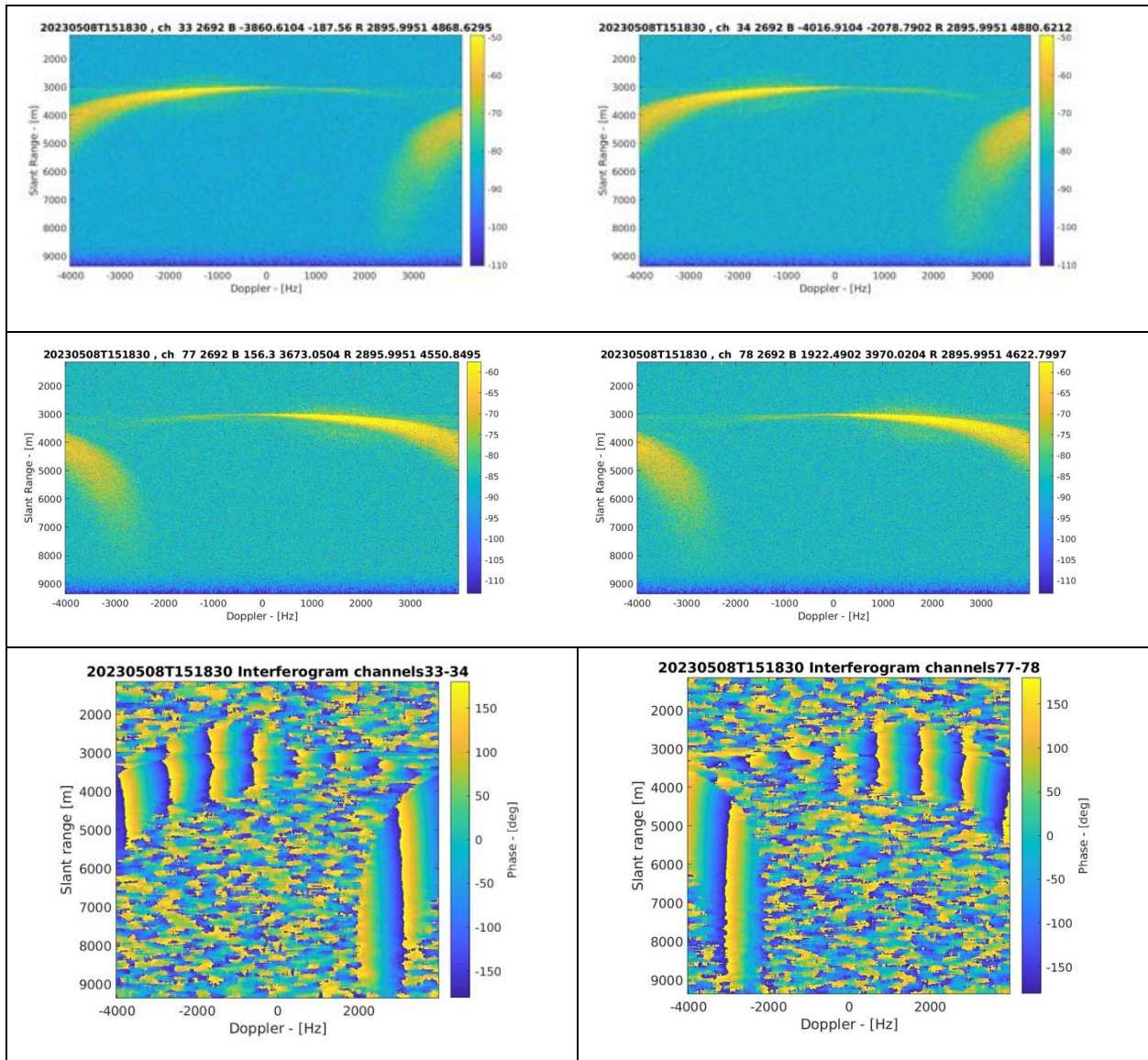


Figure 14: Healthy raw data example

We found TX/RX issue in the Zero-Doppler Channel as noted in the acquisition log show previously. Below we show the detection of this error at raw data level in track number 20230508T145818 of May 08.

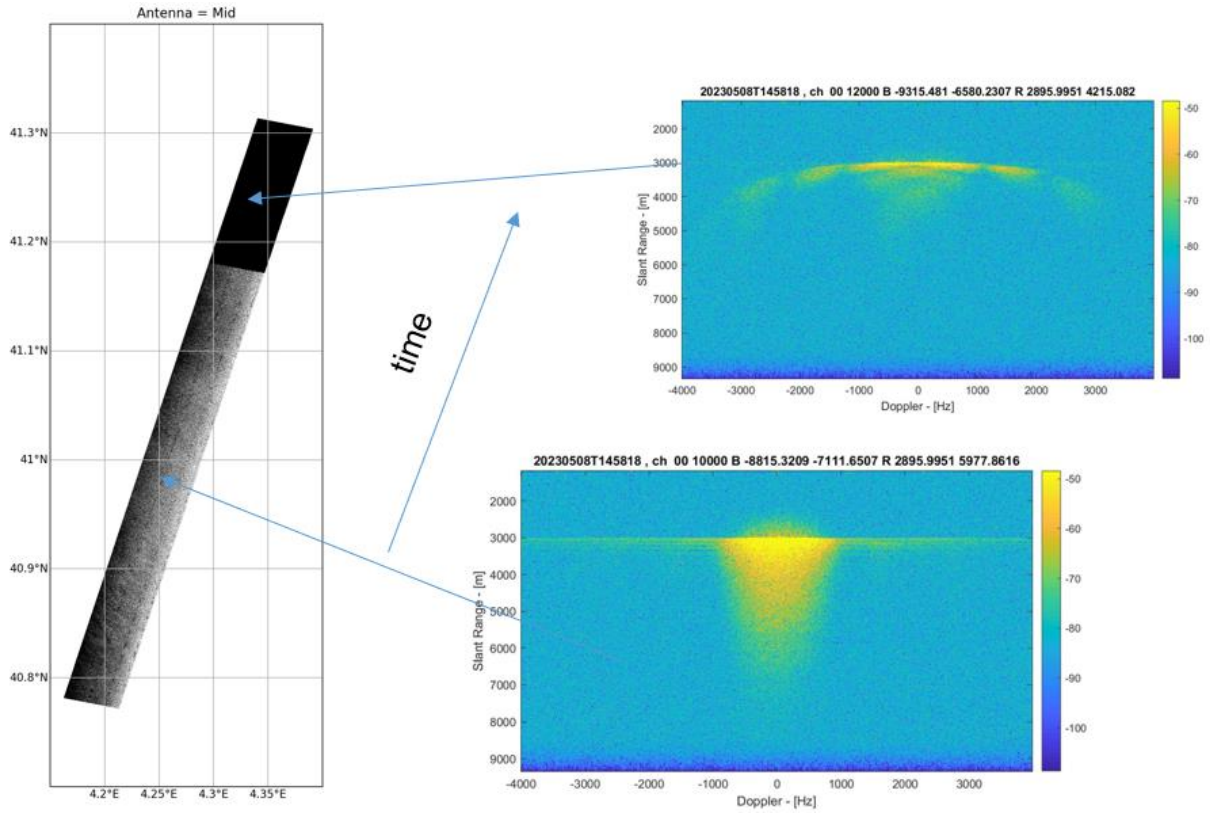


Figure 15: TX/RX failure example.

Also we show the Gimbal error (off25) issue as reported in the acquisition log. The cause is related to a mis-behavior of the gimbal which did not point to the correct angles, but with an offset of -25 deg. (off25) as illustrated below in the Roll Pitch Yaw plots. As a results the images could be processed with squint 0, -45 and 45 degrees. Instead we processed correctly the images with -25, -70, 20 degrees, accordingly.

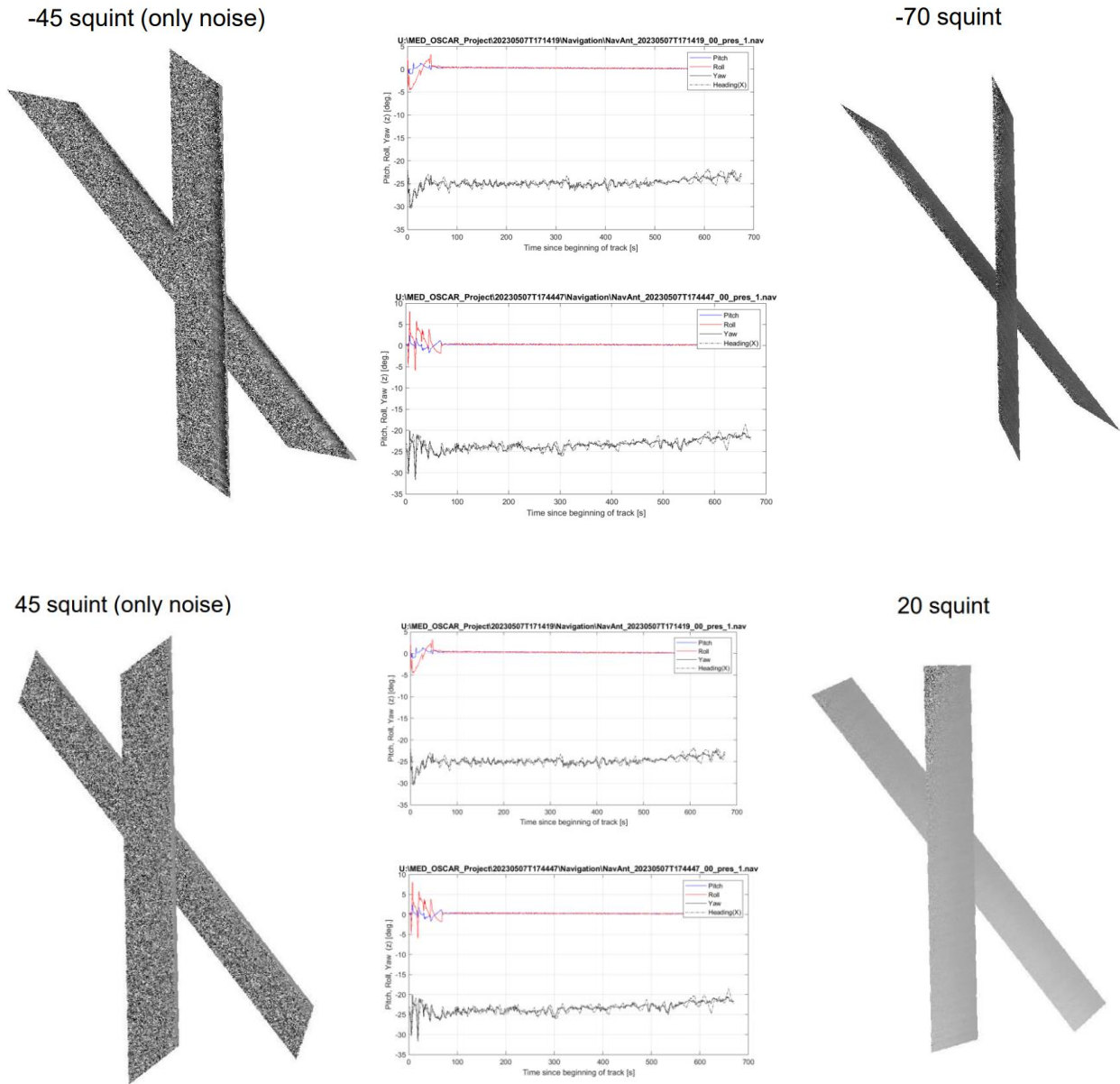


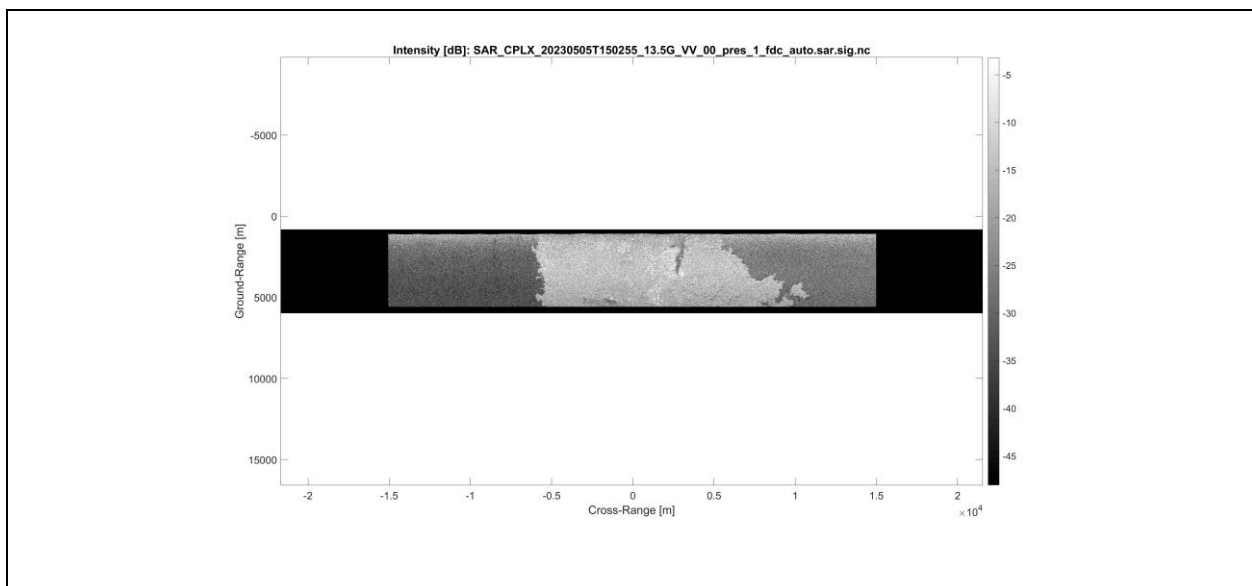
Figure 16: Gimbal error issue and corresponding effects in the image processed with the nominal squint and actual squint.

### 4.3 Processed Data

The data of all beams have been processed within the maximum possible available swath. The data are processed using the OSCAR processor, developed by MetaSensing, and making use of the GBP (Global Back Projection) algorithm. The data are processed up to L1a level, i.e. radiometrically (sigma-0) and geometrically calibrated SLC. The data are back projected in the same grid and therefore intra-coregistered.

The processed data are delivered together with the metadata encapsulated in the NetCDF file format [3]. The processed data have 8m x 8m spacing and 11.5 m x 8 m slant range x azimuth resolution (after Hanning windowing), respectively. The look angle can be adjusted to be between 28 to 68 degrees.

The figures below show an example of the SLC SAR images for all the 3 beams for one of the calibration tracks and also the corresponding interferograms for the squint channels. It is possible to note that the antenna pattern has been removed accordingly, in fact the backscatter is uniform along range and slightly higher at near range as expected.





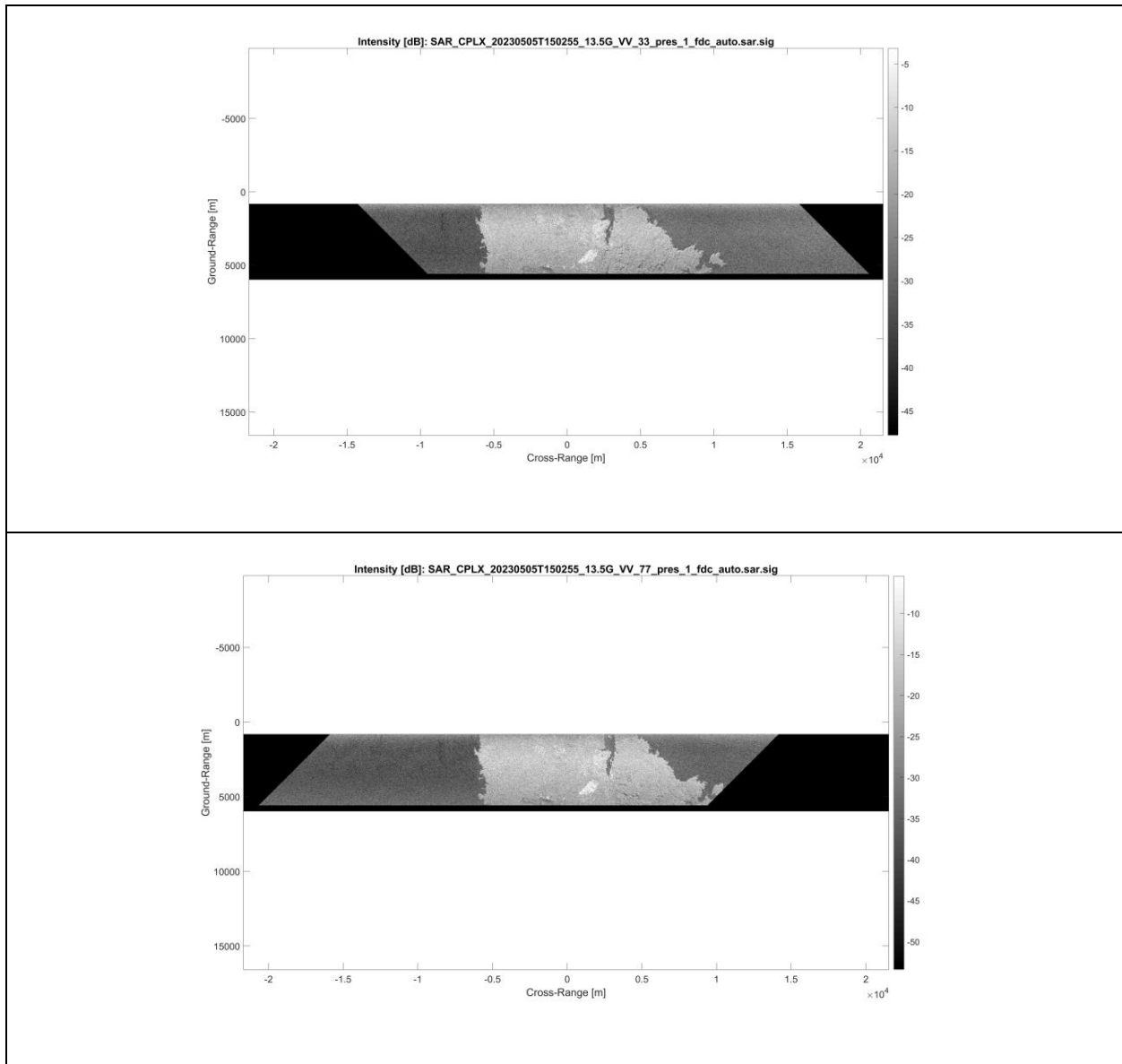
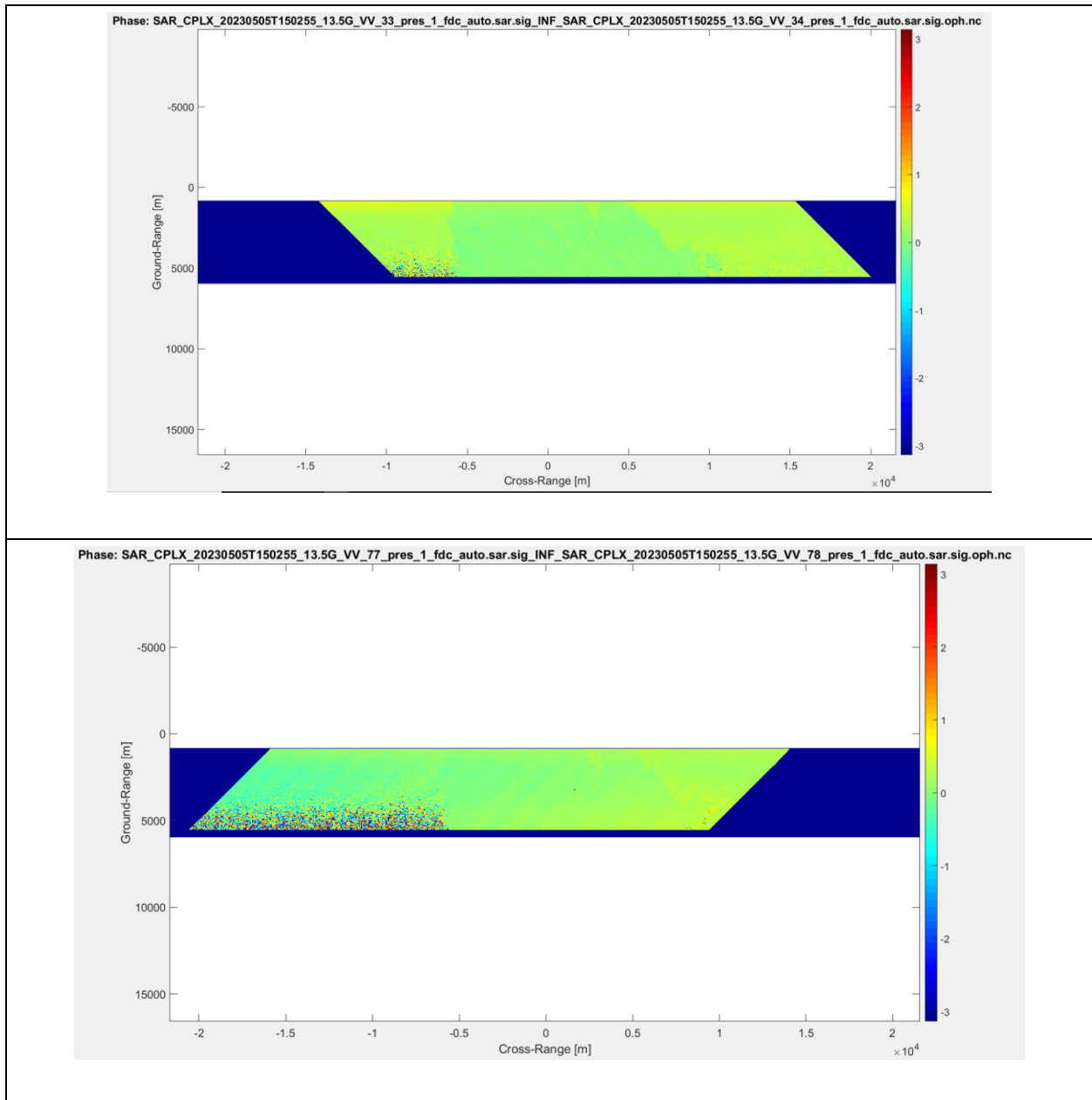


Figure 17: Intensity SAR image example for all channels



*Figure 18: SAR interferograms for the squinted channels*



## 5 Conclusions

This Data Acquisition Report - DAR provided the information related to system set-up, configuration and field work in order to process and analysis the data.

The DAR proves that the SAR data of the SeaSTARex-Med were correctly acquired with the OSCAR instrument by showing navigation statistics, RD maps and images examples up to level 1. Some issues and their causes were found and reported.

Finally, the processing of the collected data with the OSCAR processor shall deliver data within the SeaSTARex project requirements.

## 6 References

- [1] C. Gommenginger, et al, “SEASTAR: A Mission to Study Ocean Submesoscale Dynamics and Small-Scale Atmosphere-Ocean Processes in Coastal, Shelf and Polar Seas”, Proposal selected for Phase 0 of Earth Explorer 11 candidate mission, ESA-ESTEC.
- [2] Ocean Surface Current Airborne Radar Demonstrator (OSCAR) – Statement of Work, Appendix 1 to AO/1- 8309/15/NL/BJ.
- [3] MetaSensing NetCDF. File Format Description. MS-SAR-NetCDF-FFD\_v3.

# **ANNEX K) PAPER SUBMITTED TO OCEAN SCIENCE**

# **A new airborne system for simultaneous high-resolution ocean vector current and wind mapping: first demonstration of the SeaSTAR mission concept in the macrotidal Iroise Sea**

5 David. L. McCann<sup>1</sup>, Adrien C. H. Martin<sup>1,2</sup>, Karlus Macedo<sup>3</sup>, Ruben Carrasco<sup>4</sup>, Jochen Horstmann<sup>4</sup>, Louis Marié<sup>5</sup>, José Márquez-Martínez<sup>6</sup>, Marcos Portabella<sup>7</sup>, Adriano Meta<sup>3</sup>, Christine Gommenginger<sup>1</sup>, Petronilo Martin-Iglesias<sup>8</sup>, Tania Casal<sup>8</sup>

<sup>1</sup>National Oceanography Centre, Liverpool, L55DA, United Kingdom

10 <sup>2</sup>NOVELTIS, Labège, 31670, France

<sup>3</sup>Metasensing BV, Noordwijk, 2201 DK, Netherlands

<sup>4</sup>Helmholtz-Zentrum Hereon, Geestacht, 21502, Germany

<sup>5</sup>Ifremer, Plouzané, 29280, France

<sup>6</sup>Radarmetrics SL, Santander, 39005, Spain

15 <sup>7</sup>Institut de Ciències del Mar, Barcelona, 08003, Spain,

<sup>8</sup>European Space Agency, European Space Research and Technology Centre, Noordwijk, 2201 AZ, Netherlands

*Correspondence to:* D. L. McCann ([david.mccann@noc.ac.uk](mailto:david.mccann@noc.ac.uk))

**Abstract.** Coastal seas, shelf seas and marginal ice zones are dominated by small-scale ocean surface dynamic processes that play a vital role in the transport and exchange of climate-relevant properties like carbon, heat, water and nutrients between land, ocean, ice and atmosphere. Mounting evidence indicates that ocean scales below 10 km have far-ranging impacts on air-sea interactions, lateral ocean dispersion, vertical stratification, ocean carbon cycling, and marine productivity – governing exchanges across key interfaces of the Earth System, the global ocean and atmosphere circulation and climate. Yet, these processes remain poorly observed at the fine spatial and temporal scales necessary to resolve them. The Ocean Surface Current Airborne Radar (OSCAR) is a new airborne instrument with the capacity to inform these questions by mapping vectorial fields of total ocean surface currents and winds at high resolution over a wide swath. Developed for the European Space Agency (ESA), OSCAR is the airborne demonstrator of the satellite mission concept ‘SeaSTAR’, which aims to map total surface current and ocean wind vectors with unprecedented accuracy, spatial resolution and temporal revisit across all coastal seas, shelf seas and marginal ice zones. Like SeaSTAR, OSCAR is an active microwave Synthetic Aperture Radar Along-Track Interferometer (SAR-ATI) with optimal three-azimuth sensing enabled by unique highly-squinted beams. In May 2022, OSCAR was flown over the Iroise Sea, France, in its first scientific campaign as part of the ESA-funded SEASTARex project. The campaign successfully demonstrated the capabilities of OSCAR to produce high-resolution 2D images of total surface current vectors and near-surface ocean vector winds, simultaneously, in a highly dynamic, macrotidal coastal environment. OSCAR current and wind vectors show excellent agreement against ground-based X-band radar derived surface currents, numerical model outputs and NovaSAR-1 satellite SAR imagery, with Root-Mean-Square differences against X-band radar better than  $0.2 \text{ m s}^{-1}$  for currents at 200 m resolution. These results are the first demonstration of simultaneous retrieval of total current and wind vectors from a high-squint three-look SAR-ATI instrument, and the first geophysical validation of the OSCAR and SeaSTAR observing principle. OSCAR presents a remarkable new ocean observing capability to support the study of small-scale ocean dynamics and air-sea interactions across the Earth’s coastal, shelf and polar seas.

## 40 **1 Introduction**

The Earth’s coastal and shelf seas and marginal ice zones are dominated by dynamic surface processes that exist on much shorter spatial and temporal scales than in the open ocean (Schulz-Stellenfleth and Stanev, 2016; Kozlov et al., 2019). These small-scale dynamics (order of 1–10 km) play a key role in the exchange and transport of essential ocean and climate variables, biogeochemical processes, vertical mixing and air-sea interactions (Martin and Richards, 2001; Levy et al., 2012; Sasaki et al., 2014;), however global observations of dynamics at these scales are rare (McWilliams, 2016). Ocean surface currents and winds and their resultant air-sea interactions show increased complexity in coastal seas (Bricheno et al., 2018), shelf seas and in the vicinity of sea ice. The limited spatial resolution of wind predictions, model forcing and validation data have direct impacts on the ability to predict storms (Mass et al., 2002; Maskell, 2012) and assess wind power resources in developing areas (Ruiz et al., 2022). Wind observations are particularly lacking in coastal seas where satellite scatterometry is unable to make useful measurements within  $\sim 10$  km of the coast (Martin et al., 2018). Simultaneous measurements of total current and

wind vectors at fine scale are needed to improve understanding and predictive capability of coastal and shelf sea processes (Samleson, 2019; Villas Bôas et al., 2019; Hauser et al., 2023). With ocean prediction systems aspiring to resolve small scale processes operationally across the Earth's coastal, shelf and polar seas by the end of the decade (Holt et al., 2017), high-resolution mapping of these key physical properties will become increasingly important to validate and improve the numerical models used for short-term forecasting and climate change projections. There is therefore a clear and present need for synoptic measurements of currents and winds to meet the scientific, economic and societal challenges of the future.

SeaSTAR is a satellite mission concept submitted to the European Space Agency (ESA) Earth Explorer program to study these fast-changing, small scale ocean surface dynamics across the world's coastal oceans, shelf seas and marginal ice zones (Gommenginger et al., 2019). SeaSTAR is based on the principle of Synthetic Aperture Radar Along-Track Interferometry (SAR-ATI) applied in three highly squinted directions in azimuth. SAR-ATI measures the Doppler shift of ocean microwave backscatter signals from pairs of complex SAR images separated by a short time lag. The measured Doppler shift (interferogram) relates to the motion of the ocean surface in the radar line-of-sight, which contains the total ocean surface current and the motion of microwave scatterers on the ocean surface (known as the wave Doppler or Wind-wave induced Artefact Surface Velocity 'WASV'; Martin et al., 2016). SAR-ATI has a long heritage, from the first broadside-only ATI measurements of ocean surface velocity by Goldstein and Zebker (1987), through to the two-look 'Wavemill' concept (Buck, 2005) and the SeaSTAR three-look concept (Martin et al., 2018; Gommenginger et al., 2019). To date, no three-look SAR-ATI system has ever been flown in space. SeaSTAR represents a ground-breaking ocean observing system that would apply the cutting-edge performance and spatial resolution of SAR-ATI to deliver simultaneous fine-scale images of total surface current and wind vectors to inform these vital but poorly observed ocean processes.

The Ocean Surface Current Airborne Radar (OSCAR) instrument is a unique, 3-look SAR-ATI, airborne system operating at Ku-band (13.5 GHz). Built and operated by MetaSensing BV in Italy and the Netherlands, OSCAR was developed for ESA to demonstrate the three-look SAR-ATI principle and the ability to simultaneously observe total surface current vectors (TSCV) and ocean surface vector winds (OSVW) in two dimensions, at high accuracy and fine resolution, in a single pass, from an airborne platform (Trampuz et al., 2018). Within ESA Earth Explorer 11 Phase 0 activities, the SEASTARex project performed OSCAR airborne campaigns to increase the scientific readiness level of the SeaSTAR mission concept and act as the first scientific demonstration and validation of the OSCAR instrument and the high-squint 3-look SAR-ATI capability. Involving airborne OSCAR acquisitions, in situ observations, ground-based remote sensing, numerical modelling and earth observation, SEASTARex drew together expertise from nine international scientific institutions and specialists in the field of oceanography, airborne and ground-based remote sensing, engineering and earth observation sciences. This paper presents the activities and results from the scientific airborne campaign of the OSCAR instrument over the Iroise Sea in May 2022, representing the first instance of simultaneous retrieval of total surface current vectors and ocean surface vector winds based on experimental measurements from a high-squint three-look airborne SAR-ATI instrument.

## 2 OSCAR airborne system and data

### 2.1 OSCAR instrument

85 OSCAR is a unique, high-squint, 3-look SAR-ATI instrument operating at Ku-band (13.5 GHz), featuring two pairs of  
interferometric antenna squinted at  $\pm 45^\circ$  ('fore' and 'aft') from the aircraft broadside, and a conventional 'zero-Doppler'  
antenna pointing broadside ('mid'). All antennas pointed to the port (left) side of the aircraft and transmitted and received in  
vertical polarisation ('VV'). The instrument is mounted on a 3-axis gimbal (Fig. 1a) with a mounted Inertial Measurement  
Unit (IMU) paired with high-precision Global Navigation Satellite System (GNSS) receiver to stabilize the instrument pointing  
90 relative to the aircraft and resolve the pointing of the beams to a high precision. The antennas and gimbal are mounted in a  
purpose-built radome specifically designed for interferometry at Ku-band and Ka-band frequencies. OSCAR was installed on  
a PA-31 Piper Navajo airframe owned and flown by Metasensing BV (Figure 1b).

### 2.2 Data processing: simultaneous current and wind vector retrieval

The simultaneous retrieval of total surface current vector (TSCV) and ocean surface vector wind (OSVW) was performed  
95 using the SeaSTAR project in Python (Martin et al., 2023), which is based on the simultaneous wind-current retrieval method  
of Martin et al. (2018), adapted for the OSCAR 3-look configuration. At the centre of the simultaneous wind-current retrieval  
method is the minimization of the cost function  $J$ , defined here as:

$$J(u_{10}, c) = \frac{1}{N_S + N_D} \sum_{i=1}^{N_S} \left( \frac{KuMod(u_{10}, \chi_i, \theta_i, p_i) - \sigma_{obs,i}^0}{\Delta\sigma_i^0} \right)^2 + \frac{1}{N_S + N_D} \sum_{i=1}^{N_D} \left( \frac{KuDop(u_{10}, \chi_i, \theta_i, p_i) + c_{||i} - RSV_{obs,i}}{\Delta RSV_i} \right)^2 \quad (1)$$

100 where  $i$  is the beam index in a given azimuth direction (fore, mid, aft),  $\sigma_{obs,i}^0$  is the observed Normalised Radar Cross Section  
(NRCS) in VV polarization for the beam index  $i$ ,  $RSV_{obs,i}$  is the measured Radial Surface Velocity for the beam index  $i$  (in  
this case only fore and aft),  $u_{10}$  is the stress-equivalent OSVW at 10 m height,  $c$  is TSCV,  $N_S$  is the total number of observations  
for NRCS,  $N_D$  is the total number of observations for RSV,  $KuMOD$  is the predicted NRCS using the chosen Geophysical  
Model Function (GMF) for Ku-band,  $KuDOP$  is the predicted RSV using the chosen GMF for Ku-band WASV,  $\chi$  is the  
105 azimuth look direction,  $\theta$  is the incidence angle from nadir,  $p$  is the radiometric polarisation (in this case VV) and  $c_{||i}$  is the  
component of TSCV along azimuth look direction for beam index  $i$ . For the results presented in this paper the  $KuDOP$  GMF  
used for Equation 1 is the C-band 'CDOP' model of Mouche et al. (2012) adapted for Ku-band frequencies, and for the  
 $KuMOD$  GMF the NSCAT-4DS model (Wentz and Smith, 2019) is used.

The parameters  $\Delta\sigma^0 = k_p \sigma^0$  (where  $k_p$  is the radiometric resolution) and  $\Delta RSV$  represent the uncertainties in the  
110 measurements. Here  $k_p$  was estimated as a combination of contributions from instrument noise and geophysical noise (Mejia  
et al., 1999). Instrument noise was estimated via a robust estimator of distribution (normalized interquartile range) of measured

$\sigma^0$  for each look direction. Geophysical noise was estimated via comparison of measured  $\sigma^0$  with the predicted NRCS using NSCAT-4DS.  $\Delta RSV$  was estimated using open-ocean OSCAR data from the SEASTARex campaign and ground truth data from an Acoustic Doppler Current Profiler (ADCP) mooring at 48.256°N, 5.249°W to estimate the observed WASV and comparing this to the predicted WASV from Mouche et al. (2012). The estimated noise parameters used in this study were  $k_p = 20\%$  and  $\Delta RSV = 0.2 \text{ m s}^{-1}$ .

The cost function  $J$  is a unit-less function of 4 unknown variables ( $\vec{u}_{10}, \vec{c}$ ). Minimising the cost function finds the values of TSCV ( $c$ ) and OSVW ( $u_{10}$ ) that best reduce the quadratic differences between the measured observables ( $\sigma_{obs,i}^0, RSV_{obs,i}$ ) and the predicted quantities ( $KuMod, KuDop$ ). As in scatterometry, the minimisation returns up to four solutions (Portabella et al., 2002; Martin et al., 2018), leading to a well-known ambiguity problem and the requirement for an ambiguity removal procedure. A usual procedure to remove these ambiguities is to use additional geophysical information, e.g., from wind forecasts (Portabella and Stoffelen, 2004). In the case of the work presented within this paper a simple ambiguity removal method was implemented, selecting the solution for  $J$  closest in  $\vec{u}_{10}$  space to wind vectors taken from the MétéoFrance operational Application of Research to Operations at Mesoscale (AROME) atmospheric wind model (Seity et al., 2011).

### 125 3. Iroise Sea airborne campaign

The SEASTARex airborne campaign was conducted between the 17<sup>th</sup>–26<sup>th</sup> May, 2022 over the Iroise Sea, west of Brest, France, from the home airport of Morlaix, Brittany. Macrotidal and relatively shallow, the Iroise Sea is dominated by strong tidal currents and prevailing Atlantic swell interacting with complicated coastline morphology and bathymetry of the area (Muller et al., 2009). The island of Ushant (Ouessant in French) and its coastal waters, at the westerly end of the Molène archipelago in the Iroise sea, experience some of the fastest tidal flows on the North European shelf, often exceeding  $3 \text{ m.s}^{-1}$  (Sentchev et al., 2013) and frequent westerly and south-westerly Atlantic storms. Figure 1c shows the location of the study area and the bathymetry (in metres below mean sea level) from the European Marine Observation and Data Network (EMODNet) harmonized digital terrain model.

The airborne scientific campaign consisted of four flight days of repeat acquisitions of OSCAR data over three main areas of interest: a site around the Island of Ushant with highly dynamic, macrotidal and hydrodynamically heterogeneous currents; a site south of La Jument lighthouse (Fig. 1d), with temporally and spatially homogeneous conditions and deployed in situ buoy measurements (48.256°N, 5.249°W); and a long, open-ocean flight further south to coincide with measurements from the ASCAT satellite scatterometer. This paper focuses on the results from the OSCAR flights over the dynamic tidal race around Ushant (flight tracks from Figure 1d) on the 17<sup>th</sup> and 22<sup>nd</sup> of May 2022 .

#### 140 3.1 OSCAR data acquisitions

The OSCAR flights were scheduled to occur at an altitude above sea level of 3,000 m for all days, however a low cloud ceiling on the 17<sup>th</sup> May forced the aircraft to acquire data at an altitude of 1,950 m. Acquisitions on the 22<sup>nd</sup> may were obtained at the



scheduled altitude of 3,050 m. All flights were performed at a mean ground speed of  $80 \text{ m s}^{-1}$ . The flights over Ushant were scheduled to capture peak tidal flows, with the aircraft passing over the island at 09:32 UTC on the 17<sup>th</sup> and 05:48 UTC on the 22<sup>nd</sup> May. OSCAR was configured to generate SAR imagery at 8 m pixel resolution in a 5 km swath, with incidence angles varying between 22–69° for the fore and aft squinted channels and between 16–61° for the mid channel. Level 0 processing (e.g. SAR focusing) and radiometric and interferometric calibration of the OSCAR acquisitions were performed by Metasensing BV and Radarmetrics SL. Radiometric calibration was performed via targeted flights over corner reflectors of a known radar cross section, with these data being recorded on each flight day before the scientific acquisitions took place. Additional flights over the corner reflectors were performed at the end of each flight to check that calibration parameters had not changed. Additional residual calibration of NRCS was performed using OSCAR data from the open ocean flights and computing the incidence-angle dependent bias with respect to NSCAT-4DS. Interferometric calibration was performed using over-land OSCAR data to assess the recorded Doppler velocities of static land reflections (which should theoretically be zero). Level-1 single-look complex Doppler images were spatially smoothed using a 7-pixel (56 m) windowed mean and down-sampled to 200 m ground resolution (using the mean value in each 200 m cell) for input to the simultaneous retrieval. This resolution was chosen as a trade-off between capturing sub-mesoscale hydrodynamic features and computation time for the cost function. All campaign data is classified according to its stage in the processing chain, with Level-1 (L1) data corresponding to SAR-processed data in instrument (i.e., local) coordinates, Level-1c (L1c) data corresponding to calibrated data on a shared grid and Level-2 (L2) data corresponding to retrieved geophysical parameters in a global coordinate system.

160

### 3.2 X-band marine radar

As part of the SEASTARex project, a marine radar was installed on La Jument lighthouse overlooking the tidal race to the south-west of Ushant, which is an ideal location for observing the extreme tidal dynamics of the area (Filipot et al., 2019). The coherent-on-receive X-band (9.3 GHz) radar (Horstmann et al., 2021) was mounted on the lighthouse at a height of 48 m above mean sea level and covered a radius between 52 m and 3150 m corresponding to grazing angles between 40° and 0.78° (equal to incidence angles of 50° and 89.22° respectively). During the campaign the radar was operated in its rotational mode, acquiring radar backscatter intensity and radial Doppler velocity maps with a repetition rate of approximately 0.5 Hz. All radar data were collected at a pulse length of 0.5 ns and with a pulse repetition frequency of 2 kHz at VV polarization with a 2.3 m slotted waveguide antenna, resulting in an azimuthal resolution of 1.2°. Radar data were acquired at 20 MHz, resulting in a range resolution of 7.5 m. The radar was operated on 17<sup>th</sup> May 2022 between 6:41–12:00 UTC collecting six 10-minute video sequences every hour, which were used to compute surface current fields. One of these sequences was coincident with an OSCAR flight overpass of the radar at 09:38 UTC.

The surface current maps are derived from the wave signal within a 10-minute marine radar image sequence which is then transformed from the spatial-temporal domain to the wave number-frequency domain by a 3D Fast Fourier Transform (FFT).

175

Within this 3D radar image spectrum, the wave signal is located on an inverted cone; the so-called dispersion shell defined by the linear dispersion relation of surface waves. In the case of deep water with respect to the wavelength this dispersion shell is solely dependent on the surface current (Senet et al., 2001; Huang et al., 2016). The 2D fields of current vectors are determined by an algorithm that searches for the current that maximizes the energy on the dispersion shell using a brute-force optimization algorithm (Streßer et al., 2017) and considering wave lengths between 15–125 m and wave periods of between 4–20 s. The spatial window used for one individual current measurement spans over an area of 500 x 500 m, and the individual windows overlap by 200 m, which corresponds to the pixel ground resolution (posting) in the resulting 2D current map.

### 3.3 Numerical models

Data from two numerical models were used: the MARS2D depth-averaged hydrodynamic model (Lazure and Dumas, 2008) run operationally by the Laboratory for Ocean Physics and Satellite remote sensing (LOPS), and the MeteoFrance operational AROME wind model (Seity et al., 2011). MARS2D depth-average currents were provided at 15-minute intervals at a ground resolution of 250 m. Hourly AROME wind forecasts were provided for an altitude of 10 m ( $u_{10}$ ) at a ground resolution of 0.025° (approx. 2 km).

### 3.4 Spaceborne SAR imagery

NovaSAR-1 is a UK-funded technology demonstration satellite owned and operated by Surrey Satellite Technology Ltd. (SSTL) that delivers high-resolution S-band SAR imagery . NovaSAR-1 was commissioned to acquire images over the study site, resulting in an overpass at 10:30 UTC on 17<sup>th</sup> May 2022, coinciding with the OSCAR flight over Ushant with only an hour difference. The NovaSAR-1 data were commissioned and accessed thanks to the support of Martin Cohen at Airbus Defence and Space Ltd.

## 4 Results

### 4.1 OSCAR results for ebb tide on 17 May 2022

Figure 2 shows the retrieved TSCV (Fig. 2a) and OSVW (Fig. 2b) at 200 m ground resolution from a single OSCAR acquisition flying North (looking left) over the Island of Ushant during ebb tide at 09:38 UTC on the 17<sup>th</sup> May 2022. Sea state conditions at the time of acquisition consisted of a moderate swell from the south-west with a significant wave height of 2.5 m and a peak period of 11 s. Winds were approximately 7 m s<sup>-1</sup> from the south-east. The vectors on Figures 2a and 2b are plotted with a sub-sampled posting of 400 m for clarity. The trapezoidal shape of the OSCAR swath is due to the squinted look direction ( $\pm 45^\circ$  in azimuth) of the fore and aft ATI channels and their orthogonal combination to compute the L2 current and wind vectors. For comparison, Figure 2c shows depth-average current vectors at 250 m ground resolution (vector posting at 500 m) from the MARS2D ocean circulation model at 09:30 UTC and Figure 2d shows predicted stress-equivalent wind vectors at 10 m above

205 the sea surface ( $u_{10}$ ) at 2 km ground resolution from the hourly MeteoFrance AROME operational wind forecast model at 09:00 UTC. The OSCAR L2 swath can be seen outlined in black, overlain on both model outputs.

Overall, very good visual agreement can be seen between OSCAR and the two models, both in the magnitude and direction of both TSCV and OSVW. OSCAR features additional complexity in the observed current field than the model, with sharper  
210 gradients and a separate sub-mesoscale filament close to land in the northern jet north of the island. To the south of the domain, the counter-rotating eddy predicted by the model data ( $\sim 48.38^\circ\text{N}$ ) is also captured in the OSCAR TSCV, albeit with subtle spatial differences and lower magnitude in the observations. Importantly, OSCAR reveals tidal currents north of the island that are both more intense and further from land (due to leeward sheltering of the tidal flow). For OSVW, good similarity can be seen between the retrieved OSVW from OSCAR (Fig. 2b) and AROME model data (Fig. 2d), with fine scale variations in the  
215 near-surface winds present in the OSCAR data, especially around the western tips of the island which could originate from local orographic perturbation. The large-scale north-south gradient in wind speed present in the numerical model is also observed in the OSCAR data, albeit with much finer-scale detail due to the extreme difference in resolution.

Further evidence of the exceptional accuracy of OSCAR to correctly measure complex hydrodynamic structures around Ushant  
220 is shown in Figure 3 via comparison and validation against surface current vectors derived from the X-band radar on La Jument lighthouse. Figure 3a shows surface currents derived from 10 minutes of sequential X-band intensity imagery acquired over a radius of 3.1 km around the lighthouse at 09:30 UTC on the 17<sup>th</sup> May, shown with a pixel ground resolution of 200 m, a vector posting of 400 m and the coincident OSCAR L2 swath overlain. Figure 3b shows co-located and superimposed vectors from both sensors plotted at 400 m posting. The two instruments show very good agreement, with a root mean square difference  
225 (RMSD) between the data of  $0.18 \text{ m s}^{-1}$  for current velocity and  $5.27^\circ$  for current direction (Figure 3c). Both the OSCAR system and the X-band radar measure the southern tidal jet further west than appears in the model (Fig. 2c) and a northward shift in the counter-rotating flow. This is reflected by the RMSD between MARS2D and the measurements from these two remote sensing systems, which report an RMSD of  $0.61 \text{ m s}^{-1}$  and  $6.5^\circ$  between OSCAR and the model, and  $0.47 \text{ m s}^{-1}$  and  
230  $16.6^\circ$  between the X-band and the model for current velocity and current direction respectively. The high level of agreement between the two independent remote sensing measurements demonstrates the value of these systems to reveal and resolve inaccuracies that can occur in models of high energy coastal environments.

More detailed examination of Figure 3b indicates that the best agreement can be seen at the western edge of the OSCAR swath, which corresponds to higher incidence angles. The comparison around the position of the high tidal flow (at lower, or steeper  
235 incidence angles) is better for TSCV magnitude than it is for direction, with a clear shift in measured current direction between OSCAR and the X-band radar data. The validation of TSCV components from OSCAR and the X-band radar (Figure 3c) reveals good agreement in U (east component;  $R^2 = 0.7$ ) and excellent agreement in V (north component;  $R^2 = 0.96$ ) across a wide range of flow conditions. The combined RMSD between the two sensors for TSCV at 200m ground resolution is found

to be  $0.19 \text{ m s}^{-1}$ . The departure between the two sensors in negative component velocities is related to the different OSCAR  
240 TSCV directions observed in the southern tidal jet..

Further validation of the ability of OSCAR to accurately measure fine-scale hydrodynamic structures in such a dynamic coastal  
environment is seen in Figure 4. Here OSCAR TSCV vectors from 09:38 UTC on the 17<sup>th</sup> May are overlain over a geo-  
registered SAR image from the NovaSAR-1 satellite around Ushant. The satellite image was acquired at 10:30 UTC, less than  
245 an hour after the OSCAR track, but still within the same ebb-tidal flow regime. The NovaSAR-1 S-band  $\sigma^0$  image displays  
variations in Normalised Radar Cross Section ( $\sigma^0$ ) linked to the modulation of the ocean surface roughness by strong horizontal  
shear in the flow, producing clear intensity gradients that are coincident with these hydrodynamic structures. Excellent spatial  
correlation can be observed between the OSCAR TSCV vectors and these gradients in the SAR image, with good  
correspondence in the positions of both northern and southern tidal jets around Ushant in the spaceborne SAR  $\sigma^0$  and OSCAR  
250 data. The NovaSAR-1 image also displays lighter gradients that coincide with both the counter-rotating flow to the south-west  
of Ushant and the small flow ‘filament’ that are observed in the OSCAR data but are not present in the MARS2D output. The  
comparison with NovaSAR-1 confirms the validity of OSCAR TSCV placing the intense horizontal shear of the ebb-tidal jet  
north of the island ( $\sim 48.48^\circ\text{N}$ ) approximately 1 km northward of the position predicted with MARS2D (Fig. 2c). The same is  
true for the position of the southern tidal jet towards the lower extremity of the OSCAR swath. This is an important result, as  
255 the exact position of such strong gradients in tidal flows such as these can be challenging to accurately predict using numerical  
models.

#### 4.2 OSCAR results for flood tide on 22 May 2022

Figure 5 shows TSCV and OSVW results from an OSCAR acquisition flying north (looking left) covering part of the flood-  
260 tidal regime around Ushant on the 22<sup>nd</sup> May, 2022 at 05:48 UTC. Sea state conditions at the time of acquisition consisted of a  
light swell from the south-west with a significant wave height of 1 m and a peak period of 9 s. The wind was generally from  
the north-east around  $5\text{--}6 \text{ m.s}^{-1}$ . Figure 5a and Figure 5b show OSCAR retrieved TSCV and OSVW respectively. Figure 5c  
shows MARS2D simulated currents around Ushant at 05:45 UTC and Figure 5d shows forecast  $u_{10}$  wind vectors at 06:00  
UTC from the AROME model. Once again, OSCAR present very good overall agreement with the two models, both in the  
265 magnitude and direction of both TSCV and OSVW. Moreover, the results confirm the ability of OSCAR to resolve not only  
high tidal currents but also current fields in quiescent areas, for example in the shallow coastal areas around western Ushant  
that are sheltered from the northward flood tide which is present in both the predicted and observed TSCV fields. Similar to  
the ebb-tide case on the 17<sup>th</sup> May (previous section), the OSCAR TSCV field shows a more northerly extent of the accelerated  
tidal flow within the imaged swath than in the predicted data; highlighting the stark differences that can be obtained between  
270 observations and numerical models in such dynamic coastal areas. The OSCAR OSVW (Fig. 5b) captures the same general  
north-south trend and variability seen in the forecast AROME wind data (Fig. 5d), with the reduction in wind speeds to the lee  
of the island clearly visible in both the OSCAR results and the predictions.

On the 22<sup>nd</sup> May, three OSCAR acquisitions were made over the same area to the west of Ushant within a period of 15 minutes, with two passes in a southerly direction and one travelling north. The objective was to demonstrate the consistency of the OSCAR L2 products between successive passes and in different orientations. Figure 6 shows the comparison of TSCV for the three tracks (shown as coloured vectors) co-located on the same grid and overlain on MARS2D predicted currents (black vectors). The swath outlines are in orange for the northward track at 05:48 UTC and in blue for the southward tracks at 05:39 UTC and 05:54 UTC (for clarity only one swath is outlined for the two southwards tracks). The agreement between successive passes is excellent, with different TSCV vectors nearly always perfectly superposed and quasi-undistinguishable at most grid points. The TSCV median sample standard deviation between the three flights (with each TSCV vector treated as an independent measurement, i.e.,  $n = 3$ ) is  $0.10 \text{ m s}^{-1}$  for current velocity and  $1.18^\circ$  for current direction. It is worth noting that the radar lines-of-sight relative to the wind were not particularly favourable in this instance. As the wind direction was from the north-east (Fig. 5d), the antenna squint angles  $45^\circ$  and the flight directions either north or south, the southward flights at 05:39 and 05:54 UTC (blue and green) correspond to one squinted beam looking crosswind and the other looking up-wind, whereas the northward flight at 05:48 UTC (orange) had one squinted beam looking crosswind and the other downwind. This is important, as the performance of the three-look concept is known to be impacted when one of the azimuth lines-of-sight is aligned with the wind (Stoffelen and Portabella, 2006; Martin et al., 2018). However, the consistency between the TSCV obtained with up-wind (blue and green) and down-wind (orange) lines-of-sight is seen to be very good at those points where the swaths from the northward and southward flights overlap.

## 5 Discussion, conclusions and future work

This paper presents the results of the first scientific airborne campaign of the OSCAR high-squint, three-look SAR-ATI instrument and represents the first demonstration of simultaneous retrieval of TSCV and OSVW in a single pass using a SeaSTAR-type observing concept in a highly dynamic coastal marine environment. The results are extremely promising, with OSCAR and the SeaSTAR inversion algorithm reporting a high degree of accuracy and self-consistency over a large swath in highly inhomogeneous coastal conditions. The OSCAR instrument demonstrates the capability to provide quantitative information about fine scale dynamics that are not correctly represented with numerical models and are difficult to observe with ground-based sensors alone. In situ observations of hydrodynamics in high energy, macrotidal environments are costly and challenging (Neil and Hashemi, 2018) and provide only limited spatial detail needed to understand frontal dynamics in areas of strong spatial gradients. HF radars could provide synoptic information about ocean currents but their coverage is patchy and limited to a few coastal regions in some industrialised countries. Whilst HF radar data was recorded during the campaign, coverage around the island of Ushant, the focus of this paper, is unfortunately lacking; especially in the area to the West of the island that sits in the radio shadow of the HF ground stations on the French mainland. HF coverage of the open-ocean homogeneous site sampled in the campaign was good, however, and their analysis and comparison with OSCAR will

305 be a subject of future work. The quality of the OSCAR data obtained from these four flights spanning two days is notably impressive. Comparisons of the three flights for the 22<sup>nd</sup> May, acquired within a short time over roughly the same ground track but with radically different radar viewing directions with respect to the wind, give confidence in the OSCAR and SeaSTAR current and wind vector retrieval. Comparisons with high-resolution data from X-band radar, NovaSAR-1 and models demonstrate that the OSCAR airborne instrument and the SeaSTAR mission concept clearly bring great additional capability  
310 to the research community and present great promise for increasing our understanding of small scale processes in coastal and shelf seas and marginal ice zones.

It is noteworthy that the retrieval returns excellent results within this exceptionally heterogeneous coastal environment whilst using the open-ocean wind-dependent WASV correction by Mouche et al. (2012). Importantly, no specific adjustments were  
315 made to account for additional sea state dependency of the WASV on factors like fetch, wave age, wave breaking at fronts or wave-current interactions over shallow bathymetry. Our results align with prior suggestions from Martin et al (2017) that indicate that the effects on SAR-ATI of strong current gradients and wave age may hold secondary importance in these highly dynamic areas. There is a common perception that the accuracy of available open-ocean GMFs may be insufficient to predict the WASV in areas of strong surface current gradients, and may require mixed-polarisation sensor capability to correctly  
320 address additional Doppler effects at fronts (Kudryavstev et al., 2014; Martin et al., 2018). A surprising result of our work is the consistency of TSCV retrieved using the C-DOP GMF of Mouche et al. (2012) and its predicted WASV in such a dynamic coastal tidal environment. The C-DOP GMF captures the average behaviour of the WASV based on a large globally distributed dataset of Envisat ASAR Doppler measurements over the open ocean (i.e., hydrodynamically homogenous, microtidal environments) and as such does not contain the WASV response to shallow water dynamics, wave-current interactions, strong  
325 tidal shear, etc. The quality of the OSCAR retrieved TSCV in the complicated Iroise Sea environment suggests that the assumed sensitivities of the WASV to hydrodynamic processes are perhaps not as important. Future work will consider other GMFs to compute the WASV that include dependence on ocean wave parameters such as has been developed by Yurovsky et al. (2019). TSCV retrieval performance is especially sensitive to the choice of WASV at steep incidence angles (Martin et al, 2018), so a different GMF may further improve the OSCAR results in the near-range parts of the swath. The full wind and waves  
330 parametrised model for Yurovsky et al (2019) has not been tested with OSCAR data at this time but will be the basis of a future larger validation study.

All results of this study were obtained using the simultaneous retrieval of current and wind vectors that is the chosen baseline algorithm for OSCAR and SeaSTAR Level-2 inversion. But other inversion approaches exist, for example one can consider a  
335 sequential retrieval approach where ancillary wind information (for example from AROME) serves to correct the WASV directly in each line-of-sight, before recovering the current vector (as in Martin et al., 2017). In this instance, computation time is almost instantaneous, versus a typical ~30 minutes computation on a 20-core machine to apply simultaneous inversion to a single track at 200m resolution. However, our tests (not shown) indicate that the quality of the TSCV is degraded when using

sequential approach. The degradation is visible in the poorer performance against X-band marine radar currents, but also in  
340 the mis-localisation of OSCAR retrieved current gradients with the visible roughness gradients in NovaSAR-1 imagery. This  
is particularly noticeable at steep incidence angles and may be linked to errors inherent to the WASV GMF mentioned  
previously.

The comparison between OSCAR and ground-based X-band radar data is excellent, especially when considering the  
345 differences in frequency and imaging mechanisms between the two systems. Some consideration should be given to these  
differences and how they may account for a proportion of the scatter seen in Figure 3c. For the X-band radar (e.g., using the  
methods of Streßer et al., 2017), the resulting derived currents represent a weighted mean over the upper ocean, where the  
greatest weight is assigned to the surface and the effective depth of the current relates to the maximum ocean wavelengths  
imaged by the radar and considered in the current fit. For OSCAR, the TSCV derives from Doppler shifts in backscatter at  
350 moderate, non-grazing, angles (incidence angle as steep as  $22^\circ$ ) where there are combined effects from small-scale surface  
roughness and longer ocean wavelengths, particularly wind waves around 10 m (Chapron et al., 2005). Further investigations  
are needed to better understand differences in TSCV measured by different sensors, including also HF radars and other ocean  
current sensors like ADCP, and how to accommodate these differences when validating new sensors like OSCAR.

355 This paper presents only a preliminary validation of the OSCAR data to demonstrate the innovative and promising spatial  
mapping capabilities of this new system in the extreme macrotidal coastal environment close to Ushant. Fuller validation of  
the OSCAR L2 results is necessary however to quantitatively compare the OSCAR data against established ocean  
measurements from ADCP and HF radar also collected during the SEASTARex project. For this, the focus of the validation  
must shift south, to a second instrumented site set up during SEASTARex to validate OSCAR in a geophysically homogenous  
360 site to the south of Ushant (centred on  $48.256^\circ\text{N}$ ,  $5.249^\circ\text{W}$ ). Those larger datasets and comparisons will be the object of a  
separate publication. More recently still, OSCAR flew in its second scientific campaign in May 2023 in the north-west  
Mediterranean Sea (north of the island of Menorca, Spain) famous for strong sub-mesoscale ocean dynamics. The OSCAR-  
Med airborne flights were timed to coincide with overpasses of the Surface Water and Ocean Topography (SWOT) mission  
during its 1-day fast-repeat Cal/Val phase, and in situ measurements from the BioSWOT-Med oceanographic ship campaign  
365 (Doglioli and Gregori, 2023). The results of the OSCAR-Med campaign will be the subject of a future study. Finally, given  
the scientific objectives of the SeaSTAR mission concept to measure TSCV and OSVW in marginal ice zones, the team is  
currently exploring opportunities to fly a new OSCAR scientific campaign close to the sea ice edge.

### **Code availability**

The repository for the SeaSTAR processing software used for the work in this study is available at  
370 <https://doi.org/10.5281/zenodo.10026593>



### **Data availability**

OSCAR data can be provided by the corresponding author upon request.

### **Author contribution**

375 AM, CG, JH, LM, JM, MP and AMe planned the campaign, TC and PM-I managed the campaign and provided oversight, AMe managed the recording of the airborne data, DM, AM, KM and RC developed the processing software, KM, JM and MP performed the OSCAR level-1 data processing and calibration, AM and DM performed the OSCAR level-2 data processing, RC, JH and LM recorded and processed the ground truth data, DM wrote the manuscript, RC and JH provided text input for the manuscript, DM, AM and CG reviewed and edited the manuscript.

### **Competing interests**

380 The authors declare that they have no conflict of interest.

### **Acknowledgements**

The authors would like to thank Christian Trampuz (formerly of Metasensing BV), Hugo Kerhuel and Thomas Jamne for the preparation and execution of the OSCAR Iroise Sea campaign in May 2022. The authors would also like to thank: Nicholas Gebert from ESA who was the initial Technical Officer for the OSCAR system development, Rui Duarte and team at France 385 Energie Marine (FEM) who provided essential access to La Jument lighthouse and support for the installation and operation of the X-band radar, Thiago Luiz at Metasensing BV for his work in the SAR processing of OSCAR data and Guiseppe Greco at ICM-CSIC, Spain and Wenming Lin at NUIST, China for their help with the radiometric calibration of OSCAR data. Many thanks to Clive Neil at NOC for his essential assistance in setting up the Seastar project software repository.

### **Financial support**

390 This study was supported by the SEASTARex contract from the European Space Agency (400017623/22/NL/IA). The OSCAR instrument was developed by Metasensing BV under funding from the European Space Agency in the OSCAR contract (4000116401/16/NL/BJ).

## References

- Bricheno, L. M., Soret, A., Wolf, J., Jorba, O., and Baldasano, J. M.: Effect of high-resolution meteorological forcing on nearshore wave and current model performance, *J. Atmos. Ocean. Tech.*, 30(6), 1021–1037, doi: 10.1175/jtech-d-12-00087.1, 2013
- Buck, C.: An extension to the wide swath ocean altimeter concept, in *Geoscience and Remote Sensing Symposium, 2005. IGARSS '05. Proceedings. 2005 IEEE International*, vol. 8, 5436–5439, IEEE, N. Y., doi:10.1109/IGARSS.2005.1525970, 2005
- Doglioli, A. and Gregori, G.: BioSWOT-Med cruise, RV L'Atalante, doi: 10.17600/18002392, 2023
- Filipot, J.-F., Guimaraes, P., Leckler, F., Hortsmann, J., Carrasco, R., Leroy, E., Fady, N., Accensi, M., Prevosto, M., Duarte, R., Roeber, V., Benetazzo, A., Raoult, C., Franzetti, M., Varing, A. and Le Dantec, N.: La Jument lighthouse: a real-scale laboratory for the study of giant waves and their loading on marine structures, *Philos. T. Roy. Soc. A*, 377: 20190008, doi: 10.1098/rsta.2019.0008, 2019
- Goldstein, R., and Zebker, H.: Interferometric radar measurement of ocean surface currents, *Nature*, 328, 707–709, doi: 10.1038/328707a0, 1987
- Gommenginger, C., Chapron Bertrand, Hogg, A., Buckingham, C., Fox-Kemper, B., Eriksson, L., Soulat, F., Ubelmann, C., Ocampo-Torres, F., Nardelli, B. B., Griffin, D., Lopez-Dekker, P., Knudsen, P., Andersen, O., Stenseng, L., Stapleton, N., Perrie, W., Violante-Carvalho, N., Schulz-Stellenfleth, J., Woolf, D., Isern-Fontanet, J., Arduin, F., Klein, P., Mouche, A., Pascual, A., Capet, X., Hauser, D., Stoffelen, A., Morrow, R., Aouf, L., Breivik, Ø., Fu, L.-L., Johannessen, J. A., Aksenov, Y., Bricheno, L., Hirschi, J., Martin, A. C. H., Martin, A. P., Nurser, G., Polton, J., Wolf, J., Johnsen, H., Soloviev, A., Jacobs, G. A., Collard, F., Groom, S., Kudryavtsev, V., Wilkin, J., Navarro, V., Babanin, A., Martin, M., Siddorn, J., Saulter, A., Rippeth, T., Emery, B., Maximenko, N., Romeiser, R., Graber, H., Azcarate, A. A., Hughes, C. W., Vandemark, D., da Silva, J., van Leeuwen P. J., Naveira-Garabato, A., Gemmrich, J., Mahadevan, A., Marquez, J., Munro, Y., Doody, S. and Burbidge, G.: SEASTAR: A Mission to Study Ocean Submesoscale Dynamics and Small-Scale Atmosphere-Ocean Processes in Coastal, Shelf and Polar Seas. *Front. Mar. Sci.*, 6, doi: 10.3389/fmars.2019.00457, 2019
- Hauser, D., Abdalla, S., Arduin, F., Bidlot, J.-F., Bourassa, M., Cotton, D., Gommenginger, C., Evers-King, H., Johnsen, H., Knaff, J., Lavender, S., Mouche, A., Reul, N., Sampson, C., Steele, E. C. C. and Stoffelen, A.: Satellite Remote Sensing of Surface Winds, Waves, and Currents: Where are we Now?, *Surv. Geophys.*, doi: 10.1007/s10712-023-09771-2, 2023

- Holt, J., Hyder, P., Ashworth, M., Harle, J., Hewitt, H., Liu, H., New, A. L., Pickles, S., Porter, A., Popova, E., Allen, J. I., Siddorn, J. and Wood, R.: Prospects for improving the representation of coastal and shelf seas in global ocean models, *Geosci. Model Dev.*, 10(1), 499–523, doi: 10.5194/gmd-10-499-2017, 2017
- 430
- Horstmann, J., Bödewadt, J., Carrasco, R., Cysewski, M., Seemann, J., and Stresser, M.: A coherent on receive x-band marine radar for ocean observations, *Sensors*, 21(23), 7828, doi: 10.3390/s21237828, 2021
- Huang W, Carrasco R, Chengxi S, Gill EW and Horstmann J.: Surface current measurements using X-band marine radar with vertical polarization, *IEEE T. Geosci. Remote*, 54, 2988–2996. doi:10.1109/TGRS.2015.2509781, 2016
- 435
- Kudryavtsev, V., Kozlov, I., Chapron, B. and Johannessen, J.: Quad-polarization SAR features of ocean currents. *J. Geophys. Res-Oceans*, 119(9), 6046–6065, doi: 10.1002/2014JC010173, 2014
- 440
- Lazure, P. and Dumas, F.: An external–internal mode coupling for a 3D hydrodynamical model for applications at regional scale (MARS), *Adv. Water Resour.*, 31(2), 233–250, doi: 10.1016/j.advwatres.2007.06.010, 2008
- Lévy, M., R. Ferrari, P. J. Franks, A. P. Martin, and P. Rivière.: Bringing physics to life at the submesoscale. *Geophysical Research Letters*, 39 (14), 2012.
- 445
- Martin, A. and Richards, K.: Mechanisms for vertical nutrient transport within a North Atlantic mesoscale eddy, *Deep-Sea Res. Pt II*, 48, 757–773, doi: 10.1016/S0967-0645(00)00096-5, 2001
- Martin, A.C.H., Gommenginger, C., Marquez, J., Doody, S., Navarro, V., and Buck, C.: Wind-Wave induced velocity in ATI SAR Ocean Surface Currents: First experimental evidence from an airborne campaign, *J. Geophys. Res-Oceans*, 121(3), 1640–1653, doi: 10.1002/2015JC011459, 2016
- 450
- Martin, A.C.H. and Gommenginger, C.: Towards wide-swath high-resolution mapping of total ocean surface current vectors from space: Airborne proof-of-concept and validation, *Remote Sens. Environ.*, 197, 58–71, doi: 10.1016/j.rse.2017.05.020, 2017
- 455
- Martin, A.C.H., Gommenginger, C. and Quilfen, Y.: Simultaneous ocean surface current and wind vectors retrieval with squinted SAR interferometry: Geophysical inversion and performance assessment, *Remote Sens. Environ.*, 216, 798–808, doi: 10.1016/j.rse.2018.06.013, 2018

Martin, A. C. H., McCann, D. L., Gommenginger, C., Macedo, K. A. C., and Le Merle, E.: Seastar project, Zenodo [code], doi: 10.5281/zenodo.10026593, 2023

Maskell, J.: Modelling storm surges in the Irish and Celtic seas using a finite element model (TELEMAC). Ph.D. dissertation, University of Liverpool, 280 pp, 2012

Mass, C. F., Owens D., Westrick K., and Colle B. A.: Does increasing horizontal resolution produce more skillful forecasts? Bull. Amer. Meteor. Soc., 83, 406–430, doi: 10.1175/1520-0477(2002)083<0407:DIHRPM>2.3.CO;2, 2002

Mejia, C., Badran, F., Bentamy, A., Crepon, M., Thiria, S. and Tran, N.: Determination of the geophysical model function of NSCAT and its corresponding variance by the use of neural networks. J. Geophys. Res-Oceans, 104, 11539–11556, doi: 10.1029/1998JC900118, 1999

Mouche, A.C.H., Collard, F., Chapron, B., Dagestad, K-F., Guitton, G., Johannessen, J., Kerabol, V. and Hansen, M.W.: On the use of Doppler shift for sea surface wind retrieval from SAR, IEEE T. Geosci. Remote, 50(7), 2901–2909, doi: 10.1109/TGRS.2011.2174998, 2012

Muller, H., Blanke, B., Dumas, F., Lekien, F. and Mariette, V.: Estimating the Lagrangian residual circulation in the Iroise Sea, J. Marine Syst., 78, S17–S36, doi: 10.1016/j.jmarsys.2009.01.008, 2009

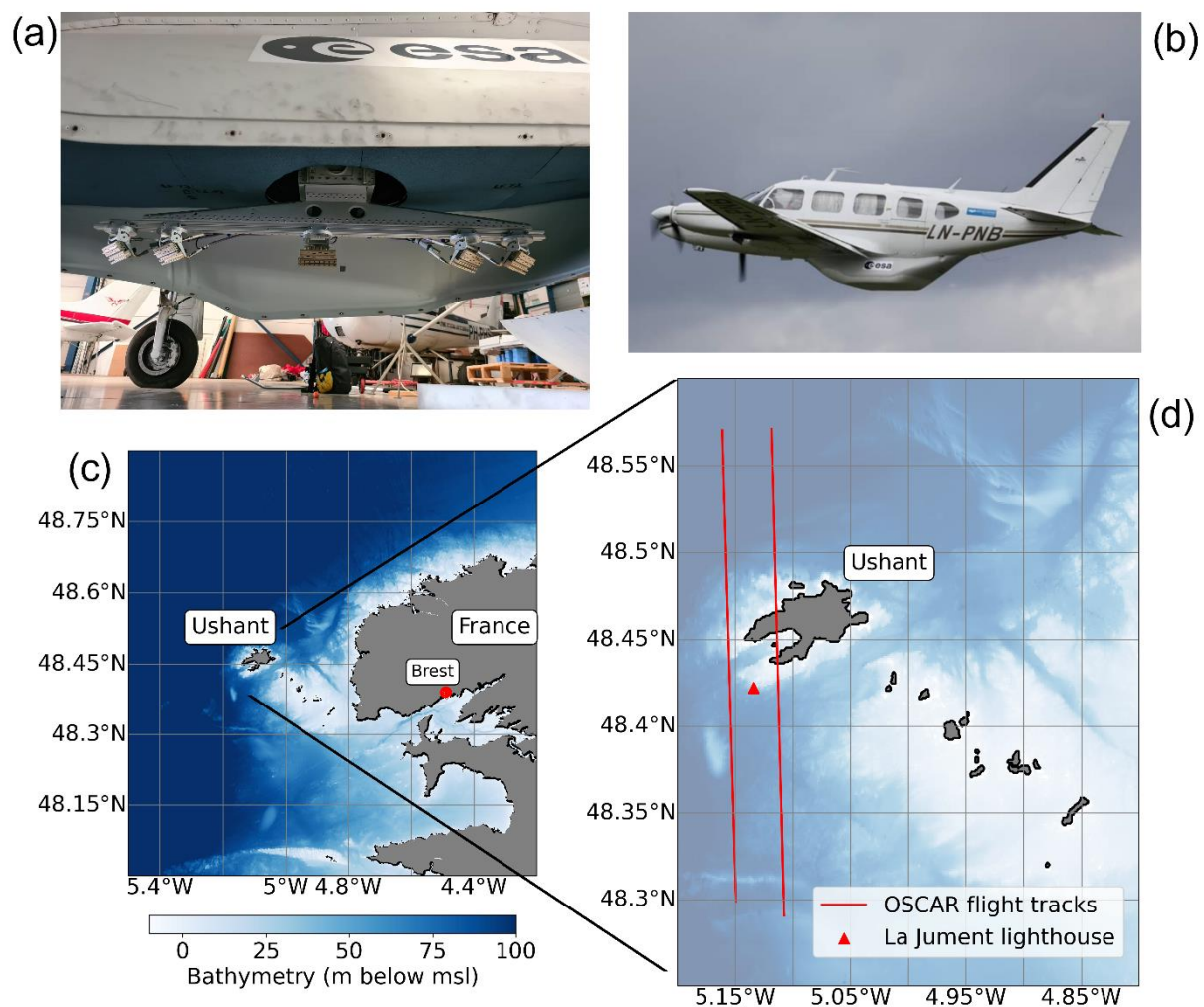
Neil, S. P. and Hashemi, M. R.: Chapter 8 - Ocean Modelling for Resource Characterization, in: Fundamentals of Ocean Renewable Energy, Academic Press, 193–235, doi: 10.1016/B978-0-12-810448-4.00008-2, 2018

Portabella, M., Stoffelen, J. and Johannessen, A.: Toward an optimal inversion method for synthetic aperture radar wind retrieval, J. Geophys. Res-Oceans, 107(C8), 3086, doi: 10.1029/2001JC000925, 2002

Portabella, M., Stoffelen, A.: A probabilistic approach for seawinds data assimilation. Q. J. Roy. Meteor. Soc., 130, 127–152, doi: 10.1256/qj.02.205, 2004

Ruiz, S. A. G., Barriga, J. E. C. and Martínez, J. A.: Assessment and validation of wind power potential at convection-permitting resolution for the Caribbean region of Colombia, Energy, 244(B), 123127, doi: 10.1016/j.energy.2022.123127, 2022

- Samelson, R. M.: Challenges and opportunities in coastal prediction, *EOS* 100, doi: 10.1029/2019EO113841, 2019
- 495
- Sasaki, H., Klein, P. and Sasai, Y.: Impact of oceanic-scale interactions on the seasonal modulation of ocean dynamics by the atmosphere, *Nat. Commun.*, 5, doi: 10.1038/ncomms6636, 2014
- Seity, Y., Brousseau, P., Malardel, S., Hello, G., Bénard, P., Bouttier, F., Lac, C. and Masson, V.: The AROME-France Convective-Scale Operational Model, *Mon. Weather Rev.*, 139(3), 976–991, doi: 10.1175/2010MWR3425.1, 2011
- 500
- Senet, C., Seemann, J., and Ziemer, F.: The near-surface current velocity determined from image sequences of the sea surface. *IEEE Trans. Geosci. Remote Sensing*, 39, 492–505, doi: 10.1109/36.911108, 2001
- Sentchev, A., Forget, P., Barbin, Y. and Yaremchuk, M.: Surface circulation in the Iroise Sea (W. Brittany) from high resolution HF radar mapping, *J. Marine Sys.*, vol. 109–110, S153–S168, doi: 10.1016/j.jmarsys.2011.11.024, 2013
- Stoffelen, A. and Portabella, M.: On Bayesian scatterometer wind inversion. *IEEE T. Geosci. Remote*, 44, 1523–1533, doi: 10.1109/TGRS.2005.862502, 2006
- 510
- Streßer, M., Carrasco, R., and Horstmann, J.: Video-based estimation of surface currents using a low-cost quadcopter. *IEEE Geosci. Remote S.*, 14(11), 2027–2031, doi: 10.1109/LGRS.2017.2749120, 2017
- Trampuz, C., Gebert, N., Placidi, S., Izzy Hendricks, L., Speziali, F., Navarro, V., Martin, A. C. H., Gommenginger, C., Suess, M. and Meta, A.: OSCAR - The airborne interferometric and scatterometric radar instrument for accurate sea current and wind retrieval, *EUSAR 2018; 12th European Conference on Synthetic Aperture Radar*, Aachen, Germany, 4–7 June 2018
- 515
- Villas Bôas, A. B., Arduin, F., Ayet, A., Bourassa, M. A., Brandt, P., Chapron, B., Cornuelle, B. D., Farrar, J. T., Fewings M. R., Fox-Kemper, B., Gille, S. T., Gommenginger, C., Heimbach, P., Hell. M. C., Li, Q., Mazloff, M. R., Merrifield, S. T., Mouche, A., Rio, M. H., Rodriguez, E., Shutler, J. D., Subramanian, A. C., Terrill, E. J., Tsamados, M., Ubelmann, C. and van Seville, E.: Integrated observations of global surface winds, currents, and waves: requirements and challenges for the next decade. *Front. Mar. Sci.*, 6, doi: 10.3389/fmars.2019.00425, 2019
- 520
- Wentz, F. and Smith, D.: A model function for the ocean-normalized radar cross section at 14 GHz derived from NSCAT observations, *J. Geophys. Res-Oceans*, 104(C5), 11499–11514, doi: 10.1029/98JC02148, 2019
- 525



530

**Figure 1:** (a) The OSCAR 3-look Ku-Band SAR instrument and 3-axis stabilisation gimbal; the two fore and aft ATI antenna pairs can be seen to the left and right of the boom with the scatterometer mid antenna in the centre. (b) The OSCAR instrument within the radome pod mounted to MetaSensing's Piper Navajo airframe. (c) The study area of the Iroise Sea, France, bathymetry in metres below mean sea level from EMODnet. (d) The island of Ushant with positions of La Jument lighthouse and the over-island flight tracks marked.

535

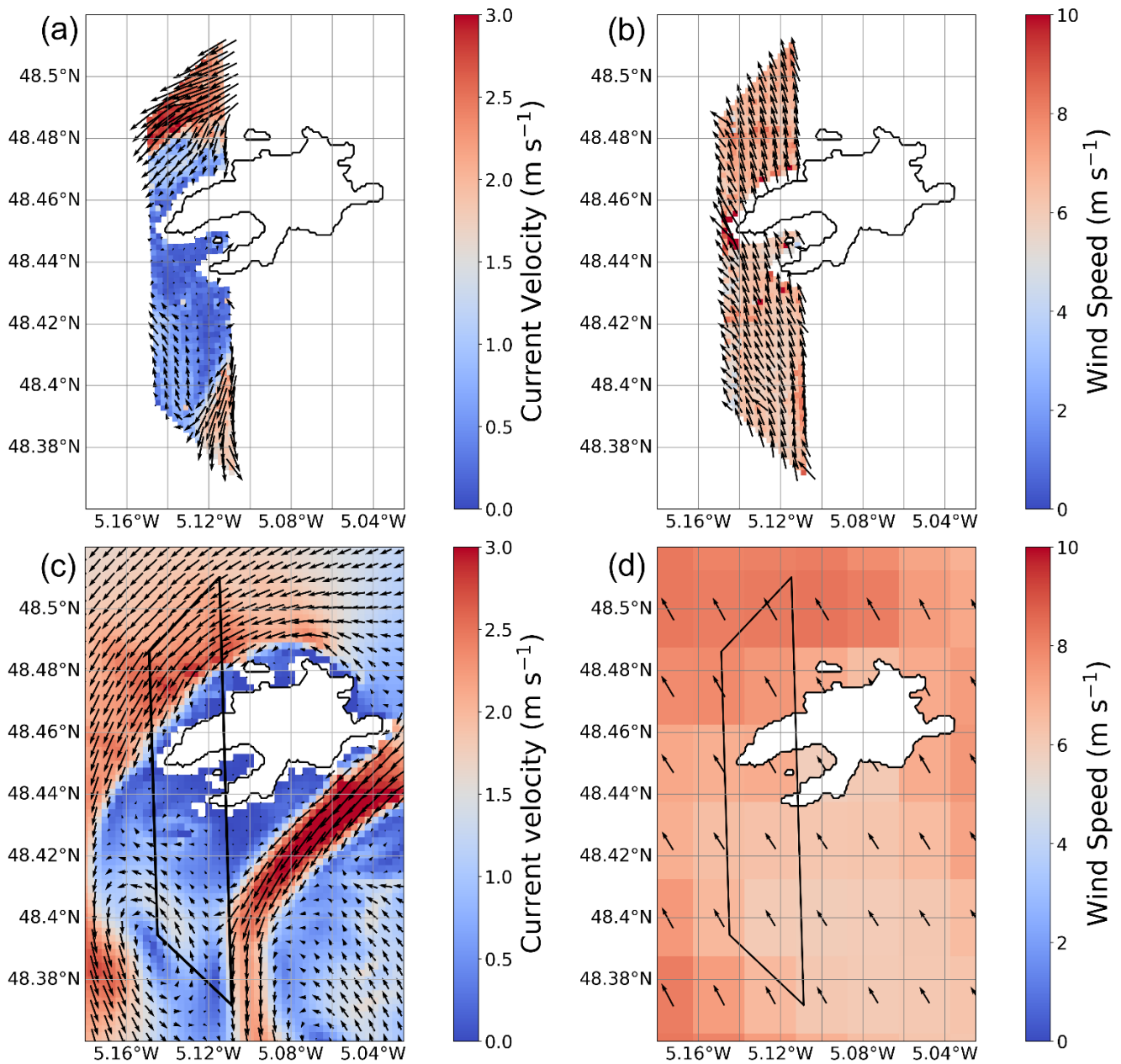
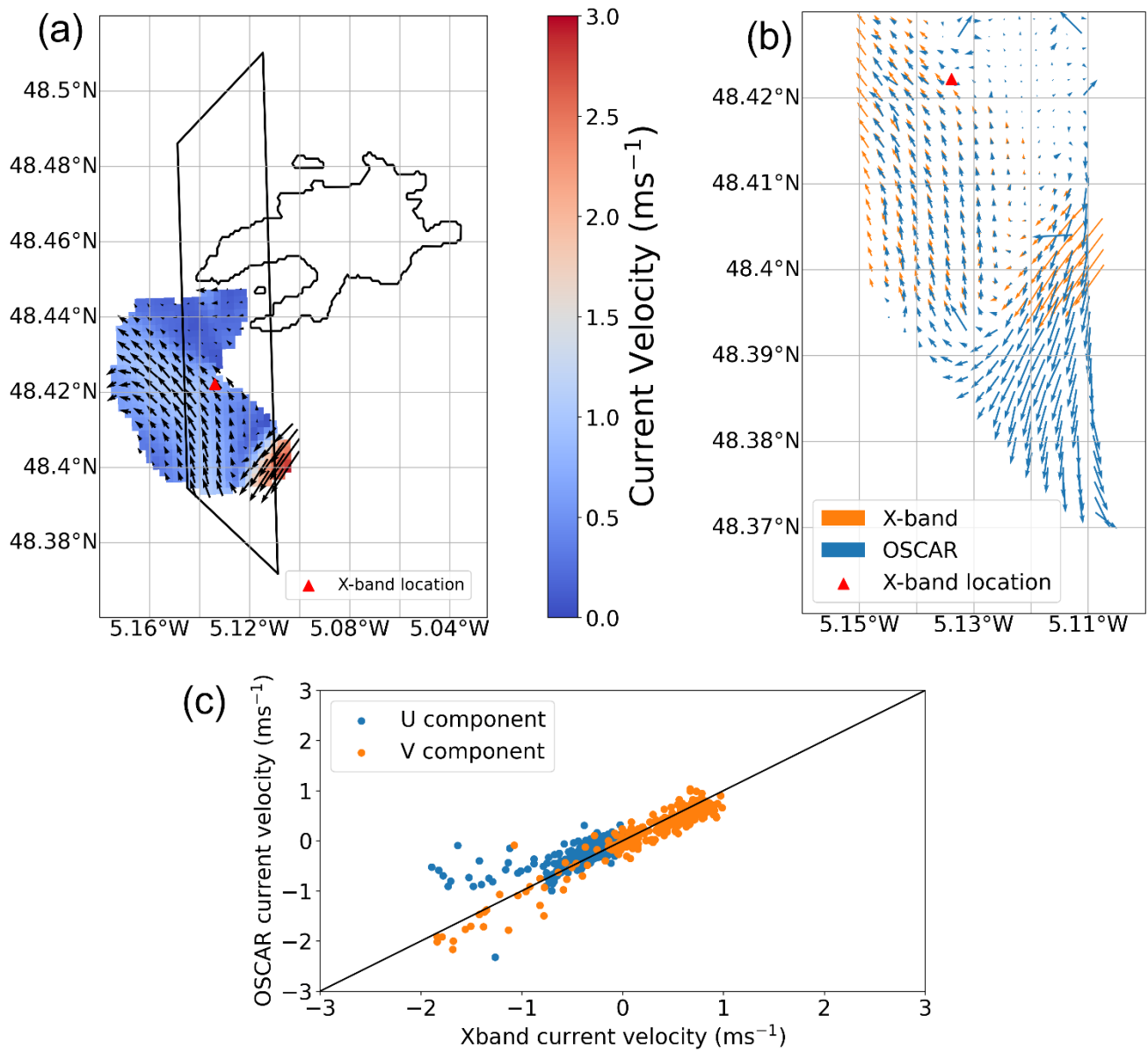


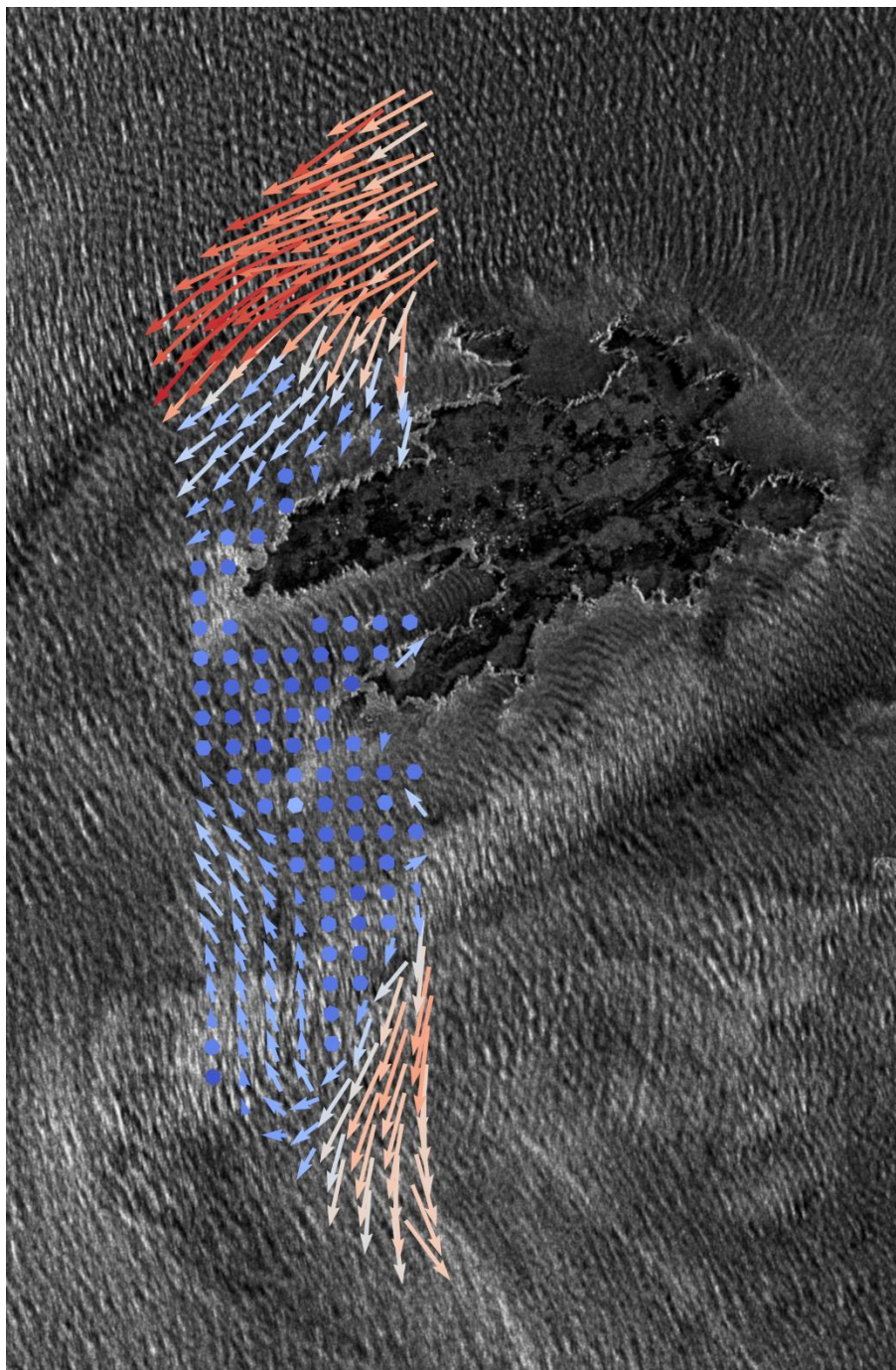
Figure 2: Simultaneously-retrieved L2 data products from a single OSCAR acquisition over Ushant at 09:38 UTC on 17th May 2022 during an ebb tide: (a) OSCAR total surface current vector, (b) OSCAR ocean surface vector wind, (c) depth-average current velocity from the MARS2D model at 09:30 UTC and (d) Wind speed ( $u_{10}$ ) from the AROME operational wind model at 09:00 UTC. The outline of the OSCAR L2 swaths are shown in black on the two model outputs.

540



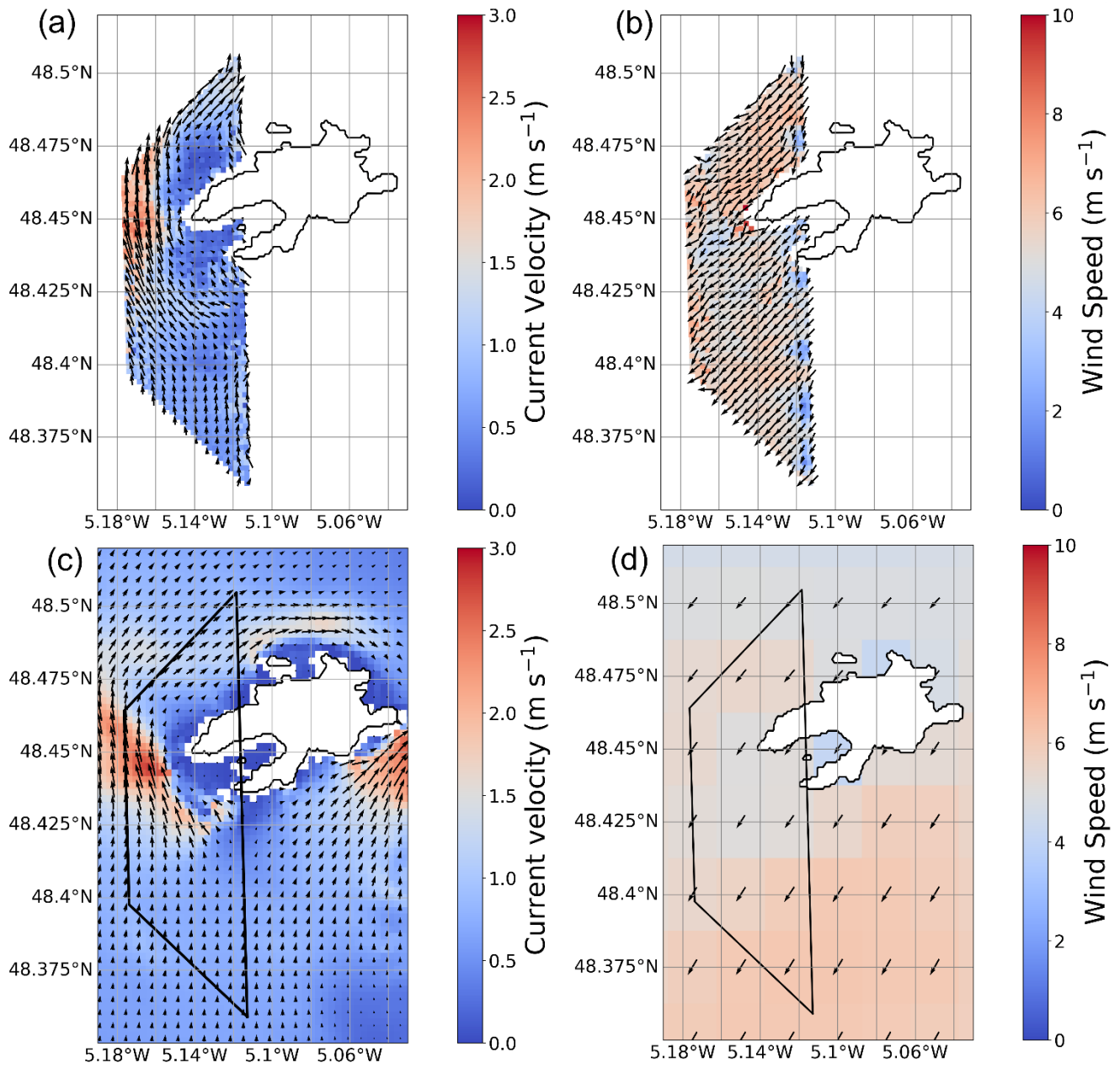


**Figure 3: (a) X-band derived surface current vectors from La Jument lighthouse from 10 minutes of radar data at 09:30 UTC on the 17th May 2022, (b) Co-located OSCAR total surface current vectors at 09:38 UTC and X-band current vectors, (c) U (east) and V (north) current component direct comparison between the two sensors.**



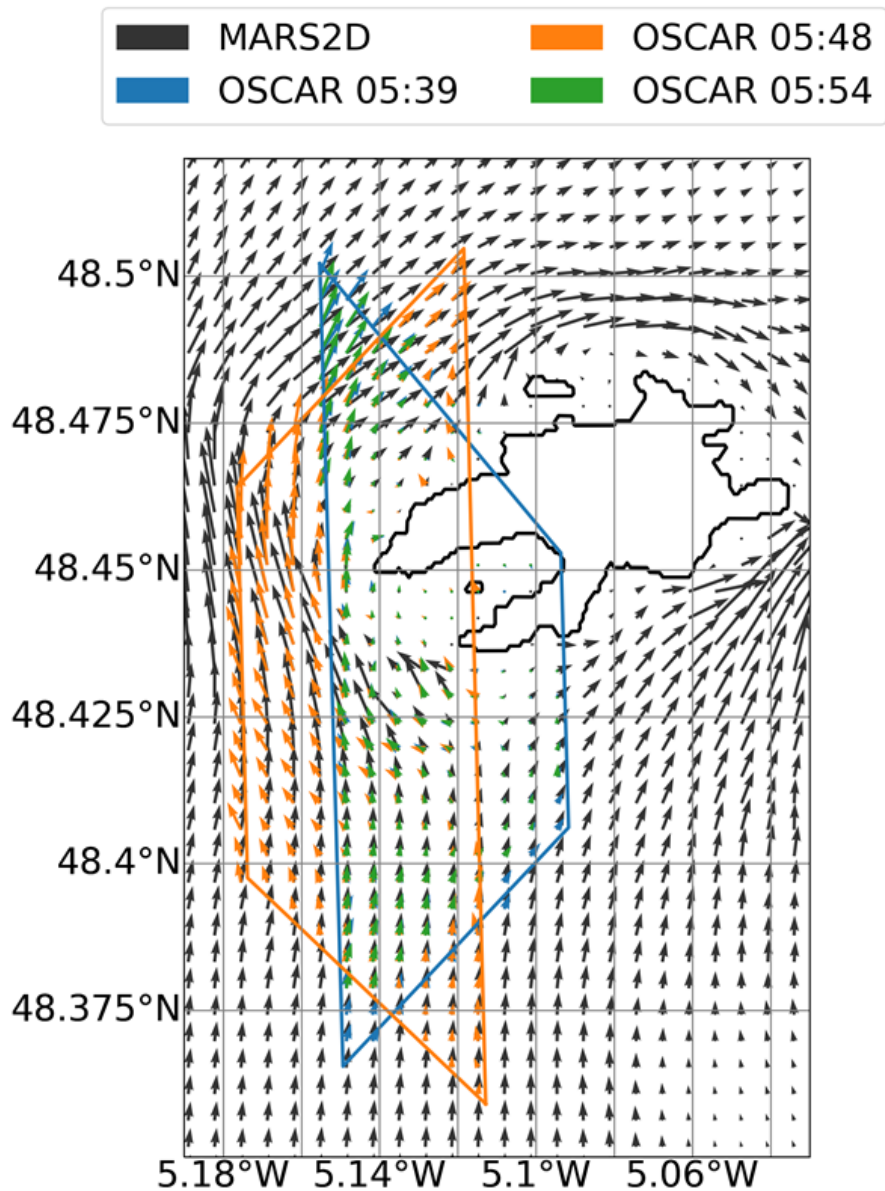
545

**Figure 4.** OSCAR total surface current vectors from 09:38 UTC on the 17th May 2022, overlain on a NovaSAR-1 S-band  $\sigma^0$  image acquired at 10:30 UTC of Ushant and the surrounding waters during a period of ebb-tidal flow. NovaSAR-1 image courtesy of SSTL and Airbus.



550

**Figure 5: Simultaneously-retrieved currents and winds from a single OSCAR acquisition over Ushant at 05:48 UTC on 22nd May 2022 during a flood tide: (a) OSCAR total surface current vector, (b) OSCAR ocean surface vector wind, (c) depth-average current velocity from the MARS2D model at 05:45 UTC and (d) Wind speed ( $u_{10}$ ) from the AROME operational wind model at 0600 UTC. The outline of the OSCAR L2 swaths are shown in black on the two model outputs.**



555

**Figure 6: Total surface current vector comparison between three successive OSCAR tracks on the 22nd May, co-located onto a common grid and overlain on MARS2D current vectors from 05:30 UTC (black arrows). OSCAR swath outlines are depicted in their corresponding vector colour (blue, 05:39 UTC; orange, 05:48 UTC; green, 05:54 UTC) . The tracks from 05:39 UTC and 05:54 UTC sharing the same swath outline.**

560

National Oceanography Centre, European Way, Southampton, SO14 3ZH  
United Kingdom +44 (0)23 8059 6666

Joseph Proudman Building, 6 Brownlow Street, Liverpool, L3 5DA  
United Kingdom +44 (0)151 795 4800

National Oceanography Centre is a company limited by guarantee,  
set up under the law of England and Wales, company number 11444362.  
National Oceanography Centre is registered as a charity in England and Wales,  
charity number 1185265, and in Scotland, charity number SC049896.

© National Oceanography Centre